ERDC TR-23-9

US Army Corps
of Engineers®
Engineer Research and
Development Center

ERDC
ENGINEER RESEARCH & DEVELOPMENT CENTER

Flood and Coastal Storm Damage Reduction Program

Load and Resistance Factors from Reliability Analysis Probability of Unsatisfactory Performance (*PUP*) of Flood Mitigation, Batter Pile-Founded T-Walls Given a Target Reliability Index (β)

Robert M. Ebeling, Barry C. White, John E. Hite, James R. Tallent,
Locke M. Williams, Brad C. McCoy, Aaron Hill, Cameron Dell,
Jake Bruhl, and Kevin McMullen

June 2023

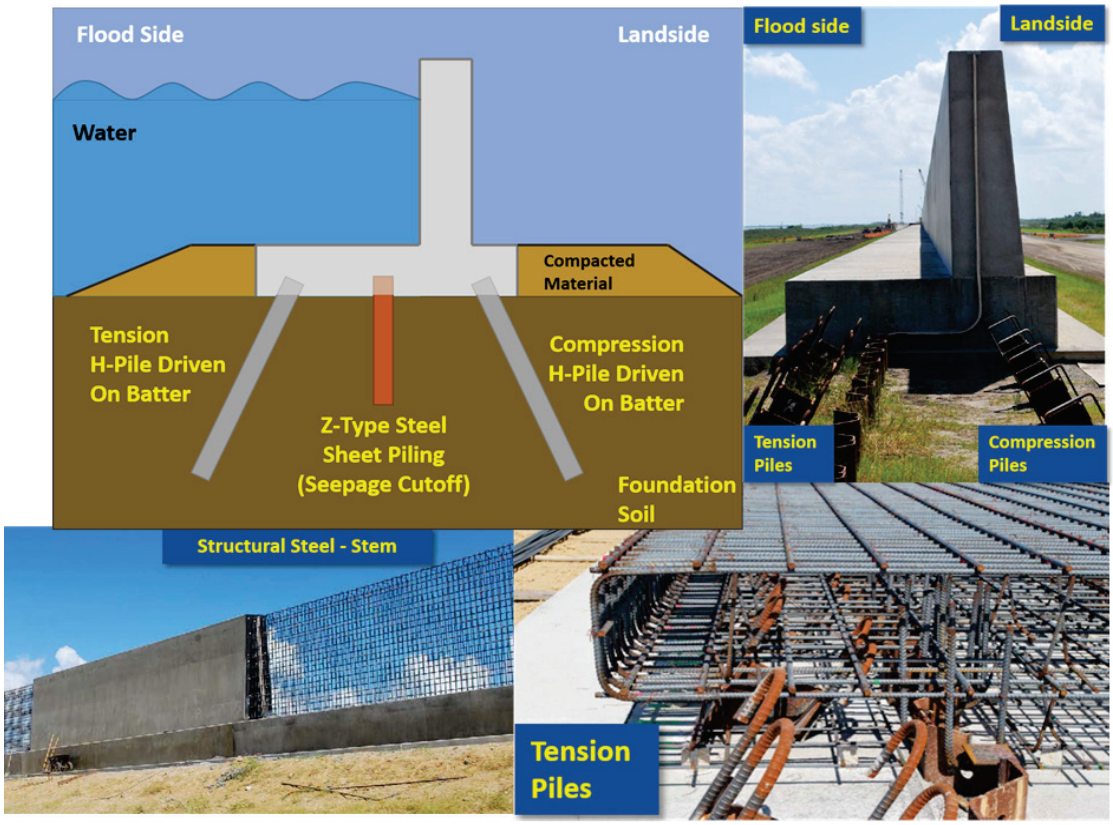

Approved for public release; distribution is unlimited.

Engineer Research and
Development Center

The US Army Engineer Research and Development Center (ERDC) solves the nation's toughest engineering and environmental challenges. ERDC develops innovative solutions in civil and military engineering, geospatial sciences, water resources, and environmental sciences for the Army, the Department of Defense, civilian agencies, and our nation's public good. Find out more at www.erdc.usace.army.mil.

To search for other technical reports published by ERDC, visit the ERDC online library at https://erdclibrary.on.worldcat.org/discovery.

ERDC TR-23-9
June 2023

Load and Resistance Factors from Reliability Analysis Probability of Unsatisfactory Performance (*PUP*) of Flood Mitigation, Batter Pile-Founded T-Walls Given a Target Reliability Index (β)

Robert M. Ebeling, Barry C. White, and James R. Tallent

Information Technology Laboratory
US Army Engineer Research and Development Center
3909 Halls Ferry Road
Vicksburg, MS 39180-6199

John E. Hite and Locke M. Williams

Coastal and Hydraulics Laboratory
US Army Engineer Research and Development Center
3909 Halls Ferry Road
Vicksburg, MS 39180-6199

Brad C. McCoy, Aaron Hill, Cameron Dell, Jake Bruhl, and Kevin McMullen

United States Military Academy, West Point
606 Thayer Road
West Point, New York 10996

Final report

Approved for public release; distribution is unlimited.

Prepared for Navigation Systems Research Program (NavSys)
Vicksburg, MS 39180-6199

Under Funding Account Code: U4375151; AMSCO Code 031391

Abstract

This technical report documents the research and development (R&D) study in support of the development of a combined Load and Resistance Factor Design (LRFD) methodology that accommodates both geotechnical and structural design limit states for design of the US Army Corps of Engineers (USACE) batter pile-founded, reinforced concrete flood walls. Development of the required reliability and corresponding LRFD procedures has been progressing slowly in the geotechnical topic area as compared to those for structural limit state considerations, and therefore this has been the focus of this first-phase R&D effort. This R&D effort extends reliability procedures developed for other non-USACE structural systems, primarily bridges and buildings, for use in the design of batter pile-founded USACE flood walls. Because the foundation system includes batter piles under flood loading, the design procedure involves frame analysis with significant soil structure interaction. Three example batter pile-founded T-Wall flood structures on three different rivers have been examined considering 10 geotechnical and structural limit states. Numerical procedures have been extended to develop precise multiple limit state Reliability calculations and for complete LRFD analysis of the example batter pile-founded, T-Wall reinforced concrete, flood walls.

DISCLAIMER: The contents of this report are not to be used for advertising, publication, or promotional purposes. Citation of trade names does not constitute an official endorsement or approval of the use of such commercial products. All product names and trademarks cited are the property of their respective owners. The findings of this report are not to be construed as an official Department of the Army position unless so designated by other authorized documents.

DESTROY THIS REPORT WHEN NO LONGER NEEDED. DO NOT RETURN IT TO THE ORIGINATOR.

Contents

Abstract ii

Figures and Tables vii

Preface xxi

1 Introduction 1

1.1 Background 1
1.2 Objective 2
1.3 Approach 2
1.4 Report contents 2

2 Reliability Analysis as It Relates to Load and Resistance Factor Design (LRFD) of the USACE Flood Mitigation Structures 4

2.1 LRFD 4
2.1.1 A brief introduction to LRFD *4*
2.1.2 A general form of LRFD *4*
2.2 An interrelationship between nominal and mean loads, resistance, and bias factors 6
2.3 Limit states for batter pile-founded, reinforced concrete T-Wall flood mitigation structures 9
2.4 Reliability analysis 10
2.5 Performance function, dimensionless variables, and the Probability of Unsatisfactory Performance (*PUP*) 13
2.6 The interrelationship between LRFD and reliability index for a single Ultimate Limit State (ULS) 20
2.7 A numerical procedure to calculate the reliability Index 27
2.7.1 Advanced Second Moment (ASM) for uncorrelated, normal distributions *28*
2.7.2 Dealing with non-normal distributions for X_i *31*
2.7.3 Dealing with correlated random variables X_1 and X_2 ..... *32*
2.7.4 ASM algorithm *34*
2.7.5 ASM caveats *34*
2.8 Numerical methods for the calculation of β and load and resistance factors given uncorrelated load and resistance PDF curves 35
2.9 Individual limit state procedure for computing load and resistance distributions from material properties and determining load factors 37
2.10 Proportioned load individual limit state procedure for computing load and resistance distributions from material properties and determining load factors 39
2.11 Reliability analysis with multiple limit states 41
2.12 Implication of multiple limit states on the computed *PUP* 45
2.13 Published design values for reliability index β and/or *PUP* 52
2.13.1 1994 Reliability analysis of proposed dikes of James Bay hydroelectric project in Quebec, Canada *55*
2.13.2 Revisited reliability calculations of the proposed dikes for the James Bay hydroelectric project in Quebec, Canada *59*

2.13.3 Probabilistic slope stability analysis calculations of a Syncrude Tailings Dike on pre-sheared clay-shale in Fort McMurray, Canada 61
2.13.4 Reliability-based target design criteria in the 2014 Canadian Highway Bridge Design Code (CHBDC) 63
2.13.5 Reliability-based target design criteria in the American Society of Civil Engineers (ASCE) design code for buildings 71
2.13.6 Reliability-based target design criteria in the 2010 American Association pf State Highway and Transportation Officials (AASHTO) LRFD bridge design specifications 73
2.13.7 Comparison of CHBDC, AASHTO, and ASCE reliability criteria for a 100-year design life 75
2.13.8 Resistance factor development background for individual and pile group founded bridge foundations 75

3 Historical Summary of the AASHTO LRFD for Pile-Founded Bridges 78
3.1 Transition from Allowable Stress Design (ASD) to LRFD and calibration of LRFD 78
3.1.1 Calibration methods 79
3.1.2 Use of reliability theory for driven pile resistance factors 82
3.2 Reliability analysis 82
3.2.1 Reliability analysis techniques 82
3.2.2 Design life considerations 85
3.3 Post-2005 changes to AASHTO driven-pile LRFD 86
3.3.1 Summary 86
3.3.2 Strength limit states 86
3.3.3 Serviceability limit states 89
3.3.4 Regional adjustments for accuracy 91

4 Structural Variables with Respect to Limit States 93
4.1 Introduction 93
4.2 Introductory observations for three structural limit states 94

5 Sea Wave Forces on Vertical Walls using the Goda-Takahashi Procedure 99
5.1 Introduction 99
5.2 Goda's laboratory setup of an instrumented caisson within a laboratory wave flume 102
5.3 Examples of wave pressure data recorded in Goda's laboratory flume 104
5.4 Wave force calculation for loading on vertical walls 111
5.4.1 Original Goda (1974) formula 111
5.4.2 The Takahashi extension of Goda's Formula to include the impulsive pressure term 120
5.4.3 Example calculation of wave forces on T-Wall 121
5.4.4 Converting a trapezoidal pressure distribution acting on a discrete segment of the I-Wall face into equivalent end point forces 130
5.4.5 Calibration with prototype breakwaters 131
5.5 Effects of scale and aeration 137
5.6 Coefficient of variation for the Goda-Takahashi wave pressure formula 138

6 Example Calculation of Wind-Induced Inland Wave Forces on Vertical Walls using the Goda-Takahashi Procedure 151

6.1 Introduction 151
6.2 Existing guidance for inland hydraulic structures 151
6.3 Wave force calculation for loading on vertical inland wall structures 152
6.4 Significant wave height and period estimation 153
6.4.1 Wind wave generation 153
6.4.2 Extreme-value estimation of wind speed 154
6.4.3 Minimum duration of wind speeds to produce wave heights 157
6.4.4 Wind fetch estimation 158
6.4.5 Re-evaluating the historical wind record 160
6.5 Returning to the Generalized Extreme Value (GEV) analysis 164
6.6 Design wave height and period estimation 168
6.7 Wave load estimation 170

7 Reliability Analysis and Load and Resistance Factors Analysis of Flood Mitigation, Batter Pile-Founded T-Walls 176

7.1 Introduction 176
7.2 Designing a pile-based T-Wall system 176
7.2.1 Establishment of limit states 176
7.2.2 T-Wall geometry - Grand Forks Red River of the North site 177
7.2.3 System variables 179
7.2.4 Pile selection and computation of properties 180
7.2.5 Stem capacities (limit states 1 and 2) 181
7.2.6 Soil distributions and capacities (limit states 3 and 4) 182
7.2.7 Computation of allowable capacities (limit states 5 through 10) 193
7.2.8 Searching for a semi-optimal deterministic design 199
7.3 Designing for the Red River of the North site, in Grand Forks, ND 203
7.3.1 System variable distributions for the Red River of the North site, in Grand Forks, ND 204
7.3.2 Deterministic results for a section with a pair of 40 ft piles 210
7.3.3 Reliability results for a section with 40 ft compression and tension piles 216
7.3.4 Computing Load and Resistance Factors for a section with 40-ft compression and tension piles 220
7.3.5 Searching for Optimal Pile Lengths for the Red River of the North site, in Grand Forks, North Dakota 229
7.3.6 Solving for the Red River of the north site, in Grand Forks, ND, using 39 ft compression and 10 ft tension piles 235
7.4 Designing for the Red Wood River site in Marshall, MN 241
7.4.1 Design of the Red Wood River pile-founded T-Wall 241
7.4.2 System variable distributions for the Red Wood River site in Marshall, MN 245
7.4.3 Deterministic results for a Red Wood River T-Wall section with a 35 ft compression pile and a 10 ft tension pile 249
7.4.4 Reliability results for the Red Wood River pile-founded T-Wall section with 35 ft compression and 10 ft tension piles 253
7.4.5 Computing load and resistance factors for the Red Wood River site section with 35 ft compression and 10 ft tension piles 256

7.4.6 Computing load and resistance factors for the Red Wood River site section with 35 ft compression and 15 ft tension piles....262
7.5 Designing for the Mississippi River site in St. Paul, MN 267
7.5.1 Design of the St. Paul pile-founded T-Wall....267
7.5.2 System variable distributions for the Mississippi River site in St. Paul, MN....272
7.5.3 Deterministic results for a Mississippi River at St. Paul, MN, T-Wall section with a 32 ft compression pile and a 10 ft tension pile....275
7.5.4 Reliability results for the Mississippi River at St. Paul, MN, pile-founded T-Wall section with 32 ft compression and 10 ft tension piles....279
7.5.5 Computing load and resistance factors for the Mississippi River at St. Paul, MN, site section with 32 ft compression and 10 ft tension piles....282

8 Summary, Conclusions, and Research Recommendations....289
8.1 Summary....289
8.2 Conclusions....293

References....300

Appendix A: Computing Probabilities....313

Appendix B: Wind-Induced Wave Loading Assessments Made at Select Inland USACE Flood Mitigation Structure Sites....346

Appendix C: Using Sparse Data to Determine Geotechnical Soil Property Distributions/Statistics....435

Appendix D: Values for Coefficient of Variation and Scale of Fluctuation for Soils....442

Unit Conversion Factors....464

Acronyms and Abbreviations....465

Report Documentation Page

Figures and Tables

Figures

Figure 2-1. Capacity vs. demand related to the *PUP* (after Nowak and Collins [2013]). 14
Figure 2-2. The normalized, Normal-Gaussian distribution for two independent variables, X_1 and X_2. 16
Figure 2-3. A 3-D rendering of a normalized, Normal-Gaussian PDF distribution for two independent variables, X_1 and X_2. 17
Figure 2-4. Cross section along the position of the limit state response surface through the PDF distribution in a 3-D rendering and the location of the design point — view from underneath. 18
Figure 2-5. PDF and CDF for a normalized, Normal-Gaussian single variate. 20
Figure 2-6. Reliability Index defined as the shortest distance from the origin of the transformed basic variable space to the design point on the limit state response surface function g(*r,l*) (after Nowak and Collins [2013]). 22
Figure 2-7. Relationships among nominal load, mean load, and factored load (after Nowak and Collins [2013]). 25
Figure 2-8. Relationships among nominal resistance, mean resistance, and factored resistance (after Nowak and Collins [2013]). 25
Figure 2-9. Finding the position of equivalent cumulative probability for a normal distribution as from a non-normal distribution (after Ang and Tang [1984]). 32
Figure 2-10. Plan view of the transformed basic variable space for the variables X'_1 and X'_2 and response surfaces for a two-limit states – overhead view. 42
Figure 2-11. A 3-D rendering of a normalized, Normal-Gaussian PDF distribution for two independent variables, X_1 and X_2 and two limit state response surfaces. 42
Figure 2-12. A 3-D rendering of a normalized, Normal-Gaussian PDF distribution for two independent variables, X_1 and X_2, and the second limit state response surface. 44
Figure 2-13. Cross section along the position of the limit state response surface through the PDF distribution in a 3-D rendering and the location of the design point for the response surface of limit state 2– view from underneath. 44
Figure 2-14. Cross sections along the position of the two limit state response surfaces through the PDF distribution in a 3-D rendering – view from underneath. 45
Figure 2-15. Mapping the integrated PUP from the multivariate hyperplane to a single Gaussian distribution. 47
Figure 2-16. Mapping the integrated PUP from the multivariate hypersphere to a single Gaussian distribution. 48
Figure 2-17. Finding the overlap region A given limit state *I* with respect to limit state *J*. 49
Figure 2-18. Finding the overlap region B given limit state *J* with respect to limit state *I*. 50
Figure 2-19. Spatial subdivision for numerical integration and computation of a PUP value with two variables with Gaussian distributions given a single hyperplanar limit state. 52

Figure 3-1. Probability of failure and reliability index (after Allen [2005]). 81
Figure 4-1. Interaction diagram for a steel HP pile (after Ebeling et al. [2012]). 97
Figure 5-1. Breaking wave for non-zero wave approach angle demonstrates non-uniformity (after Oten Lucas). 100
Figure 5-2. Influence of incident wave angle on wave pressure. 101
Figure 5-3. Section view of Goda's (1972) laboratory setup of an instrumented model caisson in wave basin (units in meters). 103
Figure 5-4. Goda's wave pressure distribution on vertical caisson wall (after Goda [1974]). 104
Figure 5-5. Idealized vertical distribution of (a) water and (b) wave pressures along the vertical face of a caisson (after Goda and Kakizaki [1966]). 105
Figure 5-6. Vertical distribution of peak pressures during wave crests and at wave troughs for waves of period 1.302 sec (after Goda and Fukumori [1972]). 106
Figure 5-7. Vertical distribution of peak pressures during wave crests and at wave troughs for waves of period 2.007 sec (after Goda and Fukumori [1972]). 106
Figure 5-8. Total weight WTotal of caisson with SWL-induced horizontal boundary water pressures acting normal to both vertical faces of the caisson and a uniform uplift boundary water pressure distribution along its base. 109
Figure 5-9. Buoyant weight of caisson acting below SWL elevation with an SWL on both sides of the caisson. 110
Figure 5-10. Illustration of terms in Goda's original pressure formulation. 112
Figure 5-11. Breaking wave height location in Goda's equation. 114
Figure 5-12. Path of Hurricane Harvey. 116
Figure 5-13. Data buoy locations in the western Gulf of Mexico monitored by along the NOAA National Data Buoy Center. 116
Figure 5-14. Normalized sea wave height frequency distribution for year 2017 with identification of H_{Mean}, $H_{1/3}$ and $H_{1/10}$ using sort and average method. Data from NOAA Buoy 42019, Freeport, TX (N = 8697). 117
Figure 5-15. Normalized histogram of sea wave heights for year 2017 with superimposed Rayleigh distribution and Rayleigh estimation of $H_{1/3}$ and $H_{1/10}$ values. Data from NOAA Buoy 42019, Freeport TX (N = 8697). 118
Figure 5-16. Normalized wave period frequency distribution for year 2017 with identification of the significant wave period ($T_{1/3}$) using sort and average method. Data from NOAA Buoy 42019, Freeport TX (N = 8697). 119
Figure 5-17. Normalized wave propagation direction frequency distribution for year 2017 with identification of the Hurricane Harvey dominant directions. Data from NOAA Buoy 42019, Texas (N = 8697). 120
Figure 5-18. T-Wall used in example wave force calculation. 122
Figure 5-19. Pressure distribution on T-Wall. 125
Figure 5-20. Resultant forces of wave pressure distribution per unit length of T-Wall. 126
Figure 5-21 Definition of wave pressure moment arm terms on T-Wall. 127
Figure 5-22. Distribution of stress acting normal to a discrete segment *k* of the wall face. (a) Trapezoidal pressure distribution. (b) Equivalent nodal point forces. (after Ebeling et al. [2018]). 131
Figure 5-23. Safety factor against sliding for the data base of field deployed caissons performance during ocean storms and analyzed using Goda's wave

loading pressure distribution relationship (after Goda [2010]). 132
Figure 5-24. Island of Alderney and the Admiralty Breakwater. 134
Figure 5-25. Admiralty Breakwater under high-sea event (after Neil Howard [2009]). 134
Figure 5-26. Admiralty Breakwater cross section (after Bullock et al. [2003]) 135
Figure 5-27. Safety factor against sliding for the data base of field deployed caissons performance during ocean storms and analyzed using Minikin's wave loading pressure distribution relationship (after Goda [1973]). 136
Figure 5-28. Frequency distribution of force measured divided by force calculated (F_M/F_C) for all four datasets combined. 139
Figure 5-29. Combined datasets of the F_M/F_C to H_i/d_{SWL} relationship for 926 data points. 140
Figure 5-30. Coefficient of variation F_M/F_C as a function of H_i/d_{SWL} for each of the five data bins containing 926 data points. 140
Figure 5-31. Statistical review of each of the four datasets used for the 926 data points in Figure H.12. 142
Figure 5-32. Wave transition zones as defined by Yamada et.al. (1968) and Goda (1972) with defined boundaries of datasets used in this study. 143
Figure 5-33. Illustration of plunging-type wave profile during energy dissipation process (after Tallent [1990]). 145
Figure 5-34. H.17 Leading edge velocity characteristics for solitary plunger. The notation of (a–f) correspond to Figure 5-33 (a-f) (after Tallent [1990]). 146
Figure 5-35. Summary of COV for the Goda-Takahashi predictive method. 148
Figure 5-36. Proposed simplification of COV to relative wave height parameter (Hi/d_{SWL}) relationship. 149
Figure 5-37. Nearshore breaking wave where H_i/d_{SWL} is an order of magnitude of 1.0. 149
Figure 6-1. Aerial image of Melvin Price Lock and Dam with superimposed hypothetical flood structure located along the southwest riverbank (red). The wind direction of primary concern in wave loading estimation is shown in yellow. 155
Figure 6-2. Historical wind-speed record for the combined St. Louis Airport and St. Charles Airport (1998–2019). Wind direction is presented for directions +/- 20° from normal to the design structure. 155
Figure 6-3. Maximum annual wind speeds for the combined St. Louis Airport and St. Charles Airport Wind Records (1983–2019). Wind speeds included in this analysis are incident to the structure (+/- 20°). 156
Figure 6-4. GEV and Gringorten estimation for maximum annual wind speed derived from 36-year record of incident wind direction to hypothetical structure. 157
Figure 6-5. Fetch length measurements for hypothetical T-Wall located at Melvin Price Lock and Dam complex. 159
Figure 6-6. The T_{min} relation for incident fetch length of 0.93 mile derived from Equation 6.1. 160
Figure 6-7. Example fully developed windstorm at mean speed of 38 mph for a duration of approximately 18 min. 161
Figure 6-8. Shows that the T_{MIN} duration required for a U_{10} wind speed of 38 mph and fetch length of 0.93 mile is approximately 22 min. 162
Figure 6-9. Demonstration of extracting the T_{min} range from the wind-speed range

using the T_{min} curve derived for the site of Interest. 162
Figure 6-10. Combined St. Louis Airport and St. Charles Airport wind records (1983–2019) for the condition of T_{min} = 30 min. 163
Figure 6-11. Comparison of annual peak wind speed versus T_{min} filtered annual wind speed. 164
Figure 6-12. T_{min} satisfied GEV and Gringorten estimation derived from 36-year record of incident wind direction to hypothetical structure for hypothetical T-Wall located adjacent to Melvin Price Lock and Dam complex. 164
Figure 6-13. The GEV estimate bounded by the standard error estimates derived from 36-year record of incident wind direction to hypothetical structure for hypothetical T-Wall located adjacent to Melvin Price Lock and Dam complex. 167
Figure 6-14. Goda's formula pressure distribution on vertical T-Wall. 171
Figure 6-15. Structural and hydrological parameters used in Goda (2010) wave-force calculation. 171
Figure 6-16. Comparison of equivalent hydrostatic force to equivalent wave-induced force for 100-year statistics. 175
Figure 7-1. shows the pile-founded T-Wall geometry in the initial configuration. Top of T-Wall is at EL 836.9 ft. Figure 7-1 ..... (a) close-in view and (b) complete view of the geometry of the wall cross section with 40 ft pile lengths. 179
Figure 7-2. Mean soil S_u properties with depth and distribution curves from -6σ to +6σ based on $COV_{Spatial}$ (40 ft compression and tension piles). 184
Figure 7-3. Normalized variance reduction factor. 186
Figure 7-4. Computation of axial compression force capacity for 40 ft compression pile as a function of top of layer four S_u (using CAXPILE). 187
Figure 7-5. Computation of axial tension force for 40 ft compression pile as a function of top of layer four S_u (using CAXPILE). 188
Figure 7-6. Incremental plot of P/Q_{ult} values with respect to C_{33} for a 40 ft compression pile. 192
Figure 7-7. Incremental Plot of P/Q_{ult} values with respect to C_{33} for a 40 ft tension pile. 193
Figure 7-8. Collected ACE data for site-specific data for the Red River of the North site, in Grand Forks, ND. 204
Figure 7-9. PDF Histogram from the Site-specific ACE data for the Red River of the North site, in Grand Forks, ND, compared with simulated data from the ACE data. 205
Figure 7-10. PDF for 100-year Chance of Exceedance values. 206
Figure 7-11. Comparison of MVP engineer estimate with ERDC simulation 100-year Chance of Exceedance values. 207
Figure 7-12. Deterministic design results for the 40 ft long HP 14 × 89 compression pile. 210
Figure 7-13. Deterministic design results for the 40 ft. long HP 14 × 89 tension pile. 213
Figure 7-14. Resulting Load (L) and Resistance (R) Curves for SSI Limit State 3 from Reliability Analysis and computed (R-L) curve. 223
Figure 7-15. Fixed Load (L) and Scaled Resistance (R) Curves for SSI Limit State 3 for β_{target}=3.5 and computed (R-L) curve (R_{SF} = 1.283210). 224

Figure 7-16. Fixed Load (L) and Scaled Resistance (R) Curves for SSI Limit State 3 for β_{target}=4.0 and computed (R-L) curve (R_{SF} = 1.792815). 225
Figure 7-17. Initial design for the site-specific data for the Red Wood River site in Marshall, MN. 242
Figure 7-18. Mean soil S_u properties with depth and distribution curves from -6σ to +6σ based on $COV_{Spatial}$ (for a 35 ft compression pile). 243
Figure 7-19. Mean soil S_u properties with depth and distribution curves from -6σ to +6σ based on $COV_{Spatial}$ (for a 10 ft piles). 244
Figure 7-20. Comparison of OCR and mean S_u soil properties for the Red River of the North with the Red Wood River characterization. 245
Figure 7-21. Comparison of mean S_u soil properties for the Red River of the North with the Red Wood River characterization: (a) compression piles, (b) tension piles. 245
Figure 7-22. Collected ACE data for site-specific data for the Red Wood River site in Marshall, MN. 246
Figure 7-23. PDF Histogram from the site-specific ACE data for the Red Wood River site in Marshall, MN, compared with simulated data from the ACE data. 246
Figure 7-24. PDF for 100Year Chance of Exceedance values at Red Wood River site in Marshall, MN. 247
Figure 7-25. Deterministic design results for the 35 ft long HP 14 × 89 compression pile. 250
Figure 7-26. Deterministic design results for the 10 ft long HP 14 × 89 tension pile. 251
Figure 7-27. Resulting load (L) and resistance (R) curves for SSI Limit State 3 from Reliability analysis and computed (R-L) curve at the Red Wood River site. 258
Figure 7-28. Fixed load (L) and scaled resistance (R) curves for SSI Limit State 3 for β_{target}=3.5 and computed (R-L) curve (R_{SF} = 0.928945) at the Red Wood River site. 258
Figure 7-29. Fixed load (L) and scaled resistance (R) curves for SSI Limit State 3 for β_{target}=4.0 and computed (R-L) curve (R_{SF} = 1.541625) at the Red Wood River site. 259
Figure 7-30. Initial design for the site-specific data for the Red Wood River site in Marshall, MN. 268
Figure 7-31. St. Paul mean soil S_u properties with depth and distribution curves from -6σ to +6σ based on $COV_{Spatial}$ (for a 35 foot Compression Pile). 269
Figure 7-32. St. Paul site mean soil S_u properties with depth and distribution curves from -6σ to +6σ based on $COV_{Spatial}$ (for a 10 ft piles). 270
Figure 7-33. Comparison of overconsolidation ratios and mean S_u soil properties for the Mississippi River at St. Paul, MN, with the Red River of the North and the Red Wood River characterization. 271
Figure 7-34. Comparison of mean S_u soil properties for the Mississippi River at St. Paul, MN, with the Red River of the North and the Red Wood River characterization for the compression pile. 271
Figure 7-35. Collected ACE data for site-specific data for the Mississippi River site in St. Paul, MN. 272
Figure 7-36. PDF histogram from the site-specific ACE data for the Mississippi River site in St. Paul, MN, compared with simulated data from the ACE data. 272
Figure 7-37. PDF for 100-year chance of exceedance values at Mississippi River site

in St. Paul, MN. 273

Figure 7-38. Deterministic design results for the 32 ft long HP 14 x 89 compression pile. 276

Figure 7-39. Deterministic design results for the 10 ft long HP 14 x 89 tension pile. 277

Figure 7-40. Resulting load (L) and resistance (R) curves for SSI Limit State 3 from Reliability analysis and computed (R-L) curve (R_{SF} = 0.613423) at the Mississippi River at St. Paul, MN, site. 284

Figure 7-41. Fixed load (L) and scaled resistance (R) curves for SSI Limit State 3 for β_{target}=3.5 and computed (R-L) curve (R_{SF} = 0.931970) at the Mississippi River at St. Paul, MN, site. 284

Figure 7-42. Fixed load (L) and scaled resistance (R) curves for SSI Limit State 3 for β_{target}=4.0 and computed (R-L) curve (R_{SF} = 1.446940) at the Mississippi River at St. Paul, MN, site. 285

Figure 8-1. Computation of Goda-Takahashi pseudo-static wave pressure distribution for the Red Word River batter pile-founded T-Wall. 297

Figure A.1. PDF and CDF of histogram data. 313

Figure A.2. Histogram data and the Gaussian (normal) distribution. 314

Figure A.3. The *G*(*X'*) function is used to determine *PUP*. 315

Figure A.4. A 2-D example of the *PUP* region and the hyperplane description using α and β. 316

Figure A.5. A 2-D example of multiple limit states with closest approach of length $|\beta|$. 317

Figure A.6. Finding the contribution of area A to overlapping probabilities of $g_i(X)$ and $g_j(X)$. 321

Figure A.7. Finding the contribution of area A to overlapping probabilities of $g_i(X)$ and $g_j(X)$. 322

Figure A.8. Gridding the Gaussian multivariate space to determine the *PUP* based on a single limit state response surface. 324

Figure A.9. Symmetric probability for pairs of bins equidistant from the mean, section view. 325

Figure A.10. Symmetric probability of the Gaussian normal curve at any distance in the multivariate space at all points on the hypersphere surface, plan view. 326

Figure A.11. A 2-D demonstration of the hypersphere calculation of *PUP*. 327

Figure A.12. Calculating dimensions for integrating spherical coordinate 3-D space. 330

Figure A.13. Distribution plots with respect to radius for 3-D sphere: (a) sphere shell volume, (b) point distribution probability, (c) probability density for the sphere shell, (d) number of divisions of the sphere density where each shell division would have 1.0e-10 probability. 332

Figure A.14. Example limit states and βs for unfactored loads and resistances. 333

Figure A.15. A uniform scale factor (S) is applied to the βs for the limit state design points. 334

Figure A.16. Applying variable axis scale factors to adjust probabilities. A scale factor applied to Limit State 1 causes slope changes in the response surfaces for Limit State 2 and 3. 336

Figure A.17. The first test case for *PUP* estimation. 337

Figure A.18. The second test case for *PUP* estimation. 343

Figure B.1-1. T-Wall used in example wave force calculation (tension and compression piles not shown). 346
Figure B.1-2 Wind speed and direction collection site at GFI. 348
Figure B.1-3. Floodwall along Red River near XS 148. 349
Figure B.1-4. Fetch and wind direction determined for the Red River of the North floodwall. 349
Figure B.1-5. Extreme wind-speed estimation for GFI. 352
Figure B.1-6. Wind frequency from Gumbel Type 1 Distribution with Gringorten's Method. 353
Figure B.1-7. Wind frequency curves based on yearly maximum average 0.25 hr wind speed for GFI data. 354
Figure B.1-8. Wave height vs. wind speed from Smith's NARFET model. 356
Figure B.1-9. Wave height vs. wind speed from Goda's (2010) procedure for a flood level, SWL, of EL 833.9. 358
Figure B.1-10. Illustration of terms in Goda's (2010) original pressure formulation. 361
Figure B.1-11. Breaking wave height location in Goda's (2010) equation. 362
Figure B.1-12. Pressure distribution on T-Wall (batter piles not shown). 365
Figure B.1-13. Red River of the North stage vs. ACE at Grand Forks, SD. 368
Figure B.1-14. River stages at Red River of the North near Grand Forks, ND, between 2007 and 2020. 369
Figure B.1-15. Number of maximum average 0.25 hr wind speed occurrences per month from 1973 to 2020 for Red River of the North floodwall. 370
Figure B.2-1. Floodwall used in example wave force calculations (tension and compression piles not shown). 371
Figure B.2-2. Wind speed and direction collection site at MML in relation to floodwall project. 372
Figure B.2-3. Fetch and wind direction determined for the Red Wood River floodwall. 375
Figure B.2-4. Extreme wind-speed estimation for MML wind data. 380
Figure B.2-5. Wind frequency from Gumbel Type 1 Distribution with Gringorten's method for MML wind data. 381
Figure B.2-6. Wind frequency curves based on yearly maximum average 0.1 hr wind speed for MML data. 382
Figure B.2-7. Fetch and wind direction for the Red Wood River floodwall used in the NARFET model. 383
Figure B.2-8. Wave height vs. wind speed from Goda's procedure for Red Wood River floodwall. 386
Figure B.2-9. Illustration of terms in Goda's original pressure formulation adopted for Red Wood River floodwall. 388
Figure B.2-10. Breaking wave height location in Goda's (2010) equation adopted for Red Wood River floodwall. 389
Figure B.2-11. Pressure distribution on Red Wood River T-Wall (batter piles not shown). 392
Figure B.2-12. Red Wood River stage vs. ACE at Marshall, MN. 396
Figure B.2-13. River Stages at Red Wood River near Marshall, MN, between 2011 and 2020. 397

Figure B.2-14. Number of maximum average 0.1 hr wind speed occurrences per month from 1984 to 2020 for Red Wood River floodwall. 398
Figure B.3-1. Floodwall used in example wave force calculations for Mississippi River at St. Paul, MN (tension and compression piles not shown). 399
Figure B.3-2. Wind speed and direction collection site at MSP in relation to floodwall project. 400
Figure B.3-3. Location 1 – fetch and wind direction determined for the Mississippi River floodwall. 403
Figure B.3-4. Location 2 – fetch and wind direction determined for the Mississippi River Floodwall. 403
Figure B.3-5. Extreme wind-speed estimation for MSP wind data. 411
Figure B.3-6. Extreme wind-speed estimation for MSP wind data. 412
Figure B.3-7. Location 1 – wind frequency from Gumbel Type 1 Distribution with Gringorten's method for MSP wind data. 413
Figure B.3-8. Location 2 – wind frequency from Gumbel Type 1 Distribution with Gringorten's method for MSP wind data. 413
Figure B.3-9. Location 1 – wind frequency curves based on yearly maximum average 0.5 hr wind speed for MSP data. 414
Figure B.3-10. Location 2 – wind frequency curves based on yearly maximum average 0.47 hr wind speed for MSP data. 415
Figure B.3-11. Location 1 – fetch and wind direction for the Mississippi River floodwall used in the NARFET model. 417
Figure B.3-12. Location 2 – fetch and wind direction for the Mississippi River floodwall used in the NARFET model. 417
Figure B.3-13. Location 1 – wave height vs. wind speed from Goda's (2010) procedure for Mississippi River floodwall. 420
Figure B.3-14. Location 2 – wave height vs. wind speed from Goda's (2010) procedure for Mississippi River floodwall. 421
Figure B.3-15. Illustration of terms in Goda's (2010) original pressure formulation adopted for Mississippi River floodwall. 425
Figure B.3-16. Breaking wave height location in Goda's (2010) equation adopted for Mississippi River floodwall. 426
Figure B.3-17. Pressure distribution on Mississippi River T-Wall (batter piles not shown). 430
Figure C-1. Development of average, average plus one standard deviation, and average minus one standard deviation strength envelopes using the 2-σ rule (N_σ= 4). 437
Figure D-1. Inherent soil variability of the geotechnical engineering soil property undrained shear strength (S_u) at depth z; (a) point estimate; (b) random field (after Li [1992]). 445
Figure D-2. Graphical definition of inherent soil variability (w) with depth, z, within a soil layer (after Phoon and Kulhawy [1999a]). 446
Figure D-3. Estimation of vertical scale of fluctuation (after Phoon and Kulhawy [1999a]). 449

Tables

Table 2-1. Reliability Index (β) and PUP – normal distribution. 29
Table 2-2. Target probability of slope failure and reliability index for a dike with a life of 100 years – based on the historical rate of failure of dams. 57
Table 2-3. Consistent factors of safety associated with target probability of slope failures and reliability Indices for a dike with a life of 100 years. 57
Table 2-4. Computed expected factors of safety, annual probability of failure and reliability indices for the proposed single stage construction of a 12 m high embankment dike at the proposed James Bay project. 60
Table 2-5. Values of the expected value and standard deviation of the FoS (FS) against sliding failure, *PUP*, reliability index and corresponding Syncrude Tailings Dike performance in terms of horizontal deformation. 62
Table 2-6. The 2014 CHBDC ULS and SLS consequence factor values (after Fenton et al. [2016]). 64
Table 2-7. The 2014 CHBDC geotechnical design ULS consequence factor values and reliability criteria (after Fenton et al. [2016]). 65
Table 2-8. Expanded table of 2014 CHBDC geotechnical design ULS consequence factor values and reliability criteria. 66
Table 2-9. Comparisons of reliability indices for the 2014 CHBDC geotechnical design ULS with a 75-year design life and for a 100-year design life. 67
Table 2-10. The 2014 CHBDC SLS consequence factor values and reliability criteria (after Fenton et al. 2016). 69
Table 2-11. Expanded table of 2014 CHBDC SLS consequence factor values and reliability criteria. 69
Table 2-12. Comparisons of reliability indices for the 2014 CHBDC geotechnical design SLS with a 75-year design life and for a 100-year design life. 70
Table 2-13. ASCE-7-10 acceptable reliability for non-earthquake – Risk Category I, temporary storage. 71
Table 2-14. ASCE-7-10 acceptable reliability for non-earthquake – Risk Category II, normal. 71
Table 2-15. ASCE-7-10 acceptable reliability for non-earthquake – Risk Category III, assembly. 72
Table 2-16. ASCE-7-10 acceptable reliability for non-earthquake – Risk Category IV, hospitals. 72
Table 2-17. AASHTO 2010 LRFD Bridge Design Specification reliability criteria extended to 50-year and 100-year β values – ULS. 74
Table 2-18. Comparison of reliability criteria data for conventionally designed detailed bridges with typical consequence level to that for normal buildings – ULS. 75
Table 3-1. LFD and LRFD load factors used for resistance factor calibration (after Allen [2005]). 79
Table 3-2. Reliability index and probability of failure by component type (after Allen [2005]). 85
Table 3-3. AASHTO resistance factor summary. 87
Table 4-1. Probabilistic models for concrete and steel reinforcement strength* (after Ellingwood). 95

Table 4-2. Resistance models (after Ellingwood).....96
Table 5-1. Description of terms in Goda's original pressure formula. 112
Table 5-2. Results of $H_{1/3}$ and $H_{1/10}$ estimation using the simple sort and average and Rayleigh methods. 118
Table 5-3. Parameters used in example wave force calculation (imperial and metric units included). 122
Table 5-4. Calculation summary. 127
Table 5-5. Summary of resultant forces and moment arms for the Goda pressure components values in this calculation example. 128
Table 5-6. Pressure and resultant force terms for original Goda and Goda-Takahashi modified methods. 130
Table 5-7. Summary of COV for binned data of the relative wave height parameter (H_I/d_{SWL}) for the 926 data points. 141
Table 5-8. Summary of COV for the Goda-Takahashi predictive method for the four individual datasets 142
Table 5-9. Summary of simplified COV as a function of the relative wave height parameter (H_I/d_{SWL}). 150
Table 6-1. Fetch angles and lengths measured for hypothetical T-Wall of Figure 6-5. Incident angle shown in yellow highlight. 159
Table 6-2. Results from wind-speed analyses for Melvin Price Lock and Dam. 167
Table 6-3. Wave height and wave period for combined airport data (SLR and SCC)* derived using the Goda procedure. 169
Table 6-4. Wave height and wave period for combined airport data (SLR and SCC) derived using the NARFET procedure. 169
Table 6-5. Structural, bathymetric, and hydrological parameters used in example wave force calculation (imperial and metric units included). 172
Table 6-6. Wave force calculation results based on input parameters of Table 6-5 and statistics of Table 6-4. 172
Table 6-7. Wave equivalent force location calculations based on Ebeling et al. (2018). Pressure (P_4) is zero since no wave overtopping was allowed 173
Table 7-1. Nucor HP 14 × 89 pile properties 180
Table 7-2. Derived pile properties from Nucor HP 14 × 89. 181
Table 7-3. Mobilized strength ratio computed for each of the 10 limit states in the deterministic T-Wall design with flood EL 836.9 ft for a pair of 40 ft long batter piles and section width of 4 ft. 215
Table 7-4. Reliability results for 100,000 Monte Carlo simulation runs using three Chance of Exceedance curves for a 40 ft compression and tension batter pile-founded T-Wall 216
Table 7-5. Annual and 100 year *PUP* and β values for the primary limit states for 40 foot compression and tension batter pile founded T-Wall 219
Table 7-6. Conversion of annual β_{Target} to 100 year $\beta_{Target.}$ 221
Table 7-7. Deterministic Design Load propagation to individual Limit States 222
Table 7-8. Computation of local resistance factor (ϕ_L). 227
Table 7-9. Deterministic assessment for different compression (C) and tension (T) pile lengths for the Red River of the North example problem. 229

Table 7-10. Mobilized strength ratio computed for each of the 10 limit states in the deterministic T-Wall design with flood EL 836.9 ft. for a 39 ft long compression and 5 ft long tension batter piles and section width of 4 ft. 232

Table 7-11. Reliability results for 100,000 Monte Carlo simulation runs using three chance of exceedance curves for a 39 ft compression and 5 ft tension batter piles founded T-Wall. 232

Table 7-12. Annual and 100-year *PUP* and β values for the primary limit states for 39 ft compression and 5 ft tension batter pile founded T-Wall. 234

Table 7-13. Deterministic assessment for 39 ft compression (C) and 10 ft tension (T) pile lengths for the Red River of the north example problem. 235

Table 7-14. Mobilized strength ratio computed for each of the 10 limit states in the deterministic T-Wall design with flood EL 836.9 ft. for a 39 ft long compression and 10 ft long tension batter piles and section width of 4 ft. 236

Table 7-15. Reliability results for 100,000 Monte Carlo simulation runs using three Chance of Exceedance curves for a 39 ft compression and 15 ft tension batter piles founded T-Wall. 237

Table 7-16. Annual and 100-year *PUP* and β values for the primary limit states for 39 ft compression and 10 ft tension batter pile-founded T-Wall. 238

Table 7-17. Deterministic design load propagation to individual limit states. 239

Table 7-18. Computation of local resistance factor (ϕ_L) for a more optimized design using 39 ft compression pile and 10 ft tension pile. 239

Table 7-19. Mobilized strength ratio computed for each of the 10 limit states in the deterministic Red Wood River T-Wall design with flood EL 22.1 ft. for a pair of 35 ft long compression and 10 ft long tension batter piles and section width of 3.8 ft. 253

Table 7-20. Reliability results for 100,000 Monte Carlo simulation runs using two Chance of Exceedance curves for a 35-ft compression and 10-ft tension batter piles founded T-Wall. 254

Table 7-21. Annual and 100-year *PUP* and β values for the primary limit states at the Red Wood River site for 35 ft compression and 10 ft tension batter pile-founded T-Wall. 255

Table 7-22. Deterministic design load propagation to individual limit states at the Red Wood River site with 10 ft tension pile and 35 ft compression pile. 257

Table 7-23. Computation of local resistance factor (ϕ_L). 260

Table 7-24. Mobilized strength ratio computed for each of the 10 limit states in the deterministic Red Wood River T-Wall design with flood EL 22.1 ft. for 35 ft long compression and 15 ft long tension batter piles and section width of 3.9 ft. 263

Table 7-25. Reliability results for 100,000 Monte Carlo simulation runs using two chance of exceedance curves for a 35 ft compression and 15 ft tension batter piles founded T-Wall. 263

Table 7-26. Annual and 100-year PUP and β values for the primary limit states at the Red Wood River site for 35 ft compression and 15 ft tension batter pile-founded T-Wall. 264

Table 7-27. Deterministic design load propagation to individual limit states at the Red Wood River site with 15 ft tension pile and 35 ft compression pile. 265

Table 7-28. Computation of local resistance factor (ϕ_L) for Red Wood River example problem with 35 ft compression and 15 ft tension pile. 266

Table 7-29. Mobilized strength ratio computed for each of the 10 limit states in the deterministic Mississippi River at St. Paul, MN, T-Wall design with flood EL 714.5 ft. for a pair of 32 ft long compression and 10 ft long tension batter piles and section width of 3.6 ft. 279

Table 7-30. Reliability results for 100,000 Monte Carlo simulation runs using two chance of exceedance curves for a 32 ft compression and 10 ft tension batter piles founded T-Wall. 280

Table 7-31. Annual and 100-year *PUP* and β values for the primary limit states at the Mississippi River at St. Paul, MN, site for 32 ft compression and 10 ft tension batter pile founded T-Wall. 281

Table 7-32. Deterministic design load propagation to individual limit states at the Red Wood River site with 10 ft tension pile and 32 ft compression pile. 283

Table 7-33. Computation of local resistance factor (ϕ_L) for Mississippi River at St. Paul, MN. 286

Table 8-1. Site-based comparison with different compression pile lengths of computed $COV_{Spatial}$ values using a 5 ft vertical scale of fluctuation and the ratio of $COV_{Spatial}$ to COV_{Point}. 292

Table 8-2. Site-based comparison with different tension pile lengths of computed $COV_{Spatial}$ values using a 5 ft vertical scale of fluctuation and the ratio of $COV_{Spatial}$ to COV_{Point}. 292

Table 8-3. A comparison of Limit State 3 (compression pile SSI) LRFD ϕ results for different pile lengths with system γ = 1.3 and target β = 3.5. 294

Table 8-4. A comparison of Limit State 3 (compression pile SSI) LRFD ϕ results for different pile lengths with system γ = 1.3 and target β = 4.0 294

Table 8-5. A comparison of Limit State 4 (tension pile SSI) LRFD ϕ results for different pile lengths with system γ = 1.3 and target β = 3.5. 296

Table 8-6. A comparison of Limit State 4 (tension pile SSI) LRFD ϕ results for different pile lengths with system γ = 1.3 and target β = 4.0. 296

Table 8-7. Unscaled PUP and Beta with the designed structure. 298

Table 8-8. ϕ_R values for γ_L value = 1.3. 298

Table A.1. *PUP* values for hyperplanar limit state and hypersphere *PUP* estimations with increasing accuracy. 328

Table A.2. Hypersphere *PUP* estimate error as a multiple of the actual hyperplanar *PUP*. 328

Table B.1-1. Yearly maximum average 0.25 hr wind speed, GFI. 350

Table B.1-2. Results from wind-speed analysis for Red River Floodwall. 354

Table B.1-3. Wave height and wave period from Smith's NARFET Model. 355

Table B.1-4. Significant wave height and significant wave period from Goda's (2010) formulations for a flood level, SWL, of el 833.9. 358

Table B.1-5. Parameters used in Goda (2010) procedure for example wave force calculation (imperial and metric units included) for a flood level, SWL, of EL 833.9. 359

Table B.1-6. Wave force and pressure distribution computations using Goda's (2010) procedure for data in Table 1-4 for a flood level, SWL, of EL 833.9. 367

Table B.2-1. Sample of wind-speed and direction data downloaded from Iowa State website for MML. 374

Table B.2-2. Sample of processed wind-speed and direction file. 376
Table B.2-3. Yearly maximum average 0.1 hr wind speed, MML.... 377
Table B.2-4. Example of determining maximum average 0.1 hr (6 min) value from wind speeds reported multiple times per hour.... 379
Table B.2-5. Example of determining maximum average 0.1 hr (6 min) value interpolated from wind speeds reported hourly.... 379
Table B.2-6. Results from wind-speed analysis for Red Wood River floodwall. 382
Table B.2-7. Wave height and wave period from Smith's NARFET Model for Red Wood River floodwall. 384
Table B.2-8. Significant wave height and significant wave period from Goda's formulations for Red Wood River floodwall. 385
Table B.2-9. Parameters used in Goda (2010) procedure for example wave force calculation (imperial and metric units included) for a flood level gage reading of 19.1, SWL = 19.1. 387
Table B.2-10. Wave force and pressure distribution computations using Goda's (2010) procedure for data in Table B.2-9 for a flood level, SWL, of EL 21.2. 395
Table B.3-1. Sample of wind-speed and direction data downloaded from Iowa State website for MSP.... 402
Table B.3-2. Sample of processed wind-speed and direction file for location one. 404
Table B.3-3. Location 1 – Yearly maximum average 0.5 hr wind speed, MSP. 406
Table B.3-4. Location 2 – Yearly maximum average 0.47 hr wind speed, MSP. 408
Table B.3-5. Example of determining maximum average 0.5 hr (30 min) value from wind speeds reported multiple times per hour.... 410
Table B.3-6. Example of determining maximum average 0.5hr (30min) value interpolated from wind speeds reported hourly.... 410
Table B.3-7. Location 1 – results from wind speed analysis for Mississippi River floodwall. 415
Table B.3-8. Location 2 – results from wind-speed analysis for Mississippi River floodwall. 416
Table B.3-9. Location 1 – wave height and wave period from Smith's NARFET model for the Mississippi River floodwall. 418
Table B.3-10. Location 2 – wave height and wave period from Smith's NARFET model for the Mississippi River floodwall. 418
Table B.3-11. Location 1 – significant wave height and significant wave period from Goda's (2010) formulations for Mississippi River floodwall.... 419
Table B.3-12. Location 2 – significant wave height and significant wave period from Goda's (2010) formulations for Mississippi River floodwall.... 420
Table B.3-13. Location 1 – parameters used in Goda (2010) procedure for example wave force calculation (imperial and metric units included) for a flood level gage reading of 713.5, SWL = 713.5).... 422
Table B.3-14. Location 2 – parameters used in Goda (2010) procedure for example wave force calculation (imperial and metric units included) for a flood level gage reading of 713.5, SWL = 713.5).... 423
Table B.3-15. Location 1 – wave force and pressure distribution computations using Goda's (2010) procedure for data in Table B.3-12 for a flood level, SWL, of EL 713.5. 433

Table B.3-16. Location 2 – wave force and pressure distribution computations using Goda's (2010) procedure for data in Table B.3-13 for a flood level, SWL, of EL 713.5. 434

Table C-1. Values of sample range (N_σ) for normally distributed variable with $\sigma = 1$ and n sample measurements (after Tippett [1925] and Burington and May [1970]). 439

Table D-1. Summary of autocorrelation and scale of fluctuation distances of some geotechnical engineering soil properties charactering the strength of soils. 451

Table D-2. Generalizations on the magnitude of the vertical and horizontal scale of fluctuation distances of select geotechnical engineering soil properties charactering the strength of soils. 455

Table D-3. Generalizations on the magnitude of the vertical and horizontal autocorrelation distances of select geotechnical engineering soil properties charactering the strength of soils. 455

Table D-4. A summary of Phoon and Kulhawy (1999b; Table 5) approximate guidelines for design soil property variability. 462

Preface

The engineering and reliability formulation-based Load and Resistance Factor Design (LRFD) developmental effort reported herein was authorized by Headquarters, US Army Corps of Engineers, and was conducted from October 2019 through September 2021 under the Infrastructure Resiliency and Reliability Research Program (Work Unit 65FG6J). Dr. Julie D. Rosati (US Army Engineer Research and Development Center, Coastal and Hydraulics Laboratory [ERDC-CHL]) was the Lead Civil Works Technical Director for (Research and Development) R&D and for Flood and Coastal Risk Management R&D during the time of research and publication of this report. Funding was provided by the Infrastructure Resiliency and Reliability Research Program under the Flood and Coastal Storm Damage Reduction (FCSDR) Research and Development Program in the focus area title Balanced Design of Flood Structures under Funding Account Code U4375151, AMSCO Code 031391. The program manager for FCSDR was Dr. Brandon M. Boyd, ERDC-CHL.

The research was performed by the Computational Science and Engineering Division, ERDC Information Technology Laboratory (ITL). During the time of research, Dr. Jerrell R. Ballard was chief, and at the time of publication, Dr. Jeffrey L. Hensley was chief, respectively. The deputy director of ERDC-ITL was Dr. Jackie S. Pettway, and the director was Dr. David A. Horner.

Mr. Kent D. Hokens, of the USACE St. Paul District, provided input, site-specific data, and information regarding District needs during this research.

COL Christian Patterson was the commander of ERDC, and the director was Dr. David W. Pittman.

1 Introduction

1.1 Background

The US Army Corps of Engineers (USACE) has been relying on an allowable stress design (ASD) methodology for design of the various structural features comprising its flood mitigation structures. In ASD, also referred to as working stress design, factors of safety (FoS) are implicit through the use of allowable stresses during the structural design process. Allowable stresses are specified for use in the various design limit states for the USACE three categories of design load cases of Usual, Unusual, and Extreme.[1] In the USACE design guidance for geotechnical-dominated limit states and engineering issues, the use of FoS against Ultimate Limit States (ULS) is more straightforward than in the structural design guidance. The appropriate value for the FoS is explicitly stated in this portion of the USACE guidance.

The USACE is currently transitioning to a structural design methodology based on Load and Resistance Factor Design (LRFD). The advantage for LRFD is that it formally takes into consideration the variability in the loads and the resistances separately. LRFD has become an accepted mode of implementation of probability-based limit state design in structural steel and reinforced concrete design. Three of the most recently developed and prominent examples of the LRFD-based building and bridge design criteria are the following:

- American Society of Civil Engineers (2010), ASCE/SEI 7-10 *Minimum Design Loads for Buildings and Other Structures*
- Canadian Standards Association (2014), *Canadian Highway Bridge Design Code*, CAN/CSA-S6-14
- American Association of State Highway and Transportation Officials (2010, 2020) *AASHTO LRFD Bridge Design Specifications*.

Development of these three LRFD-based design criteria has been led by the structural engineering community within the civil engineering profession. In recent years, researchers have been proposing means for extending LRFD into geotechnical ULS designs. However, to date, there are no LRFD-based geotechnical design criteria.

[1] One definition of a limit state is "a structural condition beyond which it no longer fulfills the specified design criteria."

USACE batter pile-founded flood mitigation structures such as reinforced concrete T-Walls are founded on piles. Consequently, the design of this category USACE flood mitigation structure involves significant soil structure interaction (SSI). Generally speaking, SSI is a specialized topic associated with foundation features for the structure. Currently, no LRFD methodology exists for SSI analysis of the USACE-type of batter pile-founded flood mitigation structure.

1.2 Objective

This technical report discusses research in support of the development of a combined LRFD methodology that accommodates structural as well as geotechnical design limit states (especially the ULSs) as used in the design of the USACE batter pile-founded flood mitigation T-Wall structures. To this end, this research and development (R&D) effort intends to extend reliability procedures that have been developed for other non-USACE structural systems to encompass USACE batter pile-founded flood mitigation T-Wall structures. Additionally, procedural methods for accurate estimation of reliability are assessed for application to the to-be-developed combined LRFD methodology.

1.3 Approach

The authors of this technical report have gathered applicable reliability methodologies and supporting data from the civil engineering LRFD technical community. These methodologies and data come from many structural and geotechnical fields and are interpreted for ultimate use in a combined LRFD application to the USACE batter pile-founded, flood mitigation T-Wall structures. Numerical procedures to facilitate accurate reliability calculations are also devised to accommodate reliability analysis of the USACE batter pile-founded, flood mitigation structures multiple limit states.

1.4 Report contents

- Chapter 2 discusses reliability analysis as it relates to LRFD of the USACE flood mitigation structures. An introduction to considerations for reliability analysis with multiple limit states is included.
- Chapter 3 provides a historical summary of the American Association of State Highway and Transportation Officials (AASHTO) Load and

Resistance Factor Design (LRFD) Bridge Design Specification (2020 being the most recent edition) for piling used in pile-founded bridges.

- Chapter 4 summarizes the moment and shear capacity relationships for use in these two structural limit states for reinforced concrete structures such as those used in the stem of the T-Wall as well as the combined loading of axial load with bending in the steel HP piling of the compression pile and tension pile.
- Chapter 5 summarizes a procedure for computing sea wave forces on vertical walls using the Goda-Takahashi procedure. An assessment of the statistical dispersion in sea force is included.
- Chapter 6 summarizes a procedure for computing wind-induced inland wave forces on vertical walls using the Goda procedure. An assessment of the statistical dispersion in wave force is included for a hypothetical T-Wall at a USACE project site.
- Chapter 7 discusses the application of the devised reliability analyses and a LRFD assessment accommodating geotechnical as well as multiple structural design limit states for design to example USACE batter pile-founded, reinforced concrete flood mitigation T-Walls structures. Design of these flood mitigation T-Wall structures involves consideration of up to 10 geotechnical and structural limit states. Because of the batter piles foundation feature of these reinforced concrete T-Walls, the design of these flood mitigation structures involves significant soil structure interaction. The devised reliability methodology computes a systems Probability of Unsatisfactory Performance (*PUP*) value for the T-Wall structures being analyzed as well as resistance factors for a prescribed global hydraulic load factor γ value of 1.3.
- Chapter 8 summarizes the Research and Development (R&D) findings discussed in this report and conclusions to be made from the research conducted.
- Appendix A discusses individual and multiple Limit States and the computation of the *PUP* using numerical procedures.
- Appendix B presents example computational assessments of wind induced wave loading made at select inland USACE flood mitigation structure sites.
- Appendix C discusses the determination of geotechnical soil property distributions/statistics for sparse data.
- Values for Coefficients of Variation (COV) for a variety of different soil types are collected and tabulated in Appendix D, along with typical vertical and horizontal scales of fluctuation.

2 Reliability Analysis as It Relates to Load and Resistance Factor Design (LRFD) of the USACE Flood Mitigation Structures

2.1 LRFD

2.1.1 A brief introduction to LRFD

The equations governing homogeneous soil regions are introduced in this section. The first subsection introduces a general form of the LRFD equation while the second describes the interrelationship between nominal and mean loads and resistance and introduces a bias factor.

2.1.2 A general form of LRFD

The general form of a single ULS (Fenton et al. 2016) in the context of an LRFD design requires that the resistance (i.e., the capacity) be greater than or equal to the load:

$$\phi * R_n \geq \sum_{i=1}^{j} \eta_i * \gamma_i * L_{ni} \tag{2.1}$$

where

ϕ = is the resistance factor to account for variability in the resistance
R_n = is the nominal resistance; (Fenton et al. [2016] refer to this as the characteristic resistance, $\hat{R}$)[2]
η_i = is a load modifier factor to account for load combinations, the effects of ductility, redundancy, and operational importance (used in some types of LRFD formulations)
γ_i = is a load factor that accounts for variability in each load i, among the j loads, to which it is assigned
L_{ni} = is the nominal load i of j different loads; (Fenton et al. [2016] refer to this as the characteristic load, $\hat{L}_{ni}$).

[2] Fenton et al. (2016) prefers to use the term *characteristic* rather than *nominal* because it suggests a value that characterizes a design parameter that is uncertain (e.g., a random resistance or load). They believe that the word *nominal* (or design) does not convey the underlying randomness of the design parameter.

Safety is assured if the factored resistance is at least equal to the factored load. The Equation 2.1 design factors are intended to cover uncertainties or to compensate for the lack of complete information.

Observe in Equation 2.1 that separate factors of ϕ and γ_i are defined for resistance and loading, respectively, and an equation of this form is unique to each ULS. These partial factors ϕ and γ_i are individually related to the variability of the resistance and load quantities, respectively, that they are factoring and are used to scale the nominal (or characteristic) design values to more conservative values so that the probability of a particular ULS occurring is acceptably small and within a magnitude acceptable to the USACE. The *PUP* value for a ULS may be equivalently expressed in terms of a reliability index (β) value. Determining the acceptable *PUP* and β values is one of the research topics discussed in this report. Section 2.12 reviews a limited number of published values for β and/or *PUP* that are associated with select designs or calculated for constructed, non-USACE project systems. The necessary design factor procedure is to be developed for the USACE to obtain designs that achieve a prescribed level of reliability. Looking forward, the level of a flood mitigation structural system's reliability will be indicated by values for *PUP* and β in this report.

The authors of this ERDC technical report recognize that multiple ULSs are considered during the design of the USACE flood mitigation structures. When considered alone, each ULS has a unique *PUP* and β value. The important ULSs will be identified in Section 2.2. A structural system PUP_{system} for the flood mitigation structure can be computed from the conjoined ULSs. The results from research into this topic is discussed later in this chapter and computations made by the authors of this report for example USACE batter pile-founded flood mitigation T-Wall structures are discussed in Chapter 7.

The load and resistance factors (γ_i and ϕ) are determined using statistics, reliability concepts, and a pre-selected value for probability of failure or, equivalently, β. These relationships are summarized in Section 2.4 for a single ULS. Generally, a factor of unity (1) or less is assigned to ϕ that is applied to the resistances of the material (including soil resistance), and a factor of unity or greater is assigned to γ_i that is applied to the nominal loads L_{ni}, loads i = 1 through j. An example taken from the structural discipline of LRFD design for L_i with i equal to 1 and to 2 would be dead and live, respectively, nominal loads.

When considering a single, displacement-based, Serviceability Limit State (SLS) in foundation design for routine, non-USACE structures, Baecher and Christian (2003) recognize that the LRFD methodology requires that the tolerable (nominal) displacement, δ_{tn}, be greater than or equal to the estimated (nominal) displacement, δ_{ni}:

$$\phi * \delta_{tn} \geq \sum_{i=1}^{j} \eta_i * \gamma_i * \delta_{ni} \quad (2.2)$$

where

ϕ = is the resistance factor to account for variability in the tolerable displacement (i.e., a *resistance* factor)
δ_{tn} = is the tolerable displacement (viewed as a nominal resistance)
η_i = is a load-induced, displacement modifier factor to account for load combinations, the effects of ductility, redundancy, and/or operational importance (used in some types of LRFD formulations)
γ_i = is a factor that accounts for variability in each displacement induced by nominal load i, among the j loads, to which it is assigned (i.e., a *load factor*)
δ_{ni} = is the estimated displacement resulting from load i of j of the different nominal loads.

An example of what Baecher and Christian (2003) refer to as a routine design would be the foundation design for a low-rise building system. Safety is assured if the factored tolerable displacement is at least equal to the sum of displacements for all the nominal loads.

2.2 An interrelationship between nominal and mean loads, resistance, and bias factors

The calculated nominal resistance R_n can differ from the mean value of measured resistance. This is particularly true for structural systems in contact with the earth that involve SSI-type of engineering computations. A good example of this is in the case of axially loaded pile foundations, as discussed in Federal Highway Administration FHWA HI-98-032 (FHWA 2001). To account for this discrepancy between measured resistance R_m and nominal resistance R_n, a bias factor is introduced:

$$R_m = \lambda_R * R_n \quad (2.3)$$

where λ_R represents the resistance bias factor. The bias factor may also be viewed as a correction factor. In the FHWA (2001) axially loaded driven pile foundation example, λ_R was determined as the ratio of the axial pile load capacities measured in the field (i.e., R_m) divided by the axial ULS.

$$\lambda_R = \frac{R_m}{R_n} \tag{2.4}$$

The ULS may be computed using either empirical correlations combined with traditional geotechnical field exploration test data (R_n) or computer programs and geotechnical soil strength data.[3]

FHWA (2001) provides a computational method to compute λ_R. One value for λ_R was generated for each pile load test location. The Standard Penetration Test (SPT) data were recovered for various soil stratum in one soil boring location near to the select pile load test and were converted into a (calculated) axial pile capacity estimate for R_n using Meyerhoff's (1976) procedure, an established geotechnical engineering correlation.[4] For each pile load test location, an R_m value was measured, and a corresponding R_n calculation was made using the SPT data recovered from the soil boring made close to the specified pile load test (Table 3-2 in FHWA [2001]). Thus, one λ_R value was computed for each pile load test location using the pairs of R_m and R_n data using Equation 2.4. Statistical processing of the collection of λ_R values was then performed generating mean and standard deviations for the bias factor λ_R based for each pile load test location. For the FHWA (2001) example cited, 24 pile load tests were used in the evaluation of λ_R. The mean (μ), standard deviation (σ), and COV of the ratio of the measured to predicted capacities are 1.22, 0.66, and 54%, respectively. Because the mean λ_R value equals 1.22, this implies that the Mayerhof's method tends to underpredict, on average, the pile resistance. In summary, there is a difference between what is predicted and what is measured, and the value for λ_R is used to quantify this difference.

[3] Pile (ultimate) axial capacity calculations for R_n may be made using the USACE Computer-Aided Structural Engineering (CASE) computer program CAXPILE (Dawkins 1984) combined with soil strength data. Pile load tests conducted at the site result in a different and more accurate ultimate pile capacity value, designated R_m. FHWAs (2001) logic to apply a bias factor λ_R in their Reliability methodology is an ingenious way to devise a "correction factor" to be applied to the predicted pile capacity calculated using site-specific soil strength data and the geotechnical procedure and/or software (e.g., CAXPILE) that computes ultimate pile capacity.

[4] The SPT is a common in situ testing method used to determine the geotechnical engineering properties of subsurface soils. It is a simple and inexpensive test to estimate (through correlations) the approximate shear strength parameters for soils as well as relative density of cohesionless soils.

When performing an example reliability analysis of a pile foundation, FHWA (2001) expanded on Equation 2.4 to become

$$\bar{R} = \lambda_R * R_n \tag{2.5}$$

where $\bar{R}$ is the mean value of resistance and λ_R is the resistance bias factor. Similarly, the ith mean load $\bar{L}_i$is given in FHWA (2001) to be

$$\bar{L}_i = \lambda_{Li} * L_{ni} \tag{2.6}$$

Rearranging, Equations 2.5 and 2.6 become

$$R_n = \frac{\bar{R}}{\lambda_R} \tag{2.7}$$

and

$$L_{ni} = \frac{\bar{L}_i}{\lambda_{Li}} \tag{2.8}$$

Introducing Equations 2.6 and 2.7, the generalized LRFD Equation 2.1 is transformed to

$$\phi * \frac{\bar{R}}{\lambda_R} \geq \sum_{i=1}^{j} \eta_i * \gamma_i * \frac{\bar{L}_i}{\lambda_{Li}} \tag{2.9}$$

Equation 2.9 allows for the introduction of resistance and/or load bias in an LRFD analysis. When no bias is present, the bias factors may be set equal to unity. In this case and by Equations 2.5 and 2.6, Equation 2.9 reverts to Equation 2.1 with $\bar{R} = R_n$ and $\bar{L}_i = L_{ni}$, respectively.

The FHWA (2001) example discussed above, in the context of the introduction of Equation 2.4 into this report, demonstrates how introduction of a bias factor λ_R into the reliability formulation (Equation 2.9) allows for the correction of limit state model(s). Numerous reliability formulations proposed and/or used in the different civil engineering disciplines (e.g., structural, geotechnical) make use of bias factors when formulating and conducting reliability analyses.

There have been significant research and proposed code developmental activity across the civil engineering community, particularly within the last 25 years, that is resulting in a variety of proposed reliability-based LRFD

methodologies for specific structural systems and/or types of structures. Some of the proposed methodologies have been or are being adopted by organizations that provide structure specific design guidance. In general, the LRFD methodologies are not *one size fits all* but are tailored to the system type and to the historical design practice of the agency overseeing the design methodology for the specific structural system type of interest. Fenton et al. (2016) observe that some non-USACE structural system design codes and Civil Engineer researchers developing LRFD-based design procedures specify that the nominal (or characteristic) load is equal to the mean; others suggest using a cautious estimate of the mean while others specify the use of an upper (or lower) fractile (whichever yields the most conservative result). Their second, companion observation is that the nominal (or characteristic) resistance may be computed using mean strength parameters or using fractiles of the strength parameters. In summary, the bias factor captures the difference between the nominal design value and the mean for both resistance and load terms.

2.3 Limit states for batter pile-founded, reinforced concrete T-Wall flood mitigation structures

In general, there are five significant categories of ULSs considered in the design of the USACE batter pile-founded reinforced concrete flood mitigation T-Wall structures. They are the following:

- Flexural hinging of individual structural members
- Shear failure of individual structural members
- Compression or tensile failure of individual structural pile foundation members subjected to axial compressive or tensile loading
- Axial capacity soil-structure interaction failure of the pile foundation
- Excessive displacement of the structural system in its entirety.

The first three are evaluated on a structural member-by-member basis. The fourth is commonly associated with geotechnical aspects of the application of reliability theory to a project feature's design. This study focuses on assessing the first four limit states for the USACE batter pile-founded, reinforced concrete T-Wall flood mitigation structures because reliability-based LRFD design methodologies are not as advanced on geotechnical and geotechnical-structural system related issues as they are on solely structural related issues alone.

Two other global limit states are identified:

- Global sliding failure of the structural system in its entirety
- Overturning or rotational failure of the structural system about its foundation in its entirety.

However, these two global limit states in conjunction with the above five limit states are not pursued in this R&D effort.

2.4 Reliability analysis

Reliability studies are performed to determine the *PUP* and β values of a structural system for a limit state or limit states affecting system performance. The reliability of the system is defined as the complement of the probability of unsatisfactory performance *(1-PUP)* and is the probability of proper or satisfactory performance during which the structure behaves safely.

$$Reliability = 1 - PUP \tag{2.10}$$

Thus, the level of a flood mitigations structural systems' reliability is indicated by its *PUP* value as well as its corresponding β.

One of the major strengths of the reliability approach, according to Christian et al. (1994), is that design engineers can use statistical-based estimates (of means or expected values) and variances (equal to the square of the standard deviation, σ^2) of engineering parameters (e.g., soil strength) and design based on these uncertainties through a reliability analysis. This leads to a more efficient system design than merely assigning conservative values of the parameters. Generally speaking, the structural community has advanced the application of reliability theory in design methodologies for steel, reinforced concrete, and timber more rapidly than has the geotechnical community for pile-based soil foundations. One explanation for this was made by Fenton et al. (2016) with their observation that the ground is by far the most variable and hence uncertain of engineering materials. Nevertheless, the geotechnical profession has made progress and advanced to the stage whereby geotechnical design codes are appearing (Fenton et al. 2016). One example would be the *Canadian Highway Bridge Design Code*, published in 2014 by the Canadian Standards Association. Reliability theory serves as a basis for the quantifiable characterization of load and resistance factors in an

LRFD analysis of Canadian bridges. In this document, example values for load and resistance factors for geotechnical ULS are provided for use in the design of Canadian bridge foundations. These load and resistance factors are based on target theoretical maximum lifetime (equal to 75 years for bridges) failure probabilities and equivalent values of β. Using the information provided by Fenton et al. (2016), the authors of this ERDC report made a careful assessment of the logic behind this Canadian bridge foundation design procedure and of the details associated with its development. The assessment was made from the viewpoint of its application to combined LRFD-based design of the USACE batter pile-founded, reinforced concrete T-Wall flood mitigation structures. This assessment is summarized in the following paragraphs.

Minimum service life of 100 years: Note that in ER 1110-2-8159 (HQUSACE 1997), USACE policy requires by regulation that engineering design decisions should be made using life-cycle design as a basis for selection of all project elements such as materials, structural systems, mechanical equipment, and scour protection on all projects. These design decisions will be consistent throughout all project phases, including value engineering studies, and will be based on a minimum project service life of 100 years for major infrastructure projects such as locks, dams, and levees.

After a careful review of Dr. Fenton's description of the theory used (Fenton et al. 2016) and the decisions made during the application of reliability and LRFD theories to Canadian bridge foundation systems, the authors of this report conclude that this LRFD-based bridge foundation design procedure cannot be applied to the USACE batter pile-founded, reinforced concrete T-Wall flood mitigation structures without modification. There are four fundamental items that make the design of a USACE flood mitigation structure different from the design of a bridge foundation: (1) differences in project service life (e.g., minimum service life of 100 years for the USACE Civil Works flood mitigation structure projects according to ER 1110-2-8159 [HQUSACE 1997] versus a 75-year life for bridges); (2) approaches for consideration of the cost of the project in the reliability analysis; (3) the consequence of unsatisfactory performance; and (4) the transition of key features of the USACE current Civil Works design methodology into LRFD (versus that given in 2014 for the Canadian bridge design industry). When decisions are ultimately made regarding these four items, as well as on other details, it is anticipated that acceptable *PUP* values and their associated β values for USACE flood

mitigation structures will not be the same as those made for the 2014 *Canadian Highway Bridge Design Code*. The authors of this report anticipate that a difference in *PUP* and β values means that the load and resistance factors in the two LRFD procedures of analysis will also differ.

It is anticipated that the four factors that were mentioned regarding the 2014 *Canadian Highway Bridge Design Code*, along with other details, are to be addressed and incorporated in the USACE Civil Works transition to combined LRFD design. Recall that LRFD design methodology is being facilitated through the use of reliability theory. Because the application of LRFD to geotechnical related *PUP* calculations for ULSs is less advanced than *PUP* calculations for structural ULSs, this ERDC study focuses on details related to developing a path forward in the application of reliability theory to geotechnical ULSs and the subsequent development of load and resistance factors for use in the design of the USACE batter pile-founded, reinforced concrete T-Wall flood mitigation structures.

An SLS will occur more frequently than a ULS. Thus, the SLS *PUP* value is higher than the ULS *PUP* value. Baecher and Christian (2003) observe that because an SLS *PUP* value is higher, compared to that for the ULS, the allowable settlement of a structure rather than the ultimate bearing capacity of the soil generally controls the design of shallow foundations. They cite Duncan et al. (1989) observation that an SLS has a higher probability of occurrence because they occur at lower absolute loads. Baecher (1996) observes that most routine designs are based on specific serviceability limits, and ultimate limits are checked subsequently. However, the design of pile foundations contradicts this trend: The design of pile foundations is controlled by the ULS.

A USACE batter pile-founded, reinforced concrete T-Wall flood mitigation structure is not a routine civil engineering structure in the context of the previously discussed, routine foundation design. Three important differences are (1) the service life of a Civil Works flood mitigation structure is approximately twice the life of a routine building (100 years versus 50 years); (2) the consequences of its failure are far more significant and can impact a community; and (3) its financial investment is significantly more than for a routine building system. The design procedures differ between the two structural systems. USACE batter pile-founded, reinforced concrete T-Wall flood mitigation structures are designed for flood loading (EM 1110-2-2502) (HQUSACE 1989a). In

contrast, routine structural systems (e.g., for buildings) and bridges are typically designed for two limit states, an SLS and a ULS. Depending on the structural feature, limiting deformation considerations may be one of the limit states evaluated for USACE batter pile-founded, reinforced concrete T-Wall flood mitigation structures.

2.5 Performance function, dimensionless variables, and the Probability of Unsatisfactory Performance (*PUP*)

Consider the case of a vector $\boldsymbol{X}$ defining a set of random variables (X_1, X_2, …, X_j) of loads and resistances and a single limit state function, designated $g(\boldsymbol{X})$, among one of those listed in Section 2.2. Reliability is based on the performance of a system as the variables in $\boldsymbol{X}$ change. Therefore, it is important to know when the system achieves, for example, a ULS. ULS is often associated with system failure and its inability to perform its intended function.

In general, a limit state is the boundary between satisfactory and unsatisfactory performance of a structure (Nowak and Collins 2000, 2013). There are different types of limit states. In non-USACE, civil engineering literature, these limit states are broken into ULS as well as SLS, depending on their severity. ULS are related mostly to the system's loss of load-carrying capacity. As an example, consider the batter pile foundation of the T-Wall flood mitigation structure; a ULS state might involve exceeding the axial capacity of the pile foundation within its adjacent soil regime. It could also be associated with the bending-moment-induced flexural failure of the compression pile as well as the shear failure or bending moment failure of the reinforced concrete T-Wall at the base of its stem. Serviceability-type limit states are generally related to gradual deterioration, personal discomfort, or maintenance cost.

Each limit state boundary is represented mathematically by a performance function that is positive for satisfactory performance of the structure, negative for unsatisfactory, and 0.0 at the transition point of the limit state being investigated. As an example, the performance function can be defined with respect to the capacity of the structure, R, and the demand on the structure, L. With respect to the capacity and demand, the performance function becomes

$$g(\boldsymbol{X}) = R - L \tag{2.11}$$

with X_1 equal to L and X_2 equal to R. The Equation 2.11 difference is sometimes referred to as the margin of safety. Using this definition of the performance function, satisfactory performance occurs when the capacity *(R)* exceeds the demand *(L)*, and unsatisfactory performance occurs when the demand *(L)* meets or exceeds the capacity *(R)*. The limit state occurs when the demand is balanced by the capacity. This can be related to the probabilities of whether the system performance is satisfactory or unsatisfactory (Figure 2-1). Given that the two variables R and L are each defined by a mean, a variance (equal to the square of the standard deviation) and a distribution (e.g., normal, lognormal), the *PUP* is the portion of the resulting distribution of (R-L) that falls below zero, as depicted and labeled in Figure 2-1. Since it is a ULS, the *PUP* is also referred to as Probability of Failure, P_f, in the civil engineering literature. Note that since this is a probability density function (PDF or ϕ), the area under the (R-L) distribution is equal to 1.0, as are each of the PDF areas under the R and L distributions.

Figure 2-1. Capacity vs. demand related to the *PUP* (after Nowak and Collins [2013]).

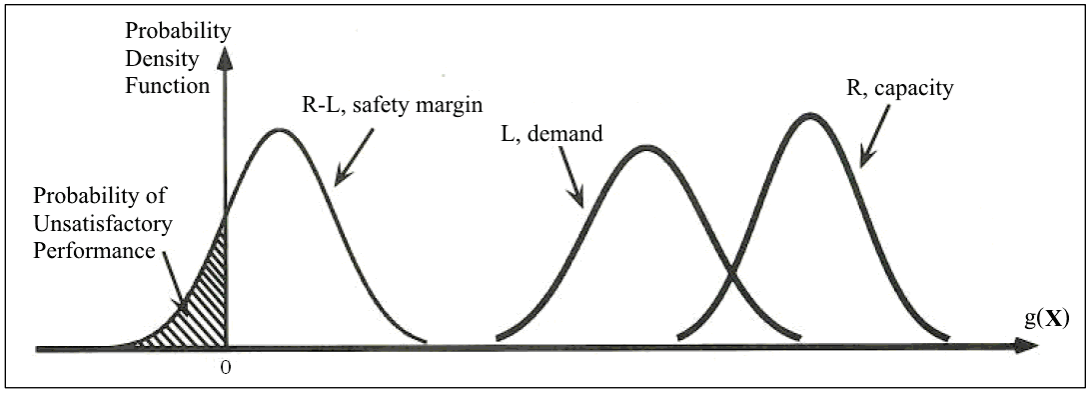

The first step in the computation of the *PUP* value (and a corresponding β) for each limit state is to apply the Hasofer-Lind approach (Hasofer and Lind 1974) of reformulating the problem in Gaussian variate space. This space is also known as the normalized, Normal-Gaussian distribution space. Generalizing, the j-dimensional space of the vector $\boldsymbol{X}$ defining random variables (X_1, X_2, …, X_j) of loads and resistances is first transformed to a vector space designated $\boldsymbol{X}'$ by the normalization

$$x'_i = \frac{x_i - \mu_{xi}}{\sigma_{xi}} \tag{2.12}$$

This transformed variable x'_i is described as a transformed basic variable (Baecher and Christian 2003) or as a reduced variable (Ellingwood[5]). Transformed basic variables have zero means and unit standard deviations (Baecher and Christian 2003). They are dimensionless variables. Rearranging, Equation 2.12 becomes

$$x_i = \mu_{xi} + x'_i * \sigma_{xi} \tag{2.13}$$

Used in this context, x'_i may be interpreted as the number of standard deviations x_i differs from mean $\mu_{x\,i}$; x'_i is expressed as a decimal fraction.

Plan view for a two-variate (i.e., X_1 and X_2) problem, the resulting transformed basic variable space of X'_1 and X'_2 (with subscript i = 1 and 2 in Equation 2.12), is shown in Figure 2-2(a) The concentric, blue circles shown in this figure represent the radially symmetric, normalized, Normal-Gaussian PDF distribution. Figure 2-2(b) shows a cross section passing through the origin, designated as I-I in Figure 2-2(a). For this two-dimensional (2-D) transformed basic variable space, the PDF has a peak value of 0.1591 the origin. The I-I cross section Figure 2-2(b) of the two variate, normalized, Normal-Gaussian PDF distribution is symmetric about its Figure 2-2(a) center (of $x'_1 = 0$, $x'_2 = 0$) having a peak value of 0.1591. This two-variate, peak PDF value is equal to $(0.3989)^2$: the square of the PDF value at the origin of a single normalized, Normal-Gaussian variate.[6] Figure 2-3 shows a three-dimensional (3-D) rendering of this Figure 2-2.a PDF distribution for a 2-D transformed variate space. Again, note the decreasing magnitude of the PDF values with increased distance in any direction away from the origin in this transformed space in Figure 2-2(b) and Figure 2-3.

[5] Ellingwood. B. R. 2015. *Procedures for Developing Reliability-Based Load Criteria for Hydraulic Steel and Concrete Structures.* Final letter report submitted to the URS Group, Inc. US Army Corps of Engineers.

NOTE: From this point forward, the document will be referred to or cited as "Ellingwood."

[6] Generalizing for *j*-variate space (where *j* is the number of variables), the normalized Normal-Gaussian PDF distribution possess a peak PDF value of $(0.3989)^j$ at its origin. The more variables, the lower the peak PDF value will be.

Figure 2-2. The normalized, Normal-Gaussian distribution for two independent variables, X_1 and X_2.

(a) Plan view of the transformed basic variable space for the variables X'_1 and X'_2 and response surface for a single limit state – overhead view.

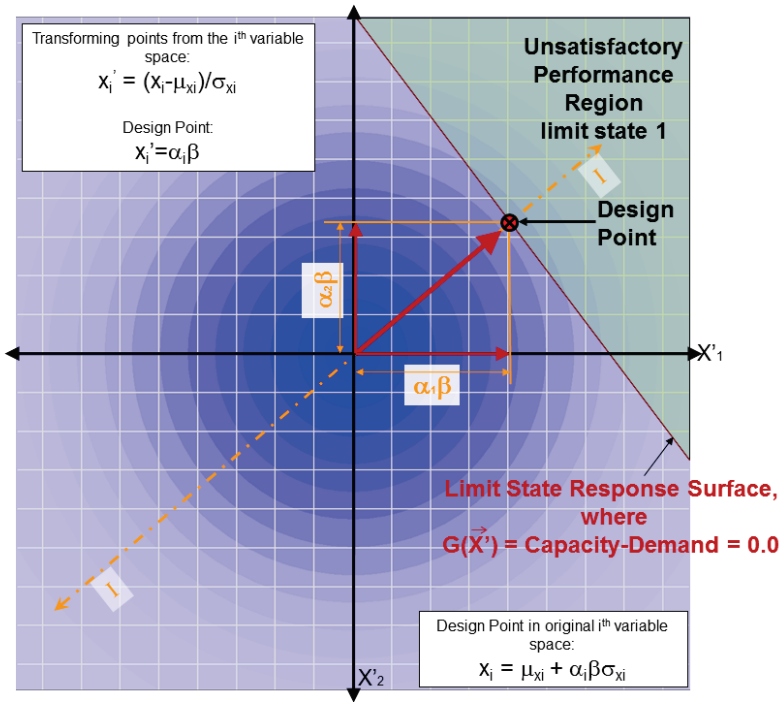

(b) The PDF distribution for cross sectional I-I passing through the origin.

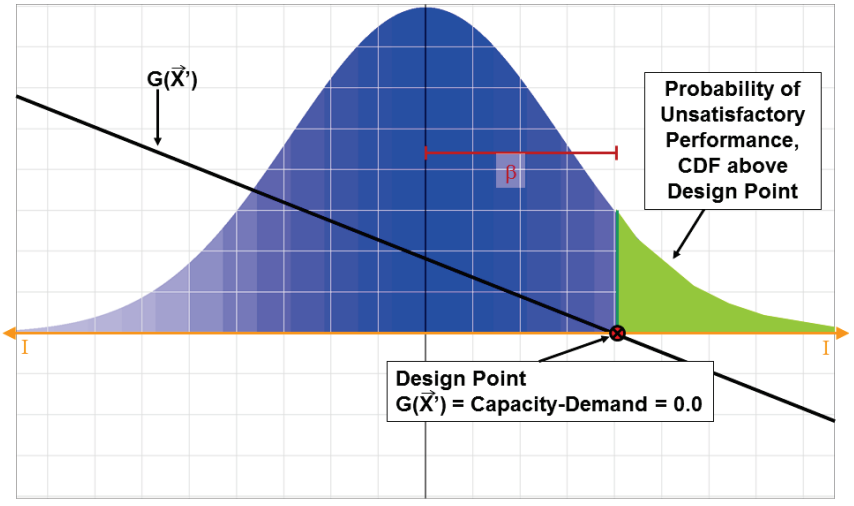

Figure 2-3. A 3-D rendering of a normalized, Normal-Gaussian PDF distribution for two independent variables, X_1 and X_2.

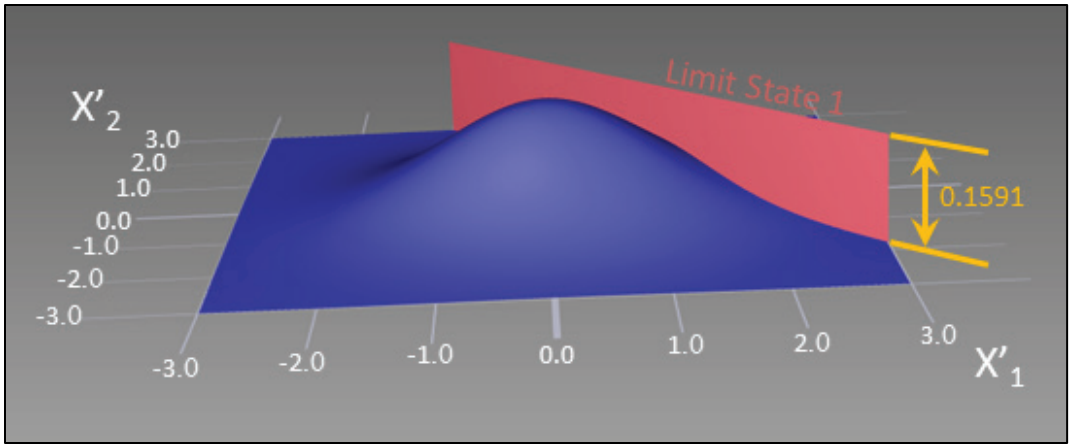

The volume under the entire Figure 2-3, 3-D PDF is 1.0. The PDF plot shown in this figure is scaled to a peak value of 0.1591 at $x'_1 = 0$, $x'_2 = 0$. The vertical plane (in red) shows the location of the limit state 1 response surface $g(X') = 0$. The height of the vertical red plane is terminated in this figure so that it is at this same height of 0.1591 as the peak PDF value. Each X'_i axis ($i = 1, 2$) is labeled using scalar values (e.g., numbers like 2.15 along an axis in this figure). Recall from the definition of x'_i by Equation 2.13 that the value of x'_i expresses the number of standard deviations σ_{xi} that a point x_i is from the mean value μ_{xi}, where x_i is given in basic variable coordinates.

The normalized, Normal-Gaussian distribution space for the example two-variable space of X'_1 and X'_2 is plotted to plus and minus 3.0 standard deviations from the mean in Figure 2-3 and many subsequent normalized, Normal-Gaussian distribution space figures in this report. Accuracy considerations in *PUP* computations by numerical method may require the variable space be extended to as much as plus and minus 8 standard deviations from the mean. This accuracy consideration will be assessed when performing example problems.

The advantage of analyzing the $g(\boldsymbol{X}) = 0$ problem in the transformed basic variable space of Figure 2-2(a) is two-fold: (1) Normal-Gaussian distribution relationships may be applied and (2) the variable axes are orthogonal; thus, the transformed variables are independent (i.e., uncorrelated).

A linear limit state response surface is depicted in Figure 2-2(a) where $g(\boldsymbol{X}')$ of capacity and demand, $(R'\text{-}L')$, is equal to zero in the transformed basic variable space. The closest distance in transformed basic variable space to the response surface $g(\boldsymbol{X}') = 0$ is designated by a unit vector times a scalar β (designated by the red vector emanating from the origin in Figure 2-2(a). The scalar β is designated as the reliability index. Its vector projection onto the X'_1 and X'_2 axes are designated as the directional cosine α_1 times β and α_2 times β, respectively, with their lengths labeled in orange in Figure 2-2(a) along each axis.

The Figure 2-2(a) point on the limit state response surface of $g(\boldsymbol{X}') = 0$ that is closest to the origin of transformed basic variable space to the response surface $g(\boldsymbol{X}') = 0$ is designated as the design point. This point is shown as a red dot and is labeled as the design point in Figures 2.2(a) and 2.2(b). Observe in Figure 2-2(a) that the unit vector times a scalar β is orthogonal to the limit state response surface at the design point. It is a point (red dot) on the limit state response surface at which the probability density of the joint random variables is greatest, as seen by the Figure 2-4 PDF (red) cross-section view. The red vector emanating from the origin of this transformed basic variable space is the unit vector times the scalar β.

Figure 2-4. Cross section along the position of the limit state response surface through the PDF distribution in a 3-D rendering and the location of the design point — view from underneath.

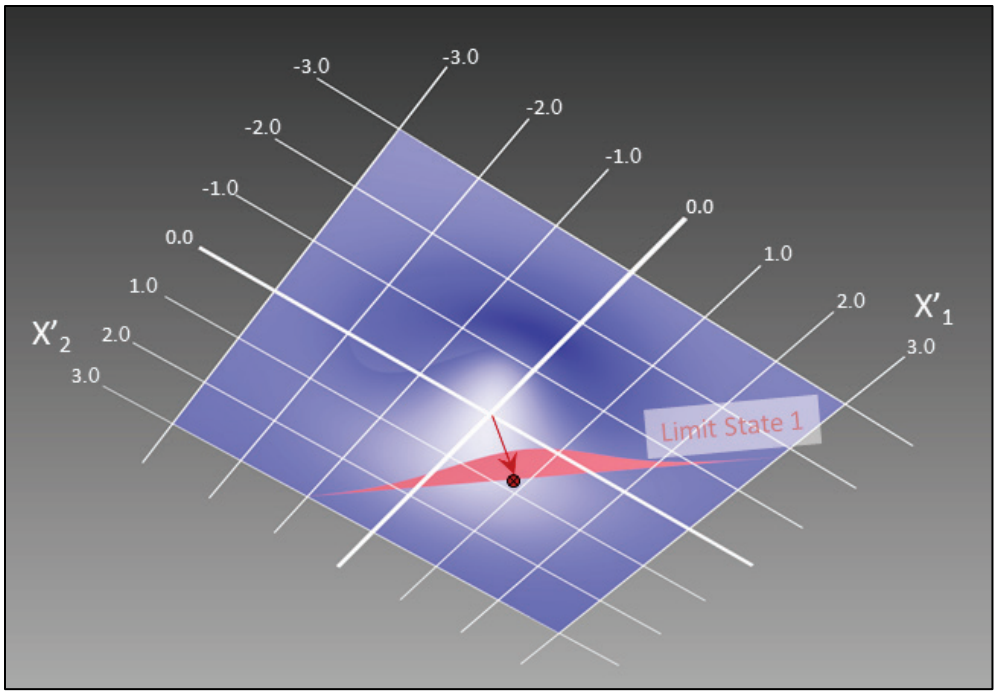

In transformed basic variable space $\boldsymbol{X}'_i$ of Figure 2-2.a, the design point is at position

$$x'_i = \alpha_i * \beta_i \tag{2.14}$$

and in the basic random variable space $\boldsymbol{X}_i$ the design point is located at

$$x_i = \mu_{xi} + \alpha_i * \beta_i * \sigma_{xi} \tag{2.15}$$

The cross section designated I-I in Figure 2-2(a) and shown in Figure 2-2(b) also identifies the position of the design point.

For a single planar response surface at a distance of magnitude β from the origin (i.e., $x'_1 = 0$, $x'_2 = 0$) in the transformed space to the design point, the *PUP* value is determined from the Cumulative Distribution Function (CDF) of β, $CDF(\beta)$, value by

$$PUP = 1 - CDF(\beta) \tag{2.16}$$

with the $CDF(\beta)$ being computed using the standard statistical tabulated data for a normalized, one-dimensional (1-D), Normal-Gaussian distribution variate or by using normal distribution functions that are available in, for example, Excel spreadsheet software. In this evaluation, a PDF with a maximum value of 0.3989 at the origin of the $x' = 0$, normalized, Normal-Gaussian PDF distribution is used (Figure 2-5). The $CDF(\beta)$ is equal to the integral of this PDF from negative infinity up to $X' = 0$ plus β (using the reduced coordinates with a unit standard deviation), as depicted in Figure 1.5. This simplified computational approach avoids the need to perform the sometimes-complex numerical integration of the Figure 2-2(a) PDF volume designated as the unsatisfactory performance region limit state 1 and identified as the olive-green region in this figure. In this computation, the PFD distribution has a peak value of 0.3989 at its origin (i.e., $x' = 0$) in transformed space of Figure 2-5. The value of the CDF is computed using the value for β associated with the design point (discussed in preceding paragraphs regarding Figure 2-2).

Figure 2-5. PDF and CDF for a normalized, Normal-Gaussian single variate.

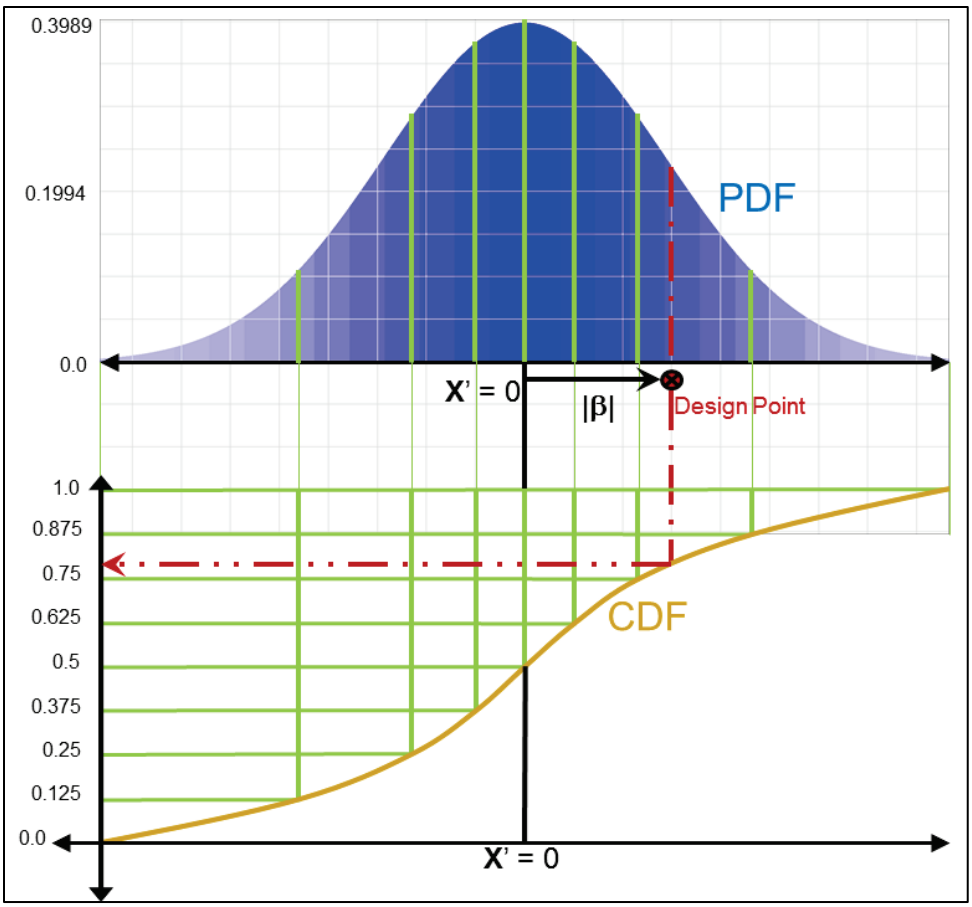

In summary, the Hasofer-Lind transformation simplifies the computational process for the PDF value and for the β value of a single limit state response surface. Its advantage is that all variables are transformed into normalized, Normal-Gaussian variate space, and these transformed variables are independent of one another.

2.6 The interrelationship between LRFD and reliability index for a single Ultimate Limit State (ULS)

The interrelationship between reliability theory and load and resistance factors used in an LRFD methodology is derived by returning to the simple ULS example of Figure 2-1 and Equation 2.11. The single limit state performance function is defined by setting Equation 2.11 equal to zero:

$$g(\boldsymbol{X}) = (R - L) = 0 \tag{2.17}$$

where R is the capacity (i.e., $X_2 = R$) and L is demand (i.e., $X_1 = L$). Recall that when $(R\text{-}L) < 0$, failure occurs. To relate the reliability index to load

and resistance factors, Ellingwood starts by expressing the limit state response surface in reduced transformed basic variable space (also known as reduced coordinates). The limit state response surface is transformed using the equations

$$r = \frac{(R-\mu_R)}{\sigma_R} \tag{2.18}$$

where r is the normalized variable for resistance in reduced coordinates, R is the basic variable, μ_R is the mean value of R, and σ_R is its standard deviation. Similarly, the reduced coordinates for the load is

$$l = \frac{(L-\mu_L)}{\sigma_L} \tag{2.19}$$

where l is the normalized variable for load in reduced coordinates, L is the basic variable, μ_L is the mean value of L, and σ_L is its standard deviation. Rearranging, Equations 2.18 and 2.19 become

$$R = \mu_R + r * \sigma_R \tag{2.20}$$

$$L = \mu_L + l * \sigma_L \tag{2.21}$$

Introducing Equations 2.20 and 2.21 to the limit state response surface Equation 2.17 yields

$$g(X) = g(R, L) = g(r, l) = (\mu_R + r * \sigma_R) - (\mu_L + l * \sigma_L) = 0 \tag{2.22}$$

Rearranging,

$$g(r, l) = (\mu_R - \mu_L) + (r * \sigma_R - l * \sigma_L) = 0 \tag{2.23}$$

Figure 2-6 shows the limit state response surface of Equation 2.23, $g(r,l) = 0$ in the 2-D, transformed basic variable space. Observe Equation 2.23 represents a straight line in r, l space.

Figure 2-6. Reliability Index defined as the shortest distance from the origin of the transformed basic variable space to the design point on the limit state response surface function g(*r,l*) (after Nowak and Collins [2013]).

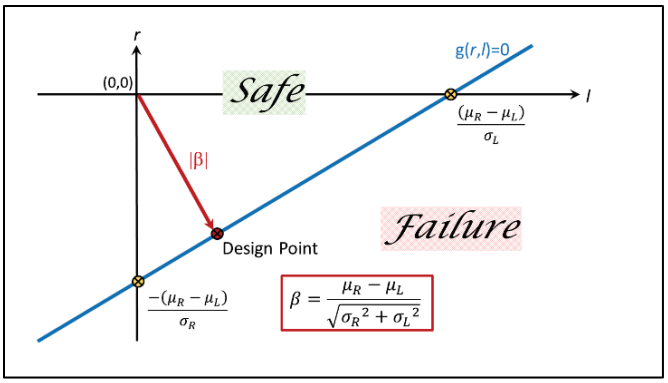

One intercept located along the transformed basic variable axis r is obtained by setting r = 0 in equation 2.23 and solving for l. This results in

$$l = \frac{(\mu_R - \mu_L)}{\sigma_L} \tag{2.24}$$

and the other intercept located along the transformed basic variable axis l is obtained by setting l = 0 in equation 2.23 and solving for r. This results in

$$r = \frac{-(\mu_R - \mu_L)}{\sigma_R} \tag{2.25}$$

These two axis intercepts of l and r axes are identified in Figure 2-6.

Using geometry of Figure 2-6, Nowak and Collins (2013) calculated the Reliability Index as the shortest distance from the origin of the transformed basic variable space to the g(r,l) limit state response surface (Equation 2.23) to be

$$\beta = \frac{\mu_R - \mu_L}{\sqrt{\sigma_R{}^2 + \sigma_L{}^2}} \tag{2.26}$$

Recall that β is a scalar value.

The Reliability Index is related to the *PUP* (equivalently, the P_f for the ULS) by

$$\beta = -\Phi^{-1}(PUP) \tag{2.27a}$$

as well as by

$$\beta = \Phi^{-1}(1 - PUP) \tag{2.27b}$$

with

$$PUP = \Phi(-\beta) \tag{2.28}$$

The safe region of satisfactory performance occurs when the capacity *(R)* exceeds the demand *(L)*. It is the region located above the blue g(*r,l*) = 0 line in Figure 2-6. Conversely, unsatisfactory performance occurs when *L* meets or exceeds *R*. It is the region located below the blue g(*r,l*) = 0 line in this figure.

Ellingwood gives the design point in transformed basic variable (i.e., reduced coordinate) space as

$$r = -\alpha_R * \beta \tag{2.29}$$

and

$$l = \alpha_L * \beta \tag{2.30}$$

where α_L and α_R are the directional cosines for *L* and *R*, respectively. Figure 2-6 supports this observation. Recognizing the (orange) vector decomposition of the red vector shown in Figure 2-2(a), a unit vector times a scalar β value, to the X'_1 and X'_2 axes, the scalar value of β is

$$\beta^2 = (\alpha_R)^2 * \beta^2 + (\alpha_L)^2 * \beta^2 \tag{2.31}$$

Dividing through by β^2,

$$(1)^2 = {\alpha_R}^2 + {\alpha_L}^2 \tag{2.32}$$

In its most general LRFD form for the basic variable coordinate space of a single limit state response surface is

$$R \geq L \tag{2.33}$$

Introducing Equations 2.20, 2.21, 2.29, and 2.30,

$$\mu_R - \alpha_R * \beta * \sigma_R \geq \mu_L + \alpha_L * \beta * \sigma_L \quad (2.34)$$

Recall that the COV is equal to the standard deviation for the variable divided by its mean value. Introducing the COV for variable *L* and *R*, Equation 2.34 becomes

$$\mu_R * (1 - \alpha_R * \beta * COV_R) \geq \mu_L * (1 + \alpha_L * \beta * COV_L) \quad (2.35)$$

This equation expresses the requirement for a reliability-based design for a single limit state response surface. The corresponding *PUP* value is calculated by Equation 2.28. The LRFD resistance factor is designated φ_R and defined as the term contained within the left-hand side (LHS) parenthesis:

$$\varphi_R = (1 - \alpha_R * \beta * COV_R) \quad (2.36)$$

Similarly, the LRFD load factor is designated γ_L and defined as the term contained within the right-hand side (RHS) parenthesis:

$$\gamma_L = (1 + \alpha_L * \beta * COV_L) \quad (2.37)$$

Recall that equations presented thus far are for *R* and *L* variables, which are normally distributed. Reviewing Equation 2.35 demonstrates that these resistance and load factors of φ_R and γ_L, respectively, are applied to the mean values of *R* and *L*.

$$\mu_R * \varphi_R \geq \mu_L * \gamma_L \quad (2.38)$$

In the specific application of LRFD to building systems, Ellingwood et al. (1982) observe that the term in parenthesis on the LHS of Equation 2.35 and on the RHS of Equation 2.36 is replaced with

$$\varphi_R = e^{-\alpha_R * \beta * COV_R} \quad (2.39)$$

thereby describing an *R* with a lognormal distribution. Similarly, describing *L* with a lognormal distribution:

$$\gamma_L = e^{\alpha_L * \beta * COV_L} \quad (2.40)$$

Another feature to be considered in a reliability analysis is to account for the difference between mean resistance μ_R and nominal resistance R_n and between mean load μ_L and nominal load L_{ni}. Nowak and Collins (2013) provide an example as to how they are related for R and L to factored loads (e.g., $\varphi_R * R_n$ and $\gamma_{Li} * L_{ni}$, respectively) as shown in Figures 2-7 and 2-8, respectively. They point out that in some recent developments in building design codes, the factored load was taken so that the shaded area in Figure 2-7 was the same for all dead and live building loads components. The factored resistance and factored load plotted in these figures assume the typical case of a φ_R less than 1 and γ_{Li} for i = 1 to loading j, to be greater than 1 for each load.

Figure 2-7. Relationships among nominal load, mean load, and factored load (after Nowak and Collins [2013]).

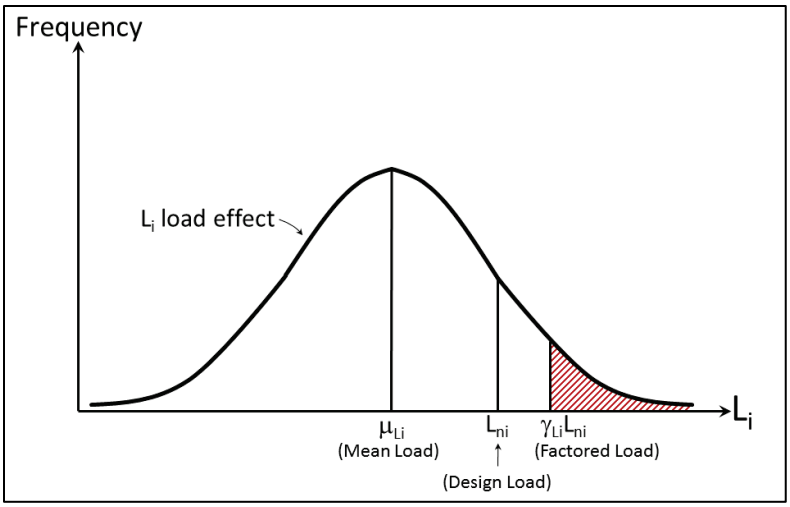

Figure 2-8. Relationships among nominal resistance, mean resistance, and factored resistance (after Nowak and Collins [2013]).

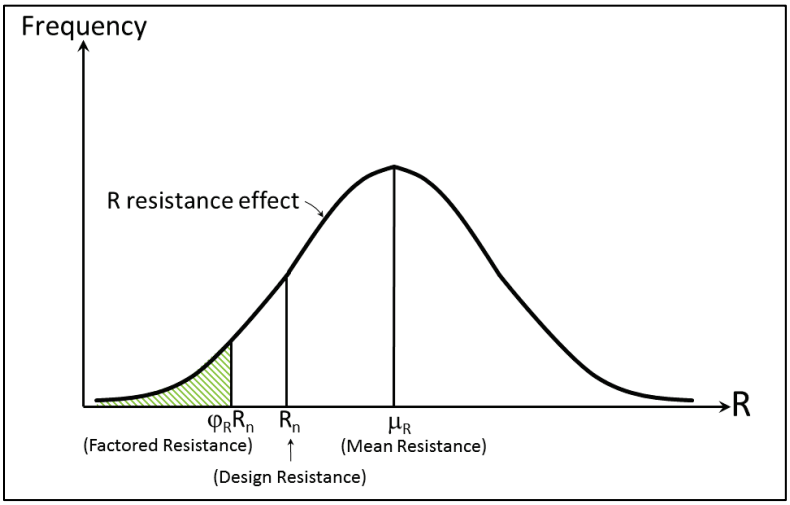

To accommodate the situations demonstrated in these two figures, engineers (e.g., Nowak and Collins 2013; Ellingwood; Fenton et al. 2016) are introducing a bias factor into the resistance and load factors of φ_R and γ_{Li} Equations of 2.36 and 2.37, respectively. The bias factor, λ, is defined as

$$\lambda = \frac{mean\ load\ value}{nominal\ (design)\ value} \tag{2.41}$$

Recall that Fenton et al. (2016) prefers to use the term characteristic (design) value in the denominator rather than nominal (design) value. Thus, for the resistance *R*, the bias factor is

$$\lambda_R = \frac{\mu_R}{R_n} \tag{2.42}$$

and for the ith load L_i, with i = 1 to j loads, each bias factor is

$$\lambda_{Li} = \frac{\mu_{Li}}{L_{ni}} \tag{2.43}$$

Thus, the LRFD resistance factor φ_R becomes

$$\varphi_R = \lambda_R * (1 - \alpha_R * \beta * COV_R) \tag{2.44}$$

and each load factor γ_{Li} becomes

$$\gamma_{Li} = \lambda_{Li} * (1 + \alpha_{Li} * \beta\ * COV_{Li}) \tag{2.45}$$

for *R* and *L* variables which are normally distributed. The generalized, governing LRFD equation for i = 1 to j loads is

$$\mu_R * \varphi_R\ \geq \sum_{i=1}^{j} \mu_{Li} * \gamma_{Li} \tag{2.46}$$

When *R* possesses a lognormal distribution, Ellingwood states that the resistance factor φ_R becomes

$$\varphi_R = \lambda_R * e^{-\alpha_R * \beta * COV_R} \tag{2.47}$$

For the two-variable problem being discussed in this section, i is set equal 1 for the single load case.

When L possesses a lognormal distribution, the load factor γ_L is

$$\gamma_L = \lambda_L * e^{\alpha_L * \beta * COV_L} \quad (2.48)$$

for the two-variable problem being discussed in this section with i set equal 1 for the single load case.

In summary, the load and resistance factors of φ_R and γ_{Li} (for i = 1 to j loads) depend on the values for β, the directional cosines α_R and α_{Li}, and the coefficients of variation COV_R and COV_{Li}, and the bias factors λ_R and λ_{Li}. Ellingwood observes that β was adopted as the reliability metric in first-generation LRFD criteria rather than a *PUP* value because β values are typically on the order of 2 to 5 while *PUP* values can be quite small, on the order of 1×10^{-4} or less.

2.7 A numerical procedure to calculate the reliability Index

A simplifying first step applied in the computation of β (and a corresponding *PUP* value) for each limit state is by using the Hasofer-Lind approach (Hasofer and Lind 1974) of transforming the problem into Gaussian variate space. This Figure 2-2(a) space is also known as the normalized, Normal-Gaussian distribution space. This space is dimensionless and has properties of symmetry and orthogonally, as well as cumulative properties for simple determination of probabilities.

Several techniques are available for calculating β, as well as the directional cosines of Figure 2-2, that define the closest design point among the various limit state response surfaces. Baecher and Christian (2003) discuss the attributes of the different techniques being for reliability analysis as well as the merits and deficiencies of each procedure. Based on experience gained during the development of the USACE CPGA-R software for reliability analysis of pile groups (Ebeling et al. 2013), procedures have been selected for possible use on the engineering problems discussed in this report:

- The First Order Second Moment (FOSM) Method. This method uses the first terms of a Taylor series expansion of the $G(\boldsymbol{X})$ performance function to estimate its expected value and variance.
- The Advanced Second Moment (ASM) Method. This is a numerical method for finding the minimum distance that a $G(\boldsymbol{X})$ performance function is from the origin of a defined vector space.

Examples of the application of FOSM procedure as applied in a reliability analysis of a slope are given in Chapter 13 of Duncan et al. (2014) and Chapter 14 of Baecher and Christian (2003). The ASM procedure is discussed in detail in the next subsection.

Alternatively, simulation methods may be used to directly estimate probabilities for exceeding these response surfaces. Simulation techniques are discussed in Ebeling et al. (2013) and Baecher and Christian (2003). The computed *PUP* value can then be converted into a β value. Simulation methods were relied upon in the USACE CPGA-R software for reliability analysis of pile groups (Ebeling et al. 2013). This approach is quite different from the FOSM and ASM methodologies (refer to Ebeling et al. 2013 for its details). It is also identified for possible usage, if deemed necessary.

2.7.1 Advanced Second Moment (ASM) for uncorrelated, normal distributions

The ASM technique, also called Advanced First Order Second Moment (AFOSM), is a method for finding the minimum distance that a capacity-vs.-demand surface, based on the function *G()*, is from the origin of a defined vector space. This differs from the FOSM technique, which approximates a nonlinear capacity-vs.-demand surface with a hyperplanar surface in multidimensional space (Melchers 1999), which forms a linear surface in 2-D space (i.e., considering two independent variables). The FOSM technique uses the linear definition of the capacity-vs.-demand surface to quickly estimate the closest surface point to the origin, without having to perform multiple iterations to find the actual nonlinear capacity-vs.-demand surface's closest point.

For a reliability analysis, the surface function is the limit state boundary function. Recall that this vector space, $\boldsymbol{X}$, can be transformed into the vector space $\boldsymbol{X}'$, where the probability of occurrence is based on the Euclidean distance from the origin. In this case, the distance is the β of the design with respect to that point (Ditlevsen 1981). The point (in the normalized vector space, $\boldsymbol{X}'$, Figure 2-2) on the surface $G(\boldsymbol{X}) = 0$ (where the design point has been transformed from X-space to X'-space) that is closest to the origin is called the design point. Values of β are shown in Table 2-1 and Figure 2-2, and the β value can be used to determine the probability that this point will be chosen from the variable distributions. In terms of reliability analysis, *PUP* can be given by $PUP = 1 - \Phi(\beta)$ for an arbitrary axis with a linear limit

state, where $\Phi()$ is the cumulative distribution function. Table 2-1 lists values of β and its corresponding *PUP* values.

Table 2-1. Reliability Index (β) and PUP – normal distribution.

β	$P_U = 1-\Phi(\beta)$
0	5.000000000000E-01
1	1.586552539315E-01
2	2.275013194818E-02
3	1.349898031630E-03
4	3.167124183678E-05
5	2.866515719235E-07
6	9.865877004245E-10
6.36	1.008768624189E-10
6.71	9.731215833142E-12
7	1.279865102788E-12
8	6.661338147751E-16
9	Out of range for a double-precision variable

The ASM technique works because any hyperplanar surface can be fully described by a directional cosine vector (α) and the distance from the origin (β) for the closest point on the hyperplanar surface (Figure 2-2(a)). The vector describing the resultant of all directional cosine vectors, α, also is identified in Figure 2-2(a). This resultant directional cosine vector (α) is perpendicular to the hyperplanar surface labeled as the ASM Response Surface (i.e., where $G(X) = 0$). This resultant directional cosine vector α is a unit vector, with the magnitude of each component vector along a variable X_i axis, $|\alpha_i|$, being a cosine value for that direction with respect to the unit vector α. The components of the directional cosine vector α_i multiplied by the distance, β, are shown for variables X_1 and X_2 in Figure 2-2(a) and lie along each respective axis. For the *x*-space, the vector *X*'s components that define the plane are given by

$$x_i = \mu_{xi} + \alpha_i * \beta_i * \sigma_{xi} \qquad (2.15 \text{ bis})$$

At the start of the reliability analysis, the directional cosine α is unknown. However, it can be estimated by determining the vector on the surface, $G(\boldsymbol{X})$, that is approaching a 0.0 value from the mean value at the fastest rate. The rate at which each component approaches the 0.0 value can be determined by computing the partial derivative of G with respect to each variable ($X1$, $X2$, ...) at the mean value.

Referring to Figure 2-2(b), which shows the 1-D cross section of a linear $G(\boldsymbol{X})$ surface, with particular attention paid to the region above the origin at the means of this 2-D normal space, a pair of partial derivatives are made numerically in the positive and negative direction of an individual axis resulting in a total of four partial derivatives for the Figure 2-2(a) two-variable problem. The direction along each variable axis with the steepest slope approaching $G(\boldsymbol{X})$ = 0.0 is selected for each variable as the direction of the vector. The magnitudes of each axis, $|\alpha_i|$, are computed according to Equation 2.50.

Recall that the response surface for vector $\boldsymbol{X}$ is defined by

$$G\left(\vec{X}\right) = 0.0 \tag{2.49}$$

This can be performed by setting

$$\alpha_i = \frac{\left(\frac{\partial G()}{\partial X_i}\right)\sigma_{X_i}}{\sqrt{\left[\sum_{i=1}^{n}\left(\frac{\partial G()}{\partial X_i}\right)^2 \sigma_{X_i}^2\right]}} \tag{2.50}$$

with the initial trial value for β set to 0.0 so that the initial vector $\boldsymbol{X}$ is composed of only the mean values. A numerical procedure, along with Equations 2.15, 2.49, and 2.50, is used to calculate the α_i values for each of the i variables.

When the directional cosine (α) has been determined, it is possible to determine β using numerical methods (e.g., the Regula-Falsi method) so that the current design point (vector $\boldsymbol{X}$) is on the response surface, where Equation 2.15 is satisfied (Figure 2-2(a).

For nonlinear performance functions, the current design point might not be the point with the minimum distance from the mean values. For this case, partial derivatives for each axis at the current design point (vector $\boldsymbol{X}$)

are computed (Equation 2.50) to determine the direction and magnitudes for a new directional cosine from the origin at the means. The β value is determined from Equation 2.15. This process is performed until the new β and the old β converge within a certain tolerance.

This solution might not reach the absolute minimum distance point to the response surface for particularly complex nonlinear surfaces, rather a local minima. Most engineering problems do not have particularly complex nonlinear response surfaces, so this ASM method will see widespread usage.

2.7.2 Dealing with non-normal distributions for X_i

To handle non-normal distributions, each non-normal distribution variable $\boldsymbol{X}$ must be changed to an equivalent normally distributed random variable $\boldsymbol{X}_{Normal}$. This is called the Rosenblatt transformation (Rosenblatt 1952). Rackwitz and Fiessler (1976 and 1978) impose two conditions on the equivalent normally distributed random variable that enable the determination of the two parameters of that distribution, μ_{Xi}^N and σ_{Xi}^N, as cited in Singh et al. (2007) and Nowak and Collins (2000, 2013). The CDFs and PDFs of the non-normal and normal distributions should be equivalent at the current design point for the performance function.

These conditions (CDF and PDF) can be expressed, respectively, in

$$\Phi\left(\frac{X_i-\mu_{Xi}^N}{\sigma_{Xi}^N}\right) = F_i(X_i) \tag{2.51}$$

$$\frac{1}{\sigma_{Xi}^N}\phi\left(\frac{X_i-\mu_{Xi}^N}{\sigma_{Xi}^N}\right) = f_i(X_i) \tag{2.52}$$

where F_i is the non-normal CDF, f_i is the non-normal PDF, Φ is the standard normal CDF, and ϕ is the standard normal PDF. From these conditions, it can be shown that the standard deviation and mean, respectively, are

$$\sigma_{Xi}^N = \frac{1}{f_i(X_i)}\phi\left(\frac{X_i-\mu_{Xi}^N}{\sigma_{Xi}^N}\right) = \frac{\phi\left(\Phi^{-1}[F_i(X_i)]\right)}{f_i(X_i)} \tag{2.53}$$

$$\mu_{Xi}^N = \mathrm{X}_i - \Phi^{-1}[F_i(X_i)] * \sigma_{Xi}^N \tag{2.54}$$

The PDF of a standard normal distribution is a continuously positive function. Bounded distributions including triangular PDFs are not. While it is possible to get equivalent CDF values between the standard normal distribution and a bounded non-normal distribution (Figure 2-9), it might be impossible to find an equivalent PDF between distributions. In this case, the standard deviation can be calculated, and the mean of the standard deviation varied to find the appropriate CDF value. The PDF in this case will be a close estimate at convergence.

Ang and Tang (1984) in their Example B.1 provided an example using annual maximum mile wind speed. This was modeled as a Type II asymptotic distribution of largest values. The CDF (Φ) of this distribution is displayed on the right side of Figure 2-9 while the CDF (Φ) of a normalized Gaussian distribution (which has a mean μ = 0.0 and standard deviation σ = 1.0) is shown on the left with positive X_{Normal} axis values growing from right to left. With fixed parameters of γ = 9.0 and β = 55 mph in the Type II asymptotic distribution equation (not shown), then for a velocity v = 60 mph, the CDF (Φ) of the Type II asymptotic distribution has a value of 0.633. This is an equivalent CDF (Φ) of the normalized Gaussian distribution at a distance of 0.38 standard deviation from the mean origin of the normalized Gaussian distribution.

Figure 2-9. Finding the position of equivalent cumulative probability for a normal distribution as from a non-normal distribution (after Ang and Tang [1984]).

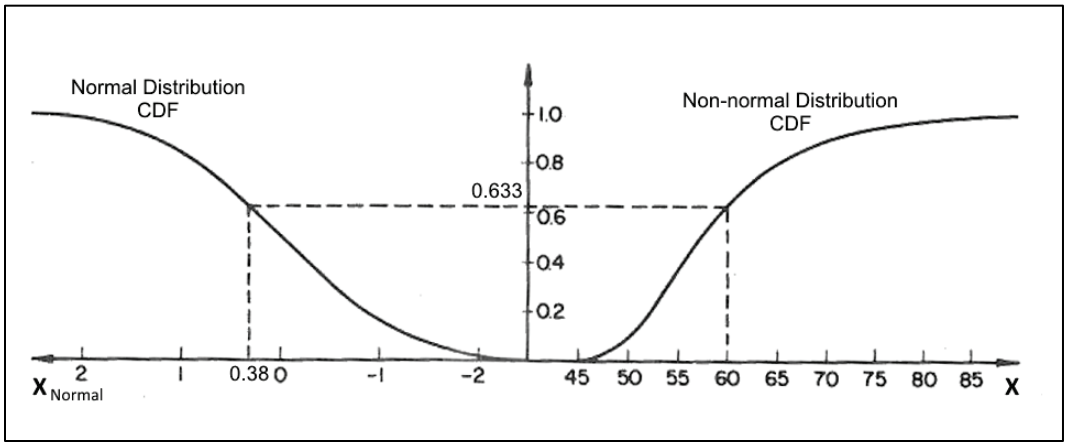

2.7.3 Dealing with correlated random variables X_1 and X_2

In certain situations, it is unrealistic to believe that variables chosen for a reliability analysis will be independent of one another. In these other instances, such as the case in which the variables are the soil material properties of the angle of internal friction and cohesion for soil layers,

variables might be related to some degree. For this discussion, a pair of variables (X_1 and X_2) is correlated with a correlation coefficient (ρ). If the two variables ($\boldsymbol{X}_i$ with i = 1, 2) have a standard normal distribution, they can be changed to a pair of non-correlated variables ($\boldsymbol{X}^*_i$) by solving for two eigenvalues and the corresponding eigenvectors as follows:

$$X_1^* = \frac{1}{2t}\left(\frac{X_1-\mu_{X_1}}{\sigma_{X_1}} + \frac{X_2-\mu_{X_2}}{\sigma_{X_2}}\right) \tag{2.55a}$$

$$X_2^* = \frac{1}{2t}\left(\frac{X_1-\mu_{X_1}}{\sigma_{X_1}} - \frac{X_2-\mu_{X_2}}{\sigma_{X_2}}\right) \tag{2.55b}$$

where $t = \sqrt{0.5}$. The variances for these two variables are equal to the eigenvalues (λ) as follows:

$$\sigma^2_{X_1^*} = \lambda_1 = 1 + \rho \tag{2.56a}$$

$$\sigma^2_{X_2^*} = \lambda_2 = 1 - \rho \tag{2.56b}$$

The directional cosines for these newly uncorrelated values must be determined from the original correlated values using

$$\alpha_{X_1^*} = \frac{\left[\left(\frac{\partial G()}{\partial V_1}\right)t\sigma_{X_1} + \left(\frac{\partial G()}{\partial V_2}\right)t\sigma_{X_2}\sqrt{1+\rho}\right]}{\left[\left(\frac{\partial G()}{\partial X_1}\right)^2\sigma^2_{X_1} + \left(\frac{\partial G()}{\partial X_2}\right)^2\sigma^2_{X_2} + 2\rho\left(\frac{\partial G()}{\partial X_1}\right)\left(\frac{\partial G()}{\partial X_2}\right)\sigma_{X_1}\sigma_{X_2}\right]^{1/2}} \tag{2.57a}$$

$$\alpha_{X_2^*} = \frac{\left[\left(\frac{\partial G()}{\partial X_1}\right)t\sigma_{X_1} - \left(\frac{\partial G()}{\partial X_2}\right)t\sigma_{X_2}\sqrt{1-\rho}\right]}{\left[\left(\frac{\partial G()}{\partial X_1}\right)^2\sigma^2_{X_1} + \left(\frac{\partial G()}{\partial X_2}\right)^2\sigma^2_{X_2} + 2\rho\left(\frac{\partial G()}{\partial X_1}\right)\left(\frac{\partial G()}{\partial X_2}\right)\sigma_{X_1}\sigma_{X_2}\right]^{1/2}} \tag{2.57b}$$

and

$$X_1 = \mu_{X_1} - \sigma_{X_1}t\beta\left(\alpha_{X_1^*}\sqrt{\lambda_1} + \alpha_{X_2^*}\sqrt{\lambda_2}\right) \tag{2.58a}$$

$$X_2 = \mu_{X_2} - \sigma_{X_2}t\beta\left(\alpha_{X_1^*}\sqrt{\lambda_1} - \alpha_{X_2^*}\sqrt{\lambda_2}\right) \tag{2.58b}$$

Ditlevsen (1981) presents a detailed derivation of these equations for transforming correlated random variables into corresponding non-correlated random values.

2.7.4 ASM algorithm

The ASM algorithm presented in this subsection has been modified from the AFOSM method to include ones for working with non-normal distributions and correlated random variables.

The ASM algorithm

1. Assign the mean value for each random variable as a starting design point value (i.e., $(X_1, X_2,..., X_i) = (\mu_1, \mu_2,..., \mu_i)$).
2. Compute the standard deviation and mean of the equivalent normal distribution for each non-normal random variable by using Equations 2.53 and 2.54 or by adjusting the mean so that an equivalent CDF is determined for the standard deviation of the original data.
3. Compute the partial derivative, $\partial G()/\partial X_i$, of the performance function with respect to each non-correlated random variable evaluated at the design point as needed to satisfy Equation 2.50.
4. Compute the directional cosine, α_i, for each non-correlated random variable as given in Equation 2.50 at the design point. For correlated pairs of random variables, Equations 2.57a and b should be used.
5. Compute β by substituting Equation 2.50 for non-correlated random variables and Equations 2.57a and b for correlated random variables into the $G()$ performance function of the vector $\vec{X}$ (Equation 2.15) and satisfying the limit state $G() = 0$ (Equation 2.49) in using a numerical root-finding method.
6. Compute a new estimate of the design point by substituting the resulting β obtained in Step 5 into Equation 2.15 for non-correlated random variables and Equations 2.58a and b for correlated random variables.
7. Repeat Steps 2 through 6 until β converges within an acceptable tolerance, δ.

2.7.5 ASM caveats

The ASM method estimates the actual *PUP*. It is accurate only if the limit state, response surface, where $G() = 0$, is linear and approximate when the limit state, response surface is nonlinear. The response surface might be nonlinear if the $G()$ function is nonlinear or if multiple limits states are included in the $G()$ function (as discussed in the next section using Figure 2-10 as an example).

2.8 Numerical methods for the calculation of β and load and resistance factors given uncorrelated load and resistance PDF curves

Several numerical methods that may be used for calculating Load and Resistance scale factors for a single limit state are described in Appendix C of Ebeling and White (2021). It is important to recognize the principal limitations for the numerical procedures discussed in this report's appendix:

1. They require a mathematically defined, continuous probability density function (PDF) distributions for load and for resistance.
2. These procedures also require that load and resistance be uncorrelated. Independent load and resistance variables satisfy this requirement.

The first numerical method discussed in Section C.2 of Ebeling and White (2021) was developed by Nowak and Collins (2013), and was restricted to single limit states, as the Load and Resistance units and distributions vary between limit states. The procedure was based on the Rackwitz and Fiessler (1976, 1978) procedure for mapping a non-normal distribution to a normal distribution with unit area. This procedure works well with continuous data and less well with histogram data because the routine requires computation of matching CDF and PDF data for the distribution with the normal distribution. This procedure allows for the scaling of the resistance distribution with respect to a fixed load distribution, adjusting the (R-L) distribution for a target value of β and its associated *PUP*.

This Nowak and Collins (2013) numerical procedure was adapted for use in solving problems involving independent load and resistance variables discussed in Ebeling and White (2021). It stands in contrast with the ASM procedure in that ASM determines a β value that corresponds to the *PUP* given fixed load and resistance distributions. Load and resistance factors are computed in the ASM approach from a design point that resides on the limit state response surface. These load and resistance factors guarantee the *PUP* for the computed value for β.

To summarize, the ASM method takes resistance and load distributions and calculates a β value for a limit state to compute load and resistance factors. In contrast, the Nowak and Collins (2013) numerical procedure iteratively scales the resistance distribution while constraining the load

distribution as fixed in reliability space allowing for calculation of load and resistance factors for a specified β value.

A supplemental procedure is discussed in Section C.3 of Ebeling and White (2021) that recognizes the fact that load and resistance factors are constants and therefore their ratio is constant. It is simpler to solve for this ratio of these two factors and then to calculate the partial load safety factor given a specified partial resistance safety factor. This safety factor ratio may be computed using the numerical procedure outlined in their Section C.2.

A numerical procedure to calculate β given variable load and resistance with distributions, which may have partial load and resistance safety factors applied, is presented to be used as a verification step (Section C.4 of Ebeling and White [2021]). To verify the computation of partial safety factors, this procedure is used by calculating β from the partial load and resistance factors applied to the load and resistance distributions. This value should then match the target β value. This second numerical procedure is also adapted to this R&D effort from a procedure described in Nowak and Collins (2013).

Section C.5 of Ebeling and White (2021) summarizes a reliability based numerical procedure for computing a value for Reliability Index β following the steps outlined in Nowak (1999). Professor Nowak originally developed this procedure over a number of years with a focus on its application to LRFD based bridge design (Nowak and Lind 1979: Nowak, 1999; Nowak and Collins 2000, 2013).

Section C.6 of Ebeling and White (2021) describes a Gaussian function superposition approach of numerically fitting normalized normal distribution functions to a non-normal PDF and computing a value for Reliability index β. This approach uses several summed Gaussian distribution values for each PDF value. The error between the non-normal distribution PDF and the summed Gaussian distributions PDF is minimized. The attractiveness of this analysis procedure is that it may be used on any form of PDF yet be able to determine a value for β that may be used in a Reliability analysis for determination of load and resistance factors.

2.9 Individual limit state procedure for computing load and resistance distributions from material properties and determining load factors

The following procedure provides a method based on Monte Carlo simulations with material variables for determination of LRFD load factors. This procedure was originally devised by Ebeling and White (2021) for the reliability analysis of a T-Wall retaining earth and is buttressed by earth, analytically modeled as a three-wedge retaining structure, with driving, structural, and resisting wedges. The Mohr-Coulomb shear strength parameters of effective angles of internal friction (ϕ'_1, ϕ'_2, and ϕ'_3) for the soils of the three respective wedges were assumed to be normally distributed, independent variables. A traditional Reliability-based (R-L) formulation of loads applied to the structural wedge containing the T-Wall was devised. Monte Carlo simulations were conducted to develop a database of corresponding resistance and load values which were then histogrammed to form PDF distributions. The resulting R and L distributions were observed to be non-normal because of the limit state computation method to calculate R and L from the three-wedge solution. Furthermore, because the three-wedge solution method was used to compute load and resistance relative to each other, the distributions exhibited correlation. Rather than attempt to sample the load and resistance distributions and try to match the Pearson (1895) correlation coefficient, the original captured samples of corresponding R and L are used to calculate a ratio of Resistance Scale Factor (R_{SF}) to the Load Scale Factor (L_{SF}). Form this ratio, and given a specified R_{SF} value, an L_{SF} value can be computed using the routine mentioned in Section 2.7 and described in Appendix C, section C.3 of Ebeling and White (2021). This procedure is referred to as the Single Limit State Simulation Fixed Load Procedure because the load distribution remains fixed while the resistance distribution is scaled.

1. Create *Gz()* function for the limit state(s) that returns total Resistance (R), total Load (L), and conditional value of unsatisfactory performance (where unsatisfactory performance occurs when $R\text{-}L < 0.0$)
2. For geotechnical design, calculate the slip plane angle for the current design conditions and determine the geo-statistical variability of soil properties (e.g., Mohr-Coulomb effective angle of internal friction) for each soil wedge (Driving, Structural, Resisting).
3. For a certain number of samples ($N_{samples}$), generate simulation soil properties and collect *Gz()* results, maintaining the order of the results so

that *R[index]* corresponds to *L[index]*. Maintaining the order means that the distributions and any correlations are included in the sample data.

4. Calculate $\mu_{Resistance}$ and μ_{Load} for the *R[]* and *L[]* simulation results.
5. For verification, calculate the $PUP_{Initial}$ for the full simulation taking the number of simulations with unsatisfactory performance and dividing by the total number of simulations. This $PUP_{Initial}$ can be run through the inverse CDF function for a Normal Distribution to arrive at a somewhat arbitrary $\beta_{Initial}$ value.
6. A β_{target} value for a normal distribution is given that can be used to determine PUP_{target}.
7. Generate a function given *R[]*, *L[]*, PUP_{target}, as well as a scale factor for Resistance R_{SF}. This function calculates the unsatisfactory performance

$$PUP_{RSF} = \frac{\sum_{i=1}^{N_{samples}} \{(R[i] * R_{SF}) - L[i]\} \begin{matrix} 0: > 0.0 \\ 1: < 0.0 \end{matrix}}{N_{samples}} \tag{2.59}$$

To judge how close PUP_{RSF} is to PUP_{target}, the function returns a value $\left|PUP_{RSF} - PUP_{target}\right|$. This value is 0.0 when PUP_{RSF} is equal to PUP_{target} and greater than 0.0 otherwise.

8. Use a numerical procedure to find a value of R_{SF} that minimizes the step 7 function. Because the function returns a minimal value of 0.0 when PUP_{RSF} is equal to PUP_{target}, the resulting value of R_{SF} is the scale factor from the original Resistance distribution *R[]* to the Resistance distribution that, combined with the original Load distribution *L[]* has the same *PUP* as PUP_{target}.
9. The R_{SF} value is a scale factor for the current design's Resistance Distribution that satisfies the PUP_{target} goal. The $\mu_{Resistance}$ and μ_{Load} values are the means of the distributions that may be correlated; therefore, their values have the same level of correlation. The deterministic design load (d_{Load}) needs to be scaled by L_{SF} to match the scaled resistance.

$$R_{sf} * \mu_{Resistance} - L_{SF} * d_{Load} = 0.0 \tag{2.60}$$

$$L_{SF} = \frac{\mu_{Resistance} * R_{SF}}{d_{Load}} \tag{2.61}$$

10. According to the Limit State equation, the Resistance to be designed for (R_{Design}) is therefore

$$R_{Design} \geq L_{SF} * d_{Load} \tag{2.62}$$

The product of the load scale factor times the design load value (i.e., the right-hand side in this equation) is viewed as the value of minimum mean capacity required to achieve the PUP_{target} value. Thus, this minimal design resistance R_{Design} is the exact minimum mean resistance required to achieve the PUP_{target} capacity.

This procedure can be used for traditional LRFD, where the load and resistance distributions can be readily defined, although this is typically a trivial case that can be solved by analytical methods. This procedure becomes more important for issues where the resistance distribution can be calculated but is highly non-linear and/or is correlated to the load distribution. In this case, the procedure based on samples more accurately captures the behavior in the tails of the distributions, assuming that the design does not change the shape and dispersion rate of the distribution. It has been adapted for Reliability analysis and LRFD factor development of the batter pile-founded T-Wall flood mitigation structures, discussed in Chapter 7 of this technical report.

2.10 Proportioned load individual limit state procedure for computing load and resistance distributions from material properties and determining load factors

The following procedure provides a method based on Monte Carlo simulations with material variables for determination of LRFD load factors. This procedure was devised by Ebeling and White (2021) for the reliability analysis of a T-Wall that retains earth and is buttressed by earth, analytically modeled as a three-wedge retaining structure, with driving, structural, and resisting wedges. The Mohr-Coulomb shear strength parameters of effective angles of internal friction (ϕ'_1, ϕ'_2, and ϕ'_3) for the soils of the three respective wedges were assumed to be normally distributed, independent variables. A traditional Reliability-based (R-L) formulation of loads applied to the structural wedge containing the T-Wall was devised. Monte Carlo simulations were conducted to develop a database of corresponding resistance and load values which were then histogrammed to form PDF distributions. The resulting R and L distributions were observed to be non-normal because of the limit state computation method to calculate R and L from the three-wedge solution. Furthermore, because the three-wedge solution method was used to compute load and resistance relative to each other, the distributions exhibited correlation. Rather than attempt to sample the load and resistance distributions and try to match the Pearson (1895) correlation

coefficient, the original captured samples of corresponding R and L are used to calculate a ratio of Resistance Scale Factor (R_{SF}) to the Load Scale Factor (L_{SF}). From this ratio, and given a specified R_{SF} value, an L_{SF} value can be computed using the routine mentioned in Section 2.7 and described in Appendix C, section C.3 of Ebeling and White (2021). This procedure is referred to as the Single Limit State Simulation Proportioned Load Procedure, because the load distribution is adjusted to maintain correlation while the resistance distribution is scaled.

The difference between the numerical routine described in this section and the one in section 2.8 are in steps 3 and 8, where the relationship of the change in load to resistance according to design changes is added to the computation in step 8.

1. Create *Gz()* function for the limit state(s) that returns total Resistance (R), total Load (L), and conditional value of unsatisfactory performance (where unsatisfactory performance occurs when $R\text{-}L < 0.0$)
2. For geotechnical design, calculate the slip angle for the current design conditions and determine the geo-statistical variability of soil properties (e.g., soil friction angle) for each soil wedge (Driving, Structural, Resisting)
3. Run a *Gz()* analysis for two different design cases (in this case, varying the base width), and collect the rate of change of μ_{Load} and $\mu_{Resistance}$ labeled Δ_{Load} and $\Delta_{Resistance}$, respectively. For greater accuracy, more runs can be made, and the rate of change values averaged.
4. For a certain number of samples ($N_{samples}$), generate simulation soil properties and collect *Gz()* results for a base design case (e.g., single base width), maintaining the order of the results so that *R[index]* corresponds to *L[index]*. Maintaining the order means that the distributions AND any correlations are included in the sample data.
5. Calculate $\mu_{Resistance}$ and μ_{Load} for the *R[]* and *L[]* simulation results.
6. For verification, calculate the $PUP_{Initial}$ for the full simulation taking the number of simulations with unsatisfactory performance and dividing by the total number of simulations. This $PUP_{Initial}$ can be run through the inverse CDF function for a Normal Distribution to arrive at a somewhat arbitrary $\beta_{Initial}$ value.
7. A β_{target} value for a normal distribution is given that can be used to determine PUP_{target}.
8. Generate a function given *R[]*, *L[]*, PUP_{target}, as well as a scale factor for Resistance R_{SF}. This function calculates the unsatisfactory performance

$$PUP_{RSF} = \frac{\sum_{i=1}^{N_{samples}} \left\{ (R[i] * R_{SF}) - (L[i] + ((R_{SF} - 1.0) * R[i]) * \frac{\Delta_{Load}}{\Delta_{Resistance}}) \right\} \begin{bmatrix} 0: > 0.0 \\ 1: < 0.0 \end{bmatrix}}{N_{samples}} \quad (2.63)$$

To judge how close PUP_{RSF} is to PUP_{target}, the function returns a value $\left| PUP_{RSF} - PUP_{target} \right|$. This value is 0.0 when PUP_{RSF} is equal to PUP_{target} and greater than 0.0 otherwise.

9. Use a numerical procedure to find a value of R_{SF} that minimizes the step 7 function. Because the function returns a minimal value of 0.0 when PUP_{RSF} is equal to PUP_{target}, the resulting value of R_{SF} is the scale factor from the original Resistance distribution *R[]* to the Resistance distribution that, combined with the original Load distribution *L[]* has the same *PUP* as PUP_{target}.
10. The R_{SF} value is a scale factor for the current design's Resistance Distribution that satisfies the PUP_{target} goal. The $\mu_{Resistance}$ and μ_{Load} values are the means of the distributions that may be correlated; therefore, their values have the same level of correlation. The deterministic design load (d_{Load}) needs to be scaled by L_{SF} to match the scaled resistance.

$$R_{sf} * \mu_{Resistance} - L_{SF} * d_{Load} = 0.0 \quad (2.60 \text{ bis})$$

$$L_{SF} = \frac{\mu_{Resistance} * R_{SF}}{d_{Load}} \quad (2.61 \text{ bis})$$

11. According to the Limit State equation, the Resistance to be designed for (R_{Design}) is therefore

$$R_{Design} \geq L_{SF} * d_{Load} \quad (2.62 \text{ bis})$$

2.11 Reliability analysis with multiple limit states

USACE flood mitigation structures are designed considering more than one limit state (e.g., multiple ULSs) occurring at the same time. Section 2.2 lists the ULSs considered during the design process. Plan view for a two-variate problem in the transformed basic variable space of X'_1 and X'_2 is shown in Figure 2-10, along with two vertical planes, one red and the other green, showing the location of each of their respective limit state response surfaces, with each possessing a $g(\boldsymbol{X}') = 0$ type relationship. The height of these vertical planes is terminated in this figure so that they are at the same height of 0.1591 (= 0.3989^2) as the maximum PDF value at $x'_1 = 0$ and $x'_2 = 0$. The concentric, blue circles shown in this figure represent

the radially symmetric, normalized, Normal-Gaussian PDF distribution. Figure 2-11 shows a 3-D rendering of this Figure 2-10 PDF distribution for this 2-D transformed Variate space. Note the decreasing magnitude of the PDF values with increased distance in any direction from the origin in Figure 2-11.

Figure 2-10. Plan view of the transformed basic variable space for the variables X'_1 and X'_2 and response surfaces for a two-limit states – overhead view.

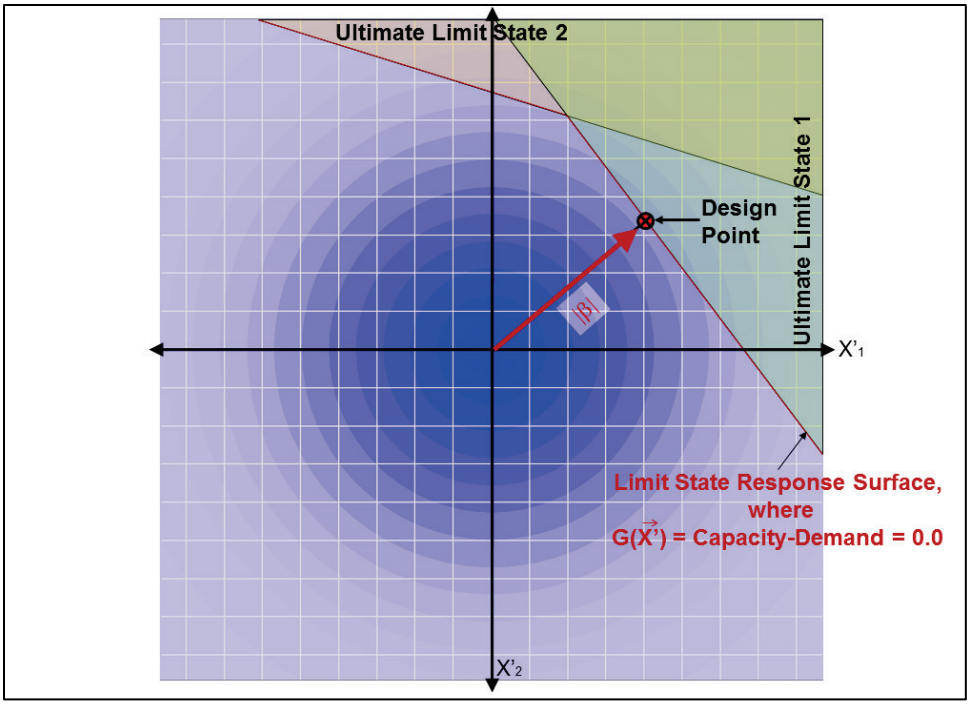

Figure 2-11. A 3-D rendering of a normalized, Normal-Gaussian PDF distribution for two independent variables, X_1 and X_2 and two limit state response surfaces.

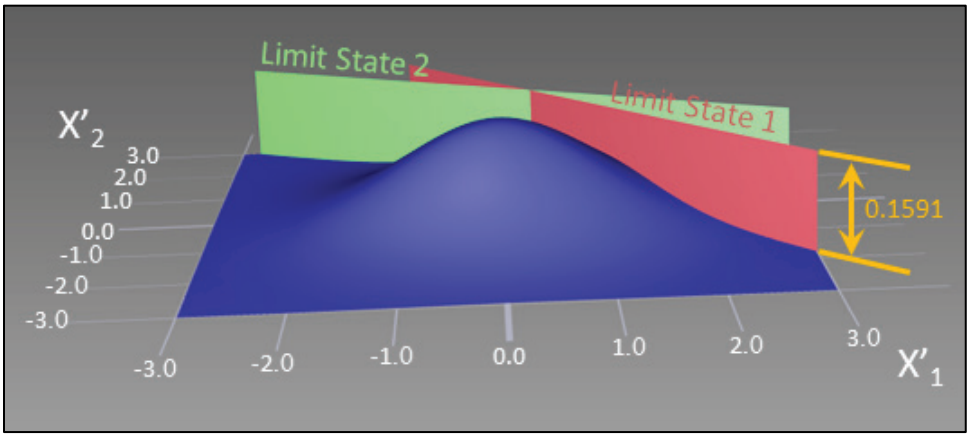

The Figure 2-10 region shaded in light brown, green, and olive green designates the failure region (i.e., $g(\boldsymbol{X}') \leq 0$). Note that regions beyond both two limit states in this figure contribute to this *PUP* volume. Conversely, the blue region in this figure designates the safe region: $g(X') > 0$. The Reliability value is again dictated by the fencing of the *PUP* volume provided by the location of these two limit states.

The closest distance in transformed basic variable space to each response surface, $g(\boldsymbol{X}') = 0$, is calculated. The distance among the two values that is closest to the ($x'_1 = 0$, $x'_2 = 0$) origin is then designated as the design point. It is located in Figure 2-10 by a unit vector times a scalar β and designated by the red vector emanating from the origin. In this case, the design point resides on limit state 1 that is located along the base of the Figure 2-11 red plane. Recall β is designated as the reliability index. Observe in Figure 2-10 that the unit vector times a scalar β is orthogonal to the limit state 1 response surface (with $g(\boldsymbol{X}') = 0$) at the design point. It is also the point on the limit state response surface at which the probability density of the joint random variables is greatest, as seen in Figure 2-4.

The Figure 2-10 designated limit state 2 is shown at its corresponding location in the 2-D PDF distribution in Figure 2-12. Its PDF distribution along the trace of limit state 2 for $g(\boldsymbol{X}') = 0$ is shown with a viewpoint from below in Figure 2-13, along with the red vector defining its closest distance as measured from the origin. Because the distance of limit state 2 is farther away than for limit state 1 (Figure 2-4), this red dot in Figure 2-13 for limit state 2 is not designated as the design point. Observe that for the green PDF distribution plotted along the location of $g(\boldsymbol{X}') = 0$ for limit state 2 in Figure 2-13, the largest PDF value occurs at the point designated by the red dot. This dot was the limit state 2 candidate for the design point.

Figure 2-12. A 3-D rendering of a normalized, Normal-Gaussian PDF distribution for two independent variables, X_1 and X_2, and the second limit state response surface.

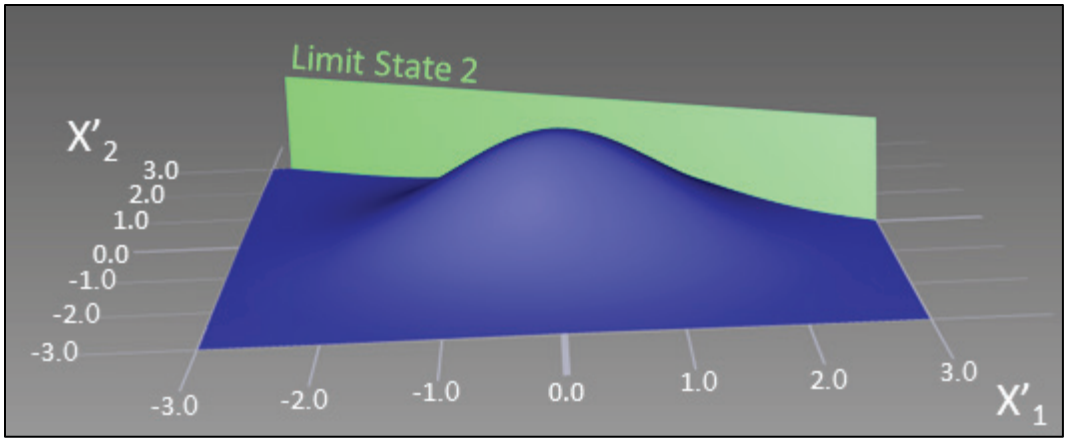

Figure 2-13. Cross section along the position of the limit state response surface through the PDF distribution in a 3-D rendering and the location of the design point for the response surface of limit state 2– view from underneath.

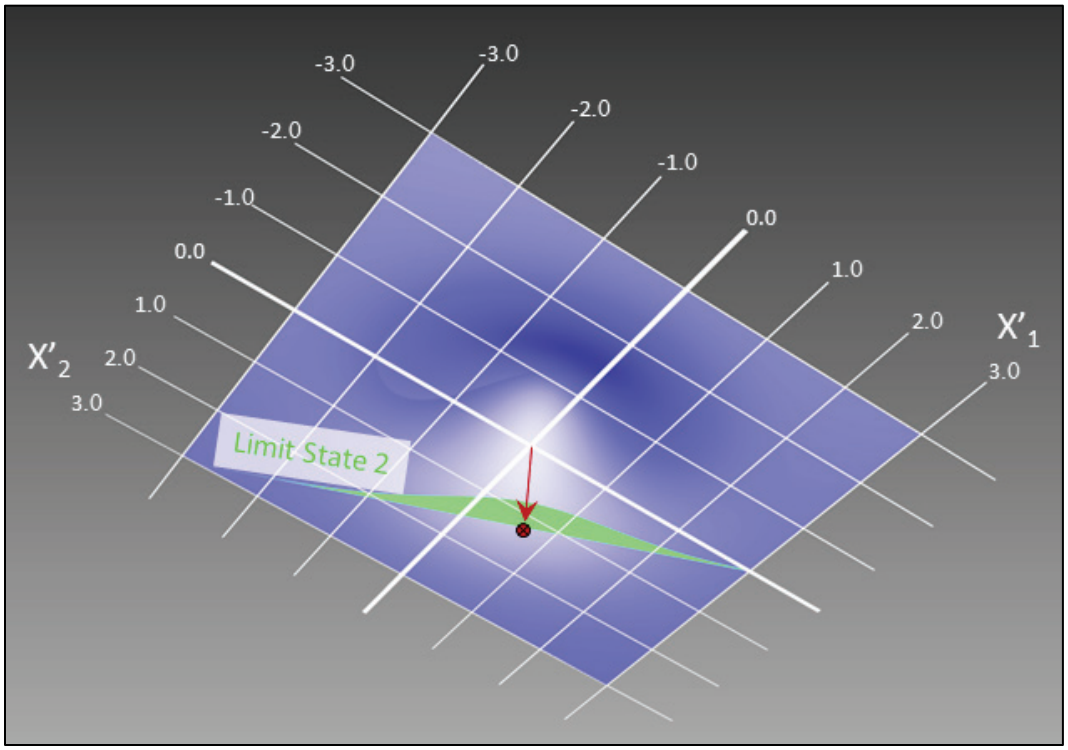

Figure 2-14 shows the cross sections along the position of the two limit state response surfaces through the PDF distribution in the 3-D PDF rendering. The viewpoint is made from below.

Figure 2-14. Cross sections along the position of the two limit state response surfaces through the PDF distribution in a 3-D rendering – view from underneath.

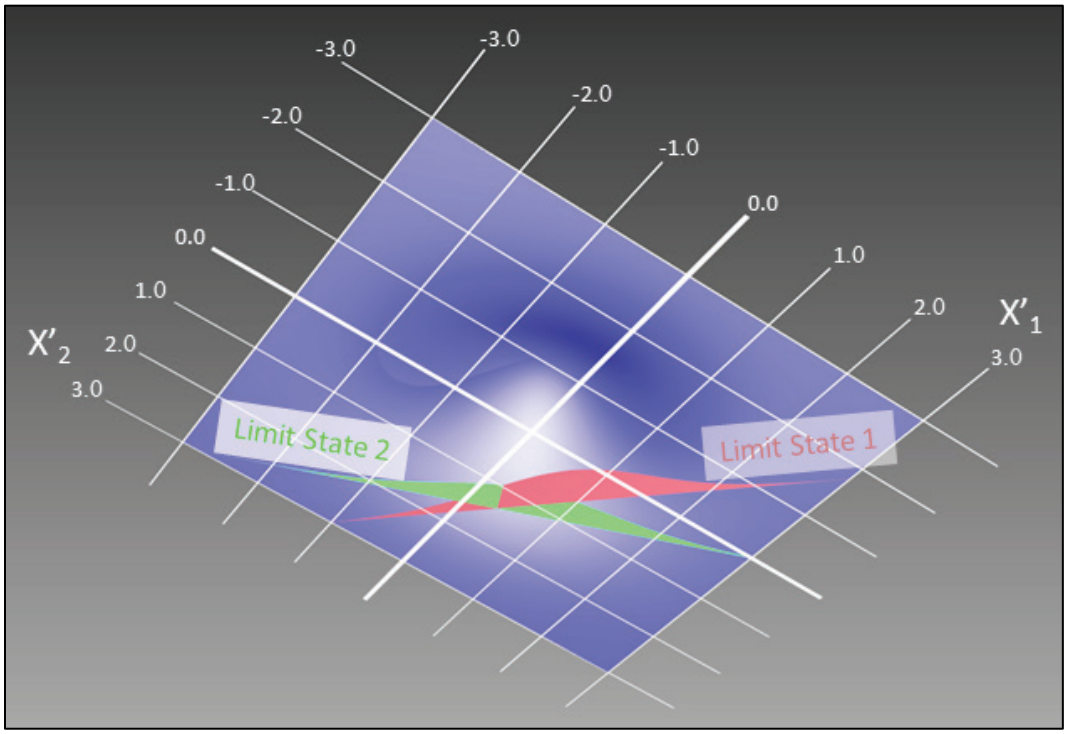

Multiple failure modes and the computation of *PUP*: The computation of the *PUP* value for this two-variable problem with two ULSs is best determined in the transformed basic variate space. Returning to the plan view of the PDF distribution in Figure 2-10, the *PUP* value is equal to the integral of the *PUP* volume up and to the right of both limit states. This region is shaded in light brown, green, and olive green. The Reliability Value is equal to the integral of the *PUP* volume for the region shaded in blue in this figure. The sum of the reliability and *PUP* values is 1.0 and equal to the volume of the entire PDF.

2.12 Implication of multiple limit states on the computed *PUP*

There are limited technical publications reporting on probabilistic investigations of multiple geotechnical limit states and multiple failure modes. Fan et al. (2014) discuss the reliability analysis of piles in spatially varying soils considering multiple failure modes. Specifically, they summarize their research into the performance state of vertical drilled

shafts under combined lateral and axial loading using a reliability analysis. The performance of the vertical pile is defined in terms of the displacements induced by external loading. They consider three performance limit states: (1) lateral pile deflection, (2) angular pile distortion, and (3) axial pile movement at the top of shaft. The unsatisfactory performance event is said to occur if the induced displacements at the top of the pile are greater than the corresponding allowable displacements. Lateral pile response is computed using the *p-y* method of pile-to-soil interaction analysis, and vertical displacements are computed using a *t-z* model for pile-to-soil interaction.[7] Uncertainties in soil deformation and strength properties are considered in their reliability analysis. Each of the soil property variables used in the analytical model is characterized by values of mean, standard deviation, and distribution type (e.g., normal, lognormal). With the statistical properties defined, a Monte-Carlo simulation method is used to conduct the reliability analysis. They apply a conventional reliability methodology of computing a *PUP* value for each of the three displacement limit states as well as a *PUP* value for the system.

One of the important findings of the Fan et al. (2014) study is that the *PUP* for the system is greater than for any of the three individual displacement limit state modes and is less than the sum of the *PUP* values of the three individual limit state modes if assuming the statistical independence among the three limit state modes. Fan et al. (2014) emphasize that the value for *PUP* will be underestimated if multiple displacement limit state modes are not considered simultaneously while the *PUP* value for the system will be overestimated if the dependence among the different displacement limit states is not considered.

The USACE batter pile-founded, reinforced concrete T-Wall flood mitigation structures are designed to resist multiple limit states, which are listed in Section 2.2. When a batter pile-founded T-Wall structure is viewed in terms of a reliability methodology, Fan's research indicates that the interrelationship between multiple performance limit states and a system *PUP* value is an important consideration. This is one of the research tasks investigated by the authors of this report, with the findings in this research study discussed in Chapter 7.

[7] Examples of the USACE CASE programs that perform lateral *p-y* analysis and axial *t-z* analysis are COM624G and CAXPILE, respectively.

Accommodating multiple limit states and/or failure modes given multiple variables in the *PUP* calculation has been shown by the Fan et al. (2014) study to be important part of a reliability analysis. Therefore, Appendix A describes different methods that have been researched and/or devised by the authors of this report for possible use in estimating the overall *PUP* values for systems with multiple limit state response surfaces.

For a single limit state with a hyperplanar Limit State Response Surface, as shown in Figure 2-15, the calculation of *PUP* is simple and accurate. Because the variables are mapped to a normalized multivariate Gaussian distribution space, the integration of the area of unsatisfactory performance on one side of the hyperplane of distance β (at the design point) from the mean origin is the same as the area for the single variable normalized Gaussian distribution beyond the design point distance β.

Figure 2-15. Mapping the integrated PUP from the multivariate hyperplane to a single Gaussian distribution.

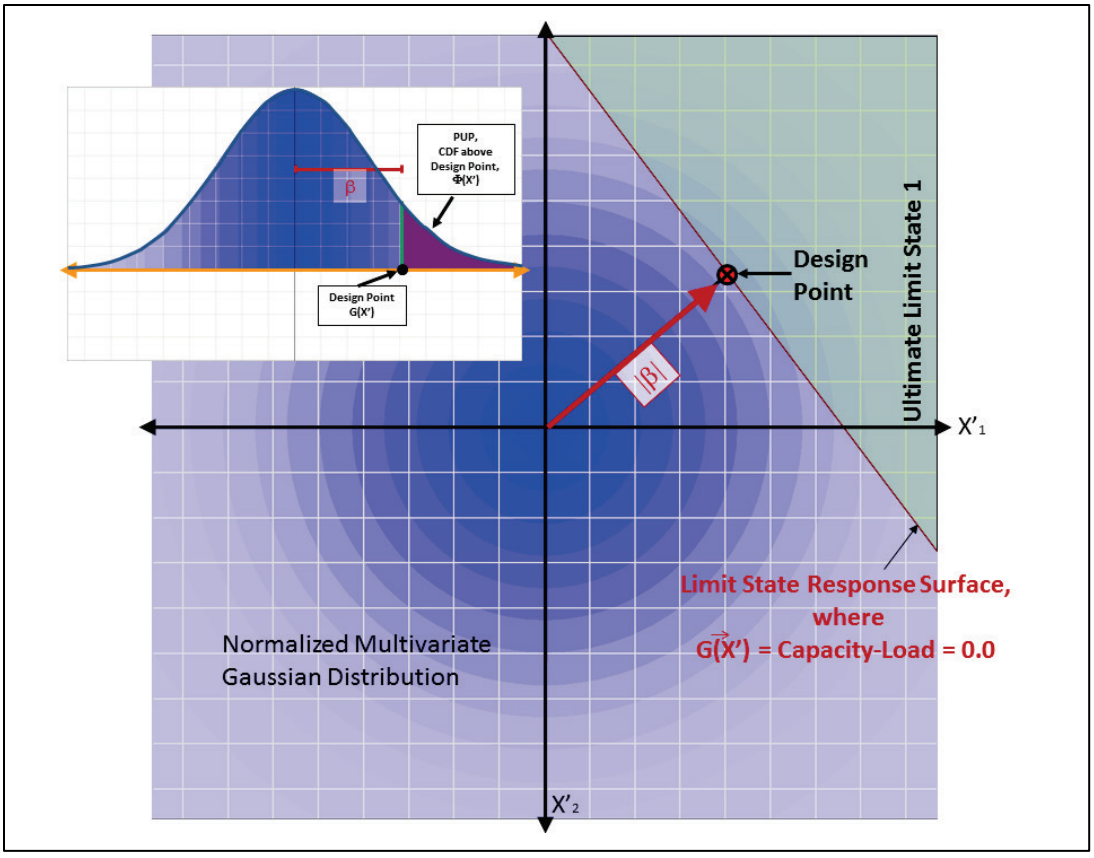

This situation becomes more complicated as non-hyperplanar limit state response surfaces are considered. Figure 2-16 shows how two hyperplanar limit states combine to create a non-hyperplanar limit state response surface. In this case, the integral of the probabilities includes the probabilities under the second limit state that does not overlap the first limit state probabilities. The probabilities of the overlap of the second limit state and the first limit state only need to be accounted for once.

Because the design point exists at the point where the limit state response surface is nearest the origin of the normalized multivariate Gaussian distribution space, a way to conservatively estimate the *PUP* so that satisfactory performance is guaranteed is the based on the probability of the hypersphere of radius β, as shown in Figure 2-16. This estimate integrates the probabilities outside of the hypersphere to determine *PUP*. This value is conservative because the hypersphere is guaranteed to be completely in the area of satisfactory performance but is not guaranteed to encompass all the satisfactory performance region.

Figure 2-16. Mapping the integrated PUP from the multivariate hypersphere to a single Gaussian distribution.

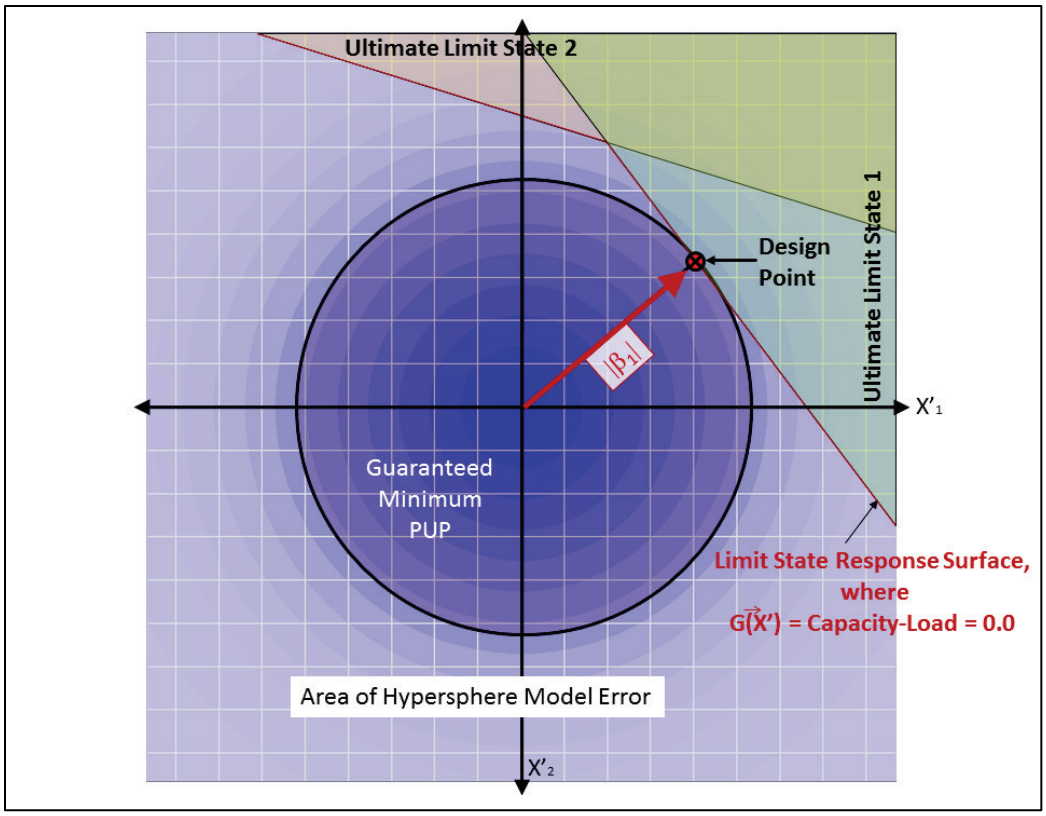

More accurate range finding *PUP* estimation methods provide a minimal range for the upper and lower bounds of the *PUP* using logical combination constraints given the limit state response surfaces, their number, and possible overlap information. The minimal range refers to the fact that the bounds are at the closest distance from each other based on the logical combinations. Choosing a value at the midpoint of the range guarantees an estimate that is accurate to within half the range width. Ang and Tang (1984) provide methods for finding the bounds of the overlap of regions based on Bayesian logic. These estimations are based on non-correlated variables, so they involve perpendicular response surfaces. The overlap regions involve the combination of comparing each limit state with respect to each other, as shown in the two-limit state, 2-D example of Figures 2.17 and 2.18. The upper and lower bounds for the overall *PUP* would be the different summations and removals of probabilities based on the Bayesian combinations of non-correlated values as described in subsection A.3.1 of Appendix A. The difference in the bounds is described by the third overlap region between overlap regions A and B from Figures 2-17 and 2-18. Note that the bounds can be found for multi-variate, multi-limit state problems.

Figure 2-17. Finding the overlap region A given limit state *i* with respect to limit state *j*.

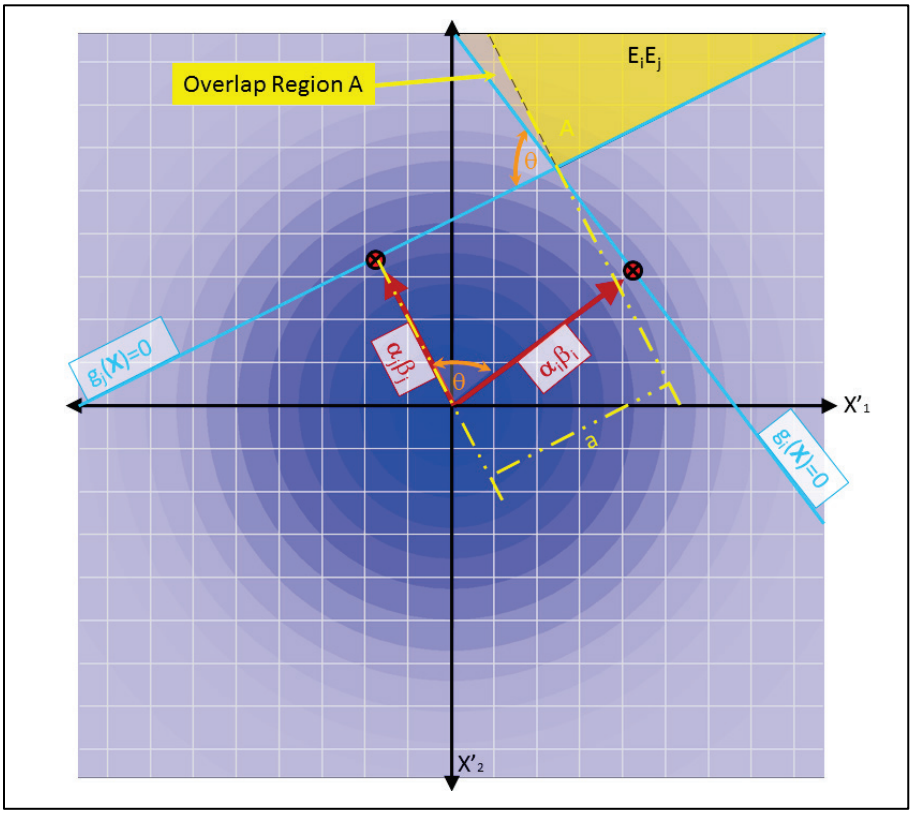

Figure 2-18. Finding the overlap region B given limit state *J* with respect to limit state *I*.

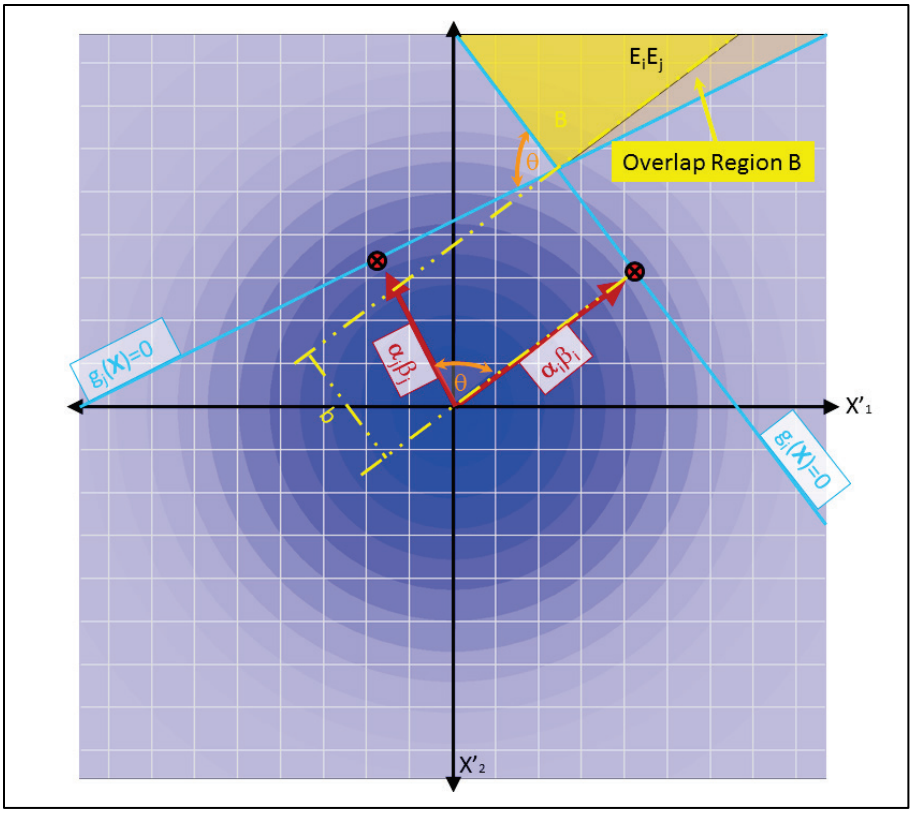

The range-finding methods were developed at a time (e.g., Ang and Tang, 1984) when computational power was not available to perform the more accurate numerical integration techniques that handle correlation between limit state response surfaces. This computational power is now available for a limited number of variables. However, range-finding methods are still useful in that they provide valuable information that bounds the range in *PUP* value with minimal computational effort.

Monte Carlo simulation methods can also be used to estimate *PUP*. Samples would be taken at random from the variable space according to each variable's distribution; then, the unsatisfactory or satisfactory result of the sample would be computed. Many samples would be taken, and the ratio of unsatisfactory results to the overall number of samples would give the *PUP* estimate. For a full Monte Carlo simulation, many samples (>10,000) would be required. The Latin Hypercube sampling method reduces the number of samples required by guaranteeing that samples are not repeatedly chosen in the same regions. Also, Importance Sampling lowers the error in calculation of the probability, by sampling about the design point, which is the point of the lowest β distance for all the limit

states (Figure 2-16), on the response surface for the combined limit states. To perform Importance Sampling, the design point, which gives the point on the closest limit state to the origin of the normalized Gaussian distribution, needs to be found. This can be done using the ASM techniques. A major concern for the simulation methods is that there are no guarantees that sample points will be generated in all the limit state unsatisfactory performance regions, when multiple limit states exist. This concern is mitigated by the fact that the limit state regions that are not covered will typically have very low probabilities.

Numerical integration can also be used to estimate *PUP* but can quickly grow to be unsolvable in a timely manner, even on the most advanced computers. The authors believe that for a small number of variables, this method may provide results in a timely manner. Figure 2-19 shows an integration method for estimating the *PUP* value. The space is divided into a hypergrid, and each grid cell probability would be added to the *PUP* if the variable values would lead to unsatisfactory performance. The two sources of error for this calculation would be the resolution of the hypergrid and the range of the calculations. By having the range vary from -5 to 5 standard deviations from the mean for each variable, the error can be minimized. A range of plus or minus 5 standard deviations corresponds to a maximum precision of 1.5E-6. If this range was increased out to plus and minus 8 standard deviations, the precision would improve to 5E-15. An improvement to the integration method utilizes the fact that the probability of a normalized Gaussian distribution stays the same at a given radius; therefore, a polar hypergrid could be used so that the probability calculations would be quicker. These numerical integration methods are described in Appendix A subsections A.3.2 and A.3.4. Because all the variable spaces are mapped for integration and the solution looks for any unsatisfactory performance in any grid cell (voxel, or volume element), this solution method works for multi-variate, multi-limit state problems.

Figure 2-19. Spatial subdivision for numerical integration and computation of a PUP value with two variables with Gaussian distributions given a single hyperplanar limit state.

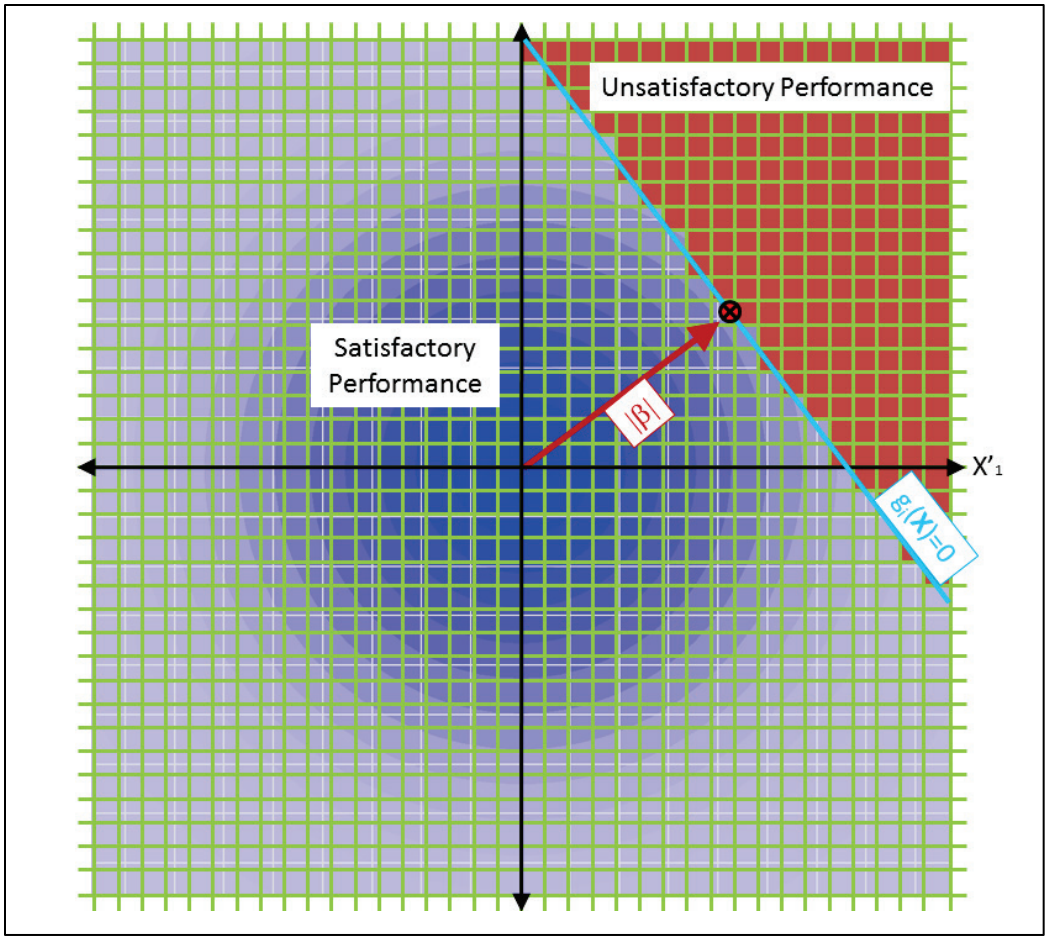

2.13 Published design values for reliability index β and/or *PUP*

The USACE batter pile-founded, reinforced concrete T-Wall flood mitigation structures are designed to resist multiple limit states, as listed in Section 2.2. Some of these design limit states fall within the sphere of influence of the structural engineering community while others are shared between the geotechnical and structural community. In general, the structural community both inside as well as outside the USACE has embraced the usage of β values whereas the geotechnical community has embraced the use of Probability of Failure, P_f, values and the use of *PUP* values. It is the viewpoint of the authors of this R&D report that this distinction has more to do with how reliability theory is being applied by the two disciplines of civil engineers when dealing with the different and distinct limit state evaluations being conducted during the design process.

The application of reliability theory to the first three design limit states listed in Section 2.2 have been dominated in the civil engineering technical literature by studies and decisions made by civil engineers within the structural community. These mechanisms are (1) flexural hinging of individual structural members, (2) shear failure of individual structural members, and (3) combined bending failure of individual structural H-Pile members. For the batter pile-founded, reinforced concrete T-Wall flood mitigation structures being designed by the USACE, the flood limit state dictates the size of the concrete base and stem members, the required amount of reinforcement steel to be placed within the individual reinforced concrete members, and the minimum compressive strength of the concrete as well as the yield strength of the steel reinforcement. For the batter piles, the size and length of piles are being dictated in the design process. In the application of reliability theory in structural limit state design, the structural engineering community tend to use a β value rather than a P_f or *PUP* value. One example taken from outside of the USACE technical literature is in the application of LRFD to the design of bridges: The bridge community of structural engineers has developed load and resistance factors so that reliability indices for bridges designed using the new (bridge design) code would be close to the a target Reliably Index β_{Target} of 3.5 referenced to a target period of 75 years (service life) by the discussions found on page 283 of Nowak and Collins (2013), on pages 48–49 in Ellingwood, and on page 245 in Fenton et al. (2016). The authors of this R&D report observe it is important to recognize that when expressing reliability-based design criteria in terms of a β design value, the value for β will need to be changed when the design life is changed. Different types of structures, as well as USACE projects, have different values for design life. The length of design life (usually 50, 75, or 100 years) is associated with the type of structure. In general, the longer the design life the more vital the structure is to society and frequently, the more costly it is to design and build.

The USACE batter pile-founded, reinforced concrete T-Wall flood mitigation structures are a significant financial investment. Consequently, these have a 100-year design life (ER 1110-2-8159) (HQUSACE 1997). Another detail for consideration is that once in place, the substructure foundations are costly to retrofit relative to the superstructure. There are often accessibility issues to the foundation. These items will need to be considered when selecting a β value for use in the design of the superstructure and for the foundation substructure. The authors of this R&D report pose this question: Should the design β values

used in the design of the superstructure and for the foundation substructure be the same?

There is also the question of redundancy for axially loaded pile groups. For example, Zhang et al. (2001) and Paikowsky et al. (2004) have concluded that target β-value for a redundant pile within a group of "significant size" (e.g., five or more axially loaded piles) can be less than the target β-value for an axially loaded single pile. The authors of this report observe that this type of pile redundancy configuration that is common to the axially loaded pile foundations of bridge columns is not a common configuration for USACE batter pile-founded T-Wall flood mitigation structures.

Regarding reliability theory, the geotechnical engineering community has been involved with the application of the theory to the limit states of (1) sliding, (2) bearing, and (3) overturning of a (shallow) foundation within the foundation soil (or rock) as well as (4) the axial capacity of (deep foundation) piles. In the past, a significant portion of the geotechnical reliability community has been making use of the probability of failure, P_f, for shallow foundation limit states (1) through (3) rather than focusing on the value of β. β is determined from the P_f value by applying reliability theory to a project feature's design for these limit states and for a specified design life and PDF distribution. The structural bridge community makes extensive use of pile foundations (i.e., deep foundations). This technical community has been a strong proponent for LRFD. Therefore, for the axial capacity of piles in deep foundations (limit state 4 listed in this paragraph), there is a penchant towards the use of reliability index β.

In their report on a reliability-based analysis of sliding and bearing limit states of a retaining structure, Sleep and Duncan (2014) observe that estimating the probability of failure is a major motive for applying probability theory in geotechnical engineering. This type of structure makes use of shallow foundation limit state theory for its limit states. They also comment that most geotechnical engineers prefer to use P_f rather than β because P_f has an easily understood relationship to likely performance and β does not.[8] The authors of this report comment that this viewpoint may not be universal, especially when project feature designs involve the mixing of structural and geotechnical disciplines. For example, Fenton et al. (2016) provide their reliability-based target design

[8]The authors of this report observe that β is a simplified probabilistic description of Reliability given a normal distribution (in a Guassian variate space).

criteria in terms of both target failure probabilities and β values when describing reliability-based geotechnical design in the 2014 Canadian highway bridge design code.

Recall that the *PUP* or P_f value is uniquely related to β by Equation 2.16, given an assumption for the distribution of the FoS (e.g., normal, lognormal). It is not unusual to see a lognormal or a normal distribution being assumed for the FoS against sliding failure in proposed reliability based, retaining wall design procedures with a focus on sliding stability (e.g., Sleep and Duncan 2014).

The authors of this R&D report observe that P_f and/or *PUP* values will need to be converted into load and resistance factors for use in LRFD design with consideration of individual and multiple limit states for the USACE batter pile founded, reinforced concrete T-Wall flood mitigation structures. Converting the *PUP* values to load and resistance factors will provide the means for a combined LRFD. It is anticipated that this computational process will involve the conversion of P_f and/or *PUP* values into reliability indices for each of the involved limit states. This can be done using reliability transformation relationships given in previous sections. For example, Equation 2.37 serves to demonstrate the conversion of a β value into a value for the load factor. In preparation for this action, this section collects reliability data from the non-USACE technical literature for geotechnical limit states: sliding, bearing, and/or overturning failures. Most of these data are expressed in terms of P_f with some also reporting β values. When unavailable, P_f values have been converted by the authors of this report into β values, assuming a normal distribution.

2.13.1 1994 Reliability analysis of proposed dikes of James Bay hydroelectric project in Quebec, Canada

In 1994, Christian et al. (1994) described a formal calculation of reliability and risk to the design of 50 km of dikes for a James Bay hydroelectric project. This slope stability assessment was used to help to decide among the alternatives to new dike construction on a soft clay foundation. These alternatives were construction of the embankment in a single stage, to either a height of 6 or 12 m with one berm. The second alternative involved the construction of the dike in multiple stages to allow the soft clay foundation to dissipate the excess pore water pressures generated during berm construction: Following the installation of vertical drains within the clay foundation, the first stage would consist of two berms built to a height

of 12 m. Then, the zone with the drains would be allowed to consolidate to 80% of primary consolidation, and the second stage would be built to a height of 23 m. Their analysis formally considered the uncertainty in soil strength parameters in the reliability-based slope stability, culminating in the calculation of a P_f for slope failure for each dike construction alternative. This study was special because of the significant geotechnical data base of soil properties and strength data for the project as well as the fact that Drs. Christian and Baecher are pioneers in the application of reliability theory to solve geotechnical foundation problems. Dr. Ladd is recognized as an expert in characterizing the strength of soft clays, which was a key aspect of the design challenge for the construction of these dikes at this project. Today, this study is considered a landmark reliability-based study by the geotechnical community even though the project was not built.

Target probability of failure: The design approach used for the dikes started with a probabilistic-based interpretation of the historical data on earthen dam failure since slope failure is one of the categories of earthen dam failures. Baecher et al. (1980) determined that earth dams seem to have probabilities of failure of approximately 10^{-4} per dam-year for a wide range of locations and times of construction. Their study suggests that approximately one-third of the failures are due to slides (with another third due to overtopping and the final third due to the category of internal erosion, piping, or seepage). Using this historical data, Christian et al. (1994) computed an overall probability of slope failure for a 100-year life, equal to 10^{-2} (= 10^{-4} times 100 years), in the absence of specific attention during design and construction to mitigate the hazards. With less than one-third of the historical failures being due to slope instability, Christian et al. suggested a target probability of failure of 10^{-3} (= 1/3 times 10^{-2} = 3.3×10^{-3}, rounded down to 10^{-3}) as being reasonable for design purposes and consistent with experience. These target reliability data are summarized in Table 2-2. The risk evaluation stage of the dike construction assessment introduced the consequences of failure into the evaluation and is summarized next.

Table 2-2. Target probability of slope failure and reliability index for a dike with a life of 100 years – based on the historical rate of failure of dams.

Project and Location	Historical Rate of Failure of Dams (per dam year)	$P_{f\text{-}100}$ (per dam life of 100 years)	Proportion of Sliding Failures to All Types of Dam Failures	Intermediate Calculation of $P_{f\text{-}100}$ (per dam life of 100 years)	Target $P_{f\text{-}100}$ for Design Purposes (per dam life of 100 years)	Reliability Index, β
Proposed dikes of James Bay hydroelectric project (Quebec, Canada); 1994	1×10^{-4}	1×10^{-2}	1/3	3.3×10^{-3}	1×10^{-3}	3.09*

*Computed by the authors of this report and assuming a normal distribution for the PDF of the FoS.

Consideration of risk and consistent factors of safety: Christian et al. (1994) recognized that a slope failure during dike construction would primarily be associated with the costs of reconstruction. However, a slope failure during operation of the hydroelectric project would involve much larger economic costs as well as other public consequences. Thus, Christian et al. introduced different target reliability indices or probability of failures for the different stages in the life of the project by informal consideration of project risk through the assignment of what they refer to as "consistent" factors of safety. This information is summarized in Table 2-3.

Table 2-3. Consistent factors of safety associated with target probability of slope failures and reliability Indices for a dike with a life of 100 years.

Project and Location	Case	Target $P_{f\text{-}100}$ for Design Purposes (per dike life of 100 years)	Consistent FoS (without model error)	Reliability Index, β
Proposed Dikes of James Bay hydroelectric project (Quebec, Canada); 1994	Single stage, H = 6 m, circular failure surface	1×10^{-2}	1.63	2.325 *
	Single stage, H = 12 m, circular failure surface	1×10^{-3}	1.53	3.09 *
	Multistage, H = 23 m, wedge failure surface	1×10^{-4}	1.43	3.718 *

*Computed by the authors of this report and assuming a normal distribution for the PDF of the FoS.

The consistent FoS listed in Table 2-3 was obtained by rearranging the Christian et al. (1994) Equation 9 into the form

$$E[F] = \frac{1.0}{1.0 - \beta * COV[F]} \quad (2.64)$$

β values are listed in Table 2-3. Values for the coefficient of variation of the FoS COV[F] are obtained from the data contained in the Christian et al. (1994) Table 7 variance in FoS for each of the three dikes. This variance in FoS comes from using Christian et al. (1994) Equation 13 (a first-order, second-moment method) in conjunction with slope stability analyses. An example of the application of the variance decomposition technique they used is outlined in their Table 5.

Note that once the design probability of failure is defined for the project feature and thus the value for the Reliability Index β, then by Equation 2.64, one only needs the value for coefficient of variation in FoS COV[F] to define the value for the consistent FoS. This equation bridges the reliability/statistical data of β and COV[F] values back into an expected FoS value, E[F].

Because of the consequences of failure of a major portion of the completed multistage, 23 m high embankment are expected to be greater than those for failure of a 12 m high embankment and because experience with staged construction is less fully evaluated for this project, the target probability for the multistage case was reduced from 10^{-3} (for the 12 m high embankment) to 10^{-4}. With this $P_{f\text{-}100}$ value, a target FoS equal to 1.43 was determined from the reliability-based slope stability data for the multistage construction by Christian et al. (1994).

Christian et al. (1994) rationalized that the consequences of failure of a portion of the smallest dike (6 m) might be only one-tenth as great as the 12 m high dike, so the target $P_{f\text{-}100}$ value was increased from 10^{-3} to 10^{-2}. With a $P_{f\text{-}100}$ value of 10^{-2}, a target FoS equal to 1.63 was determined by them from the reliability-based slope stability data for the 6 m high dike using Equation 2.64.

Christian et al. (1994) reasoned that because experience with staged construction is less fully evaluated and the consequences of failure of a major portion of the completed multistage embankment are expected to be greater than those of the failure of a 12 m high embankment, the target

probability for the multistage case was reduced by a factor of 10 to 1×10^{-4}. This value contrasts with the $P_{f\text{-}100}$ equal to 1×10^{-3} value for the 12 m high dike (Table 2-3).

The Christian et al. (1994) reliability-based slope stability results led the committee to recommend that a FoS equal to 1.5 be adopted for feasibility studies and preliminary cost estimates for both single and multistage dikes. In closing comments, they observed that a prior committee had recommended using a FoS equal to 1.4 for the minor dikes and 1.7 for the major, multistage dikes.

2.13.2 Revisited reliability calculations of the proposed dikes for the James Bay hydroelectric project in Quebec, Canada

In 2002, El-Ramly et al. (2002a) revisited the reliability-based calculation for the proposed design of the 50 km of dikes for a James Bay hydroelectric project. Only one design was re-evaluated in their study: the single stage construction of a 12 m high embankment with a slope angle of 18.4 degrees (3H:1V) and a 56 m wide berm at mid-height. Three probabilistic procedures of analysis were used: (1) an integrated slope stability analysis based on the use of a Monte Carlo simulation technique, (2) an FOSM approach in which the PDF distribution for the FoS against sliding failure was assumed to be either normal or lognormal (to the base *e*), and (3) a simplified analysis that ignored the spatial variability of soil properties. This latter analysis was made to contrast with the results of the first two analyses in which the spatial variability of soil properties was accounted for by using a variance reduction function and an autocorrelation distances (each with a corresponding scale of fluctuation distance) for soil strength along the slip plane within each of the soil layers. Their probabilistic slope stability assessment made use of the Bishop method of slices for circular slip surfaces. Note that this type of stability analysis cannot accommodate wedge-shaped and curved noncircular surfaces constructed using planar segments. The probabilistic results for the El-Ramly et al. (2002a) re-evaluation is summarized in Table 2-4 for the single stage construction of a 12 m high embankment for their FOSM reliability analysis results. Recall the Christian et al. (1994) target $P_{f\text{-}100}$ for a 100-year design life is equal to 1×10^{-3}. It is included in this table for reference. The El-Ramly Table 2-4 results using an updated reliability based, procedure of slope stability analysis show that their expected FoS values are somewhat lower than the Christian et al. (1994) results and that the annual probability of failure

values is much higher. Additionally, their reliability index values are lower than the Christian et al. (1994) target value.

Table 2-4. Computed expected factors of safety, annual probability of failure and reliability indices for the proposed single stage construction of a 12 m high embankment dike at the proposed James Bay project.

Reference	Assumed Distribution for FoS	Probability of Failure, P_f	Expected FoS E[FS]	Standard Deviation for the FoS σ[FS]	Coefficient of Variation for the FoS COV_{FS}	Reliability Index, β
Christian et al. (1994)		1×10^{-3}	1.53 *			3.09 **
El-Ramly et al. (2002a)	Normal	7.74×10^{-3} ***	1.46	0.19	0.13	2.42
Duncan et al. (2003)	Normal	1.9×10^{-1}	1.17	0.194 **	0.166	0.877 **
El-Ramly et al. (2002a)	Lognormal	2.15×10^{-3} ***	1.43	0.19	0.13	2.855 ***
Duncan et al. (2003)	Lognormal	1.9×10^{-1}	1.17	0.194 **	0.166	0.872 **

*Consistent FoS.
**Computed by the authors of this report using the PDF listed in the second column of this table.
*** Recomputed by the authors of this report to correct for computational errors made in the original paper.

Table 2-4 also includes results from the Duncan et al. (2003) re-evaluation of the El-Ramly et al. (2003a) results using yet another type of reliability-based procedure of slope stability analysis. One important feature of their slope stability evaluation was their ability to analyze wedged-shaped and curved noncircular slip plane surfaces constructed using planar segments. They found their critical slip planes to be geometrically different from the critical circular slip planes found in the El-Ramly et al. (2002a) and Christian et al. (1994) analyses. The Duncan et al. (2003) results indicate a significantly lower value for the expected FoS value of 1.17 as compared to both the Christian et al. (1994) result of 1.53 and the El-Ramly et al. (2002a) results of 1.46 and 1.43. As would be expected in the case of comparable values for the standard deviation of the FoS, the Duncan et al. (2003) computed probability of failure value of 1.9×10^{-1} is much higher than the Christian et al. (1994) target probability of failure of 1×10^{-3}. Similarly, the Duncan et al. (2003) reliability index value of 0.87 is much lower than the (approximate) target value of 3. A subsequent El-Ramly et al. (2003b) noncircular wedge slip surface evaluation using Spencer's method of slope stability analysis result of $P_{f\text{-}1} = 1.2 \times 10^{-1}$ and $\beta = 1.136$ corroborated the

Duncan et al. (2003) probabilistic results of a high probability of failure for the critical failure mechanism.

The revisited reliability-based calculations for the proposed design of the 50 km of dikes for a James Bay hydroelectric project made by El-Ramly et al. (2002, 2003b) and made by Duncan et al. (2003) provide the basis for an important observation: Both teams of engineers comment that it is absolutely essential to identify the critical failure mechanism. If the critical slip surface is not located and used in the probabilistic analysis, then no probabilistic methodology can overcome this deficiency and the computed value for the probability of failure will be meaningless.

The James Bay dike system provided a case study used for conducting a reliability-based designs/analyses for a geotechnical structural feature whose limit state is dominated by a sliding slope failure mechanism. Recall that this dike system was not constructed. Therefore, the link between design target β or conversely, *PUP* values, and field performance is not established in this example. The next subsection discusses a case study that demonstrates this link using the example of a tailings dike constructed to retain tailings sands from an oil sands mine operation in Canada.

2.13.3 Probabilistic slope stability analysis calculations of a Syncrude Tailings Dike on pre-sheared clay-shale in Fort McMurray, Canada

In 2003, El-Ramly (2003a) performed a 2-D probabilistic slope stability analysis of a 44 m (144 ft) high Syncrude Tailings Dike on a pre-sheared clay-shale foundation in Fort McMurray, Canada. The project's target FoS was 1.3. Tailings cell 23 (out of 30 cells) was completed to final design elevation in 1993. The maximum lateral movement recorded was 0.437 m (1.4 ft) in this tailings cell. The movement has been negligible since 1996, and the performance of the dike has been deemed adequate by El-Ramly et al. (2003a). An El-Ramly et al. (2002a) spread-sheet-based Monte Carlo probabilistic simulation procedure of analysis was applied to this tailings cell. This procedure of solution has its origins in the Vanmarcke (1977a, 1977b, 1980, 1983, and 2010) random field-based reliability analysis as applied to slope stability. Specifically, El-Ramly et al. (2003a) uses the variability of local averages over adjacent segments of the slip surface versus modeling the point-to-point variability of soil properties along the slip surface, which is difficult to obtain in practice. The portion of the slip surface within each soil layer is divided into segments of a length equal to the scale of fluctuation of that material. The varying soil property along an

individual segment is modeled by one random variable representing the spatial average of the property over the segment length.[9] The noncircular wedge slope stability analysis used included consideration of variability in soil strength and pore water pressures through a spatial averaging technique in which point estimates are combined with variance reduction of random fields approach (e.g., using a [horizontal] autocorrelation distance r_o of 33 m in the pre-sheared clay-shale). By Equation D.6, a r_o of 33 m corresponds to a scale of fluctuation value of 66 m (216 ft). They observed that the analytical performance of the dike was governed by uncertainties about geotechnical material properties and pore water pressures. The spreadsheet-based Monte Carlo simulation analysis resulted in a *PUP* value of 1.6×10^{-3}. The results for the El-Ramly (2003a) probabilistic study are summarized in Table 2-5.

Table 2-5. Values of the expected value and standard deviation of the FoS (FS) against sliding failure, *PUP*, reliability index and corresponding Syncrude Tailings Dike performance in terms of horizontal deformation.

Project	Project Location	E[FS]	σ[FS]	PUP	Reliability Index	Horizontal Deformation (m)	Reference
Syncrude Tailings Dike, 44 m high	Fort McMurray, Canada	1.31	0.14	1.6×10^{-3}	2.31	0.437	El-Ramly et al. (2003a)

The β value of 2.31 was computed by El-Ramly (2003a) using the relationship

$$\beta = \frac{E[FS]-1.0}{\sigma[FS]} \tag{2.65}$$

These probabilistic results indicate that the 0.437 m (1.43 ft) horizontal deformation of this 44 m high tailings dike founded on pre-sheared clay-shale, with an expected value for FoS against sliding of 1.31, has a *PUP* equal to 1.6×10^{-3} and a corresponding reliability index of 2.31. Again, considering this type of structure, the dike performance is deemed adequate in their study.

[9] By assigning slip plane segmental lengths that are equal to the scale of fluctuation, the variance reduction due to spatial averaging can be ignored, and the correlation coefficients between most of the variables representing the local averages approach zero, as per Vanmarcke (1977a).

A parametric study conducted by El-Ramly (2003a) showed that by ignoring the spatial correlation of the earth data and relying only on the means, standard deviations, and probability distribution functions resulted in a *PUP* equal to 1.6×10^{-2}. This value is one order of magnitude higher than the probabilistic analysis that considered spatial correlation (Table 2-5). This is an important detail: Christian and Baecher (2011) observe that uncertainty in soil properties is being overestimated, helping to explain why failures are less frequent than reliability studies have been predicting. Refer to Christian and Baecher (2011) for their discussion of 10 unresolved problems in geotechnical risk and reliability.

2.13.4 Reliability-based target design criteria in the 2014 Canadian Highway Bridge Design Code (CHBDC)

In 2014, a revised version of the CHBDC was published. It is of importance to this R&D effort because reliability-based criteria and procedures were used to establish the design criteria and LRFD design values. Fenton et al. (2016) provide detailed discussion of the code's reliability-based target design criteria in terms of both target failure probabilities and β values when describing reliability-based geotechnical design in the 2014 CHBDC.

Under the CHBDC LRFD approach and using Fenton et al. (2016) notation, Canadian bridge designs must satisfy

$$\varphi_g * \hat{R} = \sum_i I_i * \eta_i * \alpha_i * \hat{F}_i \tag{2.66}$$

where

φ_g = the geotechnical resistance factor with the subscript referring to *geotechnical* or *ground*
$\hat{R}$ = the characteristic geotechnical resistance based on characteristic ground parameters
I_i = is a structure importance factor for the i^{th} characteristic load effect $\hat{F}_i$
η_I = a load combination factor
α_I = the load factor
$\hat{F}_i$ = the i^{th} characteristic load effect.

Fenton et al. (2016) note that the word *characteristic* is used because it suggests a value that characterizes a design parameter that is uncertain, (e.g., a random load or resistance). They feel that the words *nominal* or

design do not convey the underlying randomness of the design parameter. In some Eurocodes, there is a specific statistical definition of the word *characteristic*, often as being the 5th or 95th percentile, whichever leads to the highest probability of failure. Eurocode 7 (CEN 2004) defines a characteristic parameter in geotechnical design as the value selected such that the probability of occurrence of the associated limit state does not exceed 5% (i.e., a reliability of 95% with respect to the performance of the structure). Hicks (2013) provides a detailed explanation of this code's characteristic values.

2.13.4.1 Ultimate Limit States (ULS)

For the ULS under the CHBDC LRFD approach, the geotechnical design for Canadian bridges will need to satisfy

$$\psi * \varphi_{gu} * \hat{R} = \sum_i I_i * \eta_i * \alpha_{iu} * \hat{F}_{iu} \quad (2.67)$$

in which the notation is the same as for Equation 2.66 but with the addition of a subscript u to designate the ULS. The consequence factor ψ, listed in Table 2-6, accounts for failure consequences. Note this consequence factor is applied to the resistance term (versus the demand/load term).

Table 2-6. The 2014 CHBDC ULS and SLS consequence factor values (after Fenton et al. [2016]).

Consequence Level	Consequence Factor, ψ
High	0.9
Typical	1.0
Low	1.1

The targeted theoretical maximum 75-year-lifetime bridge ultimate (limit state) failure probability, $p_{f\text{-}n}$ with n equal to 75 years (p_m in Fenton et al. [2016] notation) is 1/5,000 for a typical Canadian bridge foundation. Fenton et al. (2016) describes the basic idea of the consequence factor is to adjust the maximum acceptable factor of the design down (e.g., to 1/10,000) for high failure consequences (relative to a typical consequence case) or up (e.g., to 1/1,000) for low failure consequences. Table 2-7 lists the corresponding $\beta_{f\text{-}75}$ values of the foundation ULS for the three consequence levels.

Table 2-7. The 2014 CHBDC geotechnical design ULS consequence factor values and reliability criteria (after Fenton et al. [2016]).

Consequence Level	$p_{f\text{-}75}$	Reliability Index, $\beta_{f\text{-}75}$
High	1/10,000	3.7
Typical	1/5,000	3.5
Low	1/1,000	3.1

By Melchers (1999) Equation 6.17, the annual probability of limit state failure, $p_{f\text{-}1}$, can be (approximately) determined from the n = 75 years lifetime (limit state) failure probability $p_{f\text{-}75}$ using

$$p_{f-1} = \frac{p_{f-n}}{n} \tag{2.68}$$

Using Equation 2.68, the annual probability of (ULS) failure for the 2014 CHBDC criteria is computed and the results reported in Table 2-8 in the column labeled "$p_{f\text{-}1}$." The USACE batter pile-founded reinforced concrete T-Wall flood mitigation structures are designed for an n equal to 100 years (ER 1110-2-8159) (HQUSACE 1997). It is of interest to see what an equivalent CHBDC-type probabilistic criteria would be for a 100-year lifetime instead of its 75-year lifetime. In an n equal to 100-year lifetime, the probability of limit state failure, $p_{f\text{-}100}$, is determined by using Melchers (1999) Equation 6.19, which uses a binomial distribution for determining the expected probability ($p_{f\text{-}n}$) that a threshold return period ($1/p_{f\text{-}1}$) will be exceeded:

$$p_{f-n} = 1 - \left(1 - p_{f-1}\right)^n \tag{2.69}$$

Computations were made, and the results reported in Table 2-8 column labeled $p_{f\text{-}100}$. Its corresponding annual $\beta_{f\text{-}1}$ is also computed and listed in this table. Values for $p_{f\text{-}100}$ and the $\beta_{f\text{-}100}$ are computed using the Excel statistical function NORM.INV[(1-$p_{f\text{-}100}$), μ = 0, σ =1] and are listed in this table.[10]

[10] μ is the Greek symbol representing a mean value, and σ represents the standard deviation.

Table 2-8. Expanded table of 2014 CHBDC geotechnical design ULS consequence factor values and reliability criteria.

CHBDC (2014) Document				Calculated			
Consequence Level	p_{f75}		Reliability Index, β_{f75}	Pf-1 (Annual)	Annual Reliability Index, $\beta_{f\text{-}1}$	p_{f100}	Reliability Index, β_{f100}
High	1/10,000	1.0 x 10^{-4}	3.7 (3.72)*	1.33 x 10^{-6}	4.69	1.33 x 10^{-4}	3.65
Typical	1/5,000	2.0 x 10^{-4}	3.5 (3.54)*	2.67 x 10^{-6}	4.55	2.67 x 10^{-4}	3.46
Low	1/1,000	1.0 x 10^{-3}	3.1 (3.09)*	1.33 x 10-	4.2	1.33 x 10^{-3}	3.0

*$\beta_{f\text{-}75}$ value is recalculated and is reported with two decimals places for greater accuracy when used in comparisons with $\beta_{f\text{-}n}$ values for other design lives of n years.

Solving for $p_{f\text{-}1}$, Equation 2.69 becomes

$$p_{f-1} = 1 - 10^{\frac{\log_{10}(1-p_{f-n})}{n}} \tag{2.70}$$

Observe the inverse relationship between values of $\beta_{f\text{-}n}$ and $p_{f\text{-}n}$ in the Table 2-8 data for each n years: As $\beta_{f\text{-}n}$ goes up in value, the value of $p_{f\text{-}n}$ goes down. This is consistent with the characteristics of a normal distribution curve. Recall that β is the number of standard deviations from the variable's PDF mean value to the variable's value x and that $p_{f\text{-}n}$ is the PDF's area from negative infinity up to value x (and equal to the CDF value within this x-range).

$\beta_{f\text{-}75}$ ranges from a low of 3.1 to a high of 3.7 for a 75-year design life for each of the three Canadian bridge design consequence levels. The Table 2-8 data calculated for a 100-year design life shows $\beta_{f\text{-}100}$ ranges from a low of 3.0 to a high of 3.65. The two columns of data show that the design life n-value increases, the value for $\beta_{f\text{-}n}$ decreases. However, the effect of a change in design life from 75 to 100 years is minor; $\beta_{f\text{-}n}$ decreases in value by 2.9% or less for each of the three design consequence levels with this 25-year design life increase (Table 2-9).

Table 2-9. Comparisons of reliability indices for the 2014 CHBDC geotechnical design ULS with a 75-year design life and for a 100-year design life.

Consequence Level	Reliability Index, β_{f75}	Reliability Index, β_{f100}	$(\beta_{f100} - \beta_{f75})$	β_{f100}/β_{f75}
High	3.72	3.65	-0.07	0.98
Typical	3.54	3.46	-0.08	0.98
Low	3.09	3	-0.09	0.97

By the data contained in the second-to-last column of Table 2-9, the 2014 CHBDC geotechnical design ULS-based reliability criteria would translate into a reduction in the β value for a 100-year (foundation) design life that is between 0.07 and 0.09 lower than the β value for a 75-year Canadian bridge design life.

The annual $\beta_{f\text{-}1}$ ranges from a low of 4.2 to a high of 4.69 for a 75-year design life for each of the three Canadian bridge design (failure) consequence levels (Table 2-8). The difference between the annual reliability index value and that for a 75-year design life is significant, ranging in value from 21 to 26% lower values for the three design (failure) consequence levels.

2.13.4.2 Time variability of both loads and resistance and a theoretical reliability target value

Fenton et al. (2016) provide a thought-provoking discussion of the appropriate reliability index value and conclude with a basis for selection of a theoretical reliability target value. Summarizing their discussion on pages 244–245: Citing two clauses in an earlier (2006) version of the CHBDC, it specifies (in Clause 3.5.1) that calibration of load and resistance factors shall be based on a minimum annual reliability index of 3.75 for CL-625 loading (in accordance with Clause 3.8.3). If each year is considered to be independent, then for the 75-year design life, the annual $\beta_{f\text{-}1}$ value would equal 3.75 for a Canadian bridge of typical consequence (failure) level. This would correspond to $\beta_{f\text{-}75}$ equal to 2.5.[11] In actuality, each year is not actually independent. Consequently, it is unlikely that the

[11] A value of ULS Reliability Index $\beta_{f\text{-}75}$ equal to 2.5 (i.e., 2.478 before rounding) is obtained as follows: The value for $p_{f\text{-}1}$ is derived from an annual Reliability Index set equal to 3.75 for a Canadian bridge of typical consequence level. With $\beta_{f\text{-}1}$ set equal to 3.75, its corresponding $p_{f\text{-}1}$ value would be 8.84 x 10^{-5} as calculated using Excel with the equation and statistical function of [1-NORM.S.DIST(β=3.75,TRUE)]. For an n = 75-year design life and using Equation 2.69 with $p_{f\text{-}1}$ equal to 8.84 x 10^{-5}, $p_{f\text{-}75}$ is calculated to be 6.608 x 10^{-3}. Its corresponding Reliability Index $\beta_{f\text{-}75}$ is calculated to be equal to 2.478 using Excel with the statistical function of NORM.INV[(1-$p_{f\text{-}75}$), μ = 0, σ = 1].

actual lifetime reliability index is as low as 2.5. To determine the actual lifetime reliability index, Fenton et al. (2016) suggest consideration of the time variability of both loads and resistance. They observe that both structural and geotechnical systems often exhibit substantial degradation over a Canadian bridge's design life (of 75 years). They cite the continual degradation of geotechnical systems by pore-pressure variations, freeze-thaw effects, erosion, seismic motion, local liquefaction, etc. Even if the annual reliability index of 3.75 is achieved in the first year after construction, the 75-year reliability index would be a lower value for these reasons. Fenton et al. suggest that the actual 75-year reliability index will be somewhere between 2.5 (based upon assumed independence between years) and 3.75 (assuming neither degradation nor fluctuation in loads). They recognize that further research is needed on this complex issue of fluctuations and degradation with time and conclude that it is reasonable to assume that the actual reliability index will be somewhere between 2.5 (deemed a conservative estimate) and 3.75, with a recommended theoretical target of 3.5 for a 75-year lifetime. This CHBDC ULS target value is listed in Table 2-7 for a typical consequence level Canadian bridge. They feel it is reasonable to assume the lifetime reliability index will fall between 3 and 3.5 and would conservatively correspond to an annual reliability index of 3.75 for Canadian bridge (of typical consequence level). Until further research and development advance reliability methodologies and the required data on time variability of both loads and resistance to the point that it is robust enough to be formally included in design guidance (such as the CHBDC), the Fenton et al. logic described in this paragraph for a fixed target β value provides for a practical alternative.

2.13.4.3 Serviceability Limit State (SLS)

For the SLS under the CHBDC LRFD approach, the geotechnical design for bridges will need to satisfy

$$\psi * \varphi_{gs} * \hat{R} = \sum_i I_i * \eta_i * \alpha_{is} * \hat{F}_{is} \tag{2.71}$$

in which the notation is the same as for Equation 2.66 but with the addition of a subscript *s* to designate the SLS. According to the CHBDC, the SLS corresponds to behavior of the ground that causes unacceptable conditions, such as deformations, that restrict the intended use of the supported structure and/or geotechnical system. The serviceability geotechnical resistance is the load the ground can support at the SLS, usually at a predefined deformation in the ground or structure, estimated using

characteristic geotechnical parameters. Table 2-10 lists the corresponding $\beta_{s\text{-}n}$ values of the foundation SLS for the three consequence levels.

Table 2-10. The 2014 CHBDC SLS consequence factor values and reliability criteria (after Fenton et al. 2016).

Consequence Level	$p_{s\text{-}75}$	Reliability Index, β
High	1/1,000	3.1
Typical	1/500	2.9
Low	1/100	2.3

Using Equation 2.68, the annual probability of exceeding the SLS for the 2014 CHBDC is computed, and the results reported in Table 2-11, along with its corresponding annual serviceability $\beta_{s\text{-}1}$. Values for $p_{s\text{-}100}$ and the $\beta_{s\text{-}100}$ are also given.

Table 2-11. Expanded table of 2014 CHBDC SLS consequence factor values and reliability criteria.

CHBDC (2014) Document				Calculated			
Consequence Level	$p_{s\text{-}75}$		Reliability Index, $\beta_{s\text{-}75}$	$P_{s\text{-}1}$ (Annual)	Annual Reliability Index, $\beta_{s\text{-}1}$	$p_{s\text{-}100}$	Reliability Index, $\beta_{s\text{-}100}$
High	1/1,000	1.0×10^{-3}	3.1 (3.09)*	1.33×10^{-5}	4.2	1.33×10^{-3}	3.0
Typical	1/500	2.0×10^{-3}	2.9 (2.88)*	2.67×10^{-5}	4.04	2.66×10^{-3}	2.79
Low	1/100	1.0×10^{-2}	2.3 (2.33)*	1.33×10^{-4}	3.65	1.32×10^{-2}	2.22

*$\beta_{s\text{-}75}$ value is recalculated and is reported with two decimals places for greater accuracy when used in comparison with a $\beta_{s\text{-}n}$ value for a design life of n years (e.g., n = 100).

The Table 2-11 data show the same inverse relationship observed in the Table 2-8 data between values of $\beta_{f\text{-}n}$ and $p_{f\text{-}n}$ for each n years: As $\beta_{s\text{-}n}$ goes up in value, the value of $p_{s\text{-}n}$ goes down.

$\beta_{s\text{-}75}$ ranges from a low of 2.3 to a high of 3.1 for a 75-year design life for each of the three Canadian bridge design consequence levels (Table 2-11). These are lower reliability indices than for the failure limit state $\beta_{f\text{-}75}$ values. Recall from Table 2-8 that $\beta_{f\text{-}75}$ ranges from a low of 3.1 to a high of 3.7 for a 75-year design life for each of the three Canadian bridge design consequence levels. This corresponds to a 16% to 26% decrease in the three sets of $\beta_{f\text{-}75}$ to $\beta_{s\text{-}75}$ comparisons. In terms of probabilities, there is a

factor of 10 difference in the three sets of $p_{f\text{-}75}$ to $p_{s\text{-}75}$ comparisons. The SLS is more probable than the ULS.

The Table 2-11 reliability data calculated for a 100-year design life shows $\beta_{f\text{-}100}$ ranges from a low of 2.22 to a high of 3.0. The two columns of 75- and 100-year data show that as the design life n-value increases, the value for $\beta_{f\text{-}n}$ decreases. This was the same trend seen in the Table 2-8 data. The effect of a change in design life from 75 to 100 years is again shown to be minor; $\beta_{f\text{-}n}$ decreases in value by approximately 3% for each of the three design consequence levels with this 25-year design life change.

By the data contained in the second-to-last column of Table 2-12, the 2014 CHBDC geotechnical design SLS-based reliability criteria would translate into a reduction in the β value for a 100-year (foundation) design life that is between 0.09 and 0.11 lower than the β value for a 75-year Canadian bridge design life.

Table 2-12. Comparisons of reliability indices for the 2014 CHBDC geotechnical design SLS with a 75-year design life and for a 100-year design life.

Consequence Level	Reliability Index, $\beta_{s\text{-}75}$	Reliability Index, $\beta_{s\text{-}100}$	$(\beta_{s\text{-}100} - \beta_{s\text{-}75})$	$\beta_{s\text{-}100}/\beta_{s\text{-}75}$
High	3.09	3	-0.09	0.97
Typical	2.88	2.79	-0.09	0.97
Low	2.33	2.22	-0.11	0.95

The annual $\beta_{s\text{-}1}$ ranges from a low of 3.65 to a high of 4.2 for a 75-year design life for each of the three Canadian bridge design (serviceability) consequence levels (Table 2-11). The difference between the annual reliability index value and that for a 75-year design life is significant, ranging in value from 26% to 37% lower values for the three design (serviceability) consequence levels.

The three annual SLS $\beta_{s\text{-}1}$ values (Table 2-11) are smaller than the three ULS $\beta_{f\text{-}1}$ values (Table 2-8). Specifically, the $\beta_{s\text{-}1}$ values are 10% to 13% less than the $\beta_{f\text{-}1}$ values.

2.13.5 Reliability-based target design criteria in the American Society of Civil Engineers (ASCE) design code for buildings

The ASCE ASCE-7-10 (Table C.1.3.1a) acceptable reliability for non-earthquake events is listed in Table 2-13 through Table 2-16 for the risk categories associated with four different building system categories and three building (ultimate) limit states. The ASCE criteria were developed for building systems with a 50-year design life. The column labeled "$p_{f\text{-}1}$" is the ASCE annual probability of limit state failure. This value is the basis for all subsequent calculations. Also included in these tables are reliability calculations made by the authors of this report using Equation 2.69 with the design life, n, set equal to 50 years and to 100 years, and using the statistical function of NORM.INV[(1-$p_{f\text{-}100}$), $\mu = 0$, $\sigma = 1$] defined in Excel. These calculations extend the ASCE annual probability of building limit state failure criteria (i.e., $p_{f\text{-}1}$) to a design life of 100 years, which is the design life required of the foundation systems used for the USACE hydraulic and flood mitigation structures (ER 1110-2-8159) (HQUSACE 1997).

Table 2-13. ASCE-7-10 acceptable reliability for non-earthquake – Risk Category I, temporary storage.

Limit State	P_{f1} (annual)	P_{f50}	β_{f50}*	P_{f100}	β_{f100}	(β_{f100} - β_{f50})	β_{f100}/β_{f50}
Benign	1.25 x 10^{-4}	6.231 x 10^{-3}	2.5 (2.5)	1.24 x 10^{-2}	2.24	-0.26	0.9
Sudden or Severe	3 x 10^{-5}	1.499 x 10^{-3}	2.97 (3)	3 x 10^{-3}	2.75	-0.22	0.93
Sudden and Severe	5 x 10^{-6}	2.5 x 10^{-4}	3.48 (3.5)	5 x 10^{-4}	3.29	-0.19	0.95

*ASCE 10-7 values have been rounded and are reported in parentheses.

Table 2-14. ASCE-7-10 acceptable reliability for non-earthquake – Risk Category II, normal.

Limit State	P_{f1} (annual)	P_{f50}	β_{f50}*	P_{f100}	β_{f100}	(β_{f100} - β_{f50})	β_{f100}/β_{f50}
Benign	3 x 10^{-5}	1.499 x 10^{-3}	2.97 (3)	3 x 10^{-3}	2.75	-0.22	0.93
Sudden or Severe	5 x 10^{-6}	2.5 x 10^{-4}	3.48 (3.5)	5 x 10^{-4}	3.29	-0.19	0.95
Sudden and Severe	7 x 10^{-7}	3.5 x 10^{-5}	3.98 (4)	7 x 10^{-5}	3.81	-0.17	0.96

*ASCE 10-7 values have been rounded and are reported in parentheses.

Table 2-15. ASCE-7-10 acceptable reliability for non-earthquake – Risk Category III, assembly.

Limit State	P_{f1} (annual)	P_{f50}	β_{f50}*	P_{f100}	β_{f100}	(β_{f100} - β_{f50})	β_{f100}/β_{f50}
Benign	1.25×10^{-5}	6.248×10^{-4}	3.23 (3.25)	1.25×10^{-3}	3.02	-0.2	0.94
Sudden or Severe	2×10^{-6}	1×10^{-4}	3.72 (3.75)	2×10^{-4}	3.54	-0.18	0.95
Sudden and Severe	2.5×10^{-7}	1.25×10^{-5}	4.21 (4.25)	2.5×10^{-5}	4.06	-0.16	0.96

*ASCE 10-7 values have been rounded and are reported in parentheses.

Table 2-16. ASCE-7-10 acceptable reliability for non-earthquake – Risk Category IV, hospitals.

Limit State	P_{f1} (annual)	P_{f50}	β_{f50}*	P_{f100}	β_{f100}	(β_{f100} - β_{f50})	β_{f100}/β_{f50}
Benign	5×10^{-6}	2.5×10^{-4}	3.48 (3.5)	5×10^{-4}	3.29	-0.19	0.95
Sudden or Severe	7×10^{-7}	3.5×10^{-5}	3.98 (4)	**7×10^{-5}**	3.81	-0.17	0.96
Sudden and Severe	1×10^{-7}	5×10^{-6}	4.42 (4.5)	1×10^{-5}	4.26	-0.15	0.97

*ASCE 10-7 values have been rounded and are reported in parentheses.

When considering the USACE batter pile-founded reinforced concrete T-Wall flood mitigation structures, the ASCE 7-10 reliability criteria for normal, assembly and/or hospital building systems would be of more interest than that for temporary storage structures. Therefore, by the data contained in the second-to-last column of Tables 2.14 through 2.16, the ASCE-based reliability criteria would translate into a reduction in the β value for a 100-year (foundation) design life that is between 0.15 and 0.22 lower than the β value for a 50-year building design life. Recall that as the value for reliability index decreases, the probability of failure increases, given a specified design life of n years. This is observed when comparing the $p_{f\text{-}100}$ values to the $p_{f\text{-}50}$ values in these tables: They differ by a factor of two according to the data contained in these tables and by Equation 2.69 for n equal to 100 and 50 years, respectively.

2.13.6 Reliability-based target design criteria in the 2010 American Association pf State Highway and Transportation Officials (AASHTO) LRFD bridge design specifications

In 2010, the fifth edition of the AASHTO LRFD bridge design specifications was published. Although not dealing with batter pile-founded reinforced concrete T-Wall flood mitigation structures, it is of importance to this R&D effort because reliability-based criteria and procedures were used to establish the design criteria and LRFD design values. The AASHTO LRFD bridge design specification was developed for American bridges with a 75-year design life, on which the statistical derivation of transient loads is based.

Under the AASHTO LRFD specification for extreme event limit states, bridge designs must satisfy

$$\phi_n * R_n \geq \sum_i \eta_i * \gamma_i * Q_i \tag{2.72}$$

where

ϕ_n = the resistance factor
R_n = the nominal resistance
η_I = a load modifier factor: a factor relating ductility, redundancy, and operational classification
γ_I = the load factor: a statistically based multiplier applied to force effects
Q_i = the force effect.

During code development, the influence of η on the bridge girder β was estimated by observing its effect on minimum values of β calculated in a database of girder-type bridges. For discussion purposes, the girder bridge data used in the calibration of these specifications were modified by multiplying the total factored loads by η = 0.95, 1.0, 1.05, and 1.10. The resulting minimum values of β for 95 combinations of span, spacing, and type of construction were determined to be approximately 3.0, 3.5, 3.8, and 4.0, respectively. Thus, for conventionally design-detailed bridges consisting of typical steel, reinforced concrete, or pre-stressed concrete bridge girders, β is 3.5. Generally speaking, and focusing on the operational importance aspect of bridge design, the two higher β values of 3.8 and 4.0 are associated with critical or essential bridges while the lower β value of 3.0 is associated with less important bridges.

Ellingwood provides insight into and discussion of the AASHTO LRFD Bridge Design Specifications reliability index. On pages 48–49 of his letter report to the USACE, Dr. Ellingwood observes that the structural actions – moments and shears in girders are based on a quasi-system analysis in which traffic loads are distributed to the individual girders through "girder distribution factors," but the target reliabilities are comparable to those for buildings, and indeed, the reliability indices for buildings were used to benchmark the bridge girder reliabilities in the early 1990s when the LRFD method was developed and implemented for bridges. He further notes that in contrast to building structures, the bridge engineering research community believed that the service life of a typical bridge would be on the order of 75 years and chose that as a convenient period of reference for determining the maximum bridge live load and the target bridge girder reliability index. Recall that for buildings, the building community referenced their target reliability index to 50 years. Assuming (1) the load process is stationary (from a statistical point of view) and (2) no structural deterioration occurs during the service life, the four AASHTO target reliability index values of 3.0, 3.5, 3.8, and 4.0 translate to the β_n-values for n = 50 years and = 100 years as listed in Table 2-17.[12] Again, it is the data for the three AASHTO target reliability index values of 3.5, 3.8, and 4.0 that are of most interest.

Table 2-17. AASHTO 2010 LRFD Bridge Design Specification reliability criteria extended to 50-year and 100-year β values – ULS.

β_{f75}	P_{f75}	P_{f1} (annual)	P_{f50}	β_{f50}	P_{f100}	β_{f100}	(β_{f50} - β_{f75})	(β_{f100} - β_{f75})
3.0	1.35×10^{-3}	1.80×10^{-5}	9.0×10^{-4}	3.12	1.80×10^{-3}	2.91	0.12	-0.09
3.5	2.33×10^{-4}	3.10×10^{-6}	1.55×10^{-4}	3.61	3.10×10^{-4}	3.42	0.11	-0.08
3.8	7.24×10^{-5}	9.65×10^{-7}	4.82×10^{-5}	3.9	9.65×10^{-5}	3.73	0.1	-0.07
4.0	3.17×10^{-5}	4.22×10^{-7}	2.11×10^{-5}	4.1	4.22×10^{-5}	3.93	0.1	-0.07

[12] $\beta_{f\text{-}n}$ for n years is calculated according to the following steps: With $\beta_{f\text{-}75}$ set equal to 3.0, 3.5, 3.8 and 4.0, their corresponding $p_{f\text{-}75}$ values are calculated using Excel with the equation and statistical function of 1-[0.5+GAUSS($\beta_{f\text{-}75}$)] for an AASHTO n =75 years design life. Next, the annual probability of the ULS, $p_{f\text{-}1}$, is calculated using Equation 2.68. The $p_{f\text{-}1}$ value serves as the basis for converting the 75-year AASHTO reliability criteria to n = 50 years and n = 100 years: The $p_{f\text{-}n}$ value is computed using Equation 2.69 for each n = 50 years and 100 years value. Last, the corresponding $\beta_{f\text{-}n}$ value is computed using Excel with the equation and statistical function of NORM.INV([1-$p_{f\text{-}n}$],0,1).

2.13.7 Comparison of CHBDC, AASHTO, and ASCE reliability criteria for a 100-year design life

Table 2-18 compares the CHBDC Table 2-8 reliability criteria data for typical bridges of typical consequence with the Table 2-17 AASHTO reliability criteria data for a standard bridge and with Table 2-14 ASCE reliability criteria for a normal building structure. These reliability data are for a ULS. For a 100-year design life, the reliability criteria for typical/standard bridges and normal buildings provides for a range in β values of between 3.29 and 3.46. A tighter range in 100-year β values of 3.42 to 3.46 is observed for the two-bridge criteria alone.

Table 2-18. Comparison of reliability criteria data for conventionally designed detailed bridges with typical consequence level to that for normal buildings – ULS.

Type of Structure	Design Code	β_{f50}	β_{f75}	β_{f100}	(β_{f100} - β_{f50})	(β_{f100} - β_{f75})
Typical bridge	CHBDC (2014)	-	3.54	3.46*	-	-0.08
Standard bridge	AASHTO (2010)	3.61*	3.5	3.42*	-0.19	-0.08
Normal building	ASCE 7-10 (2010)	3.48	-	3.29*	-0.19	-

*Calculated β value.

By the data contained in the last column of Table 2-18, the CHBDC- and AASHTO-based reliability criteria for typical and standard bridges, respectively, would translate into a reduction in the β value for a 100-year (foundation) design life that is 0.08 lower than the β value for a 75-year bridge design life. Also, the ASCE-based reliability criteria for a normal building would translate into a reduction in the β value for a 100-year design life that is 0.19 lower than the β value for a 50-year building design life. Recall that the design life for the foundation of a USACE batter pile founded reinforced concrete T-Wall flood mitigation structure is 100 years (ER 1110-2-8159) (HQUSACE 1997).

2.13.8 Resistance factor development background for individual and pile group founded bridge foundations

The structural engineering discipline of bridge design was one of the early champions of LRFD development. Since the 1980s, the bridge community of structural engineers has been developing and then revising load and resistance factors so that reliability indices for bridges superstructure

designed using the new (bridge design) code would be close to the a target Reliably Index β_{Target} of 3.5 referenced to a target period of 75 years (service life) by the discussions found on page 283 of Nowak and Collins (2013), on pages 48–49 in Ellingwood, and on page 245 in Fenton et al. (2016). With pile foundations being an integral part of the foundation system for a significant number of bridges, LRFD R&D for both driven as well as cast-in-place pile bridge foundations therefore also became an R&D focus for LRFD development with respect to bridges. This subsection discusses some of the early bridge-centric driven pile foundation LRFD R&D results.

This subsection summary draws heavily from the material contained in and observations made by Allen (2005) on the earlier LRFD developmental work for bridge pile foundations. At the time of Allen's publication, two of the most commonly used approaches for development of resistance factors for LRFD for driven piles used in bridge design were (1) calibration by fitting to Allowable Stress Design (ASD), and (2) calibration using reliability theory. He observes that the calibration by fitting to ASD for axially loaded piles suffers from two important deficiencies; (1) there is no consideration of the probability of failure, P_f, in the analysis and (2) there is no consideration of the actual bias or variability of the load or resistance prediction methods when calibration by fitting to ASD is used. Nevertheless, calibration by fitting does attempt to analytically translate traditional deep foundation design experience into the realm of LRFD design.

Calibration using reliability theory involves the estimation of the reliability inherent in ASD design methods that were in use prior to development of the bridge design based LRFD methodologies. It is based upon selecting a target reliability that is a function of the margin of safety implied in earlier non-LRFD based ASD designs, and then determining load and resistance factors consistent with the selected target reliability. One of the early sources of the resistance factors for piles in the early LRFD-centric AASHTO LRFD Design specifications (AASHTO 2004, Section 10) was the NCHRP Report 343 by Barker et al. (1991). Resistance factors were developed using statistical data and reliability theory, and calibration by fitting to ASD. In many cases, results from calibration by fitting to ASD influenced the early LRFD era final AASHTO value selected for the resistance factors reported by Barker et al. (1991) and incorporated in the AASHTO LRFD specifications of 2004 for foundation design.

It is recognized that calibration by fitting to ASD does not meet the objective of providing a consistent level of safety in design. However, calibration by fitting provides the strongest link to previous ASD practice and provides a designer's perspective to reliability analysis results.

The load factors available at the time the original resistance factors were developed are different from the load factors specified in the current AASHTO LRFD specifications (AASHTO 2004). Chapter 3 provides a historical summary of the AASHTO load and resistance factor design for pile-founded bridges as well as a summary of the most current (2020) AASHTO guidance.

3 Historical Summary of the AASHTO LRFD for Pile-Founded Bridges

3.1 Transition from Allowable Stress Design (ASD) to LRFD and calibration of LRFD

The first AASHTO LRFD Bridge Design Specification was published in 1992 and injected a change to the geotechnical engineering world, which was accustomed to ASD and the use of factors of safety (FoS) for design. ASD and its associated FoS were largely based on engineering judgement and historical behavior. If a structural component or system failed, the FoS was increased until the failure no longer occurred (Allen 2005). The lack of a failure simply meant that the FoS stayed where it was. This led to an inconsistent level of safety. The intent of the LRFD was to provide a consistent level of safety across various limit states to design structural components. The philosophy behind LRFD was to consider sources of variability and uncertainty for loads and structural behavior separately. This was accomplished by utilizing statistical data, probability distributions, and reliability theory to determine appropriate load factors and separate resistance factors. Unfortunately, there were cases where statistical data were not available, or the available statistical data lacked sufficient adequacy to be used for reliability formulations. In those cases, load factors and resistance factors were determined by calibration by fitting to the current FoS used in ASD. While this approach did not provide a consistent level of safety, it did ensure that a structure designed using LRFD methodology achieved a similar level of safety as ones previously designed using ASD.

AASHTO LRFD Design Specifications (AASHTO 2004), Section 10, first introduced resistance factors for geotechnical foundation design. The source for the resistance factors in AASHTO (2004) is the *National Cooperative Highway Research Program* NCHRP Report 343 by Barker et al. (1991). Details for associated calibrations are in Appendix A of that report. This research project focused on developing resistance factors for the Strength I limit state considering just dead and live load as this is commonly the controlling limit state. When statistical data were available, the factors were developed using statistical data and reliability theory, and when there was a lack of data, the factors were developed by calibration to the ASD code. These resistance factors were developed considering the load factors from AASHTO Standard Specifications for Highway Bridges

(AASHTO 2002). However, the load factors changed in 2004 AASHTO (2004) (Allen 2005). Since the work conducted by Barker (1991) and Paikowsky (2004) were both completed based on the previous load factors, an update is warranted to the resistance factors (approximately a 10% reduction).

3.1.1 Calibration methods

As with any theoretical framework for engineering design, calibration of the framework is critical. There are two methods used by AASHTO to calibrate the LRFD design framework:

1. Calibration by fitting to ASD
2. Calibration using reliability theory.

Fitting to ASD is done in conjunction with fundamental changes to design philosophy in which detailed statistical data are not yet available. It is also used as a benchmark for reliability theory adjustments and often influences (or controls) the selection of resistance factors.

Table 3-1 shows the 2002 load factors used by Barker et al. (1991) to calibrate the development of resistance factors and the 2004 load factors. Pre-Allen (2005) calibrations (Barker et al. 1991; Paikowsky et al. 2004) focused on Strength I limit state – for dead load (DL) and live load (LL) only – selected because it is the most common for bridge design.

Table 3-1. LFD and LRFD load factors used for resistance factor calibration (after Allen [2005]).

	LFD Load Factors (AASHTO 2002)	LRFD Load Factors (AASHTO 2004)
Dead Load, γ_{DL}	1.30	1.25
Live Load, γ_{LL}	2.17	1.75

3.1.1.1 Calibration by fitting to ASD

There are various methods in which to calibrate by fitting to ASD that start with the traditional LRFD relationship of

$$\varphi(R) \geq (\gamma_{DL} DL) + (\gamma_{LL} LL) \tag{3.1}$$

where R is the resistance, φ is the resistance factor, DL is the dead load, γ_{DL} is the dead load factor, LL is the live load, and γ_{LL} is the live load factor.

The FoS, FoS, for ASD is calculated as

$$FoS = \frac{R}{DL+LL} \tag{3.2}$$

Substituting Equation 3.2 for R, Equation 3.1 becomes

$$\varphi(DL + LL)FoS \geq (\gamma_{DL}DL) + (\gamma_{LL}LL) \tag{3.3}$$

Collecting terms on the right-hand side, the resistance factor is defined in terms of the existing load factors as

$$\varphi = \frac{\gamma_{DL} \cdot (DL/LL) + \gamma_{LL}}{[(DL/LL)+1] \cdot FoS} \tag{3.4}$$

with the DL and the LL now expressed as a ratio DL/LL in this equation.

Using Equation 3.4, an average value resistance factor can be obtained in situations where varying load factors exist. However, there is no consideration for variability of load or resistance predictions when calibrating using this approach. Further, there is no consideration to the probability of failure. Using calibration by fitting to ASD, simply *converts* ASD to LRFD and provides the same FoS. In the absence of reliable historic data, fitting to ASD is appropriate, but when historic data become available, reliability theory should be used to develop resistance factors the drive the desired probability of failure, P_f.

3.1.1.2 Calibration using reliability theory

Reliability theory determines the likelihood that failure will occur for a given structural component, considering the selected load and resistance factor combination. This likelihood of failure is the probability of failure, P_f. Failure is defined as the loads applied to a structure or structural component exceeding the available resistance:

$$\sum \gamma_i Q_{ni} \leq \varphi R_n \tag{3.5}$$

where γ_i is a load factor applicable to a specific load type (Q_{ni}), φ is the resistance factor, and R_n is the unfactored design resistance available for the limit state considered (ultimate or otherwise). The summation of $\gamma_i Q_{ni}$ is the total factored load for the loading condition for the specific limit state considered.

Loads (Q_{ni}) and resistance (R_n) are independent random variables with assumed standard normal distributions. Calibration of the LRFD design framework to a desired probability of failure, P_f, using reliability theory estimates the combination of load and resistance factors that separates the load and resistance values such that the probability that Q is greater than R, is sufficiently small. This probability represents the overlap in the load and resistance curves shown in Figure 3-1, which would result in failure of the component or system being analyzed. The number of standard deviations between the mean safety margin and the failure limit (R-Q) is the reliability index, β. Note that β is equal to the z-test statistic for a standard normal distribution. For example, a desired P_f of 1.0% (99% probability of success) corresponds to β=2.33 for the normal distribution of R-Q (2.33 is the z-test statistic for 0.01 on a standard normal distribution). This is illustrated in Figure 3-1.

Figure 3-1. Probability of failure and reliability index (after Allen [2005]).

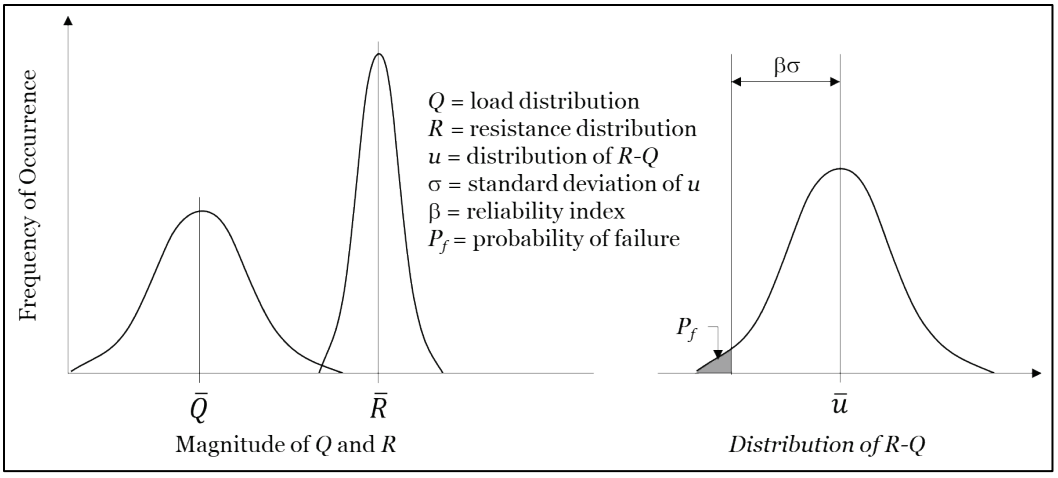

The following process to develop resistance factors is used by Baker et al. (1991) and Paikowsky et al. (2004):

1. Develop/calculate parameters.
   a. Mean, $\bar{x}$ – average of measured values

   b. Standard deviation, σ – a measure of the dispersion of a dataset relative to its mean (calculated as the square root of the variance)
   c. COV – ratio of standard deviation to the mean (shows the extent of variability in relation to the mean)
   d. Distribution type (e.g., normal, which is typically the case for DL and LL statistical distributions according to Nowak (1999); or lognormal, which is typically the case for foundation resistance according to Paikowsky et al. (2004)
2. Estimate reliability inherent in current design methods.
3. Select a target reliability based on margin of safety implied in current designs, considering need for consistency with the reliability used in development of rest of AASHTO LRFD specs, and considering levels of reliability for geotechnical design as reported in literature.
4. Determine load and resistance factors consistent with selected target reliability.

3.1.2 Use of reliability theory for driven pile resistance factors

Paikowsky et al. (2004) focused on calibration of the Strength I limit state (DL + LL), specifically to driven pile groups. This approach did not take into consideration the systematic error or spatial uncertainty as the piles were installed in a single site condition using the same installation methods. The results of the analysis yielded a ratio of 2.0 as a DL/LL ratio. The resistance factors were determined using the First Order Reliability Method from Hasofer and Lind (1974). Paikoswky et al. (2004) concluded that a target reliability index of 3 should be used for pile groups with fewer than five piles and 2.3 for pile groups with more than five piles.

3.2 Reliability analysis

3.2.1 Reliability analysis techniques

Various techniques can be used to effectively conduct reliability analysis. The techniques presented by Allen (2005) vary in theoretical accuracy and ease of implementation. Allen (2005) presents two methods in detail and presents other advanced methods found in the literature for further consideration.

1. Mean Value First Order Second Moment Method (MVFOSM).
2. Monte Carlo simulation.
3. Other advanced methods such as Rackwitz and Flessler (1978).

When discussing the reliability of a design, there are three main sources of uncertainty: spatial variability, systematic error, and design model error. Barker et al. (1991) took a first-order approach to combine the three sources of uncertainty. In this approach, Barker et al. (1991) assume that these three main sources of uncertainty are completely independent. Results of this first-order approach provided them with the final statistics, including bias and coefficients of variation, used as input into their reliability analyses. The variable λ_R is the combined bias for all sources of uncertainty affecting the resistance prediction. The COV_R is the combined COV for all the sources of uncertainty affecting the resistance prediction.

1. Statistics representative of inherent spatial variability. There is a greater variability/uncertainty in the measurement of a given property at a point than there is in the average of several measurements at various points.
2. Statistics representative of systematic error. There may be error in how data are collected; without systematic error, a new user should be able to repeat the test and get the same result.
3. Statistics representative of design model error. The theory used to develop the design model should be able to accurately estimate the resistance. Allen (2005) notes this aspect of error may be high because it is hard for models to capture the nonlinear nature of soils.

These sources of uncertainty can be combined to obtain a statistically significant value for β, a key input in reliability theory. Barker et al. (1991) settled on a DL/LL ratio of 3.0 for their analysis. They used calibration by fitting to ASD to determine resistance factors. Then, they used MVFOSM to assess the accuracy of the calibration, using the available statistical data for the level of safety, β, implied by the ASD FoS value of the limit state under question.

Using Equations 3.6 and 3.7, λ_R and COV_R can be calculated as key inputs for determining β using Equation 3.8.

$$\lambda_R = \prod \lambda_i \tag{3.6}$$

where λ_R is the combined bias for all sources of uncertainty affecting the resistance factor prediction, and λ_i are the bias values for individual sources of uncertainty affecting the resistance factor prediction. The total coefficient of variation for all sources of uncertainty affecting the resistance prediction can be calculated using the sum of squares method:

$$COV_R = \sqrt{\sum COV_i^2} \tag{3.7}$$

where COV_R is the combined COV for all sources of uncertainty affecting the resistance prediction, and COV_i are the COV values for individual sources of uncertainty. Using the calculated λ_R and COV_R, β is calculated as follows:

$$\beta = \frac{ln\left[\frac{\overline{\lambda_R} FS(Q_D/Q_L+1)}{\overline{\lambda_D} Q_D/Q_L+\overline{\lambda_{LL}}} \sqrt{\frac{1+COV_R^2+COV_{QD}^2+COV_{QL}^2}{1+COV_R^2}}\right]}{\sqrt{ln\left[(1+COV_R^2)(1+COV_{QD}^2)(1+COV_{QL}^2)\right]}} \tag{3.8}$$

where

β = reliability index
$\overline{\lambda_R}$ = mean of the resistance bias values (measured or predicted)
$\overline{\lambda_D}$ = mean of the dead load bias (measured or predicted)
$\overline{\lambda_{LL}}$ = mean of the live load bias (measured or predicted)
Q_D = nominal dead load
Q_L = nominal live load
COV_{QD} = coefficient of variation of the bias values for dead load
COV_{QL} = coefficient of variation of the bias values for live load
COV_R = coefficient of variation of the bias values for the resistance.

β is typically 3.5 for bridge and other structural designs (approximate probability of failure, P_f, of 1 in 5,000) (Allen 2005). Barker et al. (1991) found that the ASD FoS values in past geotechnical design practice for foundation were typically smaller, especially for redundant systems. They also concluded that a β of 2.3 is reasonable for a single pile within a group of significant size. Therefore, it is reasonable to consider each as an individual pile and not as part of a larger group of piles. Table 3-2 provides typical and target reliability indices, β, and the associated probability of failure, P_f, for various pile conditions and methods of calculation.

Table 3-2. Reliability index and probability of failure by component type (after Allen [2005]).

	Typical Reliability Index Factor, β	Probability of Failure, P_f
Bridge/Other structural designs	3.5	0.0002
Pile Groups		
Bearing capacity of sand footings	1.3 to 4.5	0.0968 to 0.000005
Bearing capacity of clay footings	2.7 to 5.7	0.00347 to 0
SPT estimating method	4.2	0.000015
CPT* estimating method	3.3	0.000483
Shafts		
Bearing (MVFOSM)	2.0 to 3.7	0.0228 to 0.000108
Bearing (Advanced method)	2.0 to 4.3	0.0228 to 0.00001
Pile Foundations		
Bearing (MVFOSM)	1.6 to 3.1	0.0548 to 0.000968
Bearing (Advanced method)	1.6 to 3.3	0.0548 to 0.000483
	Target β Values	Probability of Failure, P_f
Non-redundant systems (e.g., footings)	3.5	0.0002
Drilled Shafts	2.5 to 3.0	0.00621 to 0.00135
Redundant systems (e.g., pile groups)	2.0 to 2.5	0.00621

*CPT=Cone Penetration Testing

The resistance factors in the AASHTO LRFD 2004 Specifications are the Barker et al. (1991) recommended values multiplied by a λ_v factor to account for the field bearing resistance verification method used. The modifier provides a method for designers to include combinations of design and construction control methods (e.g., they can gain confirmatory testing during construction to reduce the uncertainty of the pile capacity).

3.2.2 Design life considerations

The design life for bridges is taken to be 75 years. The USACE batter pile-founded, reinforced concrete T-Wall flood mitigation structures are a significant financial investment and consequently have a 100-year design life (ER 1110-2-8159) (HQUSACE 1997). The implication on reliability analysis as well as the appropriate value of reliability index β value

considering the project design life difference is discussed in Section 2.12 of this technical report.

3.3 Post-2005 changes to AASHTO driven-pile LRFD

The following section discusses changes to driven-pile LRFD since 2005. The driven-pile methodologies and procedures discussed within this section come directly from AASHTO references (AASHTO 2007, 2020) and from the references of those direct sources.

3.3.1 Summary

The AASHTO LRFD 9th Edition (AASHTO 2020) provisions use LRFD, a reliability-based member-by-member design methodology, to ensure a pile of a given type, size, and embedment depth has a design strength that is equal to or greater than its factored load effects. This approach was initially introduced in the first edition of the LRFD Specification (1994). Mathematically, this approach is designed to ensure that a minimum level of reliability is achieved in the design of driven piles. Prior to 2006, pile design capacity derived from static design methods required the inclusion of a factor, λ. This factor varied based on the type of construction control and was not well received for adoption and implementation by the geotechnical community. It was not until 1 October 2007 that AASHTO and FHWA mandated a transition to an LRFD approach for new bridges, which is when most in the geotechnical community changed from ASD to LRFD.

3.3.2 Strength limit states

AASHTO Article 10.7.3. (2007, 2020) addresses the design strength of piles by covering axial compression, uplift, and lateral resistances of a single pile and pile group. In addition, it covers the structural resistance of a steel pile (axial, bending, and shear).

The nominal bearing resistance of a steel pile can be determined using a myriad of methods to include static load testing, dynamic testing, the wave equation analysis, and dynamic formulas. The method used to determine the nominal bearing resistance subsequently determines the geotechnical resistance factor, φ, and the associated uncertainty of the bearing resistance. AASHTO recommends using a dynamic analysis method over a static analysis method unless the dynamic methods are viewed as unsuitable for field verification of a pile's nominal bearing resistance.

Since 2005, the resistance factors used by AASHTO have stayed consistent except for slight changes in wording (e.g., lateral geotechnical resistance versus horizontal geotechnical resistance) and in the description of some of the driving criteria conditions. Table 3-3 below provides data extracted from Table 10.5.5.2.3-1 and Article 6.5.4.2 from AASHTO (2007, 2020) and demonstrates the lack of significant change throughout the years.

Table 3-3. AASHTO resistance factor summary.

Condition/Resistance Determination Method		Resistance Factor AASHTO (2020)	Resistance Factor AASHTO (2007)
Nominal Resistance of Single Pile—Dynamic Analysis and Static Load Test Methods, φ_{dyn}	Driving criteria established by successful static load test of at least one pile per site condition and dynamic testing of at least two piles per site condition but no less than 2% of the production piles. *Note: in AASHTO 2007, values varied based on site variability and number of load tests per site.	0.80	0.55 - 0.90*
	Driving criteria established by successful static load test of at least one pile per site condition without dynamic testing.	0.75	Not listed
	Driving criteria established by dynamic testing conducted on 100% of production piles.	0.75	Not listed
	Driving criteria established by dynamic testing, quality control by dynamic testing of at least two piles per site condition but no less than 2% of the production piles.		Not listed
	Wave equation analysis, without pile dynamic measurements or load test. 2020: …with field confirmation of hammer performance. 2007: …at end of drive conditions only.	0.50	0.40
	FHWA-modified Gates dynamic pile formula (End of Drive condition only).	0.40	0.40
	Engineering News dynamic pile formula (end of drive condition only).	0.10	0.10

Condition/Resistance Determination Method		Resistance Factor AASHTO (2020)	Resistance Factor AASHTO (2007)
Nominal Bearing Resistance of Single Pile—Static Analysis Methods, φ_{stat}	Side Resistance and End Bearing: Clay and Mixed Soils α-method β-method λ-method Sand Nordlund/Thurman Method *SPT*-method *CPT*-method End bearing in rock	 0.35 0.25 0.40 0.45 0.30 0.50 0.45	 0.35 0.25 0.40 0.45 0.30 0.50 0.45
Block Failure, φ_{b1}	Clay	0.60	0.60
Uplift Resistance of Single Piles, φ_{up}	Nordlund Method α-method β-method λ-method *SPT*-method *CPT*-method Static Load Test (“Load Test” in 2007) Dynamic test with signal matching	0.35 0.25 0.20 0.30 0.25 0.40 0.60 0.50	0.35 0.25 0.20 0.30 0.25 0.40 0.60 Not listed
Group Uplift Resistance, φ_{ug}	All soils (“Sand and Clay” in 2007).	0.50	0.50
Lateral Geotechnical Resistance of Single Pile or Pile Group (“Horizontal” in 2007)	All soils and rock.	1.0	1.0

Condition/Resistance Determination Method		Resistance Factor AASHTO (2020)	Resistance Factor AASHTO (2007)
Structural Limit State	Steel piles: For axial resistance of piles in compression and subject to damage due to severe driving conditions where use of a pile tip is necessary, ϕ_c.	0.50	0.50
	For axial resistance of piles in compression under good driving conditions where use of a pile tip is not necessary, ϕ_c.	0.60	0.60
	For combined axial and flexural resistance of undamaged piles: -Axial resistance, ϕ_c -Flexural Resistance, ϕ_f	0.70 1.00	0.70 1.00
Pile Drivability Analysis, φ_{da}	Steel H-piles: For resistance during pile driving	1.0	1.0

3.3.3 Serviceability limit states

AASHTO (2020) lists serviceability limit states for a driven-pile foundation as settlement due to static and downdrag loads and lateral movement due to lateral squeeze and deformations. This is consistent with AASHTO (2007). However, AASHTO (2007) considered overall stability of a driven-pile foundation a serviceability limit state. Thus, in situations where a pile foundation was constructed through an embankment, in proximity to a slope, where it was susceptible to erosion or scour, or on inclined bearing strata, overall stability of the pile-supported foundation was evaluated for serviceability, with appropriate stabilization measures taken to mitigate risk. Presently, AASHTO (2020) classifies the overall stability of a pile supported foundation as a strength limit state.

As it pertains to vertical deformation, or settlement, pile settlements are usually estimated specifically to pile groups. In addition, the settlement of a pile group will be several times greater than the settlement of a single pile carrying the same load per pile. This is because a larger area of soil around and underneath the pile group is subjected to vertical stress. Modjeski and Masters Inc. (2015) highlights the uncertainty inherent in the determination of differential settlement between multiple piles along the length of a structure. In fact, they point out that the uncertainty for differential settlement between two piles is greater than the uncertainty in

estimating the settlement of a single pile. Thus, they recommend a δ-0 approach with a load factor for deformation and the construction point concept. This involves estimating the maximum settlement of one pile, δ, using one of several approved methods, with all applicable loads in the AASHTO Service I load combination and subtracting the total foundation settlement caused before construction of the supported superstructure. This relevant total settlement from one pile is compared to a conservatively assumed deflection of 0 by the adjacent pile. Once the calculated angular distortion is adjusted by a load factor, which is a function of the probability of exceedance of the foundation deformation under consideration, one can determine the potential structural implications from the angular distortions between adjacent piles.

As mentioned earlier in this section, downdrag loads, which are axial compressive loads generated on a pile from negative skin friction, contribute to settlement and the ability for a pile or pile group to meet AASTHO serviceability limit state criteria. Factors contributing to the magnitude of the downdrag load and corresponding settlement include subsurface conditions, pile installation methods, and the pile loading sequences, to name a few. In response to the perception by some that the 6th Edition of the LRFD Bridge Design Specifications (AASHTO 2012) was too complex, Siegel et al. (2013) proposed an alternative design approach to determine the downdrag load and associated downdrag movement. Given the unfactored, permanent load acting on the pile, a clear picture of the subsurface layers, an understanding of the load-deformation response of the soil, and information on fill placement, Siegel et al. (2013) demonstrated the alternative design approach to two hypothetical examples. Hannigan et al. (2016) provides the step-by-step procedure used by Siegel et al. (2013). Note that this specific approach intentionally omits the use of load and resistance factors as they lead to erroneous predictions of both settlement and drag force. While adopted as the design method for downdrag by the FHWA, AASHTO LRFD (2020) does not mention this specific proposed alternative design approach. It does, however, reference another neutral plane method, which is described and discussed in NCHRP 393 Briaud and Tucker (1997) and Hannigan et al. (2005), which is consistent with AASHTO (2007). When dealing with cohesive soils, both the 2020 and 2007 specifications use a maximum load factor of 1.4 (α Tomlinson Method) or 1.05 (λ Method) when investigating maximum downward pile loads and use a minimum load factor of 0.25 (α Tomlinson Method) or 0.30 (λ Method) when investigating possible uplift loads.

3.3.4 Regional adjustments for accuracy

The purpose of the LRFD resistance factors for piles is to provide a sufficiently low design value for a wide range of pile types and soil conditions. The factors vary based on the method used, the type of soil, and the direction of loading. Paikowsky et al. (2004), suggested a modification to calibrated resistance factors once checked against case studies to test their validity. Since 2005, several Departments of Transportation have shifted from the AASHTO LRFD resistance factors to their own regionally calibrated resistance factors. In C10.5.5.2.1 of AASHTO (2007, 2020), modified resistance factors are encouraged based on regionally specific values if substantial statistical data or substantial successful experience is available and justified. In doing so, AASHTO (2007, 2020) reminds the designer of the historical geotechnical design practice of achieving an effective reliability index, β, of 3.0, for foundations in general and an effective reliability index of 2.3 for highly redundant systems such as pile groups. These indexes correspond with approximate probability of failures of 1 in 1,000 and 1 in 100, respectively. AASHTO (2007, 2020) states that modified resistance factors should follow this precedence.

For example, while not in the AASHTO (2020) specifications, the Washington State Department of Transportation (WSDOT) has reportedly developed an improved driving formula with a recommended resistance factor of 0.55 (Allen 2007). WSDOT conducted the study in hopes of providing users with a driving formula to estimate the bearing resistance of a pile simply and quickly while simultaneously reducing inherent inaccuracies. To achieve the desired more accurate prediction, the WSDOT pile-driving formula, shown in Equation 3.9, modifies the FHWA Gates Formula (AASHTO equation 10.7.3.8.5-1, 2020) by accounting for pile type, hammer type, and the use of different functions for the energy and driving resistance terms.

$$R_n = 6.6 \times F_{eff} \times E \times \ln(10N) \tag{3.9}$$

where

F_{eff} = hammer efficiency factor
E = nominal (or developed) energy of pile hammer, in foot-kips
N = penetration resistance, in blows/inch.

The WSDOT modifications serve as a better fit to pile load data from Paikowsky et al. (1994) whereas the FHWA Gates equation tends to

underpredict bearing resistances over 700 kips and overpredict the bearing resistance when under 700 kips (Allen 2007).

As another example of regional modifications, the Minnesota Department of Transportation has also developed and adopted a dynamic pile formula, referred to as MPF12 (Minnesota Pile Formula 2012) shown in Equation 3.10 (Paikowsky et al. 2014).

$$R_n = 20 \times \sqrt{\frac{W \times H}{1{,}000}} \times \log\left(\frac{10}{s}\right) \tag{3.10}$$

where

R_n = nominal resistance (tons)
W = weight of ram (lb)
H = stroke (height of fall)
s = set (pile permanent displacement per blow) (in.).

To determine the factored resistance, MPF12 recommends using a resistance factor of 0.60 (for blow counts between 2 and 15 blows per inch). Their formula and associated resistance factor were developed through the review of data from 28 bridges in the state. The distribution of the resistance along with the distribution of the load and established target reliability (2.33 for piles when used in groups of five or more and 3.0 for single piles and groups with four or fewer piles) was used to calculate the 0.60 resistance factor (Paikowsky et al. 2014).

After assessing load testing data from high-displacement piles from six major bridge projects in Rhode Island, Bradshaw and Davis (2013) reported the AASHTO LRFD Nordlund and SPT methods for static pile capacity were overpredicting the capacity of high-displacement piles in their region. The AASHTO LRFD (2007) static capacity methods and related resistance factors used for comparison were based on pile load test data in sands and clays, which did not accurately capture the capacity given the very silty soils found in parts of Rhode Island. Thus, the authors recommended a more rigorous Monte Carlo method and an expansion of the static loading test database at a regional level. In summary, several states are following AASHTO (2007, 2020) guidance to determine modified resistance factors to regionally specific values when there is either substantial statistical data combined with calibration or substantial successful experience leading to justification.

4 Structural Variables with Respect to Limit States

4.1 Introduction

As stated in Chapter 2, in reliability analysis the probability that a structure will fail is defined by the passive Capacity (or Resistance) and the active Demand (or Load). When the Demand exceeds the Capacity of a structural element, that structural element will have unsatisfactory performance. A response state function (sometimes referred to as a $g(\boldsymbol{X})$ function), returns the status of the system performance. The $g(\boldsymbol{X})$ function is thus defined as

$$g(\boldsymbol{X}) = R - L \tag{2.11 bis}$$

where R is the Resistance (Capacity) and L is the Load (Demand). In this case, the limit state Response Surface is defined by the point where the Resistance equals the Load, or

$$g(\boldsymbol{X}) = (R - L) = 0 \tag{2.17 bis}$$

It is important to find how to calculate the Capacity from variable engineering properties given these relationships to calculate the probability that the Capacity will be exceeded. This implies that the Resistance is a similar function taking a vector of variable properties drawn from distributions of the form

$$R = R_m(\boldsymbol{X})\lambda_R = R_m\left(f_y, f_c, E, b, c, d \ldots\right)\lambda_R \tag{4.1}$$

in which $R_m(\ldots)$ is a mechanics-based expression of strength, with probabilistic material properties (f_y,f_c,...) and λ_R is the factor representing uncertainties because of approximations in structural analysis and simplifications in the constitutive model of the material behaviors. The factor is called the resistance bias factor in subsection 2.1.2 and is defined as the ratio of the mean and nominal resistances.

$$\lambda_R = \frac{R_m}{R_n} \tag{2.4 bis}$$

4.2 Introductory observations for three structural limit states

Limit state criteria is needed for both reinforced concrete flood mitigation structures as well as for the steel piles that provide its foundation. This subsection provides introductory observations for the three structural limit states of

- shear capacity
- flexural capacity
- combined axial load and bending.

Shear capacity: The first structural limit state of interest to reinforced concrete hydraulic structures is the shear capacity of reinforced concrete members. Equation 4.2 gives an example of a resistance equation for shear capacity, V_c, computed using the simplified American Concrete Institute (ACI) (1978) equation for beam capacity (ACI 318-14; ACI Committee 318 [2014]; Equation 22.5.5.1):

$$R_m(b, d, f_c') = V_c = 2\sqrt{f_c'}bd \tag{4.2}$$

where

b = section width
d = distance from compression face to center of reinforcing steel
f'_c = concrete compression strength.

Details regarding the shear capacity and the structural HP pile shear limit state is presented in Chapter 7.

Flexural capacity: The second structural limit state of interest to reinforced concrete hydraulic structures is the flexural capacity of reinforced concrete members. Equation 4.3 gives an example of a resistance equation for flexural capacity of a reinforced concrete member, M_n:

$$R_m\left(A_s, F_y, d, f_c', b\right) = M_n = A_s F_y \left[d - \frac{\frac{A_s F_y}{0.85 f_c' b}}{2}\right] \tag{4.3}$$

where

A_s = area of reinforcing steel
F_y = yield strength of reinforcing steel
D = distance from compression face to center of reinforcing steel
f'_c = concrete compression strength
b = width of beam or design section.

Table 4-1 shows representative distributions for certain material properties given construction practice in the United States (Ellingwood). These material properties, as well as others not listed, are used in the specified $R_M(\boldsymbol{X})$ functions to calculate capacity in a probabilistic fashion.

Table 4-1. Probabilistic models for concrete and steel reinforcement strength* (after Ellingwood).

Variable	Distribution Type	Nominal (pounds per square inch [psi])	Mean (psi)	COV
Ec (4,000 psi concrete)**	Normal	3.6×10^6	3.95×10^6	0.18
Ec (6,000 psi concrete)**	Normal	4.4×10^6	4.84×10^6	0.18
fc (4,000 psi concrete)	Normal	4,000	4,800	0.15
fc (6,000 psi concrete)	Normal	6,000	7,200	0.12
ft (4,000 psi concrete)	Normal	405	443	0.20
ft (6,000 psi concrete)	Normal	496	543	0.20
fy (deformed bar)	LogNormal	60,000	66,000	0.08
fu (deformed bar)	LogNormal	90,000	104,000	0.07
Es	Normal	29×10^6	29×10^6	0.04
Effective depth of reinforcement	Normal	D	D	0.5/d***
Reinforcement cover	Normal	c	c	0.5/c***
Placement of formwork	Normal	b, h	b, h	0.25/b***

*1 psi = 6.9 megapascals

**Unit weight of concrete = 145 lb per cubic foot

***COV equals standard deviation in placement, σ, divided by nominal dimension.

The probabilistic capacities can be computed for various limits states given variable material properties can be calculated using the specified $R_m(\boldsymbol{X})$ capacity equation (e.g., flexural capacity of beams). Table 4-2 shows the results of running Monte Carlo simulations to determine distributions for several $R_m(\boldsymbol{X})$ capacity equations. The $R_m(\boldsymbol{X})$ capacity equations were performed by assigning an input vector $\boldsymbol{X}$ with values drawn from the appropriate material distributions and then a distribution was mapped to the results. This work was performed by MacGregor at al. (1983), Ellingwood and Hwang (1985), Nowak and Szerszen (2003), and others. The final statistics consider the bias of the mechanics-based expression (λ_R).

Table 4-2. Resistance models (after Ellingwood).

Limit State	Distribution Type	Mean*	COV
Flexure Capacity (beams)	LogNormal	1.10 Mn	0.12
Flexure Capacity (one-way slabs)	LogNormal	1.12 Mn	0.14
Shear Capacity (beams)	LogNormal	1.15 Vn	0.18
Shear Capacity (walls)	LogNormal	1.20 Vn	0.18
Axial load and flexure capacity (short columns, tension failure)	LogNormal	1.05 Rn	0.12
Axial load and flexure capacity (short columns, compression failure)	LogNormal	0.98 Rn	0.14
Compression Capacity (plain concrete)	LogNormal	1.20 Pn	0.15

*Mn in nominal applied moment.
Vn in nominal applied shear force.
Rn in nominal applied axial load.
Pn in nominal applied axial load.

For the resistance models in Table 4-2, the variable capacity (R) for reliability analysis can be derived by drawing from the distribution. Using Equation 2.11, if the capacity (R) exceeds the demand (L), then the $g(\boldsymbol{X})$ function is greater than 0, indicating failure.

Interaction equation: The third structural limit state of interest to the HP steel pile that provide T-Walls their foundation is the combined loading of axial load with bending, analyzed within each pile of the foundation. This is a complicated limit state because the (axial) compressive strength of the pile and the moment strength are not independent of each other. The resulting axial and moment column/pile capacity is expressed through an interaction diagram. For this reason, a single, independent resistance-only equation $R_m(\boldsymbol{X})$ cannot be generated for columns/piles as it can be for shear and flexural capacities (Equations 4.2 and 4.3, respectively).

Figure 4-1 shows the configuration of interaction diagram for an HP steel pile. The capacity of the HP steel pile is the area below the interaction curve for compression and to the left of the curve under moment. The axial load is positive for a pile in compression for CPGA-R output. Notice that as the moment increases for the pile, the compressive strength decreases. The axial load is negative for a pile in tension for CPGA-R output. The

capacity of the HP steel pile in tension is the area above the interaction curve for tension and to the left of the curve under moment.

Figure 4-1. Interaction diagram for a steel HP pile (after Ebeling et al. [2012]).

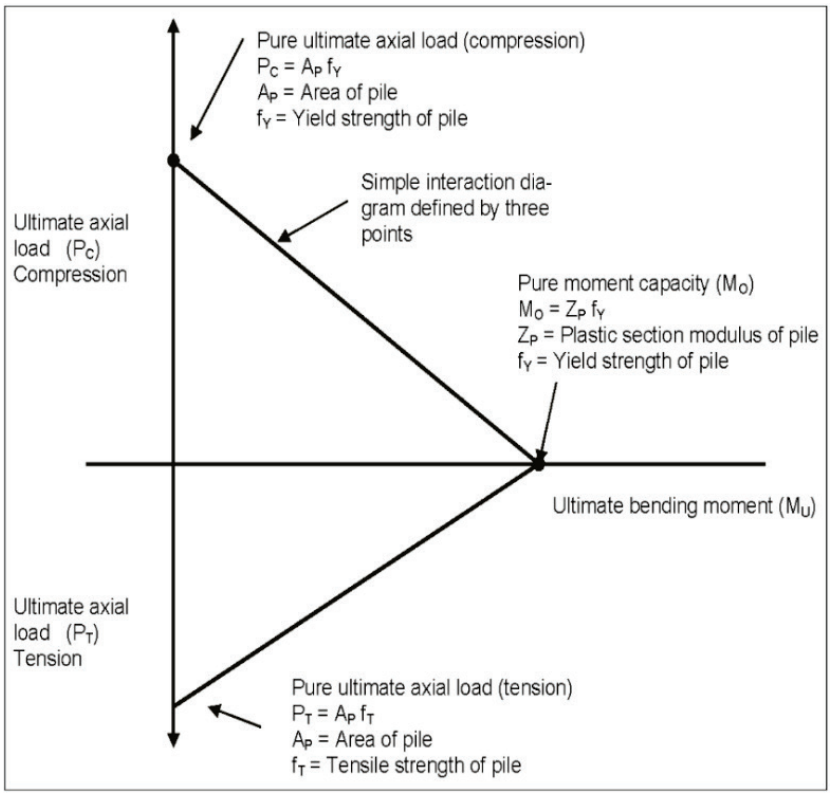

In the case of HP steel pile foundations, CPGA-R software defines the Combined Bending Factor (CBF) for piles subjected to axial compression loading and bending as

$$\text{CBF} = \left[\frac{F3}{ACC} + MF1 * \frac{|M1|}{AM1} + MF2 * \frac{|M2|}{AM2}\right] * \left(\frac{1}{OSF}\right) \tag{4.4}$$

with

$F3$ = actual axial load (a local pile axis)
$M1$ = actual bending moment about the 1 axis (a local pile axis)
$M2$ = actual bending moment about the 2 axis (a local pile axis)
ACC = allowable axial load in compression
$AM1$ = allowable bending moment about the 1 axis (a local pile axis)
$AM2$ = allowable bending moment about the 2 axis (a local pile axis)
OSF = overstress factor.

Similarly, for HP steel piles subjected to axial tension loading and bending, CPGA-R defines the CBF as

$$\text{CBF} = \left[\frac{-F3}{ATT} + MF1 * \frac{|M1|}{AM1} + MF2 * \frac{|M2|}{AM2}\right] * \left(\frac{1}{OSFT}\right) \quad (4.5)$$

where

ATT = allowable axial load in tension
$OSFT$ = overstress factor for piles in tension.

The CBF value of Equation 4.4 or 4.5 must be less than or equal to 1.0 in each HP steel compression or tension pile, respectively.

Details regarding the capacities and the HP pile structural limit states are elaborated upon in Chapter 7.

5 Sea Wave Forces on Vertical Walls using the Goda-Takahashi Procedure

5.1 Introduction

The USACE Coastal Engineering Manual (EM 1110-2-1100) (HQUSACE 2002), referred to as CEM in this chapter, currently does not provide clear guidance on the topic of estimating wave forces (breaking and non-breaking) on vertical walls. The CEM was last updated in 04/2012. In this regard, the CEM (Part VI, Change 3, 28 Sept 11, pg. VI-1-3) refers to the Shore Protection Manual (1984) in the following statement: *"*The Shore Protection Manual contains provisional guidance for estimating slamming forces on vertical walls caused by breaking waves (Minikin method). This procedure produces high forces, and it is viewed with skepticism by some. Because no commonly accepted procedure was available at the time of writing to replace Minikin's method, it was decided to not include this topic.*"*

Since a wave force estimation method (for vertical walls) is needed for this research effort and Minikin's method is now considered, by many, as obsolete and theoretically incorrect (Allsop et al. 1996) and as "somewhat out of fashion" (Bullock et al. 2004), a literature review was conducted to identify a method that is both generally accepted among the international coastal engineering community and that can be implemented with reasonable effort. The selected method, based on the literature review, is attributed to the work of Goda (1974) and Takahashi et al. (1993). This method is well established, based on a broad set of laboratory and theoretical considerations, and has been adopted by many national standards including Japan, Great Britain, and Italy (Cuomo 2007).

The current version of the Goda-Takahashi wave pressure relationship is given in Goda (2010). The mathematical relationships of this formulation are discussed in detail in Section 5.4 of this chapter. Goda's original objective was to predict the pressure components, on a vertical (e.g., caisson) wall, as a function of the wave, the bathymetry, and the still water level (SWL) for design storm conditions. Later, it was found that breaking waves could impart an implosive pressure component to a vertical wall. Bullock et al. (2004) observed that Goda's original method did not attempt to predict the short-duration peak wave pressures caused by breaking waves but assumes a trapezoidal pressure distribution that is intended to produce

a static load equivalent to that of a breaking or non-breaking wave acting on the dynamic system formed by a caisson founded on a rubble mound. The pseudo-static Goda formulation was extended by Takahashi et al. (1993, 1996) to include the implosive pressure coefficient of a breaking wave.

Goda's formulation assumes that the maximum wave induced pressure, exerted on a vertical wall, occurs at the location of the mean water level (identified as the SWL, in this chapter) and that the maximum pressure is proportional to the height of the highest wave (H_{max}) and the design wave length (L_D). Additionally, the Goda-Takahashi formulation includes the effect of the incident wave angle, which has a significant effect on reducing wave pressures imparted to the wall at impact. In Figure 5-1, a breaking wave is shown for the case of a small incident shoreline angle. This non-zero wave approach angle results in a non-uniformity wave break along the length of the wave resulting in significant lateral variability in impact pressures and an overall reduction in total force. This wave pressure/force reduction is accounted for in the Goda-Takahashi formulation through inclusion of the incident wave angle term, which has a significant effect on reducing wave pressures (Figure 5-2).

Figure 5-1. Breaking wave for non-zero wave approach angle demonstrates non-uniformity (after Oten Lucas[13]).

[13] www.pixabay.com

Figure 5-2. Influence of incident wave angle on wave pressure.

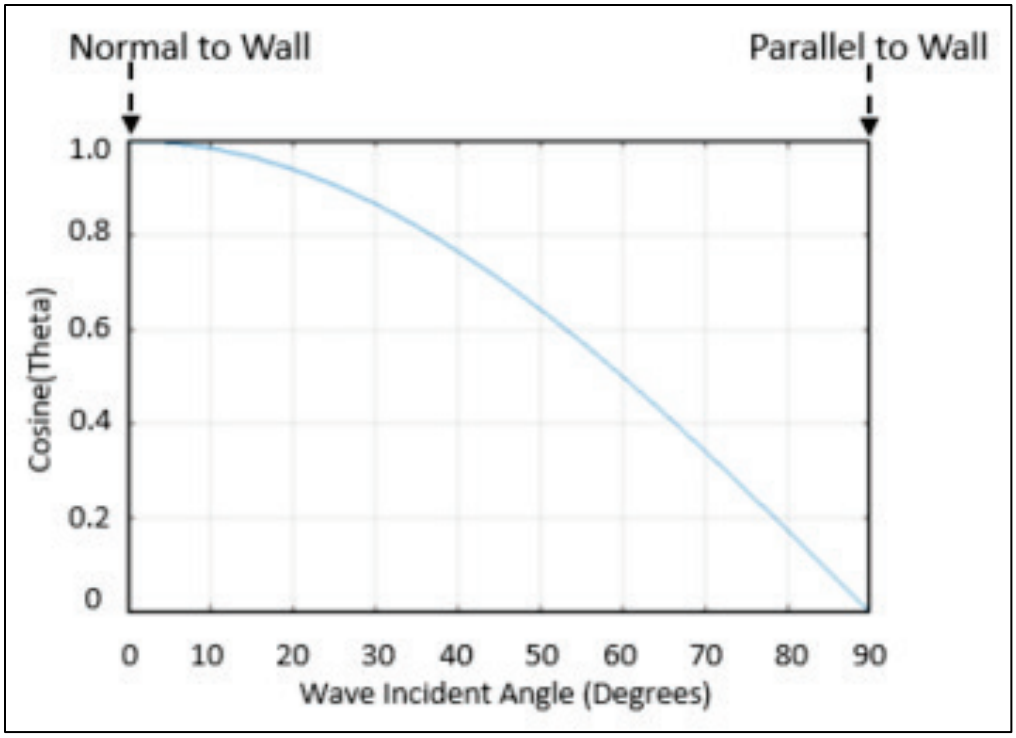

Goda and Takahashi (2010) employed laboratory scale modeling in the derivation and validation of the predictive wave pressure formula. In Section 5.2 of this report, Goda's laboratory setup, including the physical model, the pressure sensors and the data acquisition system are described. Additionally, Goda's experimental design and definitions of environmental and structural parameters are presented.

In Section 5.3, Goda's experimental results are discussed with primary focus on the measurement and interpretation of wave induced peak pressures and their vertical distribution along the wall. This quasi-static wave induced peak pressure distribution acts to exert a lateral force on the seaward side of the caisson that must be balanced by resistance at the berm level of the caisson to prevent failure by sliding. The fundamentals of this quasi-static force balance requirement are presented in Section 5.3.

In Section 5.4, Goda's wave pressure formula is presented. This formula is a combination of theoretical terms and empirically derived coefficients. The empirically derived coefficients of the Goda formulation are based on his laboratory scale experiments and verified by full-scale breakwater safety factor analysis. The impulsive pressure term added to Goda's original formula by Takahashi et al. (1993) is also discussed in Section 5.4.

As mentioned above, Goda went on to validate his predictive method by performing stability analysis on full-scale caisson type breakwaters along Japan's coastline. The breakwaters selected for analysis experienced high sea storm events of which wave records were available. The results of this analysis are impressive in that Goda's formulation adequately characterized the breakwater's susceptibility to failure in design storm conditions. The details of this validation study are given in Section 5.5.

Extrapolation of small-scale empirical results to full-scale application requires knowledge of the physical phenomena that can be influenced by scale effects. In the case of breaking waves and pressures imparted to a structure, the primary phenomena of concern here is air entrainment and air compression during the wave breaking process. This is a phenomena that has been described as the impulsive component of peak wave pressure and has been measured using high-speed data acquisition equipment. Several researchers have investigated this scale effect as discussed in Section 5.6.

In LRFD analysis, a parameter is required that represents the uncertainty in the predictive capability of a load calculation method. This parameter is known as the COV of the load, which is in this analysis the wave pressure loading. Since the Goda-Takahashi formulation is used in this procedure, it is necessary to determine the uncertainty in this predictive method. To achieve this objective, the datasets of various researchers were statistically evaluated, individually and combined, to derive a set of Goda-Takahashi wave pressure COVs as a function of the relative wave height (H_i/d_{SWL}), where H_i is the incident design wave height and d_{SWL} is the design still water depth at the structure. The results of this investigation are presented in Section 5.6 and summarized in Figures 5-35, 5-37, and Table 5-9. The authors of this technical report observed a general increase in the COV with increasing values of H_i/d_{SWL} leading to a step-like COV adjustment. For extreme values of H_i/d_{SWL}, where water depth and wave height are near equal, our statistical confidence in estimating the COV is diminished, thus requiring the coastal engineer to re-examine the summary dataset statistics shown in Figure 5-35.

5.2 Goda's laboratory setup of an instrumented caisson within a laboratory wave flume

In 1974, Goda (1974) introduced a formula to compute non-impulsive wave loading on vertical walls. His application focus was on the design of Japan's

coastal caissons used to protect its harbors from damage caused by wave loadings. It was based upon theoretical and laboratory work. With respect to the laboratory investigation, Figure 5-3 is a schematic of the wave basin test facility that Goda used to develop his initial relationship from measured wave loading on a caisson located within a laboratory flume.

In Figure 5-3, the model caisson is partially submerged with the wave generator situated on the right-hand side of the caisson and the protected zone on the left-hand side of the caisson. The right-side vertical face of the caisson was instrumented with pressure sensors. This model set up is consistent with Goda's objective of defining ocean wave loading as applied to caissons used to protect Japan's harbors from damage caused by these wave loadings.

Figure 5-3. Section view of Goda's (1972) laboratory setup of an instrumented model caisson in wave basin (units in meters).

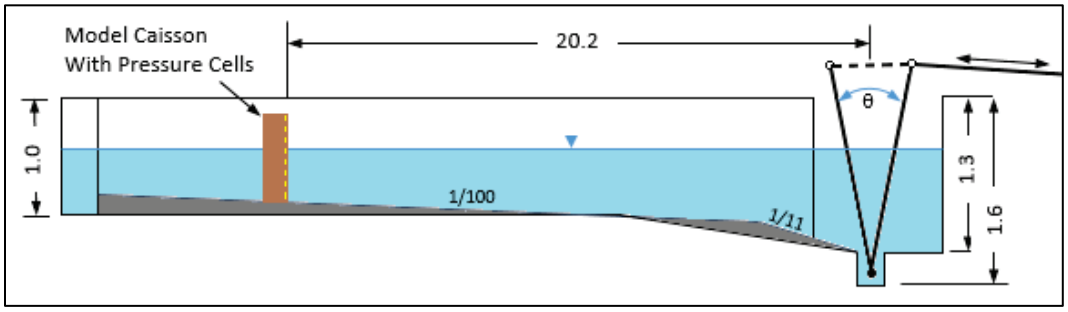

Goda (1972) describes how a model caisson was set in the flume by laying up steel boxes of 50, 30, and 15 cm in height. They were tied together and stabilized in position by weights. Pressure cells of unbonded strain gage type with diaphragms of 20 mm in diameter were used for measurement of wave pressures. Five or six pressure cells were tightly screwed onto the front steel plate of 10 mm thickness with the vertical distance of 10 cm between them. The maximum sampling rate of the pressure cell data acquisition system was 300 Hz. The measuring of wave pressures was repeated six times for each test condition. The mean values of wave pressures were calculated and analyzed with pre-calibrated incident wave heights.

Goda assumes a trapezoidal pressure distribution on vertical walls with maximum wave pressure exerted at SWL, as depicted in Figure 4-4 of Goda (2010) and Figure 4-21 of Takahashi (2002) and indicated by P_1 in Figure 5-4. The Goda wave pressure distribution applied to the vertical face of a 2-D caisson cross section is shown below in Figure 5-4. The

parameters shown in this figure will be discussed in Section 5.4 where details of Goda's equations are described.

Figure 5-4. Goda's wave pressure distribution on vertical caisson wall (after Goda [1974]).

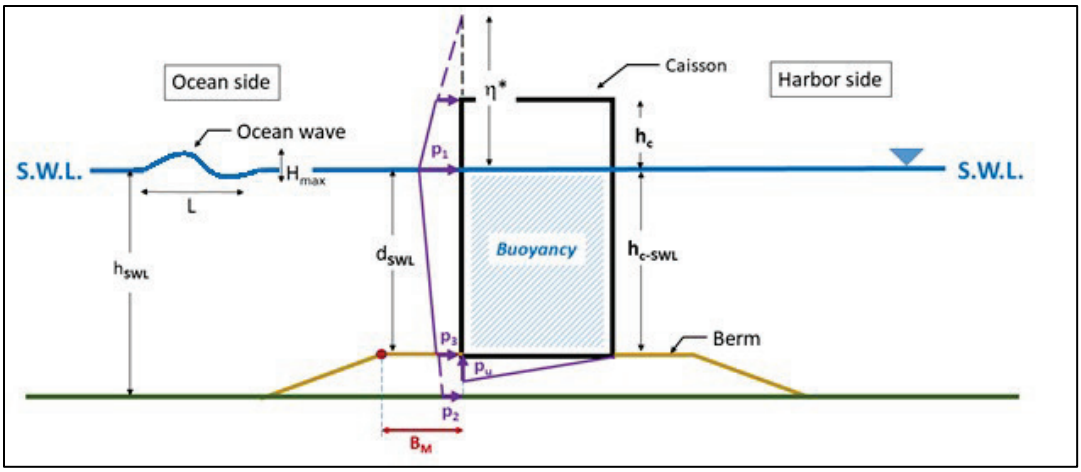

5.3 Examples of wave pressure data recorded in Goda's laboratory flume

In Figure 5-5, Goda and Kakizaki (1966) attempt to illustrate the pressure distribution on a vertical wall as a function of wave and hydrostatic components. In Figure 5-5 (a), the vertical water pressure distribution of the total water pressure with elevation is depicted for the hydrostatic water pressure at SWL as well as the total pressure distributions of water at the wave crest and wave trough events. In Figure 5-5 (b), the wave pressure portion of the total water pressure distribution is separated out by subtracting the SWL hydrostatic distribution component from the wave induced water pressure distributions at wave crest and trough events. The resulting wave distributions (Figure 5-5 (b)) indicate a net-positive pressure distribution at wave crest and a net-negative pressure distribution at wave trough events.

Figure 5-5. Idealized vertical distribution of (a) water and (b) wave pressures along the vertical face of a caisson (after Goda and Kakizaki [1966]).

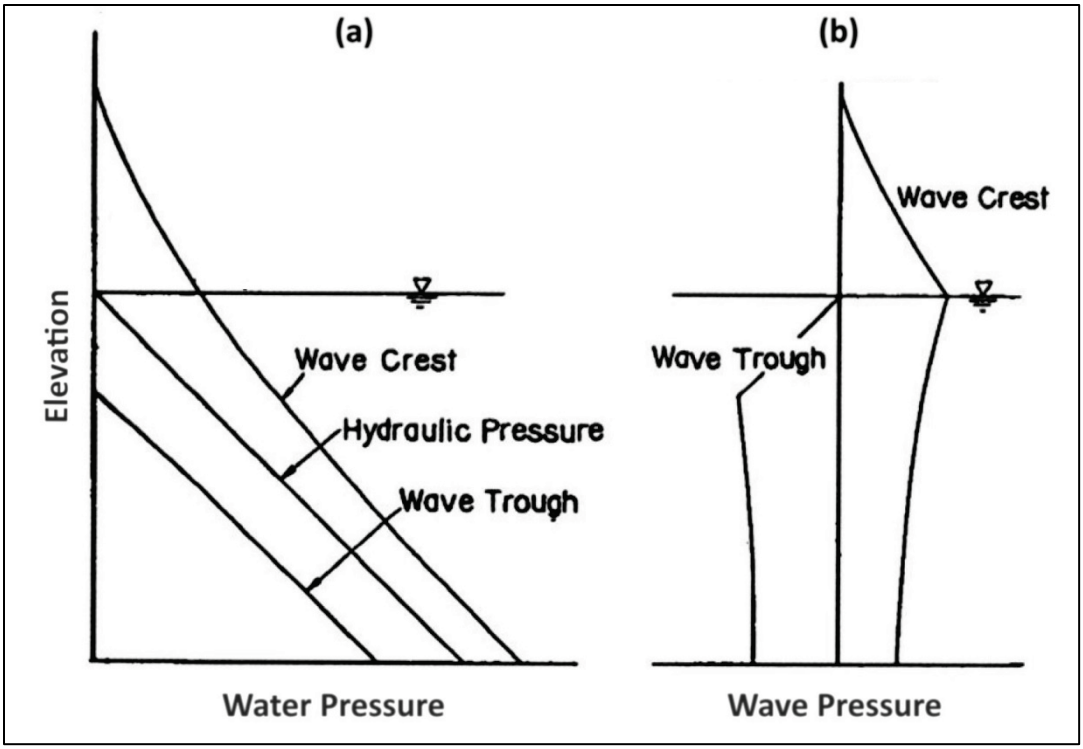

Examples of vertical distribution of peak wave pressures measured on the instrumented model caisson in the flume by Goda during wave crest and at wave trough events are shown in Figures 5-6 and 5-7. Figure 5-6 shows the peak wave pressure distributions for a wave with period of 1.302 sec. Figure 5-7 shows the peak wave pressure distributions for a wave with period of 2.007 sec. Each data point represents the average peak pressure reading of 35 to 54 waves of the same wave height and period. The authors of this technical report emphasize the importance of Goda's use of mean peak pressure, as opposed to maximum peak pressure, in the derivation of his formula. Other researchers have focused efforts on identifying the maximum peak pressure due to wave impact on a vertical wall and the associated force imparted to the wall. The authors of this technical report acknowledge that the wave-induced maximum peak pressure is an important measurement even though the duration of maximum peak pressure, acting on the vertical wall face, is typically on the order of only several milliseconds.

Figure 5-6. Vertical distribution of peak pressures during wave crests and at wave troughs for waves of period 1.302 sec (after Goda and Fukumori [1972]).

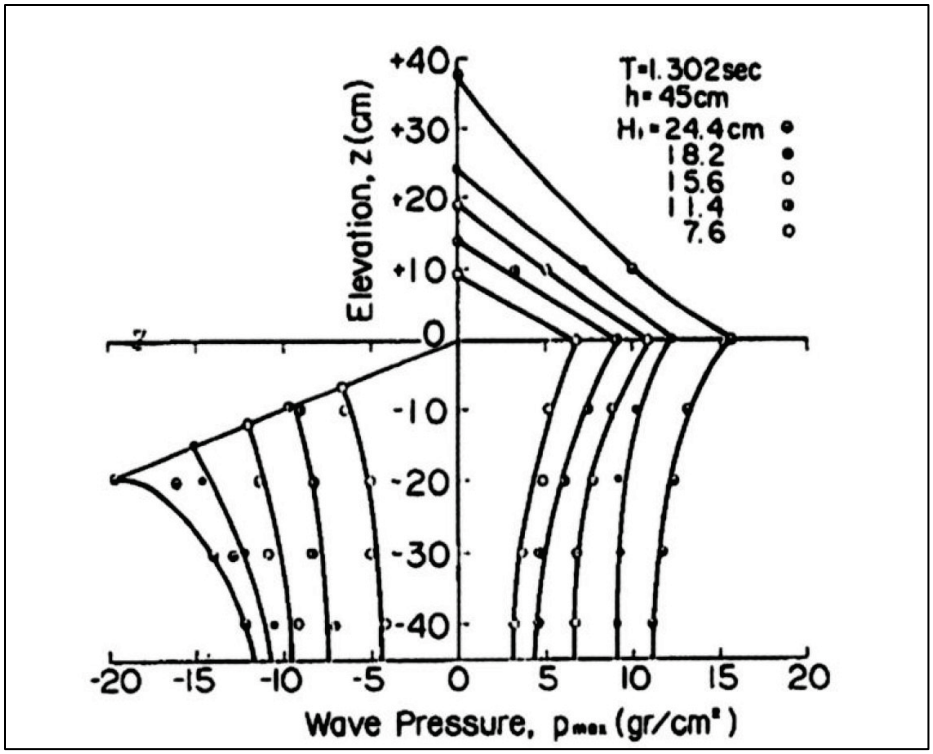

Figure 5-7. Vertical distribution of peak pressures during wave crests and at wave troughs for waves of period 2.007 sec (after Goda and Fukumori [1972]).

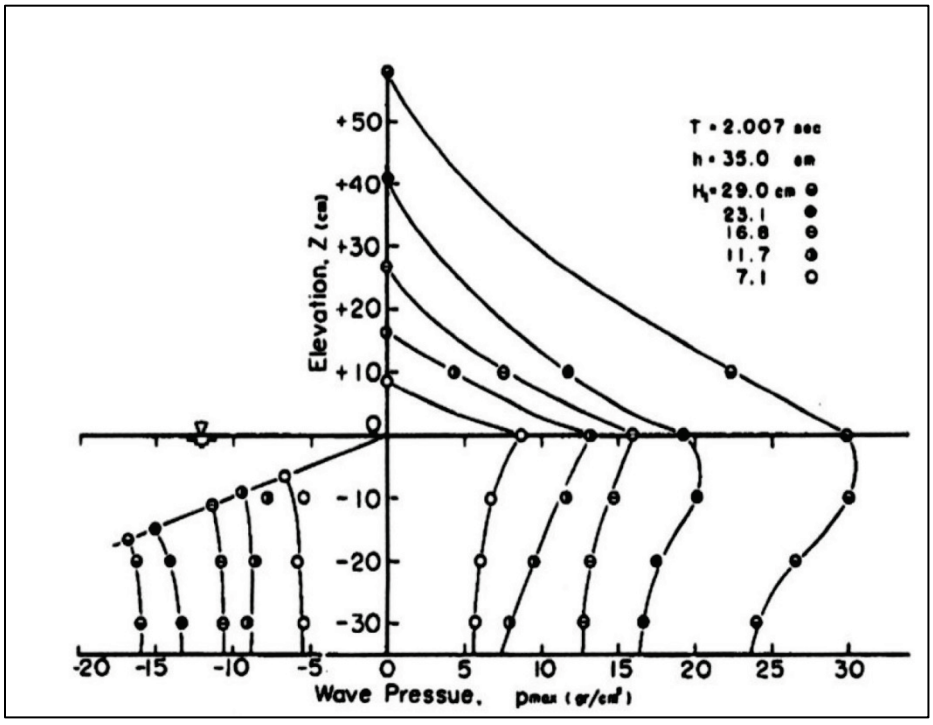

After careful examination of the laboratory data (e.g., Figures 5-6 and 5-7) combined with Figure 5-4 and Figure 5-5, as well as a study of Goda's wave equations for zero wave height, the authors of this report conclude that Goda's wave pressure relationships are reported relative to the hydrostatic water pressures of Figure 5-5 (a). These wave pressure components are idealized in Figure 5-5 (b). To arrive at the total water pressure, the Goda wave pressure component must be added to the hydrostatic water pressure at the SWL.

Japan uses caissons extensively to protect harbors from damage due to ocean waves generated by storms and typhoons. Goda developed his wave pressure relationships for use in the design of Japan's caissons subject to ocean wave loading. In his design methodology, the caisson being analyzed is subjected to both hydrostatic water pressure components acting on both vertical faces of the caisson as well as being subject to wave loading on the ocean side. These two sets of boundary water pressure distributions are defined in separate computations and applied to the caisson using the principle of superposition. The boundary water pressures corresponding to the ocean design wave component may be computed following the Goda procedure to be described in Section 5.4. Sliding and overturning limit state computations are conducted to assess the stability of a caisson during the design ocean storm. In these stability computations, the effective normal force that the caisson applies to the berm foundation is required. This computation for the self-weight of the caisson subjected to the SWL-induced water pressure component of loading is described subsequently. The wave loading pressure component depicted in Figure 5-4 and defined by application of the Goda formulation for wave pressure loading (Section 5.4) is superimposed onto the SWL caisson free body diagram component result.

Figure 5-8 shows only the hydrostatic boundary water pressures acting normal to the three exterior faces of the caisson (ocean, harbor, and bottom sides). Note that the design wave pressure components are not shown in this figure. Stability computations require knowledge of the effective weight the caisson imparts upon its berm foundation. One approach to compute this effective normal force the caisson imposes on its foundation berm is by using total unit weights and boundary water pressures, as described starting on page 119 in Cedergren (1977). For a hydrostatic SWL water condition and without the wave pressure component, the boundary water pressure

components act normal to the ocean side and harbor side vertical caisson faces, as depicted in Figure 5-8. For an SWL with hydrostatic water pressures acting in opposite directions to the ocean side and harbor side vertical caisson faces, the two resultant horizontal forces of these triangular distributions cancel each other in a stability computation. Additionally, with the ocean side and harbor side surface water being defined by the same SWL, there is no seepage within the berm foundation from one side of the caisson base to the other because of no differential total head acting across a pervious berm below the caisson. Since there is no horizontal seepage within the berm, the pore water pressure within the berm is hydrostatic, and uniform hydrostatic pore water pressures of magnitude p_{h3} act upward, normal to the base of the caisson as shown in Figure 5-8. The hydrostatic water pressure p_{h3} in this figure equals the unit weight of sea water times the depth d_{SWL} below SWL. The resultant boundary water pressure force acting upward and normal to the base (force not shown) is equal to the hydrostatic water pressure p_{h3} times the base width of the caisson and acts upward and normal to base center. The total weight W_{Total} of the caisson acting downward consists of two components of weight, W_{Top} plus W_{Bottom}. W_{Top} is equal to the moist unit weight of the caisson times its area above the elevation of the SWL, as designated in this figure. Similarly, W_{Bottom} is equal to the saturated unit weight of the caisson times its area located below the elevation of the SWL in this figure. These two forces, which sum to W_{Total}, act downward. The W_{Total} contribution to caisson stability is countered by the uplift, resultant base boundary water pressure force (not shown) due to the uniform hydrostatic boundary water pressure distribution of magnitude P_{h3} (Figure 5-8).

Figure 5-8. Total weight WTotal of caisson with SWL-induced horizontal boundary water pressures acting normal to both vertical faces of the caisson and a uniform uplift boundary water pressure distribution along its base.

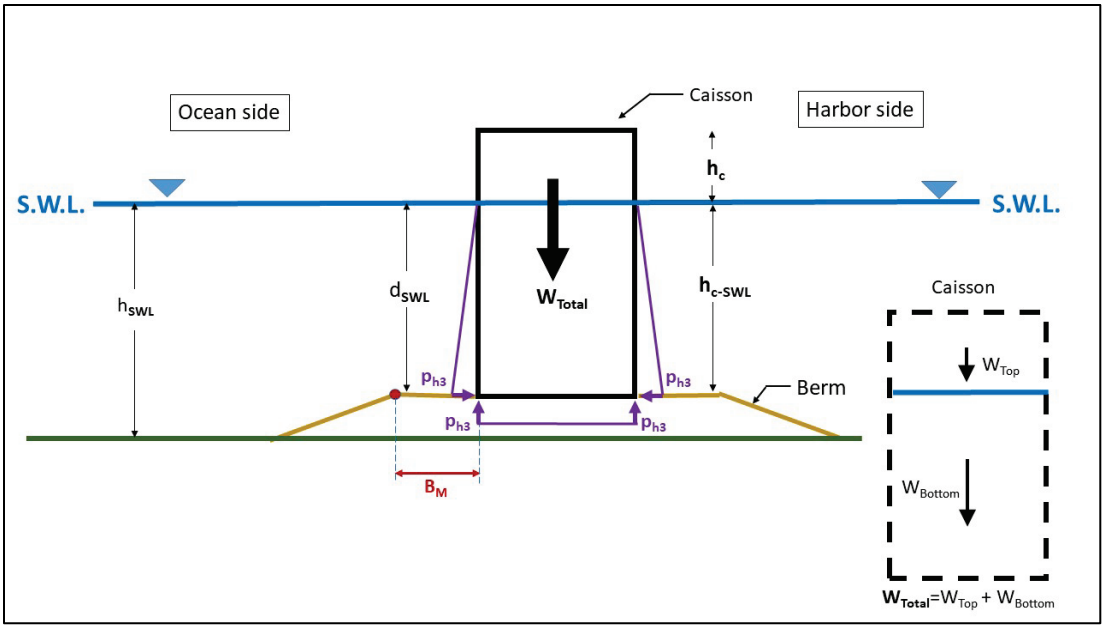

With an SWL defining the hydrostatic component of water loading applied to the ocean side and harbor side of the caisson, a total unit weight and buoyancy force-based formulation depicted in Figure 5-9 may alternatively be used to compute the net weight, W_{Net}, of the caisson. W_{Top} and W_{Bottom} total forces are computed as described previously. With an SWL hydrostatic water condition and no cracking within the reinforced concrete caisson shell, there are no seepage forces developed within the berm. An imaginary, upward-acting buoyancy force may be imposed within the submerged portion of the caisson, as depicted in Figure 5-9. The magnitude of $W_{Buoyant}$ is equal to the unit weight of water times the volume of submerged caisson. It counters the total unit weight force designated W_{Bottom} in this figure. The action of these two vertical forces W_{Bottom} minus $W_{Buoyant}$ is equivalent to the force calculated by the buoyant unit weight for the submerged caisson times the submerged caisson volume. The W_{net} force equation is given in this figure. The net effect of W_{Bottom} minus $W_{Buoyant}$ is a force equal to a force defined by the buoyant unit weight (= the saturated unit weight for the submerged caisson minus the unit weight of water) times the volume of the submerged caisson.

Figure 5-9. Buoyant weight of caisson acting below SWL elevation with an SWL on both sides of the caisson.

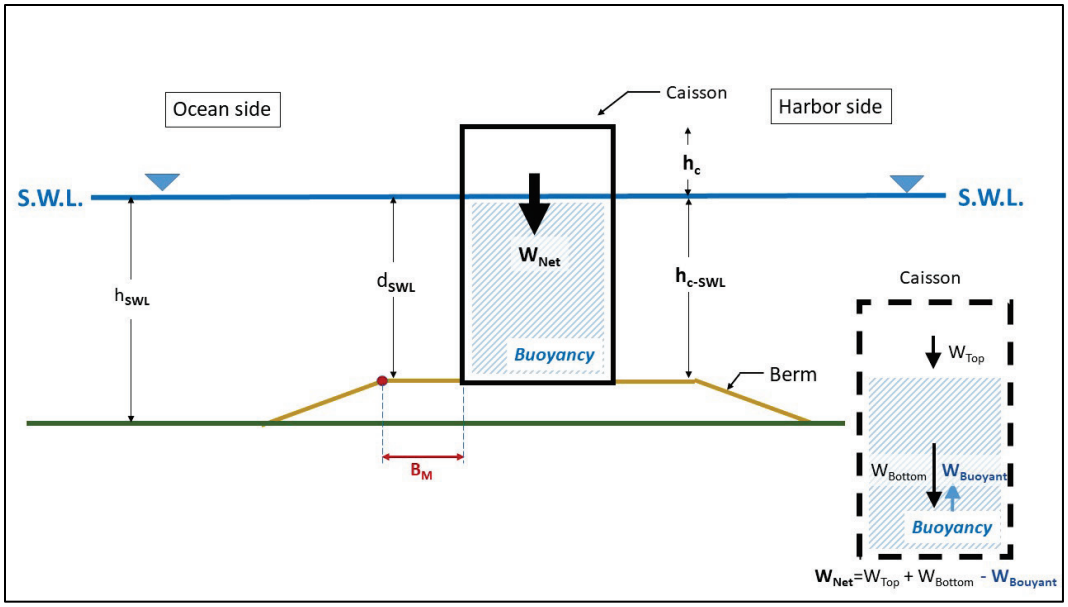

Thus, for net vertical force W_{Net} imposed by the caisson on the berm in a SWL condition, total unit weight is computed and assigned to the portion of the caisson region above SWL elevation while buoyant unit weight is assigned to the region of the caisson residing below SWL elevation as depicted in Figure 5-9. The SWL elevation defines the demarcation elevation for the Figure 5-9 caisson force component regions. This figure is more in line with that presented in the numerous Goda papers (e.g., Goda 1973, 1974, 2010) and Takahashi (2002) on caisson stability with ocean design waves defined by the Goda wave pressure relationships given in Section 5.4.

Vertical equilibrium calculations for the caisson based on the Figure 5-8 total unit weights and SWL boundary water pressure resultant forces or using the Figure 5-9 forces may be used to compute the effective vertical force W_{Net} acting on the berm. They result in the same W_{Net} force value. Last, wave pressure loading will be superimposed upon the SWL free-body diagram to define the total water pressure loading for which stability computations are carried out for the design ocean wave using an effective stress analysis-based stability computational procedure of analysis.

With an SWL defining one component of water loading and applied to the ocean side and harbor side of the caisson, a buoyant unit weight and seepage force-based formulation (see page 119 in Cedergren [1977)] may

alternatively be used to compute the net weight, W_{Net}, of the caisson. W_{Top} is computed in the usual manor. With an SWL hydrostatic water condition, there are no seepage forces, so the contribution to the net weight of the caisson by its submerged region is equal to the buoyant unit weight times the volume of the submerged caisson. This effective weight force is added to W_{Total} and results in the W_{Net} force imposed by the caisson on berm. The magnitude of force W_{Net} will be the same that is computed in the computations described in the previous paragraphs.

5.4 Wave force calculation for loading on vertical walls

5.4.1 Original Goda (1974) formula

Goda's wave pressure formulation is based on theoretical and laboratory works. He assumes a trapezoidal pressure distribution on a vertical wall as shown in Figure 5-10. Furthermore, Goda assumes that the maximum wave pressure (P_1) occurs at the SWL and that pressures linearly decay in magnitude both above and below the SWL. These assumptions are supported from laboratory data as shown in Figures 5-6 and 5-7.

Figure 5-10 and Table 5-1 introduce the pressure relations and terms of Goda's formula. The design wave height (H_D) is typically stochastically derived using, for example, a Rayleigh distribution of the wave spectrum. Similarly, the design wave length (L_D) and the design wave approach angle (β_D) are typically stochastically derived. The design wave approach angle (β_D) is measured from a line perpendicular to the structure, such that an angle of zero represents wave crest parallel to the breakwater. Goda (2010) recommends that the design wave direction (β_D) be rotated up to 15° toward the line normal to the breakwater to account for uncertainty in the estimation of design wave direction. Three depth related terms are used in the wave pressure formula to describe the design SWL at the structure, this includes the SWL on the seabed in front of the structure (h_{SWL}), the SWL at the top of the berm (d_{SWL}) and the SWL in front of the wall where the wave breaks (h_b). Note that the SWL subscript of the h_{SWL} and d_{SWL} terms are omitted for brevity purpose only in Equations 5.1 – 5.7 as noted in Table 5-1. Since the empirically derived constants of Goda's pressure formulation are dimensionless, either imperial or metric units of measure can be used in the pressure calculation. The authors of this report used the metric system in the following example calculation.

Figure 5-10. Illustration of terms in Goda's original pressure formulation.

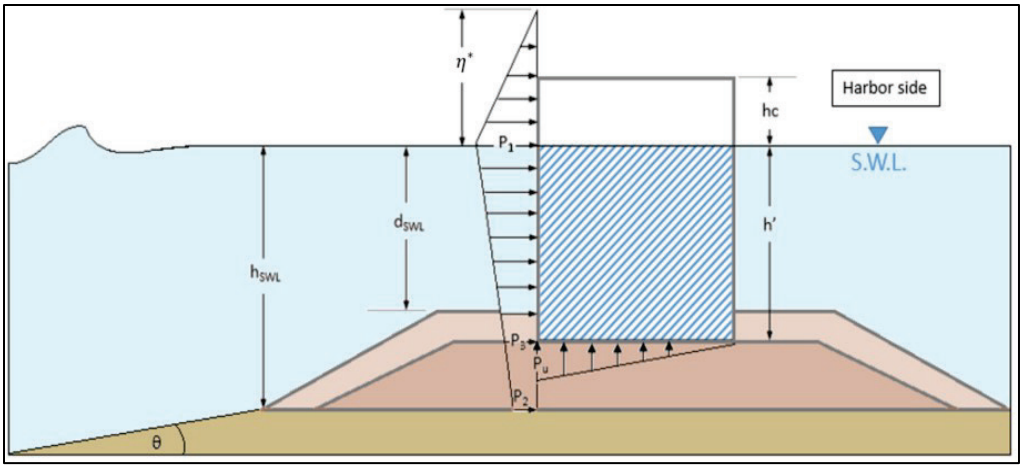

Table 5-1. Description of terms in Goda's original pressure formula.

Term	Equivalent Equation Term	Description
ρ		Density of seawater
g		Acceleration of gravity
H_D		Design wave height (discussed below)
β_D		Design wave approach angle
h_{SWL}	h	Still water depth seaward of berm (see Figure 5-3)
L_D		Design wave length (discussed below)
h_b		Still water depth where breaker height is evaluated (discussed below)
d_{SWL}	d	Still water depth at top of berm (see Figure 5-3)
θ		Mean gradient of the seabed
η^*		Elevation of wave pressure action above SWL

Goda uses three pressure terms (P_1, P_2, and P_3) to define the wave pressure distribution on the vertical face of the wall and one pressure term (P_U) to describe the uplift pressure at the toe of the wall (Figure 5-10). The P_1 pressure term represents the maximum wave pressure exerted at the SWL while P_2 and P_3 represent the linear decay in wave pressure with depth.

$$P_1 = 0.5\,(1 + \cos\beta_D)\,(\alpha_1 + \alpha_2 * cos^2\beta_D)\,\rho * g * H_D \quad (5.1)$$

$$P_2 = \frac{P_1}{\cosh(2\pi h/L_D)} \quad (5.2)$$

$$P_3 = \alpha_3 P_1 \quad (5.3)$$

$$P_u = 0.5\,(1 + cos\,\beta_D)\,\alpha_1 * \alpha_3 * \rho * g * H_D \quad (5.4)$$

where α_1 and α_2 are wave pressure coefficients derived from laboratory data. The α_1 coefficient represents the average tendency of wave pressure to increase with wave length (L), and the α_2 coefficient represents the tendency of the wave pressure to increase with the berm height. This α_2 term reflects the wave shoaling effect due to berm height and the impulsive pressure component. The α_3 coefficient describes the assumed linear pressure variation between P_1 and P_2 (Figure 5-9).

$$\alpha_1 = 0.6 + \frac{1}{2}\left[\frac{\frac{4\pi h}{L_D}}{\sinh\left(\frac{4\pi h}{L_D}\right)}\right]^2 \quad (5.5)$$

$$\alpha_2 = \min\left[\frac{h_b - d}{3h_b}\left(\frac{H_D}{d}\right)^2, \frac{2d}{H_D}\right] \quad (5.6)$$

$$\alpha_3 = 1 - \frac{h'}{h}\left[1 - \frac{1}{\cosh\left(\frac{2\pi h}{L_D}\right)}\right] \quad (5.7)$$

The Goda procedure of analysis represents the complex spectrum of sea waves by a single design wave height and length represented by H_D and L_D, respectively. The design wave height (H_D) of Goda's formula is described as the highest wave expected under given wave conditions; this wave height is also identified as H_{MAX}. H_{MAX} is determined as the lesser of 1.8 times the significant wave height ($H_{1/3}$) and the breaking wave height (H_b) (Equations 5.8 – 5.10). Where H_b is evaluated at a distance of $5H_{1/3}$ seaward of the breakwater berm as shown in Figure 5-11. The design wave length (L_D) of Goda's formula is described as the longest wave expected under given wave conditions; this wave length is also identified as L_{MAX}. In Equation 5.11, L_{MAX} is approximated using first-order wave theory and the significant wave period ($T_{1/3}$).

$$H_D = H_{Max} = min\{\alpha_h * H_{1/3},\ H_b\} \quad (5.8)$$

Where α_h is typically in the range of 1.6 to 2.0. The α_h term defines the nondeterministic characteristic of the highest wave due to the random nature of sea waves. According to Goda (2010), the value of α_h is selected based on the reliability of design storm wave estimation, the importance of the structure and the type and nature of the possible structural failure. Goda states that a value of 2.0 or greater is often used for offshore structures, such as an offshore oil rig. For the design of nearshore vertical structures Goda suggest a value of 1.8 for α_h.

$$H_b = 0.17 * L_D \left\{1 - exp\left[-1.5\frac{\pi h_b}{L_D}\left(1 + \sigma_S * tan^{4/3}\theta\right)\right]\right\} \quad (5.9)$$

Originally, Goda specified the σ_S value as a constant equal to 15 but later recommend a value of 11 based on the work of Rattanapitikon and Shibayama (2000). This reduction in the σ_S value accounts for an overprediction in the wave shoaling effect for steep bottom slopes (>1/10). Therefore, the authors of this report recommend using $\sigma_S = 11$ for bottom slopes greater than 1/50 and $\sigma_S = 15$ for bottom slopes less than 1/50.

$$h_b = h + 5 * H_{1/3} \tan\theta \quad (5.10)$$

$$L_D = L_{MAX} = \frac{g * T_{1/3}^2}{2\pi} \quad (5.11)$$

Figure 5-11. Breaking wave height location in Goda's equation.

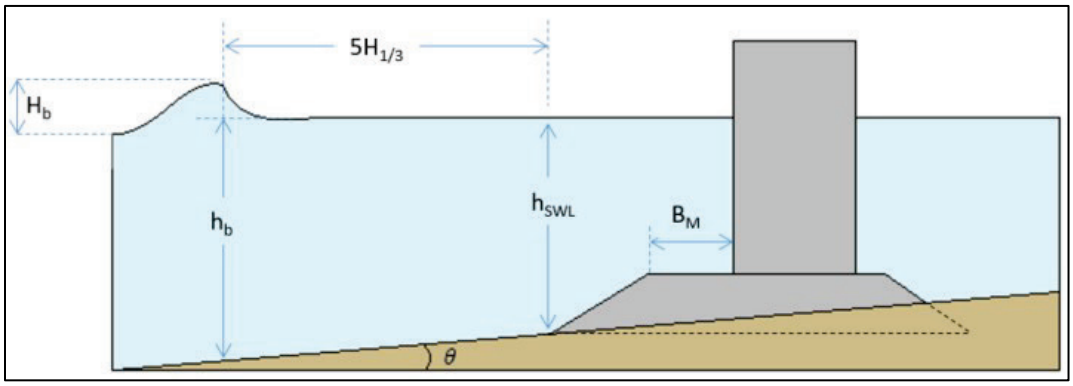

According to Goda (2010), the significant wave height ($H_{1/3}$) represents the largest one-third wave height measured in deep water. Similarly, the significant wave period ($T_{1/3}$) represents the longest one-third wave period measured in deep water. Site-specific estimates of $H_{1/3}$ and $T_{1/3}$, based on historical records, simulations, etc., can either be obtained or calculated from historical records of deep-water surface elevation changes with time. In selecting this record, it is of great importance to ensure that the record length is sufficient to include the events of interest (e.g., 100-year storm). In a simplistic analysis, the mean water level is first determined from the record followed by the identification (or separation) of individual waves using either the zero-upcrossing or zero-downcrossing methods. Once the individual waves have been identified, their heights and periods are extracted. The values of $H_{1/3}$ and $T_{1/3}$ are determined by sorting all wave heights and periods from largest to smallest, selecting the values that corresponds to the upper one-third and averaging these selected values.

This method will be demonstrated in the following discussion with field data downloaded from the National Oceanic and Atmospheric Administration (NOAA) Data Buoy Center.

A second method used to approximate the $H_{1/3}$ value is based on the generally accepted premise that the distribution of wave heights in the sea can be adequately represented by a theoretical distribution function known as the Rayleigh distribution (Equation 5.12).

$$p(x) = \frac{\pi}{2} x \exp\left[-\frac{\pi}{4} x^2\right] \tag{5.12}$$

where

$$x = \frac{H}{H_{mean}} \tag{5.13}$$

If the Rayleigh distribution is adopted, then the $H_{1/3}$ and $H_{1/10}$ values can be calculated as a function of the historical record's mean wave height (Equations 5.14 and 5.15).

$$H_{1/3} = 1.6 * H_{Mean} \tag{5.14}$$

$$H_{1/10} = 2.03 * H_{Mean} \tag{5.15}$$

An example application of $H_{1/3}$ and $T_{1/3}$ estimation is provided below for the region affected near Freemont, TX, during hurricane Harvey of August 2017. The path of the hurricane is shown in Figure 5-12, and the data buoys along the western Gulf of Mexico near the target site of Freemont, TX, are displayed in Figure 5-13. The deep-water buoy station, number 42019 (green), was selected for analysis. Hourly mean wave height, wave period and wave directional data were downloaded from the NOAA National Data Center for the entire year of 2017 (N = 8,697). In Figure 5-14, the normalized wave height frequency distribution for year 2017 is shown with identification of the H_{Mean}, $H_{1/3}$ and $H_{1/10}$ values. The $H_{1/3}$ and $H_{1/10}$ values were derived using the simple sort and average method discussed above.

Figure 5-12. Path of Hurricane Harvey.[14]

Figure 5-13. Data buoy locations in the western Gulf of Mexico monitored by along the NOAA National Data Buoy Center.[15]

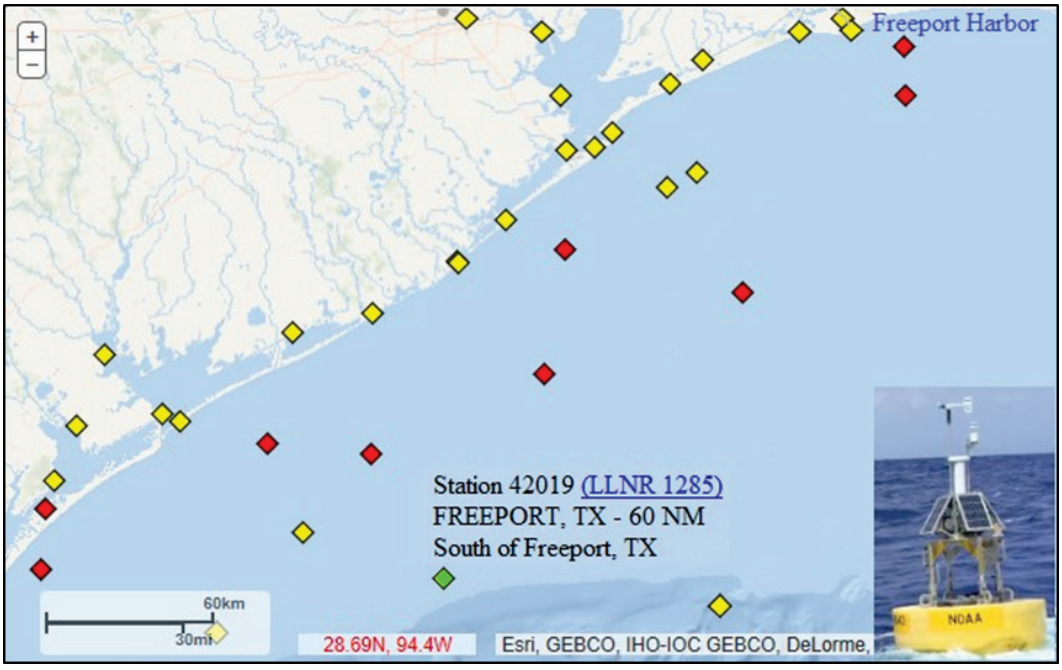

[14] https://sn56.scholastic.com/pages/news/2017-18/hurricane-harvey-hits.html, Source NOAA, Accessed 5-21-2019.

[15] https://www.ndbc.noaa.gov/ Accessed 5-13-2019.

Figure 5-14. Normalized sea wave height frequency distribution for year 2017 with identification of H_{Mean}, $H_{1/3}$ and $H_{1/10}$ using sort and average method. Data from NOAA Buoy 42019, Freeport, TX (N = 8697).

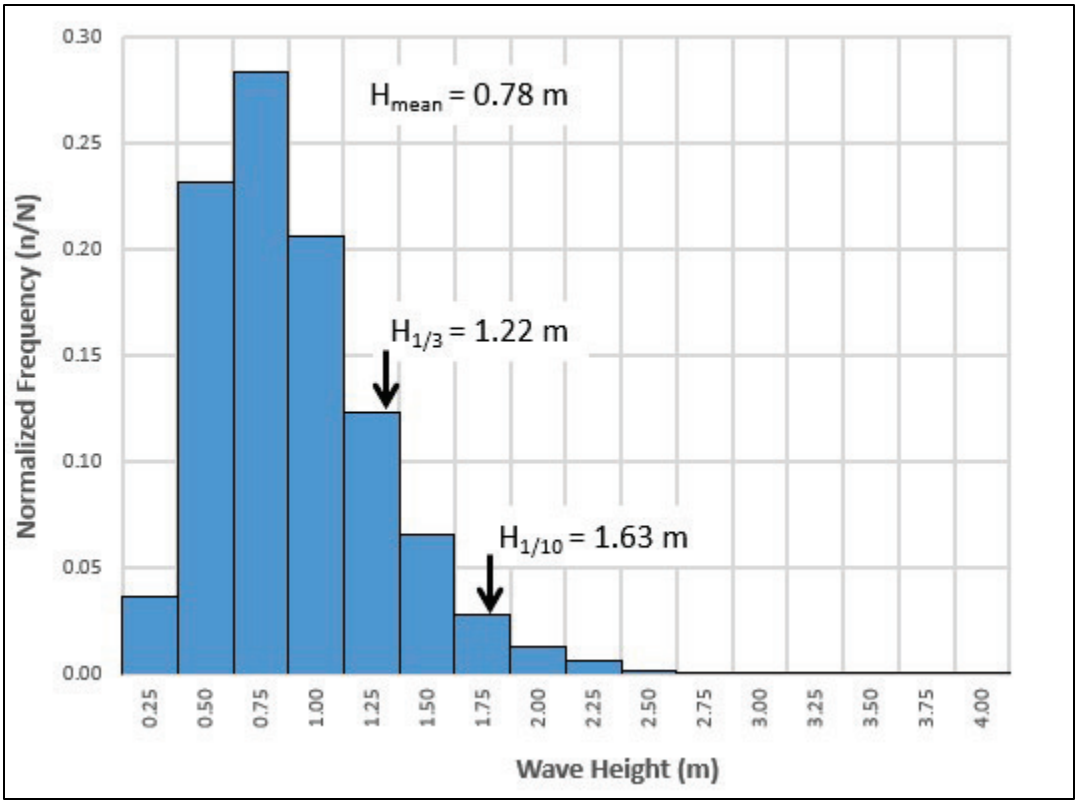

To demonstrate the Rayleigh method of approximation of the $H_{1/3}$ and $H_{1/10}$ values, a histogram of normalized sea wave heights (H/H_{MEAN}) to normalized frequency of occurrence p(H/H_{MEAN}) was constructed such that the area under the histogram is equal to unity (Figure 5-15). The ordinate of the histogram, p(H/H_{MEAN}) is given in Equation 5.16, where n represents the bin population, N represents the total population (8,697 - in our case) and D_X represents the bin width. The curved line shown in Figure 5-15 is the plot of the Rayleigh distribution, which demonstrates the relative closeness of fit to our real-world dataset.

$$\mathrm{p}\left(\frac{H}{H_{Mean}}\right) = \frac{n}{(N*D_X)} \tag{5.16}$$

Figure 5-15. Normalized histogram of sea wave heights for year 2017 with superimposed Rayleigh distribution and Rayleigh estimation of $H_{1/3}$ and $H_{1/10}$ values. Data from NOAA Buoy 42019, Freeport TX (N = 8697).

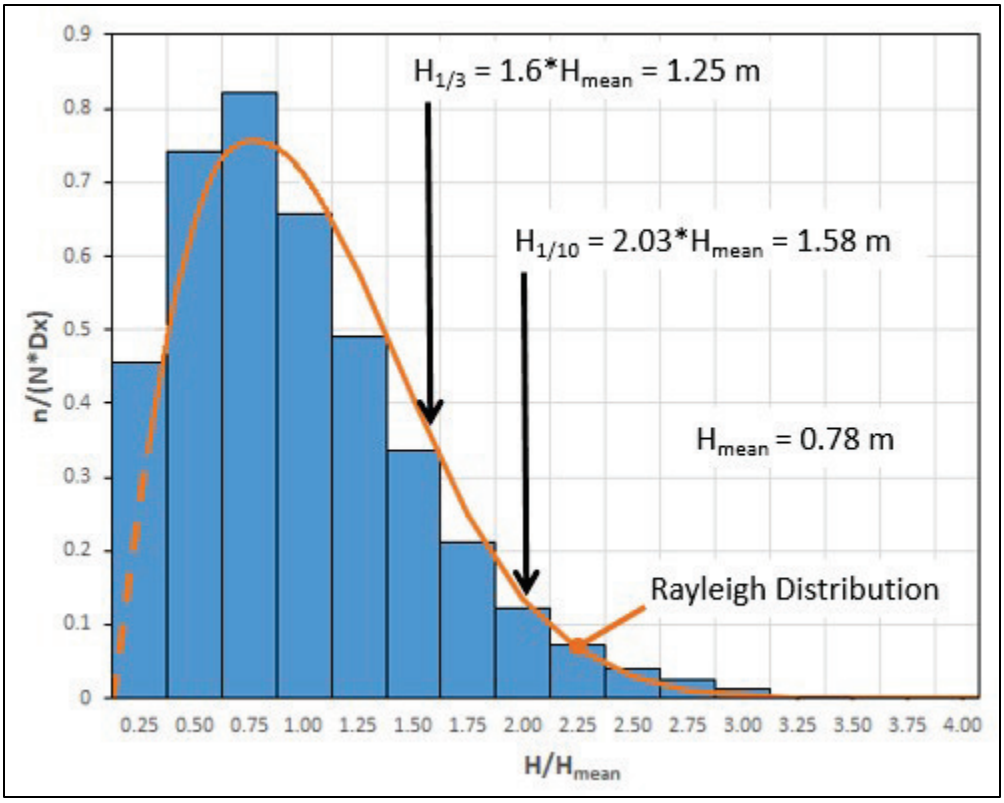

The simple sort and average and Rayleigh methods of $H_{1/3}$ and $H_{1/10}$ estimates for the wave data from NOAA Buoy 42019, Freeport, TX (N=8697), are given in Table 5-2.

Table 5-2. Results of $H_{1/3}$ and $H_{1/10}$ estimation using the simple sort and average and Rayleigh methods.

Method	$H_{1/3}$ (m)	$H_{1/10}$ (m)
Sort and Average	1.23	1.63
Rayleigh	1.25	1.58

The design wave length L_D (Equation 5.11) is used in the calculation of the breaking wave height (H_b) (Equations 5.9 and 5.10) and is based on the estimation of the $T_{1/3}$ value, which is determined using the simple sort and average method discussed above. The Rayleigh distribution is unsuitable for wave period analysis. For the case of the Freeport, TX, dataset, the normalized wave period frequency histogram is shown in Figure 5-16 along with the values of T_{Mean}, $T_{1/3}$ and $T_{1/10}$. Using Equation 5.11, the

design wavelength (L_D) is (based on $T_{1/3}$ = 5.58 sec) is estimated at approximately 48.6 m.

Figure 5-16. Normalized wave period frequency distribution for year 2017 with identification of the significant wave period ($T_{1/3}$) using sort and average method. Data from NOAA Buoy 42019, Freeport TX (N = 8697).

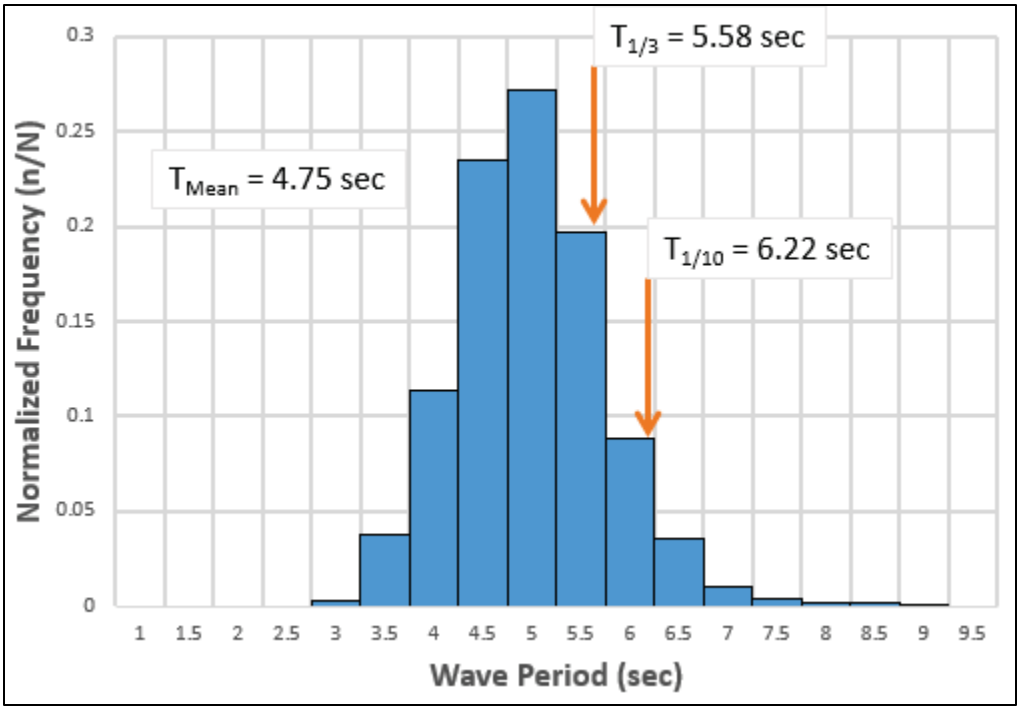

The design wave approach angle (β_D) can be estimated using both the historical wave record and knowledge of the structure orientation. For the case of the Freeport, TX, 2017 dataset used above, a normalized wave directional frequency histogram is shown in Figure 5-17 along with the range of wave directional propagation during Hurricane Harvey. From this figure, the wave propagation direction changed from an east-northeast to a west-southwest direction during Hurricane Harvey, thus making it difficult to identify a design wave direction.

Figure 5-17. Normalized wave propagation direction frequency distribution for year 2017 with identification of the Hurricane Harvey dominant directions. Data from NOAA Buoy 42019, Texas (N = 8697).

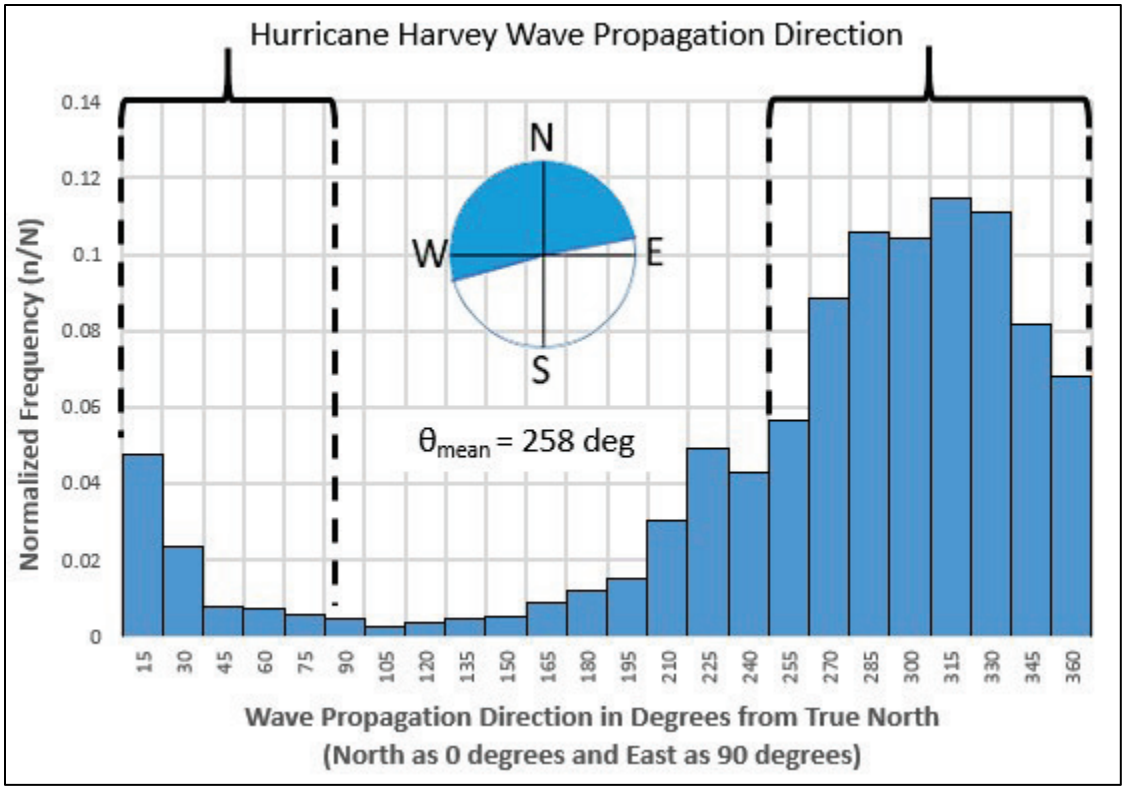

5.4.2 The Takahashi extension of Goda's Formula to include the impulsive pressure term

As mentioned in Subsection 5.4.1, the α_2 coefficient of Goda's P_1 pressure term (Equation 5.1) represents the impulsive pressure component of a breaking wave. Takahashi et al. (1993) recognized that Goda's α_2 coefficient inadequately estimated the effective pressure due to impulsive pressure under various conditions and therefore proposed a set of formulas to estimate the magnitude of impulsive pressure based on a series of laboratory test. The impulsive pressure term α^* replaces the α_2 coefficient of Goda's P_1 pressure term as shown in

$$P_1 = 0.5\,(1 + \cos\beta_D)\,(\alpha_1 + \alpha^* cos^2\beta_D)\,\rho * g * H_D \tag{5.17}$$

where

$$\alpha^* = max\{\alpha_2\,, \alpha_I\} \tag{5.18}$$

$$\alpha_I = \alpha_{IH}\,\alpha_{IB} \tag{5.19}$$

$$\alpha_{IH} = \min\left\{\frac{H_D}{d}, 2.0\right\} \tag{5.20}$$

$$\alpha_{IB} = \frac{\cos\delta_2}{\cosh\delta_1} \; when \; \delta_2 \; \leq 0 \tag{5.21}$$

or

$$\alpha_{IB} = \frac{1}{\left(\cosh\delta_1 \; \cosh{\delta_2}^{1/2}\right)} \; when \; \delta_2 \; > 0 \tag{5.22}$$

where

$$\delta_1 = 20 * \delta_{11} \; when \; \delta_{11} \; \leq 0 \tag{5.23}$$

or

$$\delta_1 = 15 * \delta_{11} \; when \; \delta_{11} > 0 \tag{5.24}$$

$$\delta_2 = 4.9 * \delta_{22} \; when \; \delta_{22} \; \leq 0 \tag{5.25}$$

or

$$\delta_2 = \; 3.0 * \delta_{22} \; when \; \delta_{22} \; > 0 \tag{5.26}$$

$$\delta_{11} = 0.93 \left(\frac{B_M}{L_D} - 0.12\right) + 0.36 \left(0.4 - \frac{d}{h}\right) \tag{5.27}$$

$$\delta_{22} = -0.36 \left(\frac{B_M}{L_D} - 0.12\right) + 0.93 \left(0.4 - \frac{d}{h}\right) \tag{5.28}$$

Goda (2010) noted that the impulsive pressure coefficient (α_I) is excessively large where the water depth (h_{SWL}) at the site is greater than $2H_{MAX}$ and recommends using a maximum h_{SWL} value of $2H_{MAX}$ in this situation.

5.4.3 Example calculation of wave forces on T-Wall

In the following example, wave forces on the seaward face of a generic T-Wall are calculated using the Goda-Takahashi method and the 2017 Freeport dataset discussed above. This dataset includes an approximate 10-year storm surge return period, attributed to Hurricane Harvey, which may not be sufficient for the actual design. This example is calculated

using the metric system and is intended for educational purpose only. The parameters h_{SWL} and d_{SWL} shown in Figure 5-18 are substituted by h and d in the equations below. Note that the T-Wall foundation batter-piles are not shown in the next sequence of figures. Figure 5-18 parameters are defined in Table 5-3.

Figure 5-18. T-Wall used in example wave force calculation.

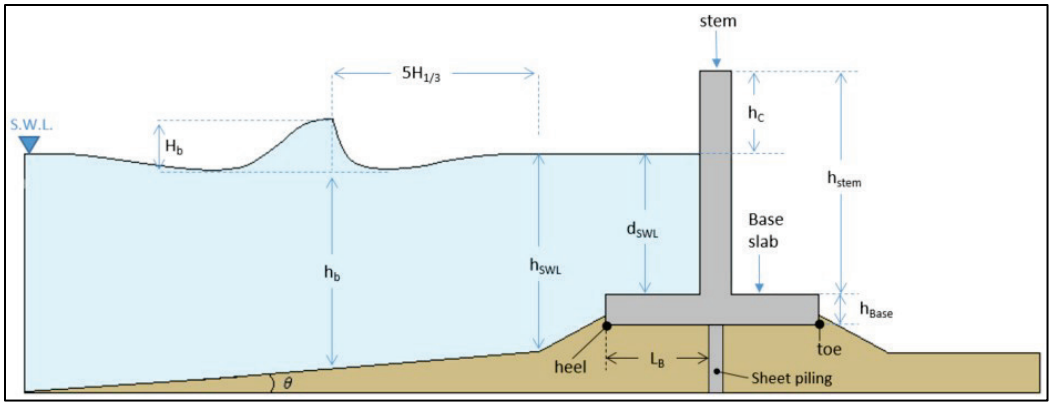

Table 5-3. Parameters used in example wave force calculation (imperial and metric units included).

Parameter	Value	Unit	Value	Unit	Description
H_{stem}	15	ft	4.57	m	T-Wall stem height (above base)
h_{Base}	2.5	ft	0.76	m	T-Wall base thickness
h_C	5	ft	1.52	m	T-Wall height above SWL
L_B	8	ft	2.4	m	Distance from heel of base slab to sheet pile distance
d (originally d_{SWL})	10	ft	3.05	m	Still water depth at base of T-Wall
h (originally h_{SWL})	15	ft	4.57	m	Still water depth at toe of berm
$\tan\theta$	1/100	N/A	1/100	N/A	Seaward slope to T-Wall (seaward of T-Wall berm)
β_D	0	deg	0	deg	Design incident wave angle
$H_{1/3}$	4.1	ft	1.25	m	Significant wave height, From Table 5-2 (1.25 m)
$T_{1/3}$	5.58	sec	5.58	sec	Significant wave period, From Figure 5-16
L_D	159.5	ft	48.6	m	Design wavelength, From $T_{1/3}$ and Eq. 5.11
ρ	64.3	lb/ft^3	1030	Kg/m^3	density of seawater
g	32.17	ft/sec^2	9.81	m/sec^2	Acceleration of gravity
h'	10	ft.	3.05	m	For the case of T-Wall: $h' = d_{SWL}$ (see Figure 5-10)

Based on the parameters given in Table 5-3 and the Goda-Takahashi equation set, the example solution is presented below. The design wave height (H_D) is the minimum of $\alpha_h H_{1/3}$ and H_b, where α_h ranges from 1.6 to 2.0. For the design of nearshore vertical structures, Goda suggests using a value of 1.8 for α_h.

$$H_D = H_{Max} = min\{\alpha_h * H_{1/3},\ H_b\} \quad (5.8\text{ bis})$$

$$H_b = 0.17 * L_D \left\{1 - exp\left[-1.5\frac{\pi h_b}{L_D}\left(1 + 15 * tan^{4/3}\theta\right)\right]\right\} \quad (5.9\text{ bis})$$

where

$$h_b = h + 5 * H_{1/3} * \tan\theta \quad (5.10\text{ bis})$$

therefore

$$\alpha_h H_{1/3} = 1.8{*}1.25\text{ m} = 2.25\text{ m (7.38 ft)}$$

and using Equations 5.10 and 5.9, the H_b parameter is derived as follows:

$$\text{hb} = 4.57\text{m} + 5{*}1.25\text{ m}{*}(1/100) = 4.63\text{ m (15.2 ft)},$$

$$H_b = 0.17 * 48.6\text{ m} * \left\{1 - exp\left[-1.5 * \frac{\pi * 4.63\text{m}}{48.6\text{m}}\left(1 + 15 * \left(\frac{1}{100}\right)^{4/3}\right)\right]\right\} = 3.06\text{ m (10.1 ft.)},$$

and finally,

$$\text{HD} = \text{HMax} = \min\{2.25\text{m}, 3.06\text{m}\} = 2.25\text{ meters (7.38 ft)}.$$

Next, the coefficients of wave pressure (α_1, α_2 and α_3) given in Equations 5.5 – 5.7 are calculated:

$$\alpha_1 = 0.6 + \frac{1}{2}\left[\frac{\frac{4\pi h}{L_D}}{\sinh\left(\frac{4\pi h}{L_D}\right)}\right]^2 \quad (5.5\text{ bis})$$

$$\alpha_2 = \min\left[\frac{h_b - d}{3h_b}\left(\frac{H_D}{d}\right)^2, \frac{2d}{H_D}\right] \quad (5.6\text{ bis})$$

$$\alpha_3 = 1 - \frac{h'}{h}\left[1 - \frac{1}{\cosh\left(\frac{2\pi h}{L_D}\right)}\right] \quad (5.7 \text{ bis})$$

Please recall that the h and d values in Equation 5.5 and 5.6 are respectively equivalent to the h_{SWL} and d_{SWL} of Table 5-3, therefore,

$$\alpha_1 = 0.6 + \frac{1}{2}\left[\frac{\frac{4*\pi*4.57m}{48.6m}}{\sinh\left(\frac{4*\pi*4.57m}{48.6m}\right)}\right]^2 = 0.92, \text{ from Equation 5.5,}$$

$$\alpha_2 = min\left[\frac{5.21m-3.05\text{m}}{3*5.21\text{m}} * \left(\frac{2.25\text{m}}{3.05\text{m}}\right)^2, \frac{2*3.05\text{m}}{2.25\text{m}}\right] = min[0.075\text{ m}, 2.71\text{ m}] = 0.075,$$

from Equation 5.6.

and finally, since $h' = d_{SWL}$,

$$\alpha_3 = 1 - \frac{3.05\text{m}}{4.57\text{m}} * \left[1 - \frac{1}{\cosh\left(\frac{2*\pi*4.57\text{m}}{48.6\text{m}}\right)}\right] = 0.9, \text{ from Equation 5.7.}$$

At this point in the solution, the calculation of the Takahashi impulsive wave force term (α^*) could be made using Equations 5.17 to 5.28; however, for the purpose of comparing final solutions, the original Goda procedure will be completed. The three lateral pressure components P_1, P_2 and P_3 (Equations 5.1 to 5.3) and the uplift pressure component (P_U) (Equation 5.4) are evaluated below.

$$P_1 = 0.5\,(1 + \cos\beta_D)\,(\alpha_1 + \alpha_2 cos^2\beta_D)\,\rho * g * H_D \quad (5.1 \text{ bis})$$

$$P_2 = \frac{P_1}{\cosh(2\pi h/L_D)} \quad (5.2 \text{ bis})$$

$$P_3 = \alpha_3 P_1 \quad (5.3 \text{ bis})$$

$$P_u = 0.5\,(1 + cos\,\beta_D)\,\alpha_1\alpha_3\rho g H_D \quad (5.4 \text{ bis})$$

The solution to P_1, P_2, and P_3 is

$$P_1 = 0.5 * (1 + \cos(0\,deg))\left(0.92 + 0.075 * cos^2(0)\right) * 1030\frac{kg}{\text{m}^3} * 9.81\frac{\text{m}}{s^2} * 2.25\text{ m} =$$
$$2{,}711\ N/\text{m}^2 = 22.7\ kN/\text{m}^2\ (474\ \text{lb/ft2})$$

$$P_2 = \frac{22.7\ kN/\mathrm{m}^2}{\cosh(2*\pi*(4.57\mathrm{m}/48.6\mathrm{m}))} = 19.23\ kN/\mathrm{m}^2\ (402\ \mathrm{lb/ft}^2)$$

$$P_3 = 0.9 * 22.7\ kN/\mathrm{m}^2 = 20.43\ kN/\mathrm{m}^2\ (427\ \mathrm{lb/ft}^2),$$

and the solution for P_U is

$$P_u = 0.5\ (1\ + cos(0\ deg))\ 0.92 * 0.9 * 1030\frac{kg}{\mathrm{m}^3} * 9.81\frac{\mathrm{m}}{s^2} * 2.25\ \mathrm{m} = 18.8\ kN/\mathrm{m}^2\ (393\ \mathrm{lb/ft}^2)$$

To calculate the total lateral force on the T-Wall, it is first necessary to determine if the pressure distribution (above SWL) extends above the crest of the T-Wall. The ΔP_1 parameter shown in Figure 5-19 represents this fraction of pressure that would be negated from the total pressure above the SWL.

Figure 5-19. Pressure distribution on T-Wall.

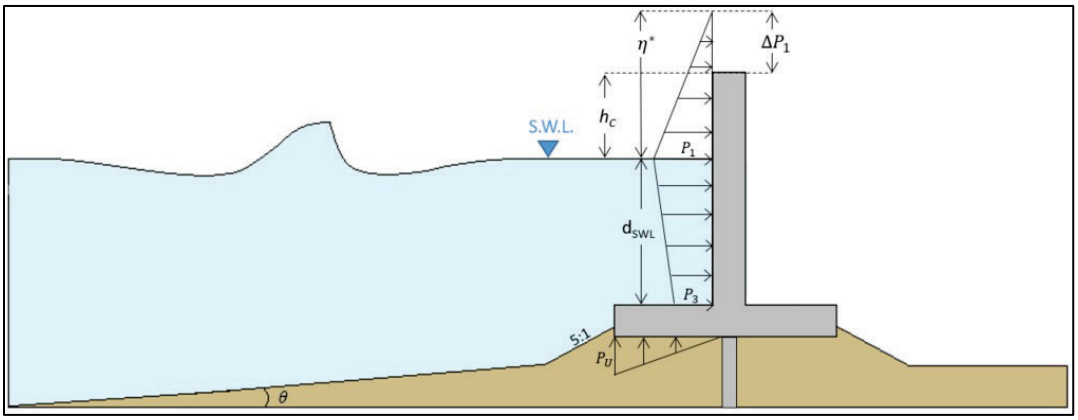

The total lateral force per linear width (F_{Lat}) on the seaward face of the T-Wall is given in Equation 5.29:

$$F_{Lat} = 0.5(P_1 + P_3)d + 0.5(P_1 + P_4)h'_C \quad (5.29)$$

where

$$P_4 = P_1\left(1 - \frac{h_C}{\eta^*}\right), if\ \eta^* > h_C \quad (5.30)$$

or

$$P_4 = 0, if\ \eta^* \leq h_C \quad (5.31)$$

$$\eta^* = 0.75(1 + \cos(\beta_D))H_D \quad (5.32)$$

$$h'_C = min\{\eta^*, h_C\} \quad (5.33)$$

Therefore, the solution for the Figure 5-20 resultant force F_{Lat} is given as

h_C = 1.52 m or 5 ft (from Table 5-2)

$\eta^* = 0.75 * (1 + \cos(0\ deg)) * 2.25$ m $= 3.38$ m (11.08 ft),
$since\ \eta^* > h_C$, from Equation 5.26

$P_4 = 22.7 * \left(1 - \frac{1.52\text{m}}{3.38\text{m}}\right) = 12.5\ kN/\text{m}^2$ (260.8 lb/ft²)

$h'_C = min\{3.38\text{ m}, 1.52\text{ m}\} = 1.52$ m (4.98 ft)

$F_{Lat} = 0.5 * \left(22.7\frac{kN}{\text{m}^2} + 20.43\ \frac{kN}{\text{m}^2}\right) * 3.05\text{ m} + 0.5 * \left(22.7\frac{kN}{\text{m}^2} + 12.5\frac{kN}{\text{m}^2}\right) * 1.52\text{ m} = 92.52\ kN/\text{m}$ (6,339 lb/ft).

The total uplift force per linear width on the T-Wall is calculated as

$$U_P = 0.5 * P_U * L_B = 0.5 * 18.82\frac{kN}{\text{m}^2} * 2.4\text{ m} = 22.6\ N/\text{m}\ (1{,}548\text{ lb/ft}).$$

Figure 5-20. Resultant forces of wave pressure distribution per unit length of T-Wall.

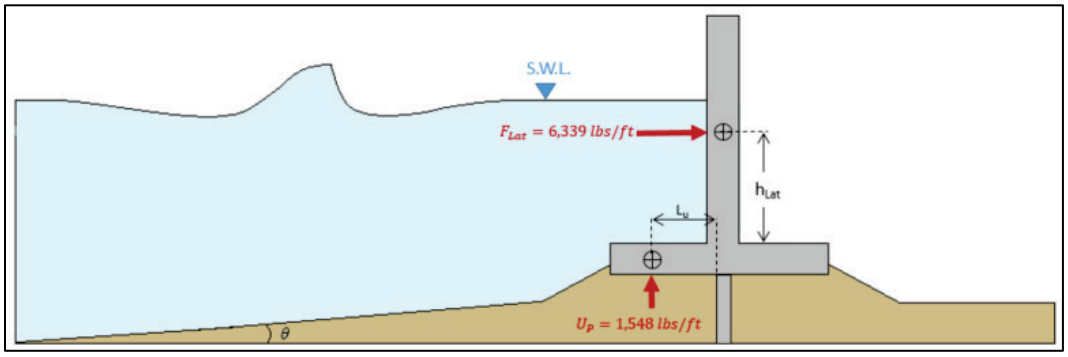

Finally, in Table 5-4, a summary of calculated parameters is provided.

Table 5-4. Calculation summary.

Variable	Term	Value	Units	Value	Units
P_1	Pressure	22.7	kN/m²	474	lb/ft²
P_2	Pressure	19.2	kN/m²	402	lb/ft²
P_3	Pressure	20.4	kN/m²	427	lb/ft²
P_4	Pressure	12.5	kN/m²	261	lb/ft²
P_U	Pressure	18.8	kN/m²	393	lb/ft²
U_P	Force/width	22.6	kN/m	1,548	lb/ft
F_{Lat}	Force/width	92.5	kN/m	6,339	lb/ft

In Figure 5-21, the pressure terms P_1, P_3, P_4, and P_U are shown acting on the T-Wall at their respective locations. The location of the lateral and uplift equivalent forces can be determined using the 1/3:1/6 method, as laid out by Ebeling et al. (2018) and described in Subsection 5.4.4. By applying this method for the lateral forces and summing moments about Point 3, Equations 5.34 is derived. Similarly, Equation 5.35 is derived for the uplift forces.

Figure 5-21 Definition of wave pressure moment arm terms on T-Wall.

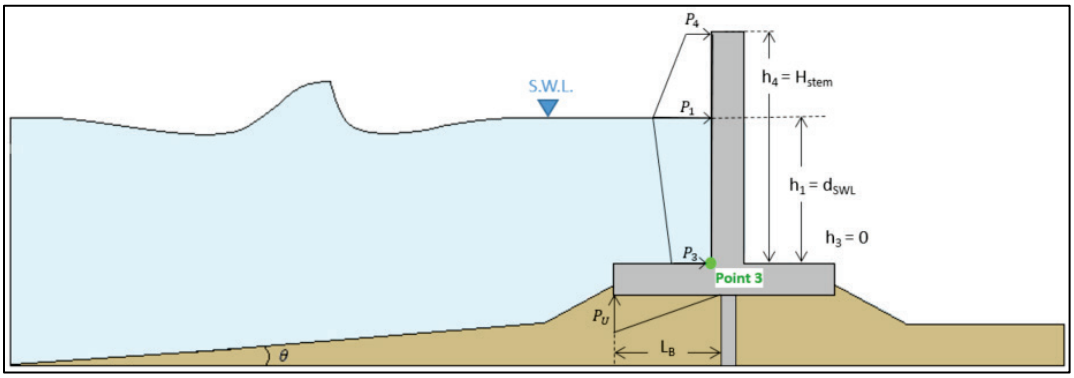

$$h_{Lat} = \frac{(h_4-h_1)\left(\frac{P_4}{3}+\frac{P_1}{6}\right)h_4+(h_4-h_1)\left(\frac{P_4}{6}+\frac{P_1}{3}\right)h_1+(h_1-h_3)\left(\frac{P_1}{3}+\frac{P_3}{6}\right)h_1}{F_{Lat}} \quad (5.34)$$

Substituting into Equation 5.29, the resultant lateral force's (P_{Lat}) moment arm (h_{Lat}) is achieved, as shown in Figure 5-20,

$$h_{Lat} = \frac{1.52m\left(\frac{12.5\frac{kN}{m^2}}{3}+\frac{22.7\frac{kN}{m^2}}{6}\right)4.57\text{m} + 1.52\text{m}\left(\frac{12.5\frac{kN}{m^2}}{6}+\frac{22.7\frac{kN}{m^2}}{3}\right)3.05\text{ m} + 3.05\text{ m}\left(\frac{22.7\frac{kN}{m^2}}{3}+\frac{20.4\frac{kN}{m^2}}{6}\right)3.05\text{ m}}{92.52\frac{kN}{m}}$$

$$h_{Lat} = 2.18\text{ m (7.16 ft)}$$

Similarly, using the 1/3:1/6 method, the equivalent force location of U_P is derived (Equation 5.30).

$$L_U = \frac{L_B^2}{3} \tag{5.35}$$

solving for L_U gives

$$L_U = \frac{2.4\text{m}^2}{3} = 1.92 \text{ m } (6.3 \text{ ft})$$

The resultant wave forces and Figure 5-20 lever arms are summarized in Table 5-5.

Table 5-5. Summary of resultant forces and moment arms for the Goda pressure components values in this calculation example.

Equivalent Pressure and Moment Arm	Result
F_{Lat}	92.5 kN/m
h_{Lat}	2.18 m from Point 3
U_P	22.6 kN/m
L_U	1.92 m from Sheet Piling

The example calculation of wave pressures on a T-Wall is now extended to include the effect of impulsive wave forces on vertical walls, as discussed in Subsection 5.4.2 above. The first step is to determine the values of δ_{11} *and* δ_{12} based on Equations 5.27 and 5.28.

$$\delta_{11} = 0.93\left(\frac{B_M}{L_D} - 0.12\right) + 0.36\left(0.4 - \frac{d}{h}\right) \tag{5.27 bis}$$

$$\delta_{22} = -0.36\left(\frac{B_M}{L_D} - 0.12\right) + 0.93\left(0.4 - \frac{d}{h}\right) \tag{5.28 bis}$$

In Equations 5.27 and 5.28, the parameter B_M represents the width of the berm seaward of the T-Wall as depicted in Figure 5-10. For the case of this example T-Wall (Figures 5-16 through 5-19), the L_B parameter will be substituted for B_M.

$$\delta_{11} = 0.93\left(\frac{2.4\text{m}}{48.6\text{m}} - 0.12\right) + 0.36\left(0.4 - \frac{3.05\text{m}}{4.57\text{m}}\right) = -0.162$$

$$\delta_{22} = -0.36\left(\frac{2.4\text{m}}{48.6\text{m}} - 0.12\right) + 0.93\left(0.4 - \frac{3.05\text{m}}{4.57\text{m}}\right) = -0.223$$

Using Equations 5.23 – 5.26 and the values of δ_{11} *and* δ_{12}, which are both less than zero,

$$\delta_1 = 20 * \delta_{11} = 20 * -0.162 = -3.24$$

and

$$\delta_2 = 4.9 * \delta_{22} = 4.9 * -0.223 = -1.09$$

since δ_2 is less than zero (Equations 5.21–5.22):

$$\alpha_{IB} = \frac{\cos\delta_2}{\cosh\delta_1} = \frac{\cos(-1.09)}{\cosh(-3.24)} = \frac{0.462}{12.78} = 0.036$$

from Equation 5.20 and the value of H_D (calculated above),

$$\alpha_{IH} = \min\left\{\frac{2.25\text{m}}{3.05\text{m}}, 2.0\right\} = 0.74$$

Then, from Equation 5.19 for the Takahashi impulsive term modification,

$$\alpha_I = 0.74 * 0.036 = 0.0265$$

In the above example, the value of α_2 (from the original Goda non-impulsive wave pressure formulation) was calculated as 0.075 (Equation 5.6). Because α_I is less than α_2 (Equation 5.18), impulsive forces are negligible and can be ignored. Note that the value of the relative wave height (H_D/d_{SWL}) evaluated at depth d_b (see Figure 5-18) is approximately 0.5, which can be considered of low to moderate potential for generating impulsive wave forces.

In the case of $\alpha_I > \alpha_2$, it would be necessary to re-calculate P_1 using Equation 5.17 followed by the recalculation of P_2, P_3, P_4, and F_{Lat}. For demonstration purpose, it is assumed that the value of α_I was calculated as 0.1, which is greater than α_2 (0.075), and follow through with the resulting solution listed in Table 5-6.

$$P_1 = 0.5\,(1 + \cos\beta_D)\,(\alpha_1 + \alpha^* cos^2\beta_D)\,\rho * g * H_D \qquad (5.17 \text{ bis})$$

$$P_1 = 0.5 * \ (1 \ + \cos(0 \ deg)) \left(0.92 + 0.1 * cos^2(0)\right) * 1030 \frac{kg}{\mathrm{m}^3}$$
$$* 9.81 \frac{\mathrm{m}}{s^2} * 2.25 \ \mathrm{m} = 23{,}189 \ N/\mathrm{m}^2 = 23.2 \ kN/\mathrm{m}^2$$

In Table 5-6, a comparison of values is given for the pressure and resultant forces terms calculated using the original Goda formulation and the Takahashi modified formulation (for the assumed case of α_I equal to 0.1). Note that in the case of a T-Wall where the landward side of the T-Wall is dry, the hydrostatic pressure component, associated with the seaward SWL, would need to be superimposed to complete the total force calculation. This hydrostatic component has been left out here as this example focus is on wave forces only.

Table 5-6. Pressure and resultant force terms for original Goda and Goda-Takahashi modified methods.

Variable	Term	Value (Goda Original)	Value (Goda Takahashi)	Units
P_1	Pressure	22.7	23.2	kN/m²
P_2	Pressure	19.2	19.6	kN/m²
P_3	Pressure	20.4	20.8	kN/m²
P_4	Pressure	12.5	12.8	kN/m²
P_U	Pressure	18.8	18.8	kN/m²
U_P	Force/width	22.6	22.6	kN/m
F_{Lat}	Force/width	92.5	94.5	kN/m

5.4.4 Converting a trapezoidal pressure distribution acting on a discrete segment of the I-Wall face into equivalent end point forces

Using the relationships given in Ebeling et al. (2018) as summarized in this subsection, the wave pressure distributions acting on the stem of the T-Wall are converted into equivalent forces. The essence of this computation uses the one-third/one-sixth (1/3:1/6) force computational procedure to convert a trapezoidal distribution of a segment of stress between the closest nodes into equivalent nodal forces. This computational procedure is summarized using the generalized trapezoidal stress distribution between node i and node i+1 acting normal to the T-Wall stem segment k, designated as $length_k$ in Figure 5-22. The equivalent nodal point forces acting at node i and node i+1 are computed to be

$$F_i^- = length_k * \left[\frac{\sigma_i^-}{3} + \frac{\sigma_{i+1}^+}{6}\right] \quad (5.36)$$

and

$$F_{i+1}^+ = length_k * \left[\frac{\sigma_i^-}{6} + \frac{\sigma_{i+1}^+}{3}\right] \quad (5.37)$$

where $length_k$ is the distance from node i to node i+1, σ_i^- is the stress normal to node i on wall segment k, and σ^+_{i+1} is the stress normal to node i+1 on wall segment k. These two relationships for equivalent end forces F_i^- and F_{i+1}^+ will exactly reflect the trapezoidal pressure diagram along its nodal pair wall segment k. The sum of these two forces equals the area under the trapezoidal pressure diagram. Moment equlibrium for the wall segment k is satisfied for the applied trapezoidal pressure distribution and these two equivalent end normal forces.

Figure 5-22. Distribution of stress acting normal to a discrete segment *k* of the wall face. (a) Trapezoidal pressure distribution. (b) Equivalent nodal point forces. (after Ebeling et al. [2018]).

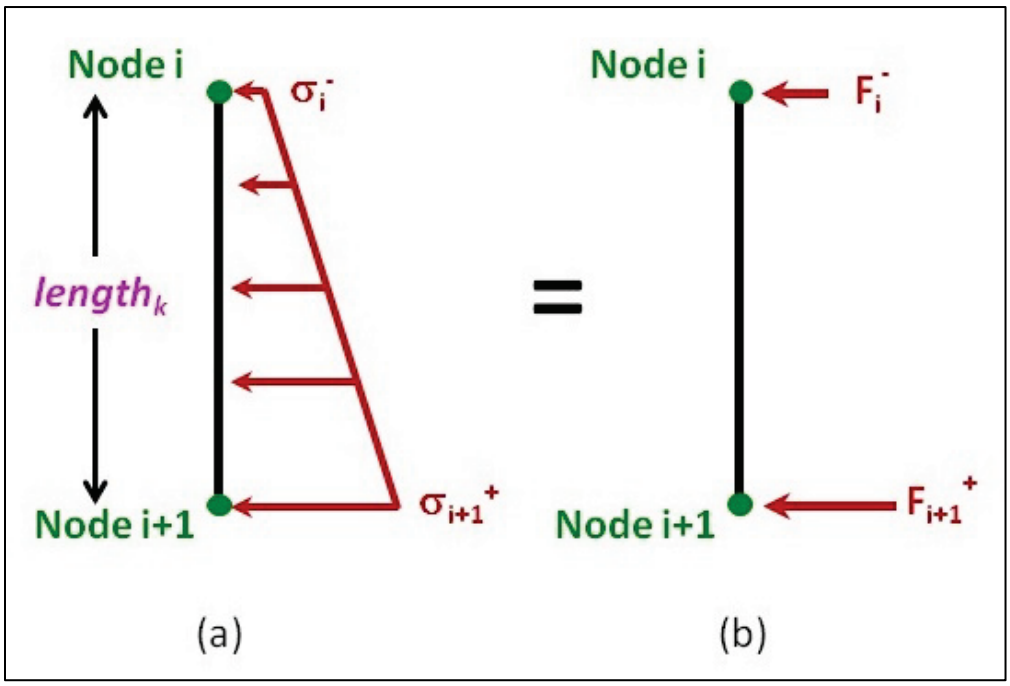

5.4.5 Calibration with prototype breakwaters

Goda (1973, 2010) combined case histories of the stability of several different prototype breakwaters (i.e., caissons) with the application of the Goda formula for wave pressure loading to validate his wave loading pressure-based formulation. For this assessment, Goda carefully

characterized the coastal engineering characteristics as per the parameters needed for Goda wave calculation input for different design sea storms and the field performance of each individual caisson during each *design* storm at various (coastal) harbors throughout Japan. Caisson performance in terms of sliding or nonsliding was noted per caisson per storm. Then, using the Goda wave pressure formula with the Takahashi breaking wave enhancement, Goda conducted a sliding stability computation for each caisson for each design storm applying Goda wave pressures and computed the safety factor against sliding. Last, the field performance of the caisson in its design storm was noted as to whether it slid in the field or not. The result of this assessment is summarized in Figure 5-23. Each letter designates a unique caisson. If the safety factor is computed to be less than or equal 1.0, the caisson is thought to slide under Goda calculation-based wave action. A filled circle designates that that caisson was observed in the field to have slid during the design ocean storm. Conversely, if safety factor is computed to be greater than 1.0, the caisson is thought to have not slid under Goda calculation-based wave action. An open circle designates that that the observation in the field was that caisson that did not slide during the design ocean storm of record. Each letter in this figure designates a unique caisson located along the coast of Japan.

Figure 5-23. Safety factor against sliding for the data base of field deployed caissons performance during ocean storms and analyzed using Goda's wave loading pressure distribution relationship (after Goda [2010]).

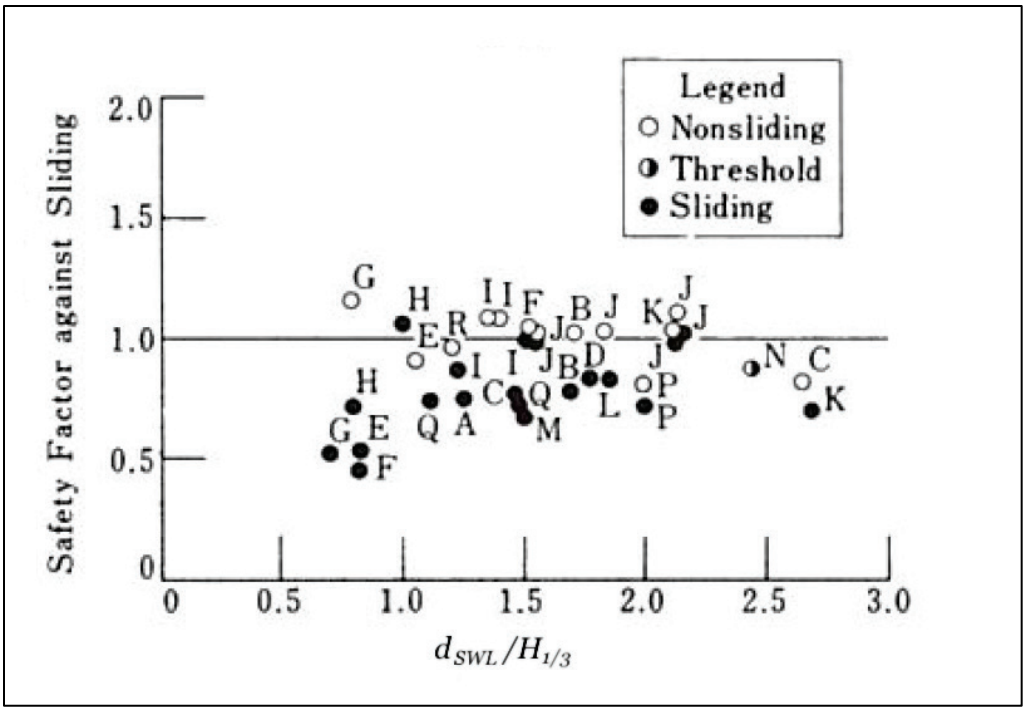

Goda (2010) observed that a separation between open and filled circles can be observed with a boundary around a safety factor equal to between 0.9 and 1.0, though some mixing remains (Figure 5-23). Also, the design sea storm for which the observed field sliding/non-sliding performance of the caisson was documented and was carefully assessed with its attributes documented in Goda (1973). Based on the results summarized in Figure 5-23, the authors of this report conclude that when the design sea storm is properly characterized in terms of the variables used as input to the Goda formulation for wave pressures with the Takahashi breaking wave enhancement, the question of if the caisson will slide or not slide for the design sea storm will be answered. It is believed that the complex effects of dynamic and time-varying ocean wave pressure distributions applied to harbor caissons are reasonably captured in an engineering sliding stability analysis of the caisson in which the Goda pseudo-static wave pressure distribution is applied. Recall that in the Goda procedure of analysis the complex spectrum of sea waves of varying amplitudes and periods are characterized by a single design wave defined by a representative wave height (H_D) and length (L_D).

Bullock et al. (2004) discusses their interpretation of measured field wave pressure data recorded during ocean storms at the Admiralty Breakwater located on the north side of Alderney Island. Alderney is the northern-most of the inhabited English Channel islands and lies 13 km off the Normandy coast of France. It is part of the Bailiwick of Guernsey, a British Crown dependency. Figure 5-24 shows the location of the Admiralty breakwater and its exposure to the North Sea. The Admiralty Breakwater is approximately 0.9 km in length, experiences significant storms events annually, and has been the subject of several studies. This breakwater is subjected to near parallel incident waves from the Atlantic and a large tidal range of approximately 7 m, therefore resulting in a wide range of wave forces Bullock et al. (2003). Figure 5-25 captures the severity of North Atlantic wave action at this breakwater. The picture is taken from the harbor side of the breakwater. Note the height of the wave splashup relative to the exposed height of breakwater and boat.

Figure 5-24. Island of Alderney and the Admiralty Breakwater[16].

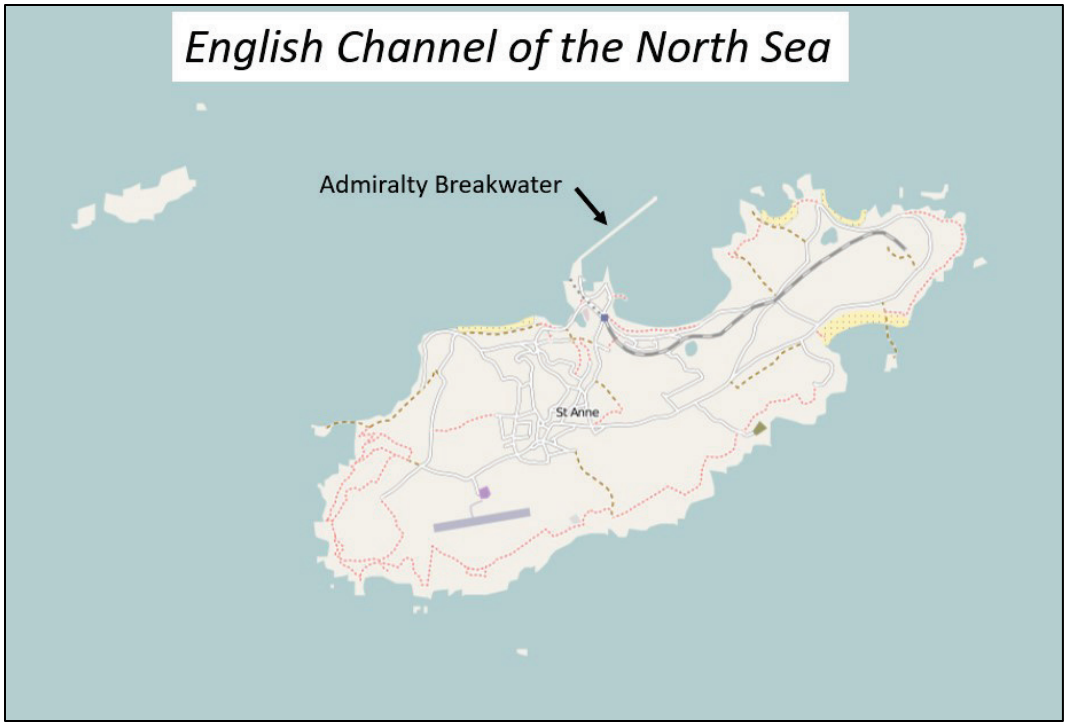

Figure 5-25. Admiralty Breakwater under high-sea event (after Neil Howard [2009][17]).

[16] Blofeld. 2010. "Location Map Alderney." Wikipedia Commons. November 2010. https://commons.wikimedia.org/wiki/File:Location_map_Alderney.png

[17] Howard, Neal. "Alderney Breakwater 2." Flickr. May 06, 2019. Accessed May 06, 2019. https://www.flickr.com/photos/neilsingapore/4131749788/in/photostream/

A 2-D array of eight pressure aeration units (PAU) had been installed on the seaward face of the masonry wall. In Figure H.10 the breakwater cross-section and PAU mounting locations are shown (Bullock et al. 2003). Each PAU was mounted vertically on one of the large granite blocks that form the wall, at an elevation that could be subject to impending waves (Figure 5-26). These PAUs measure positive and negative wave-induced pressures, conductivity, and temperature. The conductivity measurement is used to estimate the level of aeration during wave impact. In the Bullock et al. (2004) comparison of field data and design pressures, they comment that for the design sea state with H_{Si} equal to 3.1 m, Goda does not predict the peak pressures, but the overall resultant force computed within the distribution of PAUs appear to be of an appropriate order of magnitude. In their comparison, the pressure distribution predicted by the Goda relationship was based on use of an estimated H_{max} equal to 6.2 m. They also observe that usually the maximum force on the wall over the vertical range of the PAUs was found to not to occur at the time of maximum pressure. The maximum pressure Bullock et al. (2004) recorded during their reported ocean storm measurements was around 337 kPa at an elevation of 6.2 m CD[18]. However, as of 2004, the maximum impact pressure measured was 745 kPa as reported by Bullock et al. (2004).

Figure 5-26. Admiralty Breakwater cross section (after Bullock et al. [2003])

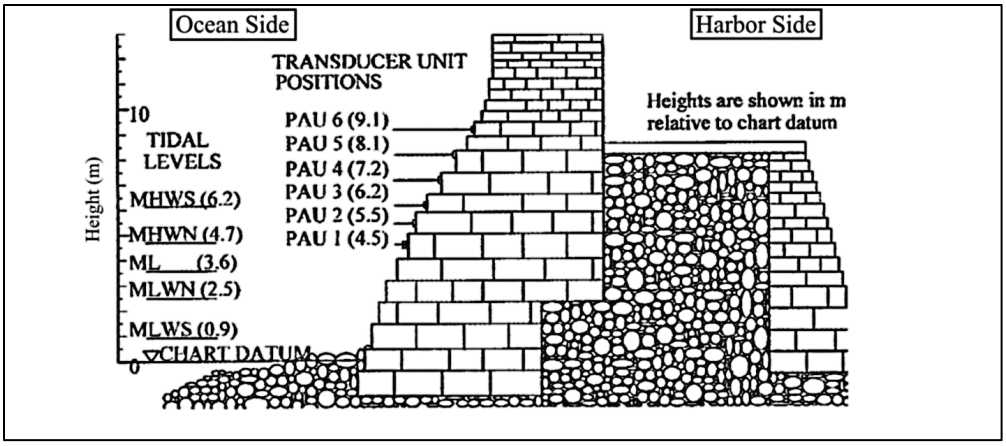

The stability of prototype breakwaters was examined by using the safety factor against sliding for a catalogue of caissons whose performance during storms was documented and analyzed by Goda (1973). The authors of this report observe that based upon subsequent (i.e., Goda [2010]) writings, it appears that the Goda (1974) tables of interpreted caisson

[18] Chart datum

performance data during the documented ocean storms and its summary figure of safety factor against sliding for the data base of caissons appears to be in error. The Goda (1973) dataset and resulting safety factor against sliding summary figure (Figure 5-23), was described in Goda's latest publication on this topic (Goda 2010). Therefore, authors of this report relied on the 1973 and 2010 Goda publications for this safety factor against sliding information for caisson that slid or did not slide during the ocean storm of record and not Goda's 1974 publication's database.

Goda (2010) performed a similar assessment of the Minikin wave pressure formula using the same field harbor data but applying the Minikin formulation in the sliding equilibrium analysis (Figure 5-27). As described in Goda (2010), the wave height for the calculation taken as the significant height yielded the poorest prediction of breakwater stability; some breakwaters remained in position with estimated safety factors less than 0.4 while others slid with safety factors of more than 2.0. Goda (2010) comments that Minikin's formula is found to be impractical, and the accuracy of the Goda formulas is judged superior to that of *conventional* pressure formulas of Hiroi and Sainflou. The Goda (1973) report contains tables of these data.

Figure 5-27. Safety factor against sliding for the data base of field deployed caissons performance during ocean storms and analyzed using Minikin's wave loading pressure distribution relationship (after Goda [1973]).

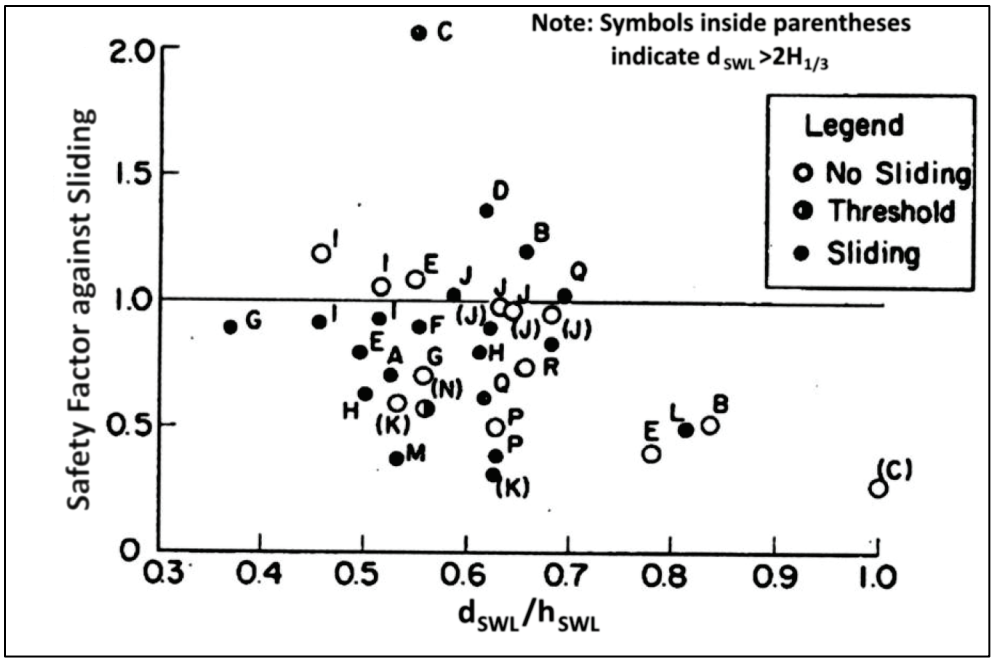

In 2004, Bullock et al. (2004) observed that Minikin's formula is out of fashion in recent years. Goda's caisson verification data as reported in Goda (1973) and discussed in Goda (1974) and most recently in Goda (2010) support this conclusion.

5.5 Effects of scale and aeration

The effect of the scale of wave-paddle-generated freshwater waves in the laboratory relative to air-entrained seawaterwaves is an important consideration when interpreting laboratory results, especially for violent breaking waves with trapped air. Bredmose et al. (2015) observe that several factors have been identified that may cause bubbles to be smaller in saltwater and seawater than in freshwater. They comment that because small bubbles tend to rise to the surface at a slower speed than large bubbles, this enables entrained air to persist for longer in seawater than in freshwater. Air is far more compressible than water. During their 2004 interpretation of wave tests conducted at a 1:4-scale in the 32 m long, 5 m wide, 7 m deep Grosser Wellenkanal large wave channel laboratory experiments in Hannover Germany, Bullock et al. (2004) commented that seawater waves are likely to contain more air than the freshwater waves generated in their laboratory test facility, and this will tend to make the fluid more compressible. Because of this, they conclude that the application of the Froude Law to wave pressure measurements made in the laboratory results in wave pressures to be overestimated in the field. It is this compressibility of air-entrained seawater that invalidates the linear Froude-scaled laboratory condition for wave pressure over a wide range of wall heights and levels of air entrainment in the seawater, as exemplified by the Bredmose et al. (2015) Figure 2 nonlinear relationship of (wave) pressure versus Froude number. In their opening comments to a paper discussing the results of field and large-scale model tests of breaking wave impacts, Bullock et al. (2004) observe that the maximum impact pressure measured by 2004 in the field is 745 kPa while pressures up to 4 MPa were measured in his large-scale flume test (1/4 scale). Such is the influence of scale and aeration effects on wave pressures. In summary, the effect of scale and air entrainment is an ongoing topic of research in the coastal engineering community.

5.6 Coefficient of variation for the Goda-Takahashi wave pressure formula

Recall that the COV is equal to the standard deviation for the variable divided by its mean value (σ/μ). In LRFD analysis, the COV plays a vital role in defining the variability of both the applied loads and resistances to these loads. In the case of a seawall or T-Wall, under design loads, the wave-induced force is the principal-loading agent, which must be evaluated for its COV. Statistically forecasted wave conditions (e.g., 100-year storm) and bathymetric conditions can provide the parameters needed to satisfy a load calculation method, but the load prediction itself has a statistical component of error that needs to be evaluated in LRFD design. The primary objective of this section is to investigate the variability in the Goda-Takahashi (Takahashi et al. 1993) wave pressure formulation (Section 5.4) resulting in recommendations in COV for LRFD application.

For years, the Goda-Takahashi wave force prediction method has been used to compare wave pressure and force predictions with modern analytical methods. For this reason, sufficient published research data are available to statistically evaluate the dispersion characteristics of the Goda-Takahashi prediction method. Because very little raw data are routinely published, most of the data used in this dispersion evaluation were extracted via digitization of published figures. Consequently, some error can be attributed to the digitizing effort. The data used in this analysis originate from Garcia (1968), Goda (1973), Cuomo et al. (2010a) and Kisacik et al. (2010). Figure 5-28 shows the binned distribution of the ratio of total force measured (F_M) to total force calculated (F_C) using the Goda-Takahashi method with a total of 926 data points from all four datasets combined. These measured forces (F_M) were computed at the time of peak measured pressure. The mean F_M/F_C value is 1.25 for the 926 all-point dataset. This implies that the total force measured is larger by 25% than the Goda-Takahashi prediction total force calculated force (i.e., by a factor of 1.25). Based on Figure 5-28, the distribution of F_M/F_C resembles a lognormal distribution with a maximum F_M/F_C value of around 9.0. Figure 5-28 also includes the statistics for the 95% CDF of the original 926 data points. The mean F_M/F_C value is 1.1 for the 846-point, reduced 95% CDF dataset. This implies that F_M is slightly larger by 10% than F_C (i.e., by a factor of 1.1). Additionally, note that the COV of F_M/F_C decreases from 0.72 to 0.47 when the upper 5% of F_M/F_C data is excluded from the COV calculation. This is a 35% reduction in COV.

Figure 5-28. Frequency distribution of force measured divided by force calculated (F_M/F_C) for all four datasets combined.

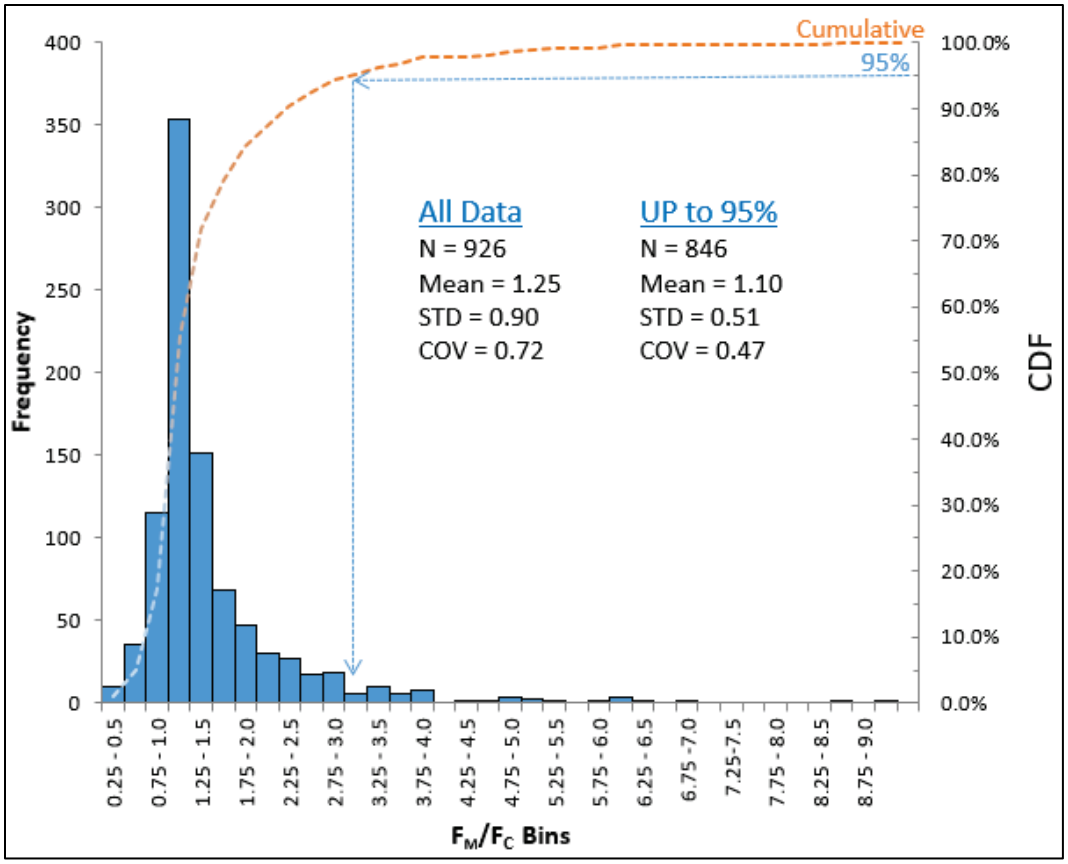

The same F_M/F_C dataset used in Figure 5-28 is presented as a function of the ratio of incident wave height to water depth H_i/d_{SWL} in Figure 5-29. In this figure, the dispersion in the F_M/F_C is observed to generally increase with H_i/d_{SWL}. Exploring this relation further, the COV is evaluated for binned ranges of H_i/d_{SWL} and shown in Figure 5-30. The data were accessed statistically for each of the five bins of H_i/d_{SWL} ranging in value from 0.1 to 1.1 in 0.2 increments. In Figure 5-30, the COV for each of the five bins at their respective bin centers is shown. The bin center is marked with black circles, and the full bin extent is indicated with a horizontal black line centered about each bin's black circle. The COV for the five bins varies from a low of 0.11 to a high of 0.75. Through these bin center data points, a trend line was added to highlight the general trend (for discussion purposes only) of increasing COVs with increasing H_i/d_{SWL} values. Table 5-7 summarizes the COV statistics for the data contained within each bin.

Figure 5-29. Combined datasets of the F_M/F_C to H_i/d_{SWL} relationship for 926 data points.

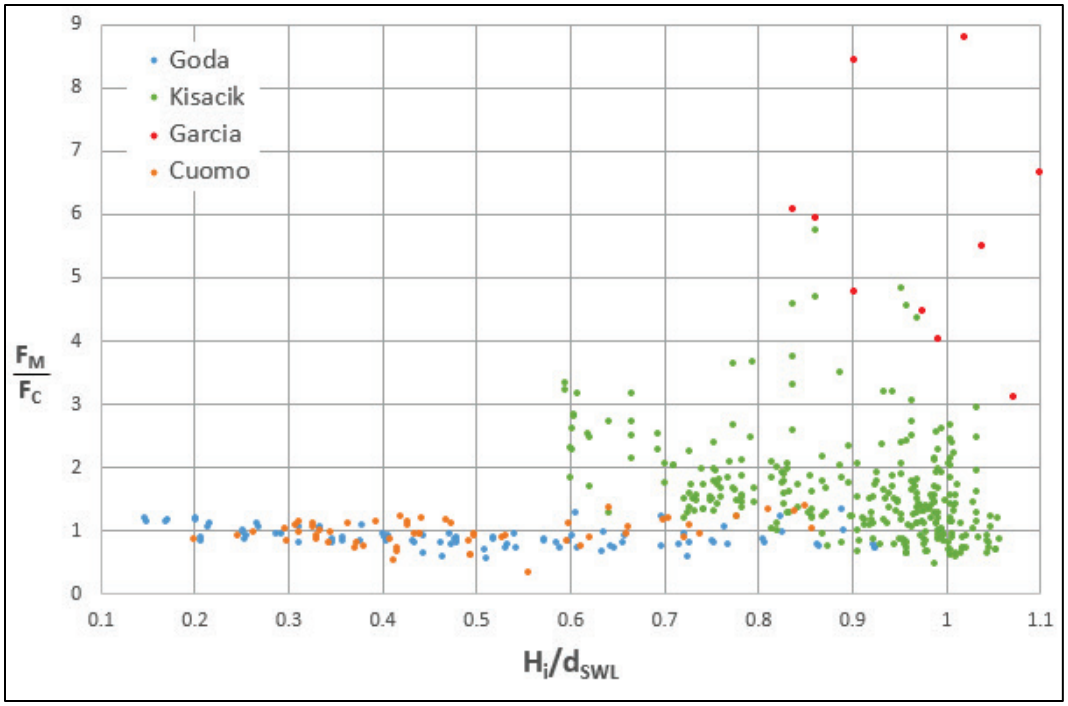

Figure 5-30. Coefficient of variation F_M/F_C as a function of H_i/d_{SWL} for each of the five data bins containing 926 data points.

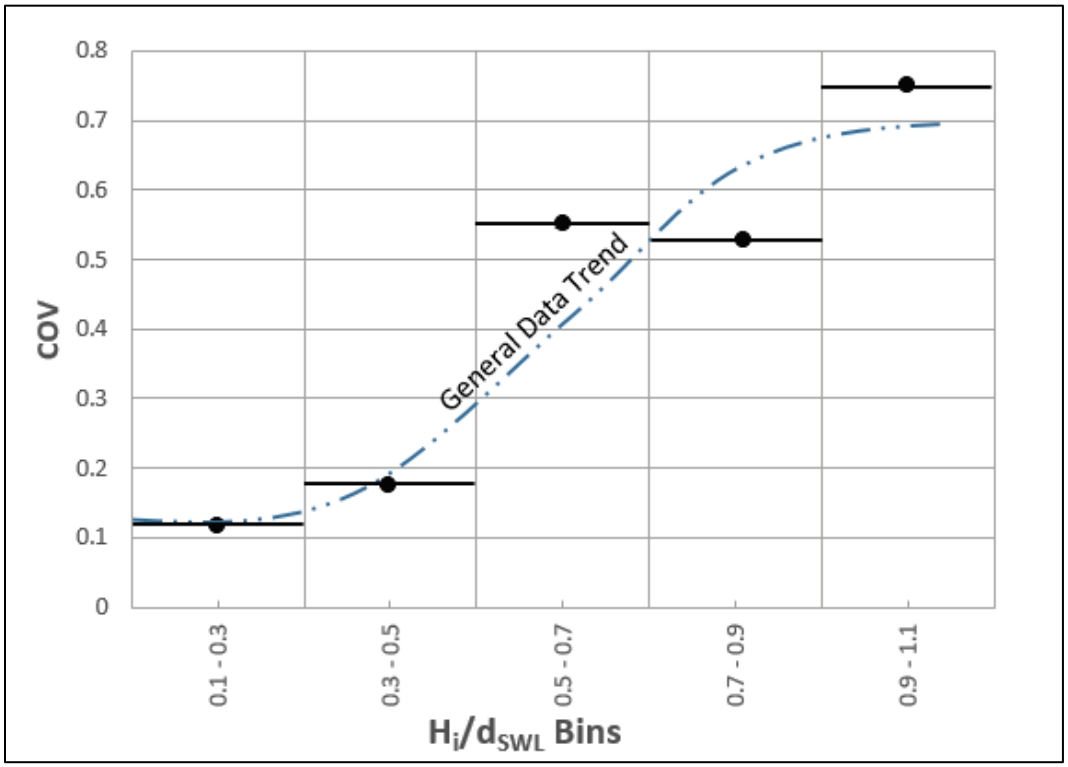

Table 5-7. Summary of COV for binned data of the relative wave height parameter (H_i/d_{SWL}) for the 926 data points.

Range of H_i/d_{SWL}	COV
0.1 – 0.3	0.11
0.3 – 0.5	0.18
0.5 – 0.7	0.55
0.7 – 0.9	0.53
0.9 – 1.1	0.75

In Figure 5-31, the four individual datasets are defined by their investigative regions of H_i/d_{SWL}, and the resulting statistics of respective F_M/F_C evaluations. Again, all four data point sets combine to a total of 926 data points. The datasets of Goda (1973) and Cuomo et al. (2010a) are similar in that their investigations both include the lower range of H_i/d_{SWL} and show very similar F_M/F_C statistics over the range of H_i/d_{SWL} even though model scales are significantly different (Goda 1/20 and Cuomo 1/4). The mean of F_M/F_C for both datasets was found to be close to 1.0 (Goda 0.9 and Cuomo 0.97). The dataset of Kisacik et al. (2010) investigated the mid to upper range of H_i/d_{SWL} and comprised approximately 65% of the data in all four datasets. The mean F_M/F_C value of the Kisacik et al. (2010) dataset increased from the Goda (1978) and Cuomo et al. (2010a) datasets by approximately 65% and the value of standard deviation by more than 400%. This finding helps to confirm the US Army Engineer Research and Development Center (ERDC) R&D team's observation of the increase in uncertainty (COV) of the Goda-Takashi predictive method with increasing H_i/d_{SWL}. Last, the dataset of Garcia (1968) investigated only the upper range of H_i/d_{SWL} and was the smallest of the four datasets comprising only approximately 2% of the data in all four datasets. The mean F_M/F_C value of the Garcia (1968) dataset increased from the Goda (1973) and Cuomo et al. (2010a) datasets by approximately 500% and the value of standard deviation by approximately 1,000%. Again, both the datasets of Kisacik et al. (2010) and Garcia (1968) confirm increasing uncertainty in the Goda-Takashi predictive method with increasing H_i/d_{SWL}. Table 5-8 summarizes the COV values for the four datasets that when combined, total 926 data points.

Figure 5-31. Statistical review of each of the four datasets used for the 926 data points in Figure H.12.

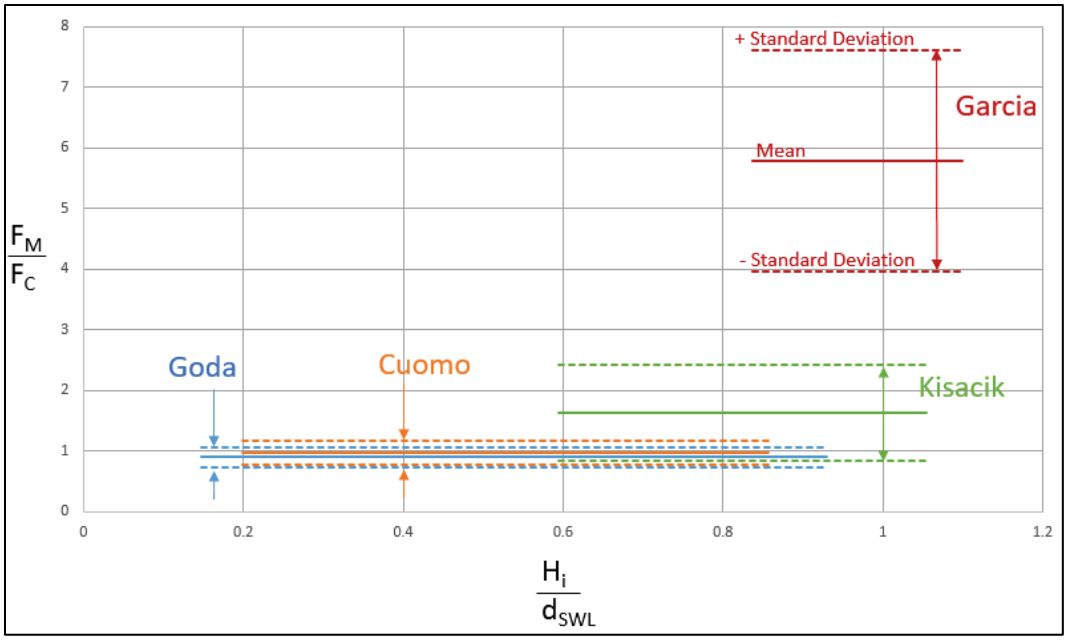

Table 5-8. Summary of COV for the Goda-Takahashi predictive method for the four individual datasets.

Range of H_I/d_{SWL}	COV	Dataset	Scale
0.16 – 0.92	0.18	Goda (1973)	Approx. 1/20
0.2 – 0.84	0.21	Cuomo et al. (2010a)	Approx. 1/4
0.59 – 1.05	0.48	Kisacik et al. (2010)	Approx. 1/20
0.84 – 1.1	0.38	Garcia (1968)	Approx. 1/20

Goda (1972) investigated wave pressure exerted on a vertical wall in relation to the wave transition from non-breaking to post-breaking. In this work, Goda observed that maximum wave pressures generally follow the theoretically derived Breaking Index by Yamada and Shiotani (1968). In Figure 5-32, Yamada's breaking index and Goda's laboratory estimates of the non-breaking and semi-breaking relations are shown. These surf-zone prediction curves of wave breaking should be considered as stochastic variables according to Smith and Kraus (1991). The regions of investigation of the four datasets used to explore the F_M/F_C COV relation are also defined in Figure 5-32 along with the COV of F_M/F_C for individual dataset. From this figure it is noted that the F_M/F_C is a function of both H_i/d_{SWL} and d_{SWL}/L_O. Note that the Garcia (1968) dataset (shown in red) employs the largest values of $H_i/d_{SWL,}$ yet the COV for this dataset falls below the Kisacik et al. (2010) COV. This is explained in Figure 5-31 by the

exceedingly large mean value of Garcia's F_M/F_C. Recall that the COV is the standard deviation divided by the mean. Although this investigation focuses solely on the F_M/F_C to H_i/d_{SWL} relationship, a more detailed relationship could be developed as a function of both H_i/d_{SWL} and d_{SWL}/L_O. The authors of this technical report attempted to devise an F_M/F_C relationship with both H_i/d_{SWL} and d_{SWL}/L_O; however, sufficient L_O data were unavailable from all but the small Garcia (2010) dataset. Therefore, this ERDC-expanded relationship developmental effort is postponed until additional L_o and H_i data sets become available.

Figure 5-32. Wave transition zones as defined by Yamada et.al. (1968) and Goda (1972) with defined boundaries of datasets used in this study.

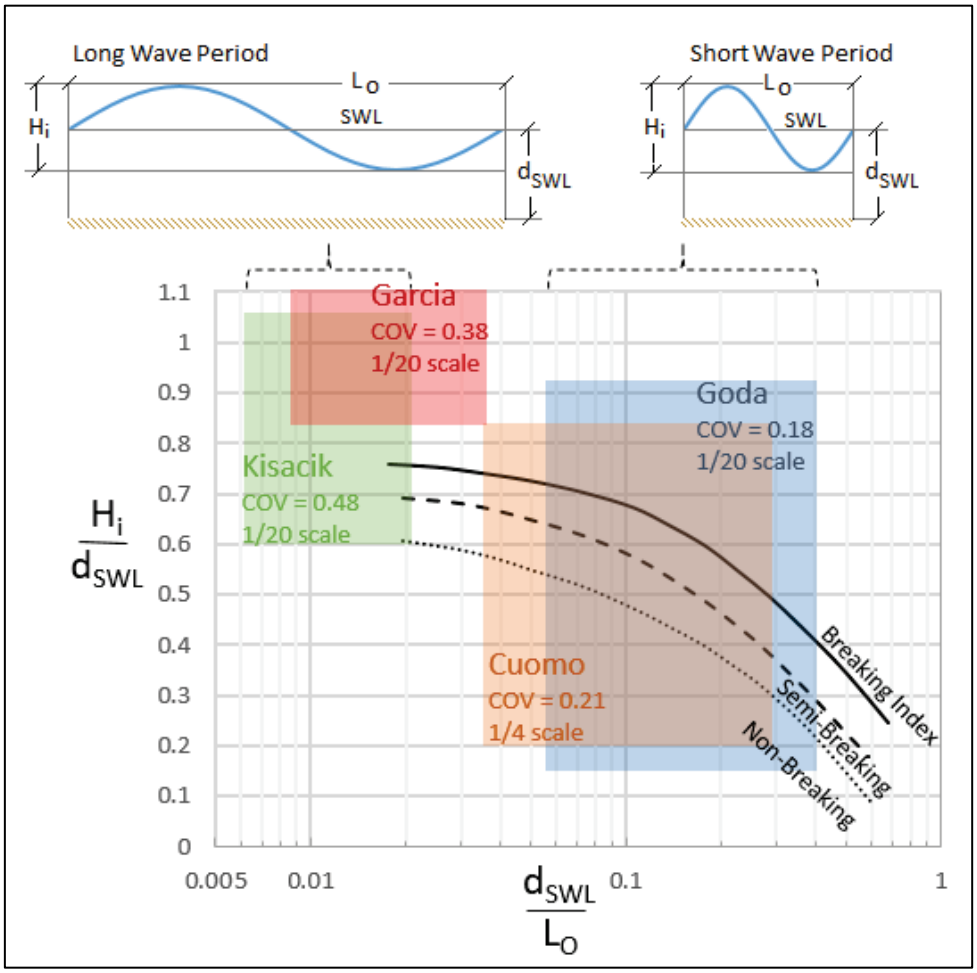

After careful study of the data the, ERDC research team concluded that the broad range in the COV (0.11 – 0.75) observed in the four datasets discussed above and shown in Figure 5-32, can be partially explained by the broad range of H_I/d_{SWL} and d_{SWL}/L_O used in the experimental studies. However, questions remain regarding the uncertainty in laboratory

measured peak pressure on the vertical wall, such as variations in model scale and variations in peak pressure sampling rate. Model scale is known to be highly correlated to peak wave pressure measurements at wave impact (Cuomo et al. 2010b; Bredmose et al. 2015). In particular, Bredmose et al. (2015) stated that the level of air entrainment of the breaking wave is likely to increase with model scale and that the volume of wave air entrainment is directly related to the magnitude of impact pressures. Cuomo et al. (2010b) describes a method to scale wave impact pressures and impact rise times based on the Bagnold number (Bagnold 1939), which is evaluated for both model and prototype scale. This scaling method requires wave profile information that is unavailable for the four datasets used in this COV evaluation conducted by the ERDC R&D team.

Takahashi et al. (1993), in their derivation of the extended Goda wave pressure formulation to include impulsive forces at wave impact, examined the wave profile prior to breaking. They found that for the same incident wave conditions in the offshore, wave pressures exerted on the vertical wall varied significantly for changes in the wave profile at impact. In Figure 5-33, consecutive wave profiles are shown detailing the breaking process of a solitary plunging wave of the type. In the work of Takahashi et al. (1993), the plunging-type breaking wave was identified as the characteristic wave profile that imparts the highest wave pressures to a vertical wall; other type of breaking wave (e.g., spilling, collapsing, surging) were not discussed in their work. The profiles of Figure H.16 were derived from high-speed imagery from research focused on the physics of wave energy transfer and dissipation (Tallent 1990). Although this study did not specifically investigate impact forces on vertical walls, it is helpful to illustrate energy dissipation and air entrainment process in wave breaking. Figure 5-33 images (a-f) are described as follows:

a. Pre-breaking wave with virtually no air entrained in the wave.
b. Wave near breaking inception with virtually no air entrained in the wave.
c. Breaking wave with a formed airpocket and little or no air entrained in the wave. This image was taken at the instant of crest-trough impact.
d. Broken wave with low to moderate air entrainment in the first eddy.
e. Broken wave with moderate air entrainment in the first eddy and initiation of the second eddy characterized by rapid air entrainment.
f. Broken wave with moderately high air entrainment in the first and second eddy and initiation of the third eddy.

Figure 5-33. Illustration of plunging-type wave profile during energy dissipation process (after Tallent [1990]).

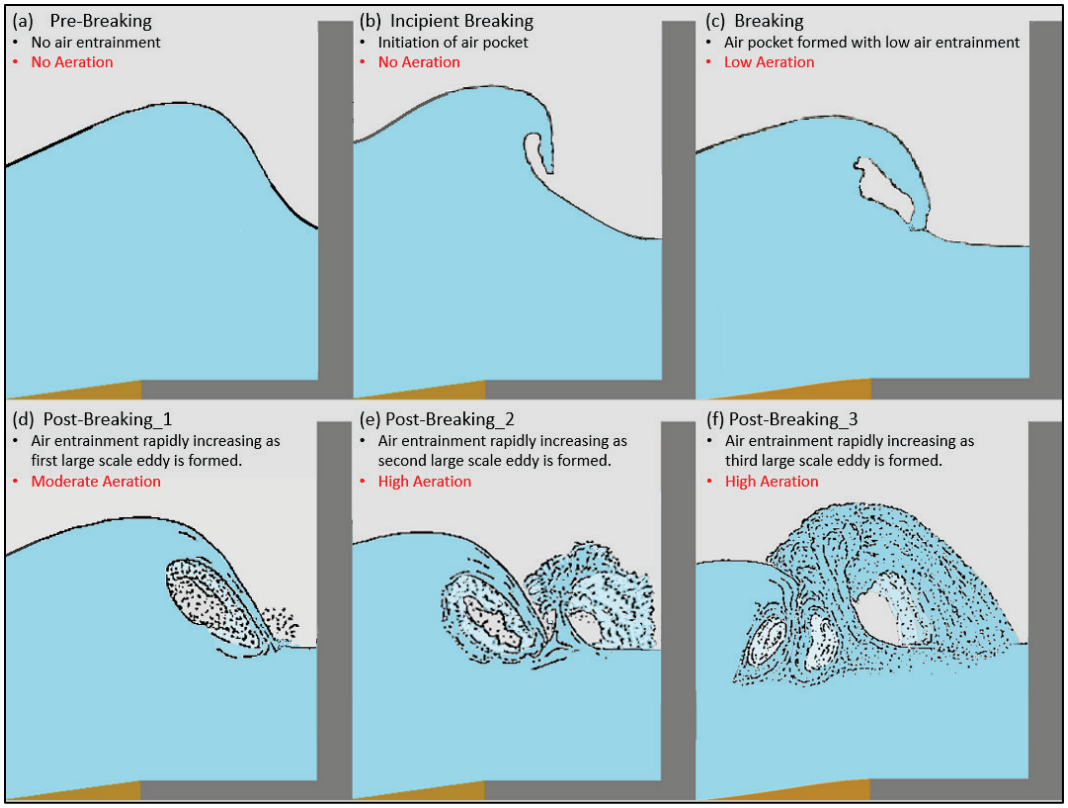

Bredmose et al. (2015) categorized the wave characteristics, at wall impact, corresponding to pressure distribution as the following:

- No aeration, resulting in a jet of water up the wall and a localized region with high impact pressure (flip-through impact), Figure 5-33 (a) and (b).
- Low aeration, resulting in high pressure distributed over the full extent of the wall, Figure 5-33 (c) and (d).
- High aeration, resulting in a lower peak pressure over a greater time duration, Figure 5-33 (e) and (f).

Takahashi et al. (1993) observed that maximum impact pressures occur for wave profiles like those depicted in 5-33 (c) and (d), where the air pocket between the wave crest and trough is fully formed and air entrainment in the wave is minimal. This scenario was used to extend the Goda wave pressure formulation to include an implosive pressure term. In Figure 5-33 (d) and (f), the wave is rapidly transformed into a series of large-scale eddies with high-level air entrainment resulting in a rapid reduction in both wave height and wave speed. This rapid velocity reduction at the

leading edge of the breaking wave is demonstrated in Figure 5-34. This velocity reduction, post (d) waves, results in lower pressures imparted to the wall due to significant aeration and vortex water particle motions.

Figure 5-34. H.17 Leading edge velocity characteristics for solitary plunger. The notation of (a–f) correspond to Figure 5-33 (a-f) (after Tallent [1990]).

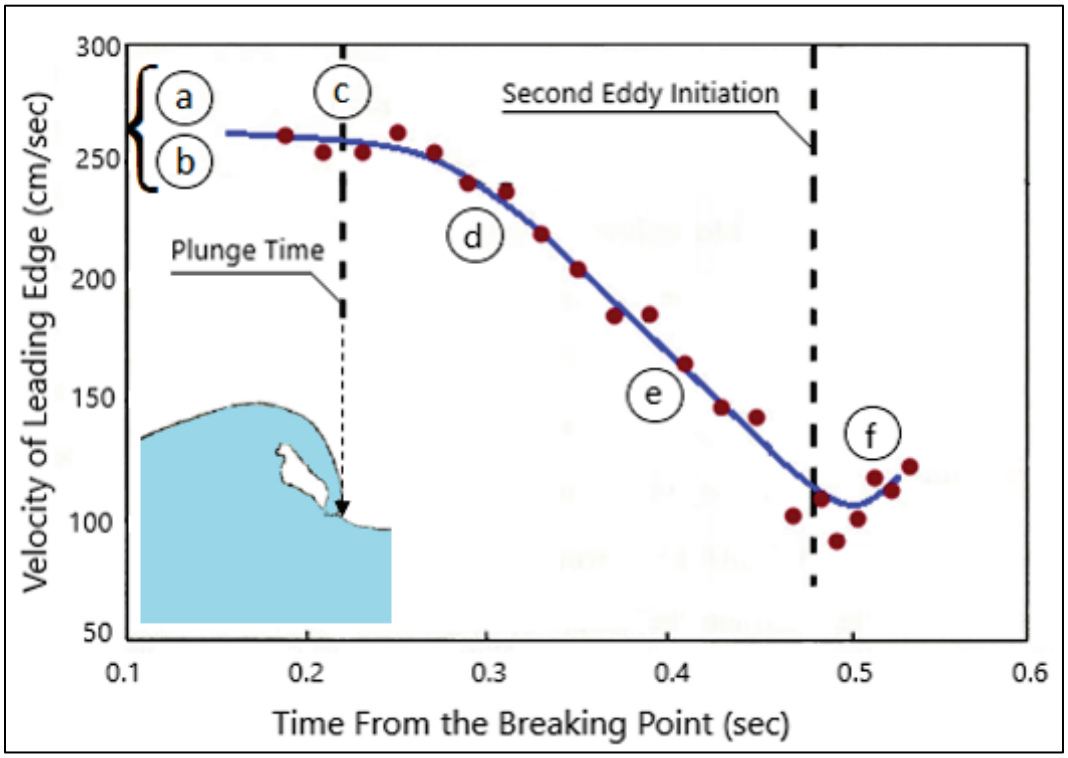

As mentioned above, significant variations in instrument capability, such as sampling rate, can lead to uncertainty in laboratory measured peak pressure. For example, in the 1960s when much of the original Goda and Garcia research was conducted, paper chart recorders were often employed. These recorders were realistically limited to sampling rates of less than 1 KHz, while in recent studies, 20 KHz sampling rates of peak wave pressure are often reported, such as in the case of Kisacik et. al. (2010). In full-scale tests, Bullock et. al. (2004) reported measuring peak impact durations of approximately 3 milliseconds. Considering that the duration of the peak pressure event at wave impact is directly related to model scale, it is somewhat doubtful that small-scale laboratory tests conducted in the 1960s could capture the peak pressure event.

To validate his then *new* wave pressure model, Goda (1974) analyzed 34 cases of prototype scale breakwaters (reinforced concrete caissons) for sliding in recorded high sea storm events. The predicted case of sliding (i.e.,

computed sliding safety factor value less than 1.0), using Goda's formula, was then compared to field observations and measurements of breakwater sliding after each design storm event for each caisson (Figure 5-23). Of the 34 case studies, only five caissons (14%) failed to satisfy Goda's prediction. The data contained in this figure imply that the uncertainty in the Goda predictive method at prototype scale can be estimated from the error in the derived safety factor for the five failed cases. The COV calculated for these five cases was found to equal 0.12 over a 0.4 to 1.0 range of H_I/d_{SWL}. The authors of this technical report recognize this is a limited dataset size to be used in a statistical COV computation.

In summary, the ERDC research team observed a relationship in the data that supports the argument that the uncertainty in the Goda-Takahashi wave pressure prediction method is primarily a function of the relative wave height parameter (H_i/d_{SWL}). Additional contributors include scale, instrumentation limitations and the complex nature of wave energy transfer and dissipation at breaking. Furthermore, considering that increasing values of relative wave height (H_i/d_{SWL}) correspond to increases in wave energy and wave instability, it is logical to assume that the COV of the Goda-Takahashi wave pressure prediction method increases with (1) increasing H_i/d_{SWL} , (2) increasing energy, and (3) increasing wave instability.

In Figure 5-35, the derived COVs for all datasets and analysis methods are combined for review. The purple lines represent the COV evaluated for binned data of H_I/d_{SWL}, as shown in Figure 5-30. Note that the COV for the largest bin ($0.9 < H_I/d_{SWL} < 1.1$) is shown as a dashed line due its limited data size (10 points), thus minimizing confidence as a representative COV for this bin. The red and black dashed lines are the upper limit COV values derived from the CDF of Figure 5-28. The red line represents the entire dataset (totaling 926 data points) used in the CDF analysis, and the black dashed line represents 95% of the CDF data points. Note that both the CDF (red and black dashed lines) COV estimates fall close to the two upper bins (purple) COV estimates. Last, the blue line represents the Goda-derived COV for prototype scale, FoS of sliding. This dataset is very small (n=5), but its validity is reinforced by the COV similarity shown in large-binned dataset of $0.1 < H_I/d_{SWL} < 0.3$. This bin's COV is designated with a purple line and labeled with its COV value of 0.11.

Figure 5-35. Summary of COV for the Goda-Takahashi predictive method.

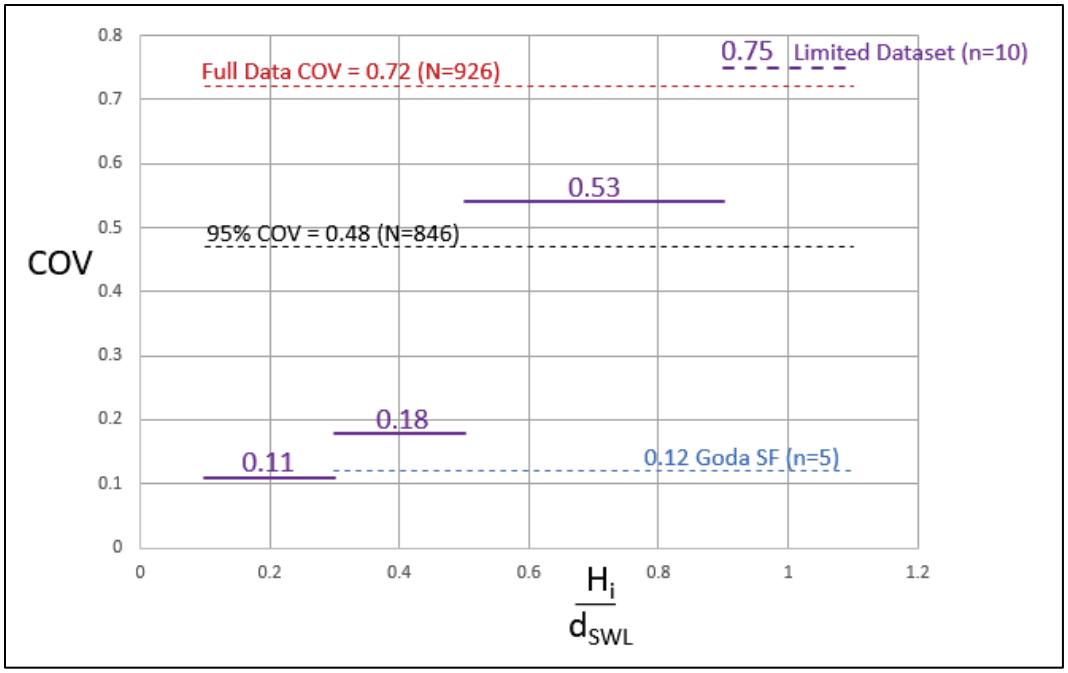

The Goda-Takahashi wave force prediction method uses design wave conditions, such as $H_{1/3}$, H_{MAX}, $T_{1/3}$, and T_{MAX}, along with design SWL conditions at the location of the structure (e.g., breakwater) to estimate the peak pressure at the time of wave impact. The ERDC R&D team assumes that the dispersion in the peak wave pressure, and resulting peak force, is greatest at the time of peak pressure. This implies that the COV is also greatest at the time of peak pressure.

To emphasize the fundamental data trend of COV for the Goda-Takahashi wave force prediction method over the range of relative wave height (H_I/d_{SWL}), the simplified relationship shown in Figure 5-36 is proposed. The COV data analyzed in this study show a relatively high statistical confidence in the region defined as $0.1 < H_I/d_{SWL} < 0.9$ (solid black line). The lower bound of 0.1 is based on both binned data (in the 0.1 to 0.3 H_I/d_{SWL} range) and full-scale tests conducted by Goda to validate his formula. The coastal engineer may choose to re-examine the statistical results presented above for $H_I/d_{SWL} > 0.9$ where a black dashed line is displayed. Recall that for this last bin ($0.9 < H_I/d_{SWL} < 1.1$), the design wave height is of the approximate same magnitude as the water depth (d_{SWL}) as demonstrated in Figure 5-37. This image shows a nearshore collapsing-type breaking wave in the proximity to the shoreline.

Figure 5-36. Proposed simplification of COV to relative wave height parameter (*Hi/dSWL*) relationship.

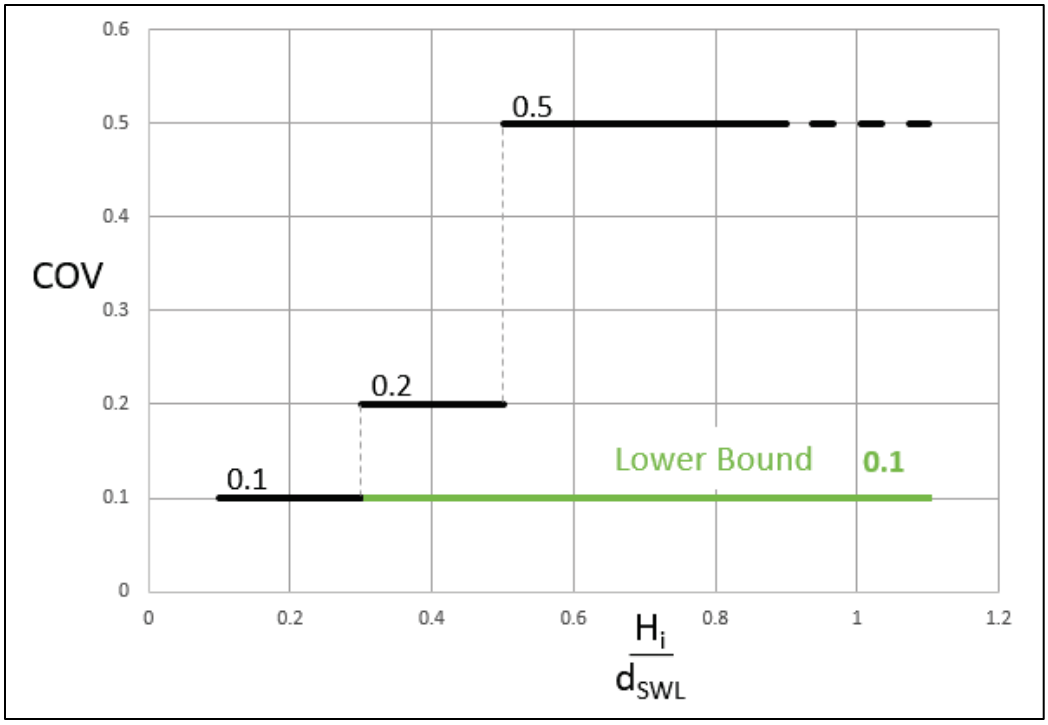

Figure 5-37. Nearshore breaking wave where H_i/d_{SWL} is an order of magnitude of 1.0.[19]

[19] Vetsikas, Dimitris. Flickr. March 21, 2016. Accessed May 07, 2019. https://pixabay.com/photos/wave-sea-water-splash-breaking-1271622/

The ERDC R&D team observed that this is the most violent wave regime of all the binned data wave regimes defined in this ERDC study, so it would be intuitive to expect large uncertainty within this wave regime. The coastal engineer is referred to the COVs shown in Figure 5-35 and its binned data for $0.9 < H_I/d_{SWL} < 1.1$ when assigning a value for COV. The ERDC R&D team is confident in stating that the COV is at least 0.5 for this bin for peak wave pressure dispersion.

The ERDC R&D team has speculated that the greater the potential for higher pressures (e.g., larger H_I/d_{SWL}) the uncertainty also increases. Figure 5-35 results led to this viewpoint. In Table 5-9, a summary of COV for ranges of H_I/d_{SWL} is provided for reference. It is consistent with Figure 5-36. The upper COV bound of 0.5 is based on both binned data and a 95% CDF of the 926 all-point dataset performed by various researchers. The lower bound of 0.1 is based on both binned data (i.e., $0.1 < H_I/d_{SWL} < 0.3$) and full-scale tests conducted by Goda to validate his formula. The coastal engineer is referred to the cautionary discussion expressed in the previous paragraph regarding the COV value in the last bin of $H_I/d_{SWL} > 0.9$.

Table 5-9. Summary of simplified COV as a function of the relative wave height parameter (H_I/d_{SWL}).

Range of H_I/d_{SWL}	Lower Bound COV	COV (from peak wave pressure)
0 – 0.3	0.1	0.1
0.3 – 0.5	0.1	0.2
0.5 – 0.9	0.1	0.5
0.9 +	0.1	0.5+

6 Example Calculation of Wind-Induced Inland Wave Forces on Vertical Walls using the Goda-Takahashi Procedure

6.1 Introduction

This chapter presents a procedure of analysis for the calculation of wind-induced wave forces acting on an inland hydraulic structure. In Chapter 5, application of the Goda-Takahashi (Goda 2010) wave force prediction method was reviewed for wind-generated sea waves on near-shore vertical-faced coastal structures (such as the T-Wall), and an example wave force calculation was included. In the example calculation contained within this chapter, the Rayleigh statistical method was employed for the purpose of estimating design wave height and period based on historical offshore wave height and period records. For the case of inland hydraulic structures where wave buoys typically do not exist, the estimation of design wave height and period is more involved due to the need to locate nearby historical records of wind speed and to process these data using both statistical and analytical methods. In this chapter, a procedure of analysis for assessing wind-induced wave force loading is laid out, and an example calculation is provided on an inland vertical-faced flood mitigation structure. The hydraulic structure used in this example problem is a hypothetical T-Wall, for flood protection purpose, oriented normal to the river channel. Analytical and statistical methods are employed in the estimation of design wave height and period along with requirements of historical wind record preparation. Finally, the Goda-Takahashi wave loading calculation results are presented for this example inland flood protection structure.

6.2 Existing guidance for inland hydraulic structures

An inland navigation projects' main purposes are to provide water depths sufficient for safe travel upstream and downstream from the project and a method or structure that allows the vessel to transit through the project. Control of river water levels is accomplished by spillway gates that are designed to withstand hydrostatic, hydrodynamic, and intermittent extreme forces acting on the gate and surrounding hydraulic structure.

Recently, Hite et al.[20] expanded on the USACE inland hydraulic design guidance by introducing the LRFD design methodology, which includes wave force loading. Hite et al. performed an analysis on an example Mississippi river spillway gate system and found that wind induced wave forces are significant and correspond to 15% and 20% of the magnitude of the hydrostatic loads (with gate closed) and the hydrodynamic loads for a 1.0 ft gate opening, respectively.

In addition to the USACE responsibility for providing inland structures for navigation purpose, such as locks and dams, the USACE is also responsible for providing inland flood mitigation structures where the need exists, such as a batter pile-founded T-Wall. These flood prevention structures are primarily designed to resist hydrostatic flood loading. In this chapter, the traditional inland flood protection structure design methodology will be extended by including wave force estimation and assessing its magnitude relative to hydrostatic loading. The current USACE guidance for determining wave load design is to use *Shore Protection Manual* (WES, CERC 1984). However, this method is now identified by the authors as insufficient as discussed in Section 5.1.

6.3 Wave force calculation for loading on vertical inland wall structures

In the following discussion, the Goda-Takahashi wave force prediction method will be applied for the case of an inland structure without detail explanation of the formulation. Therefore, the reader is expected to be somewhat familiar with the Goda-Takahashi formulation before proceeding. The derivation and application of the Goda-Takahashi wave force prediction method is thoroughly documented in Chapter 5. The primary objective of this chapter is to discuss the key difference in application of the Goda-Takahashi method between coastal and inland structure and elaborate on techniques to bridge the gap. This key difference is primarily centered on input parameter estimation to the Goda-Takahashi wave loading equations, namely, the design wave height and wave period.

[20] Hite, J. E., R. M. Ebeling, and B. C. White. In preparation. *Load Definitions for Ten Hydraulic Steel Structures, Including Probabilistic Load Characterization*. ERDC Technical Report. Vicksburg, MS: US Army Engineer Research and Development Center.

NOTE: From this point forward, the document will be referred to or cited as "Hite et al."

6.4 Significant wave height and period estimation

The Goda-Takahashi wave force prediction method uses the mean of the heights of the highest one-third waves in a wave group as the significant wave and is designated ($H_{1/3}$). The selection of the appropriate wave height used for inland structure analysis depends on wind and water characteristics such as the magnitude of the wind speed (m/s), the duration of the high wind-speed event, and the water surface distance (fetch) over which the wind blows. Additional characteristics that influence wave height prediction include water depth, water/air temperature, wind sensor elevation, etc. The wind properties must be determined from the available wind data as opposed to wave buoy data, which is typically available for coastal application. The historical wind data for many inland locations can be acquired from nearby municipal airports. Where wind records are not locally available or reliability of local record is an issue, it may be necessary to extend the statistical approach employed in this report. The authors strongly suggest employing historical wind records from multiple wind recording sites, near the project site, whenever possible. Multiple historical wind records offer opportunity to extend historical analysis, fill-in time gaps, and validate data. In the example presented below in subsection 6.4.2, historical wind records were obtained from two airports relatively close to the project site.

6.4.1 Wind wave generation

Instream waves are typically generated and driven by large-scale steady state atmospheric pressure gradients. Atmospheric pressure gradients result in air movement or wind. Air movement over a waterbody generates a water surface stress (force/unit-area) resulting in atmospheric to waterbody energy transfer. This energy transfer process produces waves of a magnitude proportional to the wind speed and the distance and time over which wind energy transfers occurs. This region is termed the *fetch* length. In general, the definition for fetch length is an open water region where the wind speed and direction are generally constant.

Numerous statistical and analytical methods have been developed for the purpose of predicting wind generated wave characteristics. The prediction methods adopted in this report are based on two key factors: historical USACE acceptance and ease of application. It may be said that prediction refinement can be achieved using modern computationally intensive modeling techniques; however, not all USACE district offices are likely to

be sufficiently equipped or have personal trained to implement and support these advanced analytical techniques.

As stated above, wind wave generation is the product of wind speed and direction, fetch lengths, bathymetry, and the physical properties of air and water. The USACE has adopted analytical methods in the past to address each of these parameters in the estimation of wave height and period estimation. The following sections of this report are intended to elaborate on each of these parameter estimation methods.

6.4.2 Extreme-value estimation of wind speed

The first objective in the prediction of waves generated by site-specific features of wind and fetch is to determine the design wind speed. The design wind speed can be defined as a statistical reoccurrence estimate for a designated time interval. For example, the 100-year windstorm reoccurrence interval is considered by the authors of this report as a plausible design return period (RP) for event-based hydraulic structural analysis. Conversely, the designer may choose to design for a 50-year event return period for economic reasons or choose a 500-year event return period for structural analysis cases of high national security. The methods employed below are not RP specific but rather allow the designer to develop the full RP statistical relationship from which the design RP is selected.

Obtaining reliable wind speed and direction records near the site of interest is the first step in this analysis. These wind records can typically be obtained from nearby municipal airports. Obviously, larger record lengths and faster sampling rates lead to an improved estimation. In the case of this analysis, two airports were identified within a few miles of the site. Both historical wind records were combined for the following purposes:

- Extending the total record length
- Improving the data sampling rate were possible
- Substitution of record where necessary.

In Figure 6-1, a hypothetical flood protection structure (T-Wall) is shown in red, and the primary wind direction (incident to the structure) is shown in yellow. The wind direction of primary interest is from the northeast at approximately 34° from north. In Figure 6-2, the summary record, for the

wind direction of interest (34° +/- 20°), is shown for combined records of two airport located near the Melvin Price Lock and Dam.

Figure 6-1. Aerial image of Melvin Price Lock and Dam with superimposed hypothetical flood structure located along the southwest riverbank (red). The wind direction of primary concern in wave loading estimation is shown in yellow.

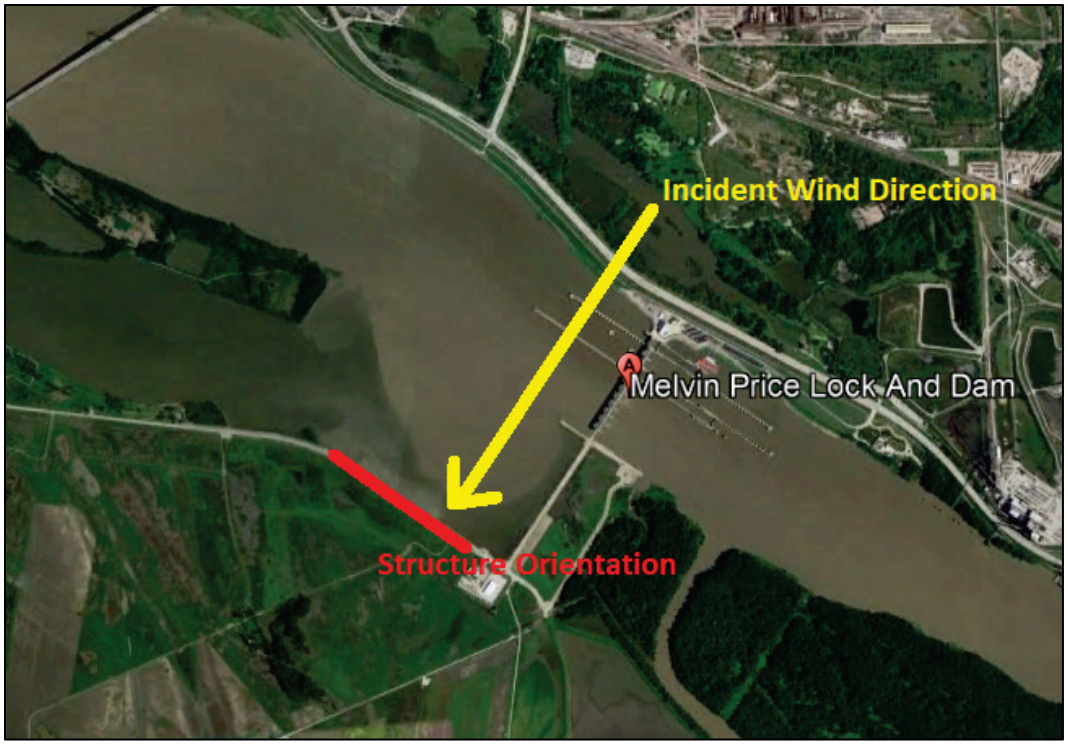

Figure 6-2. Historical wind-speed record for the combined St. Louis Airport and St. Charles Airport (1998–2019). Wind direction is presented for directions +/- 20° from normal to the design structure.

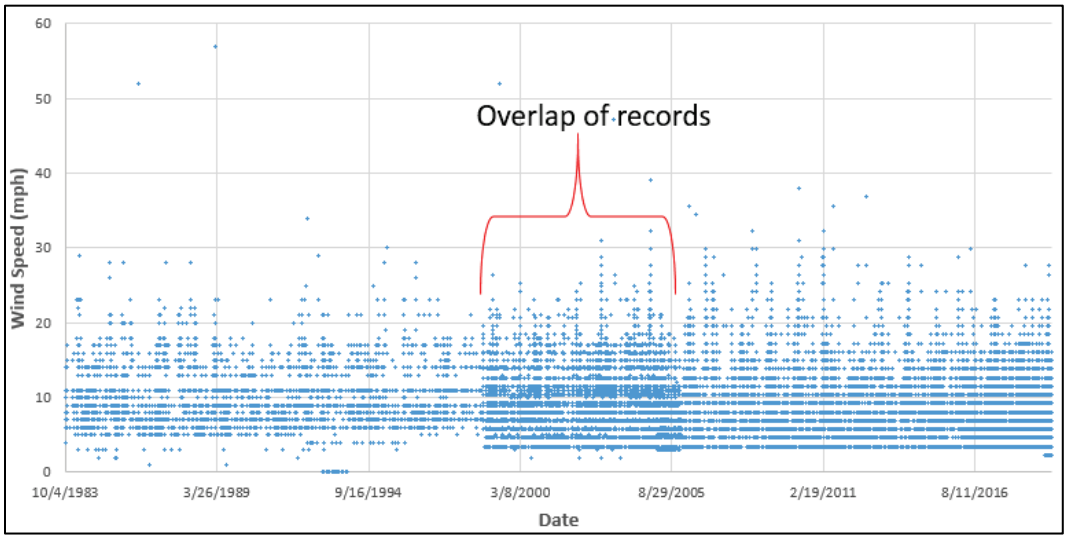

The statistical analysis method adopted for wind speeds follows the procedure used by the USACE St. Paul District in the *Oxbow-Hickson-Bakke (OHB) Levee Wind-Wave Analysis* (USACE MVP 2014). This study was performed to determine levee heights required for flood protection in the OHB community. In this study, the maximum annual wind-speed data were determined for the period of record, and the Type 1 Gumbel Distribution was used for a Generalized Extreme Value (GEV) analysis. This type of analysis is typically used to evaluate extreme, low-probability meteorological and hydrological events. The probability of non-exceedance and wind speed is plotted, and a linear regression was used to estimate values for extreme return periods. For the case of Melvin Price Lock and Dam (Figure 6-1), the maximum annual wind speeds were extracted from the 36 years of raw data (Figure 6-2) and presented in Figure 6-3. From this figure, one can observe annual maximum wind speeds ranging from 17 mph to over 55 mph.

Figure 6-3. Maximum annual wind speeds for the combined St. Louis Airport and St. Charles Airport Wind Records (1983–2019). Wind speeds included in this analysis are incident to the structure (+/- 20°).

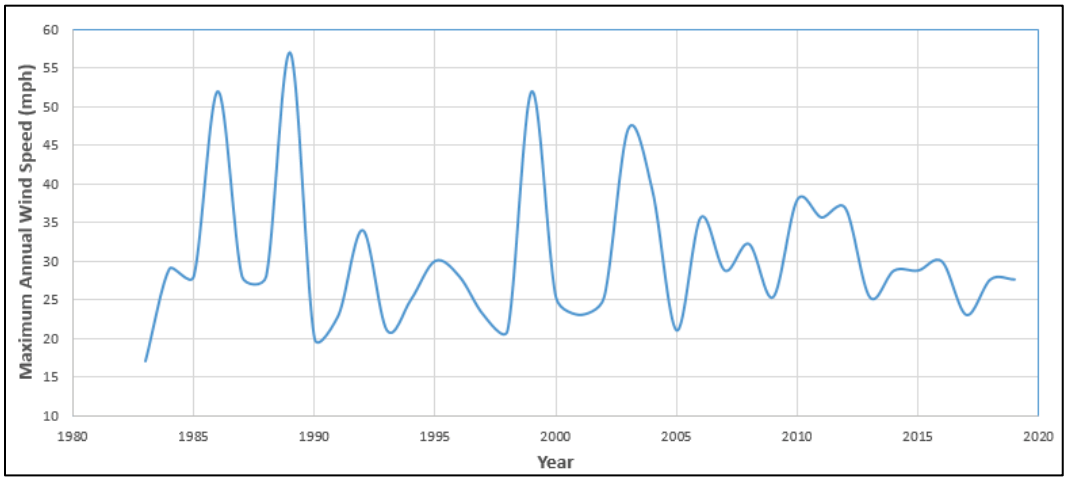

As stated above, the Type 1 Gumbel Distribution (GEV) gives an approximate return interval for extreme events. By applying the GEV method to the maximum annual wind-speed data of Figure 6-3, the resulting GEV estimation is derived and presented in Figure 6-4 along with the well-known Gringorten (1963) plotting position return period estimate. Based on this figure, an approximate 60 mph annual windstorm event can be identified as the 100-year RP wind speed.

Figure 6-4. GEV and Gringorten estimation for maximum annual wind speed derived from 36-year record of incident wind direction to hypothetical structure.

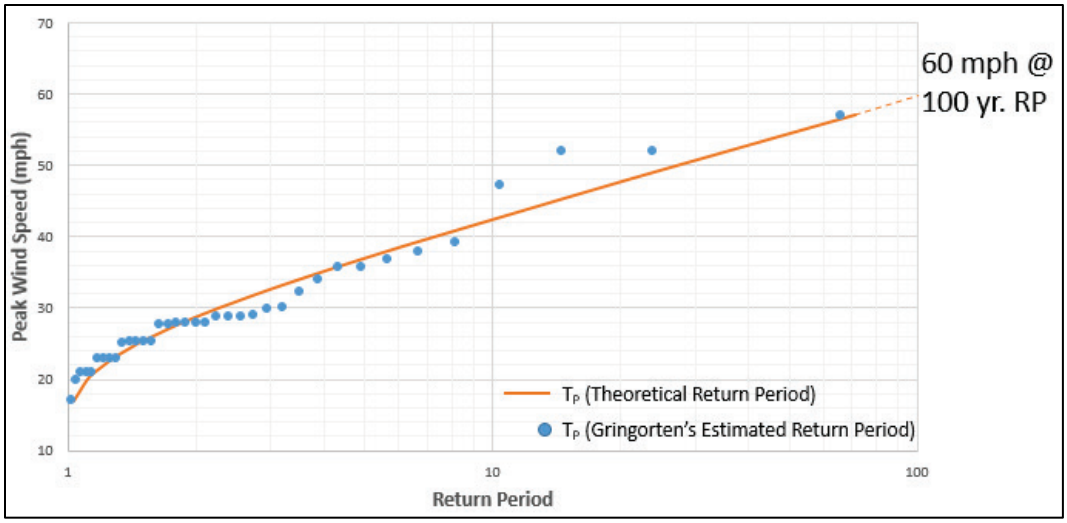

From Figure 6-4, GEV estimates of maximum annual wind speeds can be extracted for the design period of interest. For example, the 10- and 100-year RP storm events would statistically produce an approximate 42 and 60 mph wind speed in the direction incident to the hypothetical flood protection structure, respectively. If the 60 mph value were used (100-year RP) in the hypothetical structure's design calculations, it would likely be a significant overestimation of the appropriate value. The reason for this overestimation is related to a minimum wind-speed duration required to build a sustainable wave height and period. Therefore, the maximum annual wind speed used to produce the GEV of Figure 6-4 is not the statistical metric used in the final evaluation of design wind speeds, but rather it is a useful reference in the following analysis.

6.4.3 Minimum duration of wind speeds to produce wave heights

Wind-speed data, such as those shown in Figure 6-2, are typically on the order of 1 min or greater averages. These short-term wind-speed averages are insufficient to estimate wind-induced wave generation (height and period). A minimum time period (duration) of consistent wind speed is required to produce a significant and sustainable wave height and period. Goda (2010) numerically derived and experimentally validated the relation shown in Equation 6.1, which estimates this minimum duration of wind speed (T_{min}) required to generate a sustainable wave height for a fixed fetch length and wind speed.

$$T_{min} = 1.0 F_L^{\,0.73} U_{10}^{-0.46} \quad (6.1)$$

where

F_L = the fetch length in kilometers (discussed in subsection 6.4.4)
U_{10} = wind speed at the elevation of 10 m above the sea surface
T_{min} = minimum duration of wind speed (hours) required for sustainable wave height generation.

Based on Equation 6.1, the fetch length (F_L) and design wind-speed (U_{10}) values are required to calculate the minimum duration of wind speed (T_{min}). In contradiction to this requirement, a T_{min} for windstorm duration is needed to derive a representative U_{10} value from the historical wind record. Consequently, an iterative approach is applied in the evaluation of the historical wind record in the determination of U_{10} and T_{min}.

6.4.4 Wind fetch estimation

Several analytical methods are available for calculating wind-driven wave heights and periods based on fetch length(s) and wind speeds. The simplest approach requires only a single value of fetch length, the fetch length incident to the structure, while a more complicated approach requires measuring multiple fetch lengths and the associated fetch length angles to the structure (Smith 1991). In this technical report, both methods are employed in the determination of the largest design wave height and wave period for structural loading calculations. In Figure 6-5, a hypothetical T-Wall (red line) is shown adjacent to the Melvin Price Lock and Dam complex along with an array of potential fetch lengths. The yellow star shown in Figure 6-5 represents the wave loading analysis location. Notice that all fetch lines converge at this location and that the incident fetch length and fetch angle is denoted as 4,924 ft at 34° from north, respectively. The angle between consecutive fetch lengths is 6° as suggested by Smith (1991). In Table 6-1, measurements of fetch lengths and angles are listed for the case of Figure 6-5. Notice that the yellow highlight row of Table 6-1 indicates the incident fetch length.

Figure 6-5. Fetch length measurements for hypothetical T-Wall located at Melvin Price Lock and Dam complex.

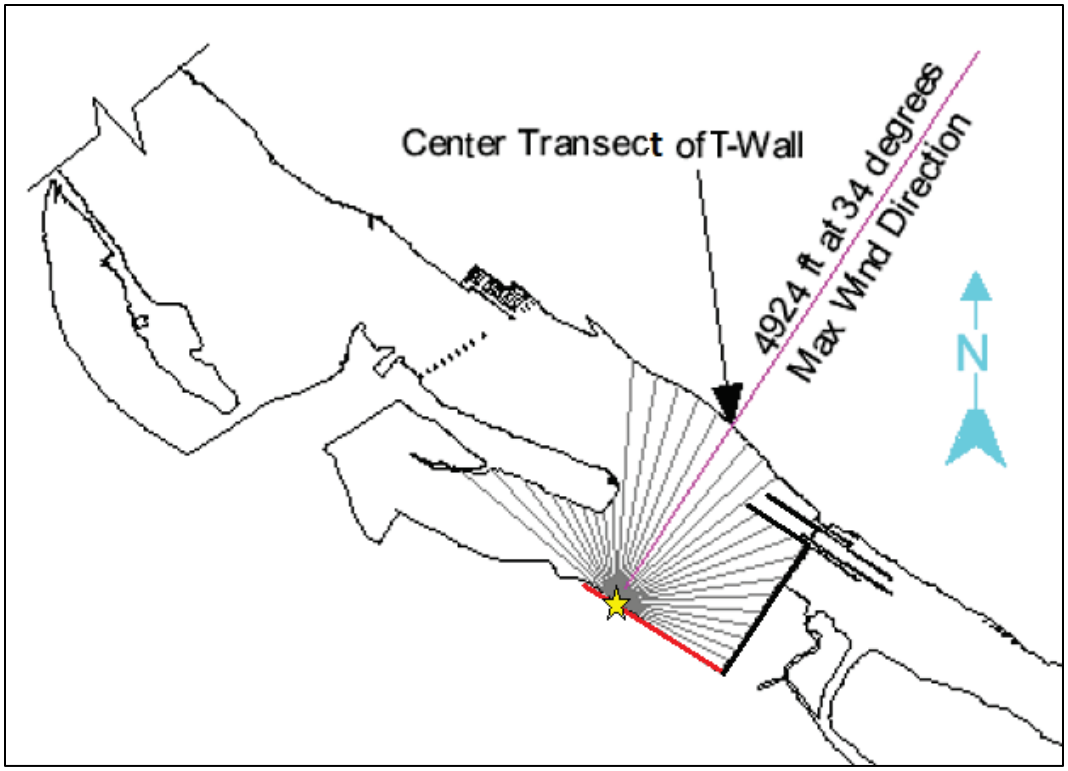

Table 6-1. Fetch angles and lengths measured for hypothetical T-Wall of Figure 6-5. Incident angle shown in yellow highlight.

Reference Number	Angle (degrees)	Length (feet)	Length (miles)	Length (km)
1	310	4720	0.89	1.44
2	316	4280	0.81	1.30
3	322	3624	0.69	1.10
4	328	2964	0.56	0.90
5	334	2618	0.50	0.80
6	340	2366	0.45	0.72
7	346	2197	0.42	0.67
8	352	2116	0.40	0.64
9	358	2421	0.46	0.74
10	4	6639	1.26	2.02
11	10	6364	1.21	1.94
12	16	6248	1.18	1.90
13	22	6120	1.16	1.87
14	28	4996	0.95	1.52
15	34	4924	0.93	1.50
16	40	4834	0.92	1.47

Reference Number	Angle (degrees)	Length (feet)	Length (miles)	Length (km)
17	46	4806	0.91	1.46
18	52	4768	0.90	1.45
19	58	3907	0.74	1.19
20	64	4121	0.78	1.26
21	70	4412	0.84	1.34
22	76	4386	0.83	1.34
23	82	3948	0.75	1.20
24	88	3662	0.69	1.12
25	94	3412	0.65	1.04
26	100	3236	0.61	0.99
27	106	3107	0.59	0.95
28	112	3022	0.57	0.92
29	118	2974	0.56	0.91

6.4.5 Re-evaluating the historical wind record

In subsection 6.4.4, the incident fetch length was measured as 0.93 mile (Table 6-1, row 15). In Figure 6-6, the incident fetch length is used to plot the T_{min} relation of Equation 6.1. Using Figure 6-6 and the complete wind record (Figure 6-2), it is possible to determine which extreme annual windstorm events satisfy the T_{min} requirement for full wave height and period generation.

Figure 6-6. The T_{min} relation for incident fetch length of 0.93 mile derived from Equation 6.1.

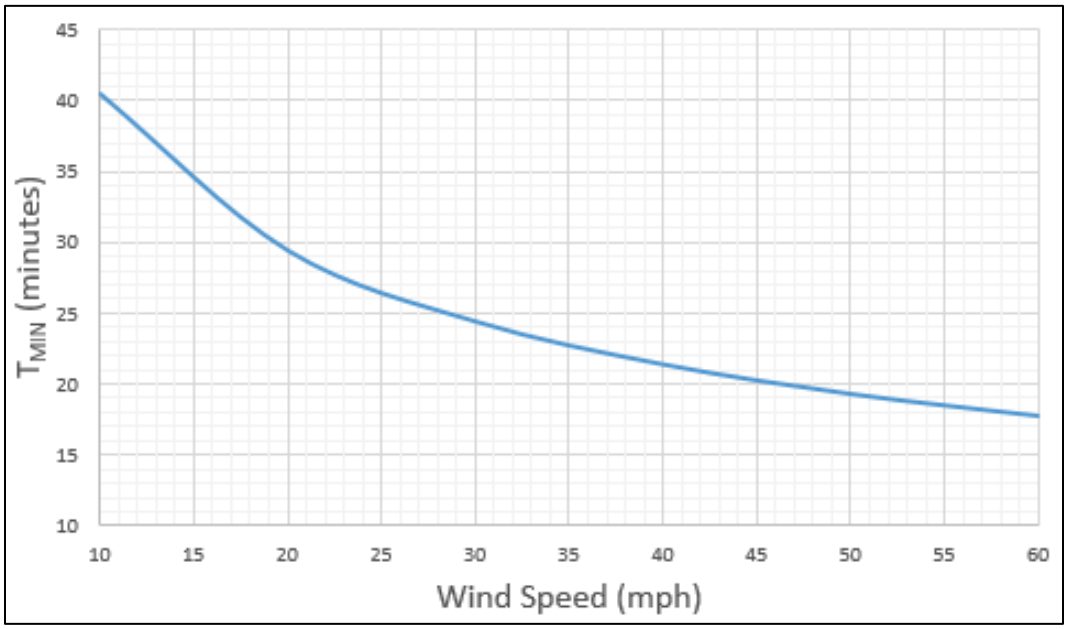

Consider the windstorm event shown in Figure 6-7 where the averaged peak wind speed is measured at approximately 38 mph and the storm duration measured at approximately 18 min. Using this example windstorm and Figure 6-6, a T_{min} requirement of approximately 22 min can be extracted as demonstrated in Figure 6-8. From this example storm, it can be concluded that the T_{min} requirement is not satisfied (18 min < T_{min} (22 min)). This Figure 6-7 storm with its mean wind speed of approximately 38 mph for a duration of 18 min is not of sufficient duration to produce a significant and sustainable wave height and period. Consequently, an iterative search of the historical record is conducted to determine the largest T_{min} value that can satisfy the annual windstorm patterns for the fetch of interest, which in the example case is approximately 34° from north and 0.93 mile in length.

Figure 6-7. Example fully developed windstorm at mean speed of 38 mph for a duration of approximately 18 min.

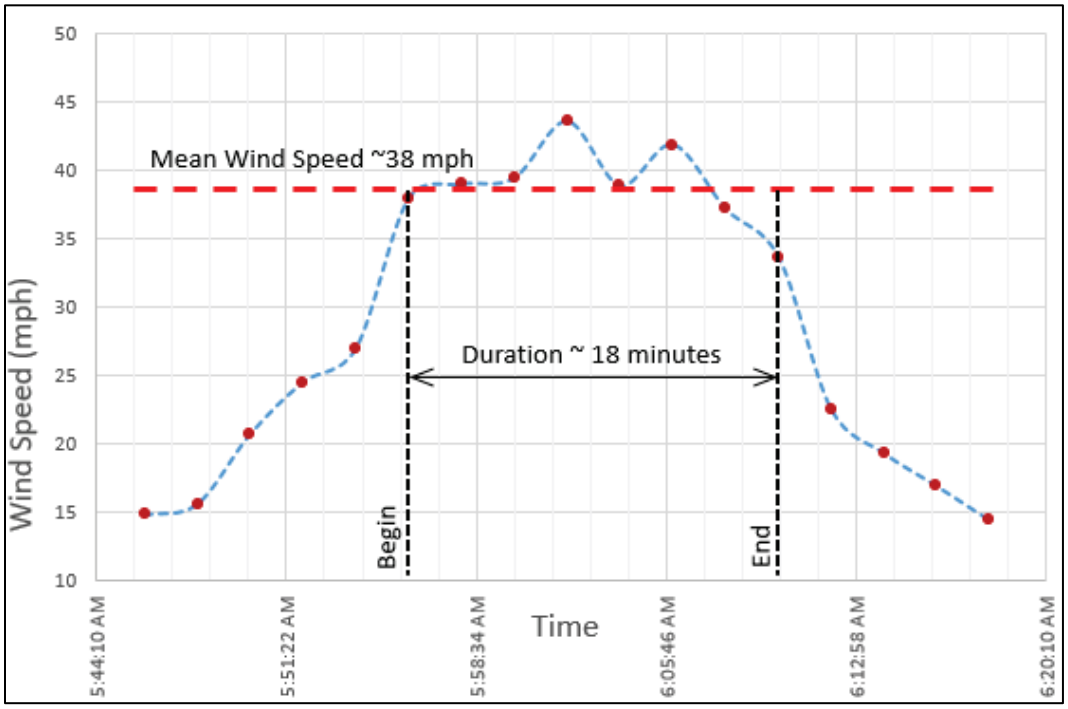

Figure 6-8. Shows that the T_{MIN} duration required for a U_{10} wind speed of 38 mph and fetch length of 0.93 mile is approximately 22 min.

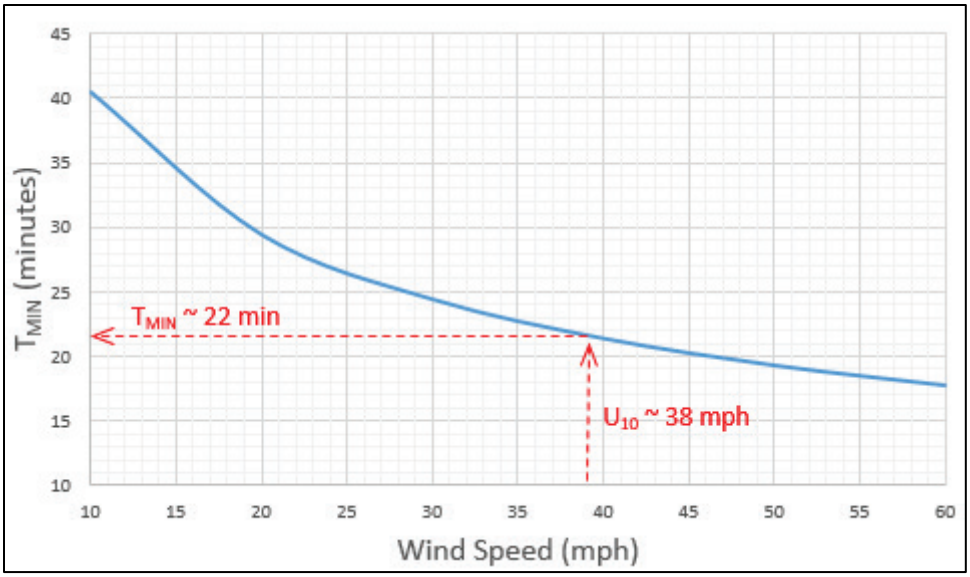

Based on a thorough review of the 36-year historical wind record for the hypothetical T-Wall located adjacent to Melvin Price Lock and Dam complex, it was determined that the maximum sustainable wind speeds of annual peak wind storm events which satisfy the T_{min} requirement ranged between 20 to 35 mph. As shown in Figure 6-9, the T_{min} range associated with the wind-speed range of 20 to 35 mph is 22 to 30 min.

Figure 6-9. Demonstration of extracting the T_{min} range from the wind-speed range using the T_{min} curve derived for the site of Interest.

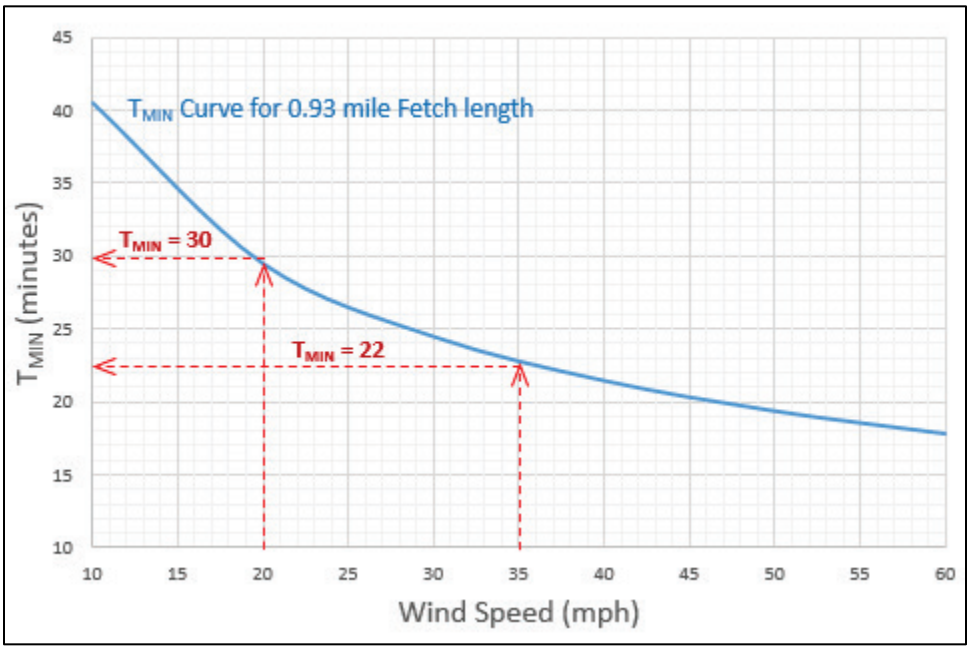

For this example analysis and for the purpose of applying conservative principles, the choice was made to set the T_{min} to the upper 30 min value shown above in Figure 6-9. In Figure 6-10, the summary annual windstorm data is presented for the case of T_{min} = 30 min. In Figure 6-11, the maximum annual wind speeds of Figure 6-3 are compared to the T_{min} filtered annual wind speeds. This figure demonstrates the importance of applying a T_{min} filter to the original peak wind-speed data. Thus, the 30 min minimum time period (duration) of consistent wind speed to produce a significant and sustainable wave height and period imposes a noticeable filter on the storms of record, resulting in few storms and lower maximum wind velocities, as shown in this figure. With this refined annual wind-speed data set, the GEV statistical technique can be applied with confidence.

Figure 6-10. Combined St. Louis Airport and St. Charles Airport wind records (1983–2019) for the condition of T_{min} = 30 min.

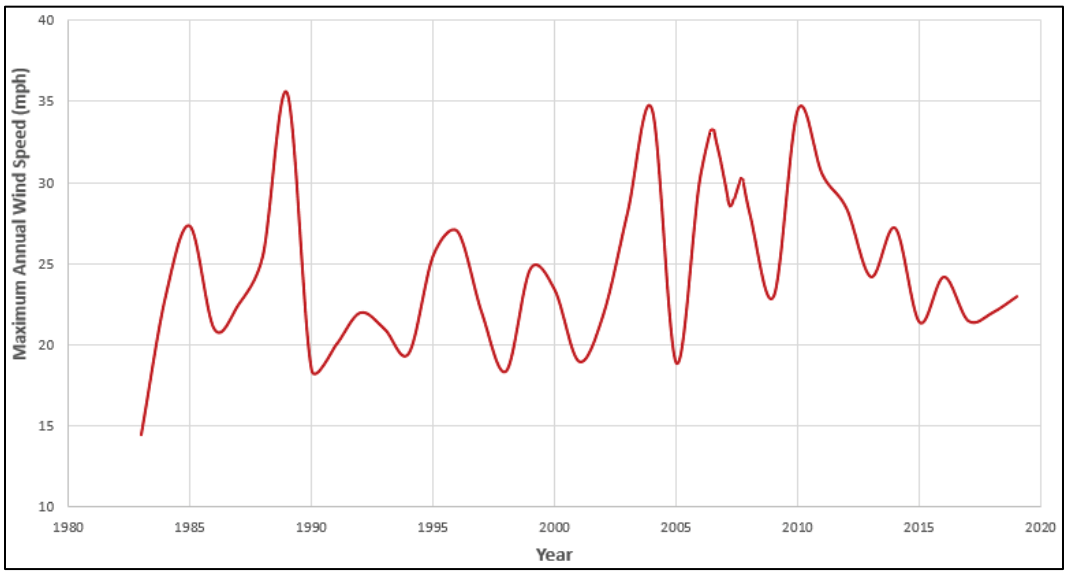

Figure 6-11. Comparison of annual peak wind speed versus T_{min} filtered annual wind speed.

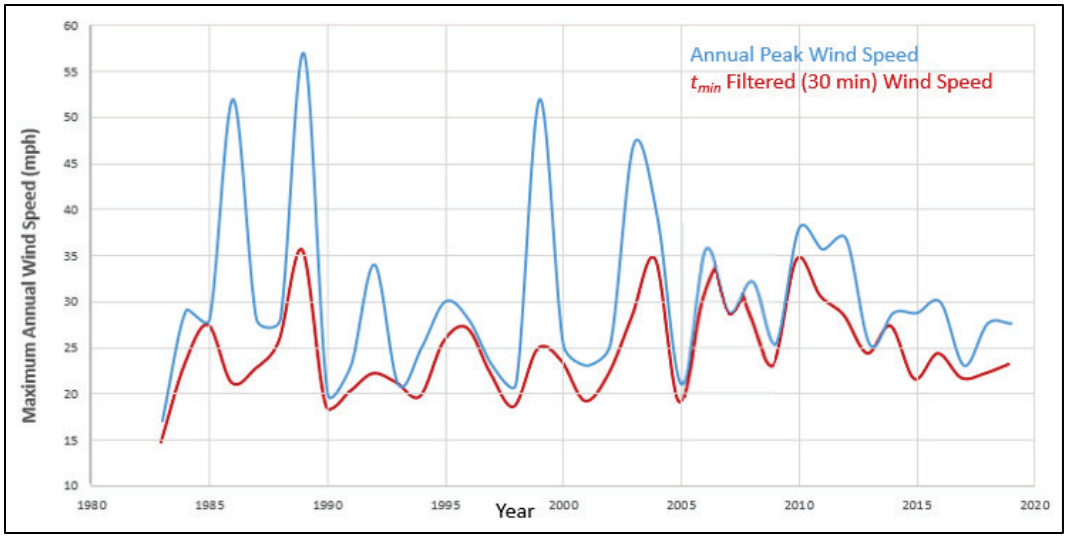

6.5 Returning to the Generalized Extreme Value (GEV) analysis

By applying the GEV method to the T_{min} filtered annual wind-speed data shown in Figure 6-9, the T_{min}-satisfied GEV relation is shown along with the Gringorten (1963) plotting position return period estimate in Figure 6-12. Based on this figure, an approximate 41 mph annual windstorm event can be identified as the 100-year return wind speed which satisfies the 30 min T_{min} requirement.

Figure 6-12. T_{min} satisfied GEV and Gringorten estimation derived from 36-year record of incident wind direction to hypothetical structure for hypothetical T-Wall located adjacent to Melvin Price Lock and Dam complex.

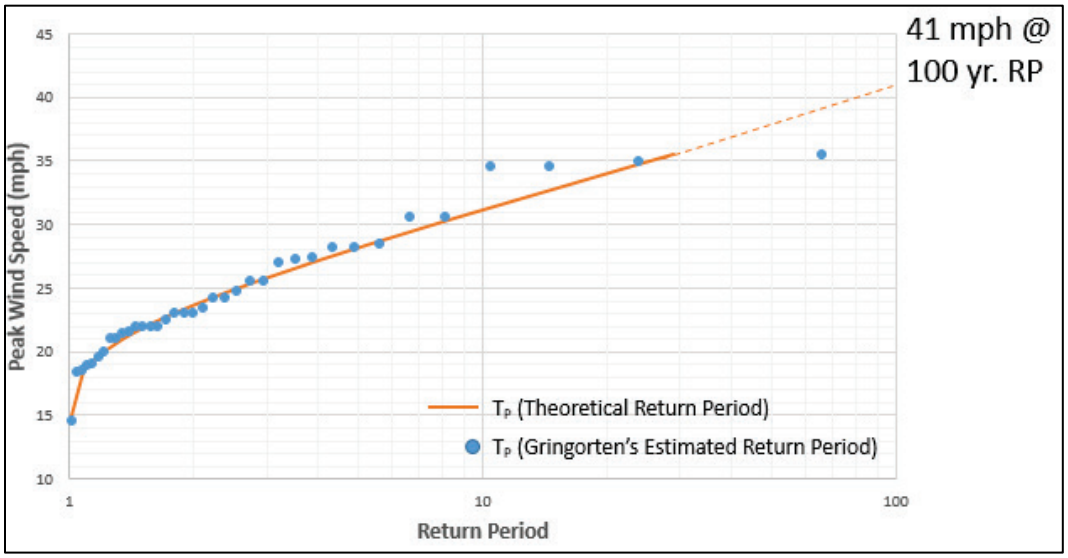

To further investigate the statistics of the return period relationship of Figure 6-12, a method was derived in Hite et al. for spillway gates to estimate the T_P standard error using both the GEV and Gringorten T_P estimates. The standard error is defined as

$$std\ error = \sqrt{\frac{\sum[U_i - U_{new}]^2}{n-1}} \tag{6.2}$$

where

U_i = the wind speed (U) value of the Gringorten T_p estimated point
U_{new} = the new value determined from a log-linear interpolation (further explanation below)
n = the number of samples.

In Standard Error Equation 6.2, the wind-speed U_{new} value of the GEV-derived orange curve is determined by a log-linear interpolation of the line segment between the T_p theoretical points (orange line in Figure 6-12). The first step is to record the value of the T_p estimated point (blue point). Next, record the closest value of T_p theoretical smaller than the selected T_p estimated point and the closest T_p theoretical value larger than the selected T_p estimated point. Now there are the values of T_p theoretical on each side of the T_p estimated point. One can think in terms of the T_p theoretical points being backward and forward of the T_p estimated point. Now the wind-speed value for each of the T_p theoretical points is recorded. These two points (backward and forward T_p theoretical values and their associated wind-speed values) are then used in the log-linear interpolation. To simplify the notation for the following discussion, let T_p theoretical backwards = $T_{p\,back}$ and T_p theoretical forward = $T_{p\,for}$. The wind-speed values will be designated U_{back} and U_{for}.

The linear interpolation will take the form

$$U_{new} = mx + b \tag{6.3}$$

The slope of the orange line segment between the two Tp theoretical points ($T_{p\,back}$ and $T_{p\,for}$) is m,

$$m = \frac{U_{for} - U_{back}}{\log 10(T_{p\,for}) - \log 10(T_{p\,back})} \tag{6.4}$$

$$x = \log 10\left(T_p\ estimated\right) - \log 10\left(T_{p\ back}\right) \quad (6.5)$$

where b = $U_{back.}$

U_{new} can now be determined, and Equation 6.2 can be used to compute the standard error.

The standard error is also referred to as the standard deviation about the *fit curve*. The standard deviation (σ) provides a way of describing how well the sample points align with a curve fitted to the data. In the case of the Gumbel Type 1 Distribution curve (T_p theoretical), this standard deviation provides an estimate of the changes in the wind speed from the fitted curve or a way to bound the values of wind speed.

Figure 6-13 shows the fitted curve bounded by plus and minus 1 and 2 standard deviations (σ) for the St. Louis Regional Airport wind data (n=36). The standard deviation was determined to be approximately 1 mph. The use of the 100-year return period plus 2 standard deviations gives a wind speed of 43.0 mph. Based on the storm-event data, the extreme event analysis, and the Gumbel Type 1 distribution analysis for the 100-year return period increased by 2 standard deviations and the discussions below, a wind speed between 41.0 and 43.0 mph seems very reasonable to the authors of this report for developing the design wave height and period. Results from the wind-speed analyses shown graphically in Figures 6-13 are summarized in Table 6-2.

Figure 6-13. The GEV estimate bounded by the standard error estimates derived from 36-year record of incident wind direction to hypothetical structure for hypothetical T-Wall located adjacent to Melvin Price Lock and Dam complex.

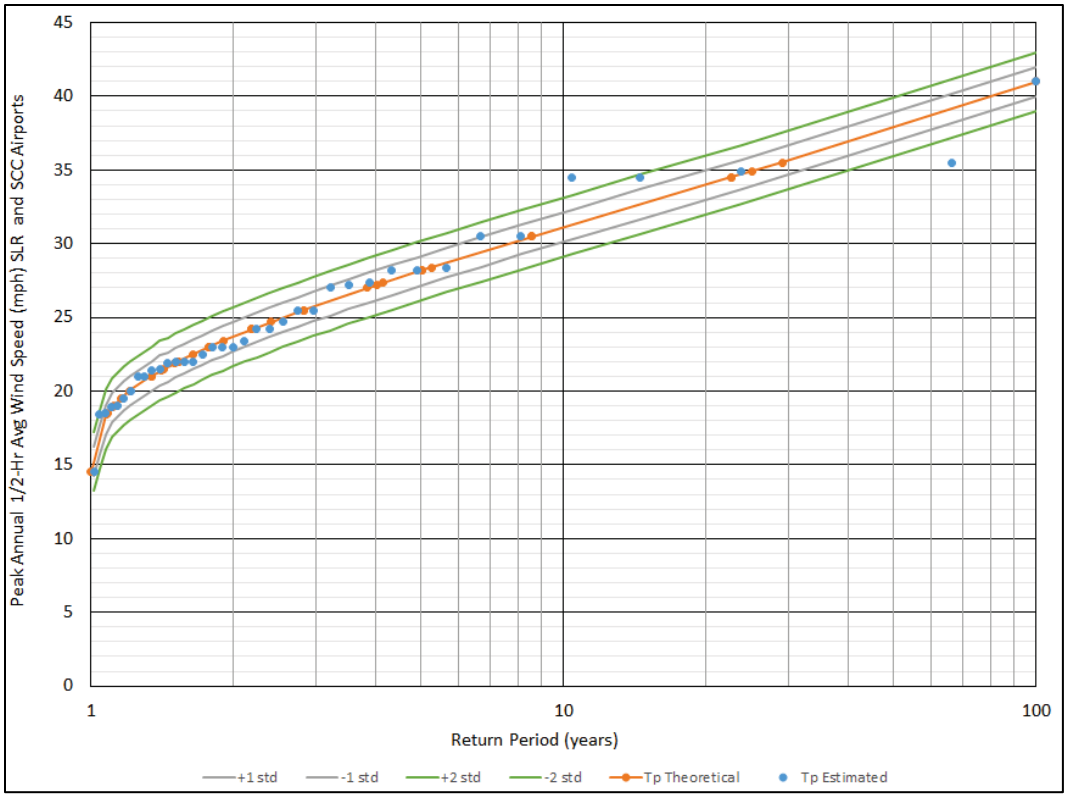

Table 6-2. Results from wind-speed analyses for Melvin Price Lock and Dam.

Statistic	100-Year Wind Speed (mph)
+2σ	43
+1σ	42
Fit Value	41
-1σ	40
-2σ	39

In summary, the following steps were used to derive the T_{min}-filtered wind speed for the 100-year return period.

1. Wind-speed data are combined from two nearby airports for the period of 1983 to 2019.
2. The T_{min} value of the wind speed is determined based on a comprehensive analysis of the historical data (as detailed above).

3. The GEV and associated standard error estimates of the annual maximum wind events are derived for a 100-year return period. These data are then used to estimate the T_{min} filtered wind speed for a 100-year return period.

The T_{min} filtered 100-year return period of wind speed will be used in section 6.6 to estimate the design wave height and wave period.

6.6 Design wave height and period estimation

To calculate wave loading on a hydraulic structure, the design wave height and period must first be known. In this section, two methods are used to predict the design wave height and period: Goda (2010) and Smith (1991). The largest wave height prediction from these two methods will then be used to calculate the wind-induced wave loading on the hypothetical T-Wall. Both methods require a design wind speed (U_{10}) and design fetch length(s). The design wind speed was derived in subsection 6.5.5 for the 100-year return interval, and the design fetch lengths were derived in subsection 6.4.4 (Table 6-1). Goda's wave height and period prediction relationships are given in Equations 6.6 and 6.7. These metric unit-based equations were numerically derived and experimentally verified as discussed in Goda (2010). Applying Equations 6.6 and 6.7 to the U_{10} values listed in Table 6-2 and the incident fetch length of Table 6-1 results in Table 6-3.

$$\frac{gH_{1/3}}{U_{10}^2} = 0.3\left\{1 - \left[1 + 0.004\left(\frac{gF}{U_{10}^2}\right)^{1/2}\right]^{-2}\right\} \tag{6.6}$$

where

g = acceleration due to gravity
$H_{1/3}$ = significant wave height (design wave height)
$T_{1/3}$ = significant wave period (design wave period)
U_{10} = wind speed at the elevation of 10 m above the sea surface
F = fetch length incident to the structure.

Table 6-3. Wave height and wave period for combined airport data (SLR and SCC)* derived using the Goda procedure.

Statistic	100-Year Wind Speed (mph)	Minimum Duration (hr)	Significant Wave Height $H_{1/3}$ (m)	Significant Wave Period $T_{1/3}$ (sec)	Significant Wave Length $L_{1/3}$ (m)	Wave Height $H_{1/3}$ (ft)
+2σ	43.0	0.5	0.57	2.14	7.15	1.87
+1σ	42.0	0.5	0.56	2.13	7.08	1.84
Fit Value	41.0	0.5	0.55	2.11	6.95	1.80
-1σ	40.0	0.5	0.54	2.10	6.89	1.77
-2σ	39.0	0.5	0.53	2.08	6.75	1.74

*SLR = St. Louis Regional Airport
SCC = St. Charles County Airport

Smith (1991) developed guidance to determine significant wave height and peak period based on wind speed and fetch. Smith developed a software tool (NARFET) to perform this calculation that employs an array of fetch lengths and angles as shown in Figure 6-5 and detailed in Table 6-1. This program input requires the radial lengths of the fetch and the angle increments for resolution of the wind direction. The radial lengths (a total of 29) determined for an angle increment of 6°. Unfortunately, the NARFET software tool was found to be incapable of running on modern Windows operating system. Consequently, the program was re-written by Dr. James Tallent in Python thus enabling NARFET to run on both Windows and Linux platform. Based on the input parameters of Tables 6-1 and 6-2, the NARFET program results are listed in Table 6-4.

Table 6-4. Wave height and wave period for combined airport data (SLR and SCC) derived using the NARFET procedure.

Statistic	100-Year Wind Speed (mph)	Minimum Duration (hr)	Significant Wave Height $H_{1/3}$ (m)	Significant Wave Period $T_{1/3}$ (sec)	Significant Wave Length $L_{1/3}$ (m)	Wave Height $H_{1/3}$ (ft)
+2σ	43.0	0.5	0.69	2.75	11.81	2.26
+1σ	42.0	0.5	0.68	2.73	11.64	2.23
Fit Value	41.0	0.5	0.66	2.70	11.38	2.17
-1σ	40.0	0.5	0.65	2.68	11.21	2.13
-2σ	39.0	0.5	0.63	2.65	10.96	2.07

Both the Goda and Smith procedures were performed. It was observed that an approximate 20% larger wave height and period were obtained by using Smith's NARFET methodology. These values of wave height and period will therefore be used to calculate the wind-induced wave loading using Goda's methodology.

6.7 Wave load estimation

The wave loading prediction method applied here is attributed to the original work of Goda (1974) and Takahashi (1993). This method is well established being based on a broad set of laboratory experiments, theoretical considerations, and field measurements and has been adopted by many national standards including Japan, Great Britain, and Italy (Cuomo 2007). The current version of the Goda-Takahashi wave pressure relationship is given in Goda (2010). The mathematical relationships of this formulation are discussed in detail in Chapter 5.

Goda's original objective was to predict the pressure components, on a vertical (e.g., caisson) wall, as a function of the wave, the bathymetry, and the SWL for design storm conditions. Later, it was found that breaking waves could impart an implosive pressure component to a vertical wall. Bullock et al. (2004) observed that Goda's original method did not attempt to predict the short-duration peak wave pressures caused by breaking waves but assumes a trapezoidal pressure distribution that is intended to produce a static load equivalent to that of a breaking or non-breaking wave acting on the dynamic system formed by a caisson founded on a rubble mound. The pseudo-static Goda formulation was extended by Takahashi et al. (1993) to include the implosive pressure coefficient of a breaking wave.

Goda formula assumes a trapezoidal pressure distribution on vertical walls with maximum wave pressure (P_1) exerted at SWL, as depicted in Figure 6-14. The wave pressure calculation parameters associated with the structural geometry of the vertical wall (T-Wall) and the associated hydrology are shown in Figure 6-15.

Figure 6-14. Goda's formula pressure distribution on vertical T-Wall.

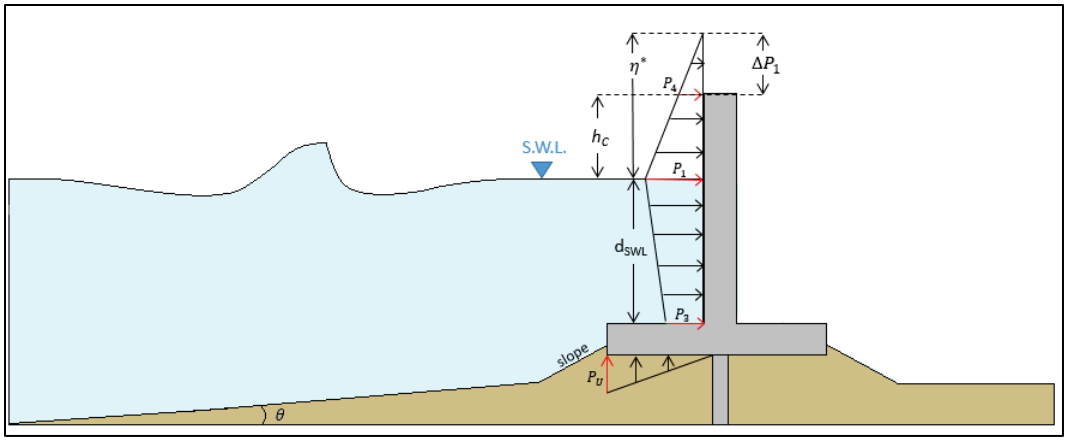

Figure 6-15. Structural and hydrological parameters used in Goda (2010) wave-force calculation.

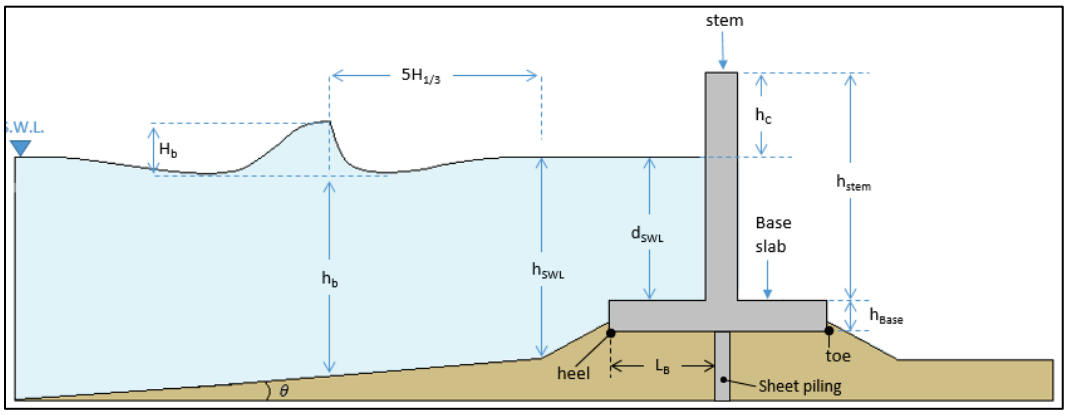

For the case of the hypothetical T-Wall located adjacent to the Melvin Price Lock and Dam complex, the primary assumptions include the following:

- The river elevation is at flood level.
- η* = h_C, meaning that wave overtopping does not occur (Figure 6-14).
- The geometry of the T-Wall is typical in design.
- The nearshore bathymetric slope is mild.

In Table 6-5, the parameters used to calculate wave loading associated with the T-Wall structural design, nearshore bathymetry, and hydrostatic conditions are listed. These parameters along with the statistics for design wave height and period (Table 6-4) are combined to produce the loading calculation results of Table 6-6. For example, for the +2σ statistic 100-year wind speed of 43 mph, the total pseudo-static hydrodynamic lateral force per 1 ft of T-Wall span is calculated as 1,514 lb. Assuming the hypothetical

T-Wall is 1 mile in length, the total wave impact force occurring every 2.75 sec is approximately 4,000 tons.

Table 6-5. Structural, bathymetric, and hydrological parameters used in example wave force calculation (imperial and metric units included).

Parameter	Value	Unit	Value	Unit	Description
h_{stem}	15	ft	4.57	m	T-Wall stem height (above base)
h_{Base}	2.5	ft	0.76	m	T-Wall base thickness
h_C	6	ft	1.83	m	T-Wall height above SWL
L_B	8	ft	2.4	m	Distance from heel of base slab to sheet pile distance
d (originally d_{SWL})	10	ft	3.03	m	Still water depth at base of T-Wall
h (originally h_{SWL})	12.5	ft	3.8	m	Still water depth at toe of berm
$\tan\Theta$	1/20	N/A	1/20	N/A	Seaward slope to T-Wall (seaward of T-Wall berm)
β_D	0	deg	0	deg	Design incident wave angle
ρ	64.3	lb/ft^3	1030	kg/m^3	Density of seawater
g	32.17	ft/sec^2	9.81	m/sec^2	Acceleration of gravity
h'	10	ft	3.05	m	For the case of T-Wall: $h' = d_{SWL}$ (see Figure 6-14)

Table 6-6. Wave force calculation results based on input parameters of Table 6-5 and statistics of Table 6-4.

Statistic	100-Year Wind Speed (mph)	Design Wave Height $H_{1/3}$ (m)	Significant Wave Period $T_{1/3}$ (sec)	Significant Wave Length $L_{1/3}$ (m)	Pseudostatic Hydrodynamic Lateral Force F_{lat} (lb/ft)
+2σ	43.0	0.69	2.75	11.81	1589
+1σ	42.0	0.68	2.73	11.64	1560
Fit Value	41.0	0.66	2.70	11.38	1508
-1σ	40.0	0.65	2.68	11.21	1473
-2σ	39.0	.63	2.65	10.96	1421

Using the relationships given in Ebeling et al. (2018) as summarized in subsection 5.4.4 of this report, the one-third/one-sixth (1/3:1/6) rule is applied to calculate the elevation of the resultant forces along the vertical face of the T-Wall (Equation 5.34). In Table 6-7, the pressure components of the Goda formula are given for all for summary statistics of the example problem along with h_{Lat} calculations from Equation 5.34.

$$h_{Lat} = \frac{(h_4 - h_1)\left(\frac{P_4}{3} + \frac{P_1}{6}\right)h_4 + (h_4 - h_1)\left(\frac{P_4}{6} + \frac{P_1}{3}\right)h_1 + (h_1 - h_3)\left(\frac{P_1}{3} + \frac{P_3}{6}\right)h_1}{F_{Lat}} \quad (5.34)$$

Table 6-7. Wave equivalent force location calculations based on Ebeling et al. (2018). Pressure (*P4*) is zero since no wave overtopping was allowed.

Statistic	Wind Speed (mph)	η*, m	P_1, N/m²	P_3, N/m²	P_4, N/m²	F_{lat}, kN/m	h_{lat}, m	P_1, lb/ft²	P_3, lb/ft²	P_4, lb/ft²	F_{lat}, lb/ft	h_{lat}, ft
+2σ	43.0	1.86	7576	3094	0	22.1	2.10	158	65	0	1590	6.9
+1σ	42.0	1.84	7461	3004	0	21.7	2.11	156	63	0	1561	6.9
Fit Value (100-year)	41.0	1.79	7239	2852	0	21	2.11	151	60	0	1508	6.9
-1σ	40.0	1.75	7092	2754	0	20.5	2.11	148	58	0	1473	6.9
-2σ	39.0	1.70	6874	2611	0	19.8	2.12	143	55	0	1422	7.0

In comparing the equivalent hydrostatic force and overturning moment resulting from an SWL of 10 ft on the T-Wall with the equivalent wave-induced force and overturning moment, note that the equivalent force imposed by wave action is approximately 50% of the hydrostatic equivalent force (Figure 6-16). Additionally, the wave-induced overturning moment is approximately equal to that of the hydrostatic overturning moment (Figure 6-16), but the resultant location for F_{lat} differ by more than a factor of 2.

Figure 6-16. Comparison of equivalent hydrostatic force to equivalent wave-induced force for 100-year statistics.

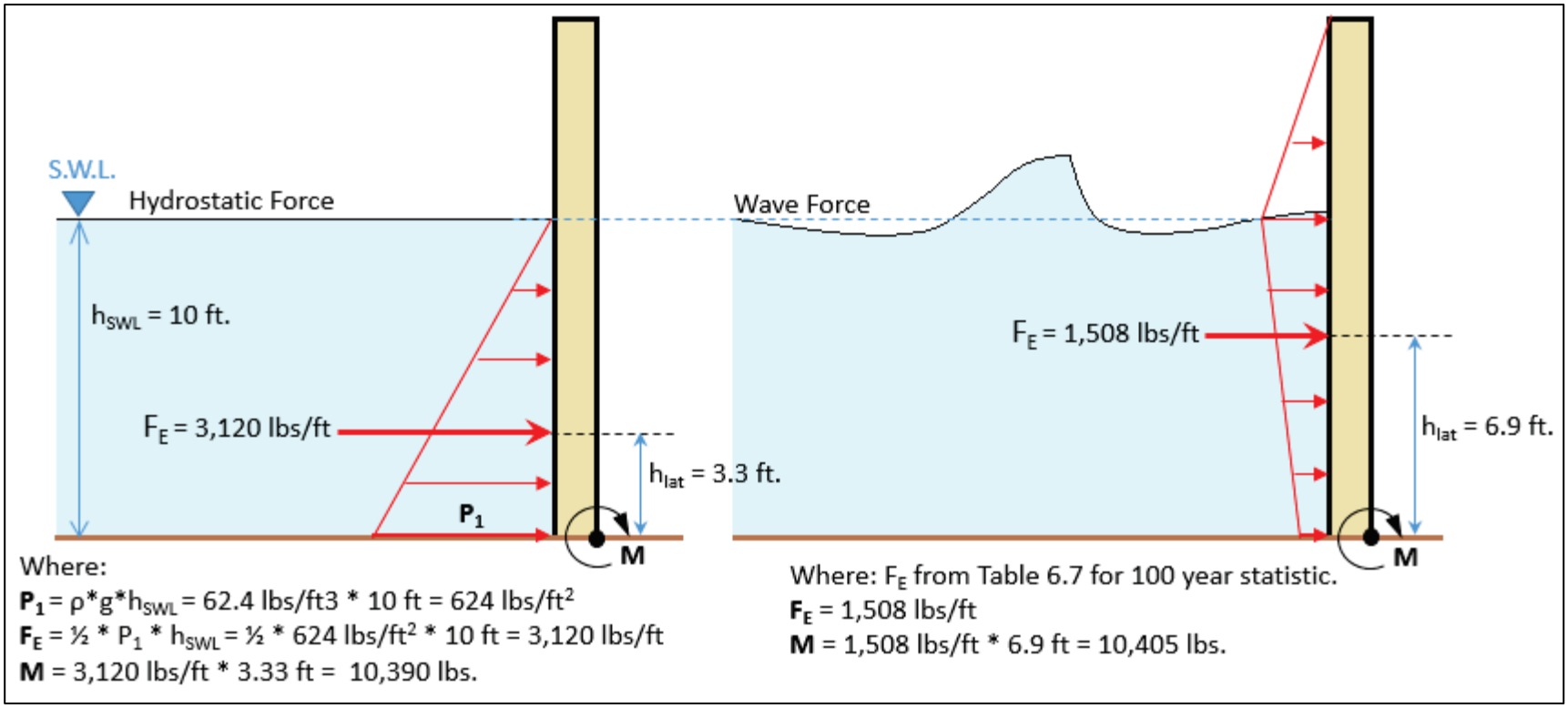

7 Reliability Analysis and Load and Resistance Factors Analysis of Flood Mitigation, Batter Pile-Founded T-Walls

7.1 Introduction

This chapter summarizes a series of Reliability analyses and an LRFD developmental effort conducted on three different batter pile group founded flood mitigation T-Walls.

7.2 Designing a pile-based T-Wall system

This section describes the engineering procedure used in the design of a batter pile-founded flood mitigation T-Wall, as practiced by USACE. Later in this chapter, the engineering procedure outlined in this first section is extended to perform a Reliability analysis and to conduct LRFD values development for this flood mitigation, batter pile-founded T-Wall project feature.

To design a pile-based T-Wall system at a specified site, certain data need to be available. These data will include site-specific foundation soil strength properties, pile sizing, and corresponding pile engineering properties, tension and compression pile lengths, and wall geometry (to include the pile cap locations and batter of connecting piles). The first of a batter pile-founded flood mitigation T-Wall to be described is for a placement on the Red River of the North site, in Grand Forks, ND.

7.2.1 Establishment of limit states

For the batter pile-founded T-Wall flood mitigation project feature, the authors have identified 10 conditions that will lead to failure of the structure to accomplish its mission. These conditions establish the engineering limit states that, if exceeded, will result in unsatisfactory performance of the pile-founded T-Wall. There are eight limit states that involve the structural components of the T-Wall (within the reinforced concrete stem wall segment and within the piles) and two geotechnical limit states (dealing with the soil structure interaction between the foundation soil and the structure's piling). These engineering limit states

are enumerated, and their descriptions are included below. This limit state enumeration is referred to throughout this chapter.

Reinforced concrete (structural)

1. Shear failure at the base of the reinforced concrete stem.
2. Flexural failure at the base of the reinforced concrete stem.

Soil-structure interaction (geotechnical)

3. Side friction and bearing capacity failure within the soil for the HP steel pile in **compression**.
4. Side friction capacity failure within the soil for the HP steel pile in **tension**.

HP steel **compression** piles (structural)

5. Shear failure at the top of the **compression** HP steel pile.
6. Compression failure at the top of the **compression** HP steel pile.
7. Bending and axial compression failure at the top of the **compression** HP steel pile.

HP steel **tension** piles (structural)

8. Shear failure at the top of the **tension** HP steel pile.
9. Tension failure at the top of the **tension** HP steel pile.
10. Bending and axial tension failure at the top of the **tension** HP steel pile.

7.2.2 T-Wall geometry - Grand Forks Red River of the North site

The wall geometry was established for the example site, East Grand Forks Red River of the North, ND, using a right-handed coordinate system. The *X*-axis is described as units of length, the *Z*-axis is described as units of height, and the *Y*-axis is described in units of width along the project T-Wall flood feature and the river channel. The units use feet in relative coordinates for the length and width, and elevation (EL) in feet, referencing National Geodetic Vertical Datum (NGVD) 29, for the *Z*-axis (in accordance with Annual Chance of Exceedance [ACE] for flood water levels). For the example problem, the heel of the wall is specified at [0.0, 0.0, 821.0]. Be aware that CPGA-R software uses an orthogonal right-

handed coordinate system in which the *Z*-axis is described in terms of positive depth, opposite sign to elevation being positive upward.

The concrete base slab section of the T-Wall was specified to have a flat base of height 2 ft and 14 ft in length. EL of the bottom and top of the base slab is 821 and 823 ft., respectively.

The T-Wall stem extends another 13.9 ft above the top of the reinforced concrete base slab. The T-Wall's reinforced concrete stem is rectangular with a length of 1 ft (referring to a CPGA-R coordinate system's *X*-axis) and is placed 8 ft from the heel. To say this another way, the thickness of the reinforced concrete stem is 1 ft, and the thickness of the base slab is 2 ft.

The steel piles of the T-Wall are placed with a tension pile centered at 2.5 ft from the heel of the T-Wall base slab, and the compression pile centered at 11.5 ft from the heel of the T-Wall base slab. Both piles have their strong axis aligned along the length of the floodwall feature (i.e., along the CPGA-R Global *Y*-axis into the T-Wall cross section). Both piles have a 4:1 (rise: run) batter with the tension pile batter proceeding in the negative Global CPGA-R *X*-coordinate direction and the compression pile batter proceeding in the positive Global CPGA-R *X*-direction.

The unit weight of concrete for the structure is given as $\gamma_{Concrete}$=150 lb/ft^3. The unit weight of water is given as γ_{Water}=62.4 lb/ft^3.

Some assumptions needed to be made for the initial deterministic design, and those assumptions would need to be reassessed and possibly changed after the deterministic design analysis is complete and has been interpreted. It was initially assumed that the distance between piles along the width of the wall (i.e., along the floodwall project feature axis and along the river channel) would be 7 ft, and therefore the section T-Wall width in the CPGA-R model would be the same width since it is the distance between center point to center point between adjacent pairs of tension and compression piles. This wall width applied to the cross section was later adjusted to 4 ft after a preliminary analysis with CPGA-R revealed that the excessive weight for the design case of a flood load at top of stem (EL 836.9 ft) would leave the 40 ft compression pile in failure for the deterministic load case. Except where noted, the Figure 7-1 example results are for the 4 ft T-Wall section width are reported. The batter pile located to the left of the stem and directly below the Figure 7-1 blue block

of floodwater is referred to as the tension pile in this chapter. The batter pile located to the right of the stem and below the dry stem delineated region is referred to as the compression pile. In the initial deterministic design with flood water to the top of stem, it was assumed that both the tension and compression pile would be of equal length. These first deterministic computations resulted in tension and compression pile lengths of 40 ft.

Figure 7-1. shows the pile-founded T-Wall geometry in the initial configuration. Top of T-Wall is at EL 836.9 ft. Figure 7-1(a) close-in view and (b) complete view of the geometry of the wall cross section with 40 ft pile lengths.

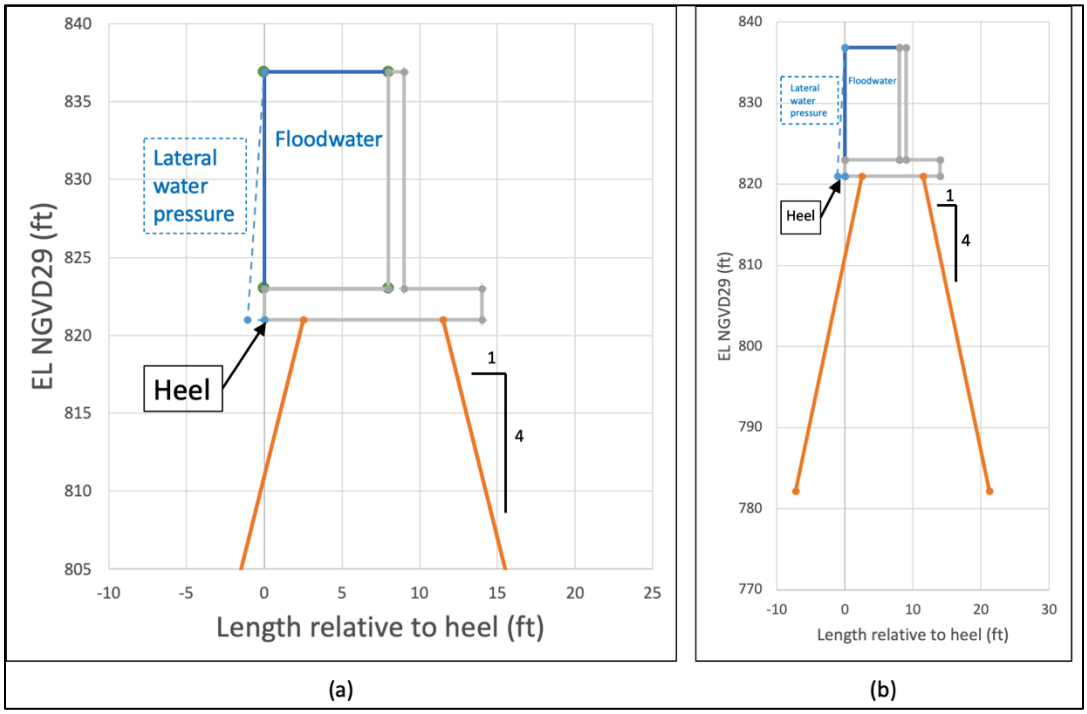

7.2.3 System variables

For a Reliability analysis in determination of LRFD factors, there is a need to identify the design characteristics with high variability that have the most significant effect on system performance. Variables are divided into two types if the loads and resistances are not correlated: those that influence LRFD loads and those that influence LRFD resistances (capacity).

The two load variables that influence the system performance of the pile-founded T-Wall are (1) the flood elevations (obtained from site-specific ACE data) and (2) wind-induced wave loading. Wind-induced wave loading and its computational variables are discussed in Chapters 5 and 6.

A wind-induced wave loading assessment for the Red River of the north site in North Dakota is discussed in subsection B.1 of Appendix B.

The capacity variables per foot run of T-Wall are

- the shear capacity at the base of the reinforced concrete stem (pound)
- the moment support at the base of the reinforced concrete stem (pound-foot)
- the effects of the soil foundations undrained shear strength (S_u in pounds per square foot) with increasing depth for the tension and compression pile
- the yield stress (pounds per square inch) of the steel in the tension and compression pile.

7.2.4 Pile selection and computation of properties

Pile selection and properties are given by the piling manufacturer, using established engineering standards. For instance, for an HP 14 × 89 pile manufactured by Nucor, the documented properties are given (Table 7-1).

Table 7-1. Nucor HP 14 × 89 pile properties.

Pile cross-section area, *pca*	26.1	(in.^{2})
Pile moment of inertia, $I_{X\text{-}X}$ (X-X strong axis)	904	(in.^{4})
Pile moment of inertia, $I_{Y\text{-}Y}$ (Y-Y weak axis)	326	(in.^{4})
Pile depth, *d*	13.8	(in.)
Pile flange width, *b*	14.7	(in.)
Pile web width, t_W	0.615	(in.)
Pile section modulus, $S_{X\text{-}X}$ (X-X strong axis)	131	(in.^{3})
Pile section modulus, $S_{Y\text{-}Y}$ (Y-Y weak axis)	44.3	(in.^{3})

Additional properties can be computed based on these values and geometry of the piles in the structure. The pile tip area is assumed to be plugged to give the maximum soil interaction with the pile. The pile shear area involves only the web area but also considers the batter of the pile, which affects the depth of the pile's web. The equations for pile perimeter (p), pile effective diameter ($d_{Effective}$), pile tip area ($a_{piletip}$), and the pile's horizontal shear area (A_{shear}) are given as, respectively,

$$p = (d \cdot 2) + (b \cdot 2) \tag{7.1}$$

$$d_{Effective} = p/\pi \tag{7.2}$$

$$a_{piletip} = d \cdot b \tag{7.3}$$

$$A_{Shear} = \frac{t_W \cdot d}{\cos\left(tan^{-1}\left(\frac{1}{batter}\right)\right)} \tag{7.4}$$

These equations, used with the HP 14 × 89 values of Table 7-1, give Table 7-2 values.

Table 7-2. Derived pile properties from Nucor HP 14 × 89.

Pile perimeter, p	57	(in.)
Pile effective diameter, $d_{Effective}$	18.14	(in.)
Pile tip area, $a_{piletip}$ (assumed plugged)	202.86	(in.^{2})
Pile shear area, A_{shear}	8.7482	(in.^{2})

7.2.5 Stem capacities (limit states 1 and 2)

In a deterministic-based design as exercised by district designers such as USACE St. Paul District (MVP), flood mitigation structures are subjected to flood loading, which is an Extreme load case defined by the site-specific ACE curve interpreted for a 750-year return period flood. A 750-year return period is stipulated for design by Figure 3-1 Load Category versus Return Period in EM 1110-2-2104 (HQUSACE 2016). In the deterministic design, this Extreme event load case is characterized by hydrostatic water pressures for flood levels that are as high as the top of T-Wall stem. It was discovered during the subsequent Reliability simulations that this condition rarely occurs for the Red River of the north flood wall, which may be subjected to typical conditions according to the ACE flood data where there is no water on the T-Wall.

The deterministic design shear and moment capacities of the T-Wall stem (provided by the 1 ft thick concrete stem and its internal steel reinforcement) are determined by the Extreme load case flood water pressures acting against the stem multiplied by a load factor taken from EM 1110-2-2104 (2016). According to Table 3-1 on page 3-10 of this engineering manual, the peak hydrostatic load that the wall stem must withstand has a load factor γ value of 1.3. This same factor is used in calculating the shear and moment capacities of the stem. This guidance sets the required capacity of the wall stem and thus the thickness of the concrete and amount of steel

reinforcement required inside the T-Wall stem. In addition, according to Table 3-1 on page 3-10 of the EM 1110-2-2104, resistance factors (ϕ) of 0.75 for shear and 0.9 for moment are stipulated.

To determine the design shear capacity of the stem, a triangular pressure diagram of hydrostatic water pressures for a flood height that is the height of the wall is created for the T-Wall stem. The flood height for the Figure 7-1 problem is 13.9 ft. That diagram is integrated over stem height, and the section width to determine the lateral shear force acting on the stem. This shear force is multiplied by the load factor γ of 1.3 and divided by the shear resistance factor ϕ of 0.75 to determine the designed shear strength of the concrete stem. The reinforced concrete stem possesses a mobilized strength ratio value ϕ/γ of 0.58 (=0.75/1.3) in this Limit State 1. This implies that 58% of the shear capacity is mobilized in a deterministic design. For the 4 ft wide Figure 7-1 example T-Wall section, the shear capacity of the stem is designed to be 50,154 lb.

The moment capacity of the stem is dependent upon the pressure diagram and the moment arm distance for the center of the factored pressure diagram from the base of the stem. Recall that the flood height for the Figure 7-1 problem is 13.9 ft. The base of the stem is the location of maximum moment dictating the size of the steel reinforcement and its spacing along the run of the T-Wall. Because the hydrostatic flood water pressures used in the deterministic design increase linearly with depth, this moment arm is one-third the distance from the stem base top of flood, which is at the top of the T-Wall or 4.63 ft for the example problem. This moment arm is multiplied by the computed lateral shear force based on flood height and section width to determine the unfactored stem base moment and then multiplied by the moment load factor γ value of 1.3 and divided by the moment resistance factor ϕ of 0.9 to define the deterministic design moment capacity of the wall stem. The reinforced concrete stem possesses a mobilized strength ratio value ϕ/γ of 0.69 (=0.9/1.3) in this Limit State 2. This implies that 69% of the moment capacity is mobilized in a deterministic design. For the 4 ft wide Figure 7-1 example T-Wall section, the moment capacity of the stem is designed to be 180,741 lb-ft.

7.2.6 Soil distributions and capacities (limit states 3 and 4)

The variable soil properties for the side friction for soil-structure interaction of a pile and bearing failure at the pile tip depend upon the

distribution of undrained shear strength (S_u) of the soil with depth. A soil strength distribution typically varies with depth. The total stress (undrained) shear strength parameters were computed for this analysis using the Stress History and Normalized Soil Engineering Parameters (SHANSEP) procedure (Ladd and Foott 1974). This procedure assumes that the soil shear strength can be normalized by the effective overburden pressure. The ratio of shear strength to the effective overburden pressure (S_u/σ'_{vo}) is dependent on an overconsolidation ratio (OCR) and a fitting parameter m assumed to be 0.8.

$$\left(\frac{S_u}{\sigma'_{v0}}\right)_{OC} = \left(\frac{S_u}{\sigma'_{v0}}\right)_{NC} \cdot OCR^m \tag{7.5}$$

where

$(S_u/\sigma'_{vo})_{NC}$ = ratio of undrained shear strength to effective overburden pressure for the normally consolidated condition

$(S_u/\sigma'_{vo})_{OC}$ = ratio of undrained shear strength to effective overburden pressure for the overconsolidated condition.

For the Grand Forks Red River example, S_u was determined assuming a normally consolidated clay with 10 ft of overconsolidated crust. The upper soil surface crust was assigned an OCR, of 20. The OCR of the soil decreased in a nonlinear fashion with depth: The OCR reduced from a value of 20 at the top to an OCR value of 10 at a 3 ft depth and finally down to an OCR of 1.0 (i.e., normally consolidated soil) at a depth of 11 ft. A hydrostatic water table was assumed to be at the top of the soil (i.e., EL 821) in the vertical effective stress computations for σ'_{vo} in these SHANSEP-based undrained shear strength S_u computations. The total unit weight of the soil was given as 122 pcf and $(S_u/\sigma'_{vo})_{NC}$ is set to 0.32.

Based on the distribution of S_u versus depth resulting from the SHANSEP computations, a set of four soil layers was used to define this site. The mean S_u layer for the top layer, layer 1, had S_u equal to 220 psf from depth 0 ft to 2 ft; S_u equal to 380 psf from depth 2 ft to 4 ft for layer 2; S_u equal to 480 psf from depth 4 ft to 10 ft in layer 3; and S_u equal to 226 psf at depth 10 ft and increasing by 18.33 psf per foot of depth in layer 4. While the SHANSEP method and variation in OCR with depth does not usually result in a constant S_u with depth within each of the top three

overconsolidated surface layers, similar S_u values were collected in each of the first three layers and averaged to determine a single S_u value assigned to that layer to simplify input for the CAXPILE software model (Dawkins 1984). This simplification provides insignificant error, due to the short lengths of the pile affected by these upper three layers encompassing a 10 ft depth as well as the averaging process being applied to these three upper layers. The mean undrained soil shear strength curve is identified in the Figure 7-2 family of S_u distribution curves with depth. The 13 Figure 7-2 S_u distribution curves with depth cover the range from the mean curve with depth minus 6 standard deviations to the mean curve with depth plus 6 standard deviations in 1 standard-deviation increments.

Figure 7-2. Mean soil S_u properties with depth and distribution curves from -6σ to +6σ based on $COV_{Spatial}$ (40 ft compression and tension piles).

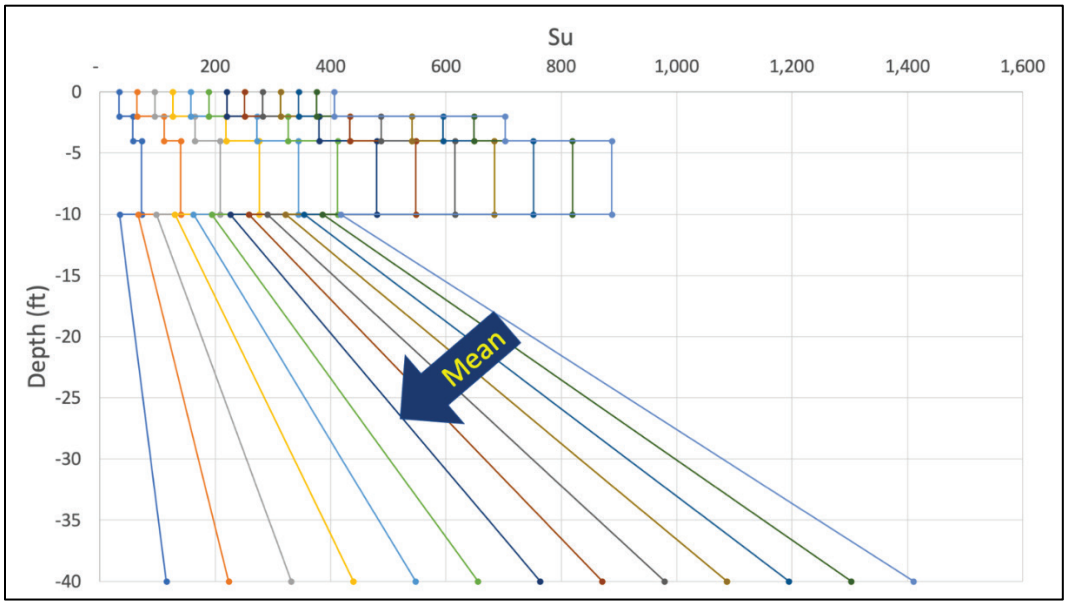

Due to a host of issues including site geology, details regarding the soil formation process, water table fluctuation, the quality of strength measurements (dependent upon minimization of disturbance introduced during soil specimen recovery from the site, quality of soil strength testing in the laboratory, etc.), undrained soil strength properties have the most variance among all the variables being considered in the Reliability analysis because they are impossible to measure exactly and can change from place to place within a soil regime. Point estimates are used to determine the coefficient of variation of soil properties at individual locations (COV_{Point}). Recall that COV is the standard deviation divided by

the mean value of a variable. A tabulation of COV_{Point} values for soils is given in Table D.4 in Appendix D.

Point estimate versus spatial average and variance reduction. Vanmarcke (1977b) points out that probabilistic distributions are primarily needed along a potential failure surface in a clay foundation for each spatially averaged geotechnical engineering soil parameter, like the undrained shear strength *Su*. A full description of these parameters is provided by a PDF from which the mean and standard deviation can be calculated. These spatial averages will have narrower PDFs than the corresponding point estimate property of a statistically homogeneous soil because the longer the distance over which this spatial averaging occurs, the uncorrelated fluctuations in S_u tend to cancel during the process of spatial averaging. This tends to cause a reduction in the standard deviation (and variance) in S_u as the size of the averaging length increases. This attribute is referred to as *variance reduction* within the zone of influence for the structure. Variance is the square of the standard deviation for a variable. Thus the statistical characterization of the variance in S_u, which can be expressed in terms of its COV value for S_u, needs to account for this variance reduction that occurs when spatial averaging estimates are made for soils properties within a zone of influence (e.g., along soil-to-pile interface) rather than for a statistical characterization of S_u at discrete points/locations (El-Ramly et al. 2003a,b). Appendix D provides background information and soil data bases regarding these issues.

Typical scale of fluctuation values for different soil strength tests have been collected and reported in Tables D.1 and D.2 in Appendix D. For these piles, a spatial COV ($COV_{Spatial}$) is used to determine the average soil strength properties along the pile.

Based on the soil data collected and tabulated in Appendix D, COV_{Point} is assumed to be 0.4 for the Red River of the North example problem site. The vertical scale of fluctuation δ is assumed to be 5 ft by the Appendix D data.

A variance reduction factor $\Gamma^2(L)$ is used to determine the effect of using pile lengths longer than the vertical scale of fluctuation for the length of the pile, *L*. When materials are chosen from a distribution in an uncorrelated fashion, the effects of those materials tend to counteract each other in an averaging fashion, as the values are chosen about the mean.

This averaging effect can be approximated using $\Gamma^2(L)$ for anisotropic materials with distances that are longer than the scale of fluctuation. The variance reduction factor is defined by

$$\Gamma^2(L) = \begin{cases} 1 : L \leq \delta \\ \frac{\delta}{L} : L > \delta \end{cases} \quad (7.6)$$

Figure 7-3 shows the relationship of variance to distance L, where L is a factor n times the scale of fluctuation δ, according to Equation 7.6. As previously discussed, this results in a distribution that has the same mean but has a smaller variance due to a reduction in the standard deviation (and variance) in S_u as the size of the averaging length increases with longer pile lengths relative to the value for the scale of fluctuation. The following equation is used to determine $COV_{Spatial}$.

$$COV_{Spatial}{}^2 = \Gamma^2(L) * COV_{Point}{}^2 \quad (7.7)$$

Figure 7-3. Normalized variance reduction factor.

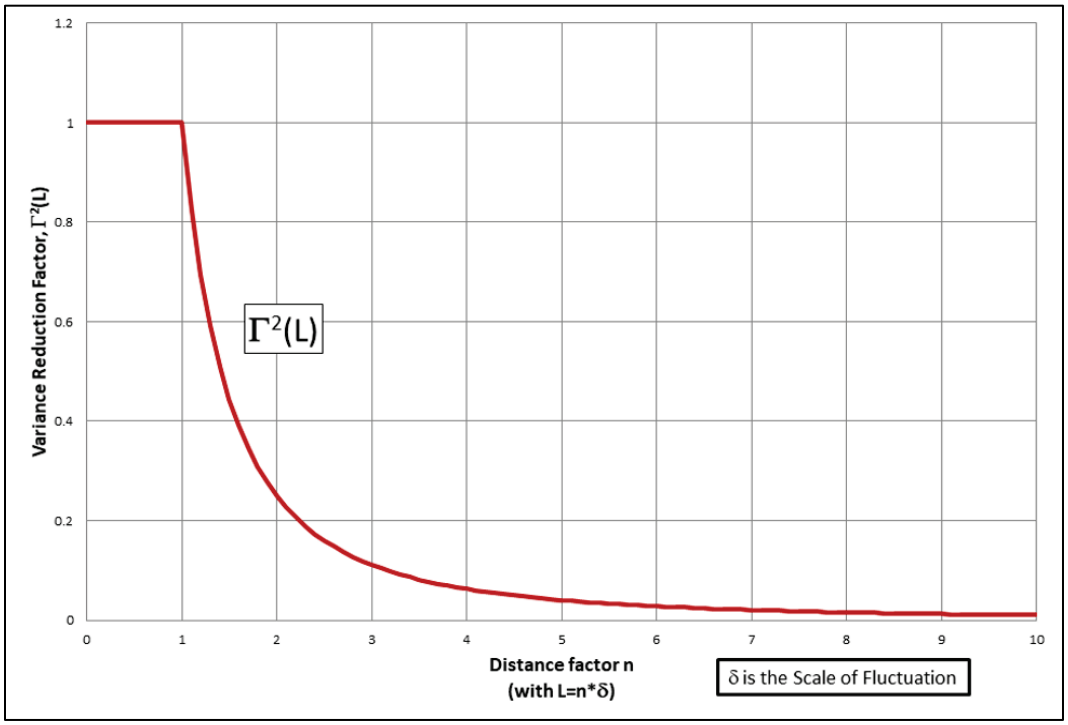

Observe in Figure 7-3 that the variance reduction factor value decreases as the ratio of pile length to scale of fluctuation (i.e., the distance factor n) increases. This results in lower values of $COV_{Spatial}$ compared to COV_{Point} as the length of pile increases. The converse is true for shorter piles; the

$COV_{Spatial}$ value approaches the value for COV_{Point} as the length of pile shortens and approaches the value for scale of fluctuation of the soil.

7.2.6.1 Axial capacity of the compression pile

Figure 7-4 shows the interpretation of CAXPILE analysis results of computing the axial compression force capacity acting through the soil-to-steel friction interface along the length of the pile as well as bearing of the pile tip at the Red River of the North site for undrained strength distributions with depth. The pile tip was assumed to be plugged for the maximum compressive force capacity acting on the pile.

Figure 7-4. Computation of axial compression force capacity for 40 ft compression pile as a function of top of layer four S_u (using CAXPILE).

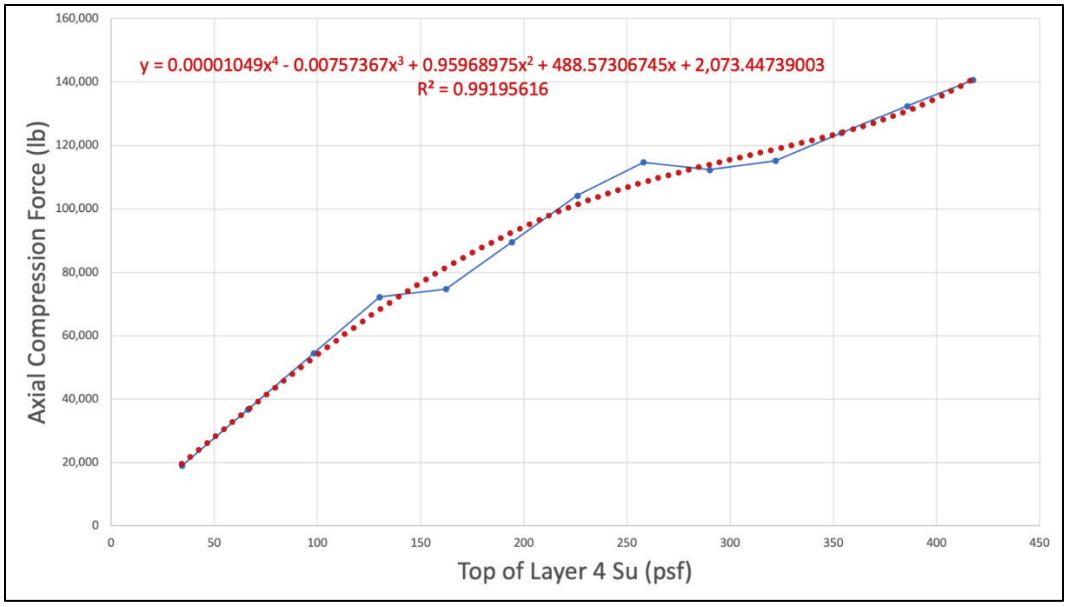

The CAXPILE software takes the properties of the example HP 14 × 89 pile and the S_u curves of Figure 7-2 to compute these forces with data points for S_u curves at ½σ intervals from -6σ to +6σ. A fourth-order polynomial curve-fit gave a good fit with an R^2 value greater than 0.99. The fitting equation is used for conversion of variable S_u to the axial compression force capacity of the soil in pounds. This curve is dependent on the length and cross-section pile geometry.

In terms of CPGA-R input, this axial compression force capacity term is approximately equivalent to the allowable compression (AC) (input in units of kips). To be specific, AC is the lower of the compression failure for the

steel of the pile or the soil. Since the soil is typically the lower capacity as compared to the compression capacity of the steel pile itself, it is used here.

7.2.6.2 Axial capacity of the tension pile

Similarly, Figure 7-5 shows the results of computing the axial tension force capacity acting through the soil-to-steel friction interface along the length of the pile. The CAXPILE software takes the properties of the example HP 14 × 89 pile and the S_u curves for the tension pile to compute these forces with data points for S_u curves at ½σ intervals from -6σ to +6σ. A fourth-order polynomial curve-fit gave a good fit with an R^2 value greater than 0.99. The fitting equation is used for conversion of variable S_u to the axial tension force capacity of the soil in pounds. This curve is dependent on the length and cross-section pile geometry.

Figure 7-5. Computation of axial tension force for 40 ft compression pile as a function of top of layer four S_u (using CAXPILE).

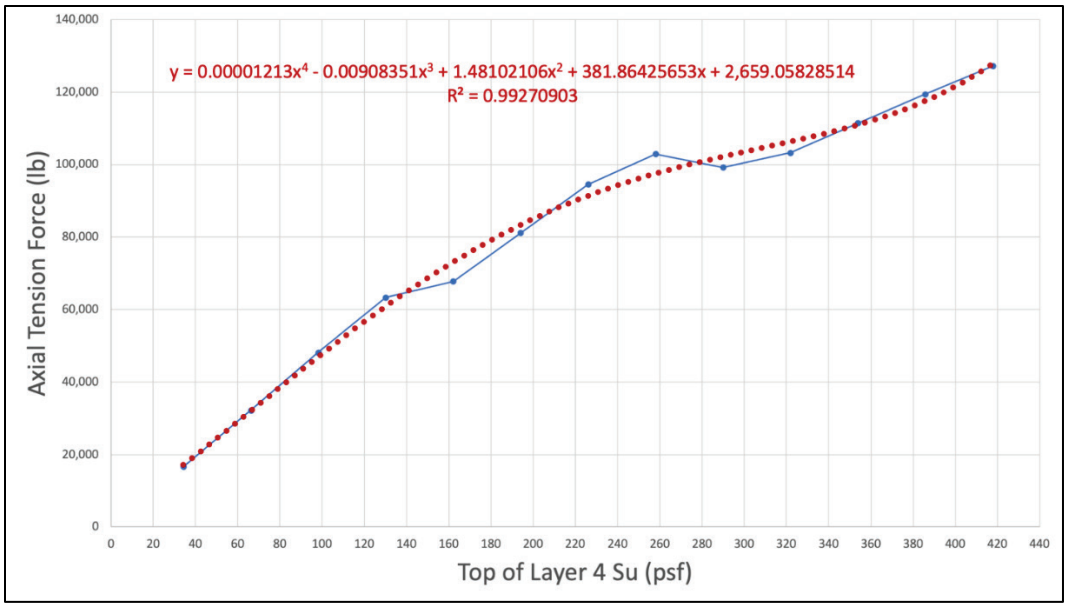

In terms of CPGA-R input, this axial tension force capacity term is approximately equivalent to the allowable tension (AT) (input in units of kips). To be specific, AT is the lower of the tension failure for the steel of the pile or the soil. Since the soil is typically the lower capacity as compared to the tension capacity of the steel pile itself, it is used here.

For a deterministic design procedure, the mean S_u is applied to the pile properties of both piles in a CAXPILE run. This generates mean capacities for compression and tension. According to EM 1110-2-2906 (HQUSACE

1989b) page 4-2 deterministic design criteria for the Extreme load case, a safety factor of 1.7 is applied to the mean capacities when site-specific pile test data are not available. The computed axial load on the pile is not allowed to exceed this value. Stipulating these scaled values in CPGA-R for AC and AT and after computation of the axial demand forces in each of the piles will result in a normalized value of axial load factor (ALF), for the pile, where a value of 1 or higher indicates a design failure of the pile. CPGA-R computes and outputs the ALF value, the ratio or the axial load in the pile divided by the user-specified axial capacity for the deterministic design. Conversely, the mean ultimate capacity values may be specified as CPGA-R input for the AC and AT values, and the computed ALF value can be checked against the value of 1/1.7 = 0.59 to determine if the deterministic design values have been exceeded. For the Figure 7-1 example with 40 ft HP 14 × 89 tension and compression piles with a T-Wall section width of 7 ft, the ALF for the tension pile was 0.04 and the ALF for the compression pile was 0.98. Because the compression pile ALF exceeded the limiting deterministic design value of 0.59, it was decided that an adjustment would be made to the pile spacing along the axis of the T-Wall and thus the T-Wall section width per pair of piles since that adjustment directly relates to the axial force acting on the piles. Adjusting the T-Wall section width to 4 ft, the ALF for the 40 ft long compression pile was 0.56, and the ALF for the 40 ft long tension pile was 0.02. Recall that the tension pile was set equal to the length of the compression pile in this deterministic design. The compression pile's ALF was slightly below the axial limiting deterministic design value of 0.59. The SSI Limit State 3 of the compression pile possesses a mobilized strength ratio value of 0.95 (=0.56/0.59) in this deterministic design. This implies that 95% of the axial SSI-based compression pile design capacity is mobilized. The 40 ft length of compression pile with a 4 ft spacing between adjacent compression piles is near optimum capacity usage in this deterministic design. The SSI Limit State 4 of the tension pile possesses a mobilized strength ratio value of 0.03 (=0.02/0.59) in this deterministic design. This implies that 3% of the axial SSI-based tension pile design capacity is mobilized. This low value of axial capacity mobilization is a result of of the excessive length for the tension pile.

7.2.6.3 CPGA-R C_{33} constants for compression and tension piles

At its root, CPGA-R is a frame analysis program developed as a reliability software extension of CPGA (Hartman et al. 1989). The axial stiffness of a pile is expressed in CPGA-R as

$$b_{33} = C_{33}\frac{A \cdot E}{L} \tag{7.8}$$

where

b_{33} = the axial pile stiffness
C_{33} = a constant that accounts for the interaction between the soil and the pile
A = the cross-section area of the pile
L = the length of the pile.

The term *(A*E/L)* is the elastic stiffness of the pile acting as a short column with no soil present. The coefficient C_{33} accounts for the stiffness of the soil-pile system. The value of C_{33} for single piles can be calculated using the following equation in conjunction with CAXPILE results:

$$C_{33} = \frac{\Delta}{\delta} \tag{7.9}$$

where

$$\Delta = \frac{P \cdot L}{A \cdot E} \tag{7.10}$$

with δ corresponding to the axial movement of the pile head due to axial load P, and P is the axial load applied to the pile in a CAXPILE analysis of a single pile at the site in question.

Using the Figure 7-2 mean undrained strength S_u distribution with depth curve, two CAXPILE models were constructed: one for the compression pile and a second for a tension pile. Pile length L used in the CAXPILE models is consistent with those used in the CPGA-R pile group model. For the CAXPILE compression pile model, an axial load was incrementally applied to the CAXPILE model up to the ultimate capacity of the pile, Q_{ult}. For each compression load increment, the axial movement of the pile head δ was computed by CAXPILE. Pairs of δ and P data were tabulated and processed using Equation 7.10 to compute Δ and then using Equation 7.9 to compute the constant C_{33}. Because of the nonlinearity of soil response in CAXPILE SSI analyses, the value for C_{33} decreases as the value for the applied load P approaches the value of the axial capacity in the CAXPILE model (i.e., Q_{ult} for the pile). With no axial load P applied to the pile, P is zero, and the ratio (P/Q_{ult}) is equal to zero as well. At the

other extreme, when the axial load applied to the CAXPILE pile SSI model is equal to Q_{ult}, the value for the ratio (P/Q_{ult}) is 1.0. Paired output data of C_{33} and (P/Q_{ult}) were obtained from the CAXPILE compression pile model results, and plots of this output data were constructed. Using this plot, an appropriate value of C_{33} was selected based upon the anticipated level of axial loading relative to the ultimate capacity for the compression pile (i.e., the value of the ratio (P/Q_{ult})). Examples of plots with C_{33} as a function of the level of site-specific axial pile loading (i.e., C_{33} versus (P/Q_{ult})) are shown in Ebeling and White (2016).

The value assigned to the C_{33} term used in the CPGA-R batter pile-founded T-Wall model is defined by a limiting deterministic design ALF value of 0.59 (=1/1.7). Recall that ALF is the ratio of the applied axial load (P) to the axial SSI limiting capacity (Q_{ult}) for the pile. The CAXPILE axial loading runs for a pile provides as output the top of pile axial deflection for each specified value for P. P is incrementally increased in the analysis by the software from a value of zero up to the limiting SSI capacity value of Q_{ult}. The CAXPILE computed results were then post-processed following the procedure given in Ebeling and White (2016), which results in C_{33} constants defined as a function of the ratio of (P/Q_{ult}). Figure 7-6 shows the result of computing C_{33} with respect to P/Q_{ult} in the incremental CAXPILE analysis for the 40 ft compression pile. For this compression pile, the CAXPILE analysis did not provide for values of forces acting on the piles that resulted in C_{33} values corresponding to a P/Q_{ult} ratio of 0.59, so the results were extrapolated from the closest pair of values to a value of 1.351.

Figure 7-6. Incremental plot of P/Q_{ult} values with respect to C_{33} for a 40 ft compression pile.

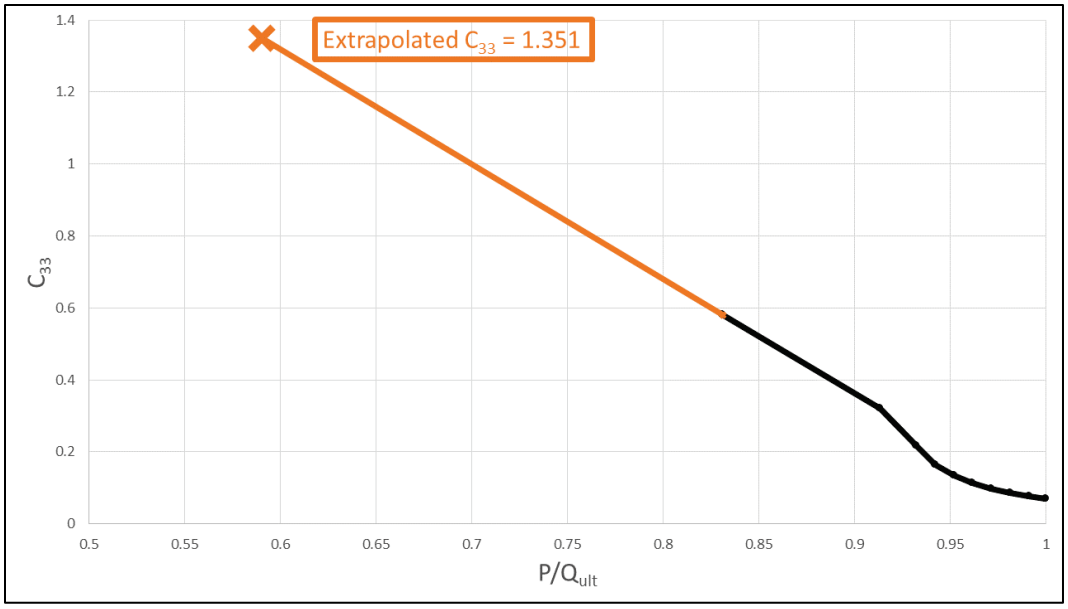

A site-specific CAXPILE tension pile axial loading model was developed and processed in the same fashion used for the compression pile following the procedure described in the previous paragraph to establish an appropriate C_{33} value for use in the CPGA-R analyses. Figure 7-7 shows the result of computing C_{33} with respect to P/Q_{ult} in the incremental CAXPILE analysis for the 40 ft tension pile. For the tension pile, the CAXPILE analysis did not provide for values of forces acting on the piles that resulted in C_{33} values corresponding exactly to a P/Q_{ult} ratio of 0.59, so the results were interpolated from the closest pair of values. Observe the asymptotic nature of this Figure 7-7 curve as the P/Q_{ult} decreases. P/Q_{ult} values below 0.6 will have a nearly constant C_{33} value of approximately 0.682. This means that computations for lower P/Q_{ult} values can be approximated with a value of 0.682.

Figure 7-7. Incremental Plot of P/Q_{ult} values with respect to C_{33} for a 40 ft tension pile.

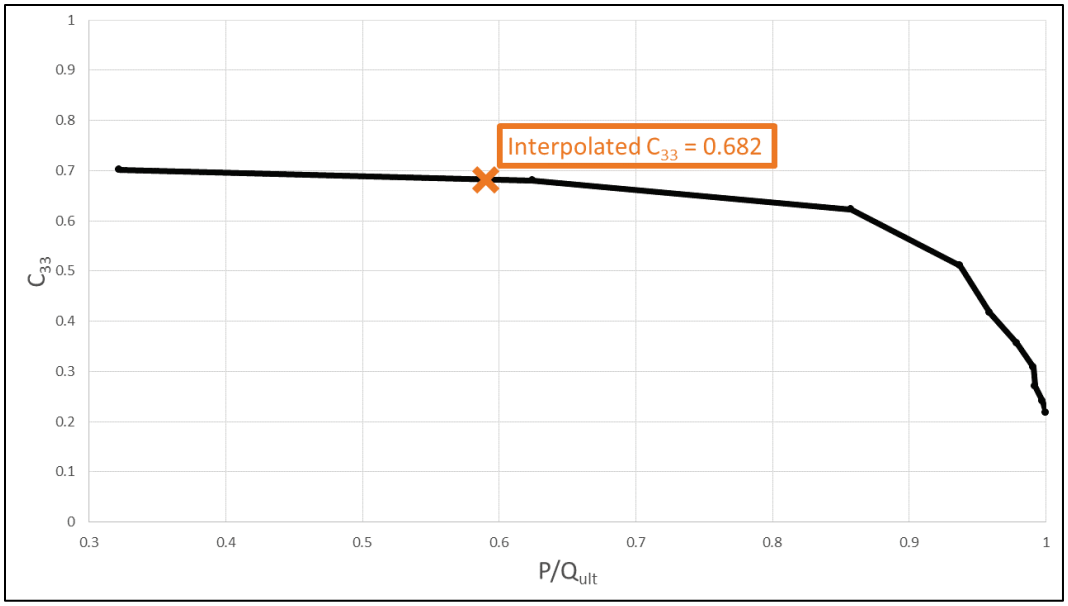

As mentioned in the previous subsection 7.2.6.2, according to EM 1110-2-2906 (HQUSACE 1989b) deterministic design criteria from section 4-2 paragraph b Loading Condition for the Extreme load case, a safety factor of 1.7 is applied to the mean capacities when site-specific pile test data are not available. This means that the relationship of ultimate force (Q_{ult}) and the currently applied force (P) has a ratio of 1/1.7 = 0.59 for the T-Wall configuration and design. Therefore, the C_{33} value for the compression and tension piles determined from the P/Q_{ult} ratio of 0.59. For CAXPILE runs where the incremental P/Q_{ult} form ranges that include the 0.59 value, the value of C_{33} can be linearly interpolated inside the range. However, if the ranges do not encompass the P/Q_{ult} = 0.59 value, then the value must be extrapolated using the closest range. Based on a series of CPGA-R deterministic analyses conducted by the authors of this report, the authors determined that the value for C_{33} should not be set to a value less than 0.01.

Summary: For the design with a 40 ft compression and 40 ft tension piles, the deterministic computation of C_{33} had to extrapolated for the compression pile and interpolated for the tension pile, with P/Q_{ult} = 0.59. The 40 ft compression pile has a C_{33} value of 1.351. The 40 ft tension pile has a C_{33} value of 0.682.

7.2.7 Computation of allowable capacities (limit states 5 through 10)

Limit States 5 through 10 deal with the capacities of the steel pile to resist shear, axial forces, or the combination of force and moment that can lead

to flexural failure. The following subsections describe these capacities both in the deterministic design process and for the Reliability assessment based on ultimate capacities.

7.2.7.1 Shear capacity of the HP compression and tension piles (Limit States 5 and 8)

These limit states are bundled together because the solution method is based entirely on the material, cross-section properties, and batter angles for the HP steel piles. The equation for capacity (*SCx*) is given as

$$SCx = \varepsilon_1 \cdot F_V \cdot A_{Shear} \tag{7.11}$$

and

$$F_V = \varepsilon_2 \cdot F_Y \tag{7.12}$$

with ε_2 is the inverse of the safety factor for I-shaped members in shear (AISC 2005; EM 1110-2-2504 [HQUSACE 1994]) and where ε_1 is an engineering scale factor (1.0 for the Ultimate capacity), F_y is the yield stress of the steel in pounds per square inch, and A_{Shear} is the pile shear area (in^2.) along a horizontal plane. For the Ultimate capacity, both ε_1 and ε_2 are set to 1.0. It is assumed for the example problem that the web of the pile is aligned along the direction of axial loading since this provides the strongest design. The HP pile shear area along a horizontal plane is given by

$$A_{Shear} = \frac{t_W \cdot d}{\cos\left(tan^{-1}\left(\frac{1}{batter}\right)\right)} \tag{7.4 bis}$$

where t_W is the web width for the pile in inches, d is the web length in inches, and *batter* is expressed as rise to run of the pile.

For the deterministic allowable stress design of the HP steel pile, F_y is set to the nominal (e.g., 50,000 psi for the HP 14 × 89 pile) yield stress of the pile. The ε_2 value is set to 0.33 times F_Y for shear stress representing 5/6 of the American Institute of Steel Construction recommended value of 1/2.5 (AISC 2005) and reflects the USACE design procedures for hydraulic steel structures (described in Chapter 6 in EM 1110-2-2504 [HQUSACE 1994]). For the Figure 7-1 batter pile-founded T-Wall example problem, the pile shear capacity (*SCx*) for the tension and compression piles is 144,345 lb.

The *Gz()* function for the pile cap shear for both compression and tension piles is

$$Gz(\quad) = SCx - Fx \tag{7.13}$$

where *Fx* is the global force acting in the *X*-direction on the pile slab from CPGA-R.

For reliability analysis of the designed structure, the shear capacity (*SCx*) is determined by the sampled F_y value from a truncated log-normal PDF possessing a mean value of 54,000 psi and with the ε_2 factor set to 1.0. This provides probabilistic uncertainty for *PUP* calculations.

The Yield Stress (F_y) distribution is collected from coupon tests conducted by Dexter et al. (2000) and Bartlett et al. (2003) on steel specimens, as descussed in Ellingwood. For ASTM A572 steel, which is assumed in this design, the yield stress has a nominal value of 50,000 psi. Based upon these test result data, Ellingwood recommends the distribution for yield stress be modeled as a truncated log-normal with a mean value of 54,000 psi, a COV of 0.07, and thus a standard deviation of 3,780 psi. The authors of this technical report reviewed the relevant steel coupon test data contained in the Dexter et al. (2000) and Bartlett et al. (2003) publications and truncated the log-normal PDF at a minimum value of 49,500 psi and at a maximum value of 69,000 psi. The authors of this report observe that selection of a different grade of steel may require modification of this PDF distribution characterization.

7.2.7.2 Axial capacity of the HP compression and tension piles (Limit States 6 and 9)

The steel axial capacity of the compression and tension piles are computed using the Yield Stress (F_y) and the total cross-section area of the pile

$$ACC = \varepsilon \cdot F_y \cdot pca \tag{7.14}$$

where *ACC* is the capacity input into CPGA-R, ε is a scale factor (1.0 for ultimate capacity), F_y is the yield stress of the pile steel, and *pca* is the pile cross-section area (26.1 in^2. for the example problem HP 14 × 89 piles).

For deterministic design, the steel axial compression capacity (ACC) is computed using the nominal (e.g., 50,000 psi for the HP 14 × 89 pile) F_y

value and an ε of 0.5. The design value for ε is provided by EM 1110-2-2906 (HQUSACE 1989b) on page 4-3. The Figure 7-1 batter pile founded T-Wall example problem ACC values for tension and compression piles are 652,500 lb.

For reliability analysis of the designed structure, the steel ACC is determined by the sampled F_y value from a truncated log-normal PDF possessing a mean value of 54,000 psi and with the ε factor set to 1.0. This provides probabilistic uncertainty for *PUP* calculations.

In CPGA-R, the steel axial capacity is usually not compared against the axial loads applied to the piles during the analysis. It is assumed that the soil capacity is far exceeded by the capacity of the steel pile; therefore, there is no need to check for steel failure. The authors include these checks in preparation for assessing all limit states of a system-based Reliability analysis of the T-Wall and recover the loads acting on the piles from CPGA-R output for comparison to the steel axial capacity. With computed ACC, axial force on the pile *F3* (from CPGA-R) and an Overstress Factor (*OSF*) of 1.0, the *Gz*() function for compression pile axial limit state becomes

$$Gz(\quad) = ACC * OSF - F3 = ACC - F3 \tag{7.15}$$

The *OSF* is set to 1 because this is not a short duration event.

Because tension forces are the inverse of compression forces (in sign convention), the tension pile axial limit state *Gz*() function is (for steel the tension capacity ATT is the same as the ACC computed values for the appropriate pile):

$$Gz(\quad) = ATT * OSF + F3 = ATT + F3 \tag{7.16}$$

Note the sign change in Equation 7.16 in contrast to Equation 7.15. This is due to the sign change in the force *F3* value being negative in tension versus positive in compression.

Like compression piles, for deterministic design the steel axial tension capacity (*ATT*) is computed using the nominal (e.g., 50,000 psi for the HP 14 × 89 pile) F_y value and an ε of 0.5. The design value for ε is provided by EM 1110-2-2906 (HQUSACE 1989b) on page 4-3. The Figure 7-1 batter

pile-founded T-Wall example problem ATT values for tension and compression piles are 652,500 lb.

For reliability analysis of the designed structure, the steel axial tension capacity (*ATT*) is determined by the sampled F_y value from a truncated log-normal PDF possessing a mean value of 54,000 psi and with the ε factor set to 1.0. This provides probabilistic uncertainty for *PUP* calculations.

7.2.7.3 Flexural capacity of the HP compression and tension piles (Limit States 7 and 10)

The flexural formulation for steel complicates the computation of loads and resistances because it combines ratios of loads to capacities, where the combined loads and capacities have different units. The Combined Bending Factor (*CBF*) in CPGA-R is computed according to the two equations. The two equations account for the fact that the pile will be in compression when *F3* is positive and in tension when *F3* is negative. The first equation is used when *F3* is positive, and the second for a negative computed value of *F3*.

$$CBF = \left[\frac{F3}{ACC} + MF1\left(\frac{|M1|}{AM1}\right) + MF2\left(\frac{|M2|}{AM2}\right)\right]\left(\frac{1}{OSF}\right) \qquad (4.4 \text{ bis})$$

$$CBF = \left[\frac{-F3}{ATT} + MF1\left(\frac{|M1|}{AM1}\right) + MF2\left(\frac{|M2|}{AM2}\right)\right]\left(\frac{1}{OSF}\right) \qquad (4.5 \text{ bis})$$

The constants *MF1* and *MF2* are Moment Amplification Factors that are set to 1.0 for fully supported piles. The *OSF* is also set to 1.0 because this is not a short-duration event.

If *CBF* goes above 1, the pile fails in flexure. In the first term of the equation, *F3/ACC* is the ratio of axial load force to the allowable axial capacity force in units of pounds. The second and third terms (*|M1|/AM1* and *|M2|/AM2*) are given as ratios of load moments and allowable capacity moments in pound-feet along the local 1-axis and 2-axis of the pile. A moment of any sign affects the stability of the structure, so the absolute value of the moment is used in the equation.

The first moment term (*|M1|/AM1*) is not considered, since a 2-D analysis is being performed and the load along the width of the structure is 0. This means that |M1| is 0, and the term may be eliminated from consideration.

Reducing by a term and substituting a value of unity for the factors, Equations 4.4 and 4.5 simplify to

$$CBF = \left[\frac{F3}{ACC} + \left(\frac{|M2|}{AM2}\right)\right] \tag{7.17}$$

$$CBF = \left[\frac{-F3}{ATT} + \left(\frac{|M2|}{AM2}\right)\right] \tag{7.18}$$

ACC is computed in Subsection 7.2.7.2 (including for the deterministic design case). Recall that for steel the tension capacity, *ATT* is the same as the *ACC*. *AM2*, the allowable moment capacity in the strong axis of the pile, is the result of equation

$$AM2 = \varepsilon \cdot F_y \cdot S_{X-X} \tag{7.19}$$

where ε is 1 for the ultimate load case and the section modulus $S_{X\text{-}X}$ is specified given for the HP pile type.

For the deterministic design steel moment capacity along the strong axis of the pile, *AM2*, is computed with the nominal (e.g., 50,000 psi for the HP 14 × 89 pile) F_y. The ε value is set to 5/9 according to EM 1110-2-2906 (HQUSACE 1989b) page 4-3. The Figure 7-1 batter pile-founded T-Wall example problem AM2 values for tension and compression piles are 3,638,889 lb-ft.

For reliability analysis of the designed structure, the steel moment capacity (*AM2*) is determined by the sampled F_y value from a truncated log-normal PDF possessing a mean value of 54,000 psi, and with the ε factor set to 1.0. This provides probabilistic capacity uncertainty for *PUP* calculations.

Notice that *CBF* is a unitless value because each term divides the load by the capacity with the same units. However, creating the *Gz*() function for the Limit State computation requires that the load and resistance (capacity) be separated to create load and resistance factors. In this case, the load and resistance need to be based on consistent units for the Reliability analysis and the collection of load and resistance sample data for the load and resistance distributions.

Substituting Equations 7.14 and 7.19 into Equations 7.17 and 7.18 and using the absolute value of *F3* under the ultimate load condition in the Reliability analysis gives

$$CBF = \left[\frac{|F3|}{F_y \cdot pca} + \left(\frac{|M2|}{F_y \cdot S_{X-X}}\right)\right] \tag{7.20}$$

At the Response Surface of the Limit State in the Reliability analysis, CBF = 1. In this case, the variable Yield Stress F_y, which is a resistance variable can be separated from the right side of Equation 7.18. Therefore, at the Response Surface, the following equation holds

$$F_y = \left[\frac{|F3|}{pca} + \left(\frac{|M2|}{S_{X-X}}\right)\right] \tag{7.21}$$

This Response Surface equation has the resistance term on the left side and the load term on the right side, all in units of stress, psi. Because the *Gz*() function has a value of zero at the Response Surface in the Reliability analysis, its formulation is

$$Gz(\quad) = F_y - \left[\frac{|F3|}{pca} + \left(\frac{|M2|}{S_{X-X}}\right)\right] \tag{7.22}$$

7.2.8 Searching for a semi-optimal deterministic design

Subsections 7.2.5, 7.2.6, and 7.2.7 give equations for determining capacities under ultimate load case design and deterministic design based on engineering guidance for the 10 defined limit states that are points of concern in a Reliability and LRFD analysis. The deterministic design based on engineering guidance equations because they are based on engineering expertise, can be used as a method to guide optimization of the wall geometry design. In Subsection 7.2.2, the wall geometry was defined using several assumptions for the example problem. Changing these assumptions could have a bearing on the deterministic capacities of the structure, bringing them closer to the mean loads. The design loads for the deterministic design are based on the Extreme load case force and moments acting on the structure. The Extreme values are determined by the 750-year flood event multiplied by a load scale factor of 1.3 from EM 1110-2-2104 (HQUSACE 2016).

7.2.8.1 Stem optimization

Subsection 7.2.5 presents that the force capacity and moment capacity acting on the stem are directly determined by multiplying a load scale factor, 1.3 (from EM 1110-2-2906 [HQUSACE 1989b]) times the Extreme load case force and moment (for a 750-year flood event) applied to the reinforced concrete stem. This is the (semi)optimal design capacity for this system since the stem is designed to the capacity and the design assumptions do not affect those capacities. Therefore, there can be no attempt to optimize the stem capacities.

7.2.8.2 Pile optimization

Subsections 7.2.6 and 7.2.7 cover the capacities that are directly implicated by soil and pile properties. However, some of these properties are varied for the Reliability analysis, namely the distribution of undrained soil strength (S_u) with depth for the soil layers used in CAXPILE analysis, and the yield stress, F_y, for the steel that the HP pile is made from. Because the undrained shear strength distribution of S_u with depth and the F_y for steel are independent variables, they cannot be considered for optimization.

It is observed that stem placement can serve to alter the distribution of the loads acting on the piles. For the purposes of this analysis, the stem placement is assumed to be a fixed part of the design.

The remaining properties of piles that can affect the capacities of the system have to do with the geometry of the piles. There are four ways to affect the geometry of the piles: changing the distance between pile groups, changing the type or size of the HP steel piles, changing the length of piles, and changing the batter of the piles.

Changing the distance between pile groups affects how much load is distributed between the pile groups. For optimization purposes, this distance should be a distance close to the response surface for first pile-based limit state, usually the compression pile SSI limit state with an ALF of 0.59 based on the Extreme value safety factor of 1.7 (from EM1110-2-2906 [HQUSACE 1989b]). This distance can be discovered quickly with a trial-and-error process varying the distance between pile groups. After this distance has been found, further optimizations based on pile lengths can be performed.

HP steel pile types/sizes are standardized and provide the cross-section geometry for the pile. Subsection 7.2.4 provides some of the geometric values for a Nucor HP 14 × 89 pile. These properties are used for determining soil-structure interactions, and therefore capacities, in CAXPILE. These properties also affect every individual pile capacity calculation.

Pile lengths are used to determine how much interactions the piles have with the subsurface soils. Longer piles have more interactions with the soil, in CAXPILE computations.

Finally, the pile batter affects the computations of cross-section areas for pile cap shear computations. This can also change the effective length of a pile in a vertical S_u range, but during computations the authors realized that this change would have insignificant effect. It was determined that the only noticeable way to increase the capacity of the pile cap in shear was to decrease the rise-to-run ratio of the pile, but pile batters larger than the 4:1 value used in the Figure 7-1 pile group would require special installation requirements that will add cost to the project. Due to these installation concerns, the authors decided to fix the batter of the piles to 4:1.

Summary: Thus, the methods for providing semi-optimal pile design had only two design parameters, the selected pile type and the lengths of the piles. These properties are optimized based on the spacing between pile groups.

7.2.8.3 Numeric deterministic design process to optimize pile lengths for batter pile-founded T-Walls

Selecting a pile type for optimizing the layout of a pile-based T-Wall is a process that is simplified by that fact that the pile types have standardized properties (e.g., cross-section area). However, selection of pile length requires that a process be defined. A numeric process can be designed that attempts to maximize these pile lengths based on steel and soil strengths engaged along with the frame action of the batter pile-founded T-Wall design. This numeric process requires computation of nonlinear soil-pile interactions with respect to depth of embedment, and the nonlinear effects of the frame design under loads. The following procedure provides a method for determination of both compression and tension pile lengths for a T-Wall configuration like Figure 7-1.

1. Create an initial deterministic design with collected data that are appropriate for the site:
   a. 750-year flood hazard to the top of the stem of the T-Wall.
   b. Use the mean soil strength distribution of S_u with depth curve, Figure 7-2.
   c. Select pile type (e.g., HP 14 × 89), which establishes the pile engineering properties.
   d. Assume a length for the compression pile and for the tension pile (Figure 7-1). The batter pile located to the left of the stem and directly below the Figure 7-1 blue block of floodwater is referred to as the tension pile in this chapter. The batter pile located to the right of the stem and below the dry stem delineated region is referred to as the compression pile.
2. Develop a layered soil model, using average S_u in each layer, from the mean soil strength distribution of S_u with depth curve derived using the SHANSEP procedure (Figure 7-2). The CAXPILE models for the compression and tension piles are developed using these S_u soil layers. Executing CAXPILE with these models computes the total SSI axial pile resistances as a function of top of pile displacement. Other output includes frictional load shedding along the length of the piles, as well as tip resistance. These properties give the soil-strength resistance parameters for side friction and tip penetration for each pile. Recall that the tension pile has no tip resistance contribution. Axial pile stresses are reduced from the top of the pile to the pile tip through transfer of the stress from the pile into the surrounding soil regime.
3. Compute the mobilized capacity value (i.e., ALF and CBF) with respect to the eight pile limit states (both internal to each pile and for SSI) using a deterministic run (with scale factors from engineering design guidance) of the CPGA-R frame analysis. This analysis provides a mobilized strength ratio of each limit states' propagated load divided by the computed resistance.
4. Determine the primary limit states that are most affected by changing the pile lengths. The SSI Limits States 3 and 4 control the pile lengths because the steel has a higher capacity than the soil. This is confirmed by comparing the ALF from CPGA-R (for SSI) with the mobilized strength ratio for Limit States 6 and 9 (i.e., axial capacities of the steel piles). This comparison shows that the ALF has a higher value (with respect to the limiting value of 0.59 for SSI).

5. Compute the new lengths of each pile (compression and tension) by taking the current length and multiplying it by the ALF (for the current length divided) by the deterministic design ALF limiting value (e.g., 0.59).
6. A Newton-Raphson numerical methodology is applied in an iterative process to help refine and converge to a required length of compression pile and tension pile. For this numerical iteration method, repeat steps 3 through 5 until a fixed Δ precision for each pile length has been reached. The Δ precision assigned in this problem is convergence to within 1 ft for pile lengths.

This procedure assumes that the frame action of the batter pile-founded T-Wall will allow the structural system to place sufficient loads on each of the limit state's members as to reach the limiting condition (e.g., 0.59 for SSI failure). In practice, steel pile member properties exceed the soil properties to an extent that steel failure is much less likely to occur than SSI failures and even prevent frame action from occurring that would cause SSI failures to occur in the tension piles.

Another reason not to use the numerical method is in the resolution of the pile lengths. Piles are placed to reduce translation and rotation of the T-Wall and provide those resistances as SSI and pile cap resisting moments.

To provide pile cap moment resistance, the pile must be at least 5 ft in length to reduce short pile ploughing action. This sets the shortest length of the pile.

In the engineering design process followedf in this report, the resolution of the lengths of the piles are specified in feet for English units. The longest piles are therefore rarely over 100 ft in length. Trial and error can be used in that range to determine the semi-optimal lengths for the piles using CAXPILE and CPGA-R software.

7.3 Designing for the Red River of the North site, in Grand Forks, ND

The first site explored using the pile group analysis methods of section 7.2 was the Red River of the North site, in Grand Forks, ND. This site served as the basis for the soil distributions of subsection 7.2.6. The following subsections discuss the collection of variable data and design choices.

7.3.1 System variable distributions for the Red River of the North site, in Grand Forks, ND

The generic system variables were established in subsection 7.2.3. This subsection provides site-specific distributions for the Red River of the north site, in Grand Forks, ND.

The truly site-specific variable distributions were the Flood Elevations drawn from ACE data and wind-induced wave loading. The other variable distributions are set by the properties of the materials used in construction of the pile-founded T-Wall.

The ACE data are collected at the site for the designed structure. The ACE provides information for the probability that an elevation will be exceeded for any given year. Figure 7-8 shows the site-specific ACE information for the Red River of the north site, in Grand Forks, ND. This same paired data set curve is presented with reversed axes in Figure B.1-12, a logarithmic horizontal scale of ACE value versus a linear vertical scale of river stage EL value. The base of slab and top of stem wall elevations are included in the plot to facilitate the observation that river stage data have a small probability of reaching the heel of the wall and even less probability of exceeding the wall height.

Figure 7-8. Collected ACE data for site-specific data for the Red River of the North site, in Grand Forks, ND.

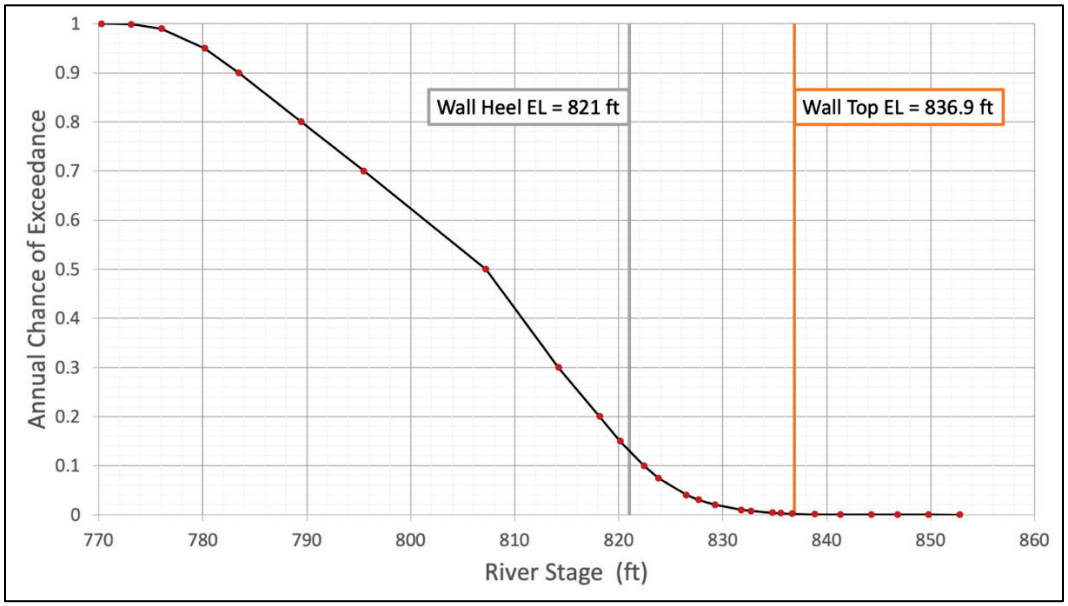

The ACE data plot is in effect a CDF since the values have been accumulated over the year for each flood level. To find the specific probability that an individual flood level will be selected, a PDF needs to be created by differentiating the CDF data. A histogram of these values was created and is shown in Figure 7-9 as a PDF distribution of the ACE values. Observe in the Figure 7-9 PDF that the bulk of the river stage PDF distribution, including the PDF center, fall below the heel EL of the T-Wall. Thus, the mean and median values of this PDF will be below the elevation of the base slab (EL 821).

This Figure 7-9 histogram is verified through simulations with the ACE curve directly, generating 100,000 uniform random variables with a value from 0 to 1 and collecting elevations from the Figure 7-8 ACE curve. The resulting samples were collected and binned to form the blue histogram in Figure 7-9. Note the consistency between the two PDFs. In addition, observe that the shape of this PDF data means that it is not acceptable to be modeled using a normal Gaussian distribution.

Figure 7-9. PDF Histogram from the Site-specific ACE data for the Red River of the North site, in Grand Forks, ND, compared with simulated data from the ACE data.

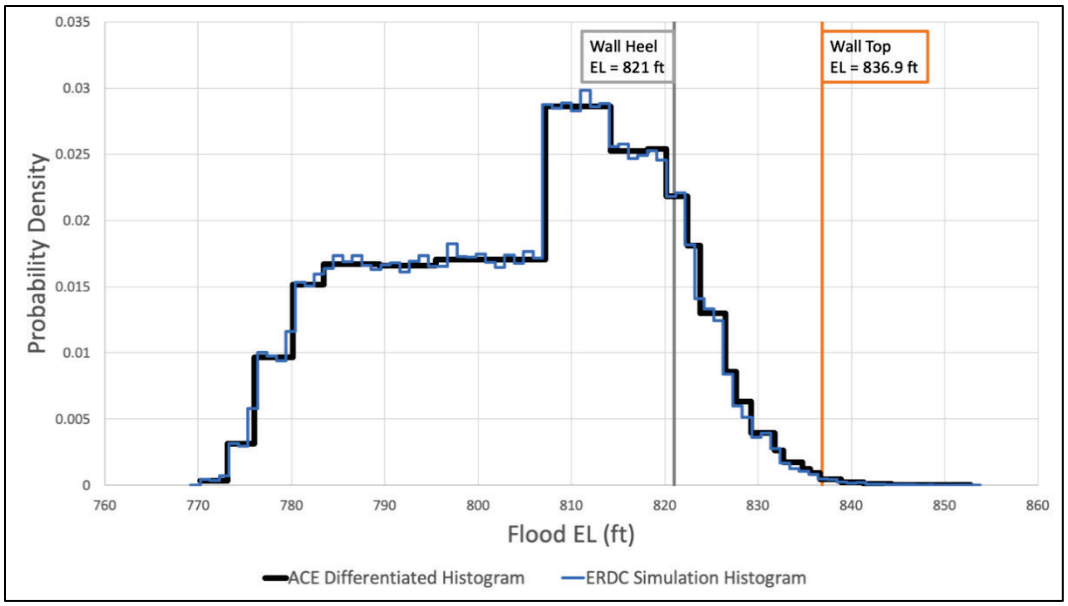

To compute LRFD factors for the minimum project service life of 100 years for major infrastructure projects such as locks, dams, and levees, a 100-year Chance of Exceedance needs to be used to determine the probability of a flood elevation during the full lifetime of the structure. Figure B.1-12 shows an estimation made by MVP of a 100-year Chance of

Exceedance, which the authors speculate as having been derived using an Extreme value function.

However, with an ACE provided by MVP, the authors of this technical report derived a 100-year Chance of Exceedance flood hazard curve from this ACE. This process was performed by finding a 100-year maximum flood value by randomly sampling the ACE 100 times and recording the maximum value. The logic is that this is a simulationof flood events each year for 100 years with a retention of the greatest flood event. Next, this simulation process was repeated 100,000 times with each 100-year maximum flood simulation result retained. Each simulation sample has a probability of 1/100,000. This database of simulations is used to construct a PDF histogram as shown in Figure 7-10.

Figure 7-10. PDF for 100-year Chance of Exceedance values.

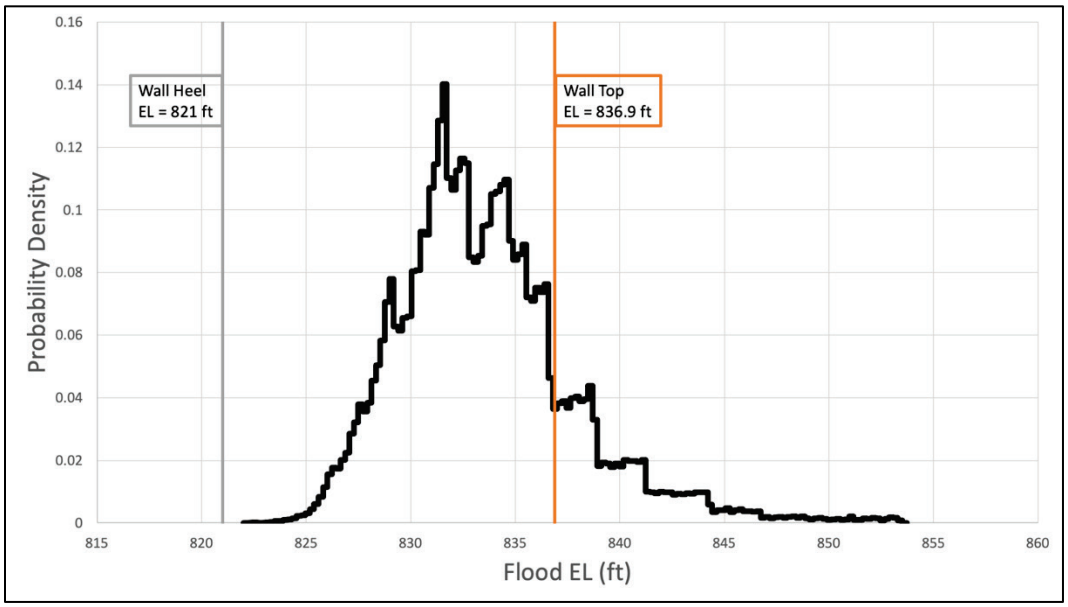

A CDF was created by integrating the 100-year flood PDF histogram. The 100-year Chance of Exceedance was derived by taking 1.0 minus the CDF. The results are shown in Figure 7-11. Figure 7-11 also provides a comparison of the 100-year chance of exceedance MVP engineering estimation and the simulation-based 100-year Chance of Exceedance taken from Figure B.1-12. The plot curves are similar with the simulation-based method providing a smaller range of flood elevations. The lower flood elevations of the simulation-based method are greater than the lower elevations of the MVP result for the higher chances of exceedance. The upper flood elevations of the simulation-based method are lower than the

upper elevations of the MVP result for the extremely low chances of exceedance. The authors believe that the ERDC simulation 100-year Chance of Exceedance curve will provide reasonable results for a Reliability analysis with the purpose of generating LRFD factors for the lifetime of the structure.

Figure 7-11. Comparison of MVP engineer estimate with ERDC simulation 100-year Chance of Exceedance values.

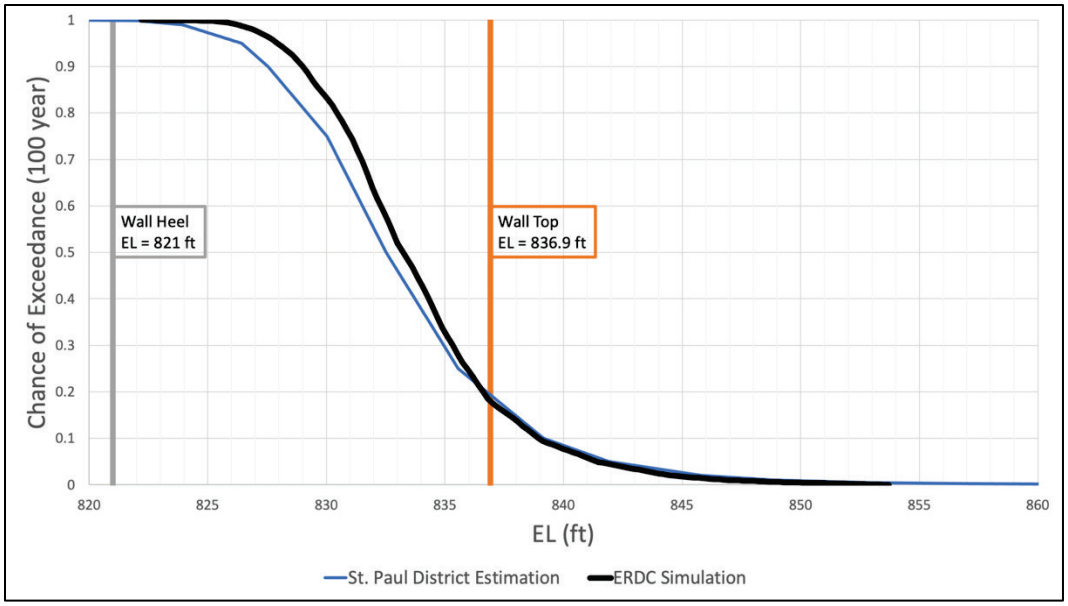

The 100-year Chance of Exceedance is also validated by comparing Reliability results from simulations with ACE and 100-year Chance of Exceedance values. For simulations with the ACE, the *PUP* per annum for the compression pile SSI limit state (#3) was determined to be approximately 0.00025. Using Equation 2.69, the 100-year *PUP* value should be 0.0247. Simulating with the 100-year Chance of Exceedance values returns a 100-year *PUP* value of 0.026. This value is within 0.013 of the predicted value and close enough to validate using the 100-year Chance of Exceedance values.

Processed wind-speed data are used in conjunction with the Goda (2010) method (Chapter 5) to generate wind-induced pseudo-static wave loading (Chapter 6). The site-specific wind data were obtained by collecting data from an airport near Grand Forks, ND, as discussed in Section B.1 of Appendix B. This wind data set was fairly complete for the years 1973 to August 2020 with wind speeds and directions reported multiple times per hour between 2012 and August 2020 and hourly from 1973 to 2012. The

range in this data was judged to be only representative of a relatively short time frame. These data were analyzed probabilistically using a Gumbel Type I distribution with Gringorten's (1963) Method to extrapolate to longer wind-speed return periods (Figure B.1-5). The winds speeds determined using the Gringorten's (1963) Method were based on a 100-year return period wind event occurring at the T-Wall. For the Red River of the North site, the data collected indicated a normal distribution with a mean 100-year wind return period wind speed of 51.0 mph and a standard deviation of 1.534 mph (Figure B.1-6). This distribution represents the variability of wind speeds only during a 100-year event and not the variability of wind speeds annually. Therefore, the value of *PUP* for each of the 10 limit states is really the *PUP* during a 100-year wind event and is likely conservative for events that occur annually.

This is an acceptable compromise given the limited time frame of wind-speed samples and the fact that wind speeds have an effect only when the water elevations reach or exceed the base elevation of the T-Wall. The authors note that in the Reliability analysis using the Figure 7-8 ACE flood curve, it has been observed that the number of flood elevations simulated to reach the stem of the T-Wall are fewer than those simulations resulting in flood ELs that reside below the base slab EL (i.e., the heel of the T-Wall).

The definition of the soil strength parameter distribution with depth has been described in Subsection 7.2.6. The functional description of the soil strength parameters for the pair of 40 ft piles as shown in Figure 7-4 and 4.5 are based on drawing information from the a Gaussian normal distribution with a mean value of 226 psf 10 ft below the ground surface combined with the S_u distribution with depth that intersects the normal distribution for S_u at this depth. These values are based on the S_u values drawn at the top of soil layer 4 in Figure 7-2. The mean value and COV are developed using SHANSEP (1974) procedure for site strength characterization. The SHANSEP-defined distribution of mean S_u with depth was assigned a COV_{point} of 0.4 based on Appendix D data that, when combined with the Variance Reduction Factor for a 40 ft pile, gave a $COV_{Spatial}$ of 0.1174. From the $COV_{Spatial}$ value, the standard deviation value of 31.9564 psf is defined at this 10 ft depth.

The Yield Stress (F_y) distribution for the HP steel piles is defined by data obtained from coupon tests conducted on steel specimens (Ellingwood). For ASTM A572 steel, which is assumed in this example, the yield stress

has a nominal value of 50,000 psi. Based upon cited test result data, Ellingwood recommends the distribution for yield stress be modeled as a truncated log-normal with a mean value of 54,000 psi and a COV of 0.07. The standard deviation is 3,780 psi. The Dexter et al. (2000) and Bartlett et al. (2003) steel coupon test data suggest that this distribution be truncated at a minimum value of 49,500 psi and at a maximum value of 69,000 psi.

The reinforced concrete stem shear and stem moment capacity distributions are based on strength assessment for the Extreme Load Case value according to Table 3-1 and Figure 3-1 of EM 1110-2-2104 (HQUSACE 2016). For a deterministic design and the two stem limit states, the hydrostatic water pressures with a flood elevation to the top of the wall from the base of the stem are computed, and the lateral force and moment are captured at the base of the stem.

The reinforced concrete Stem Shear Capacity distribution is based upon a lognormal distribution according to the Table 5-4 information provided in Ellingwood and summarized in Chapter 4 of this report. The lognormal mean capacity value is defined in a deterministic analysis for a 750-year flood load to the top of the T-Wall by multiplying the peak hydrostatic lateral force for the 13.9 ft high triangular hydrostatic flood water pressure distribution acting on the reinforced concrete stem by the load factor γ of 1.3 and a bias factor of 1.2 according to Table 3-1 in EM 1110-2-2104 (HQUSACE 2016) and Table 5-4 in Ellingwood, respectively. Recall that the height of the reinforced concrete stem is 13.9 ft. The standard deviation is computed by multiplying the mean value by the COV_{Shear} value of 0.18. This value of COV is taken from Table 5-4 in Ellingwood.

The Stem Moment Capacity distribution also uses a lognormal distribution as recommended by Ellingwood (Chapter 4 of this report summarizes this Ellingwood data). The lognormal mean capacity value is defined in a deterministic analysis for a 750-year flood load to the top of the T-Wall by multiplying the peak hydrostatic lateral force for the 13.9 ft high triangular hydrostatic flood water pressure distribution acting on the reinforced concrete stem by the load factor γ of 1.3 and a bias factor of 1.12 according to Table 3-1 in EM 1110-2-2104 (HQUSACE 2016) and Table 5-4 in Ellingwood, respectively. The standard deviation is computed by multiplying the mean moment capacity value by the COV_{Moment} value of 0.14. This value of COV is taken from Table 5-4 in Ellingwood.

7.3.2 Deterministic results for a section with a pair of 40 ft piles

A deterministic evaluation of the flood mitigation batter pile-founded T-Wall structure is required to refine the design of the structure. In this subsection, there is a summarization of the results of evaluations made using CPGA-R for the pile limit states for the Figure 7-1 structure with 40 ft long tension piles and 40 ft long compression piles.

The flood elevation was raised incrementally in a series of 17 CPGA-R deterministic analyses of the Figure 7-1 batter pile-founded T-Wall flood mitigation structure using CPGA-R. The flood elevation was raised in these analyses from EL 821 corresponding to the base of slab to the top of T-Wall El 836.9 in 1 ft increments until the last increment of 0.9 ft.

Figure 7-12 summarizes the results computed at each flood elevation analyzed for the three structural limit states of the compression pile. The three structural pile limit states are shear failure limit state 5 (blue points); axial failure Limit State 6 (orange points); and the CPGA-R Labeled Limit State 6 of CBF (black points). The strength assessment for each limit state is expressed as the ratio of the applied load within the pile divided by the structural pile capacity. In the deterministic design process, the structural steel design capacity values used for each of these three limit states listed above contain constants that reduce the ultimate steel capacity to an allowable steel capacity. Thus, a deterministic design capacity is also referred to as an allowable stress-based design capacity.

Figure 7-12. Deterministic design results for the 40 ft long HP 14 × 89 compression pile.

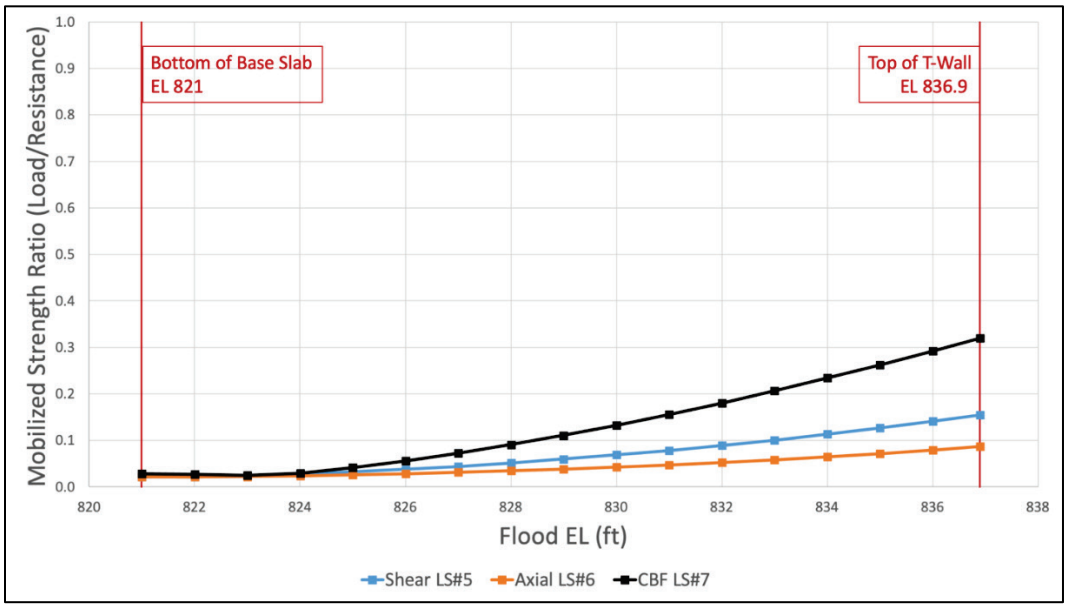

Examples of these constants are the ε_2 value set to 0.33 times F_Y for the allowable steel shear stress capacity *Fv* (Equation 7.12) used in the computation of the pile shear capacity force *SCx* along a horizontal plane (Equation 7.11); an ε of 0.5 used in steel axial design compression stress steel capacity computed using the nominal (e.g., 50,000 psi for the HP14 × 89 pile) F_y value times this ε value of 0.5 that are used in computing the design force capacity value for *ACC* (Equation 7.14); and the ε value of 5/9 used to define the design stress steel flexural capacity, equal to the nominal F_y times this ε value of 5/9, used in Equation 7.17 when computing the deterministic design steel moment capacity *AM2* along the strong axis of the pile. The inverse of these three constants may be viewed as the FoS applied to the yield stress in an allowable stress-based design.

The demand is computed for each of these three structural pile limit states and for a given flood elevation using CPGA-R. In the case of the compression pile, Limit States 5 and 6 mobilized strength ratio assessments center on the horizontal shear force and the axial force computed within the compression pile. Recall that the horizontal shear force allowable capacity *SCx* is assessed using Equation 7.11 and axial compression force allowable capacity *ACC* value is assessed using Equation 7.14. The Limit State 7 mobilized strength ratio assessment makes use of the flexure formula-based Equation 7.20 for the CPGA-R computed *CBF* value for the compression pile.

For each of the three limit states, a mobilized strength ratio value of zero in Figure 7-12 corresponds to no load occurring within the compression pile. Conversely, a value of 1 implies that the allowable stress-based deterministic design pile capacity is fully mobilized for the flood elevation being considered. Figure 7-12 CPGA-R results show that as the flood elevation rises, the demands in each of the three limit states rise (with the pile design capacities held constant). This trend is to be expected. The results shown in this figure also demonstrate that the CBF is the most critical of the three structural limit states within the compression pile for all flood elevations.

With a flood elevation reaching the top of the stem of the T-Wall at EL 836.9 ft, all three structural pile limit states possess mobilized strength ratio values are less than 1. The *CBF* mobilized strength ratio reaches a maximum value of 0.32 while the ratios for shear and for axial force loadings achieve lower mobilized, maximum strength ratio values of 0.15

and 0.09, respectively. In fact, none of these three structural pile limit states come close to mobilizing their respective structural pile design capacities.

This observed reserve capacity is due to the fact that during the deterministic design of the Figure 7-1 T-Wall flood mitigation structure, it is the SSI limit state that dictated the length of compression pile as well as its pile sizing of HP 14 × 89 for its bearing capacity footprint, as discussed at the end of subsection 7.2.6.2. The deterministic design criteria used in the CPGA-R analysis consists of checking the CPGA-R-computed *ALF* value against the limiting design value of 1/1.7 = 0.59 to determine if the SSI-based design value has been exceeded for this designated Limit State 3 of the compression pile. The compression pile length was shortened or lengthened during the deterministic design process until this limiting *ALF* design value of approximately 1 was achieved for the flood EL of 836.9 ft. The pile length (and size) was then fixed to optimize this, the most vulnerable of the limit states. Optimization refers in this case to the axial force demand equaling its SSI-based design axial capacity, reducing the capacity and therefore the construction costs. After the compression pile length and size were fixed, the three structural limit states within the HP 14 × 89 pile were then assessed (Figure 7-12) using CPGA-R-computed demands.

In summary, the deterministic design was optimized by SSI Limit State 3, corresponding to a mobilized strength ratio of nearly 1.0 for the selected 40 ft long HP 14 × 89 compression pile. The three pile structural limit states were found to be far from their optimization, as demonstrated by the Figure 7-12 mobilized strength ratio values being far less than 1 at a flood EL of 836.9 ft. This observation will have a direct impact on the computed *PUP* results for the individual limit states in the Reliability analysis of this batter pile-founded T-Wall flood mitigation structure.

Figure 7-13 summarizes the results computed at each flood elevation analyzed for the three structural limit states of the tension pile. Recall the flood elevation was raised in 1 ft increments in a series of 17 CPGA-R deterministic analyses of the Figure 7-1 batter pile-founded T-Wall flood mitigation structure, from EL 821 to El 836.9. The three structural tension pile limit states considered are shear failure Limit State 8 (blue points); axial failure Limit State 9 (orange points); and the CPGA-R-labeled Limit State 10 of the CBF (black points). Recall the strength assessment for each

limit state is expressed as the ratio of the applied load divided by the structural pile capacity.

Figure 7-13. Deterministic design results for the 40 ft. long HP 14 × 89 tension pile.

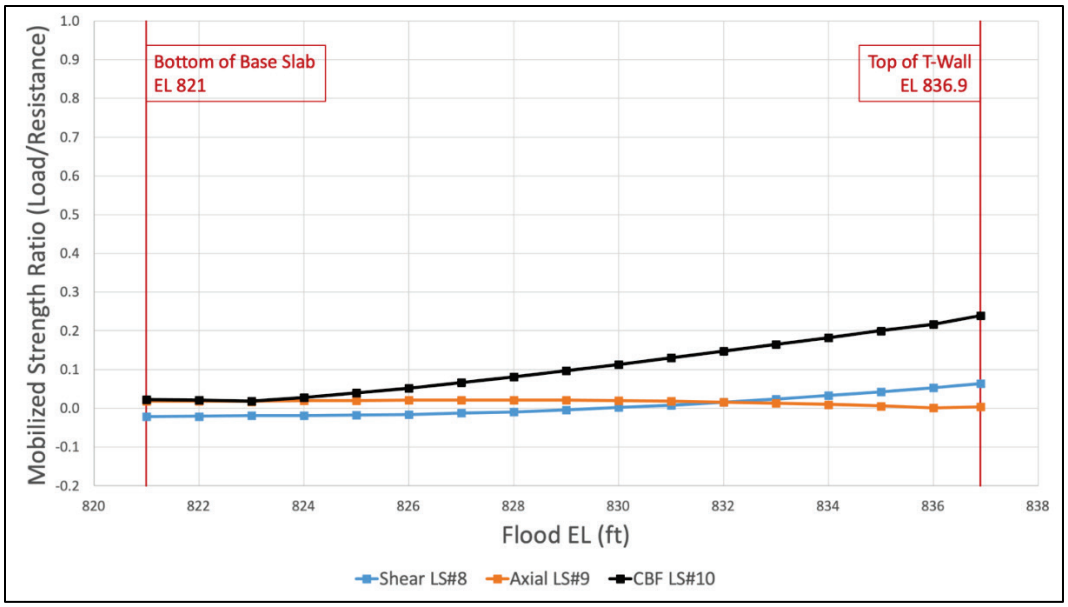

The demand is computed for each of these three structural pile limit states for a given flood elevation using CPGA-R. In the case of the tension pile, Limit States 8 and 9 mobilized strength ratio assessments center on the horizontal shear force and the axial force computed within the tension pile. The horizontal shear force capacity *SCx* is assessed using Equation 7.11, and axial force capacity *ATT* is assessed using Equation 7.14 with *ACC* set equal to *ATT* in this equation when the pile is in tension. Recall these computations are based upon allowable stresses in a deterministic design. When the pile is not in tension as in the case for low flood elevations, *ACC* is being used in Equation 7.14 to define the axial force capacity in the pile. The Limit State 10 mobilized strength ratio assessment makes use of the flexure formula-based Equation 7.20 for the CPGA-R computed *CBF* value for the tension pile.

Figure 7-13 CPGA-R results show that as the flood elevation rises, the demands in the shear and *CBF* limit states also rise. There is a sign change in the shear limit state due to a reverse in direction in this force internal to the tension pile at flood EL 829 ft. Additionally, the axial load sign changes from positive in compression to negative in tension above flood EL 836 ft (negative sign not shown in this figure). Below flood EL 836 ft, the pile is in compression under axial loading while at and above this elevation, the

pile is in tension. The axial Limit State 9 strength mobilization factor is quite low, less than 0.004 for all flood elevations considered. In lower to moderate flood elevations, the weight of water over the *wet portion* of base slab above the *tension* pile dominates its axial loading. It is only when flood elevations reach EL 836 ft and above does this Figure 7-1 left pile revert into a tension pile due to the action of the lateral water pressure force acting on the stem of the wall, counteracting the moment due to the weight of the water acting over the wet portion of the base slab.

With a flood elevation reaching the top of the stem of the T-Wall at EL 836.9 ft, all three structural tension pile limit states possess mobilized strength ratio values that are well less than 1. These Figure 7-13 results show that the *CBF* is the most critical of the three structural limit states within the tension pile at all flood elevations. The *CBF* mobilized strength ratio reaches a maximum value of 0.24 while the ratios for shear and for axial force loadings achieve lower mobilized, maximum strength ratio values of 0.06 and 0.004, respectively. Additionally, these three structural pile limit states mobilize less of their respective structural pile capacities when compared to those of the compression pile (Figure 7-12). The SSI-based Limit State 4 is less than unity because the length of the tension pile was arbitrarily set equal to the length of the compression pile in this design. Recall that it was the compression pile in Limit State 3, not the tension pile, that was optimized during the CPGA-R analyses to possess a limiting *ALF* value of 1/1.7 = 0.59 during the SSI-based limit state deterministic design process.

Table 7-3 summarizes the mobilized strength ratios for the 10 limit states of the Figure 7-1 example problem with 40 ft long tension and compression batter piles and with 4 ft section width. The limit states are ranked for criticality in the fifth column. Note that the primary failure mechanism for this structure is the SSI Limit State 3, which occurs for the compression pile.

Table 7-3. Mobilized strength ratio computed for each of the 10 limit states in the deterministic T-Wall design with flood EL 836.9 ft for a pair of 40 ft long batter piles and section width of 4 ft.

Limit State Number	Limit State Description	Component	Mobilized Strength Ratio	Limit State Ranking Number
1	Horizontal stem shear	Reinforced concrete stem	0.58	3
2	Stem moment	Reinforced concrete stem	0.69	2
3	SSI	Compression pile	0.95	1
4	SSI	Tension pile	0.03	9
5	Horizontal shear	Compression pile	0.15	6
6	Axial compression	Compression pile	0.09	7
7	CBF	Compression pile	0.32	4
8	Horizontal shear	Tension pile	0.06	8
9	Axial tension	Tension pile	0.004	10
10	CBF	Tension pile	0.24	5

In summary, the four limit states (SSI Limit State 4; shear Limit State 8; axial Limit State 9; and *CBF* Limit State 10) of the tension pile were far from optimized during the deterministic design as demonstrated by a mobilized strength ratio of much less than 1.0 (Figure 7-13) for the prescribed 40 ft long HP 14 × 89 tension pile at the flood EL of 836.9 ft. This observation will have a direct impact on the computed *PUP* results for the individual limit states in the Reliability analysis of this batter pile-founded T-Wall flood mitigation structure to be discussed next. It is also recognized that in this deterministic design, allowable stresses were used to characterize the steel pile strengths in the six structural pile limit states. In the upcoming Reliability analysis, capacities will be assessed not based upon allowable stress but on ultimate strengths. The ultimate capacity is required to conduct a Reliability analysis. This change allows for a direct comparison of the demand to ultimate strength for the materials and the development of LRFD factors.

7.3.3 Reliability results for a section with 40 ft compression and tension piles

Reliability tests were performed for the ACE and the two 100-year Chance of Exceedance flood hazard curves for the Red River of the north example problem with 40 ft compression and tension piles to determine *PUP* values for each of the 10 limit states, as well as the system *PUP* value. Table 7-4 gives the results of these *PUP* computations with appropriate β equivalents. Notice that the *PUP* and β values for the ACE are annual values and that the 100-year simulation and MVP estimates are for 100-year probabilities. Recall that higher βs mean a lower probability that a limit state will be exceeded. β values of infinity mean that probabilities are approaching the limit of 0.0.

Table 7-4. Reliability results for 100,000 Monte Carlo simulation runs using three Chance of Exceedance curves for a 40 ft compression and tension batter pile-founded T-Wall.

Limit State Number	ACE		100-Year Simulation Values		MVP 100-Year Values	
	PUP_1	PUP_1	PUP_{100}	β_{100}	PUP_{100}	β_{100}
1	0.00035	3.389579	0.03529	1.808170	0.04364	1.709924
2	0.00149	2.969793	0.12222	1.163961	0.13796	1.089531
3	0.00023	3.503029	0.02634	1.937535	0.03540	1.806758
4	0.00000	infinity	0.00000	infinity	0.00129	3.013797
5	0.00000	infinity	0.00000	infinity	0.00000	infinity
6	0.00000	infinity	0.00000	infinity	0.00000	infinity
7	0.00000	infinity	0.00000	infinity	0.00003	4.012811
8	0.00000	infinity	0.00000	infinity	0.00000	infinity
9	0.00000	infinity	0.00000	infinity	0.00000	infinity
10	0.00000	infinity	0.00000	infinity	0.00000	6.190431
System	0.00149	2.969793	0.12280	1.161103	0.13856	1.086812

These Reliability results for both the annual as well as the two 100-year flood hazard analysis curves reveal that three limit states have a greater chance of failure than the others. Limit States 1, 2, and 3 (stem shear, stem moment, and compression pile SSI, respectively) have probabilities of failure with all three flood hazard Chance of Exceedances. The Limit State 4 and 10, 100-year β values for the MVP hazard curve are so high, especially when converted to annual values using Equation 2.69, that the probabilities are extremely small.

The system *PUP* for the annual Chance of Exceedance (flood) curve is equal to the *PUP* for the limit state that has the largest individual *PUP* of reinforced concrete stem moment Limit State 2. The system *PUP* for the other two Reliability analyses using 100-year flood hazard analysis curves is slightly higher than the maximum *PUP* of the largest individual limit states belonging to stem moment Limit State 2. Each of the three flood hazard Reliability analyses whose results are summarized in Table 7-4 possess system *PUP* values that are less than the sum of all 10 Limit State *PUP*s. Results from the three Reliability analysis underscore the observations of Fan et al. (2014), who indicated that determining individual load and resistance factors may not provide a sufficient PUP_{System} for the proposed lifetime of the structural and geotechnical pile system. Fan et al. (2014) based their inference on the fact that the probability areas of the combined limit states can be greater than the probability area of any individual limit state, and that the maximum probability of failure would be the sum of the probability areas of all the Limit States, given no overlap of the failure regions.

Table 7-4 reveals that the St. Paul District estimated 100-year flood hazard curve generates a very small number of failures for Limit State 4, 7, and 10. For probabilities at the extreme upper range of the St. Paul flood hazard curve of Figure 7-11, flood elevations that are greater than the maximum ACE flood hazard elevations can be generated. The authors believe that simulations in this extreme range are responsible for the measurable, but insignificant, *PUP* values possessed by Limit State 4, 7, and 10. These values are deemed insignificant because conversion of these *PUP* values using Equation 2.70 from a 100-year value to an annual value has an annual *PUP* less than 1.5×10^{-5}.

The 100-year simulated flood hazard curve is limited to the range of the ACE curve, because samples were chosen directly from the ACE curve. This limits the extreme flood hazard elevations that can be generated in the simulation process.

The system *PUP* for the Reliability analysis using the ACE flood hazard curve is equivalent to the LS#2 (Stem Moment) *PUP*. This indicates that the stem moment failure region in Gaussian space completely overlaps the other two failure regions for stem shear (LS#1) and compression pile SSI (LS#3). The authors of this report believe Limit States 1 and 2 are directly proportional to each other, with the only difference being the application

of a moment arm applied to the lateral force due to flood loading. This reveals that the failure region with the lower *PUP* will be completely overlapped by the other, higher Limit State's *PUP* region. The authors further observe that the compression pile SSI Limit State 3 is not linearly related to the first two limit states, since its applied force is propagated through a frame analysis. Nevertheless, it is clear from the system *PUP* and individual limit state *PUP* Reliability results that stem moment Limit State 2 appears to envelop the Limit State 3 *PUP* region for the ACE flood hazard curve.

The results of the 100-year flood hazard Reliability analyses indicate that the probability regions for our Limit States partially overlap, much like the Limit States in Figure 2.10. The annual flood hazard Reliability analysis does not reveal a partial overlap, but it does not rule it out the possibility of a partial overlap that woule require extreme precision to locate.

Table 7-5 shows the results of using Monte Carlo methods to compute the probability of unsatisfactory performance (*PUP*) for the 10 limit states of subsection 7.2.1. Three Limit States were engaged in the simulation runs: The Stem Shear Limit State LS#1, the Stem Moment Limit State LS#2, and the Compression Pile SSI Limit State LS#3. The results are for 100,000 simulation runs for the three flood elevation chance of exceedance distributions.

Table 7-5. Annual and 100 year *PUP* and β values for the primary limit states for 40 foot compression and tension batter pile founded T-Wall

Limit State Number		Simulation Flood Chance of Exceedance		
		Annual Chance of Exceedance	Simulated 100-Year Chance of Exceedance	St. Paul District Estimated 100-Year Chance of Exceedance
LS#1	PUP_1	0.00035	0.00035921	0.00044611
	β_1	3.389579	3.38244916	3.32247762
	PUP_{100}	0.0344005	0.03529	0.04364
	β_{100}	1.81972431	1.80817	1.709924
LS#2	PUP_1	0.00149	0.00130274	0.00148343
	β_1	2.969793	3.01081364	2.97114989
	PUP_{100}	0.13852661	0.12222	0.13796
	β_{100}	1.08696285	1.163961	1.089531
LS#3	PUP_1	0.00023	0.0002669	0.00036035
	β_1	3.503029	3.46320024	3.38157882
	PUP_{100}	0.0227401	0.02634	0.0354
	β_{100}	2.00018582	1.937535	1.806758

The annual values for *PUP* and β (PUP_1 and β_1, respectively) and the 100-year value of *PUP* and β (PUP_{100} and β_{100}, respectively) are presented for comparisons. The values are computed from Equations 2.69 and 2.70 where they are needed, because the flood level ACE distribution computes the PUP_1 values and the 100-year Chance of Exceedance distributions compute PUP_{100} values.

The results show consistency among the three chance of exceedance distributions for simulation. The values for *PUP*, both directly simulated or computed with Equations 2.69 and 2.70, have little variation. Because the Simulated 100-year Chance of Exceedance distribution was directly drawn from the ACE, those values are minutely closer than the comparison of the St. Paul District Estimated 100-year Chance of Exceedance to the ACE, which allows for more extreme flood elevations. Also, recall that the ACE flood hazard curve results in Limit State 2 (Stem Moment) probabilities that completely overlap the other failure regions. For these reasons and after careful assessment of these three sets of computed Reliability results, the authors of this technical report prefer to use the Simulated 100-year Chance of Exceedance for LRFD factor computation. The 100-year flood Figure 7-10 PDF provides for more

density in the upper flood EL's than does the the ACE based Figure 7-9 PDF. This distinction gives the authors of this technical report more confidence that the extreme EL flood events will be more fully represented in Reliability simulations being conducted.

7.3.4 Computing Load and Resistance Factors for a section with 40-ft compression and tension piles

A procedure for deriving load and resistance factors from individual simulation runs for a target β has been developed and is described in Section 2.8 (Ebeling and White 2021). This procedure takes the load and resistance distributions (with correlation) and determines the scale factor (R_{SF}) that must be applied to the resistance values to obtain the target β, keeping the same loads. For ultimate capacity, the scaled mean resistance is equivalent to the mean design load. This design load is the mean load multiplied by a scale factor (L_{SF}). This L_{SF} is the LRFD load factor γ divided by the LRFD resistance factor ϕ.

Ellingwood recommended annual β_{Target} values of 3.5 and 4.0 for single path non-critical and critical reinforced concrete and steel hydraulic structures with 100-year design life, respectively. These β_{Target} values correspond to PUP_{Target} values of 0.000233 and 0.000032. The selection of these values sets a return period (in years) of unsatisfactory performance conditions at approximately 4,300 years and 31,570 years. For simulations based on years using the ACE values for flood levels and wind speeds, these target values are appropriate. But the ACE values provide very unsatisfactory load distributions for simulations because the same load, with flood levels below the wall, is applied a preponderance of the time. This is shown in Figure 7-9 PDF distribution of the ACE curve, where the greater part of the flood EL PDF is below the gray line indicating the base slab elevation at the heel of the T-Wall. 100-year flood events have more variation in loading and should provide better load distributions for comparison against the resistance distributions. The Figure 7-10 PDF distribution of the 100-year chance of exceedance curve shows that no flood elevations will be drawn below the gray line indicating the base slab elevation at the heel of the T-Wall.

7.3.4.1 Conversion of flood hazard annual exceedance values to 100-year exceedance values

For simulations based on 100-year chance of exceedance values, the annual β_{Target} values must be adjusted to 100-year β_{Target} values. Because the β_{Target} values represent annual return periods based on PUP_{Target} values, Equation 2.69 can be used to derive the 100-year values. These values are shown in Table 7-6. To determine the Load and Resistance Factors for annual return periods when 100-year variable are used, resulting in 100-year load and resistance distributions for the individual load states, substitute the 100-year target values into the Ebeling and White (2021) algorithm. The 100-year values will have a lower β values than the annual values. This reflects the longer time of hazard exposure.

Table 7-6. Conversion of annual β_{Target} to 100 year β_{Target}.

Annual		100-Year	
$\beta_{Target1}$	$PUP_{Target1}$	$PUP_{Target100}$	$\beta_{Target100}$
3	0.001350	0.126355	1.143792
3.5	0.000233	0.022997	1.995447
4	0.000032	0.003162	2.730474

7.3.4.2 Propagation of an externally applied deterministic design load to individual Limit State loads within structural members

To generate load and resistance factors for the designed structure, it is necessary to see how the initial design load is propagated to each of the limit state members. Following the design procedure used by St. Paul District, the initial design load is defined as the 750 year flood event (Figure 3-1 Load Category versus Return Period in EM 1110-2-2104 (HQUSACE 2016) of a hydrostatic flood level to the top of the T-Wall. Hydrostatic pressures are computed for this flood level and converted into forces and moments that are applied to the wall in the deterministic analysis. According to Table 3-1 in EM 1110-2-2104 (HQUSACE 2016), a load factor, henceforth referred to as the Global Load Factor (GLF or γ_G) will be applied to the hydrostatic pressures for computation of these forces. For the stem limit states of the structure, the flood pressures can be directly computed and converted to force and moments. The external flood force and moments translate directly to internally applied shear and moment within the reinforced concrete stem. Therefore, the Global Load Factor will scale for the internal applied stem shear and moment directly. For the limit states applied at the piles, the forces and moments need to be

analyzed using CPGA-R, which performs a frame analysis, propagating the deterministic load conditions on the structure to the loads applied at the individual limit states. Table 7-7 shows the computed propagated limit state forces, moments, and stresses for the 10 limit states, given the deterministic design load conditions, GLFs, and properties of the example T-Wall structure with 40 ft tension and compression piles. The GLF=1.3 propagated load values are used to establish the local resistance factors. Note that although the conditions of the design load do not change with design choices, the propagation to the individual limit states does change.

Table 7-7. Deterministic Design Load propagation to individual Limit States.

Limit State	GLF = 1.0	GLF = 1.3
LS#1 (Stem Shear in lb)	24,113	31,346
LS#2 (Stem Moment in ft-lb)	111,722	145,238
LS#3 (Compression Pile SSI in lb)	56,800	69,600
LS#4 (Tension Pile SSI in lb)	-2,300	-6,500
LS#5 (Compression Pile Shear in lb)	22,300	28,100
LS#6 (Compression Pile Axial in lb)	56,800	69,600
LS#7 (Compression Pile Flexure in lb-in^2)	15,959	20,521
LS#8 (Tension Pile Shear in lb)	9,200	12,900
LS#9 (Tension Pile Axial in lb)	-2,300	-6,500
LS#10 (Tension Pile Flexure in lb-in^2)	11,960	15,879

To see the effects of load propagation with different GLF values, a comparison of propagated loads is made. For Limit State 1, where there is no frame action, the ratio of the stem shears for the GLF=1.3 and GLF=1.0 is given as 31,346/24,113 = 1.3. Limit State 3 and 4 loads, which have an axial force acting on the compression pile and tension piles, respectively, subject to frame action. The Limit State 3 ratio of the loads using GLF=1.3 and GLF=1.0 is 69,600/56,800=1.23, which is less than γ_G. On the other leg of the frame, the Limit State 4 ratio of the loads using GLF=1.3 and GLF=1.0 is -6,500/-2,300=2.83, which is greater than γ_G. This reveals that the propagation of global forces and moments to local forces and moments is affected by frame action.

7.3.4.3 Computation of local member resistance factors ϕ_L using γ_G scaled deterministic design load propagated to Limit State loads and Reliability simulation results

Without applying load factors, Reliability based simulations provide *PUP* values that correspond to site-specific variable distributions. A scale factor

(R_{SF}) can be computed from simulation results using the procedure outlined in Section 2.8 and applied to the resulting reliability distribution such that the calculated *PUP* will match PUP_{Target}. Figures 7-14 through 7-16 show the effects of this scaling procedure using SSI Limit State 3 Reliability analysis results as an example. These figures use data from the 100-year simulated Flood Hazard simulations of the Red River example problem with 40 ft compression and tension piles. Figure 7-14 shows the original distributions of resistance (R) in green and load (L) in red. Additionally, the distribution of the values when each sample's load is subtracted from the resistance (R-L) is shown in gray. Any values of the R-L curve that are less than zero on the horizontal axis are in failure, as indicated by the blue line and the Failure Region indicator. The equivalent annual β for this Limit State can be found in Table 7-5 and equals 3.47053574.

Figure 7-14. Resulting Load (L) and Resistance (R) Curves for SSI Limit State 3 from Reliability Analysis and computed (R-L) curve.

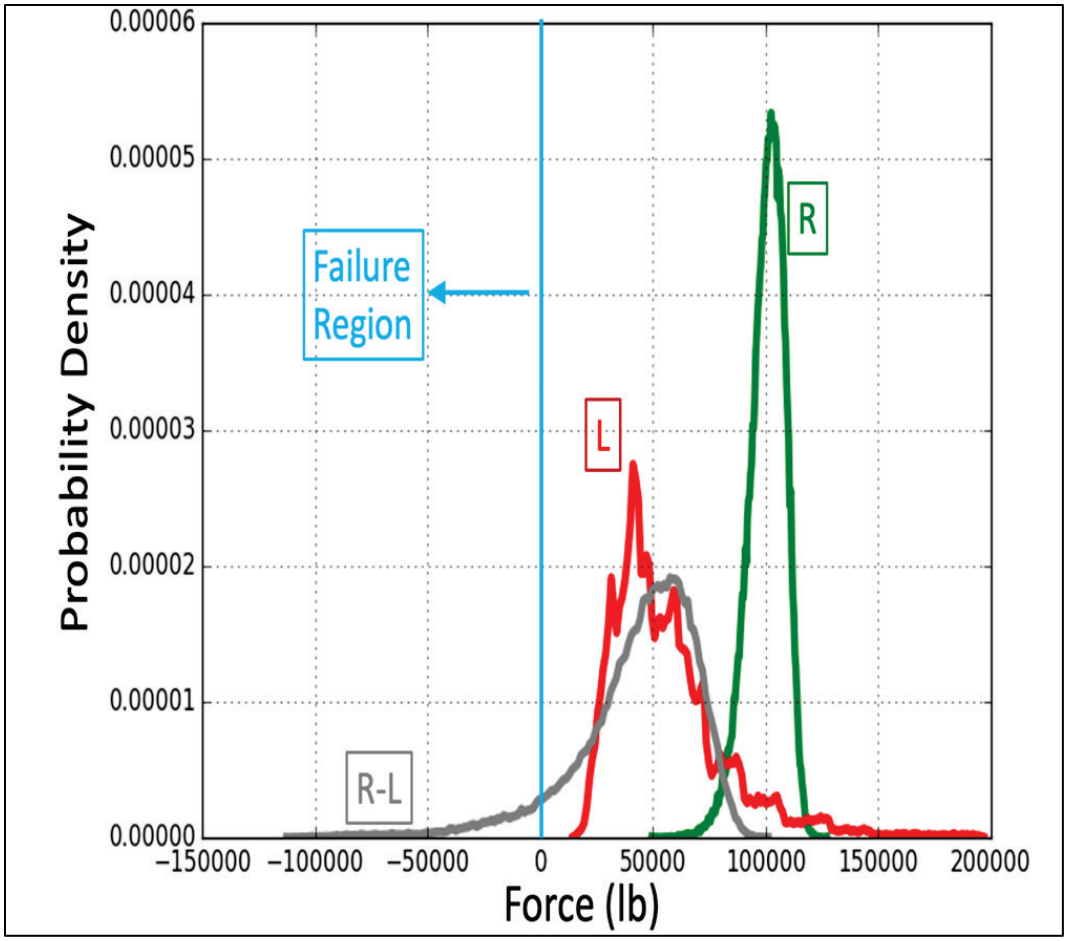

Figure 7-15. Fixed Load (L) and Scaled Resistance (R) Curves for SSI Limit State 3 for β_{target}=3.5 and computed (R-L) curve (R_{SF} = 1.283210).

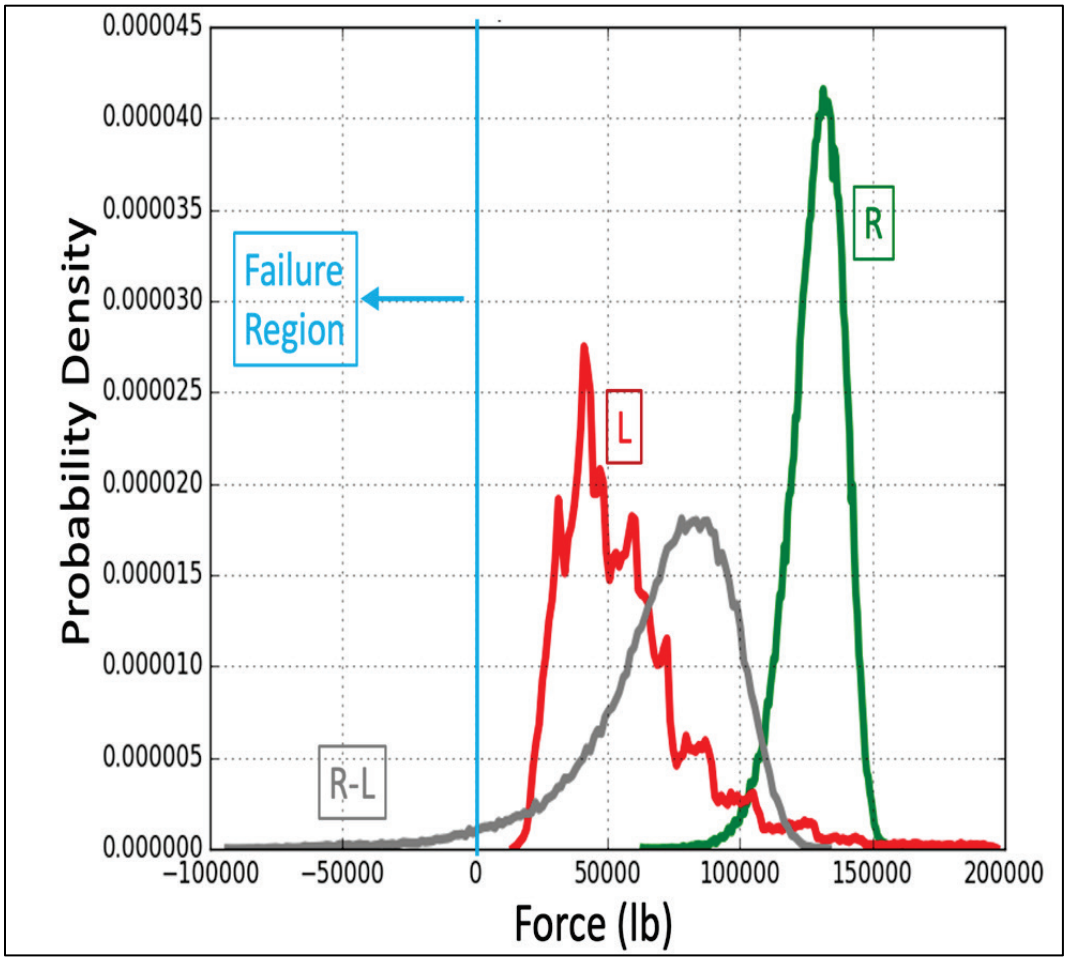

Figure 7-16. Fixed Load (L) and Scaled Resistance (R) Curves for SSI Limit State 3 for β_{target}=4.0 and computed (R-L) curve (R_{SF} = 1.792815).

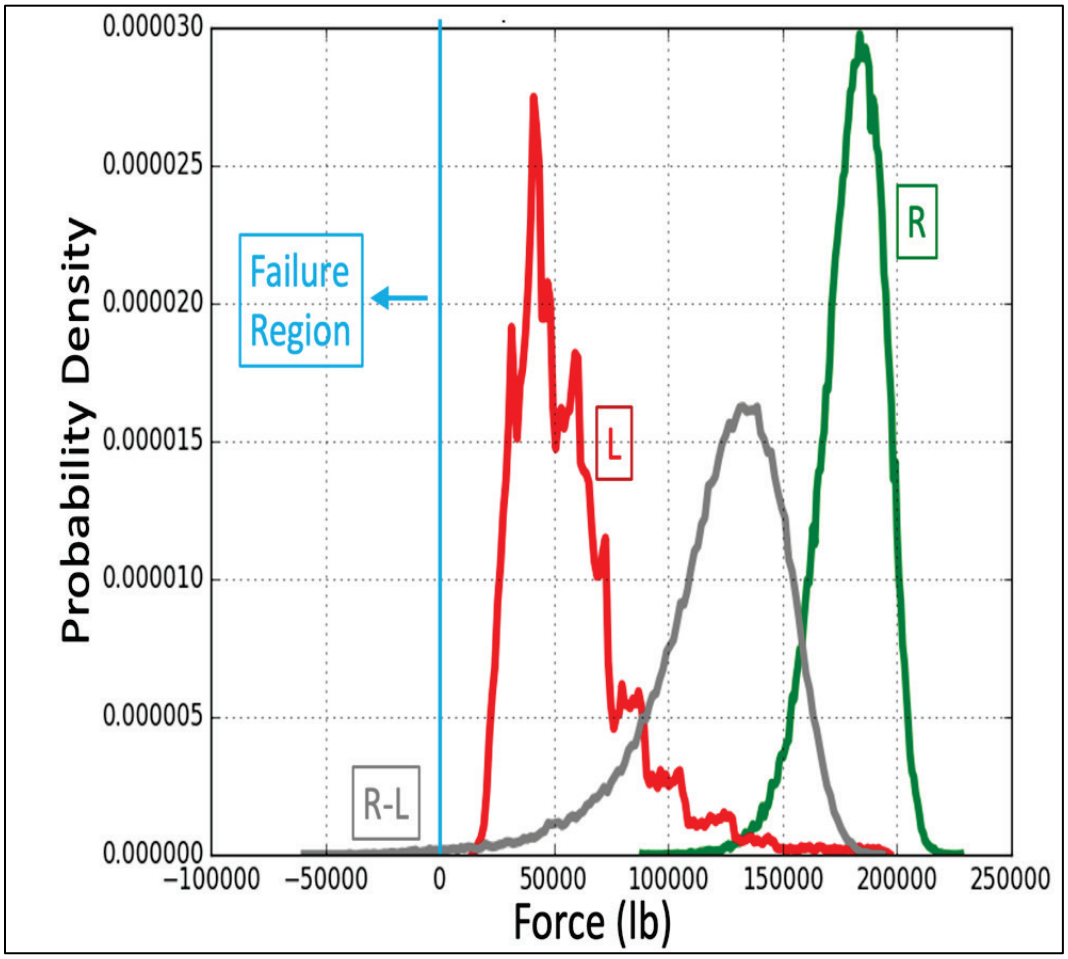

Figures 7-15 and 7-16 show the effects of using the RSF values of 1.283210 for a β_{target} of 3.5 and 1.792815 for a β_{target} of 4.0, respectively. The load curve stays the same for all three figures. While the area under the resistance curve remains the same (at 1.0), the peak probabilities of the curve become lower as an effect of scaling. Other effects are that the resistance distribution moves toward more positive values and the range of values grow greater. These last two effects are responsible for the movement and broadening of the range for the (R-L) curve, which causes the area of the (R-L) curve in the Failure Region to become less. This area is the same as the *PUP* value, and reducing the *PUP* value increases the β values.

Multiplying R_{SF} times the mean Resistance gives the target resistance, which should equal the target design load. This target design load is equal to the initial design load multiplied by a load scale factor (L_{SF}). The initial design load is specified by the condition whereby the flood elevation has

reached the top of the wall with an already applied global load factor, γ_G, of 1.3 (EM 1110-2-2104) (HQUSACE 2016), and propagated to the individual member's limit states. The target design load is divided by the initial design load to retrieve the L_{SF} value.

$$R_{sf} * \mu_{Resistance} - L_{SF} * d_{Load} = 0.0 \quad \text{(2.60 bis)}$$

$$L_{SF} = \frac{\mu_{Resistance} * R_{SF}}{d_{Load}} \quad \text{(2.61 bis)}$$

The L_{SF} is typically the local member load factor γ_L divided by the local member resistance factor ϕ_L.

$$L_{SF} = \frac{\gamma_L}{\phi_L} \quad (7.1)$$

This changes when the initial limit state load is derived from the scaled global load (i.e., GLF>1.0). At this point, the propagated Limit State load has been affected by the GLF and the local load factor γ_L is assigned a value of 1.0. This redefines the L_{SF} as

$$L_{SF} = \frac{1.0}{\phi_L} \quad (7.2)$$

For the T-Wall design with the 40 ft tension and compression piles, Limit State 1 (Stem Shear), Limit State 2 (Stem Moment), and Limit State 3 (Compression Pile SSI) are the primary failure mechanisms. Therefore Table 7-8 focuses on summarizing results for these three dominant limit states.

Table 7-8. Computation of local resistance factor (ϕ_L).

Limit State	Target	Flood Hazard	Resistance		Design Load (GLF= 1.3)	L_{SF}	
			Mean (from sims)	R_{SF}			
LS#1	3	ACE	50,142	0.669743	31,346	1.071341	0.93341
		S100	50,107	0.660672		1.056093	0.946886
		StPaul	50,156	0.685453		1.096777	0.911762
	3.5	ACE	50,142	1.124777		1.799227	0.555794
		S100	50,107	1.114492		1.78153	0.561315
		StPaul	50,156	1.198641		1.917917	0.521399
	4	ACE	50,142	1.588533		2.541065	0.393536
		S100	50,107	1.627689		2.601883	0.384337
		StPaul	50,156	1.953535		3.125806	0.319918
LS#2	3	ACE	180,931	1.041896	145,238	1.297947	0.770447
		S100	180,849	0.984926		1.226421	0.815381
		StPaul	180,568	1.043365		1.29717	0.770909
	3.5	ACE	180,931	1.637695		2.040167	0.490156
		S100	180,849	1.79653		2.237022	0.447023
		StPaul	180,568	1.964823		2.442778	0.40937
	4	ACE	180,931	2.680816		3.339641	0.299433
		S100	180,849	2.749278		3.423375	0.292109
		StPaul	180,568	3.336968		4.148705	0.241039
LS#3	3	ACE	100,507	0.702643	69,600	1.014663	0.985549
		S100	100,459	0.68299		0.985812	1.014393
		StPaul	100,477	0.705056		1.017844	0.982469
	3.5	ACE	100,507	0.990202		1.429917	0.699341
		S100	100,459	1.025439		1.480094	0.675633
		StPaul	100,477	1.098491		1.58582	0.630589
	4	ACE	100,507	1.479547		2.136564	0.468041
		S100	100,459	1.424176		2.055622	0.486471
		StPaul	100,477	1.657436		2.392733	0.417932

The rows of Table 7-8 are broken into sections based on Limit State, β_{Target}, and the Flood Hazard Chance of Exceedance distributions used. The mean resistance for each limit state set of simulations is recorded, and finally, the scale factor required to scale the simulation limit state resistance values by to achieve the β_{Target} with respect to the simulation limit state load values (R_{SF}). The limit state design load, with respect to the scaled global design load is presented next. The next column has the load scale factor (L_{SF}) that would need to be applied to the initial design load to establish an equivalence with the mean simulated resistance value times the values in the R_{SF} column. The final column reveals the limit state resistance factor ϕ appropriate for the global load factor γ_G of 1.3. The β_{Target} values of 3.0, 3.5 and 4.0 are consistent with the Ellingwood recommendation.

For the stem shear limit state (LS#1), the ϕ values range from 0.912 to 0.947 for β_{Target} = 3, 0.521 to 0.561 for β_{Target} = 3.5, and 0.32 to 0.394 for β_{Target} = 4. For the stem moment limit state (LS#2), the ϕ values range from 0.77 to 0.815 for β_{Target} = 3, 0.409 to 0.49 for β_{Target} = 3.5, and 0.241 to 0.299 for β_{Target} = 4. For the compression pile SSI limit state (LS#3), the ϕ values range from 0.982 to 1.014 for β_{Target} = 3, 0.631 to 0.699 for β_{Target} = 3.5, and 0.418 to 0.486 for β_{Target} = 4.

For the compression pile SSI limit state (LS#3) with a β_{Target} = 3.5, computed ϕ values range from 0.631 to 0.699 using the three Red River of the North flood hazard characterizations. The Table 3-3 AASHTO Nominal Bearing Resistance of Single Pile—Static Analysis Methods, φ_{stat}, values are in the range of 0.4 to 0.5. Thus 0.631 to 0.699 computed range in resistance factor is higher than the comparable AASHTO factor value range. The Reliability based 2014 Canadian Highway Bridge Design Code, as described in Fenton et al. (2016), reports compression resistance factor values for deep foundations of 0.4 and 0.45 for static analysis of soil foundations with typical and high degrees of understanding, respectively. After making a Reliability assessment, Fenton et al. (2014) conclude that the the target lifetime reliability index is approximately 3.5. The authors of this technical report conclude that both Reliability based codes provide for a consistent deep foundation, single compression pile resistance factor recommendation.

The AASHTO, Fenton et al. (2016) 2014 Canadian Highway Bridge Design Code and the ERDC T-Wall Reliability/LRFD factor analysis all provide

for ϕ values well less than 1.0. A ϕ value that is not close to 1.0 is a logical outcome for a compression pile foundation feature in the view of the authors of this technical report.

Last, it is important to recognize that the AASHTO Table 3-3 and Canadian Bridge code ϕ values reflect compilation and assessment of numerous pile foundation case studies, their resulting interpretation of group-data and subsequent committee judgement for recommended code specification. In contrast, the ϕ value computed for the compression pile SSI limit state (LS#3) reflects a single batter pile founded flood mitigation T-Wall result for the Red River of the North flood hazard.

7.3.5 Searching for Optimal Pile Lengths for the Red River of the North site, in Grand Forks, North Dakota

The 40 ft compression and 40 ft tension pile Example problem was almost designed for optimal SSI resistance for the compression pile (LS #3) with a mobilized strength ratio of 95%, or an axial load factor (ALF from CPGA-R) of 0.56 of the 0.59 deterministic limit. Table 7-9 shows the results of investigating pile lengths to find the maximum ALF and combined bending factor (CBF) for the compression and tension piles of the batter pile founded T-Wall design.

Table 7-9. Deterministic assessment for different compression (C) and tension (T) pile lengths for the Red River of the North example problem.

C Pile Length (ft)	T Pile Length (ft)	C Pile C_{33}	T Pile C_{33}	C Pile ALF	T Pile ALF	C Pile CBF	T Pile CBF
40	40	1.257	0.615	0.56	0.02	0.32	0.24
30	30	0.371	0.327	0.82	0.03	0.31	0.23
50	5	0.960	0.01	0.44	0.32	0.32	0.23
38	5	0.937	0.01	0.6	0.34	0.32	0.23
38	5	0.937	0.1	0.6	0.37	0.33	0.23
39	5	1.099	0.01	0.58	0.35	0.33	0.23
39	5	1.099	0.1	0.58	0.38	0.33	0.24

The effect that pile length has on the C_{33} term is revealed in the compression pile C_{33} terms, especially for the 30 ft compression pile length. The value of C_{33} increases from a value of 0.371 for the 30 ft compression pile length to a maximum value of 1.257 for the 40 ft

compression pile length, and then down to a value of 0.960 for the 50 ft compression pile length. This illustrates the non-linearity of the soil interactions with the compression pile as the pile length increases.

For the investigation and semi-optimization, the initial design with 40 ft compression and tension piles gave a nearly optimal ALF value (as compared to the inverse of the deterministic design FoS of 1.7, 0.59) for the compression pile. The tension pile had a very much smaller ALF value, which suggests that shortening the pile length could maximize the ALF value. The CBF values, which are normalized to 1, have values less than 0.32, suggesting that they are overdesigned by a factor of 2/3.

A second run documented in Table 7-9 with both piles shortened to 30 ft reveals that shortening the compression pile has a large effect on the ALF, but that the tension pile is still too long. The CBFs did not change for either pile.

For the third run, the length of the compression pile was made 10 ft longer than the original (40-ft.) length, since the tension pile was reduced to a minimum length of 5 ft, based on the ratio of the ALF to the target ALF of 0.59. The compression pile was lengthened to counter the assumed effects of frame action with the significantly reduced tension pile length. The ALF results reveal that the compression pile was now overdesigned, and that the tension pile was still overdesigned, but less overdesigned than before.

The compression pile length then was reduced to 38 ft based on the ratio of ALF values for the fourth run and fifth run. The tension pile length was kept at the minimum 5 ft. For the fourth run, the C33 term for the tension pile was set to a very small value of 0.01. The ALF for the compression pile of 0.6 just exceeded its limit of 0.59, but the tension pile ALF increased by only 0.02, which reveals that frame action has a minor contribution to the SSI Limit State mobilized strength ratios.

Based upon insight gained during these and previous analyses, the minimum recommened C33 term for the tension pile was increased to 0.1 for the fifth run. This change was deemed appropriate because it is apparent that the primary resistance for the T-Wall is in the compression pile. This action resulted in an increase in the SSI resistance of the tension pile, which in turn increased the load on the tension pile. This resulted in an increase in the ALF value of the tension pile by 0.03. It was presumed

that increase in tension pile load through frame action would increase the ALF of the compression pile, but the change was not noticeable to two decimal places.

The sixth and seventh runs increased the compression pile length by 1 ft, to 39 ft. The ALF of the compression pile reached a value of 0.58 or 98% of the target value. The runs were differentiated by the minimum C33 value assigned to the tension pile. These results were similar to the paired C33 tension pile value results of 38 ft compression pile runs 4 and 5, respectively, with the ALF at the tension pile being within 0.01 for the same C33 tension pile value runs (i.e., fourth and sixth; fifth and seventh).

For all seven Table 7-9 runs, the computed CBF values for the compression and tension piles had minor variations. It is assumed that the steel strength properties were much stronger than the soil strength properties, such that changes in soil loads would not be enough to mobilize the steel.

Based upon careful interpretation of the Table 7-9 results, the semi-optimized structure with HP 14 × 89 piles of 4:1 batter and loads and soil properties from the Red River of the North site was assigned a compression pile length of 39 ft and a tension pile length of 5 ft and given a minimum pile C33 value of 0.1.

Table 7-10 shows the new hierarchy of failure mechanisms based on the mobilized strength ratios for Table 7-9 run #7. These Mobiliized Strength Ratio values were computed from a deterministic analysis. Because they do not take variability into account, these strengths only provide an assessment of the mean capability of the batter pile-founded T-Wall. Observe that for the Table 7-9 run #7 batter pile foundation configuration of a 39 ft long compression pile and a 5 ft long tension pile and assigned C_{33} values, SSI tension pile Limit State 4 is now ranked third among the top-four active limit states.

Table 7-10. Mobilized strength ratio computed for each of the 10 limit states in the deterministic T-Wall design with flood EL 836.9 ft. for a 39 ft long compression and 5 ft long tension batter piles and section width of 4 ft.

Limit State Number	Limit State Description	Component	Mobilized Strength Ratio	Limit State Ranking Number
1	Horizontal stem shear	Reinforced concrete stem	0.58	4
2	Stem moment	Reinforced concrete stem	0.69	2
3	SSI	Compression pile	0.98	1
4	SSI	Tension pile	0.64	3
5	Horizontal shear	Compression pile	0.16	7
6	Axial compression	Compression pile	0.09	8
7	CBF	Compression pile	0.33	5
8	Horizontal shear	Tension pile	0.06	9
9	Axial tension	Tension pile	0.003	10
10	CBF	Tension pile	0.24	6

Table 7-11 shows the complete results of simulations with the different chance of exceedance curves for the 39 ft compression and 5 ft tension pile Example Problem. For this pile length optimization problem, the Limit State that has the highest probability of failure is the tension pile SSI limit state, LS#4. Its values for *PUP*, both annual and 100-year values, are much higher than the other limit states.

Table 7-11. Reliability results for 100,000 Monte Carlo simulation runs using three chance of exceedance curves for a 39 ft compression and 5 ft tension batter piles founded T-Wall.

Limit State Number	ACE		100-Year Simulation Values		St. Paul 100-Year Values	
	PUP1	β1	PUP100	β100	PUP100	β100
1	0.00043	3.332725	0.03431	1.820914	0.04286	1.71842
2	0.00142	2.984545	0.11853	1.182367	0.13531	1.101636
3	0.0004	3.352795	0.03199	1.852319	0.04102	1.73897
4	0.0819	1.392404	0.19109	0.873887	0.21271	0.797053
5	0.00000	infinity	0.00000	infinity	0.00000	infinity

Limit State Number	ACE		100-Year Simulation Values		St. Paul 100-Year Values	
	PUP1	β1	PUP100	β100	PUP100	β100
6	0.00000	infinity	0.00000	infinity	0.00000	infinity
7	0.00000	infinity	0.00000	infinity	0.00001	4.264891
8	0.00000	infinity	0.00000	infinity	0.00000	infinity
9	0.00000	infinity	0.00000	infinity	0.00000	infinity
10	0.00000	infinity	0.00000	infinity	0*	6.361341
System	0.0819	1.392404	0.19173	0.871539	0.21318	0.795436

*Results are truncated for limited precision

At first glance, these results would appear to be in opposition to the deterministic design tension pile ALF value, which is below design criteria (0.38 < 0.59). However, because the tension pile is the same length as the scale of fluxuation (δ), the Variance Reduction Factor $\Gamma^2(L)$ is 1.0 by Equation 7.6 and Figure 7-3. A Variance Reduction Factor of 1.0 for the tension pile-results in a distribution of the undrained shear strength (S_u) used in assigning the SSI strength along the tension pile posesses a larger standard deviation than assigned for the SSI pile strength along the much longer compression pile. This greater variance increases the scaled variable search area and thus the chance that a random variate will cause the limit state resistance to be exceeded. The authors believe that the design criteria is set for long pile behavior and that shorter piles should use a different criteria.

The results of the other limit states have not seen a significant change in probabilities of unsatisfactory performance. This further leads to the conclusion that the material properties of steel in the pile are significantly stronger than the SSI occurring between the soil and the pile.

The Table 7-11 system values of *PUP* are close to the Limit State 4 values of *PUP*, but not exactly the same for the 100-year chance of exceedance curves. This indicates again that there is significant overlap of the failure regions, but that the overlap is not complete.

Table 7-12 shows the Equation 2.69 and 2.70 transformations of the *PUP*s and βs between the annual and 100-year values. The SSI tension pile Limit State 4 annal *PUP* value of 0.0819 corresponds to a 12.21-year return period. Converting this annual *PUP* value to a 100-year *PUP* value using Equation 2.69 gives a PUP_{100} of 0.9998 (corresponding to a β value of -

3.5). This means that unsatisfactory performance is virtually guaranteed over a 100-year time frame.

The individual *PUP* values show agreement between the different Chances of Exceedance for stem shear (Limit State 1), stem moment (Limit State 2), and compression pile SSI (Limit State 3). The same cannot be said for the tension pile SSI (Limit State 4). Under the ACE distribution, the return period was given as 12.21 years. The return period for the 100-year Chance of Exceedance from simulated values was 472 years. Finally, the return period for the 100-year Chance of Exceedance from the MVP estimate was 418 years. The authors believe that this disparity between the annual exceedance values and the 100-year exceedance values is a result of the greater spatial variance of the soil strengh that is assigned to a shorter pile when a variance reduction factor is nearly one based on the scale of fluctuation (5 ft.) for the soil.

Table 7-12. Annual and 100-year *PUP* and β values for the primary limit states for 39 ft compression and 5 ft tension batter pile founded T-Wall.

Limit State Number		Simulation Flood Chance of Exceedance		
		Annual Chance of Exceedance	Simulated 100-Year Chance of Exceedance	MVP Estimated 100-Year Chance of Exceedance
LS#1	PUP_1	0.00043	0.00034906	0.00043796
	β_1	3.332725	3.39031394	3.32761754
	PUP_{100}	0.04209747	0.03431	0.04286
	β_{100}	1.72684816	1.820914	1.71842
LS#2	PUP_1	0.00142	0.00126085	0.00145279
	β_1	2.984545	3.02072591	2.97755535
	PUP_{100}	0.1324663	0.11853	0.13531
	β_{100}	1.11480827	1.182367	1.101636
LS#3	PUP_1	0.0004	0.00032508	0.00041876
	β_1	3.352795	3.40978063	3.34008558
	PUP_{100}	0.03921825	0.03199	0.04102
	β_{100}	1.7598308	1.852319	1.73897
LS#4	PUP_1	0.0819	0.0021184	0.00238873
	β_1	1.392404	2.85996645	2.8216682
	PUP_{100}	0.99980546	0.1910	0.21271
	β_{100}	-3.5473882	0.873887	0.797053

7.3.6 Solving for the Red River of the north site, in Grand Forks, ND, using 39 ft compression and 10 ft tension piles

The mobilized strength ratio values suggest that the shorter the tension pile, the less that the pile is overdesigned using USACE criteria for the tension pile SSI Limit State 4. However, simulations with a 39 ft compression pile and 5 ft tension pile reveal that the unsatisfactory performance of the tension pile SSI Limit State 4 exceeds the target values for *PUP* because the spatial variability of the pile capacity from the distribution of soil strength with depth is based on the length of the pile. This suggests that there is a tension pile length (as a multiple of the vertical scale of fluctuation) that will reduce the variability of the soil interactions and provide consistency between the annual Chance of Exceedance values and the two 100-year Chance of Exceedance values. The vertical scale of fluctuation was established to be 5 ft, so a 10 ft tension pile length would reduce the variance of the soil structure interaction by half, using the Variance Reduction Factor Equation 7.6.

Therefore, the example problem was re-examined with a compression pile length of 39 ft and a tension pile length of 10 ft. Table 7-13 shows the computed C_{33} values and ALF and CBF for both piles based on a deterministic run. Notice that the tension pile C_{33} term is greater than the original minimum limit of 0.01 proposed by the authors but less than the 0.1 limit that was later adopted by the authors of this study.

Table 7-13. Deterministic assessment for 39 ft compression (C) and 10 ft tension (T) pile lengths for the Red River of the north example problem.

C Pile Length (ft)	T Pile Length (ft)	C Pile C_{33}	T Pile C_{33}	C Pile ALF	T Pile ALF	C Pile CBF	T Pile CBF
39	10	1.099	0.0145*	0.58	0.13	0.31	0.23

*Limited to a minimum value of 0.1 in the CPGA-R analyses.

With the new pile lengths, the mobilized strength ratios changed, as shown in Table 7-14. This changed the limit state rankings, which seems to indicate that frame action is affecting the results.

Table 7-14. Mobilized strength ratio computed for each of the 10 limit states in the deterministic T-Wall design with flood EL 836.9 ft. for a 39 ft long compression and 10 ft long tension batter piles and section width of 4 ft.

Limit State Number	Limit State Description	Component	Mobilized Strength Ratio	Limit State Ranking Number
1	Horizontal stem shear	Reinforced concrete stem	0.48	4
2	Stem moment	Reinforced concrete stem	0.62	2
3	SSI	Compression pile	0.98	1
4	SSI	Tension pile	0.22	7
5	Horizontal shear	Compression pile	0.15	8
6	Axial compression	Compression pile	0.58	3
7	CBF	Compression pile	0.31	5
8	Horizontal shear	Tension pile	0.07	10
9	Axial tension	Tension pile	0.13	9
10	CBF	Tension pile	0.23	6

Using 100,000 simulations with the variable distributions provides the correct interpretation of which limit states have the greatest probability of unsatisfactory performance. Table 7-15 lists the *PUP* and β values for the simulated runs with a 39 ft compression pile and 10 ft tension pile. The results indicate that the same four primary limit states are involved (although with different *PUP*s) as for the simulation runs for the 39 ft compression pile and 5 ft tension pile.

The primary difference in values for the 10 ft tension pile is in the much lower *PUP* values for Limit State 4, as compared to the results for the 5 ft tension pile. In fact, doubling the length of the tension pile from 5 ft to 10 ft reduced the Limit State 4 *PUP* from 0.0819 for the 5 ft tension pile to a value of 0.00095 for the 10 ft tension pile (Table 7-16). This is a significant reduction factor of 86. This indicates that the length of the pile and the variance reduction in pile capacity through reduced spatial soil strength variation with depth can play a very large part in the Reliability analysis of the structure that may not be indicated by a deterministic analysis.

As previously noted, the PUP_{System} is greater than any individual limit state *PUP* but less than the sum of the individual limit state *PUP*s. This still

indicates that the individual unsatisfactory regions overlap each other in the probability space.

Table 7-15. Reliability results for 100,000 Monte Carlo simulation runs using three Chance of Exceedance curves for a 39 ft compression and 15 ft tension batter piles founded T-Wall.

Limit State Number	ACE		100-Year Simulation Values		MVPI 100-Year Values	
	PUP_1	β_1	PUP_{100}	β_{100}	PUP_{100}	β_{100}
1	0.00040	3.352795	0.03425	1.821703	0.04311	1.715683
2	0.00146	2.976037	0.12136	1.168215	0.13603	1.098331
3	0.00032	3.414071	0.03041	1.874802	0.03892	1.763359
4	0.00111	3.059104	0.09204	1.328297	0.10361	1.261247
5	0.00000	infinity	0.00000	infinity	0.00000	infinity
6	0.00000	infinity	0.00000	infinity	0.00000	infinity
7	0.00000	infinity	0.00000	infinity	0.00003	4.012811
8	0.00000	infinity	0.00000	infinity	0.00000	infinity
9	0.00000	infinity	0.00000	infinity	0.00000	infinity
10	0.00000	infinity	0.00000	infinity	0*	6.190431
System	0.00160	2.947843	0.12555	1.147682	0.14126	1.074676

*Results are truncated for limited precision

Computing the *PUP*s and βs for different time periods using the binomial equations (Equations 2.69 and 2.70) shows another difference for Limit State 4 when comparing the runs with tension pile lengths of 5 ft versus 10 ft. With less variability, the 10 ft tension pile comparison between the ACE and the simulated and MVP-estimated Chance of Exceedance shows agreement between the values. This is preferrable to to the results of the 5 ft case because it provides confidence in the assigned value, especially when using the simulations to compute a resistance scale factor (R_{SF}).

Table 7-16. Annual and 100-year *PUP* and β values for the primary limit states for 39 ft compression and 10 ft tension batter pile-founded T-Wall.

Limit State Number		Simulation Flood Chance of Exceedance		
		Annual Chance of Exceedance	Simulated 100-Year Chance of Exceedance	MVP Estimated 100 Year Chance of Exceedance
LS#1	PUP_1	0.0004	0.00034844	0.00044057
	β_1	3.352795	3.390802	3.325961
	PUP_{100}	0.03921825	0.03425	0.04311
	β_{100}	1.759831	1.821703	1.715683
LS#2	PUP_1	0.00146	0.00129296	0.0014611
	β_1	2.976037	3.013101	2.975805
	PUP_{100}	0.13593448	0.12136	0.13603
	β_{100}	1.098769	1.168215	1.098331
LS#3	PUP_1	0.00032	0.00030877	0.0003969
	β_1	3.414071	3.42379	3.354949
	PUP_{100}	0.03149838	0.03041	0.03892
	β_{100}	1.859214	1.874802	1.763359
LS#4	PUP_1	0.00111	0.00096508	0.0010932
	β_1	3.059104	3.100772	3.06367
	PUP_{100}	0.10511642	0.09204	0.10361
	β_{100}	1.252925	1.328297	1.261247
System	PUP_1	0.0016	0.0013407	0.00152173
	β_1	2.947843	3.002081	2.963314
	PUP_{100}	0.14796539	0.12555	0.14126
	β_{100}	1.045199	1.147682	1.074676

The procedure using each simulation result can be used to determine the scale factor that must be applied to the resistances R_{SF} to achieve a PUP_{Target} for each limit state. The design load is propagated to each of the limit states so that the design load scale factor (L_{SF}) multiplied by the design loads will match the intended resistance. Table 7-17 lists the propagated loads for the Example T-Wall problem with a 39 ft compression pile and a 10 ft tension pile.

Table 7-17. Deterministic design load propagation to individual limit states.

Limit State	GLF = 1.0	GLF = 1.3
LS#1 (Stem Shear in lb)	24,113	31,346
LS#2 (Stem Moment in ft-lb)	111,722	145,238
LS#3 (Compression Pile SSI in lb)	56,300	68,600
LS#4 (Tension Pile SSI in lb)	-1,900	-5,600
LS#5 (Compression Pile Shear in lb)	22,100	28,000
LS#6 (Compression Pile Axial in lb)	56,300	68,600
LS#7 (Compression Pile Flexure in lb-in^2)	15,491	19,686
LS#8 (Tension Pile Shear in lb)	9,400	13,100
LS#9 (Tension Pile Axial in lb)	-1,900	-5,600
LS#10 (Tension Pile Flexure in lb-in^2)	11,711	15,105

The results of the computation of the individual limit state R_{SF} values given different β_{Target}'s are listed in Table 7-18. Observe that as the value of β_{Target} increases in value, the resistance factor ϕ decreases in value. Recall that these ϕ values are individual limit state values for the overall load factor γ of 1.3, using the propagated loads in Table 7-17.

Table 7-18. Computation of local resistance factor (ϕ_L) for a more optimized design using 39 ft compression pile and 10 ft tension pile.

Limit State		Flood Hazard	Resistance		Design Load (GLF= 1.3)	L_{SF}	ϕ_L (γ=1)
			Mean (from sims)				
LS#1	3	ACE	50,143	0.691325	31,346	1.10589	0.90425
		S100	50,167	0.658660		1.05414	0.94864
		MVP	50,094	0.682816		1.09121	0.91642
	3.5	ACE	50,143	1.131492		1.81000	0.55248
		S100	50,167	1.105847		1.76983	0.56503
		MVP	50,094	1.192782		1.90618	0.52461
	4	ACE	50,143	1.837281		2.93903	0.34025
		S100	50,167	1.611662		2.57935	0.38769
		MVP	50,094	1.988380		3.17763	0.31470

Limit State		Flood Hazard	Resistance		Design Load (GLF= 1.3)	L_{SF}	ϕ_L (γ=1)
			Mean (from sims)				
LS#2	3	ACE	180,820	1.045422	145,238	1.30154	0.76832
		S100	180,798	0.980642		1.22074	0.81917
		MVP	180,693	1.035685		1.28851	0.77609
	3.5	ACE	180,820	1.904659		2.37128	0.42171
		S100	180,798	1.793628		2.23278	0.44787
		MVP	180,693	1.955574		2.43296	0.41102
	4	ACE	180,820	3.101063		3.86080	0.25901
		S100	180,798	2.713224		3.37753	0.29607
		MVP	180,693	3.439550		4.27920	0.23369
LS#3	3	ACE	97,105	0.718224	68,600	1.01666	0.98361
		S100	97,046	0.702498		0.99380	1.00624
		MVP	97,092	0.723841		1.02448	0.97611
	3.5	ACE	97,105	1.084037		1.53448	0.65169
		S100	97,046	1.054756		1.49213	0.67018
		MVP	97,092	1.126445		1.59430	0.62724
	4	ACE	97,105	1.351170		1.91261	0.52284
		S100	97,046	1.446050		2.04568	0.48884
		MVP	97,092	1.733650		2.45370	0.40755
LS#4	3	ACE	22,218	0.799519	5,600	3.17209	0.31525
		S100	22,203	0.454423		1.80171	0.55503
		MVP	22,215	0.473349		1.87776	0.53255
	3.5	ACE	22,218	0.879569		3.48969	0.28656
		S100	22,203	0.542973		2.15279	0.46451
		MVP	22,215	0.559592		2.21988	0.45047
	4	ACE	22,218	1.066453		4.23115	0.23634
		S100	22,203	0.618399		2.45184	0.40786
		MVP	22,215	0.639550		2.53707	0.39416

Additionally, for a β_{Target} value of 3.5, observe the similarity in the three ϕ values for the 39 ft long compression pile SSI Limit State 3 of Table 7-18 with the three ϕ values for the 40 ft long compression pile compression pile Limit State 3 listed in Table 7-8. This same trend holds true for results computed using a β_{Target} value of 4.0. The authors of this report attribute the consistency to the fact that the pile lengths differ by only 1 ft. For the same size pile used in both analyses (i.e., A and E are constant), the pile cap axial deflections have an insignificant change, but the the C_{33} term (for SSI axial capacity) is based on the axial pile deflections divided by the pile length, which will minimize the differences between the piles even further.

The Design Load for Limit State LS#4 has a sign change from Table 7-17. The sign is only an indicator of the direction along the axis of the pile. Since the capacity is given as a positive value against the axial direction of the pile, the load is negated to match those values to provide a set of positive scale factors. This matches the results of the simulations.

For Limit States LS#3 and to a greater extent LS#4, the R_{SF}'s vary a bit between the annual Chance of Exceedance simulation values and the 100-year Chance of Exceedance simulation values. The authors suggest that these changes may be due to minor changes in distribution shape as the extreme values are more likely under the longer return periods. Since these extreme events are the cases when the unsatisfactory performance is likely to occur, it seems that the 100-year Chance of Exceedance values would provide more robust estimates of capacity for design that would be preferred.

7.4 Designing for the Red Wood River site in Marshall, MN

The second site explored using the pile group analysis methods of section 7.2 was the Red Wood River site in Marshall, MN. This site distributions are discussed in this chapter and in Appendix B for the wind-induced wave loading. The following subsections discuss the collection of variable data and design choices.

7.4.1 Design of the Red Wood River pile-founded T-Wall

The Red Wood River site T-Wall is similar to the Red River of the North site in Grand Forks, ND, but with minor differences. The first noticeable difference is the change in elevations. The top of wall elevation for the Red River of the North example is 836.9 ft, and the top of wall elevation for the

Red Wood River is 22.1 ft. These elevations must be maintained to be relative to water level distributions collected for the site. The base of the T-Wall has the same thickness and length from floodside to dry side. The height and thickness of the wall stem is the same for both T-Walls, as well as its placement on the base. The pair of supporting piles have the same position and the same batter as the Red River of the North site. The assumption of the lengths of the piles from the beginning has changed to a 10 ft tension pile and a 35 ft compression pile. All this is illustrated in Figure 7-17.

Figure 7-17. Initial design for the site-specific data for the Red Wood River site in Marshall, MN.

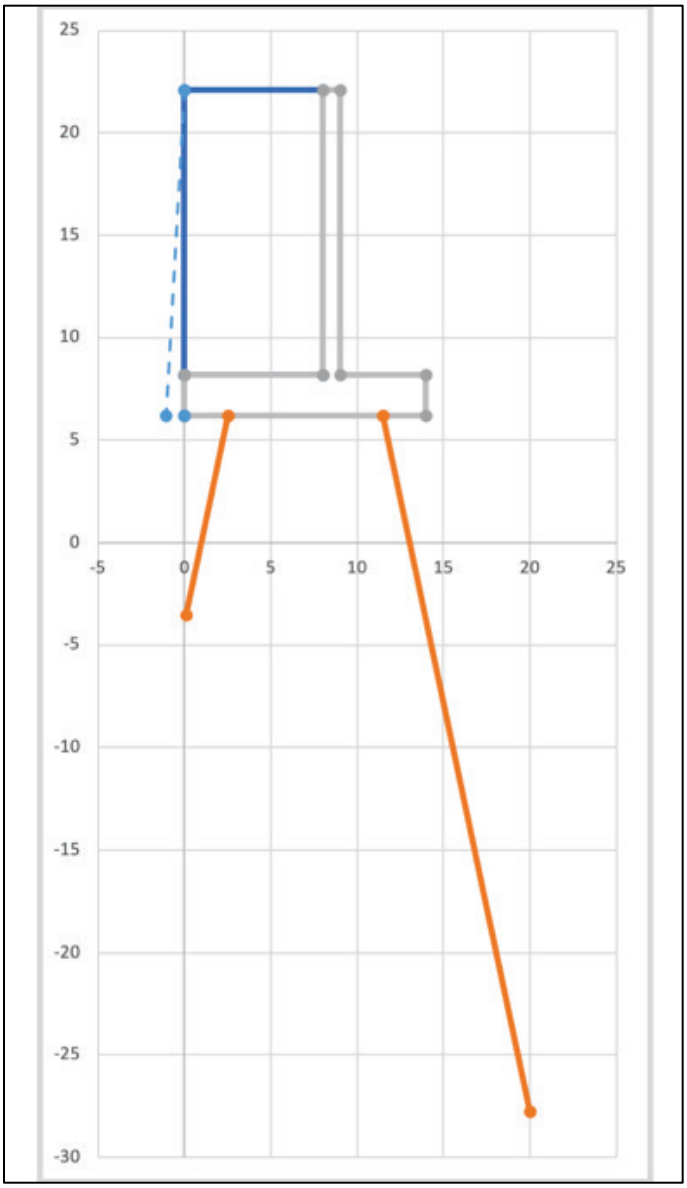

The initial estimate lengths of the piles are based on information from the previous site runs and the fact that the soil distribution was changed to reflect another site with more soil layers using SHANSEP. The distribution of S_u with depth was defined at this site using Equation 7.5 and by following the procedure outlined in subsection 7.2.6. The total unit weight of the soil was given as 122 pcf and $(S_u/\sigma'_{vo})_{NC}$ is set to 0.32. The SHANSEP-defined distribution of mean S_u with depth was assigned a COV_{point} of 0.4 based on Appendix D data which, when combined with the Variance Reduction Factor for a 35 ft compression pile and a vertical scale of fluction of 5 ft, Equations 7.6 and 7.7 result in a $COV_{Spatial}$ of 0.1512. Using the distribution of mean S_u with depth times this $COV_{Spatial}$ value, the standard deviation value is defined with depth. This same computational process is followed for the 10 ft long tension pile, maintaining a δ value to 5 ft. The resulting tension pile $COV_{Spatial}$ value equals 0.2828. Figures 7-18 and 7-19 show how the S_u varies with depth for the compression and tension piles, respectively. The tension pile distribution has a different standard deviation based on the variance reduction factor (VRF) defined by the pile's length and the scale of fluctuation (5 ft) in the soil (Equation 7.6).

Figure 7-18. Mean soil S_u properties with depth and distribution curves from -6σ to +6σ based on $COV_{Spatial}$ (for a 35 ft compression pile).

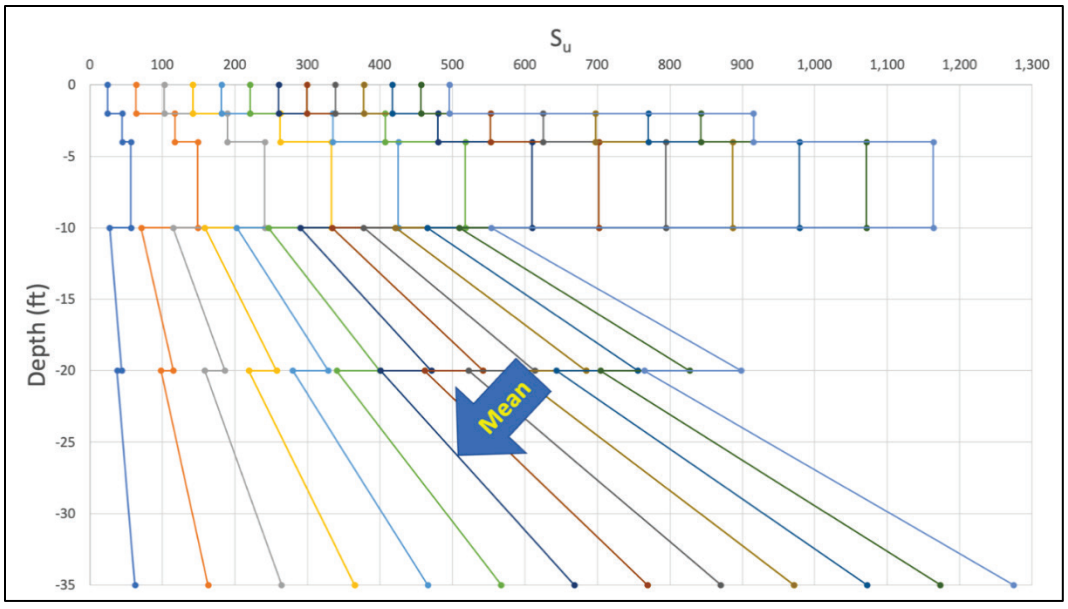

Figure 7-19. Mean soil S_u properties with depth and distribution curves from -6σ to +6σ based on $COV_{Spatial}$ (for a 10 ft piles).

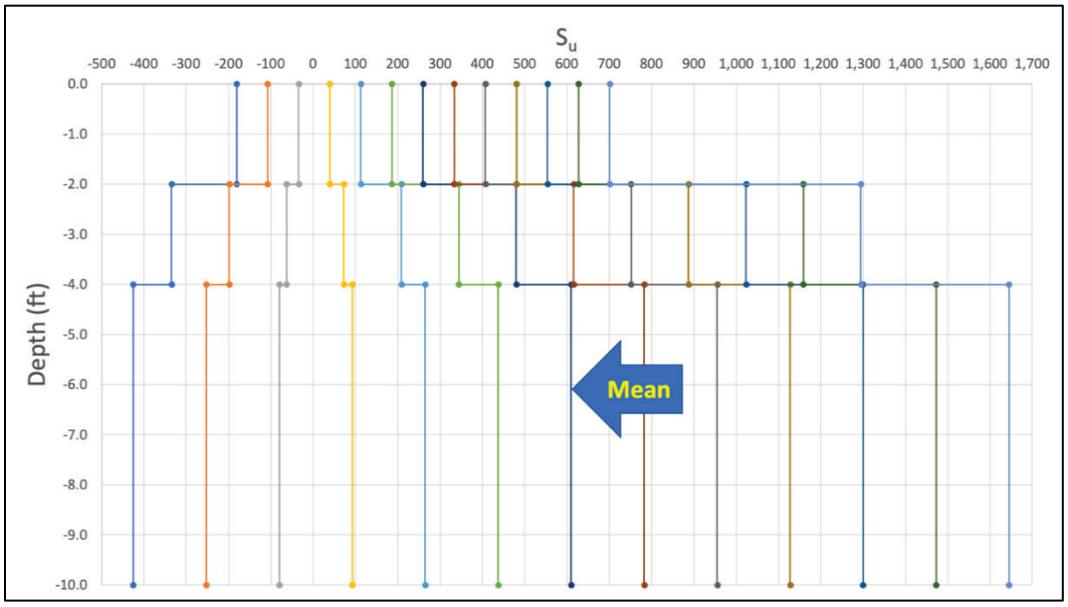

The values used for the overconsolidation ratios and full description of S_u distribution with depth using SHANSEP are shown in Figure 7-20. The upper 20 ft thick soil crust at the Red Wood River site posesses higher S_u values than the Red River of the North site with its 10 ft thick crust due to the higher assigned OCR ratios. Figure 7-21 shows a comparison of the soil site at the Red River of the north with the Red Wood River S_u characterization, as used in the software CAXPILE. Since CAXPILE has limited resources for dealing with continuous curves, the S_u characterization has been simplified. The comparison reveals that in the overconsolidated region of the soil, near the surface, the S_u values are higher.

Figure 7-20. Comparison of OCR and mean S_u soil properties for the Red River of the North with the Red Wood River characterization.

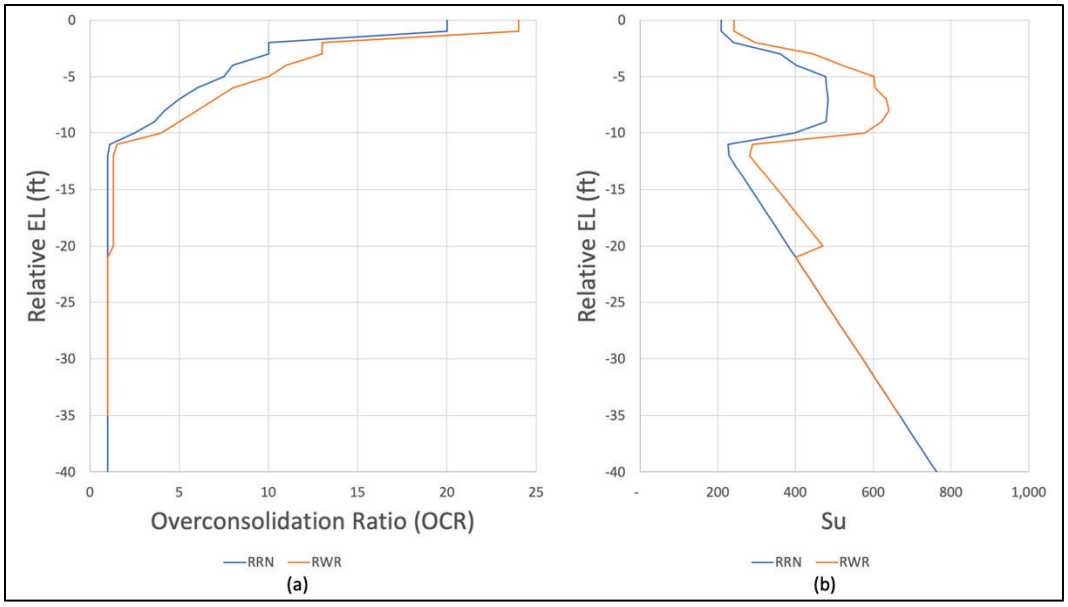

Figure 7-21. Comparison of mean S_u soil properties for the Red River of the North with the Red Wood River characterization: (a) compression piles, (b) tension piles.

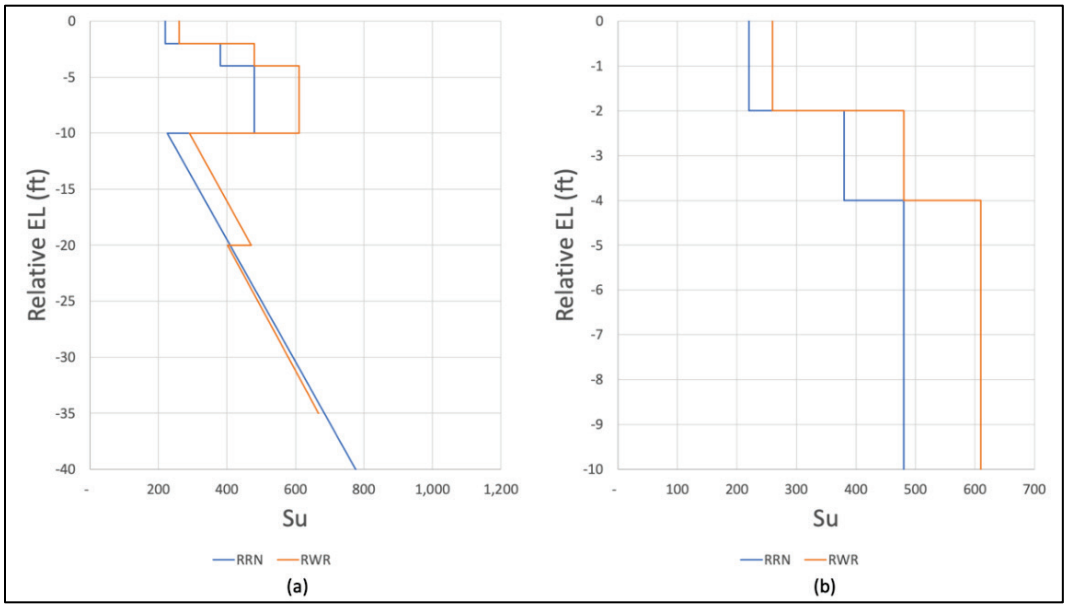

7.4.2 System variable distributions for the Red Wood River site in Marshall, MN

In a manner similar to Subsection 7.3.1, ACE values were collected for flood elevations at the Red Wood River site in Marshall, MN. These data are shown in Figure 7-22.

Figure 7-22. Collected ACE data for site-specific data for the Red Wood River site in Marshall, MN.

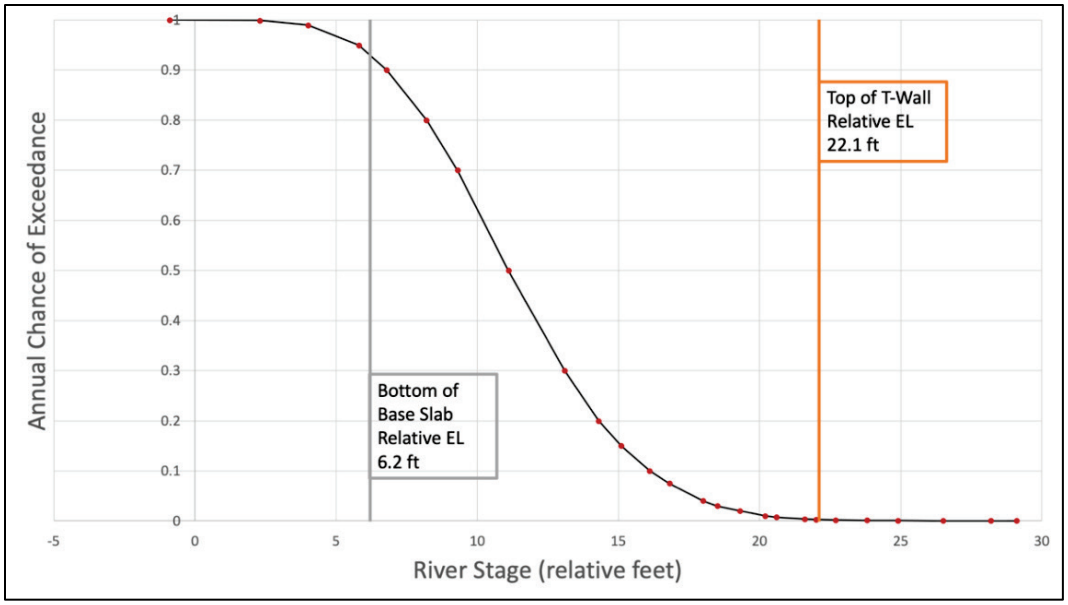

The computed PDF for the Red Wood River ACE is shown in Figure 7-23. Unlike the Red River of the north site, the majority of the distributed flood elevations are above the base of the wall. This means that on average, the wall will have some load applied.

Figure 7-23. PDF Histogram from the site-specific ACE data for the Red Wood River site in Marshall, MN, compared with simulated data from the ACE data.

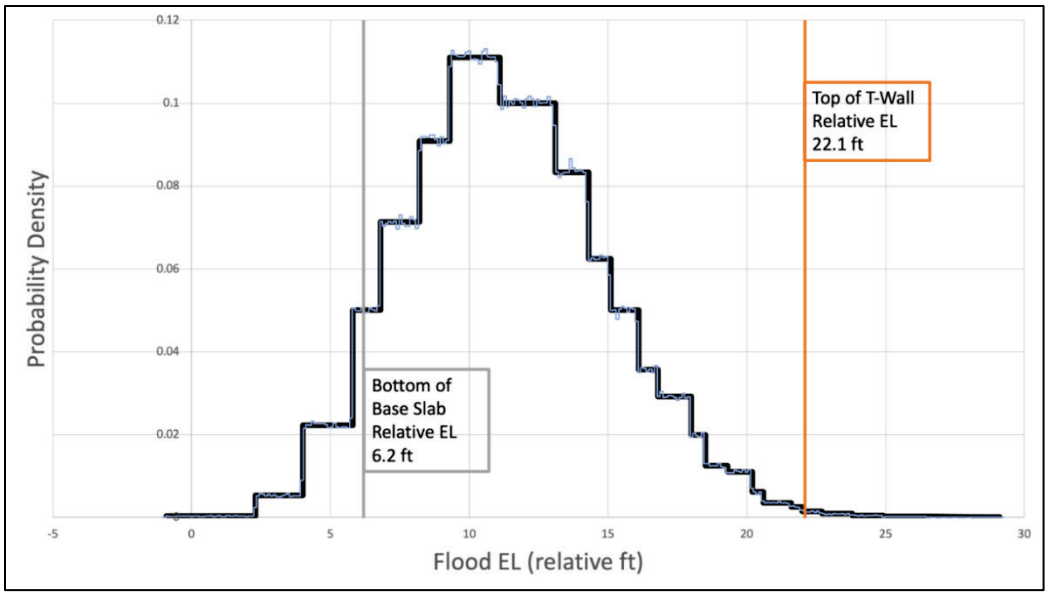

The 100-year values were recovered using simulation, as before. Figure 7-24 reveals the 100-year chance of exceedance computed in this fashion. This distribution reveals a high probability that the wall height will be exceeded.

Figure 7-24. PDF for 100-Year Chance of Exceedance values at Red Wood River site in Marshall, MN.

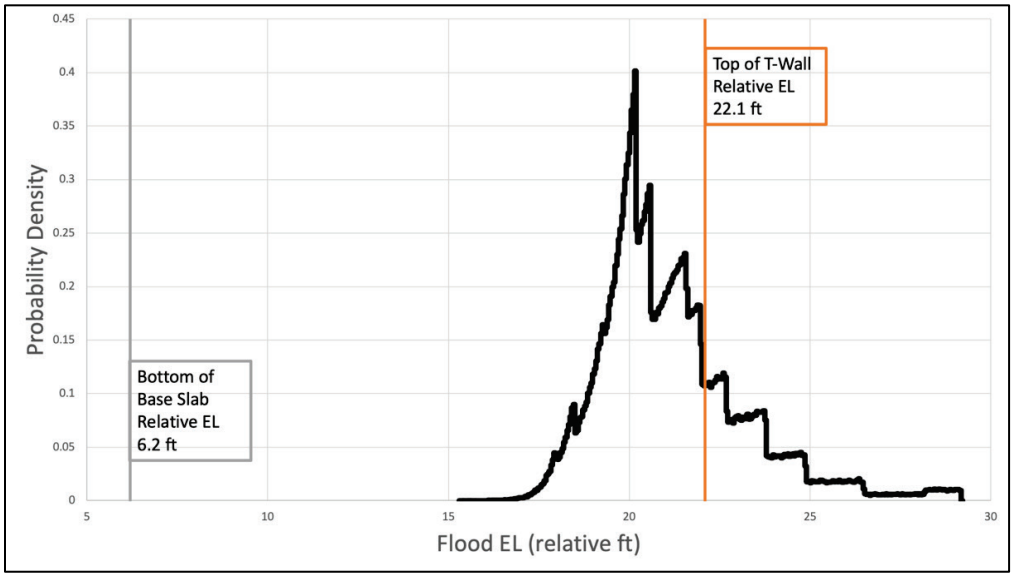

Processed wind-speed data are used in conjunction with the Goda (2010) method (Chapter 5) to generate wind-induced pseudo-static wave loading (Chapter 6). The site-specific wind data were obtained by collecting data from Marshall/Ryan Airport (MML), which is approximately 1 mile from the project at Marshall, MN, as discussed in Section B.2 of Appendix B. The data was fairly complete from 1984 to November 2020 with wind speeds and directions reported multiple times per hour between July 1996 and November 2020 and hourly from 1984 through June 1996. The range in these data was judged to be only representative of a relatively short time frame. This data were analyzed probabilistically using a Gumbel Type I distribution with Gringorten's (1963) Method to extrapolate to longer wind-speed return periods (Figure B.1-5). The winds speeds determined using the Gringorten's (1963) Method were based on a 100-year return period wind event occurring at the T-Wall. For the Red Wood River site, the data collected indicated a normal distribution with a mean 100-year wind return period wind speed of 59.0 mph and a standard deviation of 0.848 mph (Figure B.2-6). This distribution represents the variability of wind speeds only during a 100-year event and not the variability of wind speeds annually. Therefore, the value of *PUP* for each of the 10 limit states

is really the *PUP* during a 100-year wind event and is likely conservative for events that occur annually.

The Yield Stress (F_y) distribution for the HP steel piles is defined by data obtained from coupon tests conducted on steel specimens (Ellingwood). For ASTM A572 steel, which is assumed in this example, the yield stress has a nominal value of 50,000 psi. Based upon cited test result data, Ellingwood recommends the distribution for yield stress be modeled as a truncated log-normal with a mean value of 54,000 psi and a COV of 0.07. The standard deviation is 3,780 psi. The Dexter et al. (2000) and Bartlett et al. (2003) steel coupon test data suggest that this distribution be truncated at a minimum value of 49,500 psi and at a maximum value of 69,000 psi.

The reinforced concrete stem shear and stem moment capacity distributions are based on strength assessment for the Extreme Load Case value according to Table 3-1 and Figure 3-1 of EM 1110-2-2104 (HQUSACE 2016). For a deterministic design and the two stem limit states, the hydrostatic water pressures with a flood elevation to the top of the wall from the base of the stem are computed, and the lateral force and moment are captured at the base of the stem.

The reinforced concrete Stem Shear Capacity distribution is based upon a lognormal distribution according to the Table 5-4 information provided in Ellingwood and summarized in Chapter 4 of this report. The lognormal mean capacity value is defined in a deterministic analysis for a 750-year flood load to the top of the T-Wall by multiplying the peak hydrostatic lateral force for the 13.9 ft high triangular hydrostatic flood water pressure distribution acting on the reinforced concrete stem by the load factor γ of 1.3 and a bias factor of 1.2 according to Table 3-1 in EM 1110-2-2104 (HQUSACE 2016) and Table 5-4 in Ellingwood, respectively. Recall that the height of the reinforced concrete stem is 13.9 ft. The standard deviation is computed by multiplying the mean value by the COV_{Shear} value of 0.18. This value of COV is taken from Table 5-4 in Ellingwood.

The Stem Moment Capacity distribution also uses a lognormal distribution as recommended by Ellingwood (Chapter 4 of this report summarizes these Ellingwood data). The lognormal mean capacity value is defined in a deterministic analysis for a 750-year flood load to the top of the T-Wall by multiplying the peak hydrostatic lateral force for the 13.9 ft high triangular hydrostatic flood water pressure distribution acting on the reinforced

concrete stem by the load factor γ of 1.3 and a bias factor of 1.12 according to Table 3-1 in EM 1110-2-2104 (HQUSACE 2016) and Table 5-4 in Ellingwood, respectively. The standard deviation is computed by multiplying the mean moment capacity value by the COV_{Moment} value of 0.14. This value of COV is taken from Table 5-4 in Ellingwood.

7.4.3 Deterministic results for a Red Wood River T-Wall section with a 35 ft compression pile and a 10 ft tension pile

A deterministic evaluation of the flood mitigation batter pile-founded T-Wall structure is required to refine the design of the structure. In this subsection, there is a summarization of the results of evaluations made using CPGA-R for the pile limit states for the Figure 7-17 structure with 10 ft long tension piles and 35 ft long compression piles.

The flood elevation was raised incrementally in a series of 17 CPGA-R deterministic analyses of the Figure 7-17 batter pile founded T-Wall flood mitigation structure using CPGA-R. The flood elevation was raised in these analyses from EL 6.2 corresponding to the base of slab to the top of T-Wall EL 22.1 in 1 ft increments until the last increment of 0.9 ft.

Figure 7-25 summarizes the results computed at each flood elevation analyzed for the three structural limit states of the compression pile. The three structural pile limit states are shear failure Limit State 5 (blue points); axial failure Limit State 6 (orange points); and the CPGA-R labeled Limit State 6 of the Combined Bending Factor, CBF (black points). The strength assessment for each limit state is expressed as the ratio of the applied load within the pile divided by the structural pile capacity. In the deterministic design process, the structural steel design capacity values used for each of these three limit states listed above contain constants that reduce the ultimate steel capacity down to an allowable steel capacity. Thus, a deterministic design capacity is also referred to as an allowable stress-based design capacity. This analysis follows the same procedure as described in subsection 7.3.2.

Figure 7-25. Deterministic design results for the 35 ft long HP 14 × 89 compression pile.

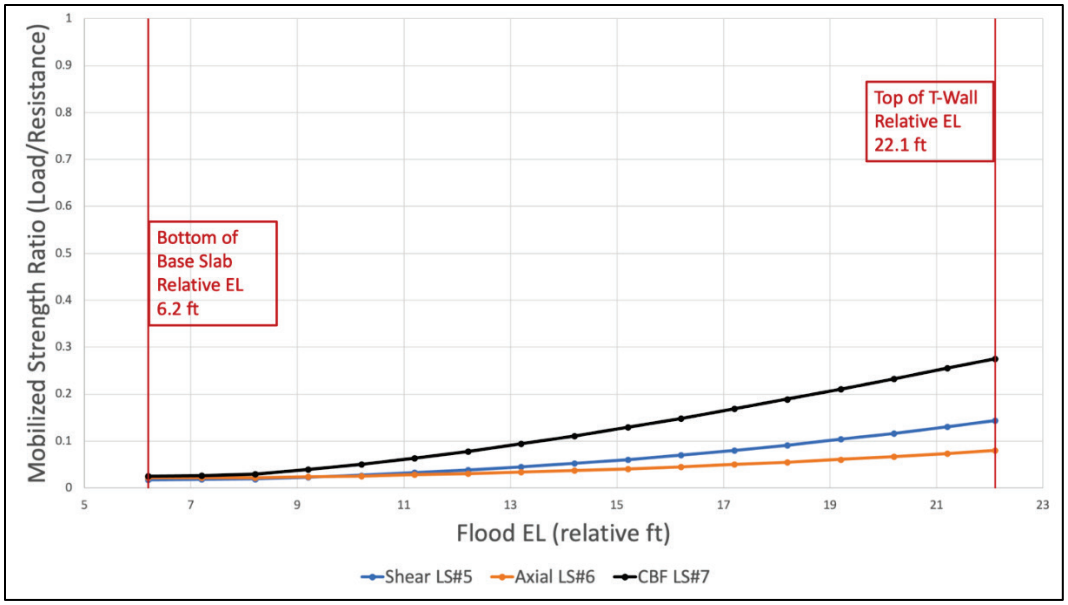

Figure 7-25 CPGA-R results show that as the flood elevation rises, the demands in each of the three limit states rise (with the pile design capacities held constant). This trend is to be expected. The results shown in this figure also demonstrate that the CBF is the most critical of the three structural limit states within the compression pile for all flood elevations.

With a flood elevation reaching the top of the stem of the T-Wall at EL 22.1 ft, all three structural pile limit states possess mobilized strength ratio values less than 1. The *CBF* mobilized strength ratio reaches a maximum value of 0.28 while the ratios for shear and for axial force loadings achieve lower mobilized, maximum strength ratio values of 0.14 and 0.08, respectively. In fact, none of these three structural pile limit states comes close to mobilizing their respective structural pile design capacities.

This observed reserve capacity is because during the deterministic design of the Figure 7-1 T-Wall flood mitigation structure, it is the SSI limit state that dictated the length of compression pile as well as its pile sizing of HP 14 × 89 for its bearing capacity footprint. This deterministic design outcome was also observed for the Red River of the North batter pile-founded T-Wall and is discussed at the end of subsection 7.2.6.2. In summary, the deterministic design was optimized by SSI Limit State 3, corresponding to a mobilized strength ratio of nearly 1.0 for the selected 35 ft long HP 14 × 89 compression pile.

Figure 7-26 summarizes the results computed at each flood elevation analyzed for the three structural limit states of the tension pile. Recall the flood elevation was raised in 1 ft increments in a series of 17 CPGA-R deterministic analyses of the Figure 7-17 batter pile-founded T-Wall flood mitigation structure, from EL 6.2 to El 22.1. The three structural tension pile limit states considered are shear failure Limit State 8 (blue points); axial failure Limit State 9 (orange points); and the CPGA-R labeled Limit State 10 of the CBF (black points). Recall the strength assessment for each limit state is expressed as the ratio of the applied load divided by the structural pile capacity.

Figure 7-26. Deterministic design results for the 10 ft long HP 14 × 89 tension pile.

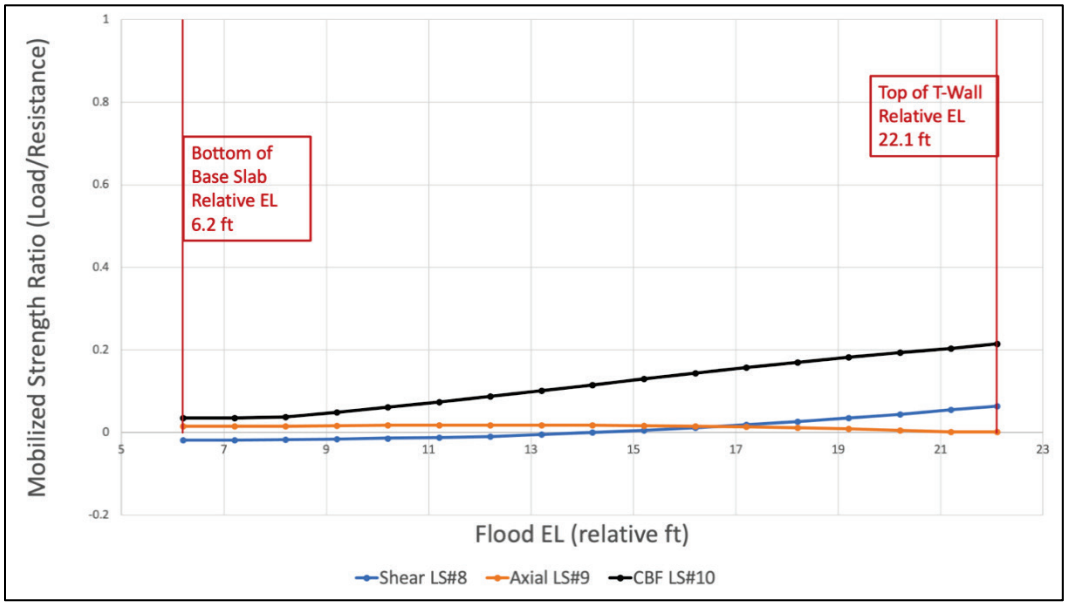

Figure 7-26 CPGA-R results show that as the flood elevation rises, the demands in the shear and *CBF* limit states also rise. There is a sign change in the shear limit state due to a reverse in direction in this force internal to the tension pile at flood EL 22.1 ft. Additionally, the axial load sign changes from positive in compression to negative in tension above flood EL 22.6 ft (negative sign not shown in this figure). Below flood EL 22.6 ft, the left-most Figure 7-17 pile is in compression under axial loading while at and above this elevation, this same pile is in tension. The axial Limit State 9 strength mobilization factor is quite low, less than 0.004 for all flood elevations considered. In lower to moderate flood elevations, the weight of water over the wet portion of base slab above the tension pile dominates its axial loading. It is only when flood elevations reach EL 22.1 ft and above does this Figure 7-1 left pile revert

into a tension pile due to the action of the lateral water pressure force acting on the stem of the wall, counteracting the moment due to the weight of the water acting over the wet portion of the base slab.

With a flood elevation reaching the top of the stem of the T-Wall at EL 22.1 ft, all three structural tension pile limit states possess mobilized strength ratio values that are well less than one. These Figure 7-26 results show that the *CBF* is the most critical of the three structural limit states within the tension pile at all flood elevations. The *CBF*-mobilized strength ratio reaches a maximum value of 0.21 while the ratios for shear and for axial force loadings achieve lower mobilized, maximum strength ratio values of 0.05 and 0.004, respectively. Additionally, these three structural pile limit states mobilize less of their respective structural pile capacities when compared to those of the compression pile (Figure 7-25). Recall that it was the compression pile in Limit State 3, not the tension pile, that was optimized during the CPGA-R analyses to possess a limiting *ALF* value of 1/1.7 = 0.59 during the SSI-based limit state deterministic design process.

Table 7-19 summarizes the mobilized strength ratios for the 10 limit states of the Figure 7-17 example problem with 10 ft long tension and 35 ft long compression batter piles and with 3.8 ft section width. The limit states are ranked for criticality in the fifth column. Note that the primary failure mechanism for this structure is the SSI Limit State 3, which occurs for the compression pile.

Table 7-19. Mobilized strength ratio computed for each of the 10 limit states in the deterministic Red Wood River T-Wall design with flood EL 22.1 ft. for a pair of 35 ft long compression and 10 ft long tension batter piles and section width of 3.8 ft.

Limit State Number	Limit State Description	Component	Mobilized Strength Ratio	Limit State Ranking Number
1	Horizontal stem shear	Reinforced concrete stem	0.48	3
2	Stem moment	Reinforced concrete stem	0.62	1
3	SSI	Compression pile	0.59	2
4	SSI	Tension pile	0.07	8
5	Horizontal shear	Compression pile	0.14	6
6	Axial compression	Compression pile	0.07	7
7	CBF	Compression pile	0.28	4
8	Horizontal shear	Tension pile	0.06	9
9	Axial tension	Tension pile	0.001	10
10	CBF	Tension pile	0.22	5

7.4.4 Reliability results for the Red Wood River pile-founded T-Wall section with 35 ft compression and 10 ft tension piles

Reliability tests were performed for the ACE and the 100-year Chance of Exceedance flood hazard curves for the Red Wood River example problem with 35 ft compression and 10 ft tension piles to determine *PUP* values for each of the ten limit states, as well as the system *PUP* value. Table 7-20 gives the results of these *PUP* computations with appropriate β equivalents. Recall that higher βs mean a lower probability that a limit state will be exceeded. β values of infinity mean that probabilities are approaching the limit of 0.0.

Table 7-20. Reliability results for 100,000 Monte Carlo simulation runs using two Chance of Exceedance curves for a 35-ft compression and 10-ft tension batter piles founded T-Wall.

Limit State Number	Annual Chance of Exceedance		100-Year Simulation Values	
	PUP_1	β_1	PUP_{100}	β_{100}
1	0.00016	3.598547	0.01376	2.204062
2	0.00172	2.925412	0.1397	1.081668
3	0.00014	3.633134	0.00833	2.394127
4	0.00037	3.374314	0.02663	1.932807
5	0.00000	infinity	0.00000	infinity
6	0.00000	infinity	0.00000	infinity
7	0.00000	infinity	0.00000	infinity
8	0.00000	infinity	0.00000	infinity
9	0.00000	infinity	0.00000	infinity
10	0.00000	infinity	0.00000	infinity
System	0.00173	2.923608	0.14075	1.076956

These Reliability results for both the annual as well as the simulated 100-year flood hazard analysis curves reveal that four limit states are engaged and that the others have infinitesimal chances of failure. Limit States 1, 2, 3, and 4 (stem shear, stem moment, compression pile SSI, and tension pile SSI, respectively) have probabilities of failure with both flood hazard chance of exceedances.

The system *PUP* for the Reliability analyses is slightly higher than the maximum *PUP* of the largest individual limit states belonging to stem moment Limit State 2. Each of the flood hazard Reliability analyses whose results are summarized in Table 7-20 possesses system *PUP* values that are less than the sum of all 10 Limit State *PUP*s.

The general observations made in subsection 7.3.1 of the probabilistic Table 7-4 results for the Red River of the north batter pile-founded T-Wall are also applicable for the Table 7-20 results for the Red Wood River flood wall assessment. Most notably is that the probability regions for the limit states partially overlap, much like the limit states in Figure 2-10. Table 7-20 results indicate that the stem moment failure (LS#2) region in Gaussian space completely overlaps the other two failure regions for stem shear (LS#1) and compression pile SSI (LS#3). The authors of this report believe Limit States 1 and 2 are directly proportional to each other with the

only difference being the application of a moment arm applied to the lateral force due to flood loading. This reveals that the failure region with the lower *PUP* will be completely overlapped by the other, higher limit state's *PUP* region. The authors further observe that the compression pile SSI Limit State 3 is not linearly related to the first two limit states, since its applied force is propagated through a frame analysis. Nevertheless, it is clear from the system *PUP* and individual limit state *PUP* Reliability results that stem moment Limit State 2 appears to envelop the Limit State 3 *PUP* region for the ACE flood hazard curve.

Table 7-21 shows the results of using Monte Carlo methods to compute the probability of unsatisfactory performance (*PUP*) for the 10 limit states of subsection 7.2.1. Four limit states were engaged in the simulation runs: The Stem Shear Limit State LS#1, the Stem Moment Limit State LS#2, the Compression Pile SSI Limit State LS#3, and the Tension Pile SSI Limit State LS#4. The results are for 100,000 simulation runs for the three-flood elevation chance of exceedance distributions.

Table 7-21. Annual and 100-year *PUP* and β values for the primary limit states at the Red Wood River site for 35 ft compression and 10 ft tension batter pile-founded T-Wall.

Limit State		Annual Chance of Exceedance	Simulated 100-Year Chance of Exceedance
LS#1	PUP_1	0.00016	0.00013855
	β_1	3.59854702	3.63582563
	PUP_{100}	0.01587394	0.01376
	β_{100}	2.14757064	2.20406177
LS#2	PUP_1	0.00172	0.00150361
	β_1	2.92541241	2.96699902
	PUP_{100}	0.15814551	0.1397
	β_{100}	1.00210887	1.08166817
LS#3	PUP_1	0.00014	8.3645E-05
	β_1	3.63313355	3.76388959
	PUP_{100}	0.01390342	0.00833
	β_{100}	2.20000071	2.39412654
LS#4	PUP_1	0.00037	0.00026987
	β_1	3.37431365	3.46021353
	PUP_{100}	0.03633046	0.02663
	β_{100}	1.79495465	1.93280682

The annual values for *PUP* and β (PUP_1 and β_1, respectively) and the 100-year value of *PUP* and β (PUP_{100} and β_{100}, respectively) are presented for comparisons. The values are computed from Equations 2.69 and 2.70 where they are needed because the flood level ACE distribution computes the PUP_1 values and the 100-year Chance of Exceedance distributions compute PUP_{100} values.

Note that Limit State 4 is engaged in the Red Wood River scenario and not in the Red River of the North scenario. The primary differences between the two example problems are the fact that the soil properties have changed and that the flood level ACE curve for the Red Wood River has greater probability for flood elevations that are above the base of the wall. Either of these conditions can have an effect on the tension pile SSI analysis. Regardless, the Limit State 4 condition has become more of a concern than the Limit State 3 condition.

7.4.5 Computing load and resistance factors for the Red Wood River site section with 35 ft compression and 10 ft tension piles

The procedure for deriving load and resistance factors from individual simulation runs for a target β in Section 2.8 (Ebeling and White 2021) has been performed for the Red Wood River example problem with 35 ft compression pile and 10 ft tension pile. The Reliability-based procedure used is described in subsection 7.3.4.

Following the design procedure, the initial design load is defined as the 750-year flood event (Figure 3-1 Load Category versus Return Period in EM 1110-2-2104 [HQUSACE 2016]) of a hydrostatic flood level to the top of the T-Wall. According to Table 3-1 in EM 1110-2-2104 (HQUSACE 2016), a load factor, referred to as the Global Load Factor (GLF or γ_G), is applied to the hydrostatic fllod water pressures for computation of internal frame forces within the batter pile-founded T-Wall CPGA-R model.

Table 7-22 shows the computed propagated limit state forces, moments, and stresses for the 10 limit states, given the deterministic design load conditions, GLFs, and properties of the example T-Wall structure with 10 ft tension and 35 ft compression piles. The GLF=1.3 propagated load values are used to establish the local resistance factors. Note that, although the conditions of the design load do not change with design choices, the propagation to the individual limit states does change.

Table 7-22. Deterministic design load propagation to individual limit states at the Red Wood River site with 10 ft tension pile and 35 ft compression pile.

Limit State	GLF = 1.0	GLF = 1.3
LS#1 (Stem Shear in lb)	22,907	29,779
LS#2 (Stem Moment in ft-lb)	106,135	137,976
LS#3 (Compression Pile SSI in lb)	52,600	64,100
LS#4 (Tension Pile SSI in lb)	-1,100	-4,500
LS#5 (Compression Pile Shear in lb)	20,700	26,100
LS#6 (Compression Pile Axial in lb)	52,600	64,100
LS#7 (Compression Pile Flexure in lb-in.^{2})	13,774	17,523
LS#8 (Tension Pile Shear in lb)	9,300	12,900
LS#9 (Tension Pile Axial in lb)	-1,100	-4,500
LS#10 (Tension Pile Flexure in lb-in.^{2})	10,754	13,922

Without applying load factors, Reliability-based simulations provide *PUP* values that correspond to site-specific variable distributions. A scale factor (R_{SF}) can be computed from simulation results using the procedure outlined in Section 2.8 and applied to the resulting reliability distribution such that the calculated *PUP* will match PUP_{Target}. Figures 7-27 through 7-29 show the effects of this scaling procedure using SSI Limit State 3 Reliability analysis results as an example. These figures use data from the 100-year simulated Flood Hazard simulations of the Red Wood River example problem with 35 ft compression and 10 ft tension piles. Figure 7-27 shows the original distributions of resistance (R) in green and load (L) in red. Additionally, the distribution of the values when each sample's load is subtracted from the resistance (R-L) is shown in gray. Any values of the R-L curve that are less than zero on the horizontal axis are in failure, as indicated by the blue line and the Failure Region indicator. The equivalent annual β for this limit state can be found in Table 7-21 and equals 3.76388959.

Figure 7-27. Resulting load (L) and resistance (R) curves for SSI Limit State 3 from Reliability analysis and computed (R-L) curve at the Red Wood River site.

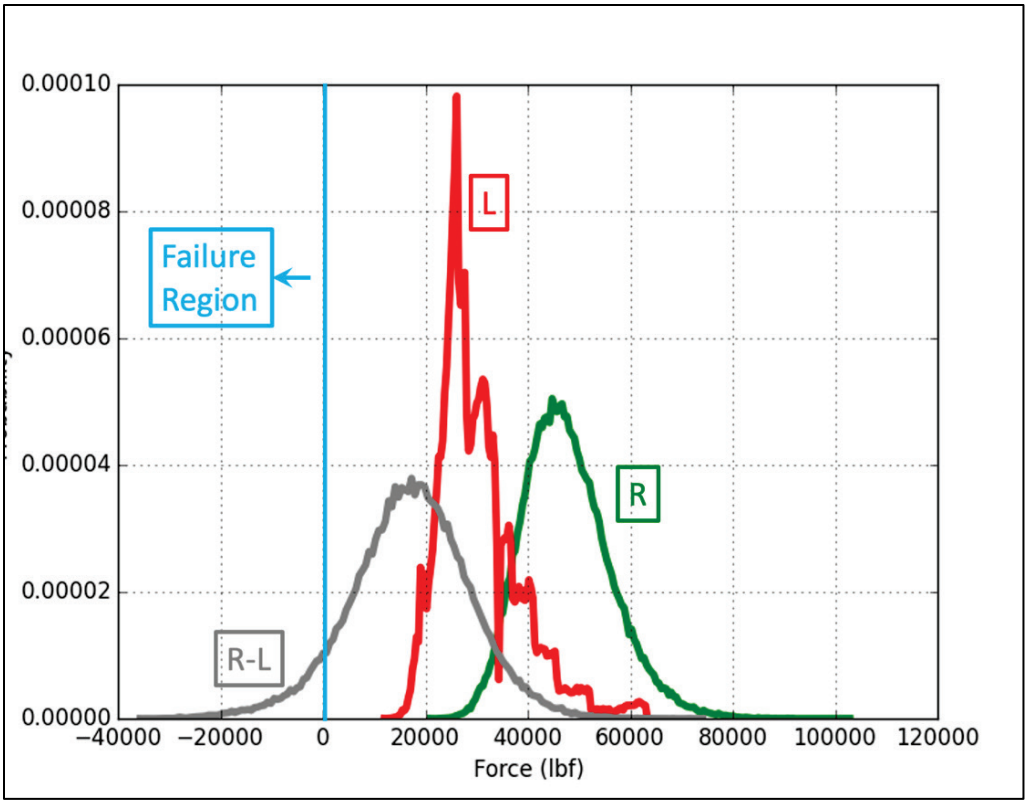

Figure 7-28. Fixed load (L) and scaled resistance (R) curves for SSI Limit State 3 for β_{target}=3.5 and computed (R-L) curve (R_{SF} = 0.928945) at the Red Wood River site.

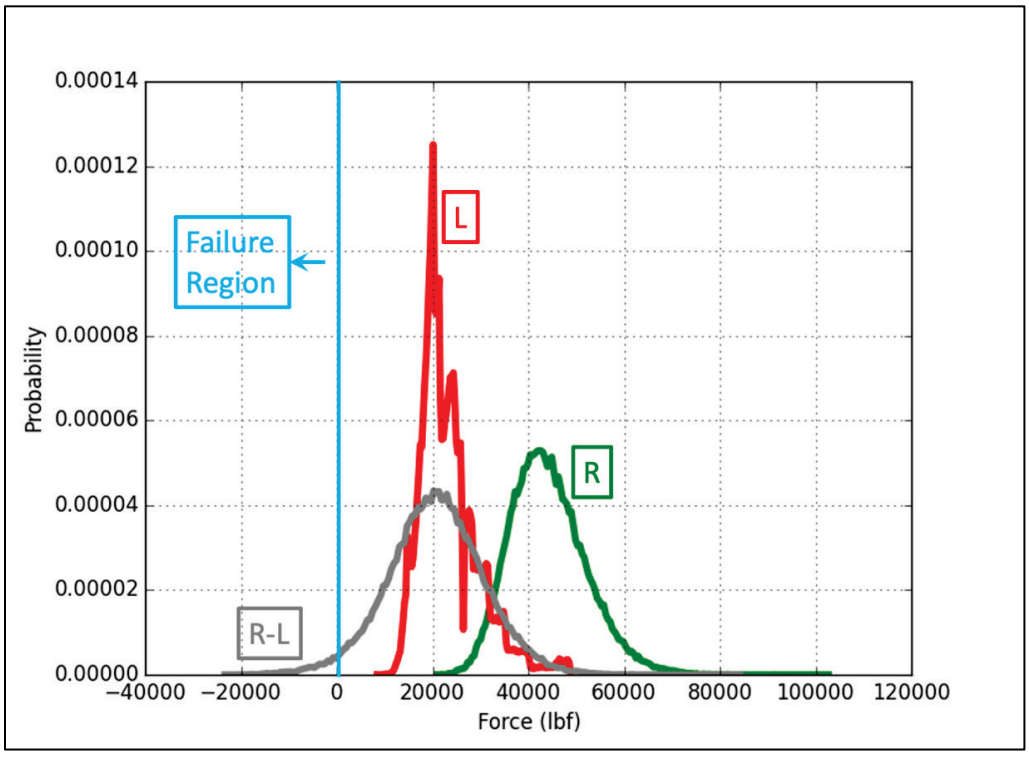

Figure 7-29. Fixed load (L) and scaled resistance (R) curves for SSI Limit State 3 for β_{target}=4.0 and computed (R-L) curve (R_{SF} = 1.541625) at the Red Wood River site.

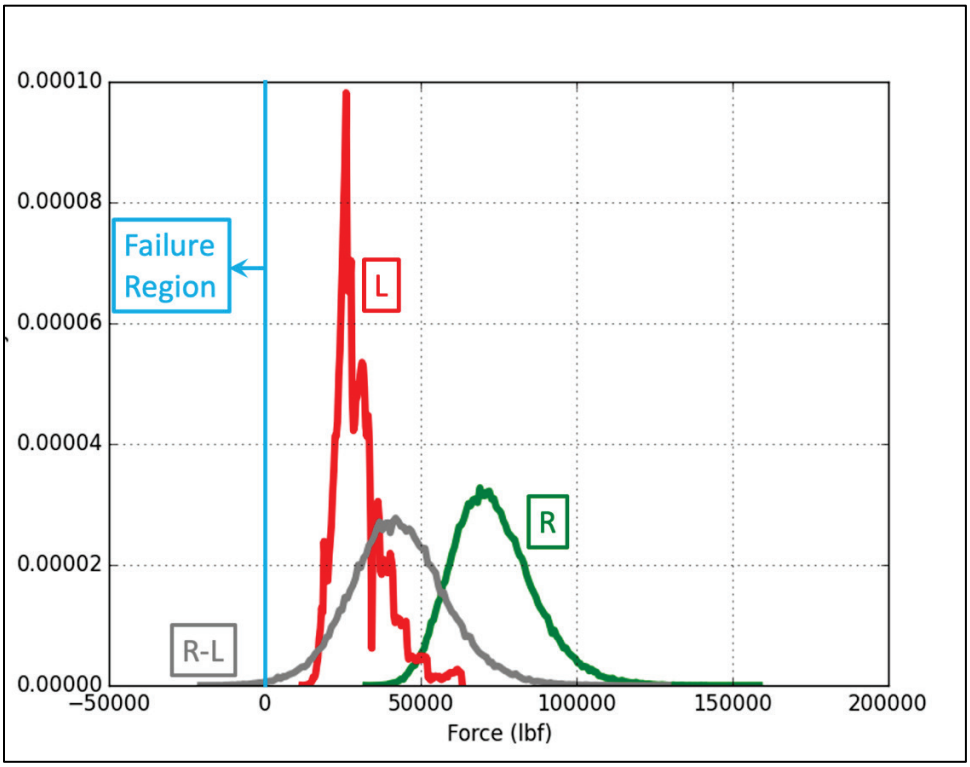

Figures 7-28 and 7-29 show the effects of using the RSF values of 0.928945 for a β_{target} of 3.5 and 1.541625 for a β_{target} of 4.0, respectively. The load curve stays the same for all three figures. While the area under the resistance curve remains the same (at 1.0), the peak probabilities of the curve are affected by the scaling. Other effects are that the mean value of the resistance distribution moves relative to the scale factor. These last two effects are responsible for the movement and broadening of the range for the (R-L) curve, which causes the area of the (R-L) curve in the failure region to become less. This area is the same as the *PUP* value and reducing the *PUP* value increases the β values.

Using this Resistance Scale Factor (RSF), the Load Scale Factor (LSF) can be computed from the Table 7-22 deterministic propagated loads with a global load factor (GLF) of 1.3. These computations are outlined in Subsection 7.3.4.3 using Equations 2.60 and 2.61, and the Load and Resistance factors are computed using Equations 7.1 and 7.2.

For the T-Wall design with the 10 ft tension and 35 ft compression piles, Limit State 1 (Stem Shear), Limit State 2 (Stem Moment), Limit State 3 (Compression Pile SSI), and Limit State 4 (Tension Pile SSI) are the

primary failure mechanisms. Therefore, Table 7-23 focuses on summarizing results for these four dominant limit states. Recall from subsection 7.3.4 that R_{SF} and L_{SF} are computed Reliability constants used in the numerical analysis process to determine the value of resistance factor ϕ for a predefined target reliability index value, β_{Target}.

Table 7-23. Computation of local resistance factor (ϕ_L).

Limit State	β_{Target}	Flood Hazard	Resistance		Design Load (GLF= 1.3)	L_{SF}	ϕ_L (γ_L=1)
			Mean (from sims)	R_{SF}			
LS#1	3	ACE	47,660	0.712445	29,779	1.14024	0.87701
		S100	47,667	0.690802		1.10576	0.90435
	3.5	ACE	47,660	0.945295		1.51290	0.66098
		S100	47,667	0.928945		1.48695	0.67252
	4	ACE	47,660	1.218142		1.94958	0.51293
		S100	47,667	1.186239		1.89880	0.52665
LS#2	3	ACE	171,866	1.062753	137,976	1.32379	0.75541
		S100	171,790	1.025077		1.27629	0.78352
	3.5	ACE	171,866	1.462209		1.82136	0.54904
		S100	171,790	1.443129		1.79680	0.55655
	4	ACE	171,866	1.798050		2.23969	0.44649
		S100	171,790	1.867682		2.32540	0.43003
LS#3	3	ACE	88497	0.737362	64,100	1.01801	0.98231
		S100	88439	0.726397		1.00221	0.99779
	3.5	ACE	88497	0.942472		1.30118	0.76853
		S100	88439	0.906013		1.25003	0.79998
	4	ACE	88497	1.088308		1.50253	0.66555
		S100	88439	1.074676		1.48273	0.67443
LS#4	3	ACE	25303	0.581563	-4,500	3.27006	0.30580
		S100	25285	0.340739		1.91457	0.52231
	3.5	ACE	25303	0.739205		4.15647	0.24059
		S100	25305	0.680126		3.82458	0.26147
	4	ACE	25303	0.977380		5.49570	0.18196
		S100	25305	0.991154		5.57359	0.17942

The rows of Table 7-23 are broken into sections based on limit state, β_{Target}, and the Flood Hazard Chance of Exceedance distributions used. The mean resistance for each limit state set of simulations is recorded, and finally, the scale factor required to scale the simulation limit state resistance values by to achieve the β_{Target} with respect to the simulation limit state load values (R_{SF}). The limit state design load, with respect to the scaled global design load is presented next. The next column has the load scale factor (L_{SF}) that would need to be applied to the initial design load to establish an equivalence with the mean simulated resistance value times the values in the R_{SF} column. The final column reveals the limit state resistance factor ϕ appropriate for the global load factor γ_G of 1.3. The β_{Target} values of 3.0, 3.5 and 4.0 are consistent with the Ellingwood recommendation.

For the compression pile SSI limit state (LS#3) with a β_{Target} = 3.5, computed ϕ values range from 0.769 to 0.8 using the two Red Wood River flood hazard characterizations. The Table 3-3 AASHTO Nominal Bearing Resistance of Single Pile—Static Analysis Methods, φ_{stat}, values are in the range of 0.4 to 0.5. Thus, 0.769 to 0.8 computed range in resistance factor is higher than the comparable AASHTO factor value range. It is important to recognize that the AASHTO Table 3-3 and Canadian Bridge code ϕ values reflect compilation and assessment of numerous pile foundation case studies, their resulting interpretation of group-data and subsequent committee judgement for recommended code specification. In contrast, the ϕ value computed for the compression pile SSI limit state (LS#3) reflects a single batter pile founded flood mitigation T-Wall result for the Red Wood River flood hazard. The Reliability-based 2014 CHBDC, as described in Fenton et al. (2016), reports compression resistance factor values for deep foundations of 0.4 and 0.45 for static analysis of soil foundations with typical and high degrees of understanding, respectively. After making a Reliability assessment, Fenton et al. (2014) conclude that the the target lifetime reliability index is approximately 3.5. The authors of this technical report conclude that both Reliability-based codes provide for a consistent deep foundation, single compression pile resistance factor recommendation.

For the tension pile SSI limit state (LS#4) with a β_{Target} = 3.5, computed ϕ values range from 0.241 to 0.261 using the two Red Wood River flood hazard characterizations. The Table 3-3 AASHTO Nominal Bearing Resistance of Single Pile—Static Analysis Methods, φ_{stat}, values are in the

range of 0.25 to 0.35. Thus, 0.241 to 0.261 computed range in resistance factor matches the lower bound value of the comparable AASHTO factor value range.

7.4.6 Computing load and resistance factors for the Red Wood River site section with 35 ft compression and 15 ft tension piles

The analysis of the Red Wood River example problem with a 10 ft tension pile and a 35 ft compression pile revealed that, for the overconsolidated soil properties used in the first 10 ft of embedment and for the flood level ACE, which has more flood events higher on the wall, the tension pile SSI limit state (Limit State 4) has a much higher chance of failure than for the same structural design implemented using the Red River of the North soils and flood conditions. In fact, the tension pile SSI limit state failure *PUP* value exceeded the compression pile SSI limit state failure *PUP*. This seemed to imply that the tension pile SSI limit state is more sensitive than the compression pile SSI limit state, possibly due to the short length of the pile. It was decided that another analysis with a longer tension pile could determine the sensitivity of the LRFD factors under these quickly changing *PUP* conditions, so another anaylsis was conducted with a longer 15 ft tension pile and 35 ft compression pile to capture the change of factors under the rapidly changing *PUP* conditions.

A deterministic analysis where the failure limit states were ranked is shown in Table 7-24. The mobilized strength ratios of the different limit states only change by the smallest of fractions and the rankings did not change from Table 7-19. This indicates that the example problems show similar mobilized strength characteristics as the example problem with the 10 ft tension pile.

Table 7-24. Mobilized strength ratio computed for each of the 10 limit states in the deterministic Red Wood River T-Wall design with flood EL 22.1 ft. for 35 ft long compression and 15 ft long tension batter piles and section width of 3.9 ft.

Limit State Number	Limit State Description	Component	Mobilized Strength Ratio	Limit State Ranking Number
1	Horizontal stem shear	Reinforced concrete stem	0.48	3
2	Stem moment	Reinforced concrete stem	0.62	1
3	SSI	Compression pile	0.59	2
4	SSI	Tension pile	0.05	8
5	Horizontal shear	Compression pile	0.15	6
6	Axial compression	Compression pile	0.02	7
7	CBF	Compression pile	0.28	4
8	Horizontal shear	Tension pile	0.06	9
9	Axial tension	Tension pile	0.048	10
10	CBF	Tension pile	0.21	5

The big change is revealed in Table 7-25. Although both problems exhibited very similar mobilized strength ratios, the *PUP* values for the tension pile SSI limit state, Limit State 4, has seen a marked change. The *PUP* value for Limit State 4 has decreased by by over a factor of 10 from Table 7-20.

Table 7-25. Reliability results for 100,000 Monte Carlo simulation runs using two chance of exceedance curves for a 35 ft compression and 15 ft tension batter piles founded T-Wall.

Limit State Number	Annual Chance of Exceedance		100-Year Simulation Values	
	PUP_1	β_1	PUP_{100}	β_{100}
1	0.00013	3.652203	0.01346	2.212386
2	0.00144	2.980264	0.14171	1.072668
3	0.00012	3.672701	0.00983	2.332774
4	0.00002	4.107480	0.00273	2.778563
5	0.00000	infinity	0.00000	infinity

Limit State Number	Annual Chance of Exceedance		100-Year Simulation Values	
	PUP_1	β_1	PUP_{100}	β_{100}
6	0.00000	infinity	0.00000	infinity
7	0.00000	infinity	0.00000	infinity
8	0.00000	infinity	0.00000	infinity
9	0.00000	infinity	0.00000	infinity
10	0.00000	infinity	0.00000	infinity
System	0.00146	2.976037	0.1427	1.068267

A comparison of the adjusted *PUP*s for the ACE and 100-year Chance of Exceedance flood events is presented in Table 7-26. The values for Limit State 4 have *PUP* values that vary by less than 0.000007, as compared to slightly less than 0.0001 for the 10 ft tension pile. The authors suggest that the closer a limit state is to failure, the more it is affected by sampling variations in the distributions but that the 100-year flood level Chance of Exceedance provides a good estimate of structural behavior because it is being paired with 100-year wind-speed Chance of Exceedance for simulations.

Table 7-26. Annual and 100-year PUP and β values for the primary limit states at the Red Wood River site for 35 ft compression and 15 ft tension batter pile-founded T-Wall.

Limit State		Annual Chance of Exceedance	Simulated 100-Year Chance of Exceedance
LS#1	PUP_1	0.00013	0.0001355
	β_1	3.65220322	3.64154212
	PUP_{100}	0.0129167	0.01346
	β_{100}	2.22870712	2.21267587
LS#2	PUP_1	0.00144	0.00152697
	β_1	2.98026406	2.96225668
	PUP_{100}	0.13420211	0.14171
	β_{100}	1.10674494	1.07266823
LS#3	PUP_1	0.00012	9.8781E-05
	β_1	3.67270126	3.72211256
	PUP_{100}	0.011929	0.00983
	β_{100}	2.25940832	2.33277419
LS#4	PUP_1	0.00002	2.7337E-05
	β_1	4.10747965	4.03469221
	PUP_{100}	0.00199802	0.00273
	β_{100}	2.87847397	2.77856255

A deterministic run was performed on the Red Wood River example problem with 15 ft tension pile and 35 ft compression pile to compute the propogated flood loads from the 750-year event at each limit state. The results are given in Table 7-27. As expected, the stem load limit states (LS#1 and LS#2) did not change from Table 7-22. The remaining propogated loads changed due to the frame action of the structural system, with reductions of force in the tension pile shear (LS #8) and flexure (LS #10) but increasing for the other limit states.

Table 7-27. Deterministic design load propagation to individual limit states at the Red Wood River site with 15 ft tension pile and 35 ft compression pile.

Limit State	GLF = 1.0	GLF = 1.3
LS#1 (Stem Shear in lb)	22,907	29,779
LS#2 (Stem Moment in ft-lb)	106,135	137,976
LS#3 (Compression Pile SSI in lb)	52,900	64,700
LS#4 (Tension Pile SSI in lb)	-1,300	-4,800
LS#5 (Compression Pile Shear in lb)	21,100	26,600
LS#6 (Compression Pile Axial in lb)	52,900	64,700
LS#7 (Compression Pile Flexure in lb-in^2)	14,245	18,224
LS#8 (Tension Pile Shear in lb)	8,900	12,400
LS#9 (Tension Pile Axial in lb)	-1,300	-4,800
LS#10 (Tension Pile Flexure in lb-in^2)	10,694	13,989

The computation of LRFD resistance factors, ϕ_L, is given in Table 7-28. A comparison with Table 7-23 reveals that the changes to the tension pile length, while having a pronounced effect on the *PUP* value for tension pile SSI Limit State 4, had a small effect on the ϕ_L values.

Table 7-28. Computation of local resistance factor (ϕ_L) for Red Wood River example problem with 35 ft compression and 15 ft tension pile.

Limit State	β_{Target}	Flood Hazard	Resistance		Design Load (GLF= 1.3)	L_{SF}	ϕ_L (γ=1)
			Mean (from sims)	R_{SF}			
LS#1	3	ACE	47,623	0.691867	29,779	1.106444	0.903797
		S100	47,684	0.691441		1.107179	0.903197
	3.5	ACE	47,623	0.917056		1.466569	0.681864
		S100	47,684	0.930155		1.489422	0.671401
	4	ACE	47,623	1.110719		1.776278	0.562975
		S100	47,684	1.187863		1.902081	0.525740
LS#2	3	ACE	171,659	1.024249	137,796	1.275955	0.783726
		S100	171,719	1.028710		1.281961	0.780055
	3.5	ACE	171,659	1.409173		1.755474	0.569647
		S100	171,719	1.444583		1.800214	0.555489
	4	ACE	171,659	1.778599		2.215685	0.451328
		S100	171,719	1.845943		2.300382	0.434710
LS#3	3	ACE	88,500	0.737369	64,700	1.008611	0.991462
		S100	88,452	0.735663		1.005732	0.994301
	3.5	ACE	88,500	0.900724		1.232057	0.811651
		S100	88,452	0.919458		1.257000	0.795545
	4	ACE	88,500	1.079041		1.475968	0.677521
		S100	88,452	1.088482		1.488074	0.672009
LS#4	3	ACE	33,373	0.457852	4,800	3.183311	0.314138
		S100	33,355	0.276248		1.919636	0.520932
	3.5	ACE	33,373	0.528100		3.671725	0.272352
		S100	33,355	0.550323		3.824172	0.261495
	4	ACE	33,373	0.792672		5.511217	0.181448
		S100	33,355	0.788431		5.478774	0.182523

7.5 Designing for the Mississippi River site in St. Paul, MN

The third site explored using the pile group analysis methods of Section 7.2 was the Mississippi River site in St. Paul, MN. This site distribution is discussed in this chapter and in subsection B.3 of Appendix B, for the 100-year site-specific, wind-induced wave loading. The following subsections discuss the collection of variable data and design choices.

7.5.1 Design of the St. Paul pile-founded T-Wall

The Mississippi River at the St. Paul, MN, site batter pile-founded T-Wall flood mitigation structure has some differences with the previous two example sites. The most noticeable difference is the height of the wall stem. For the 750-year flood event, the top of the wall needs to be at elevation 714.5 ft. For this flood EL and with the river channel bank (upward) slope and a base slab thickness height of 2 ft, the height of the stem is 12 ft. This stem height is less than the stem height of 13.9 ft used for the other two example sites (Red River of the North and Red Wood River). The base slab thickness height remains at 2 ft, but the base cross-section length is reduced from the 13.9 ft. used in the first two flood T-Walls to 12 ft. The distance from the stem to either edge of the base is kept approximately proportional for all three flood T-Walls. The distance of the piles from the ends of the base are kept the same so that the pair of supporting piles have the same position and the same batter as the previous sites. The assumption of the lengths of the piles from the beginning has changed to a 10 ft tension pile and a 32 ft compression pile. All this is illustrated in Figure 7-30.

Figure 7-30. Initial design for the site-specific data for the Red Wood River site in Marshall, MN.

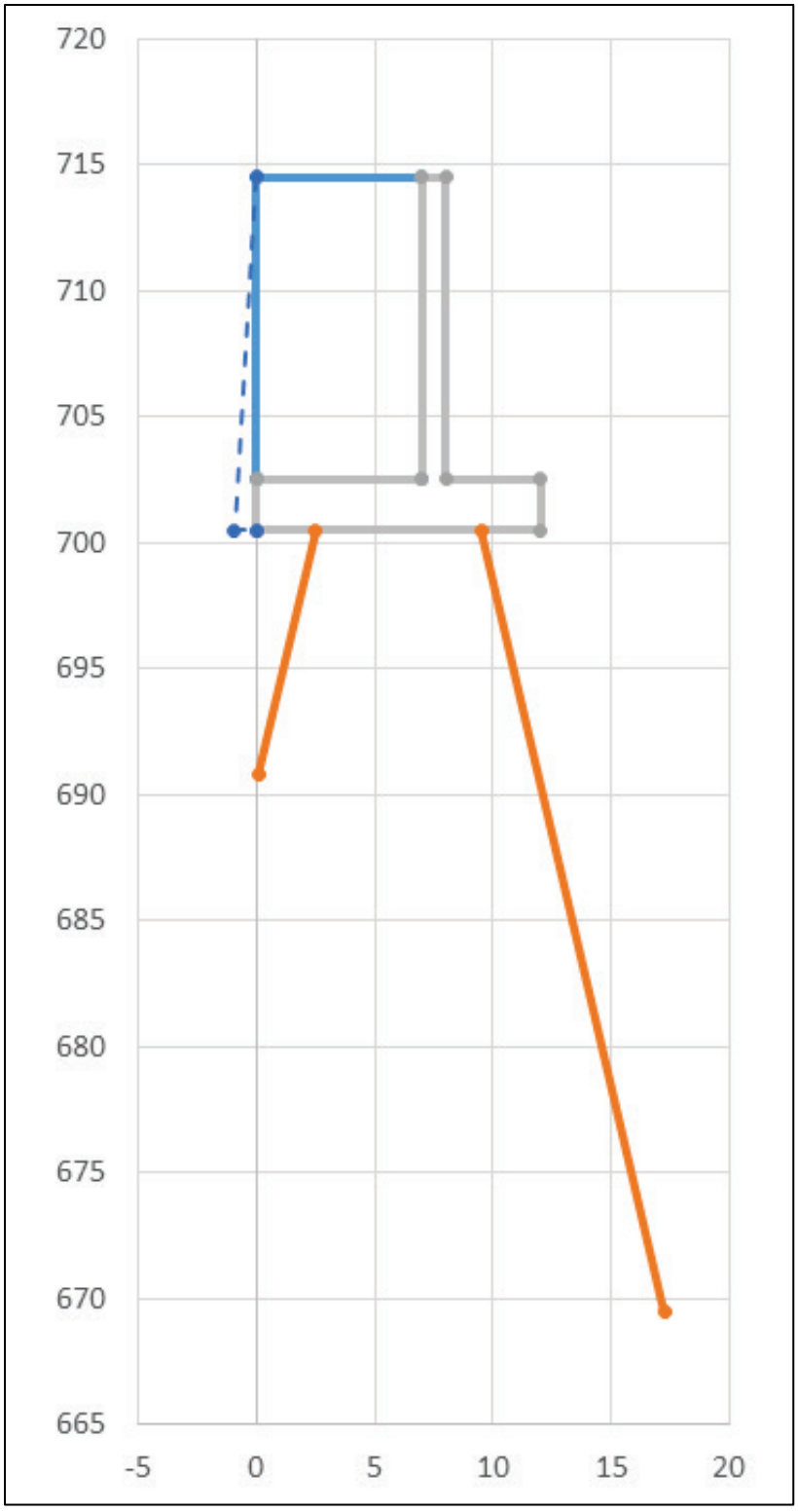

The initial estimate lengths of the piles are based on information from the previous site runs and the fact that the soil distribution was changed to reflect another site condition with more soil layers defined using SHANSEP. The distribution of S_u with depth was defined at this site using Equation 7.5 and by following the procedure outlined in subsection 7.2.6. The total unit weight of the soil was given as 122 pcf, and $(S_u/\sigma'_{vo})_{NC}$ is set to 0.32. The SHANSEP defined distribution of mean S_u with depth was assigned a COV_{point} of 0.4 based on Appendix D data which, when combined with the Variance Reduction Factor for a 32 ft compression pile and a vertical scale of fluction of 5 ft, Equations 7.6 and 7.7 result in a $COV_{Spatial}$ of 0.1581. Using the distribution of mean S_u with depth times this $COV_{Spatial}$ value, the standard deviation value is defined with depth. This same computational process is followed for the 10 ft long tension pile, maintianining a δ value to 5 ft. The resulting tension pile $COV_{Spatial}$ value equals 0.2828. Figures 7-31 and 7-32 show how the S_u varies with depth for the compression and tension piles, respectively. The tension pile distribution has a different standard deviation based on the VRF defined by the pile's length and the scale of fluctuation (5 ft) in the soil (Equation 7.6).

Figure 7-31. St. Paul mean soil S_u properties with depth and distribution curves from -6σ to +6σ based on $COV_{Spatial}$ (for a 35 foot Compression Pile).

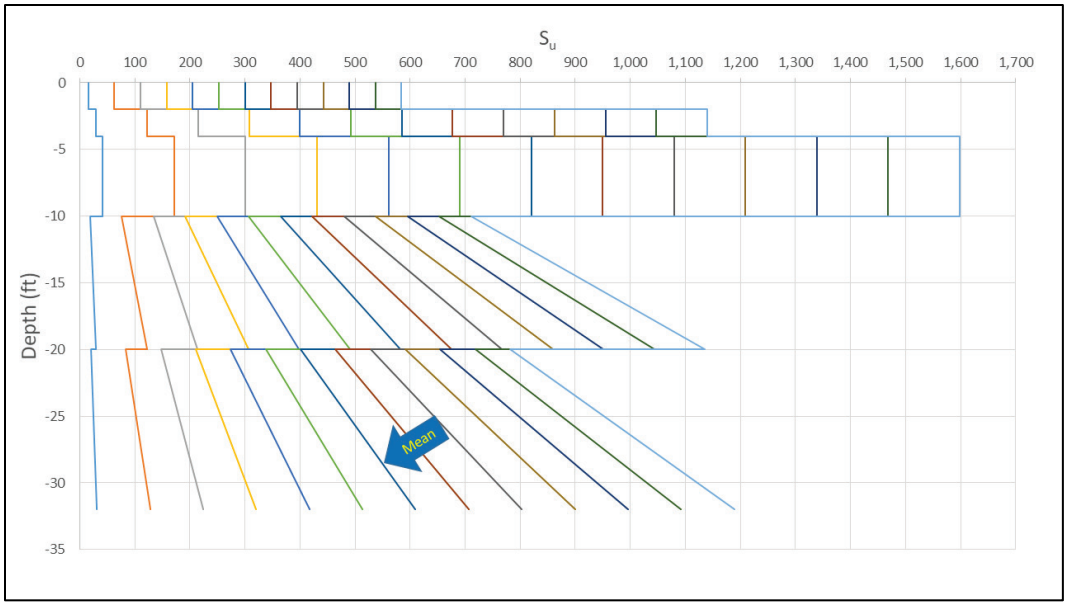

Figure 7-32. St. Paul site mean soil S_u properties with depth and distribution curves from -6σ to +6σ based on $COV_{Spatial}$ (for a 10 ft piles).

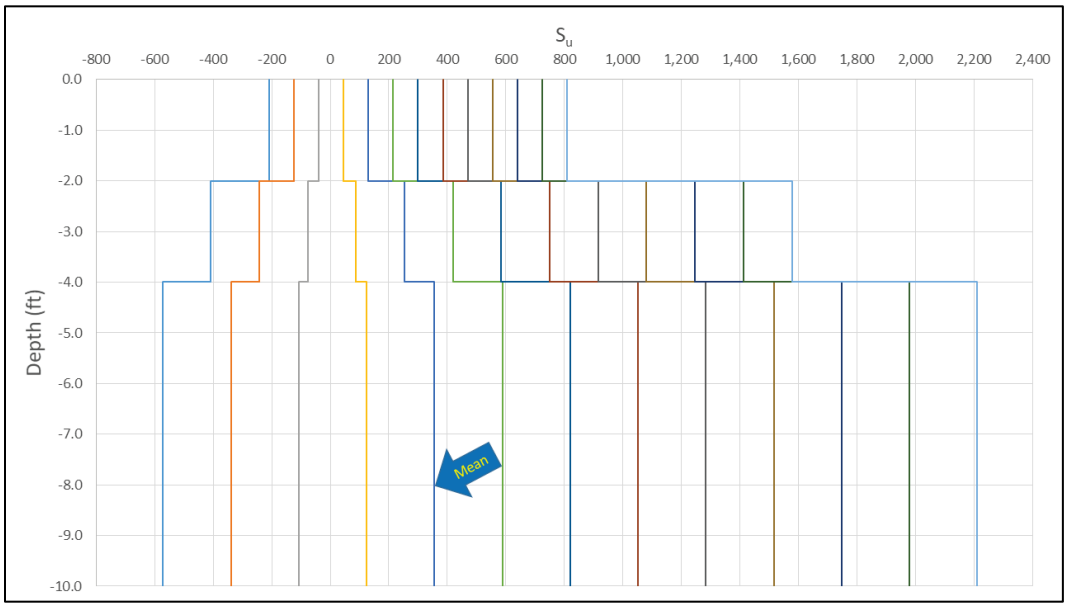

The values used for the overconsolidation ratios and full description of S_u distribution with depth using SHANSEP are shown in Figure 7-33. The data show a comparison of the Mississippi River at St. Paul S_u with depth values with the values used for the Red River of the North and Red Wood River. The upper 20 ft thick soil crust at the St. Paul site posesses higher S_u values than the other sites due to the higher assigned OCR ratios.
Figure 7-34 shows the simplified S_u characterization for the three sites as used in the software CAXPILE. Since CAXPILE has limited resources for dealing with continuous curves, the S_u characterization has been simplified. The comparison reveals that in the overconsolidated region of the soil, near the surface, the S_u values are higher.

Figure 7-33. Comparison of overconsolidation ratios and mean S_u soil properties for the Mississippi River at St. Paul, MN, with the Red River of the North and the Red Wood River characterization.

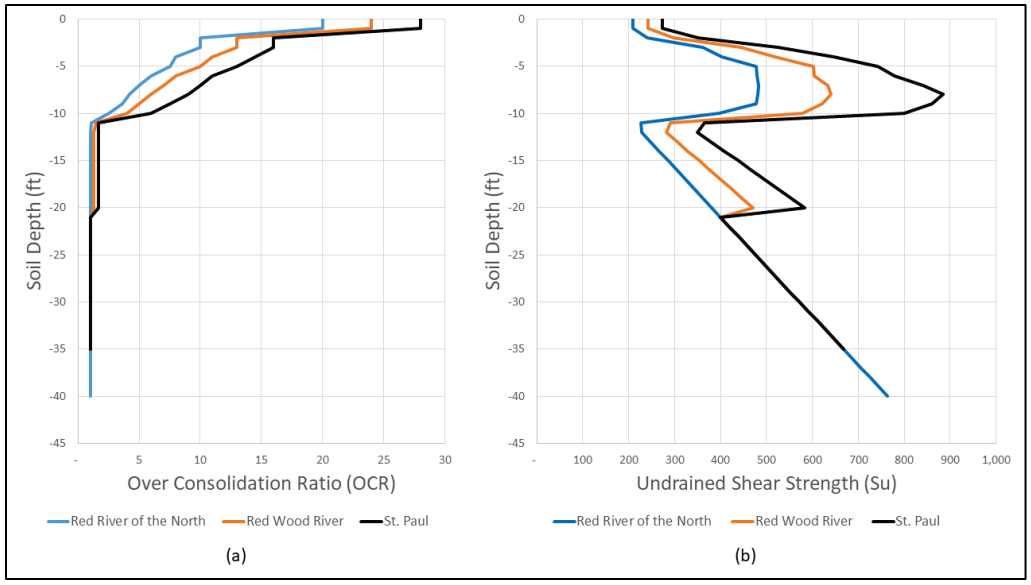

Figure 7-34. Comparison of mean S_u soil properties for the Mississippi River at St. Paul, MN, with the Red River of the North and the Red Wood River characterization for the compression pile.

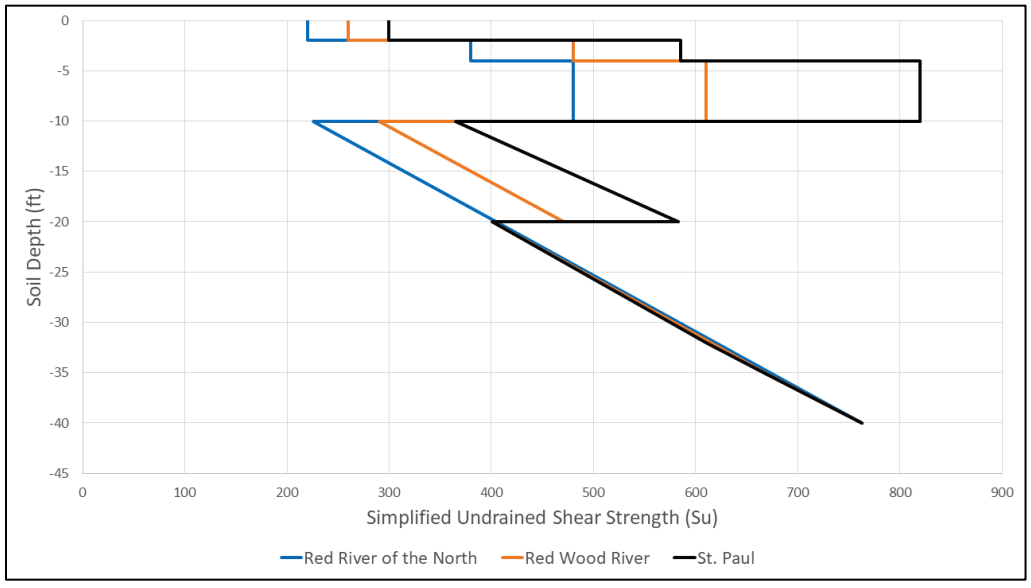

7.5.2 System variable distributions for the Mississippi River site in St. Paul, MN

In a manner like subsection 7.3.1, ACE values were collected for flood elevations at the Mississippi River flood T-Wall site in St. Paul, MN. These data are shown in Figure 7-35.

Figure 7-35. Collected ACE data for site-specific data for the Mississippi River site in St. Paul, MN.

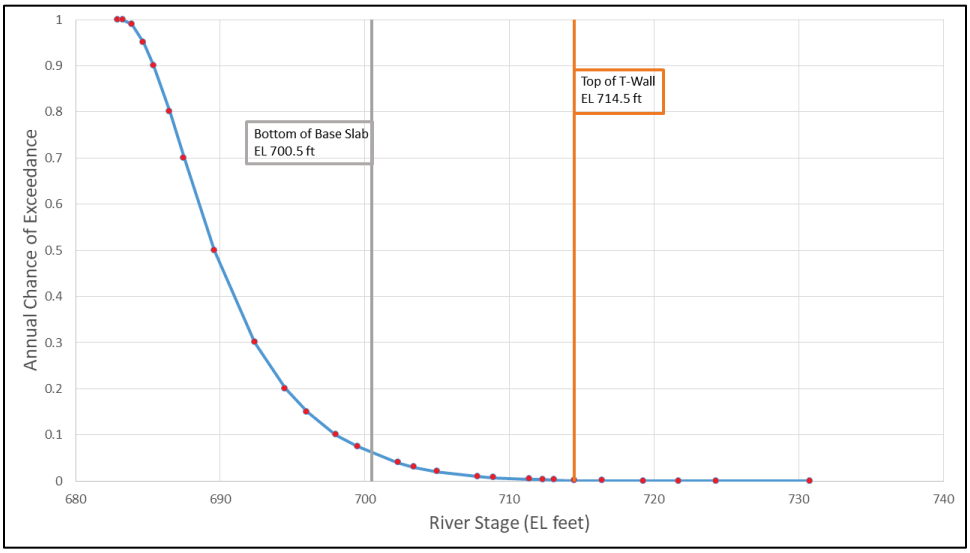

The computed PDF for the Mississippi River at St. Paul, MN, ACE is shown in Figure 7-36. Like the Red River of the North site, most of the the distributed flood elevations are below the base of the wall.

Figure 7-36. PDF histogram from the site-specific ACE data for the Mississippi River site in St. Paul, MN, compared with simulated data from the ACE data.

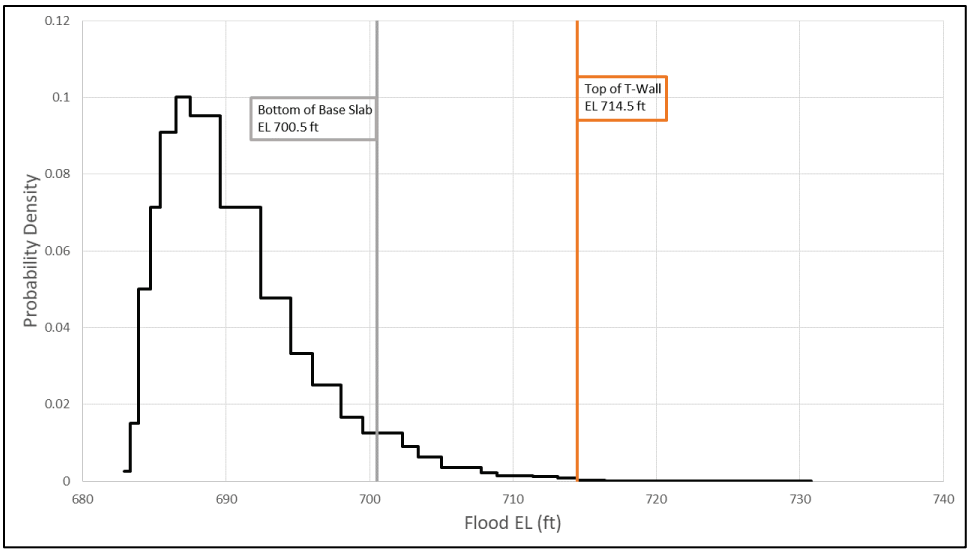

The 100-year values were recovered using simulation, as before. Figure 7-37 reveals the 100-year chance of exceedance computed in this fashion. This distribution reveals a high probability that the wall height will be exceeded.

Figure 7-37. PDF for 100-year chance of exceedance values at Mississippi River site in St. Paul, MN.

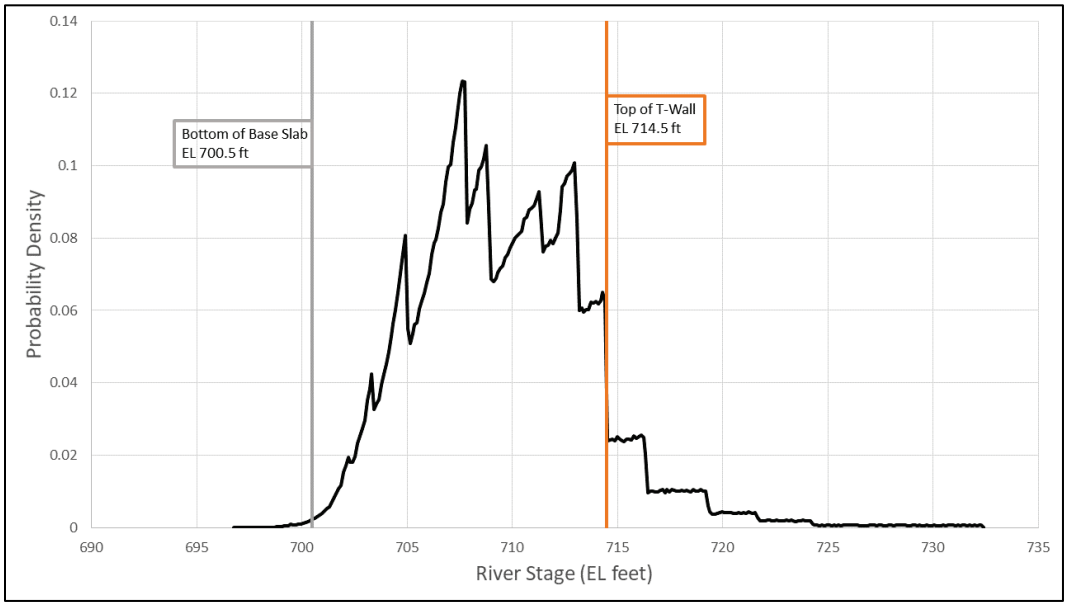

Processed wind-speed data are used in conjunction with the Goda (2010) method (Chapter 5) to generate wind-induced pseudo-static wave loading (Chapter 6). The site-specific wind data were obtained by collecting data from Minneapolis-Saint Paul International Airport (MSP), which is approximately 9 miles from the project as discussed in Section B.3 of Appendix B. The data were fairly complete from 1969 to May 2021 with wind speeds and directions reported multiple times per hour between June 1992 and May 2021 and hourly from 1969 through June 1992. The range in these data was judged to be only representative of a relatively short time frame. These data were analyzed probabilistically using a Gumbel Type I distribution with Gringorten's (1963) Method to extrapolate to longer wind-speed return periods (Figure B.3-7). The wind speeds determined using the Gringorten's (1963) Method were based on a 100-year return period wind event occurring at the T-Wall. Two locations were selected for the T-Wall based on fetch along the river. Data were collected and computed for the two locations. The second location for the T-Wall was selected as the basis for testing because of the greater extremes of the wind data at that location. For the Mississippi River site second

location at St. Paul, MN, the data collected indicated a normal distribution with a mean 100-year wind return period wind speed of 45.48 mph and a standard deviation of 0.832 mph (Figure B.3-9). This distribution represents the variability of wind speeds only during a 100-year event and not the variability of wind speeds annually. Therefore, the value of *PUP* for each of the 10 limit states is really the *PUP* during a 100-year wind event and is likely conservative for events that occur annually.

The Yield Stress (F_y) distribution for the HP steel piles is defined by data obtained from coupon tests conducted on steel specimens (Ellingwood). For ASTM A572 steel, which is assumed in this example, the yield stress has a nominal value of 50,000 psi. Based upon cited test result data, Ellingwood recommends the distribution for yield stress be modeled as a truncated log-normal with a mean value of 54,000 psi and a COV of 0.07. The standard deviation is 3,780 psi. The Dexter et al. (2000) and Bartlett et al. (2003) steel coupon test data suggest that this distribution be truncated at a minimum value of 49,500 psi and at a maximum value of 69,000 psi.

The reinforced concrete stem shear and stem moment capacity distributions are based on Strength assessment for the Extreme Load Case value according to Table 3-1 and Figure 3-1 of EM 1110-2-2104 (HQUSACE 2016). For a deterministic design and the two stem limit states, the hydrostatic water pressures with a flood elevation to the top of the wall from the base of the stem are computed, and the lateral force and moment are captured at the base of the stem.

The reinforced concrete Stem Shear Capacity distribution is based upon a lognormal distribution according to the Table 5-4 information provided in Ellingwood and summarized in Chapter 4 of this report. The lognormal mean capacity value is defined in a deterministic analysis for a 750-year flood load to the top of the T-Wall by multiplying the peak hydrostatic lateral force for the 12 ft high triangular hydrostatic flood water pressure distribution acting on the reinforced concrete stem by the load factor γ of 1.3 and a bias factor of 1.2 according to Table 3-1 in EM 1110-2-2104 (HQUSACE 2016) and Table 5-4 in Ellingwood, respectively. Recall that the height of the reinforced concrete stem is 12 ft. The standard deviation is computed by multiplying the mean value by the COV_{Shear} value of 0.18. This value of COV is taken from Table 5-4 in Ellingwood.

The Stem Moment Capacity distribution also uses a lognormal distribution as recommended by Ellingwood (Chapter 4 of this report summarizes this Ellingwood data). The lognormal mean capacity value is defined in a deterministic analysis for a 750-year flood load to the top of the T-Wall by multiplying the peak hydrostatic lateral force for the 12 ft high triangular hydrostatic flood water pressure distribution acting on the reinforced concrete stem by the load factor γ of 1.3 and a bias factor of 1.12 according to Table 3-1 in EM 1110-2-2104 (HQUSACE 2016) and Table 5-4 in Ellingwood, respectively. The standard deviation is computed by multiplying the mean moment capacity value by the COV_{Moment} value of 0.14. This value of COV is taken from Table 5-4 in Ellingwood.

7.5.3 Deterministic results for a Mississippi River at St. Paul, MN, T-Wall section with a 32 ft compression pile and a 10 ft tension pile

A deterministic evaluation of the flood mitigation batter pile-founded T-Wall structure is required to refine the design of the structure. In this subsection, there is a summarization the results of evaluations made using CPGA-R for the pile limit states for the Figure 7-28 structure with 10 ft long tension piles and 32 ft long compression piles.

The flood elevation was raised incrementally in a series of 14 CPGA-R deterministic analyses of the Figure 7-30batter pile-founded T-Wall flood mitigation structure using CPGA-R. The flood elevation was raised in these analyses from EL 700.5 corresponding to the base of slab to the top of T-Wall EL 714.5 in 1 ft increments.

Figure 7-38 summarizes the results computed at each flood elevation analyzed for the three structural limit states of the compression pile. The three structural pile limit states are shear failure Limit State 5 (blue points); axial failure Limit State 6 (orange points); and the CPGA-R labeled Limit State 6 of the CBF (black points). The strength assessment for each limit state is expressed as the ratio of the applied load within the pile divided by the structural pile capacity. In the deterministic design process, the structural steel design capacity values used for each of these three limit states listed above contain constants that reduce the ultimate steel capacity to an allowable steel capacity. Thus, a deterministic design capacity is also referred to as an allowable stress-based design capacity. This analysis follows the same procedure as described in subsection 7.3.2.

Figure 7-38. Deterministic design results for the 32 ft long HP 14 x 89 compression pile.

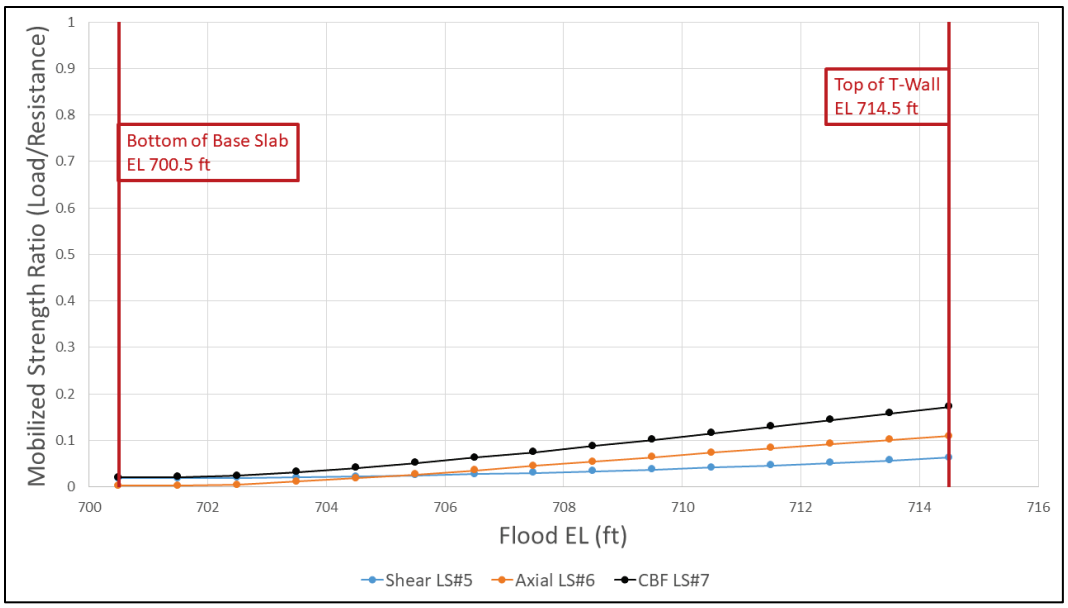

Figure 7-38 CPGA-R results show that as the flood elevation rises, the demands in each of the three limit states rises (with the pile design capacities held constant). This trend is to be expected. The results shown in this figure also demonstrate that the CBF is the most critical of the three structural limit states within the compression pile for all flood elevations.

With a flood elevation reaching the top of the stem of the T-Wall at EL 714.5 ft, all three structural pile limit states possess mobilized strength ratio values less than 1. The *CBF* mobilized strength ratio reaches a maximum value of 0.17 while the ratios for shear and for axial force loadings achieve lower mobilized, maximum strength ratio values of 0.11 and 0.03, respectively. In fact, none of these three structural pile limit states come close to mobilizing their respective structural pile design capacities.

This observed reserve capacity is because during the deterministic design of the Figure 7-28 T-Wall flood mitigation structure, it is the SSI limit state that dictated the length of compression pile as well as its pile sizing of HP 14 × 89 for its bearing capacity footprint. This deterministic design outcome was also observed for the Red River of the North batter pile founded T-Wall and is discussed at the end of subsection 7.2.6.2. In summary, the deterministic design was optimized by SSI Limit State 3, corresponding to a mobilized strength ratio of nearly 1.0 for the selected 32 ft long HP 14 × 89 compression pile.

Figure 7-39 summarizes the results computed at each flood elevation analyzed for the three structural limit states of the tension pile. Recall the flood elevation was raised in 1 ft increments in a series of 14 CPGA-R deterministic analyses of the Figure 7-30 batter pile-founded T-Wall flood mitigation structure, from EL 700.5 to El 714.5. The three structural tension pile limit states considered are shear failure Limit State 8 (blue points); axial failure Limit State 9 (orange points); and the CPGA-R labeled Limit State 10 of the CBF (black points). Recall the strength assessment for each limit state is expressed as the ratio of the applied load divided by the structural pile capacity.

Figure 7-39. Deterministic design results for the 10 ft long HP 14 x 89 tension pile.

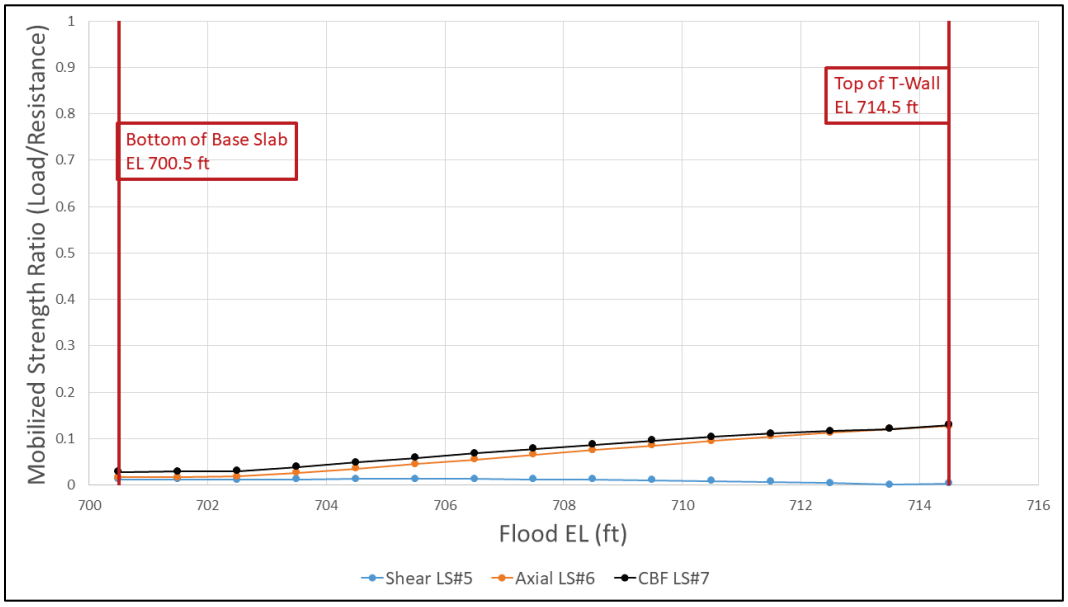

Figure 7-39 CPGA-R results show that as the flood elevation rises, the demands in the shear and *CBF* limit states also rise. There is a sign change in the shear limit state due to a reverse in direction in this force internal to the tension pile at flood EL 713.5 ft. Additionally, the axial load sign changes from positive in compression to negative in tension above flood EL 713.5 ft (negative sign not shown in this figure). Below flood EL 713.5 ft, the left-most Figure 7-28 pile is in compression under axial loading while at and above this elevation this same pile is in tension. In lower to moderate flood elevations, the weight of water over the wet portion of base slab above the tension pile dominates its axial loading. It is only when flood elevations reach EL 713.5 ft and above does this Figure 7-28 left pile revert into a tension pile due to the action of the lateral water pressure

force acting on the stem of the wall, counteracting the moment due to the weight of the water acting over the wet portion of the base slab.

With a flood elevation reaching the top of the stem of the T-Wall at EL 714.5 ft, all three structural tension pile limit states possess mobilized strength ratio values that are well less than 1. These Figure 7-37 results show that the *CBF* is the most critical of the three structural limit states within the tension pile at all flood elevations. The *CBF* mobilized strength ratio reaches a maximum value of 0.13, as does the axial force loading while the ratios for shear achieves a lower mobilized, maximum strength ratio values of 0.003. Additionally, these three structural pile limit states mobilize less of their respective structural pile capacities when compared to those of the compression pile (Figure 7-36). Recall that it was the compression pile in Limit State 3, not the tension pile, that was optimized during the CPGA-R analyses to possess a limiting *ALF* value of 1/1.7 = 0.59 during the SSI-based limit state deterministic design process.

Table 7-29 summarizes the mobilized strength ratios for the 10 limit states of the Figure 7-28 example problem with 10 ft long tension and 32 ft long compression batter piles and with 3.6 ft section width. The limit states are ranked for criticality in the fifth column. Note that the primary failure mechanism for this structure is the SSI Limit State 3, which occurs for the compression pile.

Table 7-29. Mobilized strength ratio computed for each of the 10 limit states in the deterministic Mississippi River at St. Paul, MN, T-Wall design with flood EL 714.5 ft. for a pair of 32 ft long compression and 10 ft long tension batter piles and section width of 3.6 ft.

Limit State Number	Limit State Description	Component	Mobilized Strength Ratio	Limit State Ranking Number
1	Horizontal stem shear	Reinforced concrete stem	0.48	3
2	Stem moment	Reinforced concrete stem	0.62	1
3	SSI	Compression pile	0.58	2
4	SSI	Tension pile	0.13	6
5	Horizontal shear	Compression pile	0.13	7
6	Axial compression	Compression pile	0.0631	8
7	CBF	Compression pile	0.21	4
8	Horizontal shear	Tension pile	0.06	9
9	Axial tension	Tension pile	0.003	10
10	CBF	Tension pile	0.16	5

7.5.4 Reliability results for the Mississippi River at St. Paul, MN, pile-founded T-Wall section with 32 ft compression and 10 ft tension piles

Reliability tests were performed for the ACE and the 100-year chance of exceedance flood hazard curves for the Mississippi River at St. Paul, MN, example problem with 32 ft compression and 10 ft tension piles to determine *PUP* values for each of the ten limit states, as well as the system *PUP* value. Table 7-30 gives the results of these *PUP* computations with appropriate β equivalents. Recall that higher βs mean a lower probability that a limit state will be exceeded. β values of infinity mean that probabilities are approaching the limit of 0.0.

Table 7-30. Reliability results for 100,000 Monte Carlo simulation runs using two chance of exceedance curves for a 32 ft compression and 10 ft tension batter piles founded T-Wall.

Limit State Number	ACE		100-Year Simulation Values	
	PUP_1	β_1	PUP_{100}	β_{100}
1	0.00025	3.480756	0.01969	2.060194
2	0.00070	3.194651	0.06879	1.484863
3	0.00005	3.890592	0.00641	2.488731
4	0.00014	3.633134	0.01752	2.107896
5	0.00000	infinity	0.00000	infinity
6	0.00000	infinity	0.00000	infinity
7	0.00000	infinity	0.00000	infinity
8	0.00000	infinity	0.00000	infinity
9	0.00000	infinity	0.00000	infinity
10	0.00000	infinity	0.00000	infinity
System	0.00070	3.194651	0.06908	1.482678

These Reliability results for both the annual as well as the simulated 100-year flood hazard analysis curves reveal that four limit states are engaged and that the others have infinitesimal chances of failure. Limit States 1, 2, 3, and 4 (stem shear, stem moment, compression pile SSI, and tension pile SSI, respectively) have probabilities of failure with both flood hazard chance of exceedances.

The system *PUP* for the Reliability analyses is slightly higher than the maximum *PUP* of the largest individual limit states belonging to stem moment Limit State 2. Each of the flood hazard Reliability analyses whose results are summarized in Table 7-30 possess system *PUP* values that are less than or equal to the sum of all 10 Limit State *PUP*s.

The general observations made in subsection 7.3.1 of the probabilistic Table 7-4 results for the Red River of the North batter pile-founded T-Wall are also applicable for the Table 7-30 results for the Mississippi River at St. Paul flood wall assessment. Note that the probability regions for the limit states partially overlap, much like the limit states in Figure 2-10. Table 7-30 results indicate that the stem moment failure (LS#2) region in Gaussian space completely overlaps the other two failure regions for stem shear (LS#1) and compression pile SSI (LS#3). The authors of this report believe Limit States 1 and 2 are directly proportional to each other, with the only difference being the application of a moment arm applied to the

lateral force due to flood loading. This reveals that the failure region with the lower *PUP* will be completely overlapped by the other, higher limit state's *PUP* region. The authors further observe that the compression pile SSI Limit State 3 is not linearly related to the first two limit states, since its applied force is propagated through a frame analysis. Nevertheless, it is clear from the system *PUP* and individual limit state *PUP* Reliability results that stem moment Limit State 2 appears to envelop the Limit State 3 *PUP* region for the ACE flood hazard curve.

Table 7-31 shows the results of using Monte Carlo methods to compute the *PUP* for the 10 limit states of subsection 7.2.1. Four limit states were engaged in the simulation runs: Stem Shear Limit State LS#1, Stem Moment Limit State LS#2, Compression Pile SSI Limit State LS#3, and Tension Pile SSI Limit State LS#4. The results are for 100,000 simulation runs for the three-flood elevation chance of exceedance distributions.

Table 7-31. Annual and 100-year *PUP* and β values for the primary limit states at the Mississippi River at St. Paul, MN, site for 32 ft compression and 10 ft tension batter pile founded T-Wall.

Limit State		Annual Chance of Exceedance	Simulated 100-Year Chance of Exceedance
LS#1	PUP_1	0.00025	0.000199
	β_1	3.480756	3.541613
	PUP_{100}	0.024693	0.01969
	β_{100}	1.965242	2.060194
LS#2	PUP_1	0.0007	0.000712
	β_1	3.194651	3.189559
	PUP_{100}	0.067629	0.06879
	β_{100}	1.493685	1.484863
LS#3	PUP_1	0.00005	0.00006
	β_1	3.890592	3.829108
	PUP_{100}	0.004988	0.00641
	β_{100}	2.576685	2.488731
LS#4	PUP_1	0.00014	0.000177
	β_1	3.633134	3.57256
	PUP_{100}	0.013903	0.01752
	β_{100}	2.200001	2.107896

The annual values for *PUP* and β (PUP_1 and β_1, respectively) and the 100-year value of *PUP* and β (PUP_{100} and β_{100}, respectively) are presented for comparisons. The values are computed from Equations 2.69 and 2.70 where they are needed because the flood level ACE distribution computes the PUP_1 values and the 100-year Chance of Exceedance distributions compute PUP_{100} values.

Note that Limit State 4 is engaged for the Mississippi River at St. Paul, MN, site like the Red Wood River scenario but not in the Red River of the North scenario. This indicates that the primary effective change between the example problems is the soil properties changes. This is true since both the Mississippi River and Red River of the North have a similar number of floods below the wall and engage tension pile SSI limit state (Limit State 4) differently. Regardless, the Limit State 4 condition has become more of a concern than the Limit State 3 condition.

7.5.5 Computing load and resistance factors for the Mississippi River at St. Paul, MN, site section with 32 ft compression and 10 ft tension piles

The procedure for deriving load and resistance factors from individual simulation runs for a target β in Section 2.8 (Ebeling and White 2021) has been performed for the Mississippi River at St. Paul, MN, example problem with 32 ft compression pile and 10 ft tension pile. The Reliability based procedure used is described in subsection 7.3.4.

Following the design procedure, the initial design load is defined as the 750-year flood event (Figure 3-1 Load Category versus Return Period in EM 1110-2-2104 [HQUSACE 2016]) of a hydrostatic flood level to the top of the T-Wall. According to Table 3-1 in EM 1110-2-2104 (HQUSACE 2016), a load factor, referred to as the Global Load Factor (GLF or γ_G) is applied to the hydrostatic fllod water pressures for computation of internal frame forces within the batter pile-founded T-Wall CPGA-R model.

Table 7-32 shows the computed propagated limit state forces, moments, and stresses for the 10 limit states, given the deterministic design load conditions, GLFs, and properties of the example T-Wall structure with 10 ft tension and 32 ft compression piles. The GLF=1.3 propagated load values are used to establish the local resistance factors. Note that, although the conditions of the design load do not change with design choices, the propagation to the individual limit states does change.

Table 7-32. Deterministic design load propagation to individual limit states at the Red Wood River site with 10 ft tension pile and 32 ft compression pile.

Limit State	GLF = 1.0	GLF = 1.3
LS#1 (Stem Shear in lb)	16,174	21,026
LS#2 (Stem Moment in ft-lb)	64,696	84,105
LS#3 (Compression Pile SSI in lb)	41,200	50,000
LS#4 (Tension Pile SSI in lb)	-2,000	-5,000
LS#5 (Compression Pile Shear in lb)	15,200	19,100
LS#6 (Compression Pile Axial in lb)	41,200	50,000
LS#7 (Compression Pile Flexure in lb-in^2)	8,616	10,898
LS#8 (Tension Pile Shear in lb)	6,800	9,500
LS#9 (Tension Pile Axial in lb)	-2,000	-5,000
LS#10 (Tension Pile Flexure in lb-in^2)	6,493	8,381

Without applying load factors, Reliability-based simulations provide *PUP* values that correspond to site-specific variable distributions. A scale factor (R_{SF}) can be computed from simulation results using the procedure outlined in section 2.8 and applied to the resulting reliability distribution such that the calculated *PUP* will match PUP_{Target}. Figures 7-40 through 7-42 show the effects of this scaling procedure using SSI Limit State 3 Reliability analysis results as an example. These figures use data from the 100-year simulated Flood Hazard simulations of the Mississippi River at St. Paul, MN, example problem with 32 ft compression and 10 ft tension piles. Figure 7-40 shows the original distributions of resistance (R) in green and load (L) in red. Additionally, the distribution of the values when each sample's load is subtracted from the resistance (R-L) is shown in gray. Any values of the R-L curve that are less than zero on the horizontal axis are in failure, as indicated by the blue line and the Failure Region indicator. The equivalent annual β for this limit state can be found in Table 7-31 and equals 3.890592.

Figure 7-40. Resulting load (L) and resistance (R) curves for SSI Limit State 3 from Reliability analysis and computed (R-L) curve (R_{SF} = 0.613423) at the Mississippi River at St. Paul, MN, site.

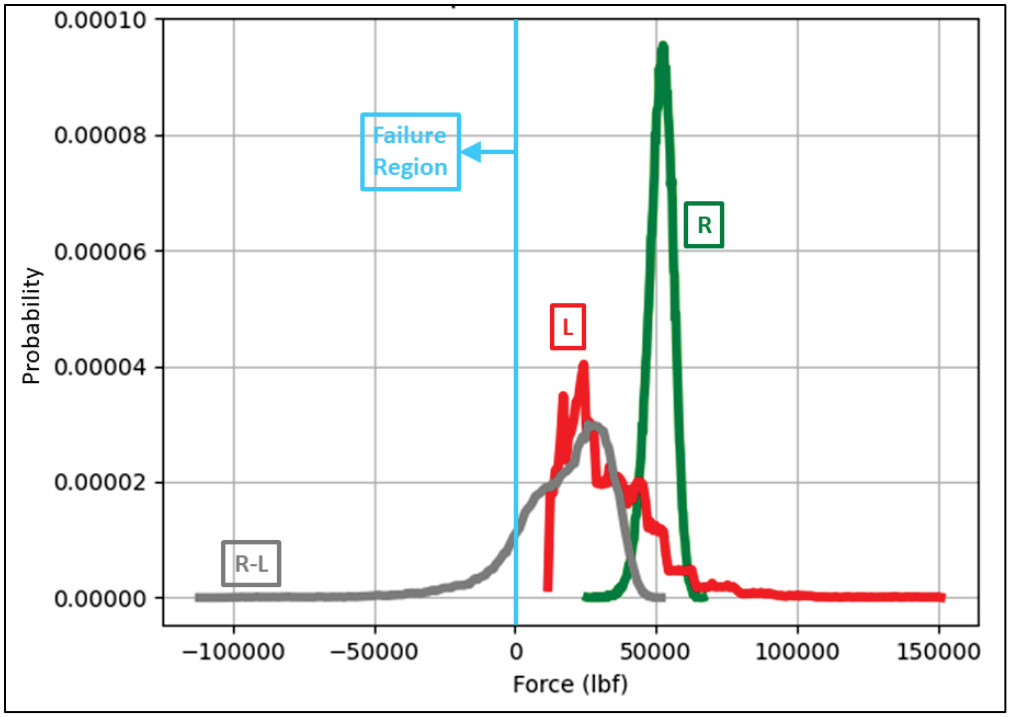

Figure 7-41. Fixed load (L) and scaled resistance (R) curves for SSI Limit State 3 for β_{target}=3.5 and computed (R-L) curve (R_{SF} = 0.931970) at the Mississippi River at St. Paul, MN, site.

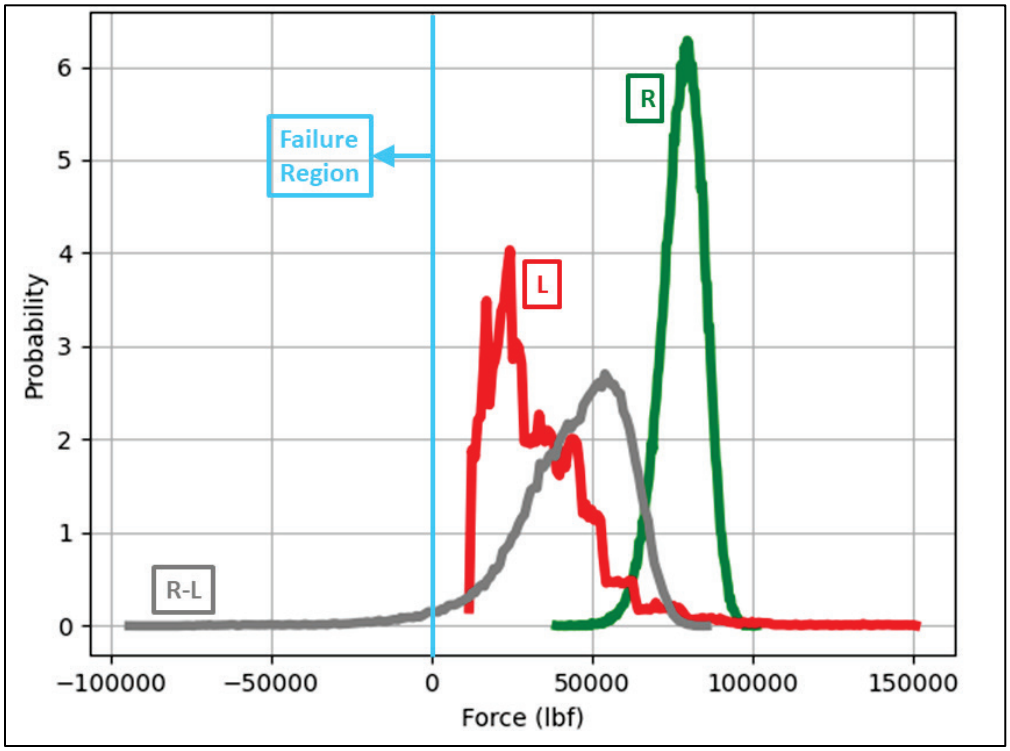

Figure 7-42. Fixed load (L) and scaled resistance (R) curves for SSI Limit State 3 for β_{target}=4.0 and computed (R-L) curve (R_{SF} = 1.446940) at the Mississippi River at St. Paul, MN, site.

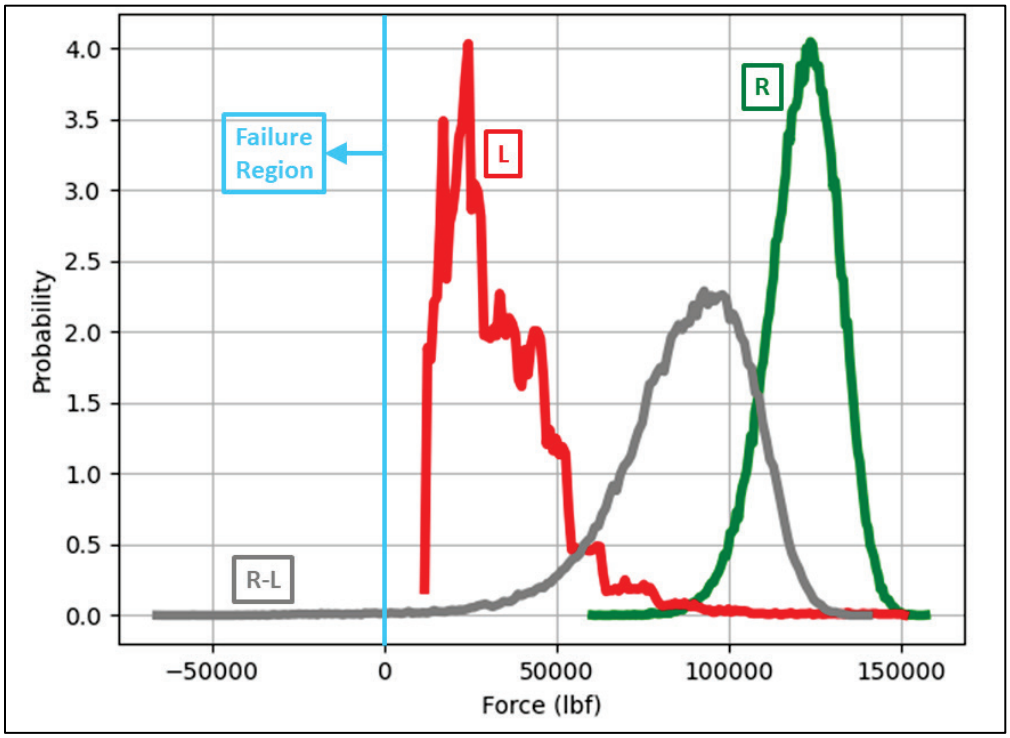

Figures 7-41 and 7-42 show the effects of using the RSF values of 0.931970 for a β_{target} of 3.5 and 1.446940 for a β_{target} of 4.0, respectively. The load curve stays the same for all three figures. While the area under the resistance curve remains the same (at 1.0), the peak probabilities of the curve are affected by the scaling. Other effects are that the mean value of the resistance distribution moves relative to the scale factor. These last two effects are responsible for the movement and broadening of the range for the (R-L) curve, which causes the area of the (R-L) curve in the Failure Region to become less. This area is the same as the *PUP* value, and reducing the *PUP* value increases the β values.

Using this RSF, the LSF can be computed from the Table 7-32 deterministic propagated loads with a GLF of 1.3. These computations are outlined in subsection 7.3.4.3 using Equations 2.60 and 2.61, and the load and resistance factors are computed using Equations 7.1 and 7.2.

For the T-Wall design with the 10 ft tension and 32 ft compression piles, Limit State 1 (Stem Shear), Limit State 2 (Stem Moment), Limit State 3 (Compression Pile SSI), and Limit State 4 (Tension Pile SSI) are the

primary failure mechanisms. Therefore, Table 7-33 focuses on summarizing results for these four dominant limit states. Recall from subsection 7.3.4 that R_{SF} and L_{SF} are computed Reliability constants used in the numerical analysis process to determine the value of resistance factor ϕ for a predefined target reliability index value, β_{Target}.

Table 7-33. Computation of local resistance factor (ϕ_L) for Mississippi River at St. Paul, MN.

Limit State		Flood Hazard	Resistance		Design Load (GLF= 1.3)		
			Mean (from sims)	R_{SF}			
LS#1	3	ACE	33,652	0.535302	21,026	0.856748	1.167204
		S100	33,632	0.536712		0.858494	1.16483
	3.5	ACE	33,652	1.015105		1.62467	0.61551
		S100	33,632	0.956975		1.530723	0.653286
	4	ACE	33,652	1.436330		2.298838	0.435002
		S100	33,632	1.593551		2.548954	0.392318
LS#2	3	ACE	104,695	0.700718	84,105	0.872263	1.146443
		S100	104,674	1.025077		1.275773	0.783838
	3.5	ACE	104,695	1.499044		1.86603	0.535897
		S100	104,674	1.529116		1.903082	0.525464
	4	ACE	104,695	2.568696		3.197546	0.31274
		S100	104,674	2.733292		3.401755	0.293966
LS#3	3	ACE	84,096	0.504957	50,000	0.849297	1.177444
		S100	84,109	0.508165		0.854825	1.16983
	3.5	ACE	84,096	0.745252		1.253454	0.797795
		S100	84,109	0.906013		1.524077	0.656135
	4	ACE	84,096	1.043951		1.755842	0.569527
		S100	84,109	1.162938		1.956271	0.511177
LS#4	3	ACE	28,664	0.403270	-5,000	2.311866	0.432551
		S100	26,103	0.276991		1.446059	0.691535
	3.5	ACE	28,664	0.858595		4.922153	0.203163
		S100	26,103	0.872194		4.553376	0.219617
	4	ACE	28,664	1.785610		10.23655	0.097689
		S100	26,103	2.014549		10.51715	0.095083

The rows of Table 7-33 are broken into sections based on limit state, β_{Target}, and the Flood Hazard Chance of Exceedance distributions used. The mean resistance for each limit state set of simulations is recorded, and finally, the scale factor required to scale the simulation limit state resistance values by to achieve the β_{Target} with respect to the simulation limit state load values (R_{SF}). The limit state design load, with respect to the scaled global design load is presented next. The next column has the load scale factor (L_{SF}) that would need to be applied to the initial design load to establish an equivalence with the mean simulated resistance value times the values in the R_{SF} column. The final column reveals the limit state resistance factor ϕ appropriate for the global load factor γ_G of 1.3. The β_{Target} values of 3.0, 3.5 and 4.0 are consistent with the Ellingwood recommendation.

For the compression pile SSI limit state (LS#3) with a β_{Target} = 3.5, computed ϕ values range from 0.656 to 0.798 using the two Mississippi River at St. Paul, MN, flood hazard characterizations. The Table 3-3 AASHTO Nominal Bearing Resistance of Single Pile—Static Analysis Methods, φ_{stat}, values are in the range of 0.4 to 0.5. Thus, the 0.656 to 0.798 computed range in resistance factor is higher than the comparable AASHTO factor value range. Note that the AASHTO Table 3-3 and Canadian Bridge code ϕ values reflect compilation and assessment of numerous pile foundation case studies, their resulting interpretation of group-data and subsequent committee judgement for recommended code specification. In contrast, the ϕ value computed for the compression pile SSI limit state (LS#3) reflects a single batter pile founded flood mitigation T-Wall result for the Mississippi River at St. Paul, MN, flood hazard. The Reliability-based 2014 CHBDC, as described in Fenton et al. (2016), reports compression resistance factor values for deep foundations of 0.4 and 0.45 for static analysis of soil foundations with typical and high degrees of understanding, respectively. After making a Reliability assessment, Fenton et al. (2016) conclude that the the target lifetime reliability index is approximately 3.5. The authors of this technical report conclude that both Reliability-based codes provide for a consistent deep foundation, single compression pile resistance factor recommendation.

For the tension pile SSI limit state (LS#4) with a β_{Target} = 3.5, computed ϕ values range from 0.203 to 0.22 using the Mississippi River at St. Paul, MN, flood hazard characterization. The Table 3-3 AASHTO Nominal

Bearing Resistance of Single Pile—Static Analysis Methods, φ_{stat}, values are in the range of 0.25 to 0.35. Thus, the 0.203 to 0.22 computed range in resistance factor is slightly lower than the lower bound value of the comparable AASHTO factor value range.

8 Summary, Conclusions, and Research Recommendations

8.1 Summary

This report summarizes the research and development of Reliability based tools and supporting software to develop LRFD values for complete batter pile-founded T-Wall flood mitigation structures. Complete hydraulic structural analysis for flood loading and wind-induced wave loading involves the structural and geotechnical SSI limit states. An example cross section of one of these flood mitigation structures is shown in Figure 7-1 with the left-most pile being referred to as the Tension pile and the right-most pile being referred to as the Compression pile, because these piles experience local tension and compression, repectively, under the system design flood load.

Ten limit states were identified that could affect the stability of the batter pile-founded T-Wall flood mitigation structure. These limit states consist of two limit states the affect the reinforced concrete section of the T-Wall stem section, two limit states that are concerned with the SSI analysis for each of the piles, and three limit states per pile for actual behavior of the pile itself. These limit states are as follows:

Reinforced concrete (Structural)

1. Shear failure at the base of the reinforced concrete stem.
2. Flexural failure at the base of the reinforced concrete stem.

Soil-structure interaction (Geotechnical)

3. Side friction and bearing capacity failure within the soil for the HP steel pile in **compression**.
4. Side friction capacity failure within the soil for the HP steel pile in **tension**.

HP steel **compression** piles (Structural)

5. Shear failure at the top of the **compression** HP steel pile.
6. Compression failure at the top of the **compression** HP steel pile.

7. Combined bending and axial compression failure at the top of the **compression** HP steel pile.

HP steel **tension** piles (Structural)

8. Shear failure at the top of the **tension** HP steel pile.
9. Tension failure at the top of the **tension** HP steel pile.
10. Combined bending and axial tension failure at the top of the **tension** HP steel pile.

Fan et al. (2014) indicated that determining individual load and resistance factors may not provide a sufficient PUP_{System} for the proposed lifetime of the structural and geotechnical pile system. This is reinforced by the results summarized in Tables 7-4, 7-11, 7-15, 7-20, and 7-25 possess system *PUP* values that are less than the sum of all 10 limit state *PUP*s. Results Example Problem Reliability analysis underscore Fan's observation. Fan et al. (2014) based their inference on the fact that the probability areas of the combined limit states can be greater than the probability area of any individual limit state and that the maximum probability of failure would be the sum of the probability areas of all the limit states, given no overlap of the failure regions.

These Reliability analyses give accurate reliability simulation load and resistance pairs for each limit state for use in the computation of Load Factors. Keeping these values as pairs keeps corresponding correlation between the loads and resistance.

Procedures for assessing these limit states are developed in Chapter 3 and with the use of the CASE Library software packages CAXPILE and CPGA-R. Chapters 4, 5, and 6 define how variable values are obtained and applied to the structural model. The variables that affect the structure are the following:

- Flood height (from ACE curves, which are also projected to 100-year chance of exceedance).
- Wind speeds (for determining wind-induced wave loading).
- Soil strength (S_u) within the foundation.
- Yield strength of the steel of the H-piles.
- Shear capacity of the reinforced concrete stem.
- Moment capacity of the reinforced concrete stem.

The first two variables affect the load on the batter pile-founded T-Wall. The last four affect the resistance of the structure.

The CASE program CAXPILE is used to define the S_u to pile capacity curves in tension as well as compression. It is also used to compute the soil-based C33 terms for pile frame interaction in CPGA-R.

The loads affecting each component are computed either directly (for the stem limit states) or through the propagation of the variable system load to the location of action for the pile-based limit states. This propagation relies on the frame-based analysis of CPGA-R.

The resistances can be computed from or have a direct relationship to their capacities. For instance, the S_u to SSI capacity at a pile is developed in equation form from a series of CAXPILE software executions, based on soil layers defined using a SHANSEP based soil strength assessment procedure. Due to spatial correlation effects of soil strength with distance (as expressed through the application of the scale of fluctuation, δ, term used in Vanmarcke's [1977a,b] Equation 7.6), a Variance Reduction Factor that is applied to the S_u point estimate COV to define the spatial COV which is assigned to the soils along the length of the pile. This conversion from point estimates to spatial estimates using Equation 7.7 results in shorter piles having a larger COV value as compared to longer piles driven into the same soil regime.

This COV difference is evidenced with the Red River of the North example problem with a scale of fluctuation of 5 ft, a COV_{Point} of 0.4 for S_u, a compression pile length of 35 ft, and a tension pile length of 10 ft. This problem has a S_u $COV_{Spatial}$ of 0.1174 and 0.2828 for the 35 ft compression pile and 10 ft tension pile, respectively, computed using Equations 7.6 and 7.7. Tables 8-1 and 8-2 show the values of S_U $COV_{Spatial}$ for both the compression and tension piles (respectively), and their ratios with COV_{Point}. In these tables, the three flood walls analyzed are based on flood sites at the Red River of the North (RRN) near Grand Forks, ND, the Red Wood River (RWR) near Marshall, MN, and the Mississipi River (STP) in St. Paul, MN.

Table 8-1. Site-based comparison with different compression pile lengths of computed $COV_{Spatial}$ values using a 5 ft vertical scale of fluctuation and the ratio of $COV_{Spatial}$ to COV_{Point}.

Site	Compression Pile Length (ft)	Tension Pile Length (ft)	COV_{Point}	Compression Pile $COV_{Spatial}$	Compression Pile $COV_{Spatial}$/ COV_{Point}
RRN	40	40	0.4	0.1414	0.3535
RRN	39	10		0.1432	0.358
RWR	35	10		0.1512	0.378
RWR	35	15		0.1512	0.378
STP	32	10		0.1581	0.3953

Table 8-2. Site-based comparison with different tension pile lengths of computed $COV_{Spatial}$ values using a 5 ft vertical scale of fluctuation and the ratio of $COV_{Spatial}$ to COV_{Point}.

Site	Compression Pile Length (ft)	Tension Pile Length (ft)	COV_{Point}	Tension Pile $COV_{Spatial}$	Tension Pile $COV_{Spatial}$/ COV_{Point}
RRN	40	40	0.4	0.1414	0.3535
RRN	39	10		0.2828	0.707
RWR	35	10		0.2828	0.707
RWR	35	15		0.2309	0.5773
STP	32	10		0.2828	0.707

Deterministic procedural computations using preliminary designs for a batter pile-founded T-Wall system were performed using a design procedure with equal length piles. The flood loads applied during the deterministic computations were set to the 750-year event for the T-Wall structure with no wave loading applied. It was determined that a design assigning equal length piles could be improved upon from a system viewpoint. Shorting the tension piles leads to more efficient structures from a system viewpoint. A method for the computation of nearly optimal pile lengths based on engineering criteria was developed and used for subsequent T-Wall example problems discussed in Chapter 7 of this report.

A Monte Carlo simulation Reliability technique was used to determine the *PUP* of each limit state and the system. Along with variable flood elevations, variable wind induced wave loadings were also used in this Reliability-based analysis. A method for determining an RSF that can be applied to each simulation sample such that the *PUP* calculation would

arrive at a target value was used. This value served as a basis for the computation of the LRFD resistance factor ϕ for each limit state based on a fixed global load factor of γ (i.e., $\gamma_G = 1.3$), which was applied to the design system load.

8.2 Conclusions

One of the most important conclusions that can be reached from the development of methods to measure limit state *PUP*s for these articulated (frame) systems is the realization that LRFD load factors can be applied to the design load of the structure, that load can be propagated to the individual members in the frame analysis, which in turn can be used to compute the LRFD resistance factor for that limit state. This reduces the number of load conditions that need to be applied to a structure in a Reliability analysis.

Deterministic analyses of batter pile-founded T-Walls on different rivers reveals that, in cross section, the design of the pile layout can be optimized, according to engineering criteria. The primary limit state for failure among the three T-Wall example problems was for SSI failure along the compression pile. This situation was first revealed in the deterministic design process for the each of the example problems, since the USACE design criteria was followed to establish the minimum length of the compression pile (LS#3). However, it was also revealed that significant overdesign of the tension pile length could easily be realized in those same analyses. This led to the development of a semi-optimized process to reduce the tension pile length. Reliability analyses based on these optimizations reveal that adjusting the tension pile length can cause very rapid changes for the *PUP* of the tension pile SSI limit state (LS#4), especially as the tension pile becomes short enough that soil variability is at its greatest.

Variable probabilities were applied from site-specific data (flood ACE and local wind speeds) and engineering characterization (S_u, steel yield strength f_y, and reinforced concrete stem shear and moment capacities). The results of these analyses revealed that unsatisfactory performance was found primarily in the first four limit states: LS#1 Stem Shear, LS#2 Stem Moment, LS#3 Compression Pile SSI, and LS#4 Tension Pile SSI. The capacity of the steel in the piles far exceeded the soil strengths, so the other limit states (LS#5-LS#10) *PUP* values were greatly exceeded by the first four limit states.

Tables 8-3 and 8-4 provide the resulting computations of the Compression Pile SSI LS#3 ϕ values for β=3.5 and β=4.0. The lowest computed ϕ values for this limit state among the three-river flood T-Wall sites is 0.65169 for β = 3.5 and 0.468041 for β= 4.0. These values are judged to be the appropriate resistance factor ϕ values for compression piles when using a flood load factor γ_G value of 1.3.

Table 8-3. A comparison of Limit State 3 (compression pile SSI) LRFD ϕ results for different pile lengths with system γ = 1.3 and target β = 3.5.

Site	Compression Pile Length (ft)	Tension Pile Length (ft)	Flood Distribution	ϕ
RRN	40	40	ACE	0.699341
			S100	0.675633
RRN	39	10	ACE	0.65169
			S100	0.67018
RWR	35	10	ACE	0.76853
			S100	0.79998
RWR	35	15	ACE	0.811651
			S100	0.795545
STP	32	10	ACE	0.797795
			S100	0.656135

Table 8-4. A comparison of Limit State 3 (compression pile SSI) LRFD ϕ results for different pile lengths with system γ = 1.3 and target β = 4.0

Site	Compression pile length (ft)	Tension pile length (ft)	Flood distribution	ϕ
RRN	40	40	ACE	0.468041
			S100	0.486471
RRN	39	10	ACE	0.52284
			S100	0.48884
RWR	35	10	ACE	0.66555
			S100	0.67443
RWR	35	15	ACE	0.677521
			S100	0.672009
STP	32	10	ACE	0.569527
			S100	0.511177

The AASHTO (2020), Fenton, et al. (2016), CHBDC 2014, and the ERDC T-Wall Reliability/LRFD factor analysis (Ebeling and White 2021) provide for ϕ values well less than 1.0. A ϕ value that is not close to 1.0 is a logical outcome for a compression pile foundation feature in the view of the authors of this technical report.

Note that the AASHTO (2020) Table 3-3 and CHBDC code ϕ values reflect compilation and assessment of numerous pile foundation case studies, their resulting interpretation of group-data and subsequent committee judgement for recommended code specification. In contrast, the ϕ value computed for the compression pile SSI limit state (LS#3) reflects a single batter pile-founded flood mitigation T-Wall result.

After making a Reliability assessment, Fenton et al. (2016 conclude that the the target lifetime reliability index (β) is approximately 3.5. The authors of this technical report conclude that both Reliability-based codes provide for a consistent deep foundation, single compression pile resistance factor recommendation.

The Table 3-3 AASHTO (2020) Nominal Bearing Resistance of Single Pile—Static Analysis Methods, φ_{stat}, values are in the range of 0.4 to 0.5. The Reliability-based 2014 CHBDC, as described in Fenton et al. (2016), reports compression resistance factor values for deep foundations of 0.4 and 0.45 for static analysis of soil foundations with typical and high degrees of understanding, respectively. The minimal ϕ value from the three different river flood site batter pile-founded T-Wall example problems of 0.65169 for the resistance factor is higher than the comparable factors from AASHTO and the CHBDC. A possible explanation for this higher value may be in the details regarding the value of and procedure used to arrive at a $COV_{Spatial}$ value assigned to the mean S_u distribution with depth used to establish the dispersion in S_u. Notice that all the computed ϕ values for the three-flood T-Walls are higher than the range of AASHTO and the CHBDC. Another possibility is that the computations made in this technical report are for laterally loaded flood walls with γ_G set equal to 1.3. Additionally, this investigation considered flood sites on three different rivers. More sites were considered in the AASHTO and CHBDC studies.

Tables 8-5 and 8-6 provide the resulting computations of the Tension Pile SSI LS#4 ϕ values for β=3.5 and β=4.0. The lowest computed ϕ values for

this limit state among the three-river flood T-Wall sites is 0.203163 for β = 3.5 and 0.095083 for β = 4.0, where values are available. As observed in the case for the compression pile, these Tension Pile ϕ values are judged to be appropriate when using a flood load factor γ_G value of 1.3.

Table 8-5. A comparison of Limit State 4 (tension pile SSI) LRFD ϕ results for different pile lengths with system γ = 1.3 and target β = 3.5.

Site	Compression Pile Length (ft)	Tension Pile Length (ft)	Flood Distribution	ϕ
RRN	40	40	ACE	<0.001
			S100	<0.001
RRN	39	10	ACE	0.28656
			S100	0.46451
RWR	35	10	ACE	0.24059
			S100	0.26147
RWR	35	15	ACE	0.272352
			S100	0.261495
STP	32	10	ACE	0.203163
			S100	0.219617

Table 8-6. A comparison of Limit State 4 (tension pile SSI) LRFD ϕ results for different pile lengths with system γ = 1.3 and target β = 4.0.

Site	Compression Pile Length (ft)	Tension Pile Length (ft)	Flood Distribution	ϕ
RRN	40	40	ACE	<0.001
			S100	<0.001
RRN	39	10	ACE	0.23634
			S100	0.40786
RWR	35	10	ACE	0.18196
			S100	0.17942
RWR	35	15	ACE	0.181448
			S100	0.182523
STP	32	10	ACE	0.097689
			S100	0.095083

For the tension pile SSI limit state (LS#4) with a β_{Target} = 3.5, the appropriate computed ϕ values range is 0.24059. The Table 3-3 AASHTO (2020) Nominal Bearing Resistance of Single Pile—Static Analysis Methods, φ_{stat}, values are in the range of 0.25 to 0.35. The computed ϕ value of 0.203163 is slightly below the comparable AASHTO lower range factor value. Examining the table of results indicates that the range of these values for the three-river site flood walls tends toward the lower end of the AASHTO tension pile range, as well.

This R&D effort developed a Reliability based procedure to compute values for resistance factors for a specified load factor, for use in design (LRFD) of the USACE next-generation, batter pile-founded T-Wall flood mitigation structures. For a Reliability analysis, one of the variables investigated for inland flood control structures is wind speed and its contribution through wind-induced wave loading (WIWL). Referring to Section 7.4, the Red Wood River flood-wall site near Marshall, MN, was one of the sites investigated for 100-year chance of exceedance wind speeds and characteristics for inputs to the Goda-Takahashi (Goda 2010) pseudo-static wave pressure equations. The geometry of the floodwall site was collected to find the fetch, sill, and the steepness of the bottom slope (Figure 8-1). The computed pseudo-static pressures acting on the wall were combined with the static flood SWL pressures to get the WIWL. For this analysis, both the inland flood elevation as well as the wind velocity were considered variables for simulations. The SWL was drawn from the 100-year chance of exceedance distribution.

Figure 8-1. Computation of Goda-Takahashi pseudo-static wave pressure distribution for the Red Word River batter pile-founded T-Wall.

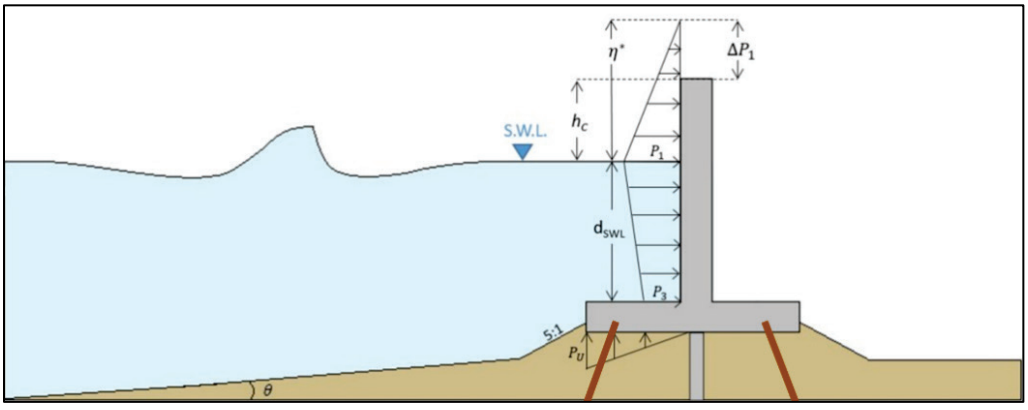

Table 8-7 provides results of Reliability analysis of the RWR site (with 35 ft long compression piles and 15 ft long tension piles) with and without consideration of WIWL. The mean peak 100-year wind was determined to be 59 mph. *PUP* and the Reliability Index, β, representing the number of standard deviations from a mean value for the limit state, are captured for each of four limit states: LS#1 stem shear, LS#2 stem moment, LS#3 compression pile soil side resistance/end bearing failure, and LS#4 tension pile soil side resistance failure.

Table 8-7. Unscaled PUP and Beta with the designed structure.

	LS#1		LS#2		LS#3		LS#4	
	PUP	β	*PUP*	β	*PUP*	β	*PUP*	β
WIWL	0.01277	2.233	0.13991	1.081	0.00961	2.341	0.00266	2.787
SWL	0.00821	2.399	0.05941	1.56	0.0062	2.501	0.00046	3.314

Table 8-7 *PUP*s increase significantly with the addition of wind-induced wave loading, by a factor of 1.55 to 5.78. The Reliability Index β value drops in an inverse non-linear relationship with *PUP*, with a decrease of between 6% to 31%, depending upon the limit state. These results demonstrate that there is a significant change caused by wind-induced wave loading and it is an important consideration for inland flood walls.

Table 8-8 provides results of LRFD factor analysis, with 100,000 simulations, of the RWR site (with 35 ft long compression piles and 15 ft long tension piles) with and without consideration of WIWL for two target β values. The computed values for LRFD load and resistance factors (γ_L and ϕ_R, respectively) are dependent on the shape of the load and resistance distributions as well as their correlation. The safety margin for the distributions is computed from the resistance minus the load distributions (R-L). With loads scaled by γ_L of 1.3, the safety margin is equal to a computed LSF which brings R-L to a target β value.

Table 8-8. ϕ_R values for γ_L value = 1.3.

		LS#1	LS#2	LS#3	LS#4
β=3.0	WIWL	0.697	0.679	0.814	0.592
	SWL	0.714	0.645	0.801	0.423
β=3.5	WIWL	0.533	0.483	0.653	0.215
	SWL	0.496	0.415	0.624	0.257

For a β value of 3.0, the ϕ_R values for Limit States 1 to 3 are nearly the same with or without WIWL effects. Limit State 4 ϕ_R values indicate that to maintain a β value of 3.0, the ϕ_R value increases when WIWL is incorporated in the LRFD analysis. This seems counterintuitive. The reason for this is that the tails of the load and resistance distributions have simulated values which contain outliers. These outliers influence the PDF of the resulting R-L curve. Similar results are observed in ϕ_R for the Reliability Index value of 3.5.

The SWL and WIWL ϕ_R values for three Limit States are nearly the same while Limit State 2 shows an observable difference. For target β values of 3.0 or above, the ϕ_R values show sensitivity to the shape of the PDF distribution for the safety margin in the tails of the distribution. However, because these effects happen in the PDF tails, the ϕ_R contribution is in the second decimal place and not the first, so its effect is noticeable but not as significant.

References

AASHTO (American Association of State Highway and Transportation Officials). 2002. *AASHTO Standard Specifications for Highway Bridges*. 17th Edition. Washington DC: American Association of State Highway and Transportation Officials.

AASHTO. 2004. *AASHTO LRFD Bridge Design Specifications,* 3rd Edition. Washington, DC: American Association of State Highway and Transportation Officials.

AASHTO. 2007. *AASHTO LRFD Bridge Design Specifications* (H. S. on B. and Structures (ed.); 4th ed.). Washington, DC: American Association of State Highway and Transportation Officials.

AASHTO. 2010. *AASHTO LRFD Bridge Design Specifications*. 5th edition, Parts I and II. Washington, DC: American Association of State Highway and Transportation Officials.

AASHTO. 2012. *AASHTO LRFD Bridge Design Specifications*. 6th Edition. Washington, DC: American Association of State Highway and Transportation Officials.

AASHTO. 2020. *AASHTO LRFD Bridge Design Specifications,* 9th Edition. American Association of State Highway and Transportation Officials. Washington, DC: American Association of State Highway and Transportation Officials.

ACI Committee 340. 1978. *Design Handbook in Accordance with the Strength Design Method of ACI 318-77, Volume 2, Columns*. ACI Publication SP-17A(78). Detroit, MI: American Concrete Institute.

ACI Committee 318. 2014. *Building Code Requirements for Structural Concrete* (ACI 318-14) and the *Commentary* (ACI 318R-14). Farmington Hills, MI: American Concrete Institute.

Allen, T. M. 2005. *Development of Geotechnical Resistance Factors and Downdrag Load Factors for LRFD Foundation Strength Limit State Design* (FHWA-NHI-05-052). http://www.wsdot.wa.gov/NR/rdonlyres/56610316-29DB-4E6F-B457-F137FDE15077/0/ResistanceFactorsFoundations.pdf

Allen, T. M. 2007. "Development of New Pile-Driving Formula and Its Calibration for Load and Resistance Factor Design." *Transportation Research Record* 2004(1): 20–27. https://doi.org/10.3141/2004-03

Allen, T. M. 2013. *AASHTO Geotechnical Design Specification Development in the USA, in Modern Geotechnical Design Codes of Practice; Implementation, Application and Development*. Edited by P. Arnold, G. A. Fenton, M. A. Hicks, T. Schweckendiek, and B. Simpson. Amsterdam, Netherlands.

Allsop, N. W. H., and J. E. Vicinanza. 1996. *Wave Forces on Vertical and Composite Breakwaters*. Strategic Research Report SR 443. Wallingford: HR Wallingford.

Alonso, E. E., and R. J. Krizek. 1975. “Stochastic Formulation of Soil Properties.” *Proc. Of the 2nd International Conference Applications of Statistics and Probability in Soil and Structural Engineering*. Aachen, F. R. Germany. Vol. 2, 9–32.

American Institute of Steel Construction. 2005 *Steel Construction Manual*. 13th Edition. https://erdclibrary.on.worldcat.org/v2/oclc/65182668

Ang, A. H-S., and W. H. Tang. 1984. *Probability Concepts in Engineering Planning and Design: Decision, Risk and Reliability*. Volume II. New York: John Wiley & Sons.

Asaoka, A., and D. A-Grivas. 1982. “Spatial Variability of the Undrained Strength of Clays.” *Journal of the Geotechnical Engineering Division, ASCE* 108(5): 743–756.

ASCE (American Society of Civil Engineers Standard). 2010. *Minimum Design Loads for Buildings and Other Structures*. ASCE/SEI 7-10. Reston, VA.

Babu, G. L. S. 2014. “Spatial Variability Using Random Fields.” Chapter 3. *Reliability Engineering*. Madras, India: National Programme on Technology Enhanced Learning (NPTEL).

Baecher, D. E. 1996. “Limit States Design for Foundations. Part I. An Overview of the Foundation Design Process.” *Canadian Geotechnical Journal* 32: 956–983.

Baecher, G. B., and J. T. Christian. 2003. *Reliability and Statistics in Geotechnical Engineering*. West Sussex, England: John Wiley & Sons, Ltd.

Baecher, G. B., M.-E. Pate, and R. de Neufville. 1980. “Risk of Dam Failure in Benefit-Cost Analysis.” *Water Resource Research* 16(3): 449–456.

Baecher, G., and J. Christian. 2006. "The Influence of Spatial Correlation on the Performance of Earth Structures and Foundations." *GeoCongress 2006: Geotechnical Engineering in the Information Technology Age, American Society of Civil Engineers*, 1-6.

Bagnold, R. A. 1939. “Interim Report on Wave-Pressure Research.” *J. Inst. Civil Eng*. 12: 202–226. ICE, London.

Bao, C. G., W. F. Huang, and Q. N. Chang. 1993. “Reliability Analysis of Bearing Capacity for a Gravity Wharf Foundation in Random Field Theory.” *Probabilistic Methods in Geotechnical Engineering: Proceedings of the Conference, Canberra*, 10-12 February 1993.

Barker, R. M., Duncan, J. M., Rojiani, K. B., Ooi, P. S. K., Tan, C. K. and Kim. S. G. 1991. *Manuals for the Design of Bridge Foundations*. NCHRP Report 343, TRB. Washington, DC: National Research Council.

Bartlett, F. M., R. J. Dexter, M. D. Graeser, J. J. Jelenek, B. J. Schmidt, and T. V. Galambos. 2003. “Updating Standard Shape Material Properties Database for Design and Reliability.” *Engineering Journal, AISC* 40(1): 2–14.

Bathurst, R. J., T. M. Allen, Y. Miyata, and B. Huang. 2013. *Lessons Learned from LRFD Calibration of Reinforced Soil Wall Structures, in Modern Geotechnical Design Codes of Practice; Implementation, Application, and Development*. Edited by P. Arnold, G. A. Fenton, M. A. Hicks, T. Schweckendiek, and B. Simpson. Amsterdam, Netherlands: IOS Press BV under the imprint Millpress.

Bergado, D. T., B. C. Patron, W. Youyongwatana, J. C. Chai, and Yudhbir. 1994. "Reliability-Based Analysis of Embankment on Soft Bangkok Clay." *Structural Safety* 13(4): 247–266.

Bradshaw, A., and S. Davis. 2013. *Assessment of Current AASHTO LRFD Methods for Static Pile Capacity Analysis in Rhode Island Soils*.

Bredmose, H., G. N. Bullock, and A. J. Hogg. 2015. "Violent Breaking Wave Impacts; Part 3; Effects of Scale and Aeration." *Journal of Fluid Mechanics* 765: 82-113.

Briaud, J.-L., and L. Tucker. 1997. *Design and Construction Guidelines for Downdrag on Uncoated and Bitumen-Coated Piles* (NCHRP Report 393). Washington, DC: National Academy Press.

Bullock, G., C. Obhrai, G. Muller, G. Wolters, H. Peregrine, and H. Bredmose. 2004. "Characteristics and Design Implications of Breaking Wave Impacts." *Proceedings of the 29th International Conference Coastal Engineering, National Civil Engineering Laboratory, Lisbon, Portugal*. Vol. 4, 3966-3978. https://doi.org/10.1142/9789812701916_0320

Burlington, R. S., and D. C. May. 1970. *Handbook of Probability and Statistics with Tables,* 2nd Edition. New York, NY: McGraw-Hill Book Company.

Cafaro, F., and C. Cherubini. 2002. "Large Sample Spacing in Evaluation of Vertical Strength Variability of Clayey Soil." *Journal of Geotechnical and Geoenvironmental Engineering, ASCE* 128(7): 558–568.

Cedergren, H. R. 1977. *Seepage, Drainage, and Flow Nets,* 2nd Edition. New York, NY: John Wiley & Sons.

CEN 2004. *Eurocode 7: Geotechnical Design. Part I: General Rules*. EN 1997-1. European Committee for Standardization (CEN).

Cherubini, C. 1997. "Data and Consideration on the Variability of Geotechnical Properties of Soils." *Proceedings of the International Conference on Safety and Reliability (ESREL) 97, Lisbon*. Vol. 2, 1583–1591.

Cherubini, C. 2000. "Probabilistic Approach to the Design of Anchored Sheet Pile Walls." *Computers and Geotechnics* 26(3–4): 309–330.

Cherubini, C., G. Vessia, and W. Pula. 2006. "Statistical Soil Characterization of Italian Sites for Reliability Analyses." *Characterization and Engineering Properties of Natural Soils, Proceedings of the Second International Workshop on Characterization and Engineering Properties of Natural Soils. Singapore, November 29 - December 1, 2006*. National University of Singapore: Taylor & Francis.

Chiasson, P., J. Lafluer, M. Soulie, and K. T. Law. 1995. "Characterizing Spatial Variability of a Clay by Geostatistics." *Canadian Geotechnical Journal* 32(1): 1–10.

Christian, J. T., and G. B. Baecher. 2001. "Factor of Safety and Reliability in Geotechnical Engineering by J. M. Duncan." *ASCE, Journal of Geotechnical and Geoenvironmental Engineering* 127(8): 700–702.

Christian, J. T., and G. B. Baecher. 2011. "Unsolved Problems in Geotechnical Risk and Reliability." *GeoRisk 2011: Geotechnical Risk Assessment and Management*. American Society of Civil Engineers. http://dx.doi.org/10.1061/41183(418)3

Christian, J. T., C. C. Ladd, and G. B. Baecher. 1994. "Reliability and Probability in Stability Analysis." *Journal of Geotechnical Engineering, ASCE* 120: 1071–1111.

Coastal Engineering Manual: https://www.publications.usace.army.mil/USACE-Publications/Engineer/Manuals/u43544q/636F617374616C20656E67696E656572696E67206D616E75616C/

CSN (Canadian Standards Association). 2006. *Canadian Highway Bridge Design Code*. CAN/CSA-S6-06. Mississauga, Ontario.

CSN. 2014. *Canadian Highway Bridge Design Code*. CAN/CSA-S6-14. Mississauga, Ontario.

Cuomo, G. 2007. "Wave Impacts on Vertical Seawalls and Caisson Breakwaters." *On Course: PIANC Magazine* 127: 25–38. nr 127, repository.tudelft.nl

Cuomo, G., W. Allsop, T. Bruce, and J. Pearson. 2010a. "Breaking Wave Loads at Vertical Seawalls and Breakwaters." *Coastal Engineering* 57(4).

Cuomo G., W. Allsop, and S. Takahashi. 2010b. "Scaling Wave Impact Pressures on Vertical Walls." *Coastal Engineering* 57(4).

Dai, S. H., and M. O. Wang. 1992. *Reliability Analysis in Engineering Applications*. New York: Van Nostrand Reinhold.

Dawkins, W. P. 1984. *User's Guide: Computer Program for Soil-Structure Interaction Analysis of Axially Loaded Piles (CAXPILE)*. Instruction Report K-84-4. Vicksburg, MS: US Army Engineer Waterways Experiment Station.

DeGroot, D. J., and G. B. Baecher. 1993. "Estimating Autocovariance of In-Situ Soil Properties." *ASCE, Journal of Geotechnical Engineering* 119(1): 147–165.

Dexter, R. J., M. Graeser, W. K. Saari, C. Pascoe, C. A. Gardner, and T. V. Galambos. 2000. *Structural Shape Material Property Survey*. Technical report for Structural Shape Producers Council. Minnesota, MN: University of Minnesota, Minneapolis.

Ditlevsen, O. 1981. *Uncertainty Modeling with Applications to Multidimensional Civil Engineering Systems*. New York: McGraw-Hill.

Doherty, P., and K. Gavin. 2010. "Statistical Review of CPT Data and Implications for Pile Design." *2nd International Symposium on Cone Penetration Testing: Volume 3. 2nd International Symposium on Cone Penetration Testing (CPT10), Huntington Beach, California, USA, May 9-11, 2010*.

Duncan, J. M. 2000. "Factors of Safety and Reliability in Geotechnical Engineering." *Journal of Geotechnical and Geoenvironmental Engineering, ASCE* 126(4): 307–316.

Duncan, J. M., C. K. Tan, R. M. Barker, and K. B. Rojiani. 1989. "Load and Resistance Factor Design of Bridge Structures." *Proceedings of the Symposium on Limit States Design in Foundation Engineering, Toronto, Canadian Geotechnical Society, Southern Ontario Section*, 47–63.

Duncan, J. M., M. Navin, and T. F. Wolff. 2003. "Probabilistic Slope Stability Analysis for Practice." Edited by H. El-Ramly, N. R. Morgenstern, and D. Cruden. *Canadian Geotechnical Journal* 40: 848–850.

Duncan, J. M., and S. G. Wright. 2005. *Soil Strength and Slope Stability*. Hoboken, NJ: John Wiley & Sons, Inc.

Duncan, J. M., S. G. Wright, and T. L. Brandon. 2014. *Soil Strength and Slope Stability*. 2nd edition. Hoboken, NJ: John Wiley & Sons, Inc.

Ebeling, R. M., and White, B. C. 2016. *Characterizing Axial Stiffness of Individual Batter Piles with Emphasis on Elevated, Laterally Loaded, Clustered Pile Groups*. ERDC/ITL TR-16-5. Vicksburg, MS: US Army Engineer Research and Development Center.

Ebeling, R. M., B. C. White, and K. Abraham. 2012. *Simplified Analysis Procedures for Flexible Approach Wall Systems Founded on Groups of Piles and Subjected to Barge Train Impact*. ERDC/ITL TR-12-3. Vicksburg, MS: US Army Engineer Research and Development Center.

Ebeling, R. M., B. C. White, and M. T. Fong. 2013. *Simulation and Advanced Second Moment Reliability Analyses of Pile Groups Using CPGA-R; Formulation, User's Guide, and Example Problems*. ERDC/ITL TR-13-2. Vicksburg, MS: US Army Engineer Research and Development Center.

Ebeling, R. M., B. C. White, and M. T. Fong. 2018. *Analysis of a Riverbank, Levee, or Floodplain I-Wall Embedded in Stratified Soil Layers during Flood Events Using Corps_I-Wall (CI-Wall) Version 2.0*. ERDC/ITL TR-18-2. Vicksburg, MS: US Army Engineer Research and Development Center

Ebeling, R. M., and B. C. White. 2019. *Load Factors for Earth Retaining, Reinforced Concrete Hydraulic Structures Based on a Reliability Index (β) Derived from the Probability of Unsatisfactory Performance; Phase 1 Study*. ERDC/ITL TR-19-5. Vicksburg, MS: US Army Engineer Research and Development Center.

Ebeling, R. M., and B. C. White. 2021. *Load and Resistance Factors for Earth Retaining, Reinforced Concrete Hydraulic Structures Based on a Reliability Index (β) Derived from the Probability of Unsatisfactory Performance; Phase 2 Study*. ERDC/ITL TR-21-1. Vicksburg, MS: US Army Engineer Research and Development Center.

Ellingwood, B., and H. Hwang. 1985. "Probabilistic Descriptions of Resistance of Safety Related Structures in Nuclear Plants." *Nuclear Engineering and Design* 88(2): 169–178.

Ellingwood, B., T. V. Galambos, J. G. MacGregor, and C. A. Cornell. 1980. *Development of a Probability-Based Load Criterion for American National Standard A58 – Building Code Requirements for Minimum Design Loads in Buildings and Other Structures*. Special Publication 577. Washington, DC: National Bureau of Standards.

Ellingwood, B., J. G. MacGregor, T. V. Galambos, and C. A. Cornell. 1982. "Probability Based Load Criteria: Load Factors and Load Combinations." *Journal of the Structural Division, ASCE* 108(ST5) Proc. Paper 17068: 978–997.

El-Ramly, H. 2001. *Probabilistic Analysis of Landslide Hazards and Risks: Bridging Theory and Practice*. Doctor of Philosophy in Geotechnical Engineering Thesis. University of Alberta, Edmonton, Canada.

El-Ramly, H., N. R. Morgenstern, and D. Cruden. 2002a. "Probabilistic Slope Stability Analysis for Practice." *Canadian Geotechnical Journal* 39: 665–683.

EL-Ramly, H., N. R. Morgenstern, and D. M. Cruden. 2002b. "Probabilistic Stability Analysis of Lodalen Slide." *Proc., 55th Canadian Geotechnical Conf., Niagara Falls*, 1053–1060.

El-Ramly, H., N. R. Morgenstern, and D. Cruden. 2003a. "Probabilistic Stability Analysis of a Tailings Dyke on Presheared Clay–Shale." *Canadian Geotechnical Journal* 40: 192–208.

El-Ramly, H., N. R. Morgenstern, and D. Cruden. 2003b. "Probabilistic Slope Stability Analysis for Practice." *Canadian Geotechnical Journal* 40: 851–855.

Fan, H., Q. Huand, and R. Liang. 2014. "Reliability Analysis of Piles in Spatially Varying Soils Considering Multiple Failure Modes." *Computers and Geotechnics* 57: 97–104.

Fenton, G. A., and D. V. Griffiths. 2008. *Risk Assessment in Geotechnical Engineering*. Hoboken, NJ: John Wiley & Sons, Inc.

Fenton, G. A., F. Naghibi, D. Dundas, R. J. Bathurst, and D. V. Griffiths. 2016. "Reliability-Based Geotechnical Design in 2014 Canadian Highway Bridge Design Code." *NRC Research Press, Canadian Geotechnical Journal* 53: 236–251.

Fenton, G. A., and E. H. Vanmarcke. 1991. "Spatial Variation in Liquefaction Risk Assessment." *Geotechnical Engineering Congress 1991, Boulder, Colorado, 10–12 June*. Geotechnical Special Publication No. 27. Vol. 1. Reston, VA: American Society of Civil Engineers.

FHWA (Federal Highway Administration). 2001. *Load and Resistance Factor Design (LRFD) for Highway Bridge Substructures; Reference Manual and Participant Workbook*. Publication No. FHWA HI-98-032. NHI Course No. 132068. https://erdclibrary.on.worldcat.org/v2/oclc/243800344

Foye, K. C., R. Salgado, and B. Scott. 2006. "Assessment of Variable Uncertainties for Reliability-Based Design of Foundations." *Journal of Geotechnical and Geoenvironmental Engineering*, *ASCE* 132(9): 1197–1207.

Gao, D. Z., and J. P. Li. 1993. "Reliability Analysis on Pile Bearing Capacity." *Probabilistic Methods in Geotechnical Engineering, Proceedings of the Conference, Canberra*, 10–12 February 1993.

Garcia, W. J. 1968. *An Experimental Study of Breaking-Wave Pressures*. Waterways Experiment Station Research Report H-68-1. Vicksburg, MS: US Army Waterways Experiment Station.

Goda, Y. 1972. "Experiments on the Transition from Nonbreaking to Postbreaking Wave Pressures." *Coastal Engineering in Japan* 15(1): 81–90.

Goda, Y. 1973. "A New Method of Wave Pressure Calculation for the Design of Composite Breakwater, Report." *Port and Harbour Research Institute* 12(3): 31–69. (in Japanese)

Goda, Y. 1974. "New Wave Pressure Formulae for Composite Breakwater." *Proc. Of 14th Int. Conf. Coastal Eng., Copenhagen, Denmark, ASCE, New York*, 1702–1720.

Goda Y. 2010. *Random Seas and Design of Maritime Structures*. 3rd Edition. Hackensak, Nj: World Scientific.

Goda, Y., and T. Fukumori. 1972. "Laboratory Investigation of Wave Pressures Exerted Upon Vertical and Composite Walls, Report." *Port and Harbour Research Institute* 11(2): 7–45. (in Japanese)

Goda, Y., and S. Kakizaki. 1966. "Study on Finite Amplitude Standing Waves and their Pressures Upon a Vertical Wall, Report." *Port and Harbour Research Institute* 5(10): 57. (in Japanese)

Gringorten, I. I. 1963. "A Plotting Rule for Extreme Probability Paper." *Journal of Geophysical Research* 68(3): 813–814.

Hannigan, P. J., G. G. Goble, G. E. Likins, and F. Rausche. 2005. *Design and Construction of Driven Pile Foundations*. Volumes I and II. (Reference for NHI Courses 132021 and 132022). Washington, DC: National Highway Institute, Federal Highway Administration.

Hannigan, P. J., F. Rausche, G. E. Likins, B. R. Robinson, and M. L. Becker. 2016. *Design and Construction of Driven Pile Foundations Reference Manual – Volume I (FHWA-NHI-16-009): Vol. I*. Washington, DC: US Department of Transportation, Federal Highway Administration. https://erdclibrary.on.worldcat.org/v2/oclc/1012132543

Hartman, J. P., J. J. Jaeger, J. J. Jobst, and D. K. Martin. 1989. *User's Guide: Pile Group Analysis (CPGA)*. Technical Report ITL-89-3. Vicksburg, MS: US Army Engineer Waterways Experiment Station.

Hasofer, A. M., and N. C. Lind. 1974. "Exact and Invariant Second Moment Code Format." *Journal of the Eng. Mech. Division, ASCE* 100(EM1): 111–121.

Hibbeler, R. C. 2014. *Mechanics of Materials*, 9th Edition. Boston, MA: Prentice Hall.

Hicks, M. A. 2013. "An Explanation of Characteristics Values of Soil Properties in Eurocode 7." *Modern Geotechnical Design Codes of Practice; Implementation, Application and Development*. Edited by P. Arnold, G. A. Fenton, M. A. Hicks, T. Schweckendiek, and B. Simpson. Amsterdam: IOS Press,

Hicks, M. A., and K. Samy. 2002. "Influence of Heterogeneity on Undrained Clay Slope Stability." *Quarterly Journal of Engineering Geology and Hydrology* 35: 41–49.

Hicks, M. A., and W. A. Spencer. 2010. "Influence of Heterogeneity on the Reliability and Failure of a Long 3D Slope." *Computers and Geotechnics* 37: 948–955.

Honjo, Y., and K. Kuroda. 1991. "A New Look at Fluctuating Geotechnical Data for Reliability Design." *Soils and Foundations* 31: 110–120.

Honjo, Y., and Y. Otake. 2013. "A Simple Method to Assess the Effects of Soil Spatial Variability on the Performance of a Shallow Foundation." *Foundation Engineering in the Face of Uncertainty*, Honoring Fred H. Kulhawy. ASCE Geotechnical Specialty Publication no. 229. Edited by J. L. Withiam, K-K Phoon, and M. H. Hussein. https://doi.org/10.1061/9780784412763.030

HQUSACE (Headquarters, US Army Corps of Engineers). 1989a. *Engineering and Design: Retaining and Flood Walls*. EM 1110-2-2502. Washington, DC.

HQUSACE. 1989b. *Engineering and Design: Design of Pile Foundations*. EM 1110-2-2906. Washington, DC.

HQUSACE. 1994. *Design of Sheet Pile Walls*. EM 1110-2-2504. Washington, DC.

HQUSACE. 1997. *Life Cycle Design and Performance*. ER 1110-2-8159. Washington, DC.

HQUSACE. 2002. Coastal Engineering Manual. EM 1110-2-1100, US Army Corps of Engineers, Washington, DC. (6 volumes). https://www.publications.usace.army.mil/USACE-Publications/Engineer-Manuals/u43544q/636F617374616C20656E67696E656572696E67206D616E75616C/

HQUSACE. 2005. *Stability Analysis of Concrete Structures*. EM 1110-2-2100. Washington, DC.

HQUSACE. 2016. *Strength Design for Reinforced Concrete Hydraulic Structures*. EM 1110-2-2104. Washington, DC.

Jaska, M. B., P. L. Brooker, and W. S. Kaggwa. 1997. "Inaccuracies Associated with Estimating Random Measurement Errors." *ASCE, Journal of Geotechnical and Geoenvironmental Engineering* 23(5): 393–401.

Jaksa, M. B., W. S. Kaggwa, and P. I. Brooker. 2000. "Experimental Evaluation of the Scale of Fluctuation of a Stiff Clay." *Applications of Statistics and Probability: Civil Engineering Reliability and Risk Analysis: Proceedings of the ICASP 8 Conference, Sydney, New South Wales, Australia*, 12-15 December 1999. Edited by R. E. Melchers, M. G. Stewart, and A. A. Sydney. Rotterdam: Balkema.

Keaveny, J. M., F. Nadim, and S. Lacasse. 1989. "Autocorrelation Functions for Offshore Geotechnical Data." *Proceedings of the 5th International Conference on Structural Safety and Reliability, San Francisco, Calif., 7–11 August*. Edited by A.H.-S. Ang, M. Shinozuka, and G.I. Schuëller. American Society of Civil Engineers, New York, NY.

Kisacik, D., P. Van Bogaert, and P. Trock. 2010. "Comparative Study on Breaking Wave Forces on Vertical Walls with Cantilever Surfaces, Coastal Engineering." *Proceedings of 32nd Conference on Coastal Engineering, Shanghai, China, No. 32*.

Kulatilake, P. H. S. W., and A. Ghosh. 1988. "An Investigation into Accuracy of Spatial Variation Estimation Using Static Cone Penetrometer Data." *Penetration Testing, 1988: Proceedings of the First International Symposium on Penetration Testing, ISOPT-1, Orlando*, 20-24 March 1988.

Kulhawy, F. H., B. Birgisson, and M. D. Grigoriu. 1992. *Reliability-Based Foundation Design for Transmission Line Structures: Transformation Models for In Situ Tests*. EPRI-EL-5507-Vol.4. Palo Alto, CA: Electric Power Research Institute.

Lacasse, S., and J. Y. de Lamballerie. 1995. "Statistical Treatment of CPT Data." *Proceedings of the International Symposium on Cone Penetration Testing, 4–5 October, Linköping, Sweden*. Vol. 2: 369–380. Swedish Geotechnical Society.

Lacasse, S., and F. Nadim. 1996. "Uncertainties in Characterizing Soil Properties." *Uncertainty in the Geologic Environment: From Theory to Practice: Proceedings of Uncertainty '96*, July 31-August 3, 1996, Madison, Wisconsin.

Ladd, C. C., and R. Foott. 1974. "A New Design Procedure for Stability of Soft Clays." *Journal of the Geotechnical Engineering Division, ASCE* 100(GT7): 763–786.

Li, K. S. 1992. "Some Common Mistakes in Probabilistic Analysis of Slopes." *Landslides*, Vol. 1. Edited by David Bell, Geology Department, University of Canterbury, Christchurch, New Zealand. *Proceedings of the Sixth International Symposium 10–14 February 1992, Christchurch, New Zealand*. Rotterdam, Brookfield: A. A. Balkema.

Li, K. S., and I. K. Lee. 1991. 'The Assessment of Geotechnical Safety." *Selected Topics in Geotechnical Engineering—Lumb Volume*. Edited by K. S. Li. Kensington. Australia: University of New South Wales.

MacGregor, J. G., S. A. Mirza, and B. Ellingwood. 1983. "Statistical Analysis of Resistance of Reinforced and Prestressed Concrete Members." *J. American Concrete Institute* 80(3): 167–176.

Matheron, G. 1962. *Traite de Geostatistique Appliquee*, Vol. 1. Paris: Technip.

Matsuo, M., and A. Asaoka. 1977. "Probability Models of Undrained Shear Strength of Marine Clay Layer." *Soils and Foundations* 17(3): 53–68.

Melchers, R. E. 1999. *Structural Reliability: Analysis and Prediction*, 2nd Edition. Chichester, UK: John Wiley and Sons, Ltd.

Meyerhof, G. G. 1976. "Bearing Capacity and Settlement of Pile Foundations." *Journal of Geotechnical Engineering Division, ASCE* 102(GT3): 197–227.

Modjeski and Masters Inc. 2015. *Bridges for Service Life Beyond 100 Years: Service Limit State Design (SHRP 2 Report S2-R19B-RW-1)*. https://doi.org/10.17226/22441

Mollon, M. G., K.-K. Phoon, D. Dias, and A.-H. Soubra. 2011. "Influence of the Scale of Fluctuation of the Friction Angle on the Face Stability of a Pressurized Tunnel in Sands, ASCE." *Georisk 2011 - Geotechnical Risk Assessment & Management*. Atlanta, GA.

Nowak, A. S., and N. C. Lind. 1979. "Practical Bridge Code Calibration." *Proceedings of the American Society of Civil Engineers, ASCE, Journal of the Structural Division* 105(ST12): 2497–2510.

Nowak, A. S. 1999. *Calibration of LRFD Bridge Design Code*. NCHRP Report 368 (1999). http://onlinepubs.trb.org/Onlinepubs/nchrp/nchrp_rpt_368.pdf

Nowak, A. S., and K. R. Collins. 2000. *Reliability of Structures*. Boston: McGraw-Hill.

Nowak, A. S., and K. R. Collins. 2013. *Reliability of Structures,* 2nd Edition. Boca Raton, FL: CRC Press, Taylor and Francis Group.

Nowak, A. S., and M. M. Szerszen. 2003. "Calibration of Design Codes for Buildings (ACI 318): Part 1 – Statistical Models for Resistance." *ACI Structural J*. 100: 377–382.

Onsiphorou, C. 2000. *Stochastic Analysis of Saturated Soils Using Finite Elements*. PhD thesis. University of Manchester, UK.

Paikowsky, Samuel G. 2004. *Load and Resistance Factor Design (LRFD) for Deep Foundations*. NCHRP Report 507. https://doi.org/10.17226/13758

Paikowsky, S. G., M. Caniff, S. Robertson, and A. S. Budge. 2014. *Load and Resistance Factor Design (LRFD) Pile Driving Project – Phase II Study*. MN/RC 2014-16. St. Paul, MN: Minnesota Department of Transportation.

Paikowsky, Samuel G., J. E. Regan, and J. J. McDonnell. 1994. *A Simplified Field Method for Capacity Evaluation of Driven Piles*. McLean, VA: Federal Highway Administration.

Paikowsky, S. G. 2004. *Load and Resistance Factor Design (LRFD) for Deep Foundations*. NCHRP (Final) Report 507. Contributions from B. Birgisson, M. McVay, T. Nguyen, C. Kao, G. Baecher, B. Ayyub, K. Stenersen, K. O'Malley, L. Chernauskas and M. O'Neil. Washington, DC: Transportation Research Board.

Pearson, Karl. 1895. "Notes on Regression and Inheritance in the Case of Two Parents." *Proceedings of the Royal Society of London* 58: 240–242.

Phoon, K. K., and F. H. Kulhawy. 1999a. "Characterization of Geotechnical Variability." *Canadian Geotechnical Journal* 36: 612–624.

Phoon, K. K., and F. H. Kulhawy. 1999b. "Evaluation of Geotechnical Property Variability." *Canadian Geotechnical Journal* 36: 625–639.

Popescu, R., J. H. Prevost, and G. Deodatis. 1997. "Effects of Spatial Variability on Soil Liquefaction: Some Design Recommendations." *Geotechnique* 47: 1019–1036.

Rackwitz, R., and B. Fiessler. 1976. "Note on Discrete Safety Checking When Using Nonnormal Stochastic Model for Basic Variables." *Loads Project Working Session*. Cambridge, MA: MIT.

Rackwitz, R., and B. Fiessler. 1978. "*Structural* Reliability under Combined Random Load Sequences." *Computer and Structures* 9(5): 489–494. Oxford: Pergamon Press. https://doi.org/10.1016/0045-7949(78)90046-9

Rattanapitikon, W., and T. Shibayama. 2000. "Verification and Modification of Breaker Height Formulas." *Coastal Engineering Journal* 42(4): 389–406.

Rosenblatt, M. 1952. "Remarks on a Multivariate Transformation." *Annals of Mathematical Statistics* 23(3): 470–472.

Schneider, H. R., and M. A. Schneider. 2013. "Dealing with Uncertainties in EC7 with Emphasis on Determination of Characteristic Soil Properties. *Modern Geotechnical Design Codes of Practice; Implementation, Application and Development*. Edited by P. Arnold, G. A. Fenton, M. A. Hicks, T. Schweckendiek, and B. Simpson. Amsterdam, Netherlands.

Siegel, T. C., R. Lamb, D. Dasenbrock, and P. J. Axtell. 2013. "Alternative Design Approach for Drag Load and Downdrag of Deep Foundations Within the LRFD Framework." *Proceedings of the 38th Annual Conference on Deep Foundations, 2013,* Phoenix, AZ. Hawthorne, NJ: Deep Foundations Institute.

Singh, V. P., S. K. Jain, and A. Tyagi. 2007. *Risk and Reliability Analysis: A Handbook for Civil and Environmental Engineers*. Reston, VA: ASCE Press.

Sleep, M., and J. M. Duncan. 2014. *Manual for Geotechnical Engineering Reliability Calculations*, 2nd Edition. CGPR #76. Blacksburg, VA: Virginia Polytechnic Institute and State University, Center for Geotechnical Practice and Research.

Smith, J. M. 1991. *Wind-Wave Generation on Restricted Fetches*. Miscellaneous Paper CERC-91-2. Vicksburg, MS: US Army Engineer Waterways Experiment Station, Coastal Engineering Research Center.

Smith, E. R., and N. C. Kraus. 1991. "Laboratory Study of Wave Breaking over Bars and Artificial Reefs." *ASCE Journal of Port, Waterway and Ocean Engineering* 17(4).

Sokolovskii, V. V. 1965. *Static of Granular Media*. New York: Pergamon Press.

Soulie, M., P. Montes, and V. Silvestri. 1990. "Modelling Spatial Variability of Soil Parameters." *Canadian Geotechnical Journal* 27: 617–630.

Takahashi, S., K. Tanimoto, and K. Shimosako. 1993. "Experimental Study of Impulsive Pressures on Composit Breakwaters – Foundational Feature of Impulsive Pressure and the Impulsive Pressure Coefficient." *Report of the Port and Harbour Research Institute* 31(5): 33–72. (in Japanese)

Takahashi, S. 2002. *Design of Vertical Breakwaters, Port and Airport Research Institute, Japan*. Original version published August 1966. Revised version 2.1 published July 2002. Reference Document No. 34. Port and Harbour Research Institute.

Tallent, J. R. 1990. *The Role of the Large-Scale Eddy in Breaking Water Waves*. Disaster Prevention Research Institute (DPRI). Doctoral Dissertation. Kyoto University, Kyoto, Japan.

Tang, W. H. 1979. "Probabilistic Evaluation of Penetration Resistances." *Journal of the Geotechnical Engineering Division, ASCE* 105: 1173–1191.

Terzaghi, K., and R. B. Peck. 1967. *Soil Mechanics in Engineering Practice*, 2nd Edition. Hoboken, NJ: Wiley.

Tippett L. H. C. 1925. "On Extreme Individuals and a Range of Samples Taken from a Normal Distribution." *Biometrika* 17(3/4): 364–387.

USACE MVP (US Army Corps of Engineers, St. Paul District). 2014. *Oxbow-Hickson-Bakke (OHB) Levee Wind-Wave Analysis*. Final draft. St. Paul, MN: US Army Corps of Engineers, St. Paul District. http://fmdam.org/wp-content/uploads/2013/09/2014-01-03_OHB_Wind-Wave_Report.pdf

Uzielli, M., G. Vannucchi, and K. K. Phoon. 2005. "Random Field Characterization of Stress-Normalized Cone Penetration Test Parameters." *Geotechnique* 55(1): 3–20.

Vanmarcke, E. 1977a. "Probabilistic Modeling of Soil Profiles." *ASCE Journal of the Geotechnical Division* 103(GT11): 1227–1246.

Vanmarcke, E. 1977b. "Reliability of Earth Slopes." *ASCE Journal of the Geotechnical Division* 103(GT11): 1247–1265.

Vanmarcke, E. 1980. "Probabilistic Stability Analysis of Earth Slopes." *Engineering Geology* 16(Special Issue Mechanics of Landslides and Slope Stability): 29–50.

Vanmarcke, E. 1983. *Random Fields: Analysis and Synthesis*. Cambridge, MA: MIT Press.

Vanmarcke, E. 2010. *Random Fields: Analysis and Synthesis*. Revised and expanded newer edition. Singapore: World Scientific Publishing Co.

Vanmarcke, E. 2011. "Risk of Limit-Equilibrium Failure of Long Earth Slopes: How It Depends on Length." GeoRisk 2011, keynote lecture. P*roceedings of GeoRisk International conference, Atlanta, GA, June 2011*. ASCE Geotechnical Specialty No. 224, June 2011, 1–29.

Vanmarcke, E. H., and N. F. Fuleihan. 1975. "Probabilistic Prediction of Levee Settlements." *Proceedings of the 2nd International Conference on Applications of Statistics and Probability in Soil and Structural Engineering, Aachen, Vol. 2*, 175–190.

Vanmarcke, E., and Y. Otsubo. 2013. “Reliability Analysis of Long Multi-Segment Earth Slopes.” *Foundation Engineering in the Face of Uncertainity*. Honoring Fred H. Kulhawy. ASCE Geotechnical Specialty Publication No. 229. Edited by J. L. Withiam, K.-K. Phoon, and M. H. Hussein. Reston, VA.

Vrouwenvelder, T., A. van Seters, and G. Hannink. 2013. “Dutch Approach to Geotechnical Design by Eurocode 7, Based on Probabilistic Analyses.” *Modern Geotechnical Design Codes of Practice; Implementation, Application and Development*. Edited by P. Arnold, G. A. Fenton, M. A. Hicks, T. Schweckendiek, and B. Simpson. Amsterdam, Netherlands: IOS Press BV under the imprint Millpress.

WES CERC (US Army Engineer Waterways Experiment Station, Coastal Engineering Research Center). 1984. *Shore Protection Manual*. Volume 1, Vicksburg, MS: US Army Engineer Waterways Experiment Station. https://repository.tudelft.nl/islandora/object/uuid:98791127-e7ae-40a1-b850-67d575fa1289

Wickremesinghe, D., and R. G. Campanella. 1993. “Scale of Fluctuation as a Descriptor of Soil Variability.” *Probabilistic Methods in Geotechnical Engineering*. Edited by K. S. Li and S. C. R. Lo. Rotterdam: Balkema.

Withiam, J. L., E. P. Voytko, R. M. Barker, J. M. Duncan, B. C. Kelly, S. C. Musser, and V. Elias. 1997. *Load and Resistance Design (LRFD) for Highway Bridge Structures*. FHWA Report DTFH61-94-C-00098. Washington, DC: Federal Highway Administration.

Wu, T. H. 1974. “Uncertainty, Safety, and Decision in Soil Engineering.” *Journal of the Geotechnical Engineering Division, ASCE* 100: 329–348.

Yamada, H., and Shiotani, T. 1968. "*On the Highest water Waves of Permanent Type, Bulletin DPRI, Kyoto Univ*. Vol. 18, Part 2, No. 135: 1–22.

Zhang, L., W. H. Tang, and C. W. W. Ng. 2001. “Reliability of Axially Loaded Driven Pile Groups.” *Journal of Geotechnical and Geoenvironmental Engineering, ASCE* 127(12): 1051–1060.

Appendix A: Computing Probabilities

A.1 The Gaussian multivariate spaces

While design and analysis procedures of structures are well defined in theory, in reality the constituent parameters have many variations, which is the reason for LRFD. Material properties (e.g., compressibility, x position) are typically chosen from a range of values that are pulled from a distribution with certain probabilities. An example distribution may be the discrete histogram idealized in Figure A.1. Each bin in the histogram presents how many times that bin has been selected from a sample data set. Dividing those values by the total number of samples drawn gives a normalized distribution where the probability of selection of any given bin (PDF) is a fraction of the total set and integrating the area under the PDF gives CDF. For the entire curve, the total area is 1.

Figure A.1. PDF and CDF of histogram data.

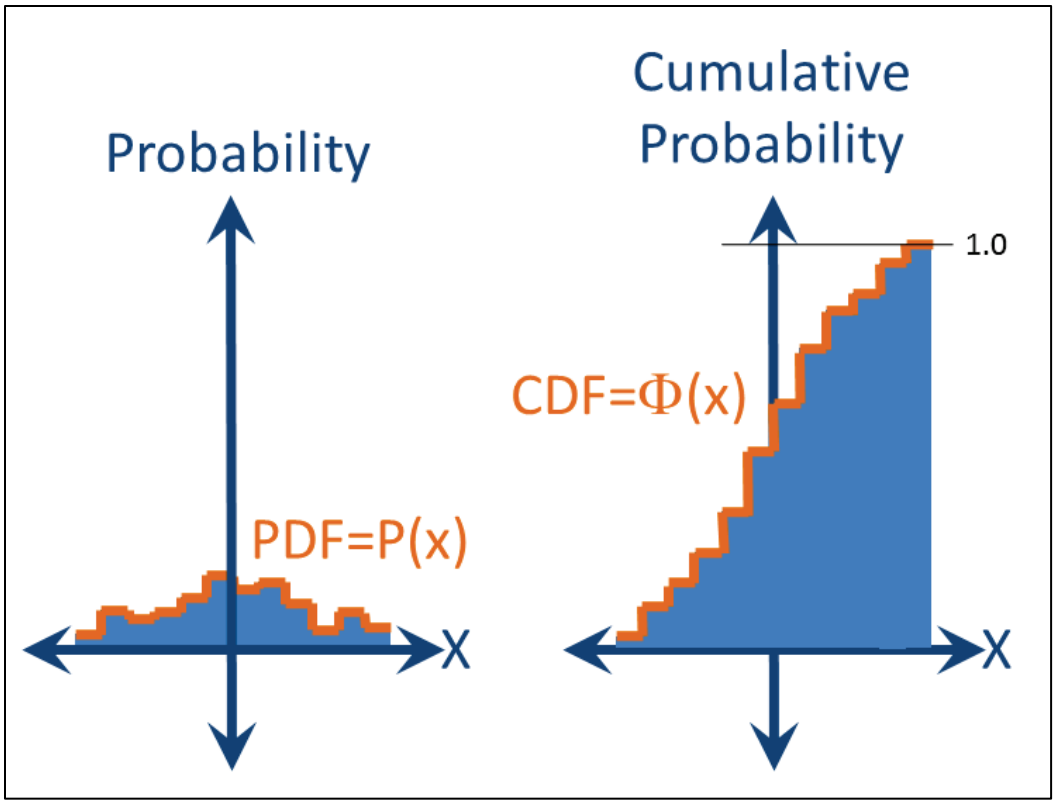

A Gaussian (also referred to as normal) distribution is given by the equation

$$f(x|\mu,\sigma^2) = \frac{1}{\sigma\sqrt{2\pi}} e^{-\frac{(x-\mu)^2}{2\sigma^2}} \quad \text{(A.1)}$$

This function provides numerous advantages when dealing with multiple orthogonal variables in LRFD, so a means to create a Gaussian distribution that approximates other distributions was established by Hasofer-Lind (1974) based on a distribution transform method by Rackwitz and Fiessler (1976, 1978). The Hasofer-Lind (1974) procedure does not find the simple mean and standard deviation of another distribution but instead maps the CDF of the non-normal distribution to the CDF of a normal distribution to get the best approximate Gaussian distribution with its own mean and standard deviation (Figures A.2 and A.3).

Figure A.2. Histogram data and the Gaussian (normal) distribution.

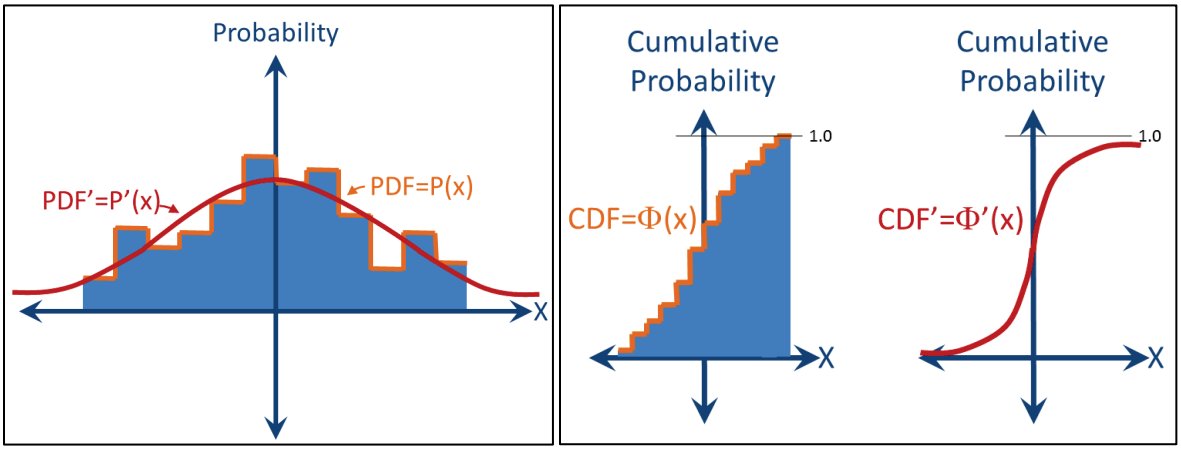

Figure A.3. The *G*(*X'*) function is used to determine *PUP*.

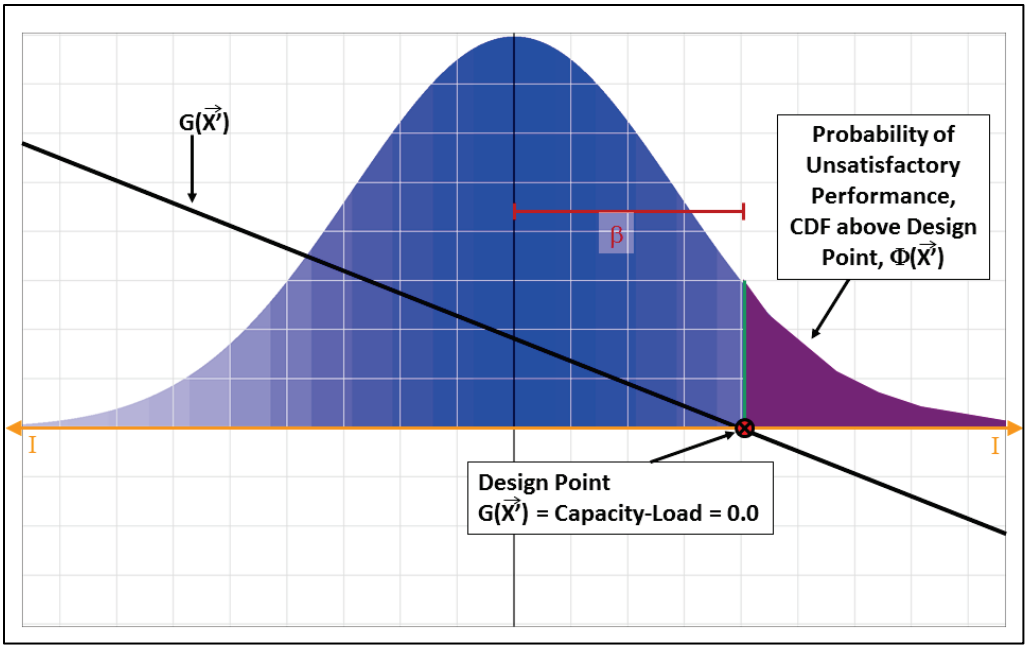

With *N* uncorrelated and orthogonal variables, an *N*-dimensional multivariate space can be formed from the distributions for those variables. With Gaussian distributions, a transformed space can be created that has a unit distance of 1σ. The following equation is used to transform the *X* value of i^{th} variable of the distribution to the transformed coordinates:

$$X_i' = \frac{(X_i - \mu_i)}{\sigma_i} \tag{A.2}$$

and conversely,

$$X_i = X_i' \sigma_i + \mu_i \tag{A.3}$$

A hyperplane can partition the multivariate Gaussian transformed space into half-spaces. The *N*-space hyperplane has the equation

$$0.0 = a_1 * X_1 + a_2 * X_2 + \cdots + a_N * X_N + c \tag{A.4}$$

This hyperplane can also be described by a vector from the origin of the multivariate space to the nearest point on the hyperplane. This vector is perpendicular to the surface of the hyperplane. The vector has length β and has unit direction component vector $\boldsymbol{\alpha}$, with N^{th} axis component of α_N (Figure A.4).

Figure A.4. A 2-D example of the *PUP* region and the hyperplane description using α and β.

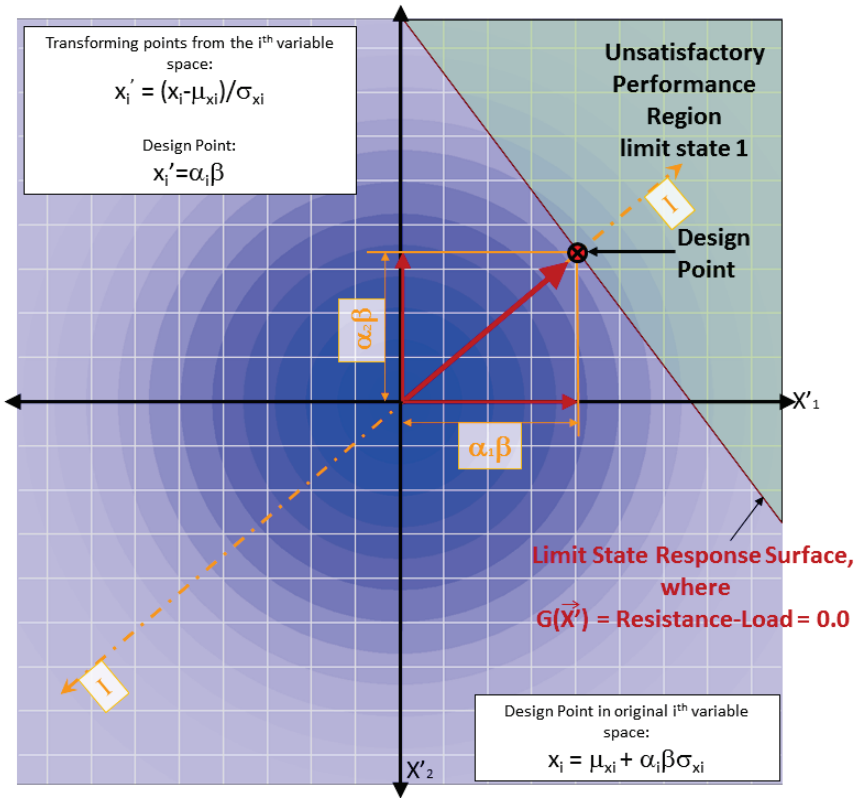

This multivariate, Gaussian transformed space has several properties that make it attractive for determining limit state probabilities, such as is done for reliability analysis and LRFD. The most important property is that for any hyperplane in the *N*-dimensional space partitions the space into two half-spaces, the integrated volume of the half-space gives the same result as the CDF(β) for a normal distribution along the hyperplane's defining vector.

A hyperplane perfectly describes the response surface of a limit state that has linear effects across multiple variable axes. For the purposes of engineering evaluation, it is assumed that each limit state has linear properties and that failure occurs because of non-linear, or plastic, response.

A.2 Limit states and *PUP*

For engineering analysis with properties that vary, described by multivariate space, a particular limit state (e.g., SSI Limit State 3 for the compression pile) can be described by the multivariate function

$$g(\boldsymbol{X}) = Capacity - Load \tag{A.5}$$

This function has positive values for satisfactory performance, negative values for unsatisfactory performance, and a value of 0.0 at the response surface, which separates the performance regions (Figure A.5). For probabilities, as discussed above, the response surface is assumed to be hyperplanar.

Figure A.5. A 2-D example of multiple limit states with closest approach of length $|\beta|$.

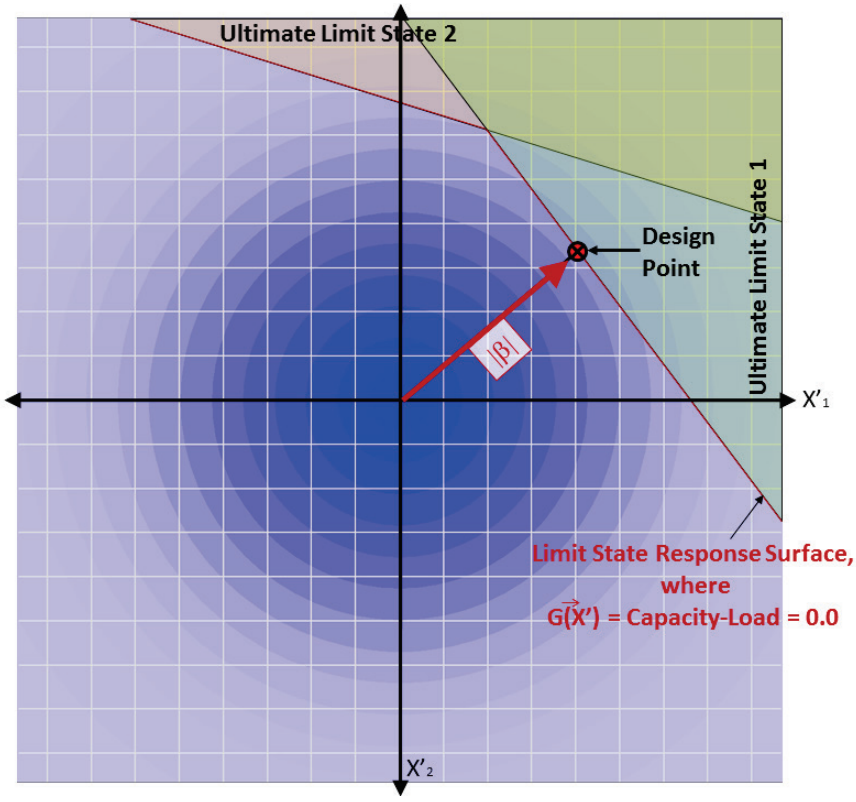

An indicator function can be created with the express purpose of providing a multiplicative identity for X vector values where there is unsatisfactory performance and a value of 0.0 at the response surface of the limit state or less.

$$i(\boldsymbol{X}) = \begin{cases} 0: g(\boldsymbol{X}) \geq 0.0 \\ 1: g(\boldsymbol{X}) < 0.0 \end{cases} \tag{A.6}$$

The function to calculate *PUP* for the Gaussian multivariate space X is

$$p_U = \Phi(\boldsymbol{X}) = \int_{\mathbb{R}^N} i(\boldsymbol{X})\, h(\boldsymbol{X}) d\boldsymbol{X} \tag{A.7}$$

where h($\mathbf{X}$) is the probability density function for the space and is given by

$$h(\boldsymbol{X}) = \prod_{n=1}^{N} h(X_n) \tag{A.8}$$

Noted previously, for a single hyperplanar surface in a Gaussian multivariate space, the *PUP* is the same as the 1-D CDF along the line through the origin that is perpendicular to the plane. For line $l = \boldsymbol{\alpha}\beta$, where $\boldsymbol{\alpha}$ is the directional cosine vector, $p_U = \Phi(\beta)$, with $\Phi(\beta)$ being the CDF for the normal Gaussian distribution.

Unfortunately, it is seldom that only one limit state is possible with the engineering design/analysis of structures and especially the USACE hydraulic structures (section 1.3). In this case, a family of limit states needs to be assessed, with each limit state having a different $g(\boldsymbol{X})$ function. In this case, combining the limit state functions gives a new, nonlinear, overall response surface, described by the boundary of the union of the half-space volumes for each limit state response surface hyperplane. For L limit states,

$$p_U = \bigcup_{n=1}^{L} \Phi_n(\boldsymbol{X}) \tag{A.9}$$

Note that these half-space sets of data are guaranteed to intersect and overlap if the hyperplane equations are not parallel and may subsume each other if the equations are parallel. This makes it difficult to get an accurate determination of the *PUP* for multiple limit states.

A.3 Estimating *PUP* for multiple limit states

A.3.1 Bounds method

Ang and Tang (1974) suggested an alternative method for estimating the *PUP* with multiple limit states based on finding the minimum and maximum bounds for the value that the *PUP* can assume. This estimation is not as accurate as the numerical Euclidean methods but can be found quickly with methods to determine a design point for each limit state, and therefore the equation for the hyperplane and the β distance to the hyperplane, resulting in the *PUP*.

$$PUP_{LSi} = \Phi(\beta_i) \tag{A.10}$$

Each limit state hyperplane divides the Gaussian multivariate space into half-spaces, with one half-space being the satisfactory performance region and the other half-space being the unsatisfactory performance region for that limit state. When there are multiple limit states, these regions in the Gaussian multivariate space overlap and combine. The probability of these combined regions having unsatisfactory performance is the probability of failure given the union of all the regions

$$PUP \cong p_u[R_1 \cup R_2 \cup \ldots \cup R_N] \tag{A.11}$$

However, as previously described, the union of the regions contains the overlapping volumes of unsatisfactory performance probabilities. This complicates the calculation of the overall *PUP*.

Because each limit state is described by a hyperplane with shortest distance β_I from the origin, the lowest bound of the overall *PUP* can be proven to be the greatest of the individual hyperplane *PUP*s of the limit states. This is true because, for a set of limit states with parallel hyperplanes, the greatest individual *PUP* subsumes the volumes of the other individual *PUP*s.

$$\max_i\big(\Phi(\beta_i)\big) \leq PUP \tag{A.12}$$

Parallel hyperplanes can have non-intersecting half-planes of unsatisfactory performance. For two such hyperplanes that do not overlap, the probability of satisfactory performance is the multiplied probabilities of satisfactory performance for each limit state. This implies that an upper limit to the *PUP* can be found by subtracting the combined probability of satisfactory performance for multiple limit states from 1.0.

$$PUP \leq 1 - \prod_i \left(1 - \Phi(\beta_i)\right) \tag{A.13}$$

Equations A.13 and A.14 establish absolute lower and upper bounds for the *PUP*, but these bounds are for limit states that are not correlated (i.e., have parallel hyperplanes in unimodal sets). In reality, the hyperplanes are seldom parallel and have complex overlapping regions. Therefore, correlation techniques can be used between pairs of hyperplanes (bimodal) to tighten the bounds about the *PUP*. With more than two hyperplanes (multimodal), the overlapping regions become much more complicated.

According to a decomposition of the union of sets using deMorgan's rule as described in Ang and Tang (1974), the bounding values for *PUP* using bimodal probabilities is

$$PUP \geq \max\left[\sum_i \{PUP_{LSi} - \sum_{j=1}^{i-1} P\left(E_i E_j\right)\}; 0.0\right] \quad \text{(A.14)}$$

and

$$PUP \leq \sum_{i=1}^{N} PUP_{LSi} - \sum_{i=2}^{N} \max_{j<i}\left(P\left(E_i E_j\right)\right) \quad \text{(A.15)}$$

Given hyperplane equations for the ith and jth limit state equations (in two dimensions for simplicity),

$$g_i(\boldsymbol{X}) = a_0 + a_1 X_1 + a_2 X_2 \quad \text{(A.16)}$$

$$g_j(\boldsymbol{X}) = b_0 + b_1 X_1 + b_2 X_2 \quad \text{(A.17)}$$

The limit state response surface is determined by setting these equations to 0.0. According to Ang and Tang (1974) in Gaussian multivariate space, the correlation coefficient can be found as the cosine of the dihedral angle (θ) between these hyperplanes.

$$\rho_{ij} = \frac{Cov(g_i, g_j)}{\sigma_{g_i}\sigma_{g_j}} = \cos\theta \quad \text{(A.18)}$$

The dihedral angle between the planes is equivalent to the angle between the vectors from the origin to the respective design points because each hyperplane is perpendicular to its design point vector. The cosine of this angle can be expressed, from the normalized design point vectors $\boldsymbol{\alpha}_i$ and $\boldsymbol{\alpha}_j$, as

$$\rho_{ij} = cos\theta = \boldsymbol{\alpha}_i \cdot \boldsymbol{\alpha}_j \quad \text{(A.19)}$$

From Figures A.6 and A.7, note that $E_i E_j \supset A$ and $E_i E_j \supset B$. The probability of $E_i E_j$ is therefore bounded by

$$\max[P(A), p(B)] \leq P(E_i E_j) \leq P(A) + P(B) \quad \text{(A.20)}$$

and, by reason of orthogonality,

$$P(A) = \Phi(-\beta_i)\Phi(-a) = \Phi(-\beta_i)\Phi\left(-\frac{\beta_j - \rho\beta_i}{\sqrt{1-\rho^2}}\right) \quad \text{(A.21)}$$

and

$$P(B) = \Phi(-\beta_j)\Phi(-b) = \Phi(-\beta_j)\Phi\left(-\frac{\beta_i - \rho\beta_j}{\sqrt{1-\rho^2}}\right) \quad \text{(A.22)}$$

Figure A.6. Finding the contribution of area A to overlapping probabilities of $g_i(X)$ and $g_j(X)$.

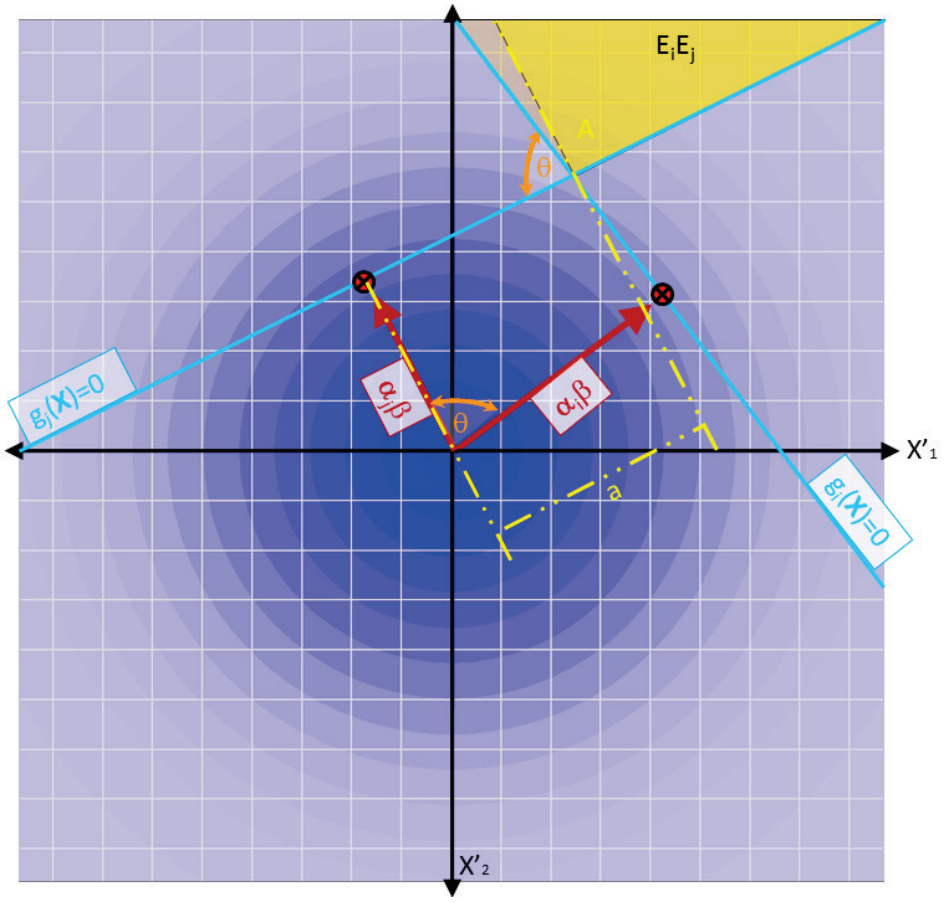

Figure A.7. Finding the contribution of area A to overlapping probabilities of $g_i(X)$ and $g_j(X)$.

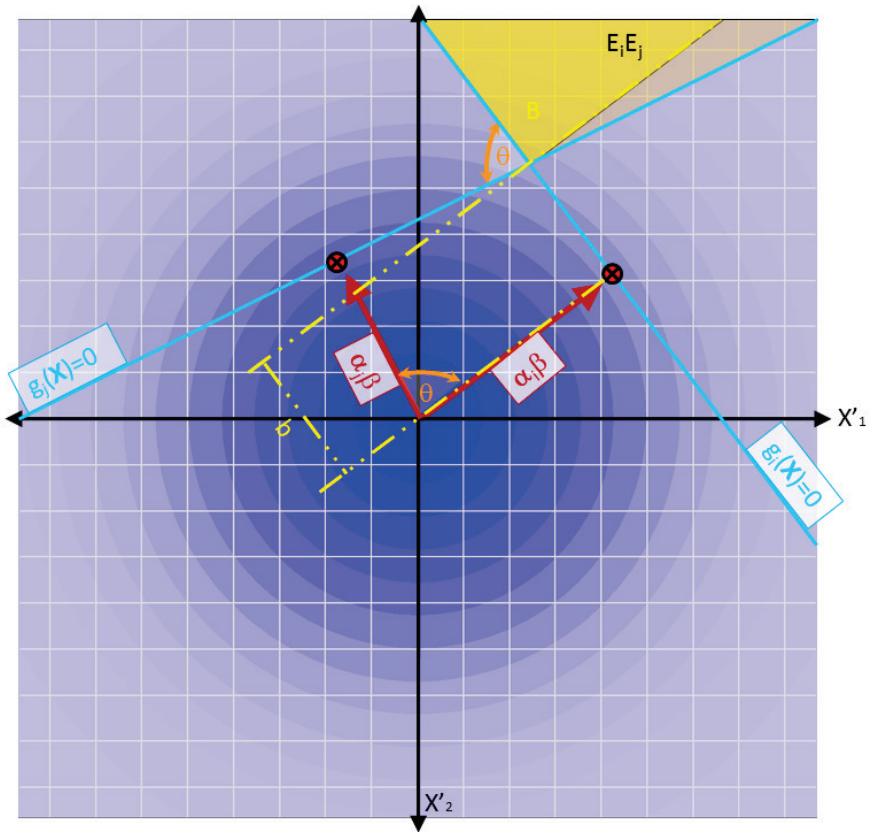

Using the relationships of Equations A.21 and A.22, the lower bound for $P(E_iE_j)$, given as

$$P(E_iE_j) = P(A) + P(B) \tag{A.23}$$

should be used in Equation A.14 for each pair of limit states, and the upper bound, given as

$$P(E_iE_j) = \max[P(A), P(B)] \tag{A.24}$$

should be used in Equation A.15 for each pair of limit states.

The results from the application of these equations are a minimum and maximum range for the overall *PUP* given multiple limit states using a bimodal analysis, using the bounds of each bimodal probabilities. The *PUP* is guaranteed to be in these ranges, so a reasonable estimate of the actual value of the *PUP* is the average of the two bounding values, giving a maximum error of half the range.

A.3.2 Euclidean numerical method

For multiple limit states, it is still possible to integrate the probabilities the spaces using Equation A.7, but there needs to be an adjustment to the indicator function specified in Equation A.6. That indicator function is defined for a single limit state function g(**X**). To work with Z multiple limit states, the overall indicator function must return the multiplicative identity if any of the Z single limit state indicator functions returns with a value of 1.

$$i_Z(\boldsymbol{X}) = 1 - \prod_{z=1}^{Z}\left(1 - i_z(\boldsymbol{X})\right) \tag{A.25}$$

$$PUP=\Phi\boldsymbol{X}=X1X2\ldots XNiZX1,X2,\ldots,XNhX1,X2,\ldots,XNdX1dX2\ldots dXN \tag{A.26}$$

It would be possible to approximate the value of the *PUP* using a Euclidean method. The Midpoint Rule Euclidean method is the one most people remember from early calculus courses, but there are other Euclidean methods (i.e., the Trapezoid Rule and Simpson's Rule) that could give a better estimation and require fewer sub-intervals.

Of course, the Euclidean methods require that the space be divided into several segments for each dimension (Figure A.8). Because the Gaussian multivariate space is orthogonal and normalized, the same number of intervals should be applied to each dimension. The greatest rate of change of the function occurs near the origin, so for efficiency, the subdivisions can be placed closer together at the origin than at the extremes. However, since most of the limit states are applied near the tails of the distributions, and therefore at extreme distances (>3.0σ), care should be taken to not spread the subdivisions too far so that accuracy and precision will be maintained. Because the probabilities become extreme at distances of greater than 3σ, the numerical solution should be satisfactory in the range of -5σ to 5σ for each variable. A range of plus or minus 5 standard deviations corresponds to a maximum precision of 1.5E-6. If this range were increased to plus and minus 8 standard deviations, the precision would improve to 5E-15.

Figure A.8. Gridding the Gaussian multivariate space to determine the *PUP* based on a single limit state response surface.

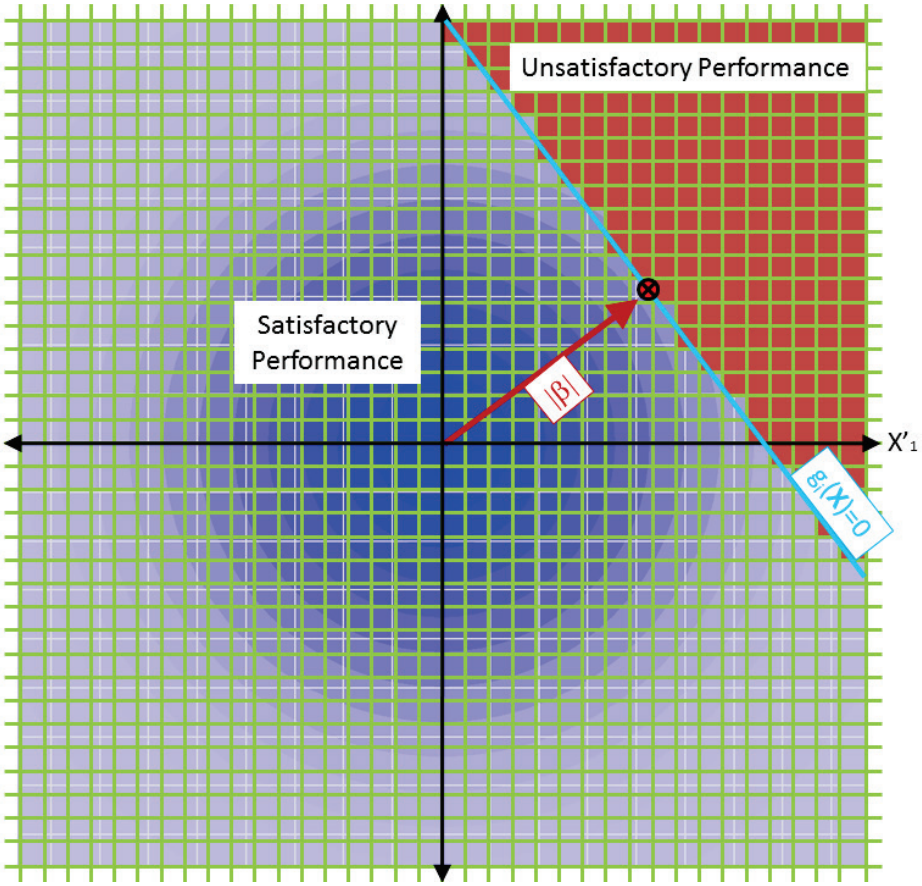

An issue with using the Euclidean approximations is the number of analyses that will need to be run. To evaluate an individual subdivision point, each of the limit state indicator functions will need to be found. If the analysis function is written correctly, these values could be collected on a single analysis execution. However, for several sub-divisions (S) and a several variables (N), the total number of runs that will need to be performed is N^S. The computational complexity of this method means that it will rarely be tractable for anything less than a high-performance computational platform. Another issue with the numerical integration is that the combined PDF for multiple variables, which are multiplied together, make numbers so small that they outstrip the precision of even double-precision floating point values in programming languages.

A.3.3 Hypersphere numerical method

So far, all the methods explored have been based on hyperplanes because there is a simple method of determining the CDF of half-spaces divided by

the hyperplane in the Gaussian multivariate space. There is another property of the Gaussian multivariate space that seems to be overlooked. For any hypersphere (also known as an n-sphere) in the space that is centered at the origin and has radius R, all of the points on the surface of the hypersphere have the same probability density function value, as shown in Figures A.9 and A.10.

$$p(\boldsymbol{X}_R) = p(R_{X1}) \times p(R_{X2}) \times \ldots \times p(R_{XN}) = p(0)^{N-1} p(R) \qquad \text{(A.27)}$$

Figure A.9 shows that the probability for any thin shell is the same at a set distance from the origin. Figure A.10 shows this thin shell in plan view. The symmetry and the properties of the Gaussian normal curve means that the probability at any distance in the multivariate space is the same at all points on the hypersphere surface.

Figure A.9. Symmetric probability for pairs of bins equidistant from the mean, section view.

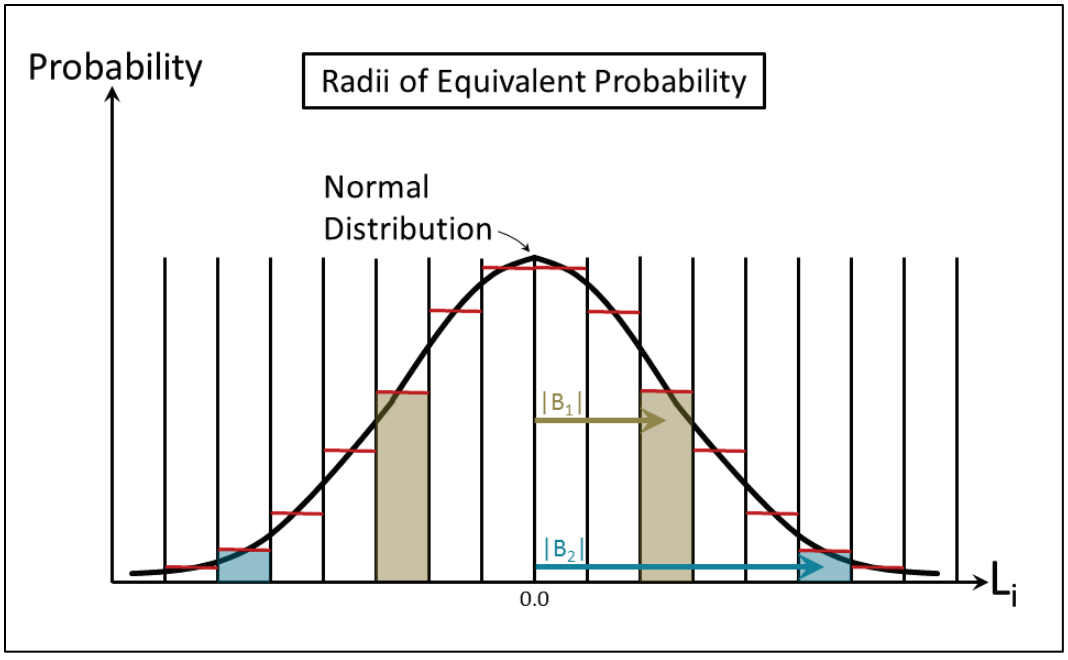

Figure A.10. Symmetric probability of the Gaussian normal curve at any distance in the multivariate space at all points on the hypersphere surface, plan view.

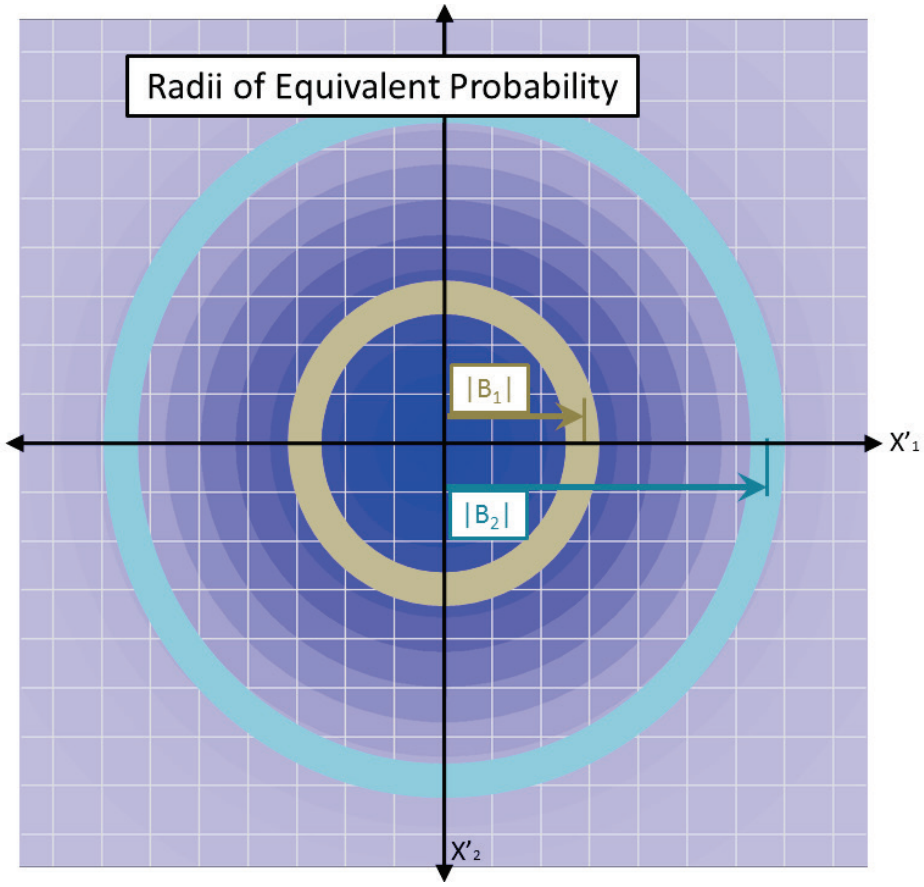

Given that the closed form equation of the surface area for the unit hypersphere with dimension N is

$$S_N = \begin{cases} \dfrac{2^{\frac{N+11}{2}}\pi^{\frac{N-1}{2}}}{(\mathrm{N}-2)!!} & for\ odd\ N, and \\ \dfrac{2\pi^{\frac{N}{2}}}{\left(\frac{1}{2}\mathrm{N}-1\right)!} & for\ even\ N \end{cases} \tag{A.28}$$

Using concentric shells, the probability of satisfactory performance of the N-dimensional hypersphere (h) with radius R in Gaussian multivariate space (Figure A.11) is

$$P_h(R) = \int_{r=0}^{R} S_N r^2 p(0)^{N-1} p(r) dr \tag{A.29}$$

which seems much more tractable for a numerical solution, the factorial divisors in Equation A.27 can grow quite large as the number of

dimensions increases. For a *PUP* given hyperplanar limit states and β radius, it follows that

$$PUP \leq (1 - P_h(\beta)) \tag{A.30}$$

Figure A.11. A 2-D demonstration of the hypersphere calculation of *PUP.*

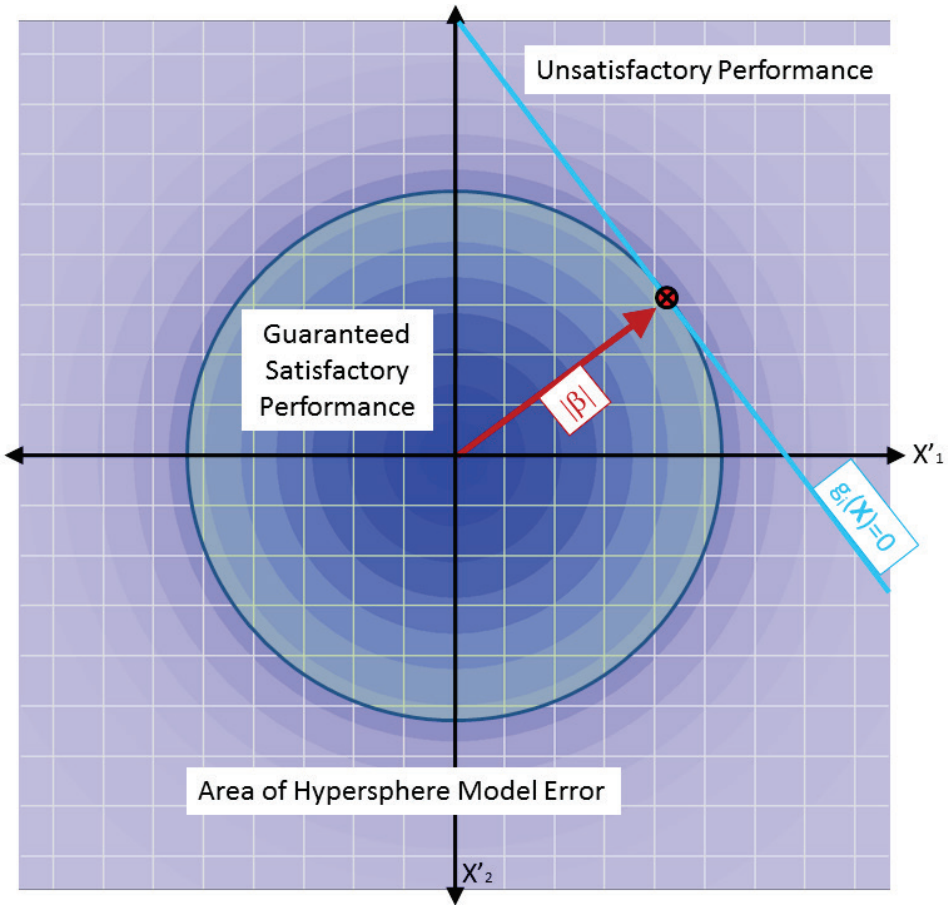

Unfortunately, this approach overestimates the *PUP,* and the error increases as the radius β increases. The error increases because the hyperplane *PUP* decreases at such a rate that any error is exacerbated at the tails of the distribution. Also, the accuracy of the hypersphere *PUP* is greatly influenced by the resolution of numerical procedure to determine its values, with greater error occurring at greater β values. Of course, higher-resolution numerical solutions also become intractable.

Table A.1 shows a quick calculation of error for a two-variable space, with hyperplanar *PUP* calculations and the numerical approximation of the integral of the hypersphere with different resolution step sizes. Recall that for a two-variable space, the hyperplane is a line, and the hypersphere is a

circle. Table A.2 shows the hypersphere estimation error as a multiple of the actual linear *PUP* value. Notice that as the hypersphere β increases, the error becomes greater. This is because the dropoff of the hyperplanar limit state CDF ($\Phi(1-\beta)$) drops off more rapidly than the CDF of the area outside the circular area in the opposite half-plane.

Table A.1. *PUP* values for hyperplanar limit state and hypersphere *PUP* estimations with increasing accuracy.

β	Hyperplanar Linear *PUP* (*LPUP*)	Hypersphere *PUP* (*HPUP*)	Hypersphere *PUP* (*HPUP*)	Hypersphere *PUP* (*HPUP*)	Hypersphere *PUP* (*HPUP*)
		(0.001 interval)	(0.0001 interval)	(0.00001 interval)	(0.000001 interval)
0.5	0.30853754	0.88207477	0.88245471	0.8824971	0.88249648
1	0.15865525	0.60604896	0.60648246	0.60653191	0.60653018
1.5	0.0668072	0.32446544	0.32463372	0.32465059	0.32465228
2	0.02275013	0.1355278	0.1353545	0.13533991	0.13533548
2.5	0.00620967	0.04439116	0.04398235	0.04394257	0.04393739
3	0.0013499	0.01168391	0.01116649	0.01111475	0.01110957
3.5	0.00023263	0.00280223	0.00224898	0.00219364	0.00218811
4	0.00003167	0.00095991	0.00039792	0.00034172	0.00033609
4.5	0.0000034	0.00066628	0.0001027	0.00004633	0.00004069
5	0.00000029	0.00063019	0.00006639	0.00000999	0.00000435

Table A.2. Hypersphere *PUP* estimate error as a multiple of the actual hyperplanar *PUP.*

β	HPUP0.001 /LPUP	HPUP0.0001 /LPUP	HPUP0.00001 /LPUP	HPUP0.000001 /LPUP
0.5	2.858889618	2.860121041	2.860258431	2.860256421
1	3.81991116	3.822643499	3.822955181	3.822944277
1.5	4.856743585	4.859262475	4.859514992	4.859540289
2	5.957231893	5.949614354	5.948973039	5.948778315
2.5	7.148714827	7.082880411	7.076474273	7.07564009
3	8.655389288	8.272086821	8.233758056	8.229920735
3.5	12.04586683	9.667626703	9.429738211	9.405966556
4	30.30975687	12.56457215	10.7900221	10.61225134
4.5	195.9647059	30.20588235	13.62647059	11.96764706
5	2173.068966	228.9310345	34.44827586	15

A.3.4 Hybrid hyperspherical-polar numerical method

The hypersphere numerical method works quickly to determine the probabilities of values occurring within a hypersphere of a defined radius and can be run to generate tables for many different radii hyperspheres for quick lookup. This method could be used to generate a quick estimate of the value to the closest design point for the most-likely-to-occur limit state but will result in a large error region.

The authors of this report have looked at a Euclidean numerical method in Cartesian space for the determination of probabilities with respect to multiple limit states. This concept can be expanded to a polar coordinate space, using

$$i_Z(r,\boldsymbol{\theta}) = 1 - \prod_{z=1}^{Z}\left(1 - i_z(r,\boldsymbol{\theta})\right) \tag{A.31}$$

$$PUP = \Phi(r,\boldsymbol{\theta}) = \int_{\boldsymbol{\theta}} \int_{r=0}^{\infty} i_Z(r,\theta_1,\theta_2,\ldots,\theta_{N-1}) h(r,\theta_1,\theta_2,\ldots,\theta_{N-1}) dr\, d\boldsymbol{\theta} \tag{A.32}$$

A numerical solution could transform the polar coordinates to Cartesian coordinates for simplification of probability calculation. This means that the *iz*() function can be determined from the Cartesian equation given in Equation A.25. The probability function *h*() is the same as Equation A.8. The rest of the equation deals with the approximation of volume occupied by a polar coordinate described shell element of *dr* thickness and all its sweep angles. Because dimensionless angles are used for these sweep angles in multiple dimensions and the angles interact within polar coordinates, the definition of $d\boldsymbol{\theta}$ needs to be rederived for each number of dimensions. The following two equations show the polar integration equations for two and three dimensions, respectively:

$$PUP = \Phi(r,\theta) = \int_{\boldsymbol{\theta}=\mathbf{0}}^{2\pi} \int_{r=0}^{\infty} i_Z(r,\theta) h(r,\theta) dr\, (r d\theta) \tag{A.32a}$$

$$PUP = \Phi(r,\theta_1,\theta_2) = \int_{\theta_2=0}^{2\pi} \int_{\theta_1=0}^{\pi} \int_{r=0}^{\infty} i_Z(r,\theta_1,\theta_2) h(r,\theta_1,\theta_2) dr\, (r d\theta_1)(r \sin(d\theta_1)\, d\theta_2) \tag{A.32b}$$

The length term *r* needs to be multiplied by each angular delta to express the shell element arc-distance for that angular sweep. For the 3-D Equation A.32b, the total sweep of angle θ_1 is reduced to make the functions one-to-one, much like latitude and longitude are described on a sphere. Figure A.12(a,b) show why the reduction of distance for the $d\theta_2$

term is required for polar coordinates. These figures use more conventional notation for 3-D axes and angles with X, Y, and Z axes representing X_1, X_2, and X_3 variable space axes, respectively, and ϕ and θ representing the θ_1 and θ_2 variable space angles, respectively. The equation derivations for Equation A.32 become more involved as more variable dimensions are included.

Figure A.12. Calculating dimensions for integrating spherical coordinate 3-D space.

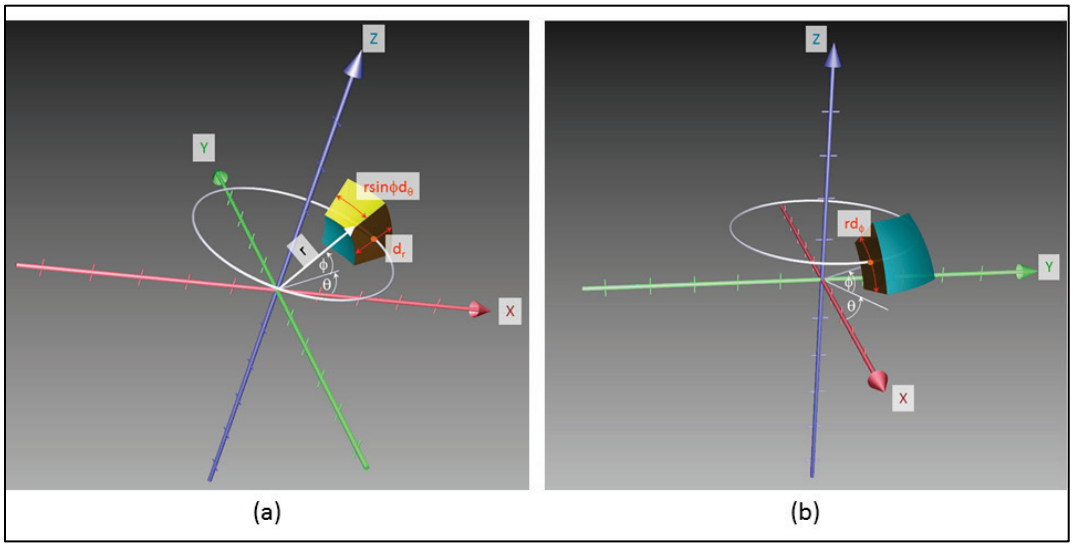

A full numerical solution along these lines would have the same issues of exponential time growth as the Euclidean method. Recall that the numerical solution could be considered complete when r equals 5σ because the probabilities are extremely small past that limit.

It is certainly possible to minimize calculation time by marrying the hypersphere calculation method with the polar coordinate method for calculating the probabilities of multiple limit states in the Gaussian multivariate space. Given the design point for the highest probability limit state defined by $\beta\boldsymbol{\alpha}$, the probability of satisfactory performance would be the hypersphere probability of radius β combined with 1 minus the polar *PUP* with r ranging from β to 5, thus limiting the polar search to a somewhat manageable area. Of course, the *PUP* is 1 minus the probability of satisfactory performance.

Another performance increase can be implemented if the limit states are guaranteed to be hyperplanar. For the hyperplanar limit states, the ASM method calculates the distance from the origin β and the unit directional cosine vector α from the origin to the hyperplane, which is normal to the

surface of the hyperplane. For multiple limit states, the limit state with the minimum β value has the highest *PUP*. The *iz*() function returns a value of 0 for every point within that minimum β value radius hypersphere. Therefore, it is only necessary to integrate from this minimum β value to 5 to get the *PUP*.

If a level of precision is specified by establishing the accuracy to a specific decimal place, another performance increase can be made by using the fact that the volume of hyperspherical shells increases with constant radial increments raised to the power of the number of dimensions n of the hyperspace while the normal distribution values get smaller by a scale factor times $e^{1/n}$. The normal distribution values at the tails of the distribution decrease faster than the volume of the hyperspherical shell grows.

Figure A.13(a) shows the exponential growth of hyperspherical shell volumes as the radius increases, with radial increment 0.001. Figure A.13(b) shows the normal distribution PDF value assigned for each of these hyperspherical shell radii. Figure A.13(c) shows the cumulative probability for the volume of the hyperspherical shell elements, computed by multiplying the shell volume by its center radius PDF value. The resulting curve shows that at the beginning, the increase of hyperspherical shell volume from volume 0 drives the shape of the curve until the PDF distribution drop off exceeds the rate of growth. At that point, the curve begins to decrease with the tails of the distribution.

Figure A.13. Distribution plots with respect to radius for 3-D sphere: (a) sphere shell volume, (b) point distribution probability, (c) probability density for the sphere shell, (d) number of divisions of the sphere density where each shell division would have 1.0e-10 probability.

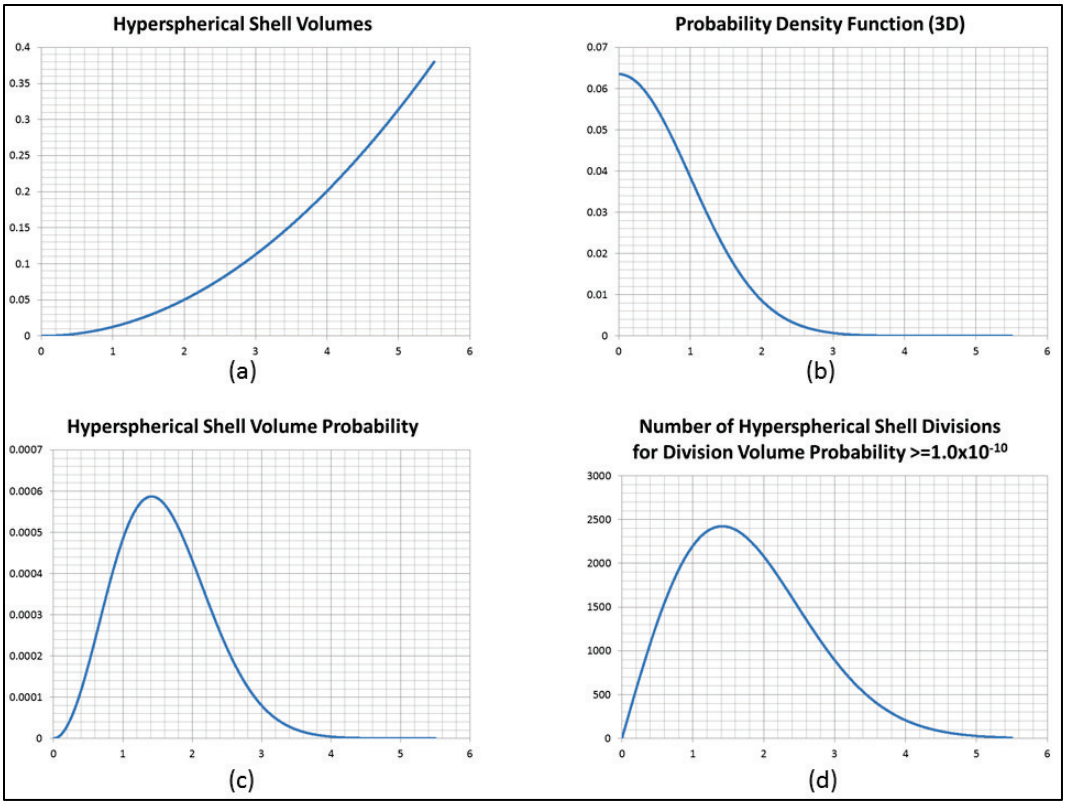

From these curves (Figure A.13(a) through (c)), it can be inferred that if equal divisions were made of each hyperspherical shell, then each division's volume probability would be equivalent. Further, these divisions (based on angular intervals) can be chosen to be equivalent or slightly less than a specified volume probability based on the precision of solution desired, simply by setting the number of divisions of the hyperspherical shell to the mathematical ceiling of the volume probability of the entire hyperspherical shell by the specified volume probability desired. For the beginning of the curve and the ends of the curve where the volume of the hyperspherical shell is extremely small and the tails of the distribution give extremely low probabilities, respectively, a minimum value for the number of divisions can be set to ensure that limit state values are accurately found. The authors suggest that this value be no less than 8 for each dimension to provide two samples per quadrant. Figure A.13(d) shows the number of shell divisions so that each division has a volume probability of 1.0×10^{-10}. Summing these divisions should give the entire ring probability to at least the tenth digit of precision. In truth, there are small errors introduced for three of more dimensions because of polar

coordinate integration, so higher precision divisions will be needed to ensure the numerical precision. From this curve, the level of integration is varied as the radius increases.

A.4 Using an estimation of *PUP* to establish LRFD factors

Because the structural probability of usability is based on the lifetime of the structure, the *PUP* can be used to establish the design limits for these structures. Under applied load cases, the design points for several limit states can be determined as a distance (in standard deviations) and direction from the mean characteristics of the structure, $\beta\alpha$. An example of this is shown in Figure A.14. The expected overall *PUP* value can be set to a limit (e.g., $\Phi(3.5)$ with $\beta = 3.5$), which guarantees the structure's lifetime integrity probability.

Figure A.14. Example limit states and βs for unfactored loads and resistances.

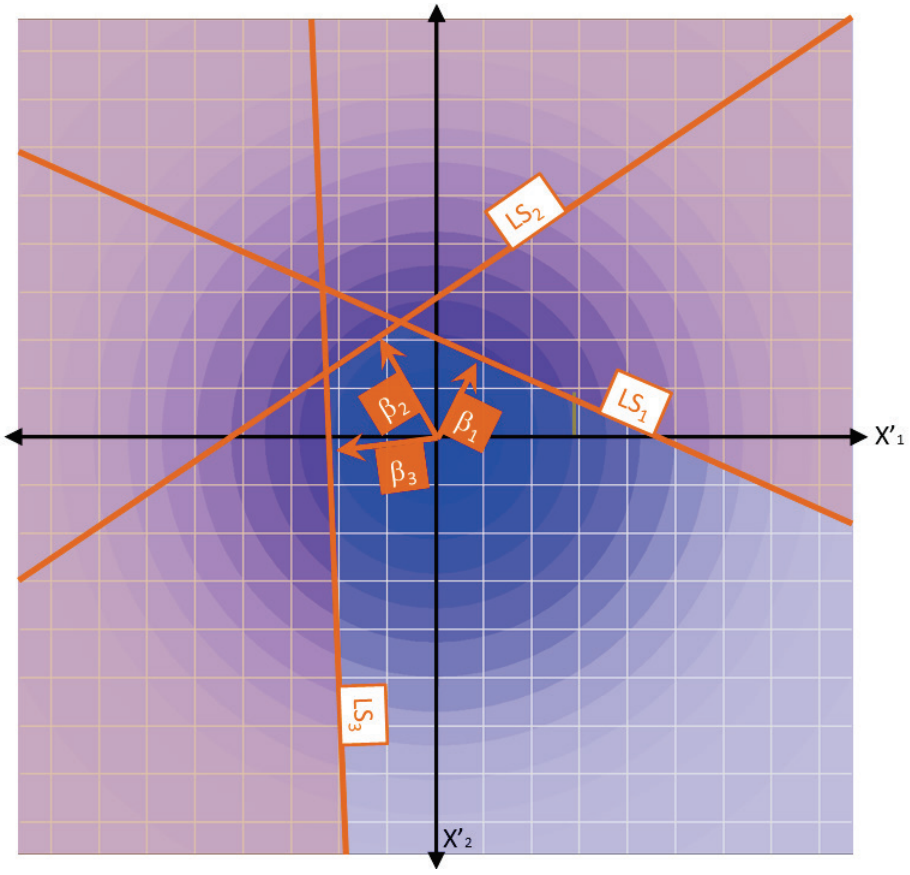

There are two ways to envision that a scale factor can be applied to the load(s) applied to a structure during its structural design. The first method assumes that the load and response directions do not change. In this case,

each variable axis has the same universal scale applied (Figure A.15). Because the factor is applied uniformly, the limit states maintain their relative positions and angles to each other in the Gaussian multivariate space. Once the limit states have been determined for the unscaled design load, the system *PUP* can be considered a function of the single applied scale factor (S) to the system.

$$PUP = f(S) \tag{A.33}$$

Figure A.15. A uniform scale factor (S) is applied to the βs for the limit state design points.

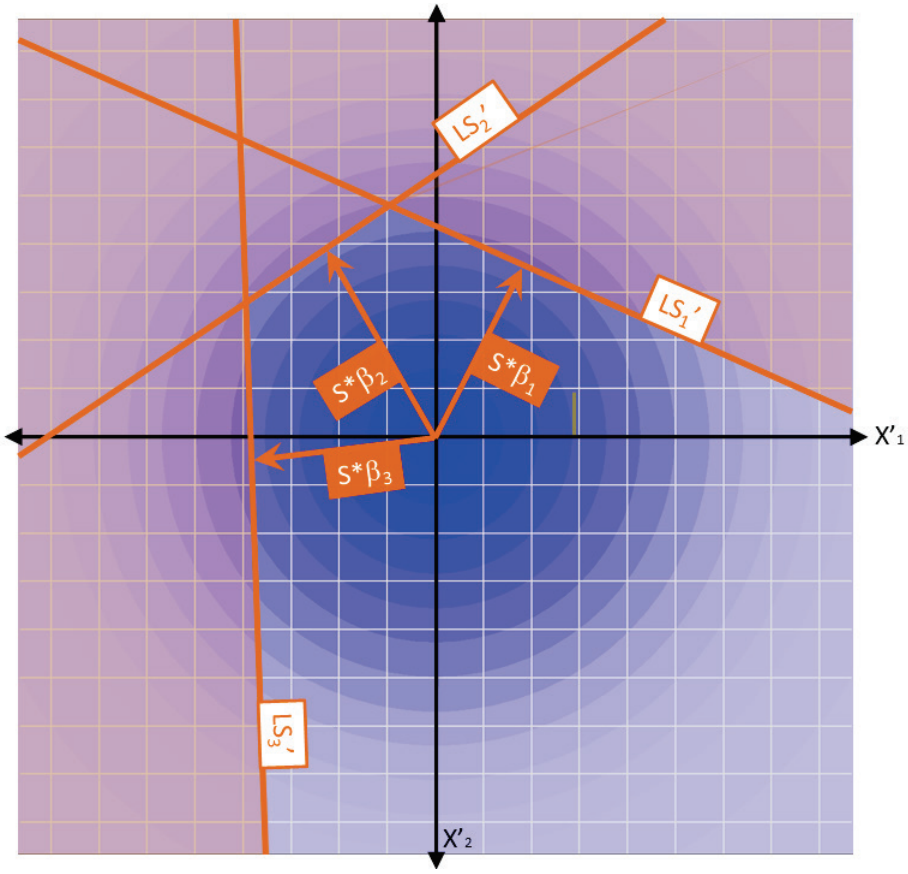

For this equation, $f(S)$ is a result of one of the multivariate, multi-limit state estimation techniques discussed in the previous section. The purpose is to make the calculated *PUP* approximately equivalent to the established limit (e.g., $\Phi(3.5)$ with $\beta = 3.5$). Each limit state response surface is described by

$$\beta_i \boldsymbol{\alpha}_{i-original} = (\beta_{i-original} \times S)\boldsymbol{\alpha}_{i-original} \tag{A.34}$$

Since the *PUP* can described by a function of a single variable (*S*), a Newtonian or secant-based numerical method can be used to adjust the design points (by changing the scale) until the solution approaches the limit set for the overall system *PUP*, in an efficient way.

The second method to apply scale factors is more complicated but can give a better overall design because all the variables are considered independently. To balance the design to the load and intended probability of failure, the initial attempt at the design must find the hyperplanar definition vectors for all the limit states, $\beta_{\text{i-original}}\boldsymbol{\alpha}_{\text{i-original}}$ (Figure A.14). When these hyperplanar descriptions are discovered, factors can be applied to the minimum β value limit state that extends the distance from the origin in the Gaussian multivariate space to the limit state hyperplane, thus lowering the *PUP* for that limit state. However, this factor affects all the limit states to varying degrees as each variable axis is extended to varying degrees by the minimum limit state's directional cosines (e.g., $\alpha_{i\text{-}original_X1}$). This is shown in Figure A.16. In this case, Equation A.34 is interpreted in a different way:

$$\beta_{i-original}\boldsymbol{\alpha}_i = \beta_{i-original}(\boldsymbol{\alpha}_{i-original} \times S) \tag{A.35}$$

Given this, each variable axis has its own scale factor

$$S_{Xi} = \alpha_{i-original_Xi} \times S \tag{A.36}$$

For this situation, the *PUP* is a function of the scale factors for each of the variables.

$$PUP = f(S_{X1}, S_{X2}, \ldots, S_{XN}) = f(\boldsymbol{S}) \tag{A.37}$$

Because of correlation between the limit state response surfaces, the concern would be that these functions can lead to local minima and maxima in a root finding because of the new slope calculations. Testing will need to be performed to find if these issues confound root-finding numerical algorithms.

Figure A.16. Applying variable axis scale factors to adjust probabilities. A scale factor applied to Limit State 1 causes slope changes in the response surfaces for Limit State 2 and 3.

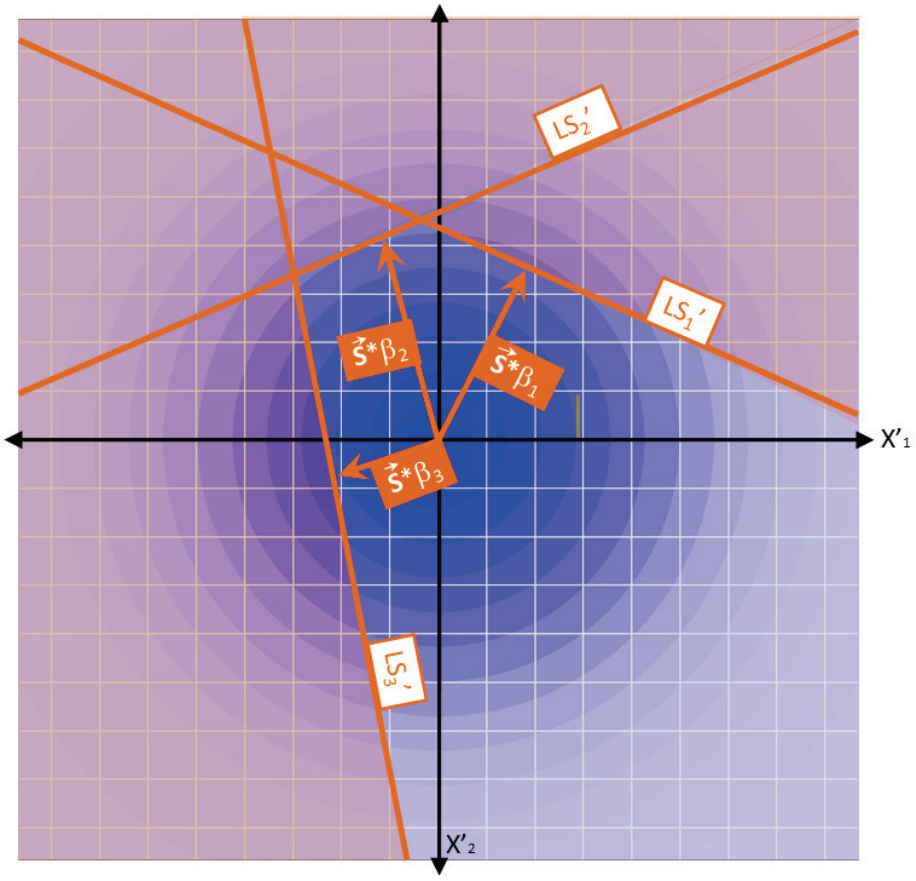

A.5 Validating *PUP* numerical estimation methods

To validate the models for *PUP* estimation, evaluate the inputs that will lead to an increase in accuracy, and to determine the resources (i.e., time) that will be needed to do these estimations, simple test cases were created. These test cases were performed with two variables and had three overlapping limit states. These tests were performed on a Dell Precision T7610 computer using Python 2.6 language for purposes of timing.

The first test case had two limit states that were perpendicular to the X_1 variable axis at distance 1.0 and -1.2 along the axis. The third limit state was perpendicular to the X_2 variable axis at distance 1.3 along the axis. For all three limit states, the unsatisfactory performance was in the half-space away from the origin of the Gaussian multivariate space. This can be seen in Figure A.17.

Figure A.17. The first test case for *PUP* estimation.

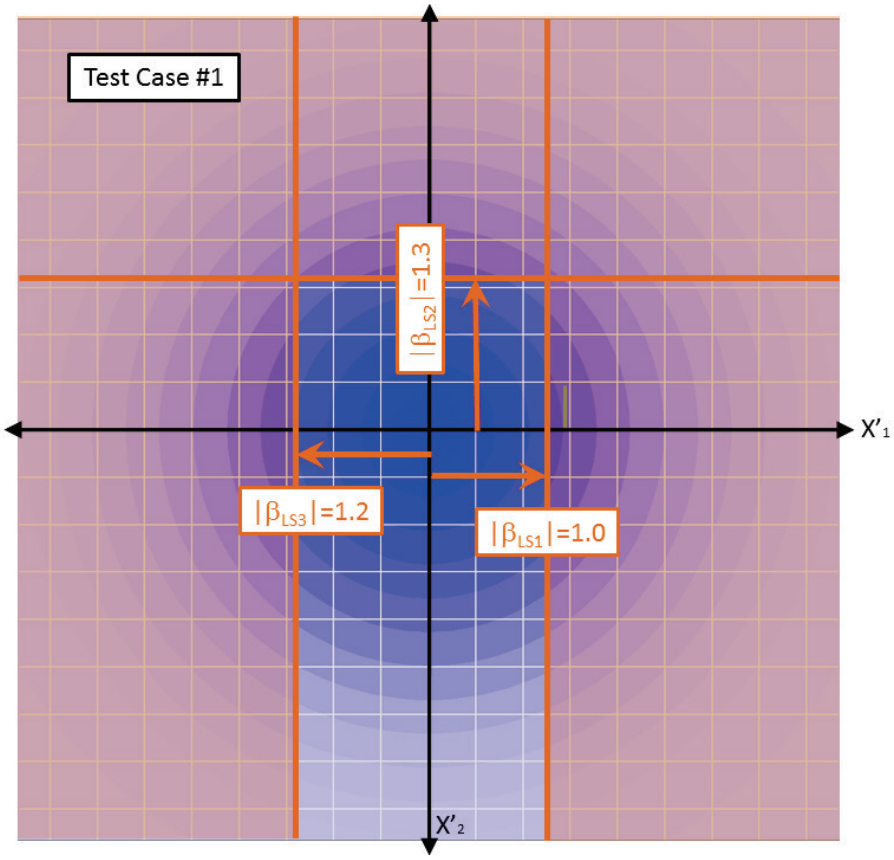

Because the limit states are perpendicular or parallel, the limit states are completely uncorrelated. This simplifies the calculation of the actual *PUP*. The probability of the overlapping area of two limit state half-spaces is the multiplication of each limit states' *PUP*. This result is shown in Equations A.21 and A.22, when ρ=0.0. This means that

$$P(E_i E_j) = \Phi(-\beta_i)\Phi(-\beta_j) \tag{A.38}$$

Therefore, for the first simple test case, the *PUP* is given by

$$PUP = \Phi(-\beta_{LS1}) + \Phi(-\beta_{LS2}) + \Phi(-\beta_{LS3}) - \Phi(-\beta_{LS1})\Phi(-\beta_{LS3}) - \Phi(-\beta_{LS2})\Phi(-\beta_{LS3}) = 0.34402870$$

Listings A.1 and A.2 show the result of performing a simple numeric integration across the test case from -5 to 5 in each dimension of the Gaussian multivariate space with step resolutions of 0.01 and 0.001, respectively. The first few lines show the calculation of the *PUP* as discussed previously. The estimated value of *PUP* with resolution 0.01

from the integration is 0.3414388654 and took 154 sec to integrate. This value is within 0.2% of the actual calculated *PUP* value. The estimated value of *PUP* with resolution 0.001 from the integration is 0.3437685994 and took 16,127 sec to integrate. This value is with 0.05% of the actual calculated *PUP* value. While the additional accuracy can make slight changes at the tails of the distribution, the solution time means that the 0.01 resolution numerical integration is preferred.

Listing A.1. Output from Euclidean numerical integration with step size 0.01.

```
===== Direct Calculation =====

PUP(LS1) = 0.15865525

PUP(LS2) = 0.11506967

PUP(LS3) = 0.09680048

E(LS1,LS3) = 0.01535791

E(LS2,LS3) = 0.01113880



PUP(Overall) = PUP(LS1)+PUP(LS2)+PUP(LS3)-E(LS1,LS3)-
E(LS2,LS3) = 0.34402870







===== Direct Numerical Integration Calculation =====

Input Parameters: Resolution=0.0100000000

numsteps=500

Solution Time=152

PUP(Overall) = 0.3414388654
```

Listing A.2. Output from euclidean numerical integration with step size 0.001.

```
===== Direct Calculation =====

PUP(LS1) = 0.15865525

PUP(LS2) = 0.11506967

PUP(LS3) = 0.09680048

E(LS1,LS3) = 0.01535791

E(LS2,LS3) = 0.01113880



PUP(Overall) = PUP(LS1)+PUP(LS2)+PUP(LS3)-
E(LS1,LS3)-E(LS2,LS3) = 0.34402870




===== Direct Numerical Integration Calculation =====

Input Parameters: Resolution=0.0010000000

numsteps=5000

Solution Time=16127

PUP(Overall) = 0.3437685994
```

Listing A.3 and A.4 show the results of pure polar integration for the same test case. Recall that polar integration can take advantage of the fact that any point on the hypersphere has the same probability in the Gaussian multivariate space for a significant speedup. The integration is performed from the center to a hypersphere of radius 5. The angle step is 0.01 for both runs, and the radius changes by steps of 0.01 and 0.001, respectively. The first few lines show the calculation of the *PUP* as discussed previously. The estimated value of *PUP* with radius resolution 0.01 from the integration is 0.3438739669 and took 217 seconds to integrate. This value is within 0.05% of the actual calculated *PUP* value and has better accuracy than the Euclidean numerical integration does with 0.001 step resolution. The estimated value of *PUP* with resolution 0.001 from the integration is 0.3440204733 and took 2,036 seconds to integrate. This value is with 0.003% of the actual calculated *PUP* value. While the additional accuracy can make slight changes at the tails of the distribution, the solution time means that the 0.01 resolution polar numerical integration is preferred and is better than the Euclidean numerical integration.

Listing A.3. Output from polar numerical integration with radius step size 0.01 and angle step size 0.001.

```
===== Direct Calculation =====

PUP(LS1) = 0.15865525

PUP(LS2) = 0.11506967

PUP(LS3) = 0.09680048

E(LS1,LS3) = 0.01535791

E(LS2,LS3) = 0.01113880



PUP(Overall) = PUP(LS1)+PUP(LS2)+PUP(LS3)-
E(LS1,LS3)-E(LS2,LS3) = 0.34402870




===== Polar Numerical Integration Calculation =====

Input Parameters: Radius Step=0.0100000000 Angle
Step=0.0010000000

Solution Time=217

PUP(Overall) = 0.3438739669
```

Listing A.4. Output from polar numerical integration with radius step size 0.001 and angle step size 0.001.

```
===== Direct Calculation =====

PUP(LS1) = 0.15865525

PUP(LS2) = 0.11506967

PUP(LS3) = 0.09680048

E(LS1,LS3) = 0.01535791

E(LS2,LS3) = 0.01113880



PUP(Overall) = PUP(LS1)+PUP(LS2)+PUP(LS3)-E(LS1,LS3)-
E(LS2,LS3) = 0.34402870




===== Polar Numerical Integration Calculation =====

Input Parameters: Radius Step=0.0010000000 Angle
Step=0.0010000000

Solution Time=2036

PUP(Overall) = 0.3440204733
```

The second test case (Figure A.18) was designed to test the Ang and Tang (1974) bounds method with correlated limit states. In this case, a design point was chosen for three hyperplanar limit states. The design points were (0.5,1.1), (-0.6,0.9), and (-0.9,-0.1) for Limit States 1, 2, and 3, respectively. The unsatisfactory performance regions were in the half-planes for the limit state response surfaces away from the origin.

Figure A.18. The second test case for *PUP* estimation.

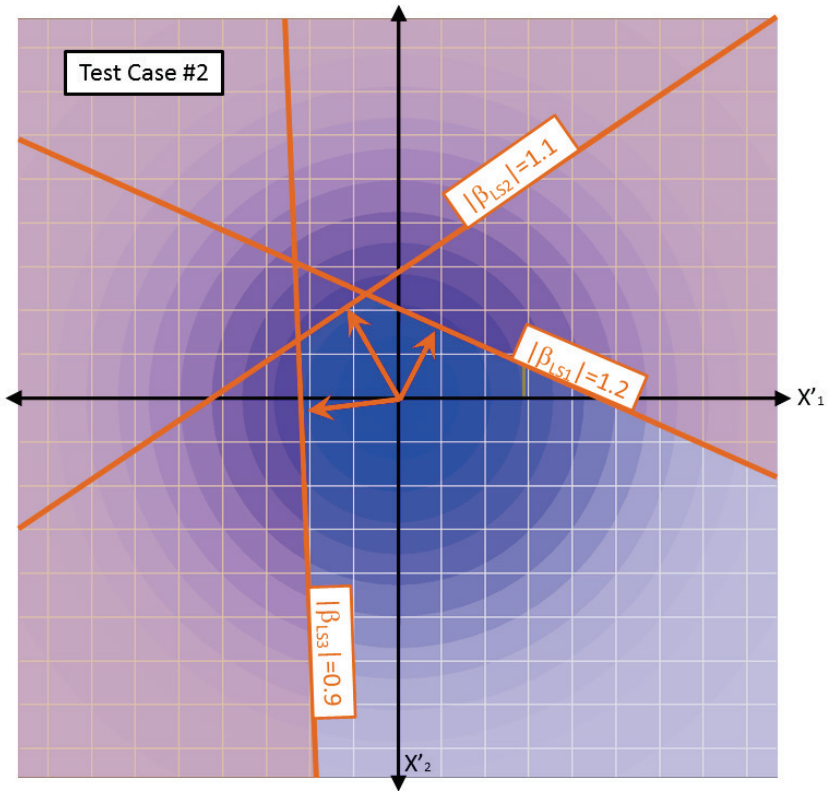

Listings A.5 shows the input design points along with the calculated β values and α vectors for the limit states. The absolute bounds for the *PUP* are calculated from Equations A.12 and A.13, resulting in 0.182590 <= *PUP* <= 0.376573, with an average value of 0.279582. Using the pairwise correlation relationships in Equations A.14 and A.15, with estimated values from Equations A.21–A.24, a tighter bound was established as 0.229335 <= *PUP* <= 0.344048, with an average value of 0.286692. Because of the correlation, an actual value was not available, so a polar integration was performed with a radius step of 0.01 and an angular step of 0.01, which resulted in a *PUP* of 0.329675.

Listing A.5 output from Ang and Tang (1974) bounds estimation compared to polar integration method.

```
===== Input Parameters =====

Limit State 1 (LS1) Design Point (0.500000 1.100000)
Beta=1.208305 Alpha = (0.413803 0.910366)

Limit State 2 (LS2) Design Point (-0.600000 0.900000)
Beta=1.081665 Alpha = (-0.554700 0.832050)

Limit State 3 (LS3) Design Point (-0.900000 -0.100000)
Beta=0.905539 Alpha = (-0.993884 -0.110432)



===== Ang and Tang Limits =====

PUP(LS1) = 0.113465

PUP(LS2) = 0.139701

PUP(LS3) = 0.182590



Absolute Bounds: 0.182590 <= PUP <= 0.376573 Average =
0.279582



Tighter Bounds: 0.229335 <= PUP <= 0.344048 Average =
0.286692



===== Numerical Analysis =====

Input Resolution: Radius step size = 0.010000 Angle step
size = 0.001000

PUP = 0.329675
```

While the bounds estimation method was simple to compute, the range of the values is too big for estimation in the tails of the Gaussian normal distribution. The averaged values also were not accurate enough for the rigorous application that would be required by an LRFD solution method.

Appendix B: Wind-Induced Wave Loading Assessments Made at Select Inland USACE Flood Mitigation Structure Sites

B.1 Example calculation of wind-induced inland wave forces Red River of the North floodwall

This sub-appendix presents a procedure to calculate wind-induced wave forces acting on an inland floodwall located on the Red River of the North in Grand Forks, ND. Application of the Goda-Takahashi (Goda 2010) wave force prediction method was chosen for this analysis. Typically, with coastal structures, buoys are available to provide data needed for the wind-induced wave force analysis. The estimation of design wave height and period for inland structures can be more involved due to the need to locate nearby historical records of wind speed. A procedure to determine wind-induced wave force loading is presented. The hydraulic structure used in this example problem is the stem of a cantilever floodwall and shown in Figure B.1-1. Analytical and statistical methods are employed in the estimation of design wave height and period along with requirements of historical wind record preparation. The wave loading calculation based on the Goda-Takahashi formulations are presented for this example inland flood protection structure.

Figure B.1-1. T-Wall used in example wave force calculation (tension and compression piles not shown).

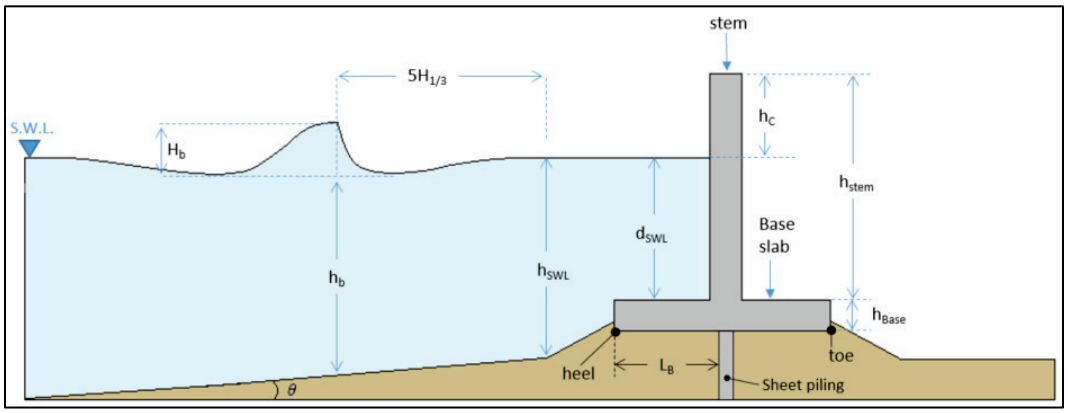

B.1.1 Details of Red River of the North floodwall

Typically, the design of an inland floodwall requires that the water level at the maximum head differential must be known. The top of the floodwall was based on a flood with a selected ACE. In this example, the top of the floodwall was set at an ACE of 0.13% (return period of 750 years). The distance from the top of the base slab to the top of the wall is 13.9 ft (h_{stem} in Figure B.1-1). The actual elevations of the top of wall and top of the base slab and bottom of the base slab are 836.9, 823, and 821, respectively. The distance from the water surface at the selected flood level to the top of wall is 3 ft, which is a water-surface elevation of 833.9.

B.1.2 Wind analysis

The selection of the appropriate wave height to use for inland structure analysis depends on wind and water characteristics. These include the magnitude of the wind speed, the duration and direction of the wind-speed event, and the open water-surface distance (fetch) over which the wind blows before reaching the floodwall. Hopefully, historical wind data from a nearby municipal airports for can be obtained. It is recommended that historical wind records from multiple wind recording sites, near the project site, be used whenever possible. Multiple historical wind records can help extend historical analysis, fill in time gaps, and validate data. In the example presented below, historical wind records were obtained from a local international airport. The following subsections describe the development of the wave height and period for the Red River of the North flood wall near Grand Forks, ND.

A detailed description of procedures used to obtain and process the wind data is provided in subsection B.2.3. This includes locating an airport, obtaining the necessary historical wind data, processing the wind data, using Goda formulation to determine minimum time (T_{min}) for wind to produce fully developed wave, determining fetch, and statistical analysis of data to obtain appropriate wind speed for wave force formulations. These steps are described below without all the background shown in subsection B.2.3.

B.1.2.1 Wind speed and fetch

The wind-speed and wind direction data were obtained from meteorological data collected between 1973 and 2020 at the Grand Forks

International Airport (GFI) in North Dakota. The GFI airport is located just over 6.7 miles west of the project. Figure B.1-2 shows the data collection site in relation to the project.

Figure B.1-2 Wind speed and direction collection site at GFI.

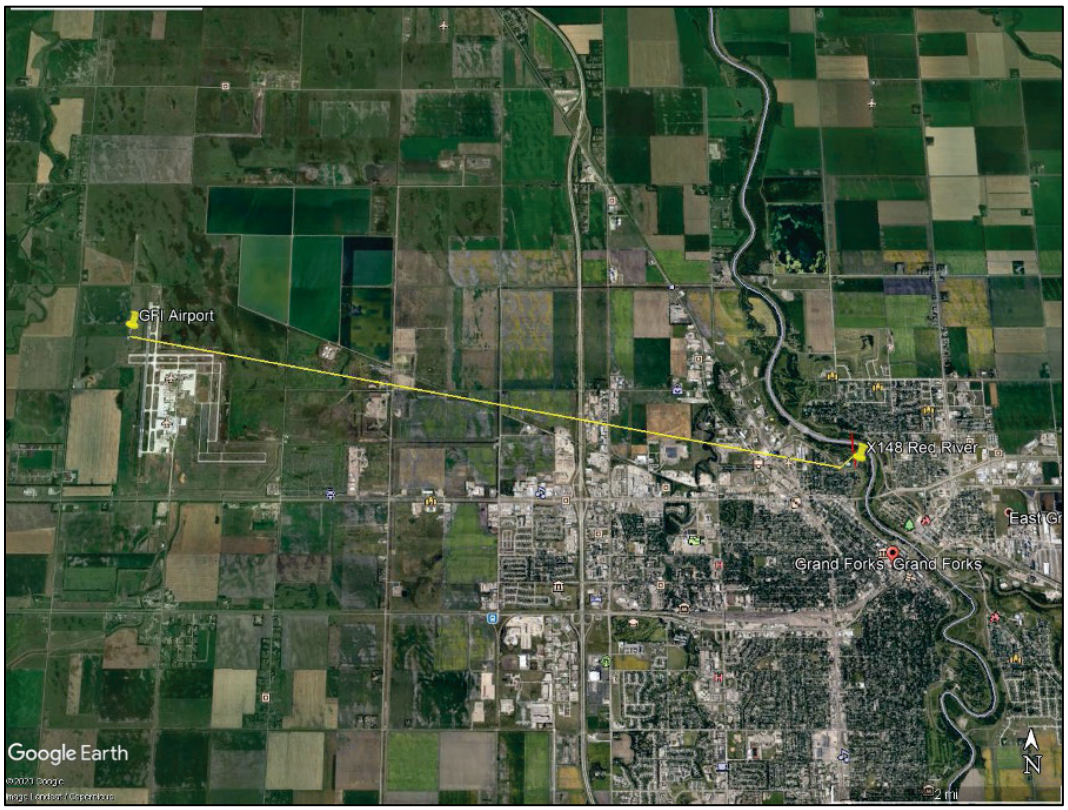

The data set was fairly complete for the years 1973 to August 2020 with wind speeds and directions reported multiple times per hour between 2012 and August 2020 and hourly from 1973 to 2012. The latitude is 47.9492, and the longitude is -97.1761. (The data were obtained from the web site supported by Iowa State University:
https://mesonet.agron.iastate.edu/request/download.phtml?network=MS_ASOS.)

Figure B.1-3 shows a portion of the Red River of the North at Grand Forks, ND, taken from a flood zone map provided by MVP. Cross section (XS) 148 (XS 148) was used for this example problem, and it is located near the middle of picture. The yellow lines in Figure B.1-4 represent the floodwall for the project. To determine the fetch, the center of XS 148 was projected normal to the floodwall as illustrated in Figure B.1-4.

Figure B.1-3. Floodwall along Red River near XS 148.

Figure B.1-4. Fetch and wind direction determined for the Red River of the North floodwall.

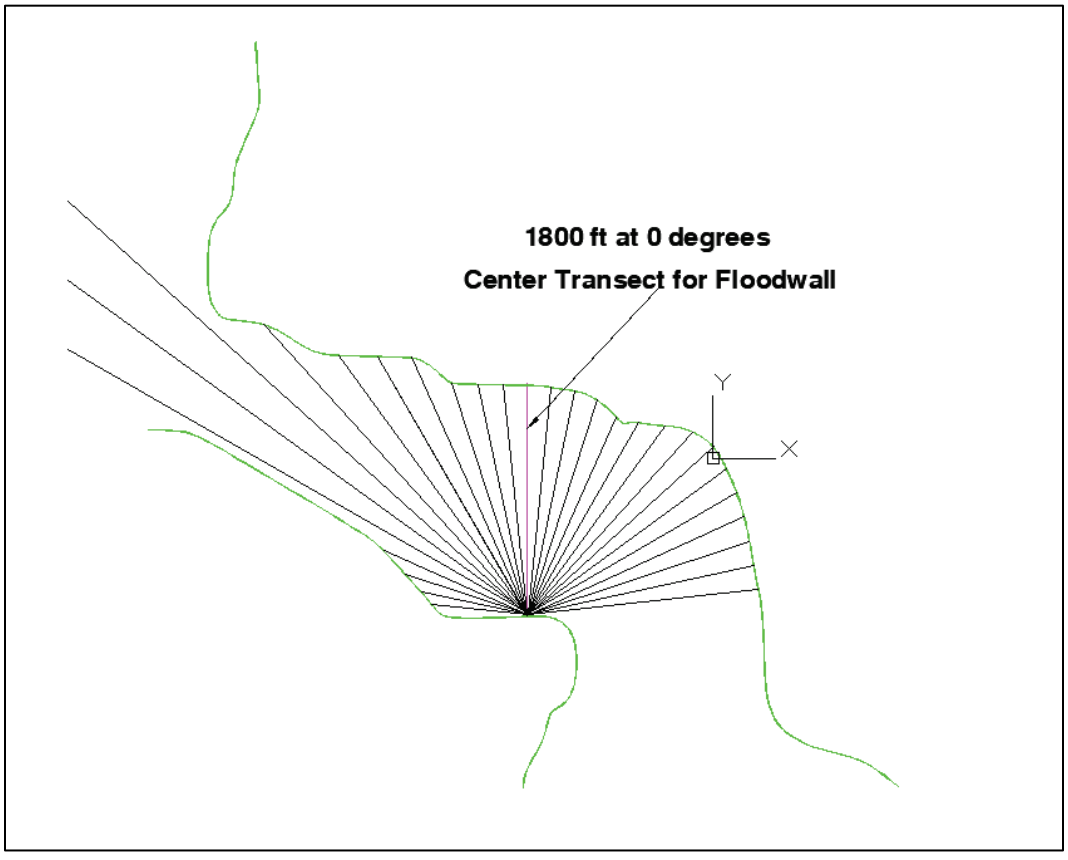

The green lines in Figure B.1-4 are the same as the yellow lines in Figure B.1-3 and represent the floodwall location. The wind direction that impacts the floodwall at this location is 0° or due north, and the fetch is 1,800 ft. Figure B.1-4 shows the input data used for the NARFET model, which computes an effective fetch length based on 6° angular offsets from the primary fetch direction. There were 14 offsets on each side of the primary direction, and the clockwise angular range was from 276° to 84°. These data are used to determine wave heights for comparison with wave heights determined using Goda (2010) procedures.

B.1.2.2 Wind-speed analyses

An appropriate wind speed needs to be determined to develop a wave height and period used to compute the wave loads. Based on recent research conducted by the authors in support of this technical report and by Hite et al. for spillway gates, the wind speed can be determined based on Goda (2010) equation and shown in Chapter 6 as Equation 6.1 where the minimum time required for a wave to fully develop is computed from the fetch. Since the fetch at this project is only 1,800 ft, the minimum time required for a wave to fully develop based on the Goda equations was 15 min or 0.25 hr. These equations are also presented in subsection B.1.4. The wind-speed data were then processed to determine the yearly maximum average 0.25 hr wind-speed value for wind directions between 340° and 20° (plus and minus 20° from the direction normal to the floodwall). Table B.1-1 shows the wind-speed values for the yearly maximum average 0.25 hr maximum for wind directions between 340° and 20°.

Table B.1-1. Yearly maximum average 0.25 hr wind speed, GFI.

Observation Period 1973–2020 (wind direction 340° to 20°)					
Date	Wind Speed (mph)	Date	Wind Speed (mph)	Date	Wind Speed (mph)
2/13/1973	34.5	1/8/1989	34.5	3/10/2005	37.95
3/15/1974	34.5	6/3/1990	29.75	7/31/2006	36.8
1/21/1975	34.5	11/2/1991	32.2	6/7/2007	37.66
3/20/1976	42.26	2/10/1992	24.44	2/9/2008	39.10
1/26/1977	40.25	12/29/1993	31.63	3/10/2009	38.67
2/14/1978	43.84	11/18/1994	30.19	1/25/2010	42.11
3/13/1979	39.68	2/10/1995	34.83	3/12/2011	37.95

Observation Period 1973–2020 (wind direction 340° to 20°)					
Date	Wind Speed (mph)	Date	Wind Speed (mph)	Date	Wind Speed (mph)
4/22/1980	36.8	1/18/1996	39.79	10/19/2012	37.66
2/7/1981	27.6	4/6/1997	46.0	2/18/2013	40.25
4/3/1982	40.25	3/13/1998	36.80	7/22/2014	40.5
8/26/1983	46.0	3/17/1999	38.38	3/29/2015	33.35
2/5/1984	40.25	3/9/2000	33.93	2/29/2016	39.10
12/26/1985	37.95	10/24/2001	34.50	5/17/2017	29.32
1/12/1986	34.5	2/12/2002	29.61	10/26/2018	40.54
10/1/1987	37.95	5/30/2003	36.94	3/14/2019	39.68
9/19/1988	33.35	12/12/2004	34.21	2/12/2020	43.01

B.1.2.3 Extreme value estimation

This first method investigated followed a procedure used by MVP (2014) in the Oxbow-Hickson-Bakke (OHB) Levee Wind-Wave Analysis. This study was performed to determine levee heights required for the flood protection project. The wind speeds shown in Table 1-1 were used for this analysis. The Type 1 Gumbel Distribution was used for a GEV analysis. This analysis is typically used to evaluate extreme, low-probability meteorological and hydrological events. The probability of non-exceedance and wind speed are plotted, and a linear regression can be used to estimate values for extreme return periods. The results from extreme value estimation using the peak annual values for the GFI data are shown in Figure B.1-5. The 100-year recurrence interval wind speed from this analysis was 53.2 mph.

Figure B.1-5. Extreme wind-speed estimation for GFI.

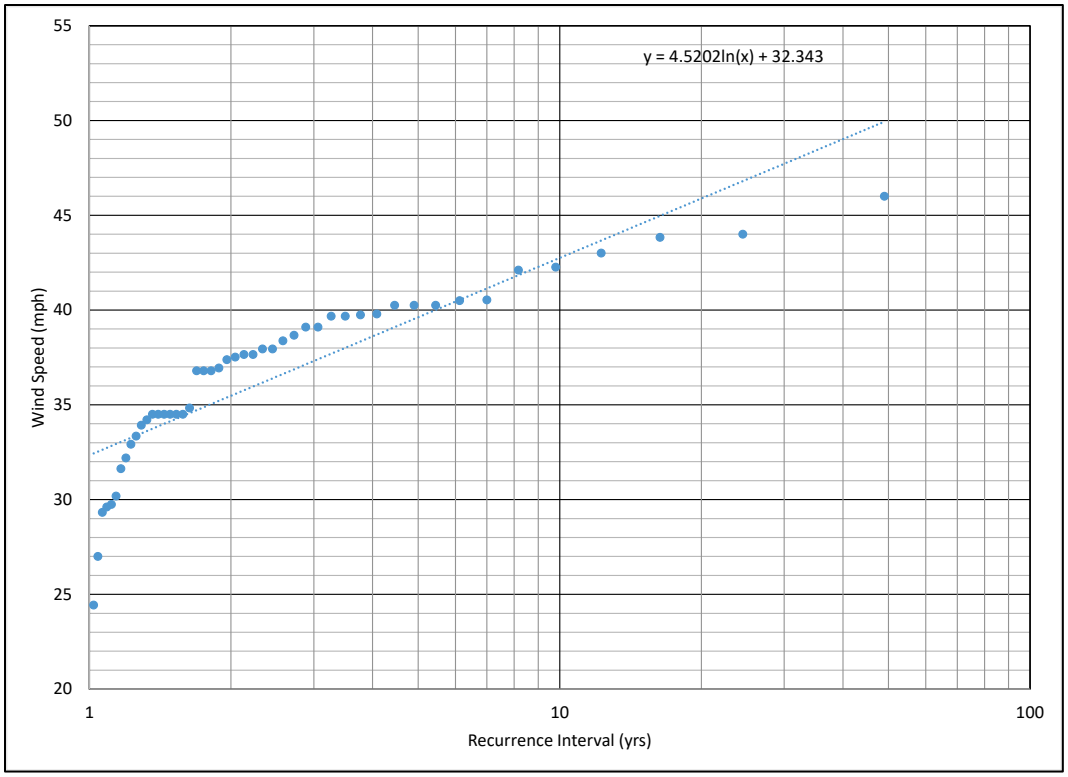

B.1.2.4 Wind frequency based on Gumbel Type 1 Distribution with Gringorten's method

Another wind-speed evaluation method was the use of the Type 1 Gumbel Distribution with Gringorten's (1963) plotting position formula. A description of this procedure is given in Chapter 6 and in Hite et al. for spillway gates. A plot of the return period vs. wind speed determined using this procedure is shown in Figure B.1-6 for the data from GFI. The wind speed for the 100-year return period was 51.0 mph.

Figure B.1-6. Wind frequency from Gumbel Type 1 Distribution with Gringorten's Method.

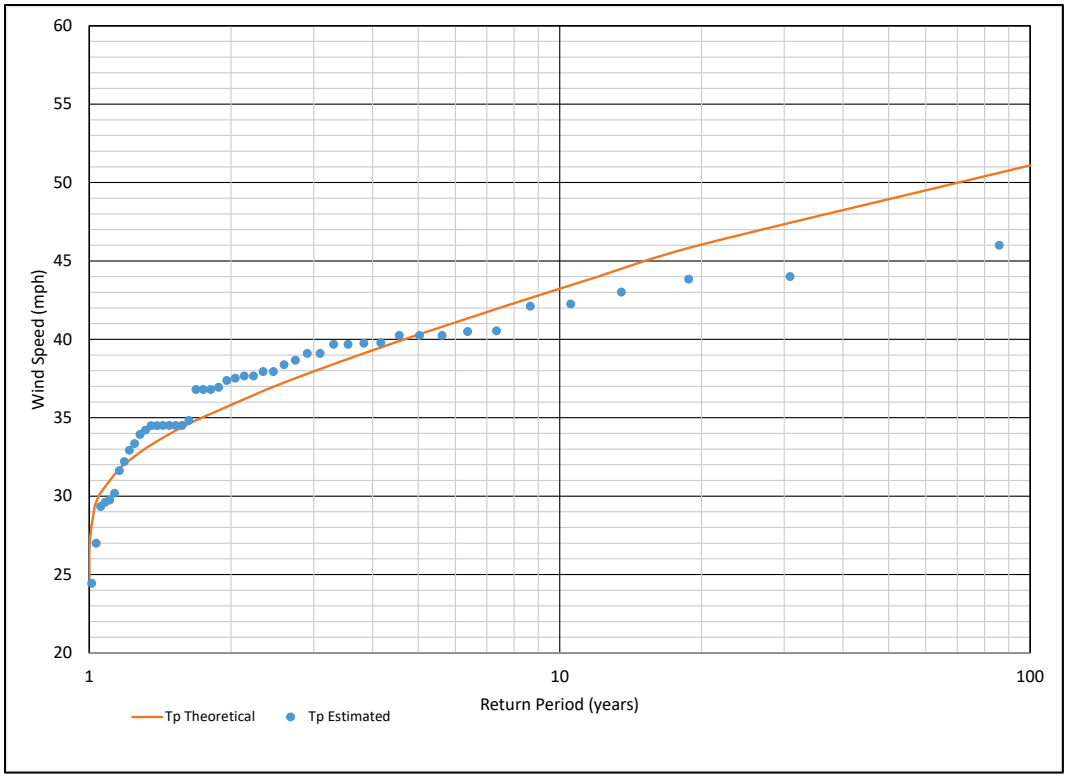

To further investigate the statistics for the wind speed, a formula to determine the standard error (deviation) was used for the data shown in Figure B.1-6. This method is presented in Chapter 6 and in Hite et al. for spillway gates. The results from this analysis are shown in Figure B.1-7 and were considered a better representation of the wind speeds to use for the wave load versus the extreme value estimation (although they were in close agreement).

Figure B.1-7. Wind frequency curves based on yearly maximum average 0.25 hr wind speed for GFI data.

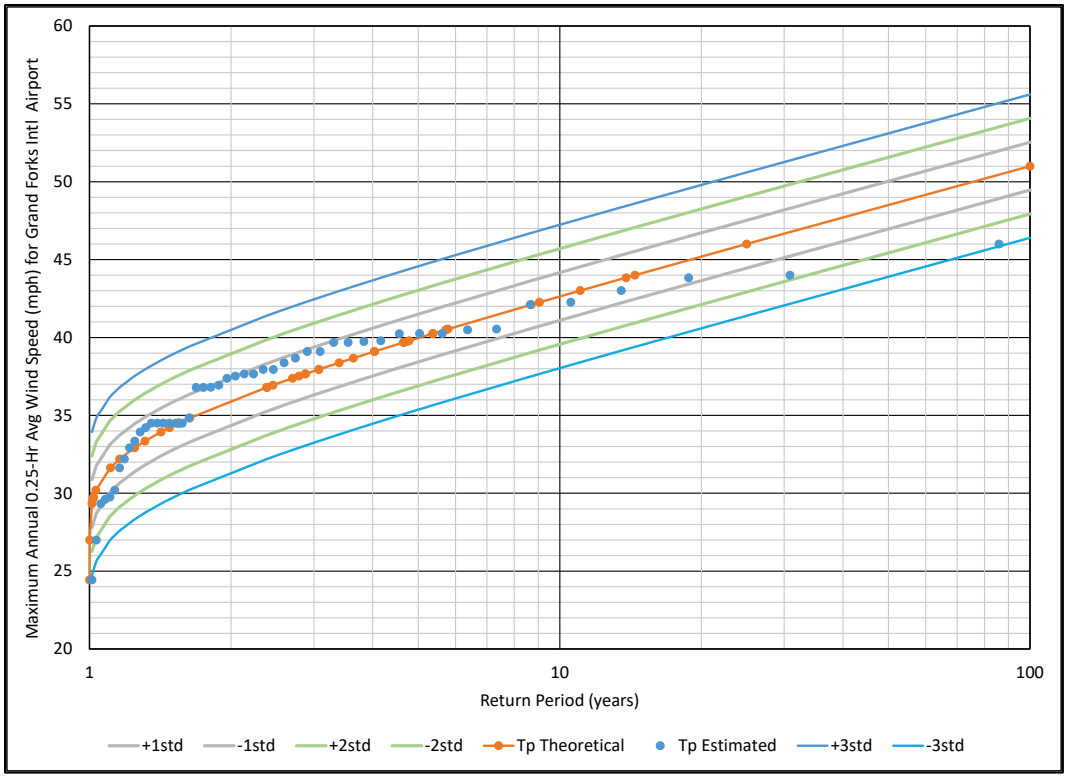

The standard deviation determined from this data (n=48) was 1.534 mph. The range of the 100-year return period for -3σ to +3σ was 46.4 mph to 55.60 mph with a mean value of 51.0 mph. These values of wind speed are shown in Table B.1-2 and were the values used in the following analysis to determine the wave loads.

Table B.1-2. Results from wind-speed analysis for Red River Floodwall.

Statistic	100-Year Wind Speed (mph)
+3σ	55.60
+2σ	54.07
+1σ	52.53
Mean	51.00
-1σ	49.47
-2σ	47.93
-3σ	46.40

B.1.3 Wave height and period assessment

Smith (1991) developed guidance to determine significant wave height and peak period based on wind speed and fetch. Dr. Tallent (unpublished) updated Smiths' NARFET fortran computer program to a more recent computer language (Python). Table B.1-3 shows the input data and results from the use of the NARFET program for the Red River of the North Floodwall at Grand Forks, ND. The program input requires the radial lengths of the fetch and the angle increments for resolution of the wind direction as depicted in Figure B.1-3. The radial lengths (a total of 29) determined for an angle increment of 6° are shown in Figure B.1-3. The significant wave height and period for the wind speeds shown in Table B.1-2 are listed in Table B.1-3. The fetch length at the maximum period or effective fetch length was 1.2 km (0.75 miles). The wave heights computed from the fit curve and plus 1, 2, and 3 standard deviations for the 100-year return period using the NARFET model are shown in Figure B.1-8.

Table B.1-3. Wave height and wave period from Smith's NARFET Model.

Wind Speed (mph)	Wave Height (m)	Wave Period (sec)
46.40	0.22	1.58
47.93	0.23	1.60
49.47	0.25	1.69
51.00	0.26	1.71
52.53	0.27	1.73
54.07	0.29	1.81
55.60	0.30	1.83

Figure B.1-8. Wave height vs. wind speed from Smith's NARFET model.

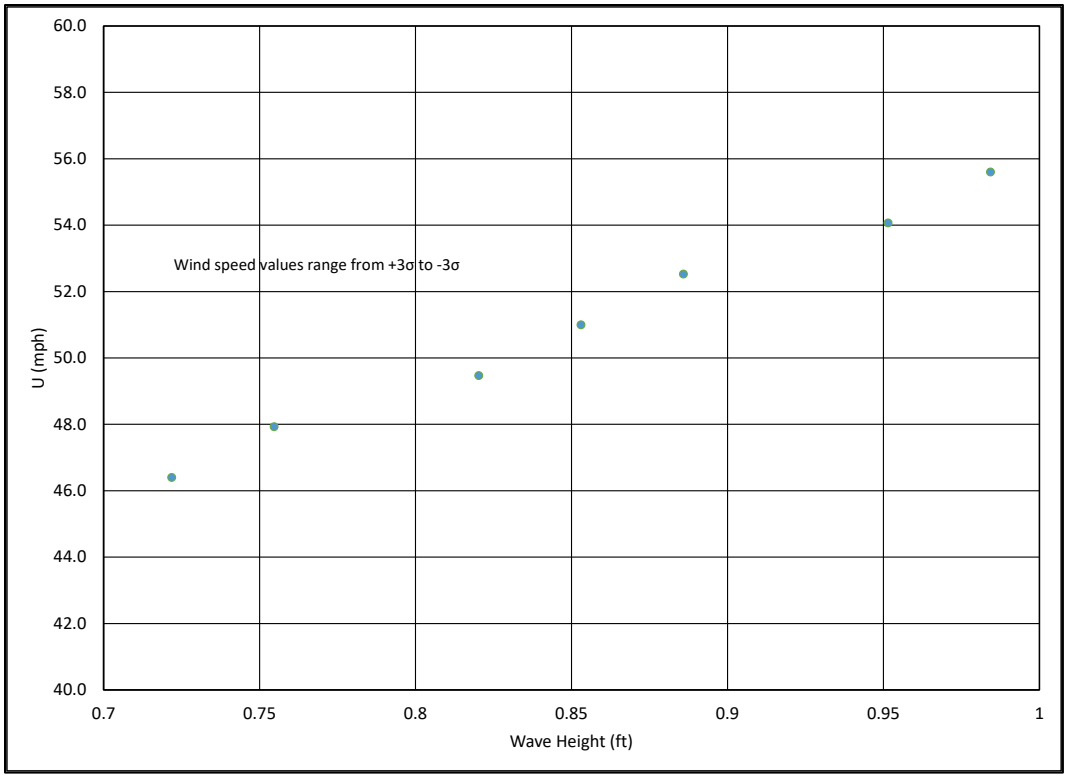

B.1.4 Pseudo-static wave load from Goda (2010)

Goda (2010) also recommended formulations to determine significant wave height and period based on wind speed and fetch. His designation for wind speed is U_{10} and represents the wind speed 10 m above the sea surface. These formulations are shown in Chapter 6 and in Hite et al. for spillway gates. Goda proposed the minimum duration (T_{min}) needed to achieve the significant wave height and significant wave period. The significant wave height and period and T_{min} computed from these equations are shown in Table 1-4. The 100-year return period wind speed was 51.0 mph, and the standard deviation was 1.534. Goda (2010) numerically derived and experimentally validated the relation shown in Equation 6.1, which estimates this minimum duration of wind speed (T_{min}) required to generate a sustainable wave height for a fixed fetch length and wind speed.

$$T_{min} = 1.0{F_L}^{0.73}U_{10}^{-0.46} \quad \text{(6.1 bis)}$$

where

F_L = the fetch length in kilometers
U_{10} = wind speed at the elevation of 10 m above the sea surface
T_{min} = minimum duration of wind speed (hours) required for sustainable wave height generation.

The fetch length used in Goda's Equation 6.1 for the design example was 548.61 m (1,800 ft). Goda's wave height and period prediction relationships are given in Equations 6.6 and 6.7. These metric unit-based equations were numerically derived and experimentally verified as discussed in Goda (2010). Applying Equations 6.6 and 6.7 to the U_{10} values listed in Table B.1-2 and the fetch length of 548.1 m (1,800 ft) results in Table B.1-4. Applying Equations 6.6 and 6.7 to Table B.1-2 data with U_{10} values in meter/sec, results in the Table B.1-4 values.

$$\frac{gH_{1/3}}{U_{10}^2} = 0.3\left\{1 - \left[1 + 0.004\left(\frac{gF}{U_{10}^2}\right)^{1/2}\right]^{-2}\right\} \quad \text{(6.6 bis)}$$

$$\frac{gT_{1/3}}{U_{10}} = 8.61\left\{1 - \left[1 + 0.008\left(\frac{gF}{U_{10}^2}\right)^{1/3}\right]^{-5}\right\} \quad \text{(6.7 bis)}$$

where

g = acceleration due to gravity (9.81 m/sec^2)
$H_{1/3}$ = significant wave height (design wave height, meters)
$T_{1/3}$ = significant wave period (design wave period, seconds)
U_{10} = wind speed at the elevation of 10 m above the sea surface (meters/second)
F = fetch length incident to the structure (meters).

Note that in Equation 6.1, F, is given in kilometers, so this needs to be converted to meters for use in Equations 6.6 and 6.7.

Table B.1-4. Significant wave height and significant wave period from Goda's (2010) formulations for a flood level, SWL, of el 833.9.

Statistic	100-Year Wind Speed (mph)	t_{min} (hr)	$H_{1/3}$ Wave Height (m)	$T_{1/3}$ Wave Period (sec)
-3σ	46.4	0.158	0.374	1.614
-2σ	47.93	0.156	0.383	1.628
-1σ	49.47	0.155	0.393	1.642
Mean	51.00	0.153	0.402	1.656
+1σ	52.53	0.151	0.411	1.669
+2σ	54.07	0.150	0.420	1.682
+3σ	55.60	0.149	0.429	1.695

A plot of wind speed (U) vs. wave height determined from Goda's recommended formulations from the statistical analysis of the wind-speed data is shown in Figure B.1-9. The values for significant wave height computed by the NARFET model were less than those using Goda's procedure, so Goda's values were used to determine the wave loads.

Figure B.1-9. Wave height vs. wind speed from Goda's (2010) procedure for a flood level, SWL, of EL 833.9.

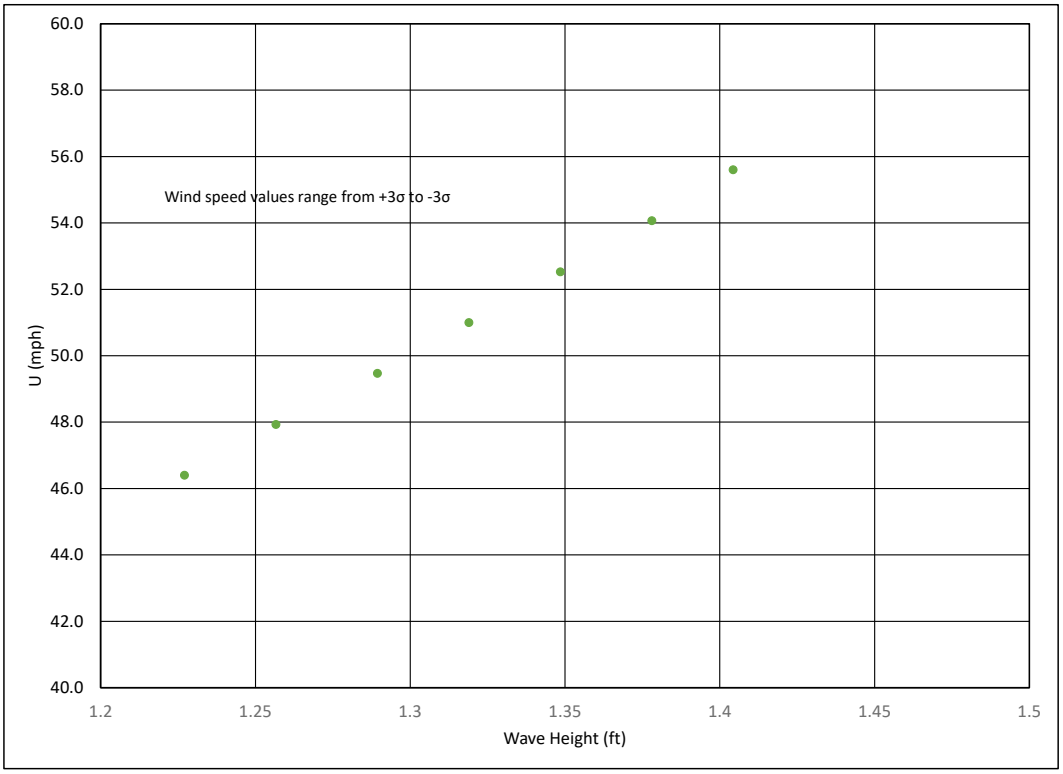

B.1.5 Example for determining pseudo-static wave load from Goda (2010) for Red River of the North floodwall

The wave pressure distribution and subsequent wave force for the floodwall gate can now be determined from the significant wave height and wave period. The complete description of this procedure is shown in Chapter 6 and in Hite et al. for spillway gates.

B.1.5.1 Example floodwall design details and parameters for Goda (2010) formulations for Red River of the North

Table B.1-5 provides a summary of the parameters used in the Goda (2010) procedure of defining a pseudo-static wind induced wave pressure acting on a floodwall. Figure B.1-1 depicts these variables.

Table B.1-5. Parameters used in Goda (2010) procedure for example wave force calculation (imperial and metric units included) for a flood level, SWL, of EL 833.9.

Parameter	Value	Unit	Value	Unit	Description
h_{stem}	13.9	ft	4.24	m	T-Wall stem height (above base)
h_{Base}	2.0	ft	0.61	m	T-Wall base thickness
h_C	3.0	ft	0.914	m	T-Wall height above SWL
L_B	8.0	ft	2.4	m	Distance from heel of base slab to sheet pile distance
d (originally d_{SWL})	10.9	ft	3.32	m	Still water depth at base of T-Wall
h (originally h_{SWL})	15	ft	4.57	m	Still water depth at toe of berm
tan θ	0	N/A	0	N/A	Floodplain slope to T-Wall (riverside of T-Wall berm)
β_D	0	deg	0	deg	Design incident wave angle
$H_{1/3}$	1.32	ft	0.402	m	Significant wave height, From Table B.1-4 (0.402 m) for a mean wind velocity of 51 mph
$T_{1/3}$	1.656	sec	1.656	sec.	Significant wave period, for a mean wind velocity of 51 mph
L_D	14.405	ft	4.282	m	Design wavelength, From $T_{1/3}$ and Eq. 5.11
ρ	62.4	lb/ft^3	1000	kg/m^3	Density of freshwater
g	32.17	ft/sec^2	9.81	m/sec^2	Acceleration of gravity
h'	10.9	ft	3.322	m	For the case of T-Wall: $h' = d_{SWL}$
H_D	2.37	ft	0.723	m	Design wave height (see Eq. 5.8)
η*	3.55	ft	1.084	m	Elevation of wave pressure action above flood level

The design wave height (H_D), is the minimum of $\alpha h H_{1/3}$ and H_b. Where αh ranges from 1.6 to 2.0. For the design of nearshore vertical structures, Goda (2010) suggests using a value of 1.8 for αh. For this example, the floodwall is 13.9 ft high (top EL 836.9), and the water-surface at the flood level is 3 ft below the top of the wall (EL 833.9). An approach depth (h and h_{SWL} in Figure B.1-1 and Table B.1-5) of 15 ft was assumed with a mild approach slope (tan θ).

The Goda (2010) wave load computation procedure adapted for an inland flood wall is described in Chapter 6 and in Hite et al. for spillway gates. Some of the parameters used in this procedure are shown in Figure B.1-1. The example computations are for the 100-year return period mean wind speed of 51 mph, a wave height of 1.319 ft (0.402 m) and a wave period ($T_{1/3}$) of 1.656 sec. As stated above, the distance from the top of the base slab to the top of the wall is 13.9 ft (h_{stem} in Figure B.1-1). The elevations of the top of wall and top of the base slab and bottom of the base slab are 836.9, 823, and 821, respectively. The distance from the water surface at the selected flood level to the top of wall is 3 ft (h_c in Figure B.1-1). The distance from the water surface at flood level to the bottom of the stem (top of base slab) was 10.9 ft (d_{SWL} in Figure B.1-1 and also referred to as d). The distance from the water surface at the flood level to the floodplain approach invert is given as 15 ft (h_{SWL} in Figure B.1-1), EL 818.9. This flood plain approach invert is 4.1 ft below the top of the base slab or 2.1 ft below the bottom of the base slab. Since θ was set equal to zero, h_b in Figure B.1-1 was equal to h_{SWL}. The significant wave height is 1.319 ft ($H_{1/3}$ in Figure B.1-1) for a mean wind velocity of 51 mph.

B.1.5.2 Pseudo-static wave pressure terms for Red River of the North floodwall

Goda (2010) uses three pseudo-static wave pressure terms (P_1, P_2, and P_3) to define the wave pressure distribution on the vertical face of the wall and one pseudo-static pressure term (P_u) to describe the uplift pressure at the toe of the wall (Figure B.1-10). The P_1 pressure term represents the maximum wave pressure exerted at the SWL while P_2 and P_3 represent the linear decay in wave pressure with depth.

Figure B.1-10. Illustration of terms in Goda's (2010) original pressure formulation.

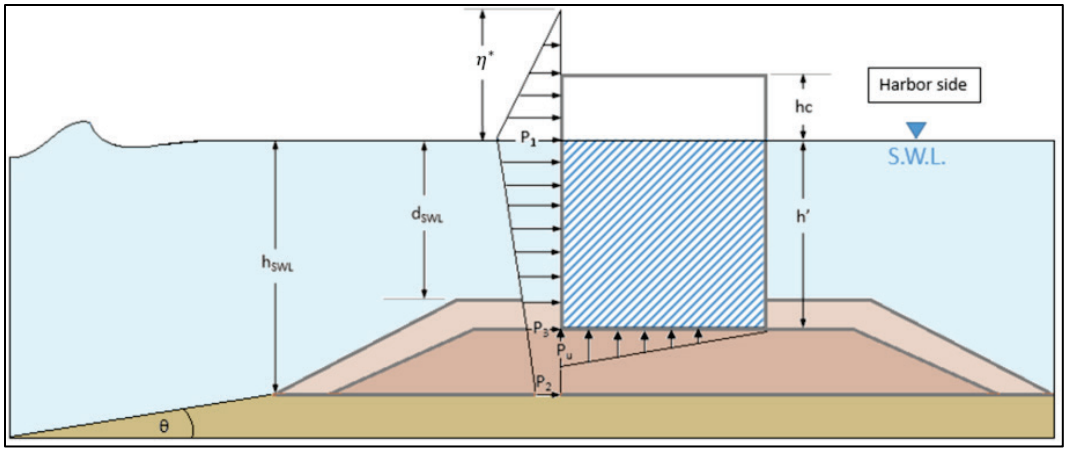

$$P_1 = 0.5\,(1\ + \cos\beta_D)\,(\alpha_1 + \alpha_2 * cos^2\beta_D)\,\rho * g * H_D \qquad (5.1\text{ bis})$$

$$P_2 = \frac{P_1}{\cosh(2\pi h/L_D)} \qquad (5.2\text{ bis})$$

$$P_3 = \alpha_3 P_1 \qquad (5.3\text{ bis})$$

$$P_u = 0.5\,(1\ + cos\,\beta_D)\,\alpha_1 * \alpha_3 * \rho * g * H_D \qquad (5.4\text{ bis})$$

where α_1 and α_2 are wave pressure coefficients derived from laboratory data. The α_1 coefficient represents the average tendency of wave pressure to increase with wavelength (L) and the α_2 coefficient represents the tendency of the wave pressure to increase with the berm height. This α_2 term reflects the wave shoaling effect due to berm height and the impulsive pressure component. The α_3 coefficient describes the assumed linear pressure variation between P_1 and P_2.

$$\alpha_1 = 0.6 + \frac{1}{2}\left[\frac{\frac{4\pi h}{L_D}}{\sinh\left(\frac{4\pi h}{L_D}\right)}\right]^2 \qquad (5.5\text{ bis})$$

$$\alpha_2 = \min\left[\frac{h_b - d}{3h_b}\left(\frac{H_D}{d}\right)^2, \frac{2d}{H_D}\right] \qquad (5.6\text{ bis})$$

$$\alpha_3 = 1 - \frac{h'}{h}\left[1 - \frac{1}{\cosh\left(\frac{2\pi h}{L_D}\right)}\right] \qquad (5.7\text{ bis})$$

The Goda (2010) procedure of analysis represents the complex spectrum of sea waves by a single design wave height and length represented by H_D

and L_D, respectively. The design wave height (H_D) of Goda's formula is described as the highest wave expected under given wave conditions; this wave height is also identified as H_{MAX}. H_{MAX} is determined as the lesser of 1.8 times the significant wave height ($H_{1/3}$) and the breaking wave height (H_b) (Equations 5.8 – 5.10), where H_b is evaluated at a distance of $5H_{1/3}$ seaward of the breakwater berm as shown in Figure B.1-11. The design wavelength (L_D) of Goda's formula is described as the longest wave expected under given wave conditions; this wavelength is also identified as L_{MAX}. In Equation 5.11, L_{MAX} is approximated using first-order wave theory and the significant wave period ($T_{1/3}$).

Figure B.1-11. Breaking wave height location in Goda's (2010) equation.

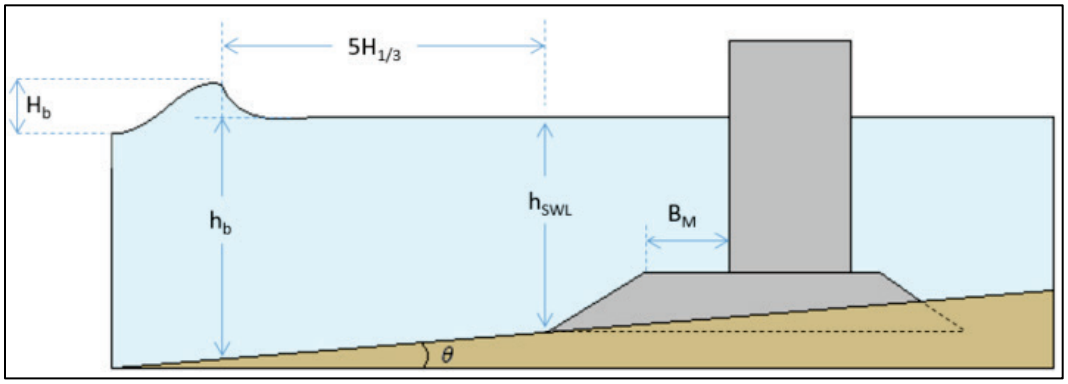

$$H_D = H_{Max} = min\{\alpha_h * H_{1/3},\ H_b\} \quad \text{(5.8 bis)}$$

where α_h is typically in the range of 1.6 to 2.0. The α_h term defines the nondeterministic characteristic of the highest wave due to the random nature of sea waves. According to Goda (2010), the value of α_h is selected based on the reliability of design storm wave estimation, the importance of the structure, and the type and nature of the possible structural failure. Goda states that a value of 2.0 or greater is often used for offshore structures, such as an offshore oil rig. For the design of nearshore vertical structures Goda suggest a value of 1.8 for α_h.

$$H_b = 0.17 * L_D \left\{1 - exp\left[-1.5\frac{\pi h_b}{L_D}\left(1 + \sigma_S * tan^{4/3}\theta\right)\right]\right\} \quad \text{(5.9 bis)}$$

Originally, Goda specified the σ_S value as a constant equal to 15 but later recommended a value of 11 based on the work of Rattanapitikon and Shibayama (2000). This reduction in the σ_S value accounts for an overprediction in the wave shoaling effect for steep bottom slopes (>1/10).

Therefore, the authors of this report recommend using $\sigma_S = 11$ for bottom slopes greater than 1/50 and $\sigma_S = 15$ for bottom slopes less than 1/50.

$$h_b = h + 5 * H_{1/3} \tan\theta \quad \text{(5.10 bis)}$$

$$L_D = L_{MAX} = \frac{g * T_{1/3}^2}{2\pi} \quad \text{(5.11 bis)}$$

According to Goda (2010), the significant wave height ($H_{1/3}$) represents the largest one-third wave height measured in deep water. Similarly, the significant wave period ($T_{1/3}$) represents the longest one-third wave period measured in deep water. Site-specific estimates of $H_{1/3}$ and $T_{1/3}$, based on historical records, simulations, etc., can either be obtained or calculated; therefore,

$\alpha_h H_{1/3}$ = 1.8*0.402 m = 0.724 meters (2.38 ft)

and using Equations 5.10 and 5.9, the H_b parameter is derived as follows:

h_b = 4.57 m + 5*0.402*(0) = 4.57 m (15.0 ft),

$H_b = 0.17 * 4.282\ \text{m}\left\{1 - exp\left[-1.5 * \frac{\pi * 4.57\text{m}}{4.282\text{m}}\left(1 + 15 * (0)^{4/3}\right)\right]\right\} =$ 0.723 m (2.37 ft),

and finally,

$H_D = H_{Max}$ = min {0.724 m, 0.723 m} = 0.723 m (2.37 ft)

Next, the coefficients of wave pressure (α_1, α_2 and α_3) given in Equations 5.5 – 5.7 are calculated. Recall that the h and d values in Equation 5.5 and 5.6 are respectively equivalent to the h_{SWL} and d_{SWL} of Table B.1-5, therefore:

$\alpha_1 = 0.6 + \frac{1}{2}\left[\frac{\frac{4*\pi*4.57\text{m}}{4.282\text{m}}}{\sinh\left(\frac{4*\pi*4.57\text{m}}{4.282\text{m}}\right)}\right]^2 = 0.60$, from Equation 5.5,

$\alpha_2 = min\left[\frac{4.57\text{m} - 3.32\text{m}}{3*4.57\text{m}} * \left(\frac{0.723\text{m}}{3.32\text{m}}\right)^2, \frac{2*3.32\text{m}}{0.723\text{m}}\right] = min[0.004\ \text{m}, 9.19\ \text{m}] =$ 0.004,

from Equation 5.6.

Finally, since $h' = d_{SWL}$,

$$\alpha_3 = 1 - \frac{3.32\text{m}}{4.57\text{m}} * \left[1 - \frac{1}{\cosh\left(\frac{2*\pi*4.57\text{m}}{4.282\text{m}}\right)}\right] = 0.275, \text{ from Equation 5.7.}$$

The three Figure B.1-12 pseudo-static wind induced lateral wave pressure components P_1, P_2, and P_3 (Equations 5.1 to 5.3) and the pseudo-static wind induced wave uplift pressure component (P_u) (Equation 5.4) are evaluated below.

The solution to P_1, P_2 and P_3 are

$$P_1 = 0.5 * (1 + \cos(0 \text{ deg})) \left(0.60 + 0.075 * cos^2(0)\right) * 1000 \frac{kg}{m^3} * 9.81 \frac{\text{m}}{s^2} * 0.723 \text{ m} = 4287 \, N/\text{m}^2 \, (89 \text{ lb/ft}^2)$$

$$P_2 = \frac{4287 \, N/\text{m}^2}{\cosh(2*\pi*(4.57\text{m}/4.282\text{m}))} = 10 \, N/\text{m}^2 \, (0.21 \text{ lb/ft}^2)$$

$$P_3 = 0.275 * 4287 N/\text{m}^2 = 1179 \text{ N/m}^2 \, (25 \text{ lb/ft}^2),$$

and the solution for P_U is

$$P_u = 0.5 \, (1 + cos(0 \text{ deg})) \, 0.60 * 0.275 * 1000 \frac{kg}{\text{m}^3} * 9.81 \frac{\text{m}}{s^2} * 0.723 \text{ m} = 1170 \, N/\text{m}^2 \, (24 \text{ lb/ft}^2)$$

To calculate the total lateral force on the T-Wall, it is first necessary to determine if the pressure distribution (above SWL) extends above the crest of the T-Wall. The ΔP_1 parameter shown in Figure A-4 represents this fraction of pressure that would be negated from the total pressure above the SWL.

Figure B.1-12. Pressure distribution on T-Wall (batter piles not shown).

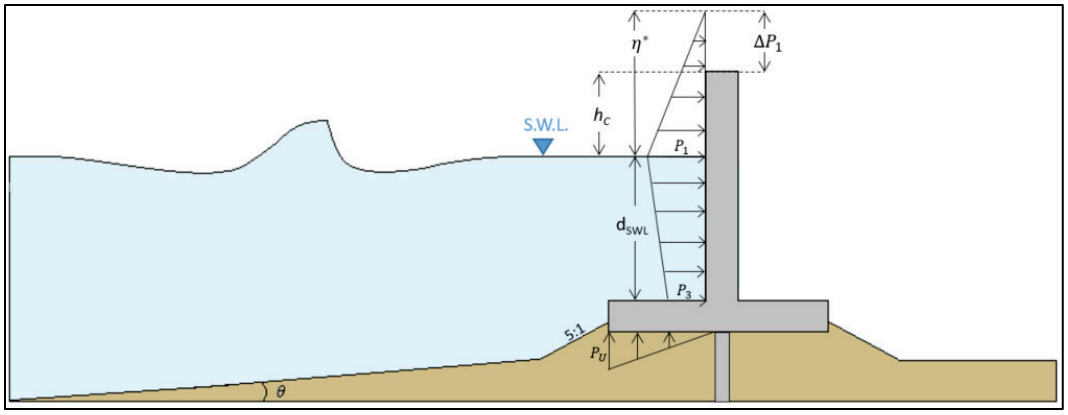

When the vertical distance η* plus the flood level SWL elevation exceeds the top of flood wall elevation, a pseudo-static horizontal water pressure P_4 is introduced at the top of wall. The total lateral force per linear width (F_{Lat}) on the seaward face of the T-Wall is given in Equation 5.29:

$$F_{Lat} = 0.5(P_1 + P_3)d + 0.5(P_1 + P_4)h'_C \quad (5.29 \text{ bis})$$

where

$$P_4 = P_1\left(1 - \frac{h_C}{\eta^*}\right), if\ \eta^* > h_C \quad (5.30 \text{ bis})$$

or

$$P_4 = 0, if\ \eta^* \leq h_C \quad (5.31 \text{ bis})$$

$$\eta^* = 0.75(1 + \cos(\beta_D))H_D \quad (5.32 \text{ bis})$$

$$h'_C = min\{\eta^*, h_C\} \quad (5.33 \text{ bis})$$

Therefore, the solution for the Figure 5-20 resultant force F_{Lat} is given as

h_C = 0.914 m or 3 ft (from Table B.1-5)

$\eta^* = 0.75 * (1 + \cos(0 \text{ deg})) * 0.723 \text{ m} = 1.084 \text{ m}$ (3.55 ft)

since $\eta^* > h_C$, from Equation 5.26,

$P_4 = 4287\ N/\text{m}\text{^}2 * \left(1 - \frac{0.914\text{m}}{1.084\text{m}}\right) = 674.6\ N/\text{m}^2$ (14.1 lb/ft²)

$$h'_C = min\{1.084\ \text{m}, 0.914\ \text{m}\} = 0.914\ \text{m}\ (3.0\ \text{ft})$$

$$F_{Lat} = 0.5 * \left(4287\,\frac{N}{\text{m}^2} + 1179\,\frac{N}{\text{m}^2}\right) * 3.322\,m + 0.5 * \left(4287\,\frac{N}{\text{m}^2} + 674.6\,\frac{N}{\text{m}^2}\right) * 0.914\ \text{m} = 11346\,N/\text{m}\ (777\ \text{lb/ft})$$

the total uplift force per linear width on the T-Wall is calculated as

$$U_P = 0.5 * P_U * L_B = 0.5 * 1170\,\frac{N}{\text{m}^2} * 2.4\ \text{m} = 1404\,N/\text{m}\ (96.2\ \text{lb/ft})$$

Using the relationships given in Chapter 6 and in Hite et al. for spillway gates, the one-third/one-sixth (1/3:1/6) rule is applied to calculate the elevation of the resultant forces along the vertical face of the T-Wall (Equation 5.34). Based on the parameters listed in Table B.1-5 and the wind speed and wave data in Table B.1-4, the pressure and lateral force acting on the floodwall were computed from the Goda (2010) formulations and are shown in Table B.1-6, along with h_{Lat} calculations from Equation 5.34.

$$h_{Lat} = \frac{(h_4 - h_1)\left(\frac{P_4}{3} + \frac{P_1}{6}\right)h_4 + (h_4 - h_1)\left(\frac{P_4}{6} + \frac{P_1}{3}\right)h_1 + (h_1 - h_3)\left(\frac{P_1}{3} + \frac{P_3}{6}\right)h_1}{F_{Lat}} \quad \text{(5.34 bis)}$$

h_{Lat} = 2.314 m = 7.59 ft

The definition of Goda's parameters shown in Table B.1-6 is illustrated in Figures B.1-12.

Table B.1-6. Wave force and pressure distribution computations using Goda's (2010) procedure for data in Table 1-4 for a flood level, SWL, of EL 833.9.

Statistic	Wind Speed (mph)	η^*, m	η^*, ft	P_1, N/m²	P_3, N/m²	P_4, N/m²	P_u, N/m²	F_{lat}, kN/m	h_{lat}, m	h_{lat}, ft	P_1, lb/ft²	P_3, lb/ft²	P_4, lb/ft²	P_u, lb/ft²	F_{lat}, lb/ft
+3σ	55.60	1.010	3.32	4487	1237	378	1088	11.96	2.324	7.62	94	26	7.9	22.7	819
+2σ	54.07	1.034	3.39	4420	1217	474	1114	11.75	2.321	7.61	92	25	9.9	23.3	805
+1σ	52.53	1.061	3.48	4353	1198	581	1144	11.55	2.317	7.60	91	25	12.1	23.9	791
Mean	51.00	1.085	3.56	4287	1179	675	1171	11.35	2.314	7.59	89	25	14.1	24.5	777
-1σ	49.57	1.101	3.61	4192	1152	740	1189	11.06	2.309	7.57	88	24	15.4	24.8	758
-2σ	47.93	1.118	3.67	4084	1122	806	1208	10.73	2.303	7.55	85	23	16.8	25.2	735
-3σ	46.40	1.134	3.72	3987	1094	872	1227	10.44	2.298	7.53	83	23	18.2	25.6	715

B.1.6 Observation of wind and flood event for Red River of the North Grand Forks, ND, floodwall

As mentioned in subsection B.1.1, the top of the floodwall was set at the flood event with an ACE of 0.13% (return period of 750 years). This relates to an elevation of 836.9. Figure B.1-13 shows the stage vs. ACE for the Red River of the North at Grand Forks, ND, and was provided by MVP. The blue dashed line represents the 50% confidence level, and the solid blue line is with all uncertainty included. The stage with 50% confidence was used for design and was used to select a top of wall elevation for a given ACE.

Figure B.1-13. Red River of the North stage vs. ACE at Grand Forks, SD.

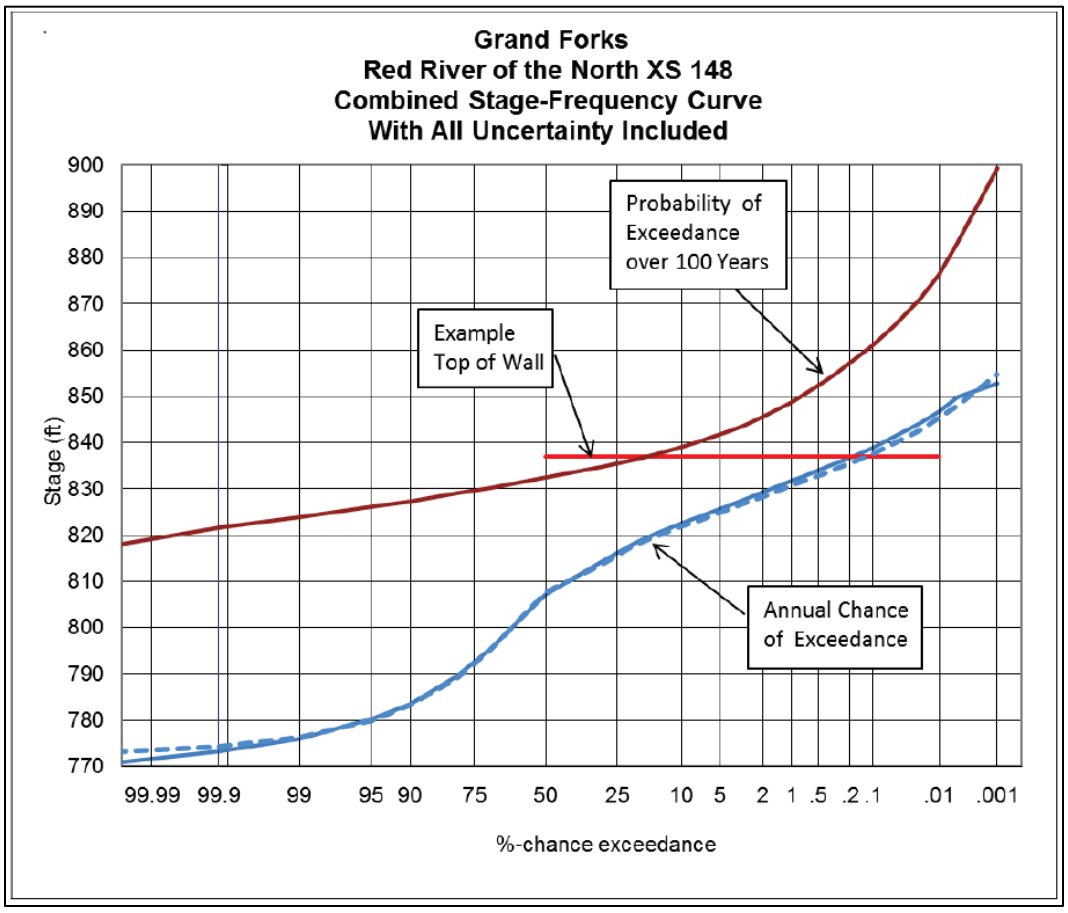

In the wind-induced wave force analysis, the SWL was evaluated for a water-surface elevation of 833.9. A water-surface elevation of 833.9 has an ACE of 0.4% (return period of 250 years). The wind speed selected for the wave force analysis was the 100-year return period (ACE of 1). A brief search of river stages at the Red River of the North Grand Forks, ND, was performed to see if there was any correlation between wind and flood

events. Figure B.1-14 shows the river stage between 2007 and 2020 and indicates there is usually a higher stage in the spring with a secondary peak near late fall or early winter. These higher stages tend to last for several days. The highest stage on this plot occurred in the spring of 2011. The elevation of gage zero was not found.

Figure B.1-14. River stages at Red River of the North near Grand Forks, ND, between 2007 and 2020.

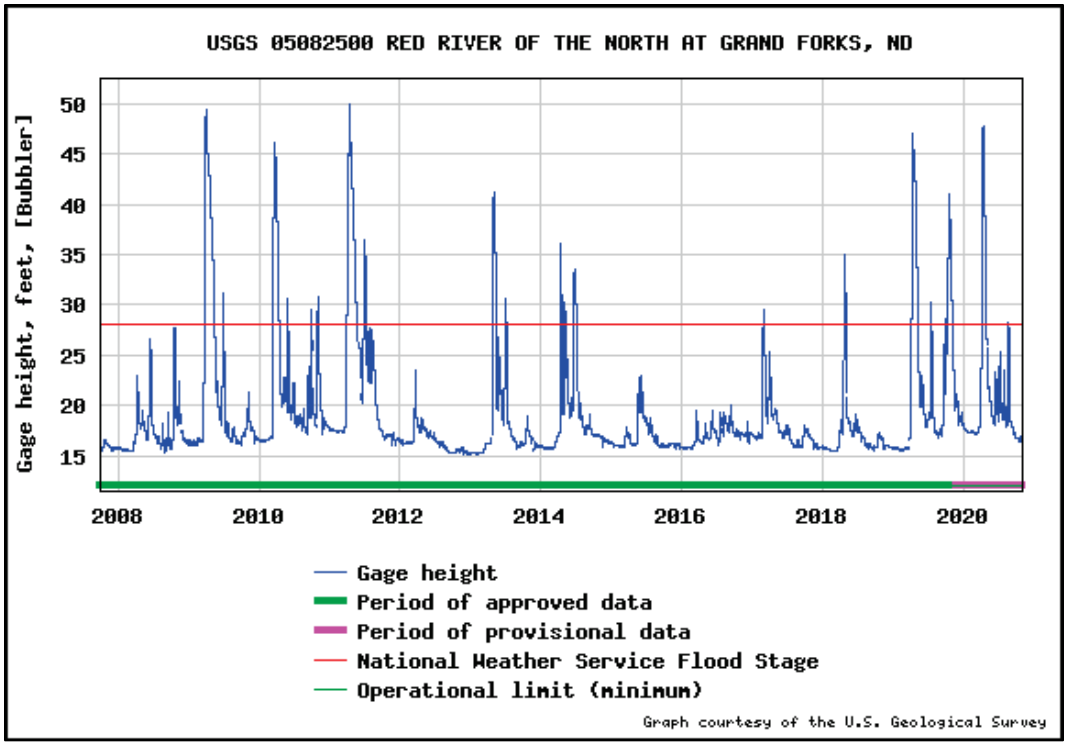

A plot of the number of maximum average 0.25 hr wind speeds that occurred per month from 1973 to 2020 is shown in Figure B.1-15. February and March had the highest number of occurrences with 11 each for the period from 1973 to 2020. From this very limited number of observations of river stage and wind speed, there appears to be a possibility that a flood event and wind event could occur at the same time since the flood event lasts for several days.

Figure B.1-15. Number of maximum average 0.25 hr wind speed occurrences per month from 1973 to 2020 for Red River of the North floodwall.

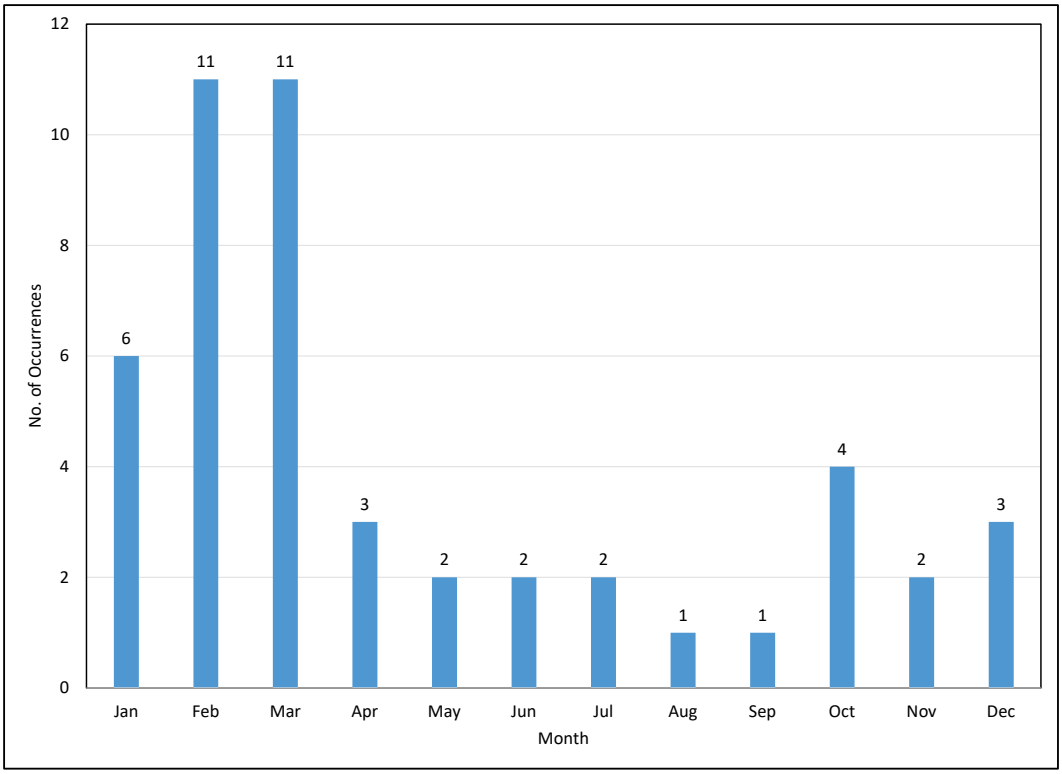

B.1.7 Summary for Red River of the North floodwall

Development of the wind-induced wave forces for the Red River of the North floodwall were presented in this sub-appendix. The analysis showed the appropriate wind speeds for the wave force computations ranged from 46.4 to 55.6 mph. These wind speeds produced wave heights from 0.374 m (1.23 ft) to 0.429 m (1.41 ft). These wave heights along with their associated wave period and wave length produced lateral forces (F_{lat}) on the floodwall of 10.44 kN/m (715 lb/ft) to 11.96 kN/m (819 lb/ft).

B.2 Example calculation of wind-induced inland wave forces, Red Wood River inland floodwall

This sub-appendix presents a procedure to calculate wind-induced wave forces acting on a hypothetical inland floodwall on the Red Wood River in Marshall, MN. The current version of the Goda-Takahashi wave pressure relationship is given in Goda (2010). Application of the Goda-Takahashi (Goda 2010) wave force prediction method was used for the example floodwall presented in section B.1 for the Red River of the North and was also used in this example analysis. The hydraulic structure used in this

example problem is the stem of a cantilever floodwall and shown in Figure B.2-1. Analytical and statistical methods are employed in the estimation of design wave height and period along with requirements of historical wind record preparation. The wave loading calculation based on the Goda-Takahashi formulations are presented for this example inland flood protection structure.

Figure B.2-1. Floodwall used in example wave force calculations (tension and compression piles not shown).

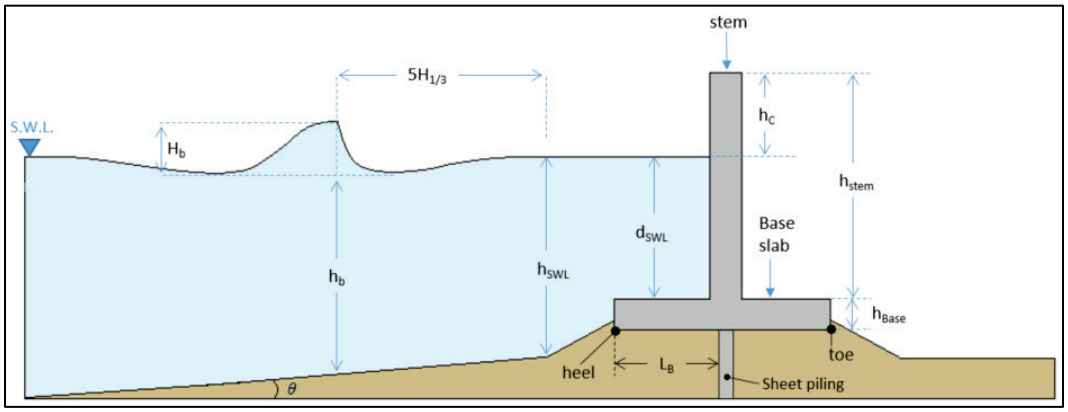

B.2.1 Floodwall details

The top of the floodwall is usually based on a flood with a selected ACE. In the example presented in this section, the top of the floodwall was set at an ACE of 0.13% (return period of 750 years). For load factor development, water to the top of the floodwall will be assumed to be the water level with the highest head differential. The distance from the top of the base slab to the top of the stem (floodwall) is 13.9 ft. In reference to a local datum, the top of wall was reported as a gage reading of 22.1 ft. This is the river stage for the ACE of 0.13% (return period of 750 years).

B.2.2 Wind-speed and direction analysis

The selection of the appropriate wave height to use for the wave force development depends on the local wind and water characteristics. These include the magnitude of the wind speed, the duration and direction of the wind-speed event and the open water surface distance (fetch) over which the wind blows before reaching the floodwall. Historical wind data from a nearby municipal airport can be very helpful for determining the wind speed and direction. It is recommended that historical wind records from multiple wind recording sites, near the project site, be used whenever possible. Multiple historical wind records can help extend historical

analysis, fill-in time gaps, and validate data. The following sections describe in detail the wind data processing needed to develop the wave height and period for the Red Wood River floodwall near Marshall, MN.

B.2.3 Steps for obtaining and processing wind data

B.2.3.1 Locating airport

The first step in the acquisition of wind data is to locate a suitable airport with a historical record of wind speed and direction. There is available online a variey of mapping tools that can locate the project and determine the closest municipal airport(s). For this example, Marshall, MN, was found on Google, and fortunately, a municipal airport was very close to the project. For the Red Wood River hypothetical floodwall project, the Marshall/Ryan Airport (MML) was approximately 1 mile from the project. Figure B.2-2 shows the data collection site in relation to the project. The latitude is 44.4500 and the longitude is -95.8200 for the airport.

Figure B.2-2. Wind speed and direction collection site at MML in relation to floodwall project.

B.2.3.2 Downloading wind data

Next, a data base needs to be found that contains the historical wind records for this airport. (The following website is supported by Iowa State University: https://mesonet.agron.iastate.edu/request/download.phtml?network=MS_ASOS. It was searched to determine if wind-speed and direction data were available for MML.) The Iowa Environmental Mesonet (IEM) maintains an archive of automated airport weather observations from around the world.)

The following steps were performed to determine if data were available.

1. Minnesota was chosen from the "Select Network" menu and [MML] Marshall/Ryan was chosen from the "Selected Stations" menu.
2. The wind speed in miles per hour and wind direction were then highlighted from the "Select From Available Data:" choices.
3. The historical period of interest was specified in the "Specific Date Range" using the "Start Date" and "End Date" options.
4. The time zone was selected from the "Timezone of Observation Times.
5. Then, the "Download Options:" was selected. The data can be displayed in the web browser or downloaded to a file. Generally, one will download the data to a file for subsequent processing.
6. The default choice for the "Limit Report Types" was chosen.
7. The "Get Data" was then activated. If available, the data are downloaded to a file(s).

B.2.3.3 Processing wind data

The wind-speed and direction data for MML were downloaded in seven separate files to avoid a very large file that would be cumbersome to process. The data were fairly complete from 1984 to November 2020 with wind speeds and directions reported multiple times per hour between July 1996 and November 2020 and hourly from 1984 through June 1996. A sample of the data downloaded from the web site is shown in Table B.2-1. The headings were changed for clarity.

Table B.2-1. Sample of wind-speed and direction data downloaded from Iowa State website for MML.

Sample No.	Date Time	Wind Direction	Wind Speed (mph)
198775	11/9/2020 11:00	350	13.8
198776	11/9/2020 11:17	330	13.8
198777	11/9/2020 11:25	10	12.65
198778	11/9/2020 11:27	10	10.35
198779	11/9/2020 11:29	20	11.5
198780	11/9/2020 11:33	10	9.2
198781	11/9/2020 11:42	360	11.5
198782	11/9/2020 11:56	10	8.05
198783	11/9/2020 12:05	360	9.2
198785	11/9/2020 13:56	350	21.85
198786	11/9/2020 14:15	330	23
198787	11/9/2020 14:30	330	18.4
198788	11/9/2020 14:35	340	19.55

The wind direction normal to the section of the floodwall being analyzed was determined next. This length of open water normal to the floodwall is referred to as the *fetch*. Figure B.2-3 shows the fetch and the direction of the wind normal to the section of floodwall used for this example. The fetch was 0.18 miles (950 ft), and the direction of the wind normal to the floodwall was 310°.

Figure B.2-3. Fetch and wind direction determined for the Red Wood River floodwall.

For the statistical analysis of the wind, all wind directions plus and minus 20° of the normal direction (310° for this example) were considered for the selection of the wind speeds. The range of wind directions from which the wind speeds were determined was from 290° to 330°. Table B.2-2 shows a sample of the data after the original wind-speed file had been processed to remove the wind directions outside the desired range. In this sample, the wind direction was 330° for approximately a 3 hr period.

Table B.2-2. Sample of processed wind-speed and direction file.

Sample No.	Date Time	Wind Direction	Wind Speed (mph)
2	1/1/2019 0:05	330	25.3
3	1/1/2019 0:10	330	31.05
8	1/1/2019 0:30	330	25.3
9	1/1/2019 0:31	330	23
12	1/1/2019 0:45	330	25.3
16	1/1/2019 1:00	330	32.2
25	1/1/2019 1:45	330	29.9
26	1/1/2019 1:46	330	28.75
29	1/1/2019 1:56	330	26.45
31	1/1/2019 2:05	330	24.15
34	1/1/2019 2:25	330	28.75
35	1/1/2019 2:30	330	28.75
43	1/1/2019 3:05	330	24.15

B.2.3.4 Selection of appropriate wind speed

From previous wind-speed statistical analyses, Chapter 6 and in Hite et al. for spillway gates, it was found that use of the maximum yearly wind-speed value for development of wave forces was produced unrealistic results. The duration of the wind speed is more important rather than the use of a maximum wind speed to achieve the fully developed wave height and wave period needed to determine the wave forces.

Goda (2010) recommended formulations to determine significant wave height and period based on wind speed and fetch. His designation for wind speed is U_{10} and represents the wind speed 10 m above the sea surface. These formulations are shown in Chapter 6 and in Hite et al. for spillway gates. Goda proposed the minimum duration (T_{min}) needed to achieve the significant wave height and significant wave period. He numerically derived and experimentally validated the relation shown in Equation 6.1, which estimates this minimum duration of wind speed (T_{min}) required to generate a sustainable wave height for a fixed fetch and wind speed.

$$T_{min} = 1.0{F_L}^{0.73}U_{10}^{-0.46} \quad \text{(6.1 bis)}$$

where

F_L = the fetch length in kilometers
U_{10} = wind speed in m/sec at the elevation of 10 m above the sea surface
T_{min} = minimum duration of wind speed (hour) required for sustainable wave height generation.

At this point in the wind data processing, the wind-speed value needed for Equation 6.1 is unknown. Since the fetch was known and the processed wind-speed and direction data contained the range of wind speeds, an estimate of the wind speed was made to determine T_{min}. For example, knowing F_L was 950 ft (0.2896 km), U_{10} was estimated at 40 mph (17.88 m/sec). The T_{min} computed from Equation 6.1 is 0.107 hr. If U_{10} is estimated at 50 mph (22.35 m/sec) and F_L remains at 950 ft (0.2896 km), then T_{min} from Equation 6.1 is 0.097 hr. Based on these values of T_{min}, the time required for the wave height and period to fully develop was approximately 0.1 hr or 6 min. This is a short time period since the fetch is so small. The actual values for T_{min} will be determined in the following sections and compared to this estimated value.

B.2.3.5 Maximum yearly average 0.1 hr wind speed

The processed wind-speed and direction data were then used to determine the maximum yearly wind speed averaged over a 6 min time period. This value was designated the yearly maximum average 0.1 hr wind speed and are shown in Table B.2-3 for the years between 1984 and 2020.

Table B.2-3. Yearly maximum average 0.1 hr wind speed, MML.

Observation Period 1984–2020 (wind direction 290° to 330°)		
Year	Month/Day	Wind Speed (mph)
1984	5/22	36.46
1985	12/23	36.47
1986	3/5	38.99
1987	1/21	34.27
1988	11/5	36.63
1989	5/5	40.91

Observation Period 1984–2020 (wind direction 290° to 330°)		
Year	Month/Day	Wind Speed (mph)
1990	1/11	39.73
1991	11/2	42.38
1992	12/25	39.96
1993	7/31	41.29
1994	11/18	45.87
1995	2/10	40.08
1996	10/30	50.26
1997	4/6	54.41
1998	11/10	51.23
1999	11/1	43.36
2000	4/5	49.57
2001	10/25	39.39
2002	2/11	46.92
2003	5/30	44.68
2004	3/14	43.18
2005	11/29	43.7
2006	1/24	40.25
2007	11/27	38.24
2008	10/26	45.14
2009	1/12	38.76
2010	6/26	46.44
2011	3/12	40.71
2012	4/16	40.54
2013	6/21	43.7
2014	4/1	43.36
2015	6/22	50.26
2016	8/4	38.53
2017	12/5	39.1
2018	6/6	34.5
2019	1/8	41.98
2020	1/5	39.1

For periods when observations of the wind speed were available multiple times per hour, a 0.1 hr (6 min) average value was determined. An example of determining the maximum average 0.1 hr (6 min) wind speed from the processed data reported multiple time per hour is shown in Table B.2-4. In Table B.2-4, the wind speed was simply the average of the two wind-speed values or (42.55 mph + 35.65 mph)/2 = 39.10 mph.

Table B.2-4. Example of determining maximum average 0.1 hr (6 min) value from wind speeds reported multiple times per hour.

Sample No.	Date Time	Wind Direction	Wind Speed (mph)
109698	1/5/2020 13:40	310	42.55
109699	1/5/2020 13:46	310	35.65
Average Wind Speed = 39.10 mph			

For periods when the wind speed was reported hourly, the 0.1 hr (6 min) average values had to be interpolated. An example for determining a maximum average 0.1 hr (6 min) wind speed from the processed data reported hourly is shown in Table B.2-5. In Table B.2-5, the wind speed was linearly interpolated to get a value 6 min after time 22:00. To get the time at 22:06, the hourly difference in the reported wind speeds in Table B.2-5 (34.5 mph [at 22:00] – 29.9 mph [at 23:00] = 4.6 mph) was determined and multiplied by 0.1. to get 0.46 mph. The wind-speed value at 22:06 was interpolated as 34.5 mph – 0.46 mph = 34.04 mph. The average of the value at 22:00 and 22:06 was then determined or (34.5 mph + 34.04 mph)/2 = 34.27 mph. This was how the maximum average 0.1 hr (6 min) wind speed shown in Table B.2-3 for the year 1987 was determined.

Table B.2-5. Example of determining maximum average 0.1 hr (6 min) value interpolated from wind speeds reported hourly.

Sample No.	Date Time	Wind Direction	Wind Speed (mph)
7407	1/21/1987 22:00	290	34.5
7408	1/21/1987 23:00	300	29.9
Linear interpolation for wind speed = 34.27 mph			

B.2.3.6 Extreme wind-speed value estimation

This first method investigated followed a procedure used by the MVP (2014) in the OHB Levee Wind-Wave Analysis. This study was performed to determine levee heights required for the flood protection project. The wind speeds shown in Table B.2-3 were used for this analysis. The Type 1 Gumbel

distribution was used for a GEV analysis. This analysis is typically used to evaluate extreme, low-probability meteorological and hydrological events.

The probability of non-exceedance and wind speed are plotted, and a linear regression can be used to estimate values for extreme return periods**.** The results from Extreme Value Estimation using the maximum average 0.1 hr wind-speed value *s* for the MML data are shown in Figure B.2-4. The 100-year recurrence interval wind speed from this analysis was 61.7 mph.

Figure B.2-4. Extreme wind-speed estimation for MML wind data.

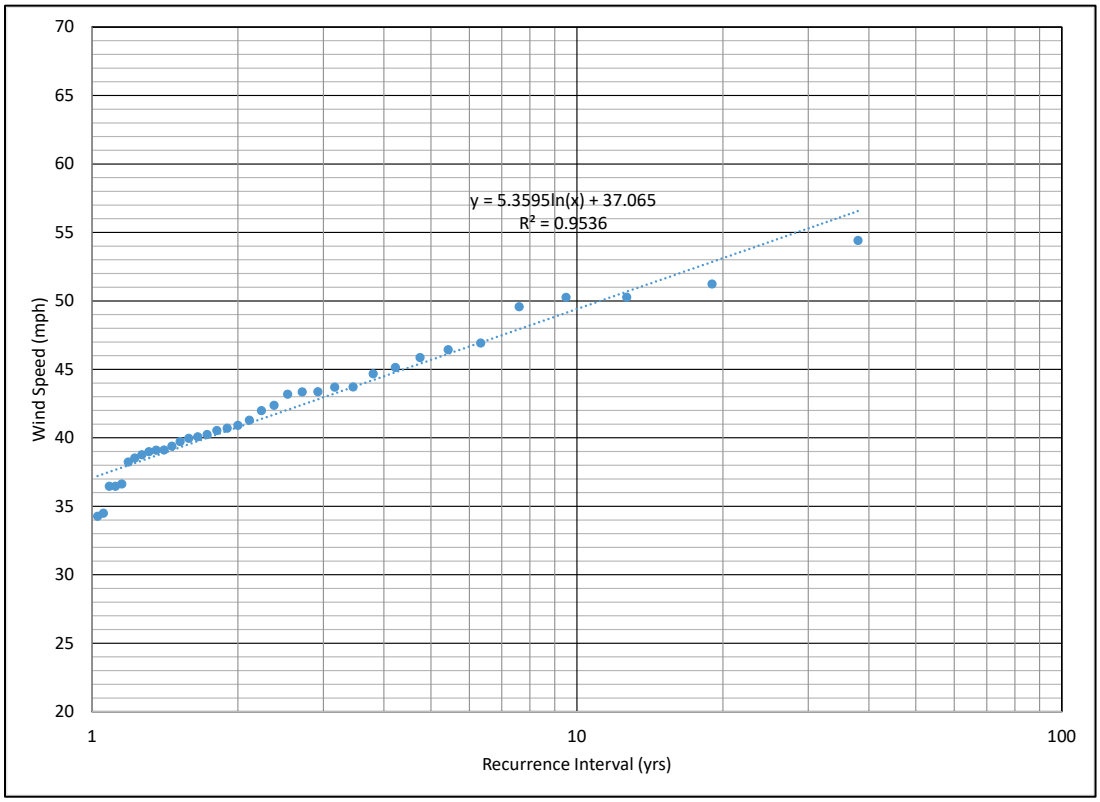

B.2.3.7 Wind frequency based on Gumbel Type 1 Distribution with Gringorten's method

Another wind-speed evaluation method was the use of the Type 1 Gumbel Distribution with Gringorten's (1963) plotting position formula. A description of this procedure is given in Chapter 6 and in Hite et al. for spillway gates. A plot of the return period vs. wind speed determined using this procedure is shown in Figure B.2-5 for the wind data from MML. The wind speed for the 100-year return period was 59.0 mph.

Figure B.2-5. Wind frequency from Gumbel Type 1 Distribution with Gringorten's method for MML wind data.

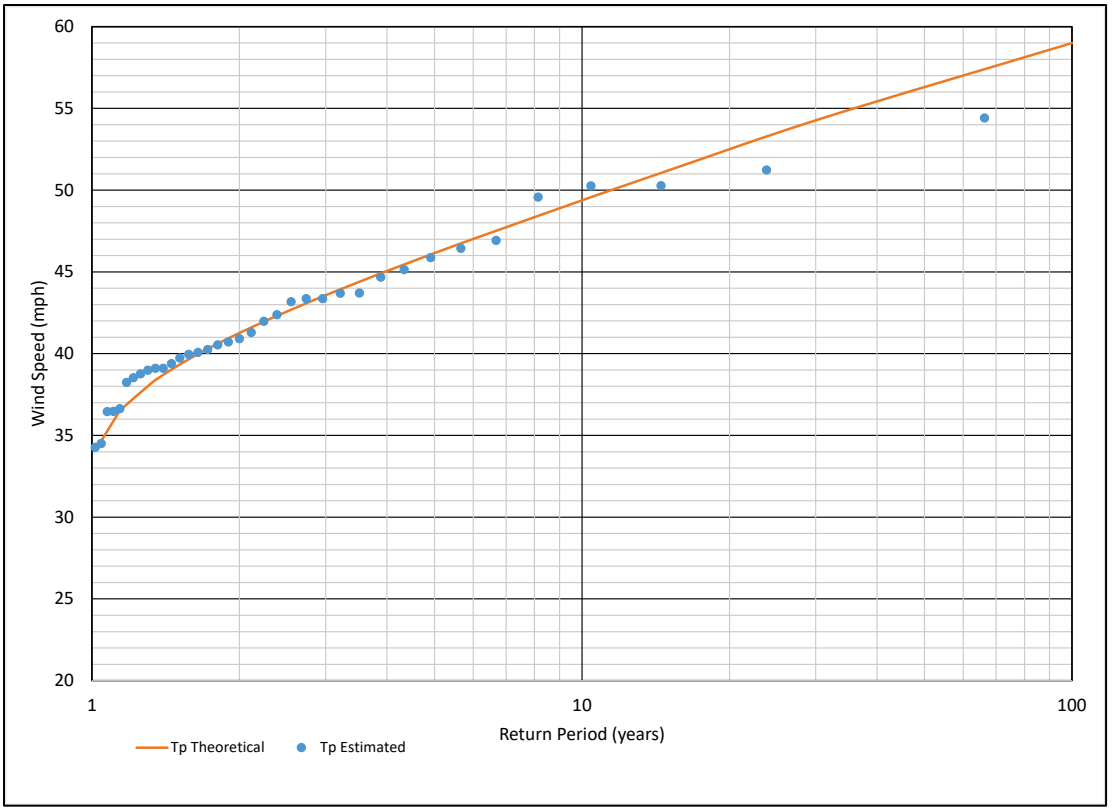

To further investigate the statistics for the wind speed, a formula to determine the standard error (deviation) was used for the data shown in Figure B.2-5. The details for this method are presented in Chapter 6 and in Hite et al. for spillway gates. The results provided the plus and minus 1, 2, and 3 standard deviations for the T_p theoretical curve in Figure B.2-5 and are presented in Figure B.2-6. These values of wind speed were considered a better representation of the wind speeds to use for the wave load versus the extreme value estimation (although they were in close agreement).

Figure B.2-6. Wind frequency curves based on yearly maximum average 0.1 hr wind speed for MML data.

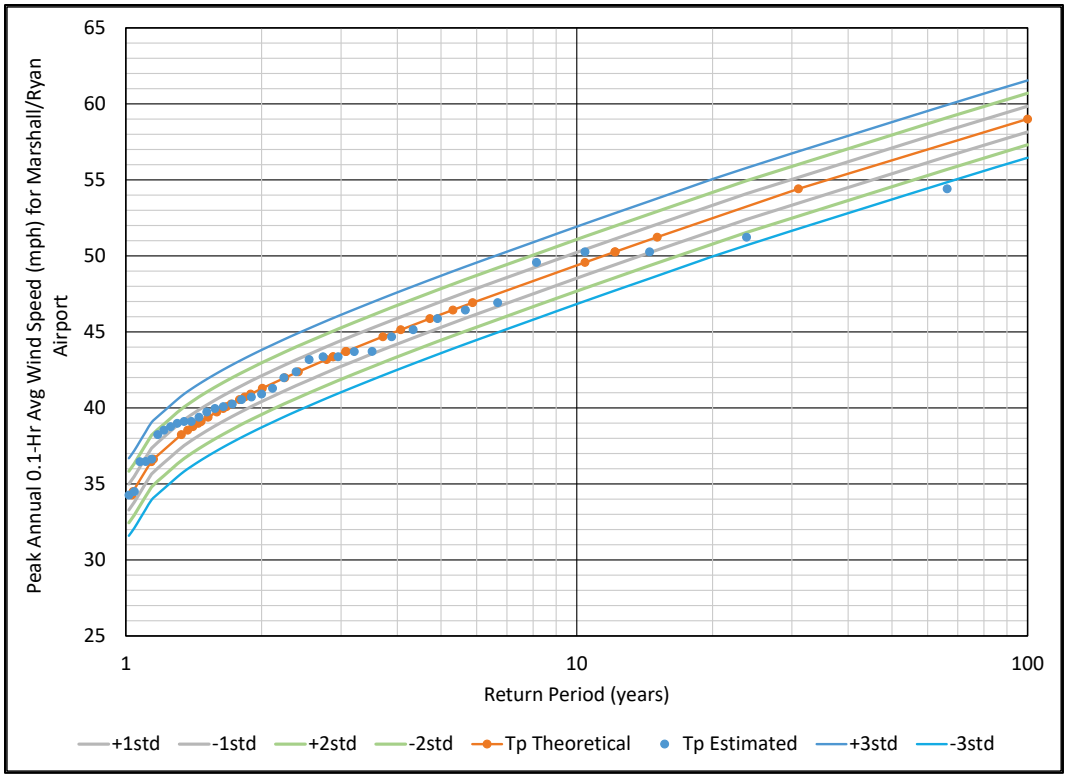

The standard deviation (σ) determined from these data (n=37) was 0.848 mph. The range of the wind speeds for the 100-year return period from -3σ to +3σ was 56.46 mph to 61.54 mph with a mean value of 59.0 mph. These values of wind speed are shown in Table B.2-6 and were used in the following analysis to determine the wave loads.

Table B.2-6. Results from wind-speed analysis for Red Wood River floodwall.

Statistic	100-Year Wind Speed (mph)
+3σ	61.54
+2σ	60.70
+1σ	59.85
Mean	59.00
-1σ	58.15
-2σ	57.30
-3σ	56.46

B.2.4 Wave height and period assessment

Smith (1991) developed guidance to determine significant wave height and peak period based on wind speed and fetch. Dr. Tallent (2019) updated Smiths' NARFET fortran computer program to a more recent computer language (Python). The program input requires the radial lengths of the fetch and the angle increments for resolution of the wind direction as depicted in Figure B.2-7. The radial segments (a total of 25) determined for an angle increment of 6° are shown in Figure B.2-7. Table B.2.7 shows the wind speeds and the wave height and wave period from the use of the NARFET program for the Red Wood River Floodwall at Marshall, MN. The fetch length at the maximum period or effective fetch length was 0.3 km (0.19 miles). The wave heights computed for the mean and plus and minus 1, 2, and 3 standard deviations were all similar, 0.4 m (1.31 ft). This was attributed to the very short fetch.

Figure B.2-7. Fetch and wind direction for the Red Wood River floodwall used in the NARFET model.

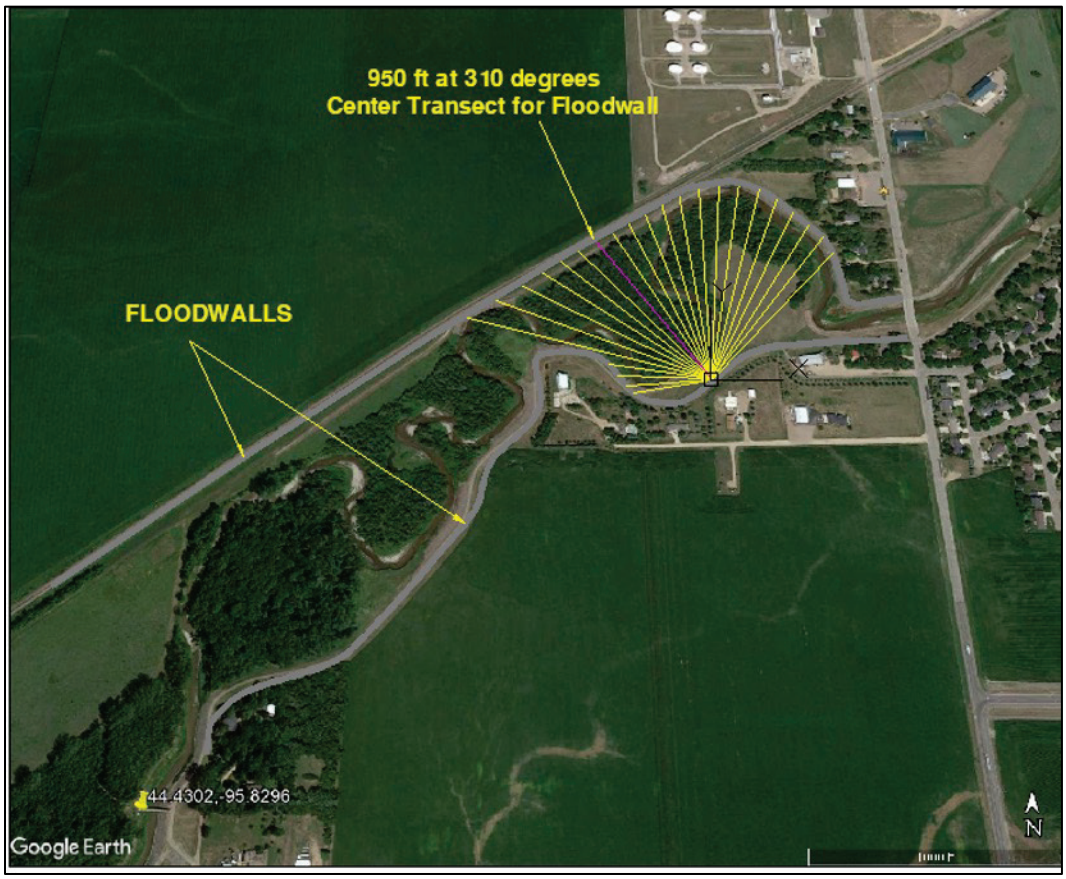

Table B.2-7. Wave height and wave period from Smith's NARFET Model for Red Wood River floodwall.

Statistic	Wind Speed (mph)	Wave Height (m)	Wave Period (sec)
-3σ	56.46	0.40	1.90
-2σ	57.30	0.40	1.90
-1σ	58.15	0.40	1.90
Mean	59.00	0.40	1.90
+1σ	59.85	0.40	1.90
+2σ	60.70	0.40	1.90
+3σ	61.54	0.40	1.90

B.2.5 Wave height and wave period from Goda (2010)

As mentioned previously, Goda (2010) also recommended formulations to determine significant wave height and period based on wind speed and fetch. The significant wave height and period and T_{min} (Equation 6.1) computed from these equations are shown in Table B.2-8. The mean 100-year return period wind speed was 59.0 mph, and the standard deviation was 0.848. Goda (2010) numerically derived and experimentally validated the relation shown in Equation 6.1, which estimates this minimum duration of wind speed (T_{min}) required to generate a sustainable wave height for a fixed fetch length and wind speed.

The fetch length used in Goda's Equation 6.1 for this design example was 289.6 m (950 ft). Goda's wave height and period prediction relationships are given in Equations 6.6 and 6.7. These metric unit-based equations were numerically derived and experimentally verified. Applying Equations 6.6 and 6.7 to the wind speed (U_{10}) values listed in Table B.2-6 and the fetch length of 289.6 m (950 ft) results in wave height and wave period values shown Table B.2-8. Applying equations 6.6 and 6.7 to Table B.2-6 data with U_{10} values in meter/sec, results in the Table B.2-8 values.

$$\frac{gH_{1/3}}{U_{10}^2} = 0.3\left\{1 - \left[1 + 0.004\left(\frac{gF}{U_{10}^2}\right)^{1/2}\right]^{-2}\right\} \qquad \text{(6.6 bis)}$$

$$\frac{gT_{1/3}}{U_{10}} = 8.61\left\{1 - \left[1 + 0.008\left(\frac{gF}{U_{10}^2}\right)^{1/3}\right]^{-5}\right\} \qquad \text{(6.7 bis)}$$

where

g = acceleration due to gravity (9.81 m/sec^2)
$H_{1/3}$ = significant wave height (design wave height, meters)
$T_{1/3}$ = significant wave period (design wave period, seconds)
U_{10} = wind speed at the elevation of 10 m above the sea surface (meters/second)
F = fetch length incident to the structure (meters).

Note that in Equation 6.1, F_L, is given in kilometers, so this needs to be converted to meters for use in Equations 6.6 and 6.7. The T_{min} values shown in Table B.2-8 were similar to the T_{min} value of 0.1 hr estimated in section B.2.3.4, so no further iterations were considered necessary.

Table B.2-8. Significant wave height and significant wave period from Goda's formulations for Red Wood River floodwall.

Statistic	100-Year Wind Speed (mph)	T_{min} (hr)	$H_{1/3}$ Wave Height (m)	$T_{1/3}$ Wave Period (sec)	$L_{1/3}$ Wave Length (m)
-3σ	56.46	0.093	0.317	1.389	3.012
-2σ	57.30	0.092	0.320	1.394	3.035
-1σ	58.15	0.092	0.324	1.400	3.059
Mean	59.00	0.091	0.327	1.1.405	3.083
+1σ	59.85	0.091	0.331	1.410	3.106
+2σ	60.70	0.091	0.334	1.416	3.129
+3σ	61.54	0.090	0.337	1.421	3.152

A plot of wind speed (U) vs. wave height determined from Goda's recommended formulations from the statistical analysis of the wind-speed data is shown in Figure B.2-8.

Figure B.2-8. Wave height vs. wind speed from Goda's procedure for Red Wood River floodwall.

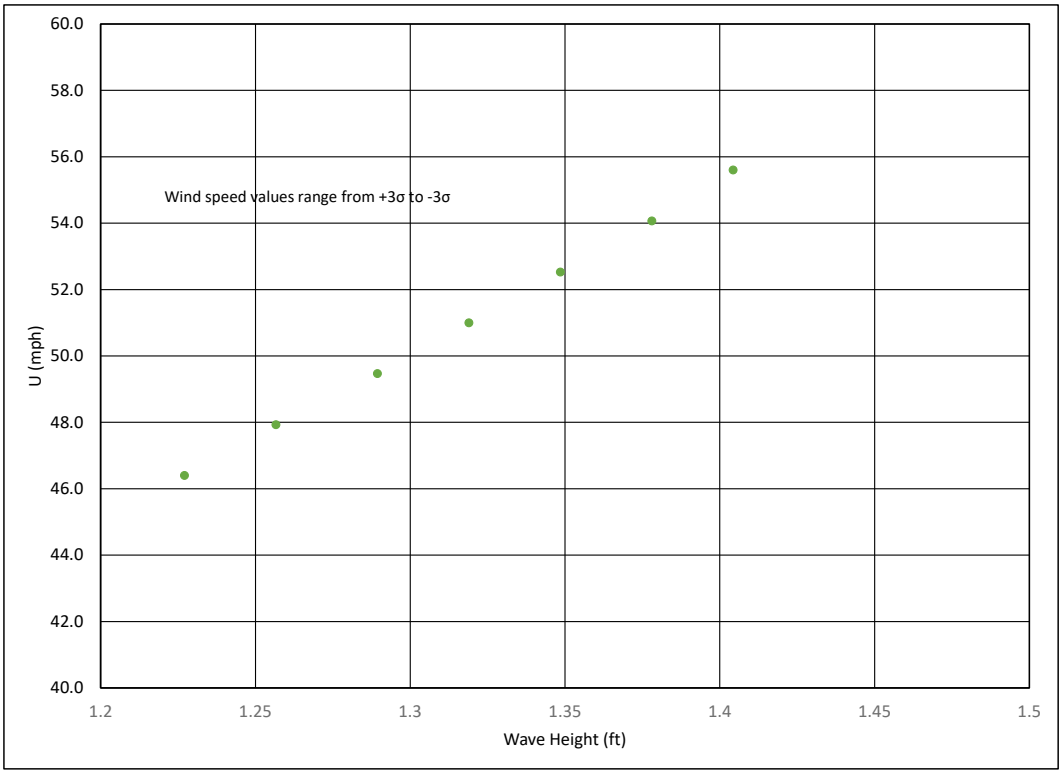

B.2.6 Example for determining pseudo-static wave load from Goda (2010)

The wave pressure distribution and subsequent wave force for the floodwall can now be determined from the significant wave height and wave period. The complete description of this procedure is shown in Chapter 6 and in Hite et al. for spillway gates.

B.2.6.1 Example floodwall design details and parameters for Goda (2010) formulations

The example computations given in this appendix are for the 100-year return period mean wind speed of 59.0 mph, a wave height of 1.073 ft (0.327 m) and a wave period ($T_{1/3}$) of 1.405 sec. In this example problem, the distance from the top of the base slab to the top of the wall is 13.9 ft (h_{stem} in Figure B.2-1). The elevations in reference to the local datum of the top of wall and top of the base slab and bottom of the base slab are 22.1, 8.2, and 6.2, respectively. The distance from the water surface at the selected flood level to the top of wall is 1 ft (h_c in Figure B.2-1). The distance from the water surface at flood level to the bottom of the stem (top of base slab) was 12.9 ft (d_{SWL} in Figure B.2-1 and also referred to as d). The distance from the water surface at the flood level to the floodplain

approach invert was chosen as 15 ft (h_{SWL} in Figure B.2-1), EL 6.1. This flood plain approach invert is 2.1 ft below the top of the base slab or 0.1 ft below the bottom of the base slab. Since θ was set equal to zero, h_b in Figure B.2-1 was equal to h_{SWL}. The significant wave height is 1.073 ft ($H_{1/3}$ in Figure B.2-1) for a mean wind velocity of 59.0 mph. Table B.2-9 provides a summary of the parameters used in the Goda (2010) procedure of defining a pseudo-static wind induced wave pressure acting on a floodwall. Figure B.2-1 illustrates these parameters.

Table B.2-9. Parameters used in Goda (2010) procedure for example wave force calculation (imperial and metric units included) for a flood level gage reading of 19.1, SWL = 19.1.

Parameter	Value	Unit	Value	Unit	Description
h_{stem}	13.9	ft	4.24	m	T-Wall stem height (above base)
h_{Base}	2.0	ft	0.61	m	T-Wall base thickness
h_C	1.0	ft	0.305	m	T-Wall height above SWL
L_B	8.0	ft	2.4	m	Distance from heel of base slab to sheet pile distance
d (originally d_{SWL})	12.9	ft	3.932	m	Still water depth at base of T-Wall
h (originally h_{SWL})	15	ft	4.57	m	Still water depth at toe of berm
tan θ	0	N/A	0	N/A	Floodplain slope to T-Wall (riverside of T-Wall berm)
β_D	0	deg	0	deg	Design incident wave angle
$H_{1/3}$	1.07	ft	0.327	m	Significant wave height, From Table B.2-8 (0.327 m) for a mean wind velocity of 59 mph
$T_{1/3}$	1.405	sec	1.405	sec	Significant wave period, for a mean wind velocity of 59 mph
L_D	10.105	ft	3.08	m	Design wave length, From $T_{1/3}$ and Equation 5.11
ρ	62.4	lb/ft^3	1000	kg/m^3	density of freshwater
g	32.17	ft/sec^2	9.81	m/sec^2	Acceleration of gravity
h'	12.9	ft	3.932	m	For the case of T-Wall: $h' = d_{SWL}$
H_D	1.72	ft	0.523	m	Design wave height (see Equation 5.8)
η*	2.57	ft	0.785	m	Elevation of wave pressure action above flood level

The design wave height (H_D) is the minimum of $\alpha_h H_{1/3}$ and H_b, where α_h ranges from 1.6 to 2.0. For the design of nearshore vertical structures, Goda (2010) suggests using a value of 1.8 for α_h. For this example, the floodwall is 13.9 ft high (top EL 22.1), and the water surface at the flood level is 1 ft below the top of the wall (el 21.1). An approach depth (h and h_{SWL} in Figure B.2-1 and Table B.2-9) of 15 ft was assumed with a mild approach slope (tan θ). The computations to determine the pseudo-static wind induced wave pressure distribution values by the Goda procedure are shown below. Their resultant forces are summarized in Table B.2-10.

B.2.6.2 Pseudo-static wave pressure terms

Goda (2010) uses three pseudo-static wave pressure terms (P_1, P_2, and P_3) to define the wave pressure distribution on the vertical face of the wall and one pseudo-static pressure term (P_u) to describe the uplift pressure at the toe of the wall (Figure B.2-9). The P_1 pressure term represents the maximum wave pressure exerted at the SWL while P_2 and P_3 represent the linear decay in wave pressure with depth.

Figure B.2-9. Illustration of terms in Goda's original pressure formulation adopted for Red Wood River floodwall.

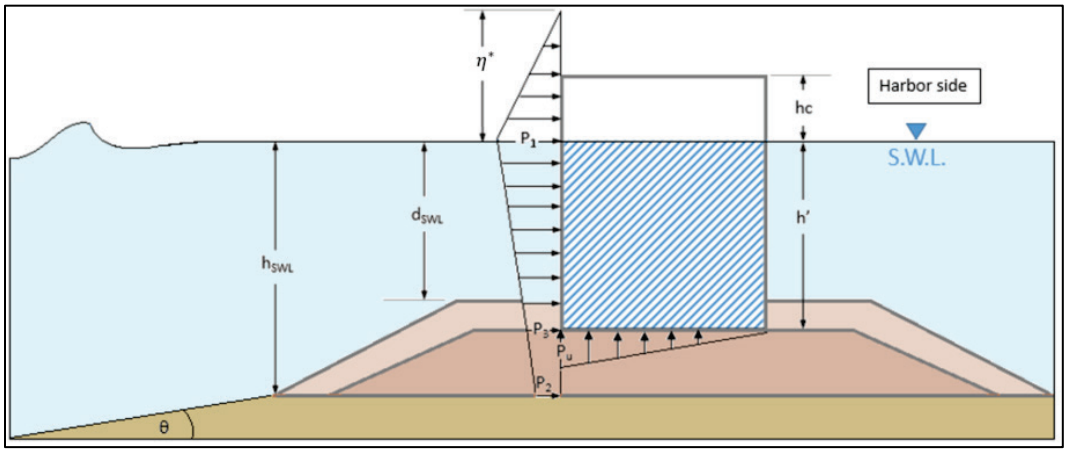

$$P_1 = 0.5\,(1 + \cos\beta_D)\,(\alpha_1 + \alpha_2 * cos^2\beta_D)\,\rho * g * H_D \qquad (5.1\text{ bis})$$

$$P_2 = \frac{P_1}{\cosh(2\pi h/L_D)} \qquad (5.2\text{ bis})$$

$$P_3 = \alpha_3 P_1 \qquad (5.3\text{ bis})$$

$$P_u = 0.5\,(1 + cos\,\beta_D)\,\alpha_1 * \alpha_3 * \rho * g * H_D \qquad (5.4\text{ bis})$$

where α_1 and α_2 are wave pressure coefficients derived from laboratory data. The α_1 coefficient represents the average tendency of wave pressure to increase with wave length (L_D), and the α_2 coefficient represents the tendency of the wave pressure to increase with the berm height. This α_2 term reflects the wave shoaling effect due to berm height and the impulsive pressure component. The α_3 coefficient describes the assumed linear pressure variation between P_1 and P_2.

$$\alpha_1 = 0.6 + \frac{1}{2}\left[\frac{\frac{4\pi h}{L_D}}{\sinh\left(\frac{4\pi h}{L_D}\right)}\right]^2 \quad \text{(5.5 bis)}$$

$$\alpha_2 = \min\left[\frac{h_b - d}{3h_b}\left(\frac{H_D}{d}\right)^2, \frac{2d}{H_D}\right] \quad \text{(5.6 bis)}$$

$$\alpha_3 = 1 - \frac{h'}{h}\left[1 - \frac{1}{\cosh\left(\frac{2\pi h}{L_D}\right)}\right] \quad \text{(5.7 bis)}$$

The Goda (2010) procedure of analysis represents the complex spectrum of sea waves by a single design wave height and length represented by H_D and L_D, respectively. The design wave height (H_D) of Goda's formula is described as the highest wave expected under given wave conditions; this wave height is also identified as H_{MAX}. H_{MAX} is determined as the lesser of 1.8 times the significant wave height ($H_{1/3}$) and the breaking wave height (H_b) (Equations 5.8 – 5.10). Where H_b is evaluated at a distance of $5H_{1/3}$ seaward of the breakwater berm as shown in Figure B.2-10. The design wave length (L_D) of Goda's formula is described as the longest wave expected under given wave conditions; this wave length is also identified as L_{MAX}. In Equation 5.11, L_{MAX} is approximated using first-order wave theory and the significant wave period ($T_{1/3}$).

Figure B.2-10. Breaking wave height location in Goda's (2010) equation adopted for Red Wood River floodwall.

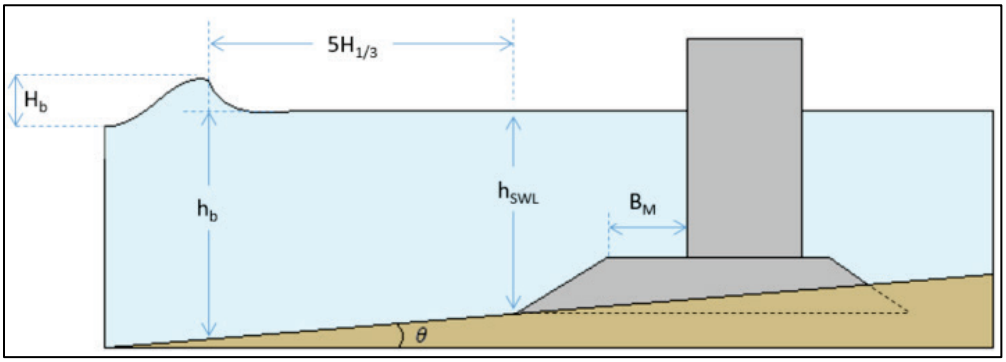

$$H_D = H_{Max} = min\{\alpha_h * H_{1/3},\ H_b\} \quad \text{(5.8 bis)}$$

where α_h is typically in the range of 1.6 to 2.0. The α_h term defines the nondeterministic characteristic of the highest wave due to the random nature of sea waves. According to Goda (2010), the value of α_h is selected based on the reliability of design storm wave estimation, the importance of the structure and the type and nature of the possible structural failure. Goda states that a value of 2.0 or greater is often used for offshore structures, such as an offshore oil rig. For the design of nearshore vertical structures, Goda suggests a value of 1.8 for α_h.

$$H_b = 0.17 * L_D \left\{1 - exp\left[-1.5\frac{\pi h_b}{L_D}\left(1 + \sigma_S * tan^{4/3}\theta\right)\right]\right\} \quad \text{(5.9 bis)}$$

Originally, Goda specified the σ_S value as a constant equal to 15 but later recommended a value of 11 based on the work of Rattanapitikon and Shibayama (2000). This reduction in the σ_S value accounts for an overprediction in the wave shoaling effect for steep bottom slopes (>1/10). Therefore, the authors of this report recommend using $\sigma_S = 11$ for bottom slopes greater than 1/50 and $\sigma_S = 15$ for bottom slopes less than 1/50.

$$h_b = h + 5 * H_{1/3} \tan\theta \quad \text{(5.10 bis)}$$

$$L_D = L_{MAX} = \frac{g * T_{1/3}^2}{2\pi} \quad \text{(5.11 bis)}$$

According to Goda (2010), the significant wave height ($H_{1/3}$) represents the largest one-third wave height measured in deep water. Similarly, the significant wave period ($T_{1/3}$) represents the longest one-third wave period measured in deep water. Site-specific estimates of $H_{1/3}$ and $T_{1/3}$, based on historical records, simulations, etc., can either be obtained or calculated from historical records of deep-water surface elevation changes with time.

Based on the parameters given in Table B.2-9 and the Goda-Takahashi equation set, the example solution is presented below. The design wave height (H_D) is the minimum of $\alpha_h H_{1/3}$ and H_b, where α_h ranges from 1.6 to 2.0. For the design of nearshore vertical structures, Goda suggests using a value of 1.8 for α_h.

$$H_D = H_{Max} = min\{\alpha_h * H_{1/3},\ H_b\} \quad \text{(5.8 bis)}$$

$$H_b = 0.17 * L_D \left\{1 - exp\left[-1.5\frac{\pi h_b}{L_D}\left(1 + 15 * tan^{4/3}\theta\right)\right]\right\} \quad (5.9 \text{ bis})$$

where

$$h_b = h + 5 * H_{1/3} * \tan\theta \quad (5.10 \text{ bis})$$

Therefore,

$\alpha_h H_{1/3}$ = 1.8*0.327 m = 0.589 m (1.931 ft)

and using Equations 5.10 and 5.9, the H_b parameter is derived as follows:

h_b = 4.57 m + 5*0.327*(0) = 4.57 m (15.0 ft),

$H_b = 0.17 * 3.082\text{ m}\left\{1 - exp\left[-1.5 * \frac{\pi * 4.57\text{m}}{3.082\text{m}}\left(1 + 15 * (0)^{4/3}\right)\right]\right\} =$ 0.523 m (1.72 ft),

and finally,

$H_D = H_{Max}$ = min {0.589 m, 0.523 m} = 0.523 m (1.72 ft).

Next, there is a calculation of the coefficients of wave pressure (α_1, α_2 and α_3) given in Equations 5.5 – 5.7. Recall that the h and d values in Equation 5.5 and 5.6 are respectively equivalent to the h_{SWL} and d_{SWL} of Table B.2-9; therefore,

$$\alpha_1 = 0.6 + \frac{1}{2}\left[\frac{\frac{4*\pi*4.57\text{m}}{3.082\text{m}}}{\sinh\left(\frac{4*\pi*4.57\text{m}}{3.082\text{m}}\right)}\right]^2 = 0.60, \text{ from Equation 5.5,}$$

$$\alpha_2 = min\left[\frac{4.57m - 3.932\text{m}}{3*4.57\text{m}} * \left(\frac{0.523\text{m}}{3.932\text{m}}\right)^2, \frac{2*3.932\text{m}}{0.523\text{m}}\right] = min[0.0008, 15.023] = 0.0008,$$

from Equation 5.6.

and finally, since $h' = d_{SWL}$,

$$\alpha_3 = 1 - \frac{3.932\text{m}}{4.57\text{m}} * \left[1 - \frac{1}{\cosh\left(\frac{2*\pi*4.57\text{m}}{3.082m}\right)}\right] = 0.140, \text{ from Equation 5.7.}$$

The three pseudo-static wind induced lateral wave pressure components P_1, P_2, and P_3 (Equations 5.1 to 5.3) and the pseudo-static wind induced wave uplift pressure component (P_u) (Equation 5.4) are evaluated below. The solution to P_1, P_2 and P_3 are

$$P_1 = 0.5 * (1 + \cos(0\ deg)) \left(0.60 + 0.0008 * cos^2(0)\right) * 1000 \frac{kg}{m^3} * 9.81 \frac{\text{m}}{s^2} * 0.523\ \text{m} = 3085\ N/\text{m}^2\ (64\ \text{lb/ft}^2)$$

$$P_2 = \frac{3085\ N/\text{m}^2}{\cosh(2*\pi*(4.57\text{m}/3.082\text{m}))} = 1\ N/\text{m}^2\ (0.02\ \text{lb/ft}^2)$$

$$P_3 = 0.140 * 3085 N/\text{m}^2 = 432\ \text{N/m}^2\ (9\ \text{lb/ft}^2),$$

and the solution for P_U is

$$P_u = 0.5\ (1 + cos(0\ deg))\ 0.60 * 0.275 * 1000 \frac{kg}{\text{m}^3} * 9.81 \frac{\text{m}}{s^2} * 0.523\ \text{m} = 431\ N/\text{m}^2\ (9\ \text{lb/ft}^2)$$

To calculate the total lateral force on the T-Wall, it is first necessary to determine if the pressure distribution (above SWL) extends above the crest of the T-Wall. The ΔP_1 parameter shown in Figure B.2-11 represents this fraction of pressure that would be negated from the total pressure above the SWL.

Figure B.2-11. Pressure distribution on Red Wood River T-Wall (batter piles not shown).

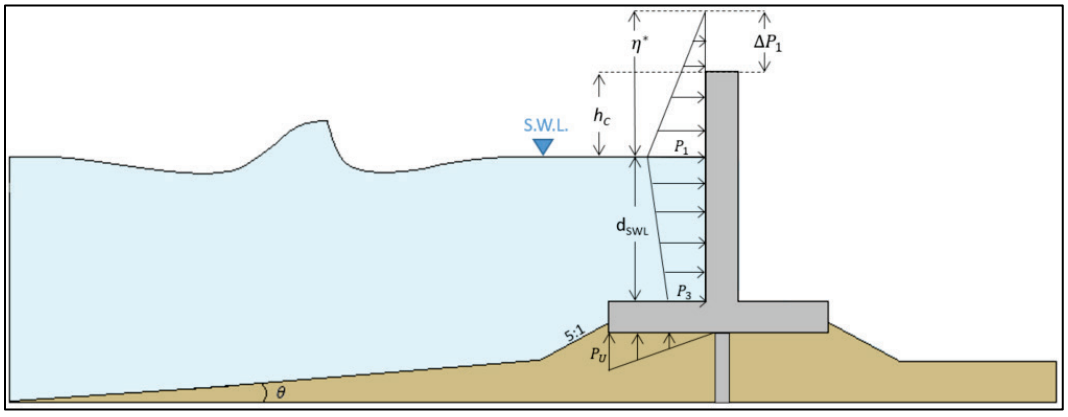

When the vertical distance η* plus the flood level SWL elevation exceeds the top of floodwall elevation, a pseudo-static horizontal water pressure P_4 is introduced at the top of wall. P_4 is a distance of h_c above P_1. The total

lateral force per linear width (F_{Lat}) on the flood side of the T-Wall is given in Equation 5.29:

$$F_{Lat} = 0.5(P_1 + P_3)d + 0.5(P_1 + P_4)h'_C \quad (5.29 \text{ bis})$$

where

$$P_4 = P_1\left(1 - \frac{h_C}{\eta^*}\right), if\ \eta^* > h_C \quad (5.30 \text{ bis})$$

or

$$P_4 = 0, if\ \eta^* \leq h_C \quad (5.31 \text{ bis})$$

$$\eta^* = 0.75(1 + \cos(\beta_D))H_D \quad (5.32 \text{ bis})$$

$$h'_C = min\{\eta^*, h_C\} \quad (5.33 \text{ bis})$$

Therefore, the solution for the Figure 5-20 resultant force F_{Lat} is given as

h_C = 0.305 m or 1 ft (from Table B.2-9)

$\eta^* = 0.75 * (1 + \cos(0 \text{ deg})) * 0.523 \text{ m} = 0.785 \text{ m}$ (2.57 ft)

$since\ \eta^* > h_C$, from Equation 5.26

$P_4 =$ 3085 N/m^2 $* \left(1 - \frac{0.305\text{m}}{0.785\text{m}}\right) = 1887\ N/\text{m}^2$ (39 lb/ft²)

$h'_C = min\{0.785 \text{ m}, 0.305 \text{ m}\} = 0.305$ m (1.0 ft)

$F_{Lat} = 0.5 * \left(3085 \frac{N}{\text{m}^2} + 432 \frac{N}{\text{m}^2}\right) * 3.932 \text{ m} + 0.5 * \left(3085 \frac{N}{\text{m}^2} + 1887 \frac{N}{\text{m}^2}\right) * 0.305 \text{ m} = 7{,}673\ N/\text{m}$ (526 lb/ft).

the total uplift force per linear width on the T-Wall is calculated as

$U_P = 0.5 * P_U * L_B = 0.5 * 431 \frac{N}{\text{m}^2} * 2.44 \text{ m} = 526\ N/\text{m}$ (35.4 lb/ft).

Using the relationships given in Chapter 6 and in Hite et al. for spillway gates, the one-third/one-sixth (1/3:1/6) rule is applied to calculate the

elevation of the resultant forces along the vertical face of the T-Wall (Equation 5.341). Based on the parameters listed in Table B.2-9 and the wind-speed and wave data in Table B.2-8 for the mean value, the pressure and lateral force acting on the floodwall was computed from the Goda (2010) formulations and are shown in Table B.2-10, along with h_{Lat} calculations from Equation 5.34.

$$h_{Lat} = \frac{(h_4 - h_1)\left(\frac{P_4}{3} + \frac{P_1}{6}\right)h_4 + (h_4 - h_1)\left(\frac{P_4}{6} + \frac{P_1}{3}\right)h_1 + (h_1 - h_3)\left(\frac{P_1}{3} + \frac{P_3}{6}\right)h_1}{F_{Lat}} \quad \text{(5.34 bis)}$$

h_{Lat} = 2.618 m = 8.59 ft.

The definition of Goda's parameters shown in Table B.2-10 is illustrated in Figure B.2-11.

Table B.2-10. Wave force and pressure distribution computations using Goda's (2010) procedure for data in Table B.2-9 for a flood level, SWL, of EL 21.2.

Statistic	Wind Speed (mph)	η^*, m	η^*, ft	P_1, N/m²	P_3, N/m²	P_4, N/m²	P_u, N/m²	F_{lat}, kN/m	h_{lat}, m	h_{lat}, ft	P_1, lb/ft²	P_3, lb/ft²	P_4, lb/ft²	P_u, lb/ft²	F_{lat}, lb/ft
+3σ	61.54	0.803	2.63	3156	442	1957	441	7.85	2.619	8.59	66	9	41	9	538
+2σ	60.70	0.797	2.61	3134	439	1936	438	7.80	2.619	8.59	65	9	40	9	535
+1σ	59.85	0.791	2.60	3107	435	1909	434	7.73	2.619	8.59	65	9	40	9	530
Mean	59.00	0.785	2.58	3085	432	1887	431	7.67	2.618	8.59	64	9	39	9	526
-1σ	58.15	0.780	2.56	3064	429	1865	428	7.61	2.618	8.59	64	9	39	9	522
-2σ	57.30	0.773	2.54	3037	425	1839	424	7.55	2.618	8.59	63	9	38	9	517
-3σ	56.46	0.767	2.52	3016	422	1817	421	7.50	2.618	8.59	63	9	38	9	514

B.2.7 Observation of wind and flood event at Red Wood River Marshall, MN, floodwall

As mentioned in section B.2.1, the top of the floodwall was set at the flood event with an ACE of 0.13 % (return period of 750 years). This relates to a gage reading of 22.1 ft. Figure B.2-12 shows the stage vs. ACE for the Red Wood River at Marshall, MN, and was provided by MVP. The blue dashed line represents the 50% confidence level, and the solid blue line is with all uncertainty included. The stage with 50% confidence was used for design and was used to select a top of wall elevation for a given ACE.

Figure B.2-12. Red Wood River stage vs. ACE at Marshall, MN.

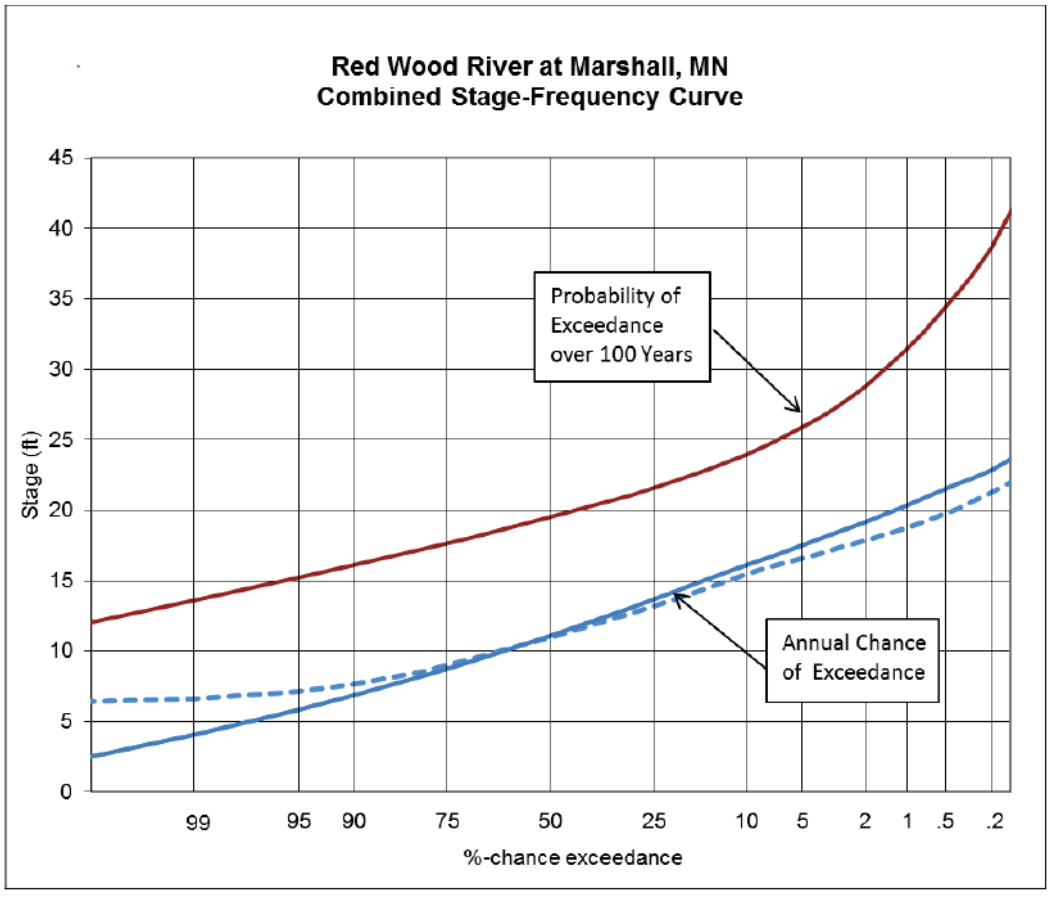

In the wind-induced wave force analysis, the SWL was evaluated for a gage reading of 21.1 ft. A gage reading of 21.1 ft has an ACE of 0.2% (return period of 500 years). The wind speed selected for the wave force analysis was the 100-year return period (ACE of 1). A brief review of the river tendencies in terms of stage heights is shown in Figure B.2-13 for 2012–2020. The plot of river stage indicates the river generally has two peaks,

one in the spring and one in the summer. The highest stage on this plot occurred in the spring of 2019.

Figure B.2-13. River Stages at Red Wood River near Marshall, MN, between 2011 and 2020.

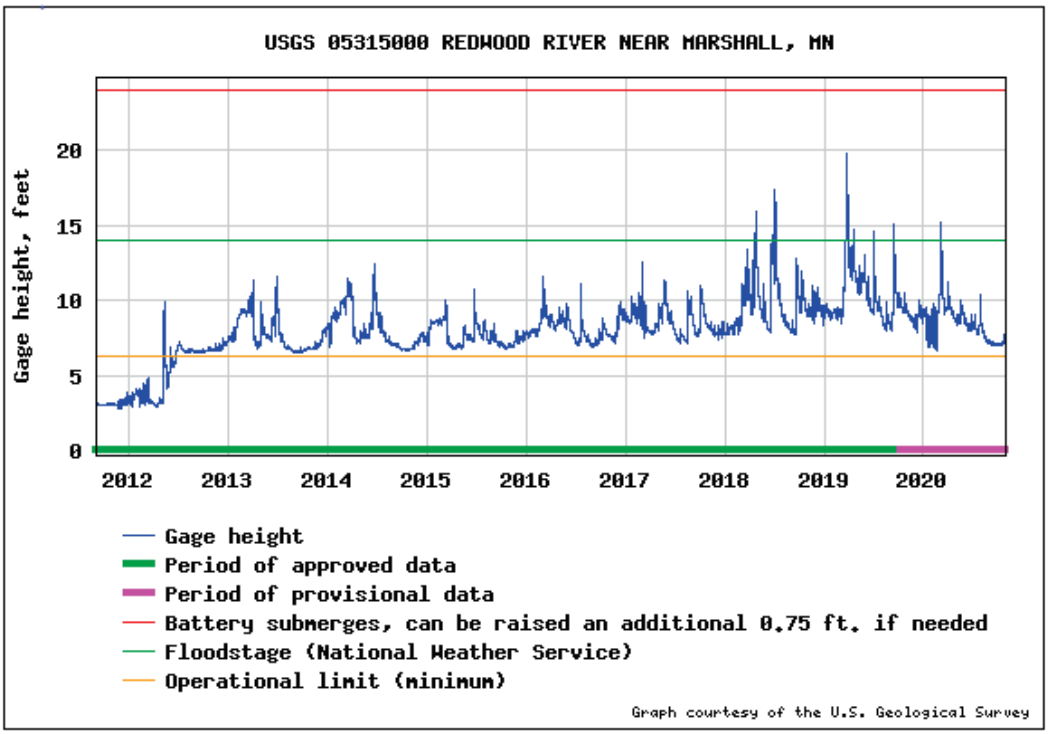

A plot of the number of maximum average 0.1 hr wind speeds that occurred per month from 1984 to 2020 is shown in Figure B.2-14. November had the highest number of occurrences with seven for the period from 1973 to 2020. From the wind-speed data listed in Table B.2-3 and shown in Figure B.2-14, there is no well-defined relationship between the month of the highest speeds per year and the associated peak river stage. Based on this limited review, it appears there is not a strong correlation between the timing of the flood event and the maximum average 0.1 hr wind event.

Figure B.2-14. Number of maximum average 0.1 hr wind speed occurrences per month from 1984 to 2020 for Red Wood River floodwall.

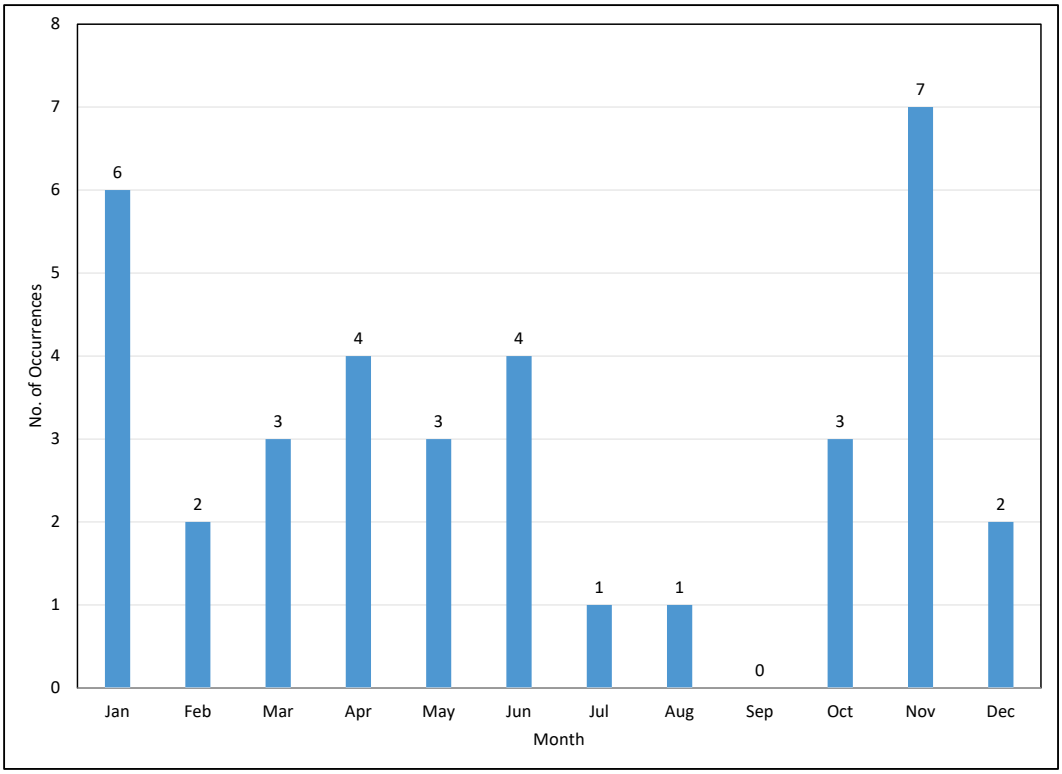

B.2.8 Summary

Development of the wind-induced wave forces for the Red Wood River hypothetical floodwall were presented in this sub appendix. The analysis showed the appropriate wind speeds for the wave force computations ranged from 56.46 to 61.54 mph. These wind speeds produced wave heights from 0.317 m (1.04 ft) to 0.337 m (1.11 ft). These wave heights along with their associated wave period and wave length produced lateral forces (F_{lat}) on the floodwall of 7.5 kN/m (514 lb/ft) to 7.85 kN/m (538 lb/ft).

B.3 Example calculation of wind-induced inland wave forces, Mississippi River inland floodwall at St. Paul, MN

This sub-appendix presents a procedure to calculate wind-induced wave forces acting on a hypothetical inland floodwall on the Mississippi River in St. Paul, MN. The current version of the Goda-Takahashi wave pressure relationship is given in Goda (2010). Application of the Goda-Takahashi (Goda 2010) wave force prediction method was used for the example floodwall presented in Appendix B subsection B.1 for the Red River of the

North, subsection B.2 for the for the Red Wood River, and was also used in this example analysis. The hydraulic structure used in this example problem is the stem of a cantilever floodwall and shown in Figure B.3-1. Analytical and statistical methods are employed in the estimation of design wave height and period along with requirements of historical wind record preparation. The wave loading calculation based on the Goda-Takahashi formulations are presented for this example inland flood protection structure.

Figure B.3-1. Floodwall used in example wave force calculations for Mississippi River at St. Paul, MN (tension and compression piles not shown).

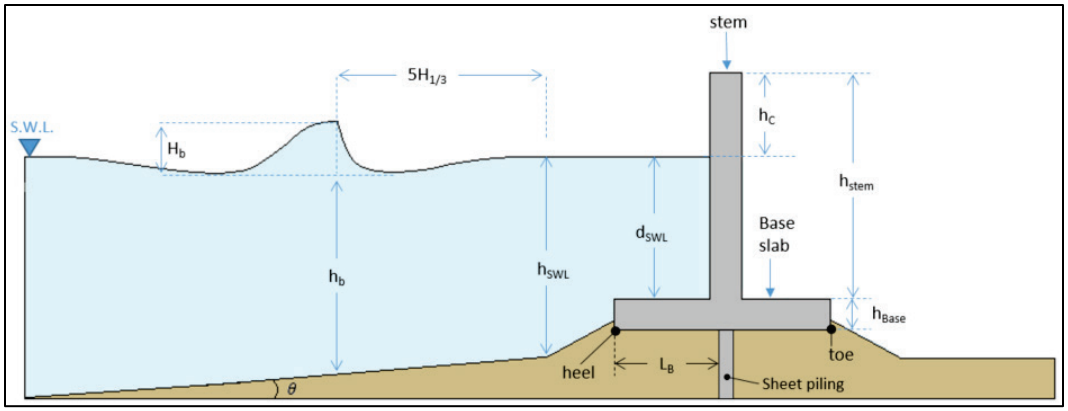

B.3.1 Floodwall details

The top of the floodwall is usually based on a flood with a selected ACE. In the example presented in this section, the top of the floodwall was set at an ACE of 0.13% (return period of 750 years). For load factor development, water to the top of the floodwall will be assumed to be the water level with the highest head differential. The distance from the top of the base slab to the top of the stem (floodwall) is 12 ft. In reference to the NGVD, the top of wall was EL 714.5. This is the river stage for the annual chance exceedance of 0.13% (return period of 750 years).

B.3.2 Wind-speed and direction analysis

The selection of the appropriate wave height to use for the wave force development depends on the local wind and water characteristics. These include the magnitude of the wind speed, the duration and direction of the wind-speed event, and the open water-surface distance (fetch) over which the wind blows before reaching the floodwall. Historical wind data from a nearby municipal airport can be very helpful for determining the wind speed and direction. It is recommended that historical wind records from

multiple wind recording sites, near the project site, be used whenever possible. Multiple historical wind records can help extend historical analysis, fill in time gaps, and validate data. The following sections describe in detail the wind data processing needed to develop the wave height and period for the Mississippi River Flood Wall in St. Paul, MN.

B.3.3 Steps for obtaining and processing wind data

B.3.3.1 Locating airport

The first step in the acquisition of wind data is to locate a suitable airport with a historical record of wind speed and direction. Google Earth Pro is very helpful tool to locate the project and determine the closest municipal airport. For this example, St. Paul, MN, was found on Google, and fortunately two municipal airports were very close to the project. For the Mississippi River hypothetical floodwall project, the St. Paul Downtown Airport (STP) was approximately 1 mile from the project, and the Minneapolis-Saint Paul International Airport (MSP) was approximately 9 miles from the project. The STP site was more desirable since it was closer to the hypothetical floodwall, but there were little to no wind data available for this airport. The MSP was chosen for the wind-induced wave analysis. There were no topographic features between this airport and the floodwall site that significantly affected the wind speed and direction. Figure B.3-2 shows the data collection site, MSP, in relation to the project. The latitude is 44.812, and the longitude is -93.222 for the airport.

Figure B.3-2. Wind speed and direction collection site at MSP in relation to floodwall project.

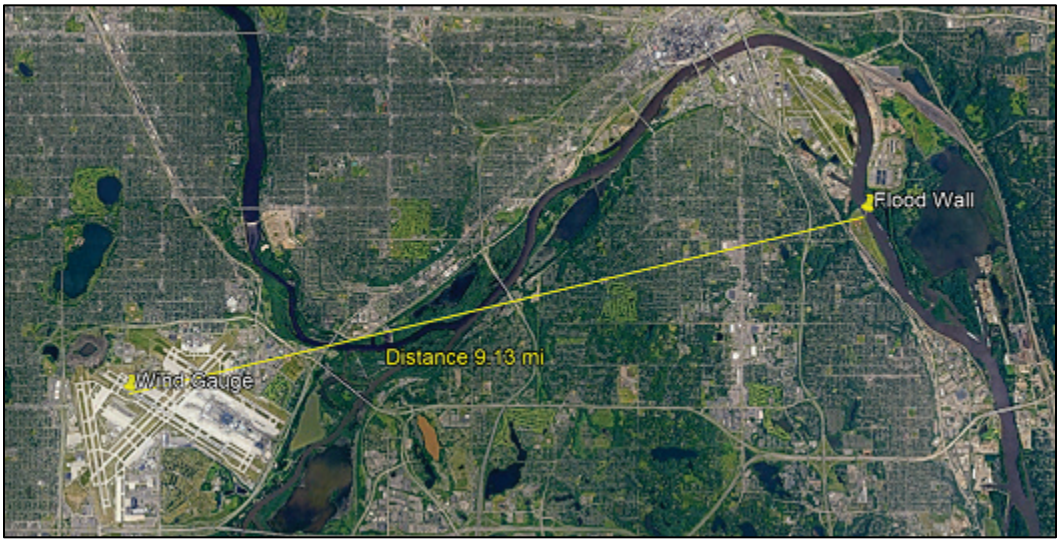

B.3.3.2 Downloading wind data

Next, a data base needs to be found that contains the historical wind records for this airport. (This web site is supported by Iowa State University: https://mesonet.agron.iastate.edu/request/download.phtml?network=MS_ASOS. It was searched to determine if wind-speed and direction data were available for MSP. The IEM maintains an archive of automated airport weather observations from around the world.)

The following steps were performed to determine if data were available.

1. Minnesota was chosen from the "Select Network" menu and [MSP] Minneapolis-Saint Paul was chosen from the "Selected Stations" menu.
2. The wind speed in miles per hour and wind direction were then highlighted from the "Select From Available Data:" choices.
3. The historical period of interest was specified in the "Specific Date Range" using the "Start Date" and "End Date" options.
4. The time zone was selected from the "Timezone of Observation Times.
5. Then, the "Download Options:" are selected. The data can be displayed in the web browser or downloaded to a file. Generally, one will download the data to a file for subsequent processing.
6. The default choice for the "Limit Report Types" was chosen.
7. The "Get Data" was then activated. If available, the data are downloaded to a file(s).

B.3.3.3 Processing wind data

The wind-speed and direction data for MSP were downloaded in 53 separate files to avoid a very large file that would be cumbersome to process. The data were fairly complete from 1969 to May 2021 with wind speeds and directions reported multiple times per hour between June 1992 and May 2021 and hourly from 1969 through June 1992. A sample of the data downloaded from the web site is shown in Table B.3-1. The headings were changed for clarity.

Table B.3-1. Sample of wind-speed and direction data downloaded from Iowa State website for MSP.

Sample No.	Date Time	Wind Direction	Wind Speed (mph)
3541	4/28/2021 1:00	360	9.2
3542	4/28/2021 1:53	20	12.65
3543	4/28/2021 2:00	20	16.1
3544	4/28/2021 2:27	30	13.8
3545	4/28/2021 2:39	10	12.65
3546	4/28/2021 2:53	10	9.2
3547	4/28/2021 3:15	30	11.5
3548	4/28/2021 3:53	10	9.2
3549	4/28/2021 4:07	350	10.35
3550	4/28/2021 4:53	360	6.9
3551	4/28/2021 5:08	20	10.35
3552	4/28/2021 5:53	20	9.2
3553	4/28/2021 6:41	10	10.35

The wind direction normal to the section of the floodwall being analyzed was determined next. This length of open water normal to the floodwall is referred to as the *fetch*. For this example, two locations along the flood wall were analyzed. The first location was normal to the right-descending flood wall and the second location was normal to the left-descending flood wall. Figures B.3-3 and B.3-4 show the fetch and the direction of the wind normal to the sections of floodwall used for this example. In Figure B.3-3, the fetch was 1.57 mi (8,290 ft), and the direction of the wind normal to the floodwall was 80°. This was designated Location 1. In figure B.3-4, the fetch was 1.55 mi (8,180 ft), and the direction of the wind normal to the floodwall was 250°. This was designated Location 2.

Figure B.3-3. Location 1 – fetch and wind direction determined for the Mississippi River floodwall.

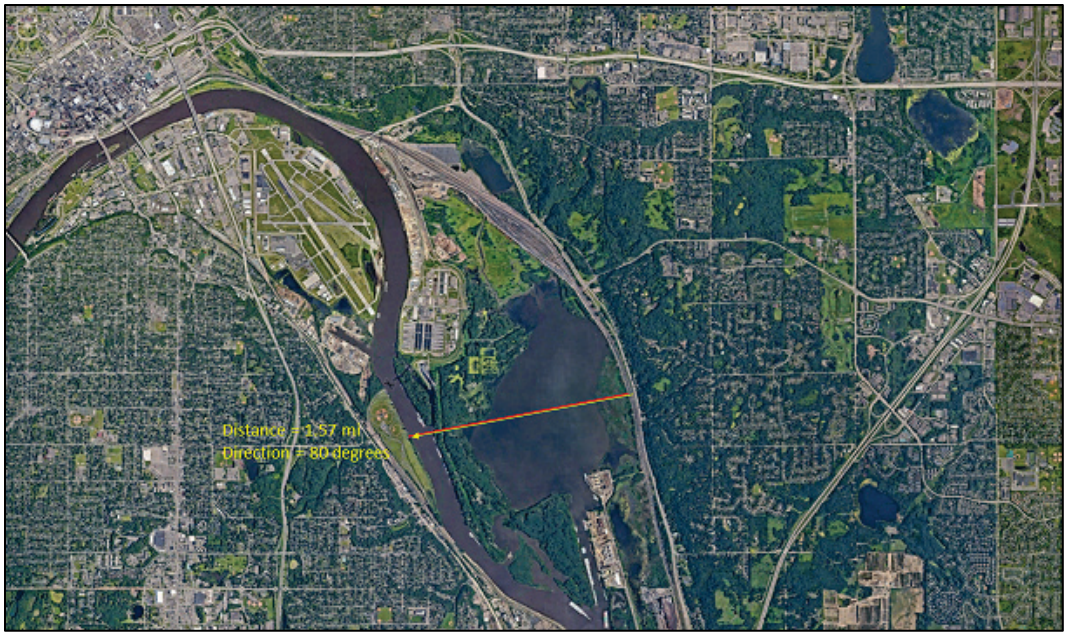

Figure B.3-4. Location 2 – fetch and wind direction determined for the Mississippi River Floodwall.

For the statistical analysis of the wind, all wind directions plus and minus 20° of the normal direction (80° and 250° for this example) were considered for the analysis of the wind speeds. The range of wind directions from which the wind speeds were determined from Location 1 was from 60° to 100°. The range of wind directions from which the wind

speeds were determined from Location 2 was from 230° to 270°. Table B.3-2 shows a sample of the data for Location 1 after the original wind-speed file had been processed to remove the wind directions outside the desired range. In this sample, the wind direction was between 60° and 90° for approximately a 0.5 hr period.

Table B.3-2. Sample of processed wind-speed and direction file for location one.

Sample No.	Date Time	Wind Direction	Wind Speed (mph)
2244	3/15/2021 18:20	90	10.35
2245	3/15/2021 18:34	90	11.5
2246	3/15/2021 18:53	90	11.5
2247	3/15/2021 19:05	80	13.8
2248	3/15/2021 19:12	90	12.65
2249	3/15/2021 19:20	90	11.5
2250	3/15/2021 19:27	90	12.65
2251	3/15/2021 19:37	80	12.65
2252	3/15/2021 19:53	70	11.5
2253	3/15/2021 20:06	60	10.35
2254	3/15/2021 20:43	90	17.25
2255	3/15/2021 20:49	90	13.8
2256	3/15/2021 20:53	90	13.8

B.3.3.4 Selection of appropriate wind speed

From previous wind-speed statistical analyses, Chapter 6 and in Hite et al. for spillway gates, the use of the maximum yearly wind-speed value for development of wave forces was considered unrealistic unless this speed occurred for a 0.5 hr period. The duration of the wind speed is more important to achieve the fully developed wave height and wave period needed to determine the wave forces.

Goda (2010) recommended formulations to determine significant wave height and period based on wind speed and fetch. His designation for wind speed is U_{10} and represents the wind speed 10 m above the sea surface. These formulations are shown in Chapter 6 and in Hite et al. for spillway gates. Goda proposed the minimum duration (T_{min}) needed to achieve the significant wave height and significant wave period. He numerically

derived and experimentally validated the relation shown in Equation 6.1 which estimates this minimum duration of wind speed (T_{min}) required to generate a sustainable wave height for a fixed fetch and wind speed.

$$T_{min} = 1.0 F_L^{\,0.73} U_{10}^{-0.46} \qquad \text{(6.1 bis)}$$

where

F_L = the fetch length in kilometers
U_{10} = wind speed in m/sec at the elevation of 10 m above the sea surface
T_{min} = minimum duration of wind speed (hour) required for sustainable wave height generation.

At this point in the wind data processing, the wind-speed value needed for Equation 6.1 is unknown. Since the fetch was known and the processed wind-speed and direction data contained the range of wind speeds, an initial estimate of the wind speed was made to determine T_{min}. For Location 1, knowing F_L was 8,290 ft (2.53 km), U_{10} was estimated at 40 mph (17.88 m/sec). The T_{min} computed from Equation 6.1 is 0.507 hr. If U_{10} is estimated at 50 mph (22.35 m/sec) and F_L remains at 8,290 ft (2.53 km), then T_{min} from Equation 6.1 is 0.47 hr. Based on these values of T_{min}, the time required for the wave height and period to fully develop was approximately 0.5 hr (30 min).

The same logic was used for Location 2 to obtain the T_{min} value. Knowing F_L was 8,180 ft (2.49 km), U_{10} was estimated at 45 mph (20.12 m/sec). The T_{min} computed from Equation 6.1 is 0.482 hr. If U_{10} is estimated at 55 mph (24.59 m/sec) and F_L remains at 8,180 ft (2.49 km), then T_{min} from Equation 6.1 is 0.451 hr. Based on these values of T_{min}, the time required for the wave height and period to fully develop was approximately 0.47 hr (28 min). This is a slightly shorter time period since the fetch is smaller. The actual values for T_{min} will be determined in the following sections and compared to this estimated value.

B.3.3.5 Yearly maximum average wind speed

The processed wind-speed and direction data were then used to determine the maximum yearly wind speed averaged over a 30 min time period for Location 1 and over a 28 min time period for Location 2. These values designated the yearly maximum average wind speed are shown in Tables B.3-3 and B.3-4 for the years between 1969 and 2021.

Table B.3-3. Location 1 – Yearly maximum average 0.5 hr wind speed, MSP.

Observation Period 1969–2021 (wind direction 60° to 100°)		
Year	Month/Day	Wind Speed (mph)
1969	7/7	18.208
1970	4/12	28.175
1971	4/27	17.825
1972	12/30	25.875
1973	5/27	23.575
1974	6/9	20.125
1975	3/23	28.750
1976	1/1	19.550
1977	3/4	22.425
1978	4/17	24.150
1979	4/11	27.600
1980	6/27	26.450
1981	7/15	20.125
1982	3/19	23.575
1983	5/1	32.775
1984	4/12	27.025
1985	3/4	31.050
1986	4/14	25.300
1987	3/18	30.188
1988	3/12	26.450
1989	4/28	21.275
1990	5/19	26.450
1991	8/7	25.875
1992	6/17	23.575
1993	11/25	24.150
1994	11/27	28.750
1995	4/15	29.325
1996	1/28	24.533
1997	6/7	28.558
1998	10/5	24.150

Observation Period 1969–2021 (wind direction 60° to 100°)		
Year	Month/Day	Wind Speed (mph)
1999	4/10	27.408
2000	4/19	21.275
2001	11/27	24.725
2002	4/28	25.517
2003	4/3	24.725
2004	9/15	21.083
2005	1/1	24.533
2006	4/16	25.300
2007	2/24	23.767
2008	4/10	29.736
2009	3/31	24.150
2010	5/22	27.042
2011	4/15	28.091
2012	5/5	28.367
2013	5/19	20.037
2014	4/28	29.838
2015	6/22	27.025
2016	4/27	28.750
2017	4/19	22.425
2018	4/14	28.392
2019	4/11	33.350
2020	3/28	24.315
2021	3/14	19.550

Table B.3-4. Location 2 – Yearly maximum average 0.47 hr wind speed, MSP.

Observation Period 1969–2021 (wind direction 230° to 270°)		
Year	Month/Day	Wind Speed (mph)
1969	6/27	24.943
1970	4/16	27.065
1971	10/31	32.359
1972	2/23	26.529
1973	10/12	24.631
1974	7/3	19.650
1975	11/10	35.611
1976	8/11	19.650
1977	11/20	33.965
1978	2/15	33.945
1979	5/17	31.288
1980	8/19	28.595
1981	4/1	26.688
1982	3/13	31.130
1983	8/29	28.641
1984	4/28	32.280
1985	4/21	23.949
1986	11/8	34.500
1987	2/2	27.994
1988	8/2	27.923
1989	1/8	26.972
1990	6/3	29.603
1991	9/18	30.137
1992	6/17	29.325
1993	10/1	24.729
1994	11/18	37.573
1995	8/4	36.225
1996	4/25	29.444
1997	4/6	23.773
1998	5/31	29.028

Observation Period 1969–2021 (wind direction 230° to 270°)		
Year	Month/Day	Wind Speed (mph)
1999	7/3	32.746
2000	11/2	29.523
2001	4/7	29.444
2002	5/9	29.365
2003	6/24	33.786
2004	9/23	24.725
2005	9/13	21.275
2006	10/30	25.379
2007	8/28	45.773
2008	6/6	30.594
2009	6/27	25.174
2010	10/27	34.579
2011	2/18	21.083
2012	6/11	23.230
2013	6/22	31.050
2014	11/4	27.679
2015	7/18	27.124
2016	12/26	27.600
2017	3/7	30.217
2018	5/25	36.114
2019	7/12	24.190
2020	10/14	25.191
2021	3/30	23.773

For periods when observations of the wind speed were available multiple times per hour, a 0.5 hr (30 min) average and a 0.47 hr (28 min) average value was determined. An example of determining the maximum average 0.5 hr (30 min) wind speed from the processed data reported multiple time per hour is shown in Table B.3-5. In Table B.3-5, the wind speed was the average of the two wind-speed values or (27.6 mph + 21.85 mph)/2 = 24.725 mph.

Table B.3-5. Example of determining maximum average 0.5 hr (30 min) value from wind speeds reported multiple times per hour.

Sample No.	Date Time	Wind Direction	Wind Speed (mph)
9591	11/27/2001 00:10	60	27.6
9592	11/27/2001 00:40	60	21.85
Average wind speed = 24.725 mph			

For periods when the wind speed was reported hourly, the 0.5 hr (30 min) average and 0.47 hr (28 min) average values had to be interpolated. An example for determining a maximum average 0.5 hr (30 min) wind speed from the processed data reported hourly is shown in Table B.3-6. In Table B.3-6, the wind speed was linearly interpolated to get a value 30 min after time 21:00. To get the time at 21:30, the absolute hourly difference in the reported wind speeds in Table B.3-6 (26.45 mph [at 22:00] – 29.9 mph [at 22:00] = 3.45 mph) was determined and multiplied by 0.5 to get 1.725 mph. The wind-speed value at 21:30 was interpolated as 29.9 mph – 1.725 mph = 28.175 mph. This was how the maximum average 0.5hr (30min) wind speed shown in Table B.3-6 for the year 1970 was determined.

Table B.3-6. Example of determining maximum average 0.5hr (30min) value interpolated from wind speeds reported hourly.

Sample No.	Date Time	Wind Direction	Wind Speed (mph)
2442	4/12/1970 21:00	90	26.45
2443	4/12/1970 22:00	90	29.9
Linear interpolation for wind speed = 28.175 mph			

B.3.3.6 Extreme wind speed value estimation

This first method investigated followed a procedure used by the MVP (2014) in the OHB Levee Wind-Wave Analysis. This study was performed to determine levee heights required for the flood protection project. The wind speeds shown in Tables B.3-3 and B.3-4 were used for this analysis. The Type 1 Gumbel Distribution was used for a GEV analysis. This analysis is typically used to evaluate extreme, low-probability meteorological and hydrological events.

The probability of non-exceedance and wind speed is plotted, and a linear regression can be used to estimate values for extreme return periods**.** The results from Extreme Value Estimation for Location 1 using

the maximum average 0.5 hr wind-speed values for MSP data are shown in Figure B.3-5. The 100-year recurrence interval wind speed from this analysis was 38.82 mph.

Figure B.3-5. Extreme wind-speed estimation for MSP wind data.

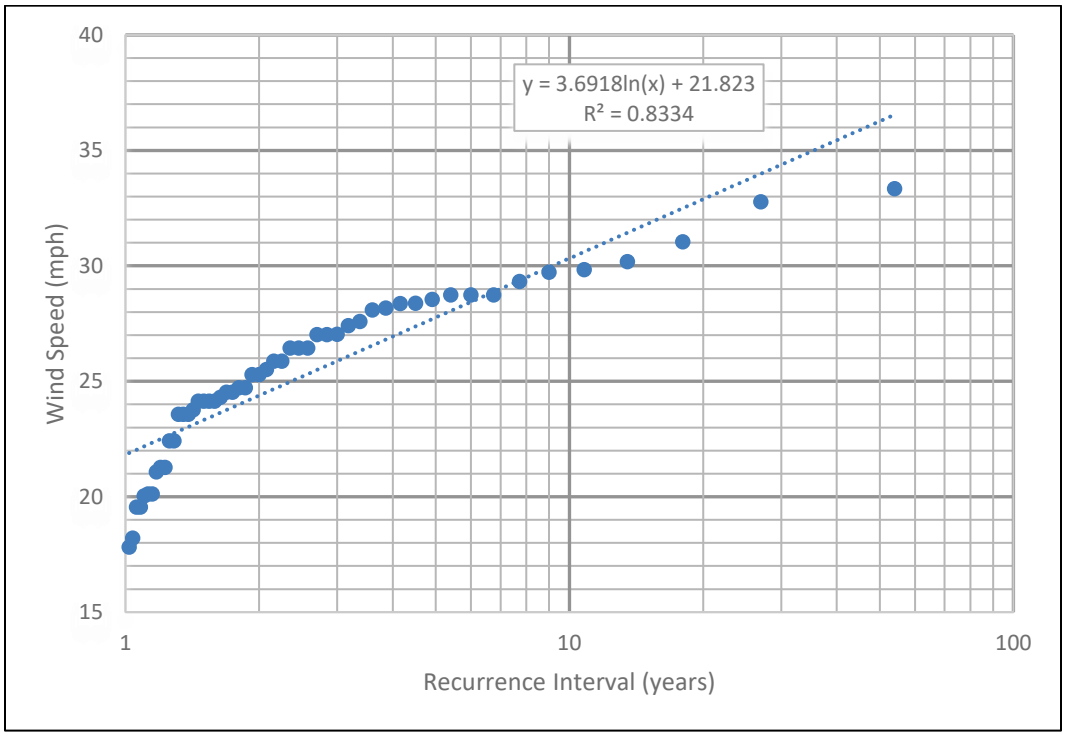

The results from Extreme Value Estimation for Location 2 using the maximum average 0.47 hr wind-speed values for MSP data are shown in Figure B.3-6. The 100-year recurrence interval wind speed from this analysis was 48.07 mph.

Figure B.3-6. Extreme wind-speed estimation for MSP wind data.

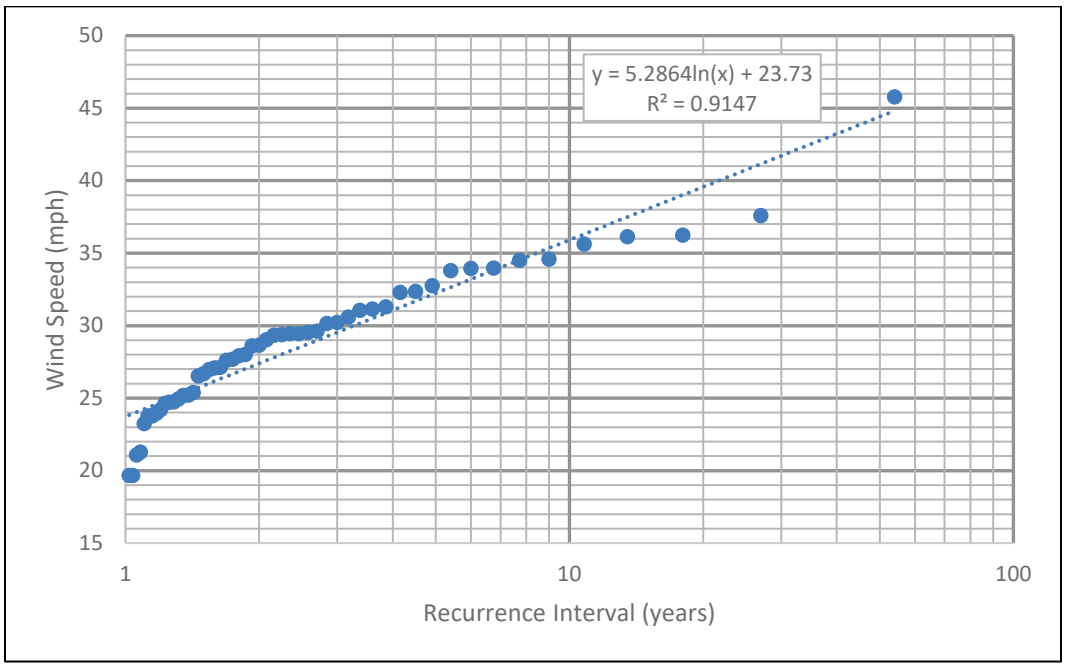

B.3.3.7 Wind frequency based on Gumbel Type 1 Distribution with Gringorten's (1963) method

Another wind-speed evaluation method was the use of the Type 1 Gumbel Distribution with Gringorten's (1963) plotting position formula. A description of this procedure is given in Chapter 6 and in Hite et al. for spillway gates. A plot of the return period vs. wind speed determined using this procedure is shown for Location 1 in Figure B.3-7 and for Location 2 in Figure B.3-8. The wind speed for the 100-year return period was 38.0 mph for Location 1 and 45.5 mph for Location 2.

Figure B.3-7. Location 1 – wind frequency from Gumbel Type 1 Distribution with Gringorten's method for MSP wind data.

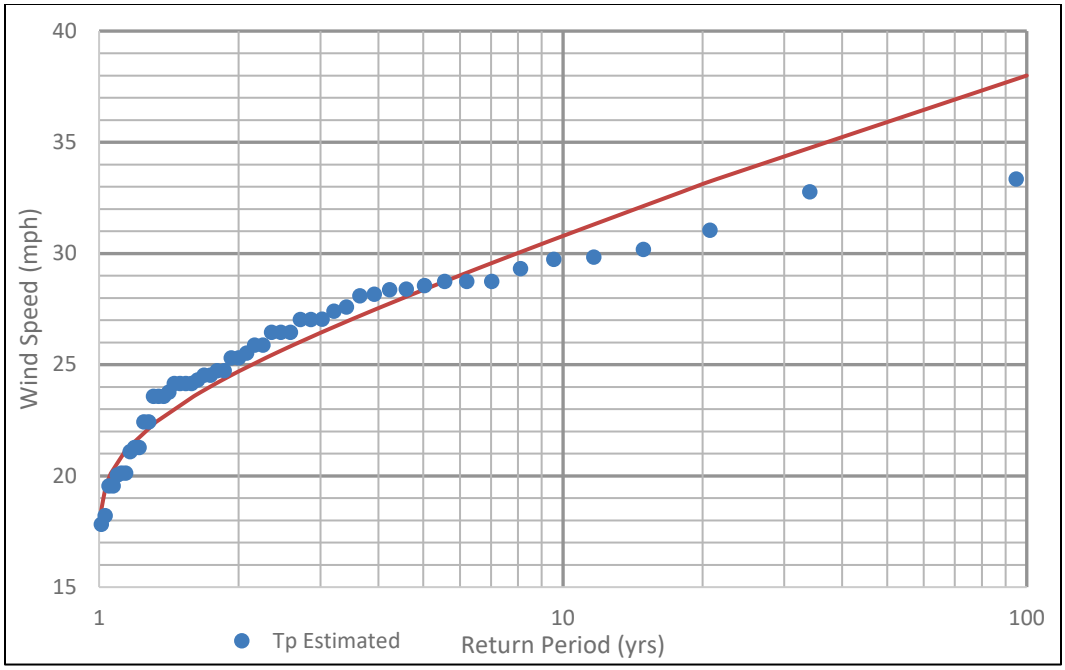

Figure B.3-8. Location 2 – wind frequency from Gumbel Type 1 Distribution with Gringorten's method for MSP wind data.

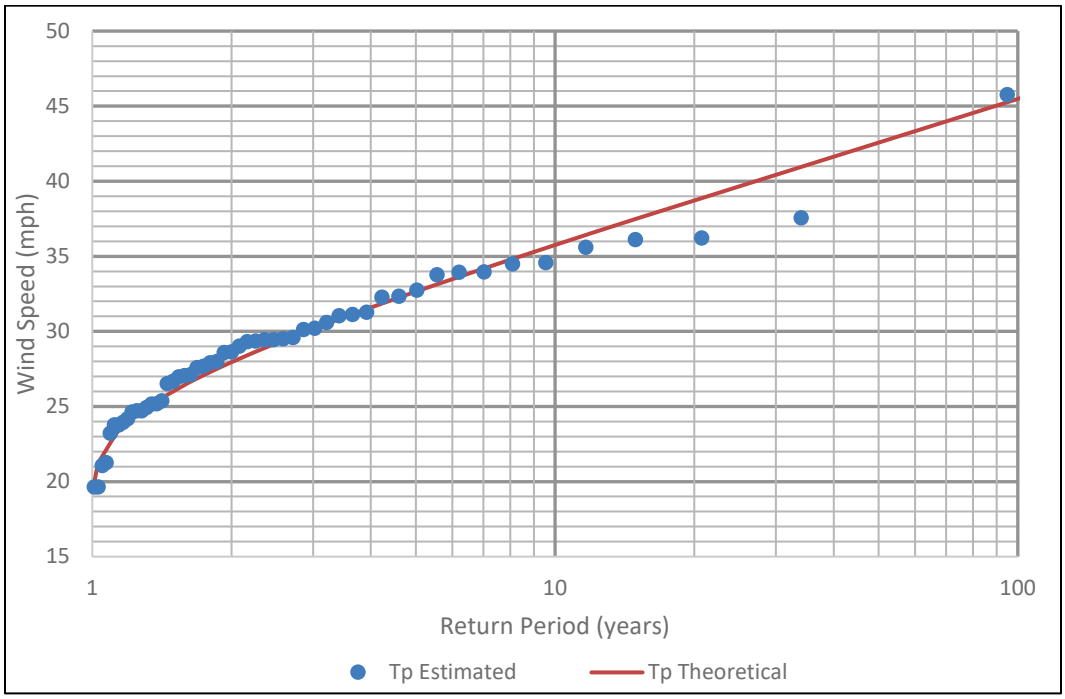

To further investigate the statistics for the wind speed, a formula to determine the standard error (deviation) was used for the data shown in Figure B.3-6. The details for this method are presented in Chapter 6 and in Hite et al. for spillway gates. The results provided the plus and minus 1, 2, and 3 standard deviations for the T_p theoretical curve in Figures B.3-6 and B.3-7 and are presented in Figures B.3-9 and B.3-10, respectively. These values of wind speed were considered a better representation of the wind speeds to use for the wave load versus the extreme value estimation (although they were in close agreement).

Figure B.3-9. Location 1 – wind frequency curves based on yearly maximum average 0.5 hr wind speed for MSP data.

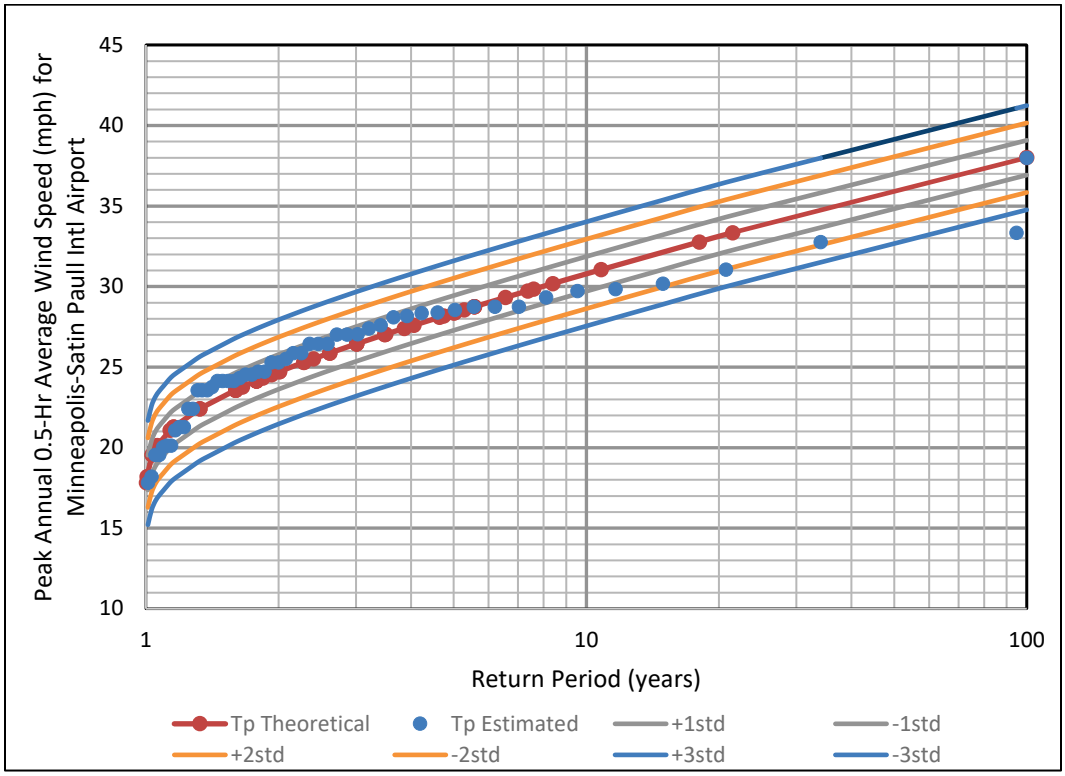

Figure B.3-10. Location 2 – wind frequency curves based on yearly maximum average 0.47 hr wind speed for MSP data.

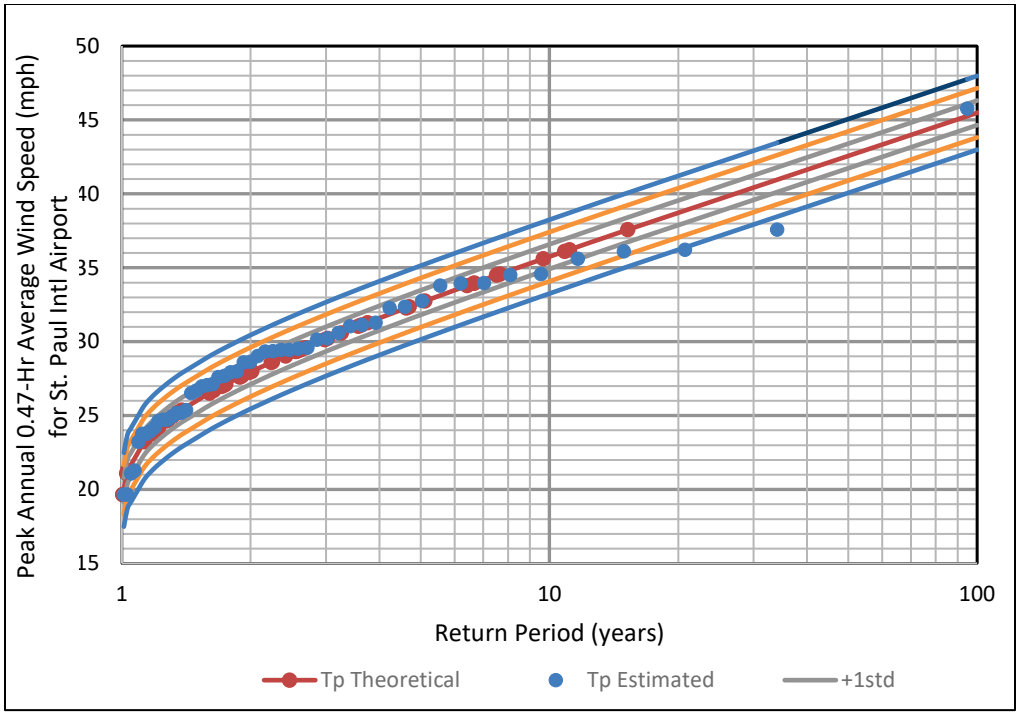

For Location 1, the standard deviation (σ) determined from these data (n=53) was 1.079 mph. The range of the wind speeds for the 100-year return period from -3σ to +3σ was 34.76 mph to 41.24 mph with a mean value of 38.0 mph. For Location 2, the standard deviation (σ) determined from this data (n=53) was 0.832 mph. The range of the wind speeds for the 100-year return period from -3σ to +3σ was 42.98 mph to 47.98 mph with a mean value of 45.48 mph. These values of wind speed are shown in Tables B.3-7 and B.3-8, respectively, and were used in the following analysis to determine the wave loads.

Table B.3-7. Location 1 – results from wind speed analysis for Mississippi River floodwall.

Statistic	100-Year Wind Speed (mph)
+3σ	41.24
+2σ	40.16
+1σ	39.08
Mean	38.00
-1σ	36.92
-2σ	35.84
-3σ	34.76

Table B.3-8. Location 2 – results from wind-speed analysis for Mississippi River floodwall.

Statistic	100-Year Wind Speed (mph)
+3σ	47.98
+2σ	47.15
+1σ	46.31
Mean	45.48
-1σ	44.65
-2σ	43.82
-3σ	42.98

B.3.4 Wave height and period assessment

Smith (1991) developed guidance to determine significant wave height and peak period based on wind speed and fetch. Dr. Tallent updated Smith's NARFET Fortran computer program to a more recent computer language (Python). The program input requires the radial lengths of the fetch and the angle increments for resolution of the wind direction as depicted in Figures B.3-11 (Location 1) and B.3-12 (Location 2). The radial segments (a total of 25) determined for an angle increment of 6° are shown in Figures B.3-11 and B.3-12. Tables B.3-9 and B.3-10 show the wind speeds and the wave height and wave period from the use of the NARFET program for the Mississippi River floodwall at St. Paul, MN. The wave heights computed for the mean and plus and minus 1, 2, and 3 standard deviations varied by approximately 0.12 m (0.394 ft) for Location 1 and 0.09 m (0.295 ft) for Location 2.

Figure B.3-11. Location 1 – fetch and wind direction for the Mississippi River floodwall used in the NARFET model.

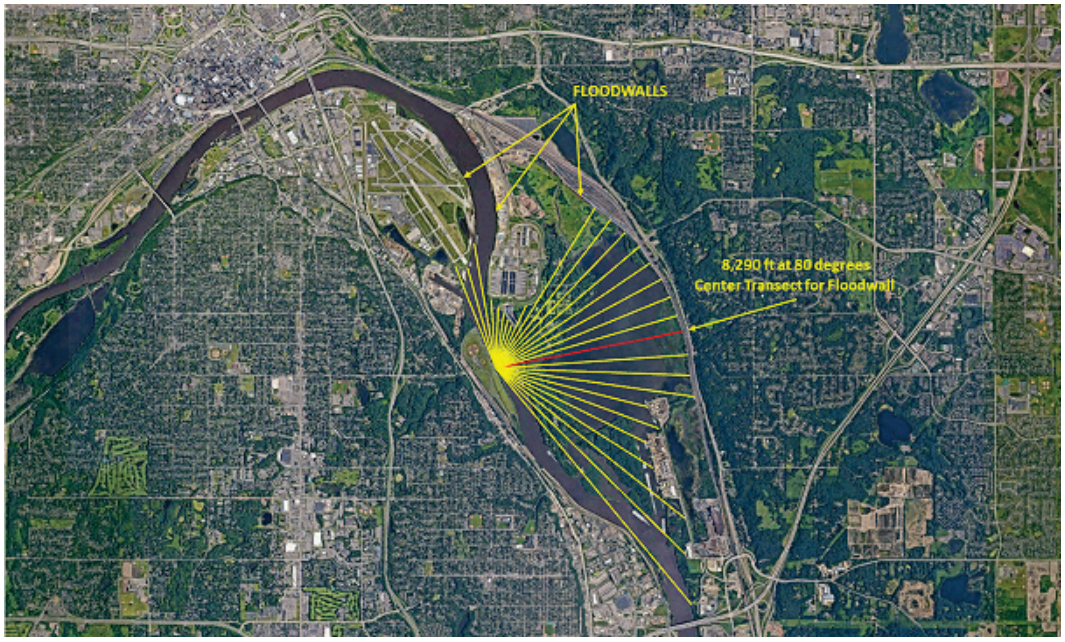

Figure B.3-12. Location 2 – fetch and wind direction for the Mississippi River floodwall used in the NARFET model.

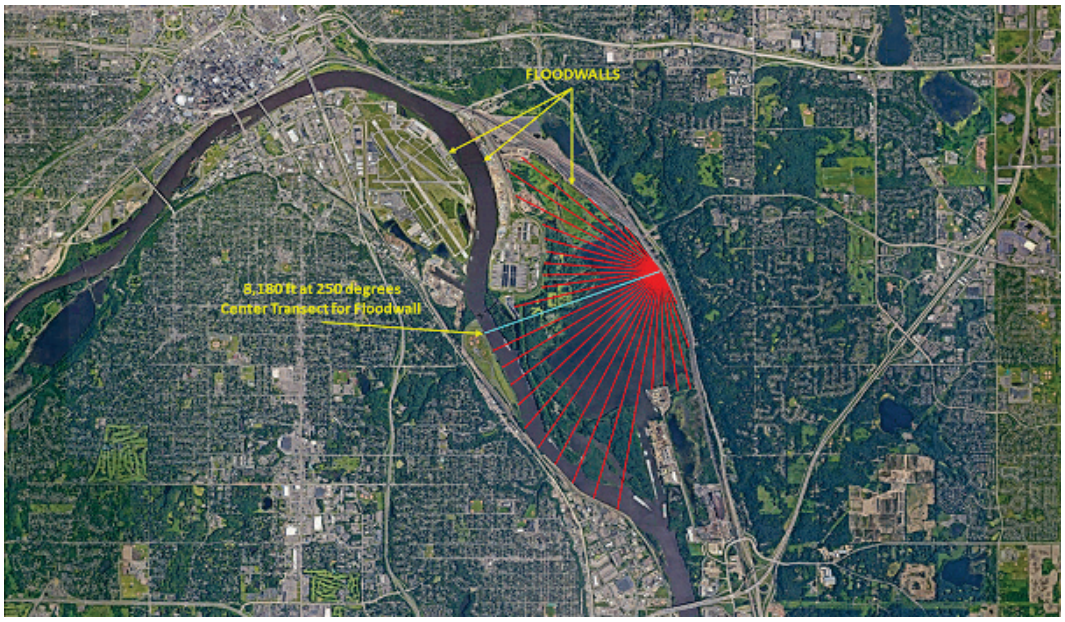

Table B.3-9. Location 1 – wave height and wave period from Smith's NARFET model for the Mississippi River floodwall.

Statistic	Wind Speed (mph)	Wave Height (m)	Wave Period (sec)
-3σ	34.76	0.70	2.83
-2σ	35.84	0.72	2.87
-1σ	36.92	0.74	2.90
Mean	38	0.76	2.93
+1σ	39.08	0.78	2.97
+2σ	40.16	0.80	3.00
+3σ	41.24	0.82	3.03

Table B.3-10. Location 2 – wave height and wave period from Smith's NARFET model for the Mississippi River floodwall.

Statistic	Wind Speed (mph)	Wave Height (m)	Wave Period (sec)
-3σ	42.98	0.83	3.04
-2σ	43.82	0.84	3.07
-1σ	44.65	0.86	3.09
Mean	45.48	0.87	3.11
+1σ	46.31	0.89	3.13
+2σ	47.15	0.90	3.16
+3σ	47.98	0.92	3.18

B.3.5 Wave height and wave period from Goda (2010)

As mentioned previously, Goda (2010) also recommended formulations to determine significant wave height and period based on wind speed and fetch. The significant wave height and period and T_{min} (Equation 6.1) computed from these equations are shown in Table B.3-11 for Location 1 and B.3-12 for Location 2. For Location 1, the mean 100-year return period wind speed was 38.0 mph, and the standard deviation was 1.08. For Location 2, the mean 100-year return period wind speed was 45.48 mph, and the standard deviation was 0.832. Goda (2010) numerically derived and experimentally validated the relation shown in Equation 6.1, which estimates this minimum duration of wind speed (T_{min}) required to generate a sustainable wave height for a fixed fetch length and wind speed.

The fetch length used in Goda's Equation 6.1 for the Location 1 design example was 2,530 m (8,300 ft) and 2,500 m (8,200 ft) for Location 2. Goda's wave height and period prediction relationships are given in

Equations 6.6 and 6.7. These metric unit-based equations were numerically derived and experimentally verified. Applying Equations 6.6 and 6.7 to the wind speed (U_{10}) values listed in Tables B.3-7 and B.3-8, the fetch lengths of 2,530 m and 2,500 m result in wave height and wave period values shown Tables B.3-11 and B.3-12, respectively. Applying Equations 6.6 and 6.7 to Tables B.3-7 and B.3-8 data with U_{10} values in meter/sec, results in the Tables B.3-11 and B.3-12 values, respectively.

$$\frac{gH_{1/3}}{U_{10}^2} = 0.3\left\{1 - \left[1 + 0.004\left(\frac{gF}{U_{10}^2}\right)^{1/2}\right]^{-2}\right\} \quad \text{(6.6 bis)}$$

$$\frac{gT_{1/3}}{U_{10}} = 8.61\left\{1 - \left[1 + 0.008\left(\frac{gF}{U_{10}^2}\right)^{1/3}\right]^{-5}\right\} \quad \text{(6.7 bis)}$$

where

g = acceleration due to gravity (9.81 m/sec²)
$H_{1/3}$ = significant wave height (design wave height, meters)
$T_{1/3}$ = significant wave period (design wave period, seconds)
U_{10} = wind speed at the elevation of 10 m above the sea surface (meters/second)
F = fetch length incident to the structure (meters).

Note that in Equation 6.1, F_L, is given in kilometers, so this needs to be converted to meters for use in Equations 6.6 and 6.7. The T_{min} values shown in both Tables B.3-11 and B.3-12 were similar to the T_{min} value of 0.5 hr and 0.47 hr estimated in section B.3.3.4, so no further iterations were considered necessary.

Table B.3-11. Location 1 – significant wave height and significant wave period from Goda's (2010) formulations for Mississippi River floodwall.

Statistic	100-Year Wind Speed (mph)	T_{min} (hr)	$H_{1/3}$ Wave Height (m)	$T_{1/3}$ Wave Period (sec)	$L_{1/3}$ Wave Length (m)
-3σ	34.76	0.531	0.628	2.383	8.870
-2σ	35.84	0.526	0.643	2.405	9.031
-1σ	36.92	0.521	0.658	2.426	9.189
Mean	38	0.516	0.673	2.447	9.345
+1σ	39.08	0.511	0.688	2.467	9.500
+2σ	40.16	0.506	0.702	2.486	9.651
+3σ	41.24	0.501	0.717	2.506	9.801

Table B.3-12. Location 2 – significant wave height and significant wave period from Goda's (2010) formulations for Mississippi River floodwall.

Statistic	100-Yr Wind Speed (mph)	T_{min} (hr)	$H_{1/3}$ Wave Height (m)	$T_{1/3}$ Wave Period (sec)	$L_{1/3}$ Wave Length (m)
-3σ	42.98	0.490	0.735	2.526	9.961
-2σ	43.82	0.487	0.747	2.540	10.073
-1σ	44.65	0.484	0.757	2.554	10.183
Mean	45.48	0.481	0.768	2.567	10.292
+1σ	46.31	0.478	0.779	2.581	10.400
+2σ	47.15	0.475	0.790	2.594	10.507
+3σ	47.98	0.472	0.800	2.607	10.613

A plot of wind speed (U) vs. wave height determined from Goda's recommended formulations from the statistical analysis of the wind-speed data is shown in Figures B.3-13 and B.3-14, respectively.

Figure B.3-13. Location 1 – wave height vs. wind speed from Goda's (2010) procedure for Mississippi River floodwall.

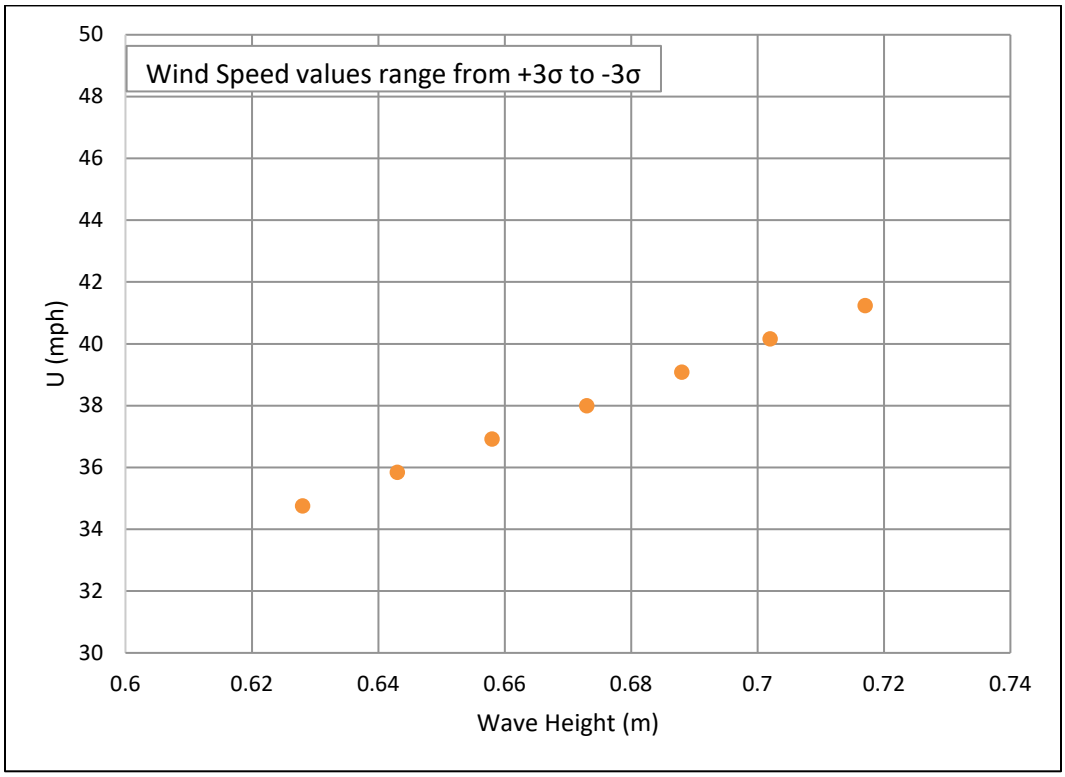

Figure B.3-14. Location 2 – wave height vs. wind speed from Goda's (2010) procedure for Mississippi River floodwall.

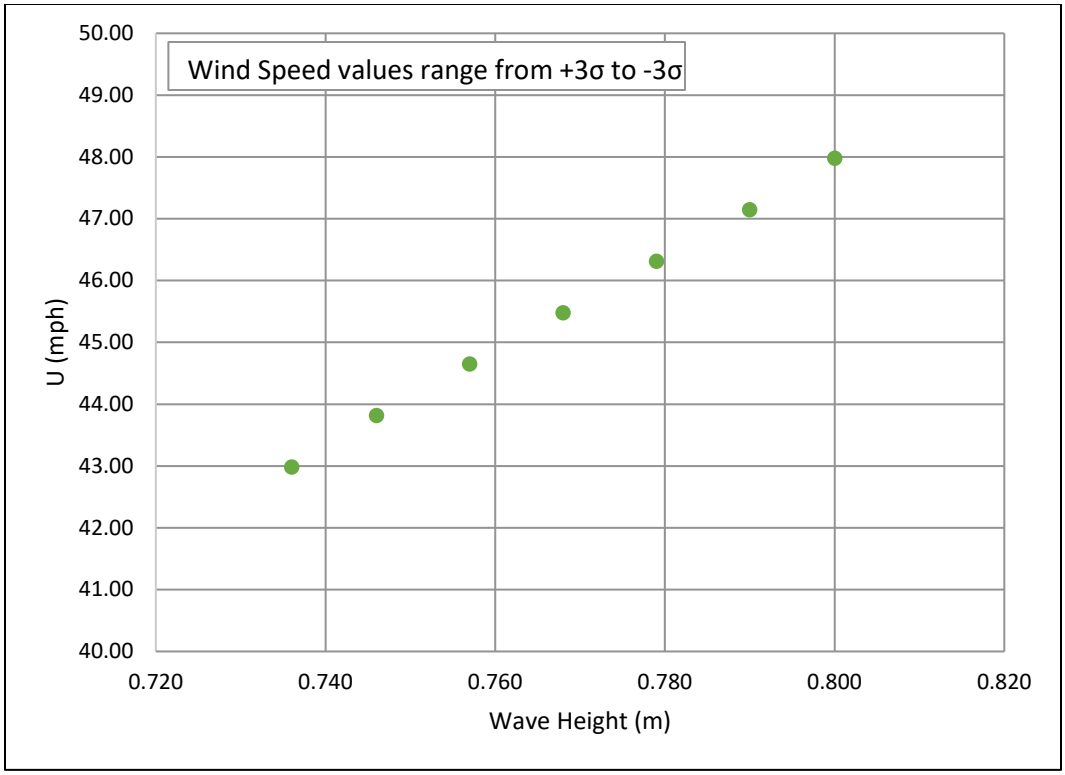

B.3.6 Example for determining pseudo-static wave load from Goda (2010)

The wave pressure distribution and subsequent wave force for the floodwall can now be determined from the significant wave height and wave period. The complete description of this procedure is shown in Chapter 6 and in Hite et al. for spillway gates.

B.3.6.1 Example floodwall design details and parameters for Goda (2010) formulations

Location 1 will be discussed first. The example computations for Location 1 given in this appendix are for the 100-year return period mean wind speed of 38.0 mph, a wave height of 0.673 ft (0.205 m), and a wave period ($T_{1/3}$) of 2.447 sec. In this example problem, the distance from the top of the base slab to the top of the wall is 12 ft (h_{stem} in Figure B.3-1). The elevations in reference to the local datum of the top of wall and top of the base slab and bottom of the base slab are 714.5, 702.5, and 700.5, respectively. The distance from the water surface at the selected flood level to the top of wall is 1 ft (h_c in Figure B.3-1). The distance from the water surface at flood level to the bottom of the stem (top of base slab) was 11 ft

(d_{SWL} in Figure B.3-1 and also referred to as d). The distance from the water surface at the flood level to the floodplain approach invert was chosen as 15 ft (h_{SWL} in Figure B.3-1), EL 699.5. This flood plain approach invert is 2.1 ft below the top of the base slab or 0.1 ft below the bottom of the base slab. Since θ was set equal to zero, h_b in Figure B.3-1 was equal to h_{SWL}. The significant wave height is 2.21 ft ($H_{1/3}$ in Figure B.3-1) for a mean wind velocity of 38.0 mph. Table B.3-13 provides a summary of the parameters used in the Goda (2010) procedure of defining a pseudo-static wind induced wave pressure acting on a floodwall. Figure B.3-1 illustrates these parameters.

Table B.3-13. Location 1 – parameters used in Goda (2010) procedure for example wave force calculation (imperial and metric units included) for a flood level gage reading of 713.5, SWL = 713.5).

Parameter	Value	Unit	Value	Unit	Description
h_{stem}	12	ft	3.658	m	T-Wall stem height (above base)
h_{Base}	2.0	ft	0.61	m	T-Wall base thickness
h_C	1.0	ft	0.305	m	T-Wall height above SWL
L_B	8.0	ft	2.4	m	Distance from heel of base slab to sheet pile distance
d (originally d_{SWL})	11	ft	3.353	m	Still water depth at base of T-Wall
h (originally h_{SWL})	15	ft	4.57	m	Still water depth at toe of berm
tan θ	0	N/A	0	N/A	Floodplain slope to T-Wall (riverside of T-Wall berm)
β_D	0	deg	0	deg.	Design incident wave angle
$H_{1/3}$	2.21	ft	0.673	m	Significant wave height, From Table B.2-8 (0.673 m) for a mean wind velocity of 38 mph
$T_{1/3}$	2.447	sec	2.447	sec	Significant wave period, for a mean wind velocity of 38 mph
L_D	30.68	ft	9.35	m	Design wave length, From $T_{1/3}$ and Equation 5.11
ρ	62.4	lb/ft^3	1000	kg/m^3	Density of freshwater
g	32.17	ft/sec^2	9.81	m/sec^2	Acceleration of gravity
h'	11	ft	3.353	m	For the case of T-Wall: $h' = d_{SWL}$
H_D	3.97	ft	1.211	m	Design wave height (see Eq. 5.8)
η*	5.96	ft	1.817	m	Elevation of wave pressure action above flood level

For Location 2, the example computations given in this appendix are for the 100-year return period mean wind speed of 45.48 mph, a wave height of 2.52 ft (0.205 m), and a wave period ($T_{1/3}$) of 2.567 sec. In this example problem, the distance from the top of the base slab to the top of the wall is 12 ft (h_{stem} in Figure B.3-1). The elevations in reference to the local datum of the top of wall and top of the base slab and bottom of the base slab are 714.5, 702.5, and 700.5, respectively. The distance from the water surface at the selected flood level to the top of wall is 1 ft (h_c in Figure B.3-1). The distance from the water surface at flood level to the bottom of the stem (top of base slab) was 11 ft (d_{SWL} in Figure B.3-1 and also referred to as d). The distance from the water surface at the flood level to the floodplain approach invert was chosen as 15 ft (h_{SWL} in Figure B.3-1), EL 699.5. This flood plain approach invert is 2.1 ft below the top of the base slab or 0.1 ft below the bottom of the base slab. Since θ was set equal to zero, h_b in Figure B.3-1 was equal to h_{SWL}. The significant wave height is 2.52 ft ($H_{1/3}$ in Figure B.3-1) for a mean wind velocity of 45.48 mph. Table B.3-14 provides a summary of the parameters used in the Goda (2010) procedure of defining a pseudo-static wind induced wave pressure acting on a floodwall. Figure B.3-1 illustrates these parameters.

Table B.3-14. Location 2 – parameters used in Goda (2010) procedure for example wave force calculation (imperial and metric units included) for a flood level gage reading of 713.5, SWL = 713.5).

Parameter	Value	Unit	Value	Unit	Description
h_{stem}	12	ft	3.658	m	T-Wall stem height (above base)
h_{Base}	2.0	ft	0.61	m	T-Wall base thickness
h_C	1.0	ft	0.305	m	T-Wall height above SWL
L_B	8.0	ft	2.4	m	Distance from heel of base slab to sheet pile distance
d (originally d_{SWL})	11	ft	3.353	m	Still water depth at base of T-Wall
h (originally h_{SWL})	15	ft	4.57	m	Still water depth at toe of berm
tan θ	0	N/A	0	N/A	Floodplain slope to T-Wall (riverside of T-Wall berm)
β_D	0	deg	0	deg	Design incident wave angle
$H_{1/3}$	2.52	ft	0.768	m	Significant wave height, From Table B.2-8 (0.673 m) for a mean wind velocity of 38 mph
$T_{1/3}$	2.567	sec	2.567	sec	Significant wave period, for a mean wind velocity of 38 mph

Parameter	Value	Unit	Value	Unit	Description
L_D	33.76	ft	10.29	m	Design wave length, From $T_{1/3}$ and Eq. 5.11
ρ	62.4	lb/ft^3	1000	kg/m^3	Density of freshwater
g	32.17	ft/sec^2	9.81	m/sec^2	Acceleration of gravity
h'	11	ft	3.353	m	For the case of T-Wall: h' = d_{SWL}
H_D	4.53	ft	1.382	m	Design wave height (see Equation 5.8)
η*	6.80	ft	2.074	m	Elevation of wave pressure action above flood level

For both locations, the design wave height (H_D), is the minimum of $\alpha_h H_{1/3}$ and $H_{b,}$ where α_h ranges from 1.6 to 2.0. For the design of nearshore vertical structures, Goda (2010) suggests using a value of 1.8 for α_h. For this example, the floodwall is 12 ft high (top EL 714.5), and the water surface at the flood level is 1 ft below the top of the wall (EL 713.5). An approach depth (h and h_{SWL} in Figure B.3-1 and Tables B.3-13 and B.3-14) of 15 ft was assumed with a mild approach slope (tan θ). The computations to determine the pseudo-static wind induced wave pressure distribution values by the Goda procedure are shown below. Their resultant forces are summarized in Table B.3-15 and B.3-16 for Locations 1 and 2, respectively.

B.3.6.2 Pseudo-static wave pressure terms

Goda uses three pseudo-static wave pressure terms (P_1, P_2, and P_3) to define the wave pressure distribution on the vertical face of the wall and one pseudo-static pressure term (P_u) to describe the uplift pressure at the toe of the wall (Figure B.3-15). The P_1 pressure term represents the maximum wave pressure exerted at the SWL while P_2 and P_3 represent the linear decay in wave pressure with depth.

Figure B.3-15. Illustration of terms in Goda's (2010) original pressure formulation adopted for Mississippi River floodwall.

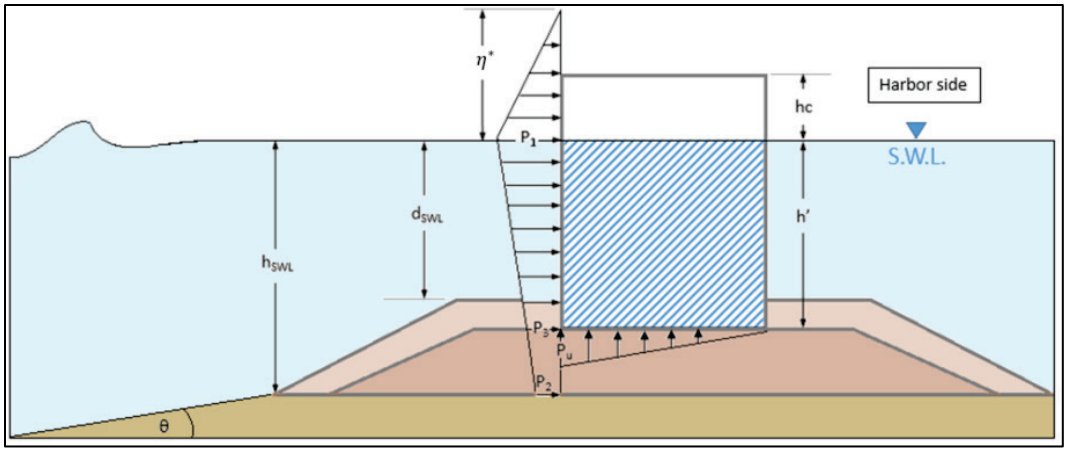

$$P_1 = 0.5\,(1\ + \cos\beta_D)\,(\alpha_1 + \alpha_2 * cos^2\beta_D)\,\rho * g * H_D \qquad (5.1\text{ bis})$$

$$P_2 = \frac{P_1}{\cosh(2\pi h/L_D)} \qquad (5.2\text{ bis})$$

$$P_3 = \alpha_3 P_1 \qquad (5.3\text{ bis})$$

$$P_u = 0.5\,(1\ + cos\,\beta_D)\,\alpha_1 * \alpha_3 * \rho * g * H_D \qquad (5.4\text{ bis})$$

where α_1 and α_2 are wave pressure coefficients derived from laboratory data. The α_1 coefficient represents the average tendency of wave pressure to increase with wave length (L_D), and the α_2 coefficient represents the tendency of the wave pressure to increase with the berm height. This α_2 term reflects the wave shoaling effect due to berm height and the impulsive pressure component. The α_3 coefficient describes the assumed linear pressure variation between P_1 and P_2.

$$\alpha_1 = 0.6 + \frac{1}{2}\left[\frac{\frac{4\pi h}{L_D}}{\sinh\left(\frac{4\pi h}{L_D}\right)}\right]^2 \qquad (5.5\text{ bis})$$

$$\alpha_2 = \min\left[\frac{h_b - d}{3h_b}\left(\frac{H_D}{d}\right)^2, \frac{2d}{H_D}\right] \qquad (5.6\text{ bis})$$

$$\alpha_3 = 1 - \frac{h'}{h}\left[1 - \frac{1}{\cosh\left(\frac{2\pi h}{L_D}\right)}\right] \qquad (5.7\text{ bis})$$

The Goda (2010) procedure of analysis represents the complex spectrum of sea waves by a single design wave height and length represented by H_D and L_D, respectively. The design wave height (H_D) of Goda's formula is described as the highest wave expected under given wave conditions; this wave height is also identified as H_{MAX}. H_{MAX} is determined as the lesser of 1.8 times the significant wave height ($H_{1/3}$) and the breaking wave height (H_b) (Equations 5.8 – 5.10), where H_b is evaluated at a distance of $5H_{1/3}$ seaward of the breakwater berm as shown in Figure B.3-16. The design wave length (L_D) of Goda's formula is described as the longest wave expected under given wave conditions; this wave length is also identified as L_{MAX}. In Equation 5.11, L_{MAX} is approximated using first-order wave theory and the significant wave period ($T_{1/3}$).

Figure B.3-16. Breaking wave height location in Goda's (2010) equation adopted for Mississippi River floodwall.

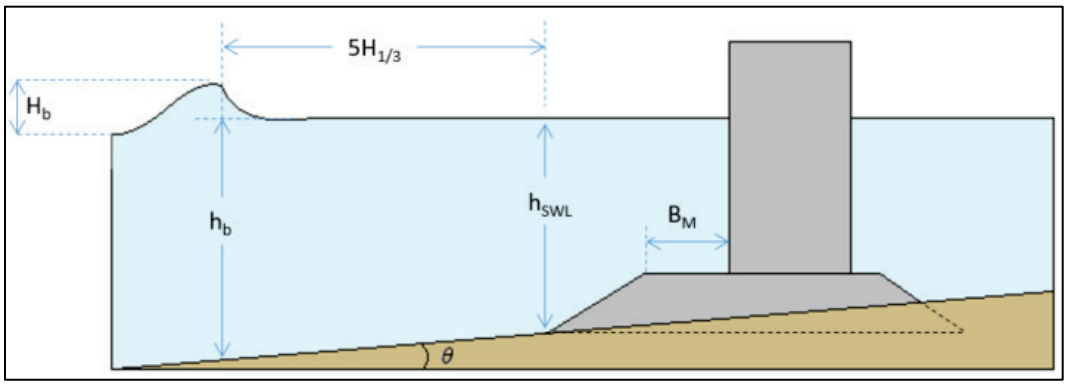

$$H_D = H_{Max} = min\{\alpha_h * H_{1/3},\ H_b\} \quad (5.8\ bis)$$

where α_h is typically in the range of 1.6 to 2.0. The α_h term defines the nondeterministic characteristic of the highest wave due to the random nature of sea waves. According to Goda (2010), the value of α_h is selected based on the reliability of design storm wave estimation, the importance of the structure and the type and nature of the possible structural failure. Goda states that a value of 2.0 or greater is often used for offshore structures, such as an offshore oil rig. For the design of nearshore vertical structures Goda suggest a value of 1.8 for α_h.

$$H_b = 0.17 * L_D \left\{1 - exp\left[-1.5\frac{\pi h_b}{L_D}\left(1 + \sigma_S * tan^{4/3}\theta\right)\right]\right\} \quad (5.9\ bis)$$

Originally, Goda specified the σ_S value as a constant equal to 15 but later recommend a value of 11 based on the work of Rattanapitikon and

Shibayama (2000). This reduction in the σ_S value accounts for an overprediction in the wave shoaling effect for steep bottom slopes (>1/10). Therefore, the authors of this report recommend using $\sigma_S = 11$ for bottom slopes greater than 1/50 and $\sigma_S = 15$ for bottom slopes less than 1/50.

$$h_b = h + 5 * H_{1/3} \tan\theta \quad \text{(5.10 bis)}$$

$$L_D = L_{MAX} = \frac{g * T_{1/3}^2}{2\pi} \quad \text{(5.11 bis)}$$

According to Goda (2010), the significant wave height ($H_{1/3}$) represents the largest one-third wave height measured in deep water. Similarly, the significant wave period ($T_{1/3}$) represents the longest one-third wave period measured in deep water. Site-specific estimates of $H_{1/3}$ and $T_{1/3}$, based on historical records, simulations, etc., can either be obtained or calculated from historical records of deep-water surface elevation changes with time.

The current version of the Goda-Takahashi wave pressure relationship is given in Goda (2010). Based on the parameters given in Table B.3-14 and the Goda-Takahashi (Goda 2010) equation set, the example solution is presented below. The design wave height (H_D) is the minimum of $\alpha_h H_{1/3}$ and H_b, where α_h ranges from 1.6 to 2.0. For the design of nearshore vertical structures, Goda (2010) suggest using a value of 1.8 for α_h.

$$H_D = H_{Max} = min\{\alpha_h * H_{1/3},\ H_b\} \quad \text{(5.8 bis)}$$

$$H_b = 0.17 * L_D \left\{1 - exp\left[-1.5\frac{\pi h_b}{L_D}\left(1 + 15 * tan^{4/3}\theta\right)\right]\right\} \quad \text{(5.9 bis)}$$

where

$$h_b = h + 5 * H_{1/3} * \tan\theta \quad \text{(5.10 bis)}$$

therefore,

Location 1: $\alpha_h H_{1/3}$ = 1.8*0.673 m = 1.211 m (3.973 ft)

Location 2: $\alpha_h H_{1/3}$ = 1.8*0.768 m = 1.382 m (4.534 ft)

and using Equations 5.10 and 5.9 the H_b parameter is derived as follows:

Location 1: h_b = 4.572 m + 5*0.673*(0) = 4.572 m (15.0 ft.)

Location 2: h_b = 4.572 m + 5*0.768*(0) = 4.572 m (15.0 ft.),

Location 1: $H_b = 0.17 * 9.349\text{m}\left\{1 - exp\left[-1.5 * \frac{\pi * 4.572\text{m}}{9.349\text{m}}\left(1 + 15 * (0)^{4/3}\right)\right]\right\} = 1.431$ m (4.695 ft.)

Location 2: $H_b = 0.17 * 10.289\text{m}\left\{1 - exp\left[-1.5 * \frac{\pi * 4.572\text{m}}{10.289\text{m}}\left(1 + 15 * (0)^{4/3}\right)\right]\right\} = 1.536$ m (5.039 ft.),

and finally,

Location 1: $H_D = H_{Max}$ = min {1.211 m, 1.431 m} = 1.211 m (3.973 ft)

Location 2: $H_D = H_{Max}$ = min {1.382 m, 1.536 m} = 1.382 m (4.534 ft).

Next, the coefficients of wave pressure (α_1, α_2 and α_3) given in Equations 5.5 – 5.7 are calculated. Recall that the h and d values in Equation 5.5 and 5.6 are respectively equivalent to the h_{SWL} and d_{SWL} of Tables B.3-13 and B.3-14; therefore,

Location 1: $\alpha_1 = 0.6 + \frac{1}{2}\left[\frac{\frac{4*\pi*4.572m}{9.349m}}{\sinh\left(\frac{4*\pi*4.572m}{9.349m}\right)}\right]^2 = 0.60$, from Equation 5.5

Location 2: $\alpha_1 = 0.6 + \frac{1}{2}\left[\frac{\frac{4*\pi*4.572m}{10.288m}}{\sinh\left(\frac{4*\pi*4.572m}{10.288m}\right)}\right]^2 = 0.60$, from Equation 5.5

Location 1: $\alpha_2 = min\left[\frac{4.572m - 3.353m}{3*4.572m} * \left(\frac{1.211m}{3.353m}\right)^2, \frac{2*3.353m}{1.211m}\right] = min[0.0008, 15.023] = 0.012$

Location 2: $\alpha_2 = min\left[\frac{4.572m - 3.353m}{3*4.572m} * \left(\frac{1.382m}{3.353m}\right)^2, \frac{2*3.353m}{1.382m}\right] = min[0.0008, 15.023] = 0.015$, from Equation 5.6.

and finally, since $h' = d_{SWL}$,

Location 1: $\alpha_3 = 1 - \frac{3.353m}{4.572m} * \left[1 - \frac{1}{\cosh\left(\frac{2*\pi*4.572m}{9.349m}\right)}\right] = 0.334$, from Equation 5.7

Location 2: $\alpha_3 = 1 - \frac{3.353m}{4.572m} * \left[1 - \frac{1}{\cosh\left(\frac{2*\pi*4.572m}{10.288m}\right)}\right] = 0.356$, from Equation 5.7.

The three pseudo-static wind induced lateral wave pressure components P_1, P_2, and P_3 (Equations 5.1 to 5.3) and the pseudo-static wind-induced wave uplift pressure component (P_u) (Equation 5.4) are evaluated below. The solution to P_1, P_2, and P_3 are

Location 1: $P_1 = 0.5 * (1 + \cos(0 \text{ deg})) \left(0.60 + 0.012 * cos^2(0)\right) * 1000 \frac{kg}{\text{m}^3} * 9.81 \frac{\text{m}}{s^2} * 1.211 \text{ m} = 7272 \ N/\text{m}^2$ (151.9 lb/ft²).

Location 2: $P_1 = 0.5 * (1 + \cos(0 \text{ deg})) \left(0.60 + 0.015 * cos^2(0)\right) * 1000 \frac{kg}{\text{m}^3} * 9.81 \frac{\text{m}}{s^2} * 1.382 \text{ m} = 8354 \ N/\text{m}^2$ (174.5 lb/ft²)

Location 1: $P_2 = \frac{7272 \ N/\text{m}^2}{\cosh(2*\pi*(4.572\text{m}/9.349\text{m}))} = 672 \ N/\text{m}^2$ (14.0 lb/ft²)

Location 2: $P_2 = \frac{8354 \ N/\text{m}^2}{\cosh(2*\pi*(4.572\text{m}/10.288\text{m}))} = 1020 \ N/\text{m}^2$ (21.3 lb/ft²)

Location 1: $P_3 = 0.334 * 7272 N/\text{m}^2 = 2432$ N/m² (50.79 lb/ft²)

Location 2: $P_3 = 0.356 * 8354 N/\text{m}^2 = 2975$ N/m² (62.14 lb/ft²)

and the solution for P_U is

Location 1: $P_u = 0.5 (1 + cos(0 \text{ deg})) 0.60 * 0.334 * 1000 \frac{kg}{\text{m}^3} * 9.81 \frac{\text{m}}{s^2} * 1.211 \text{ m} = 2386 \ N/\text{m}^2$ (49.82 lb/ft²)

Location 2: $P_u = 0.5 (1 + cos(0 \text{ deg})) 0.60 * 0.356 * 1000 \frac{kg}{\text{m}^3} * 9.81 \frac{m}{s^2} * 1.382 \text{ m} = 2902 \ N/\text{m}^2$ (60.62 lb/ft²).

To calculate the total lateral force on the T-Wall, it is first necessary to determine if the pressure distribution (above SWL) extends above the crest of the T-Wall. The ΔP_1 parameter shown in Figure B.3-17 represents

this fraction of pressure that would be negated from the total pressure above the SWL.

Figure B.3-17. Pressure distribution on Mississippi River T-Wall (batter piles not shown).

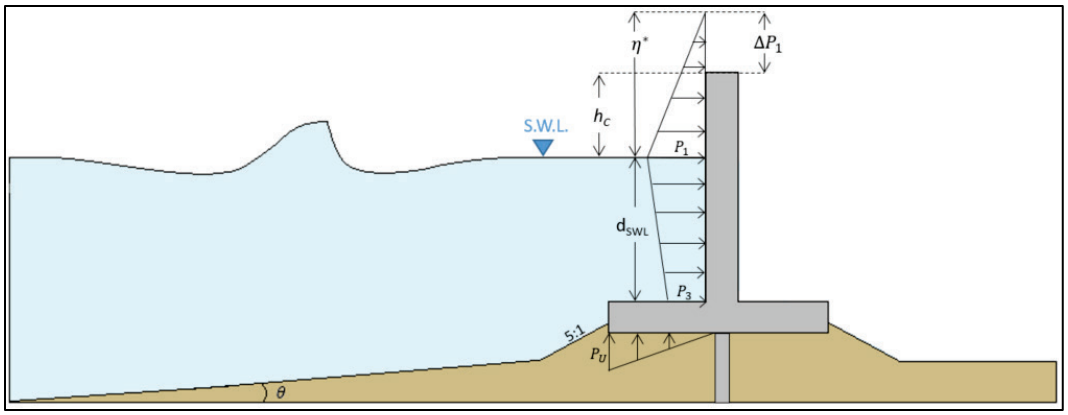

When the vertical distance η* plus the flood level SWL elevation exceeds the top of floodwall elevation, a pseudo-static horizontal water pressure P_4 is introduced at the top of wall. P_4 is a distance of h_c above P_1. The total lateral force per linear width (F_{Lat}) on the flood side of the T-Wall is given in Equation 5.29:

$$F_{Lat} = 0.5(P_1 + P_3)d + 0.5(P_1 + P_4)h'_C \quad (5.29 \text{ bis})$$

where

$$P_4 = P_1\left(1 - \frac{h_C}{\eta^*}\right), if\ \eta^* > h_C \quad (5.30 \text{ bis})$$

or

$$P_4 = 0, if\ \eta^* \leq h_C \quad (5.31 \text{ bis})$$

$$\eta^* = 0.75(1 + \cos(\beta_D))H_D \quad (5.32 \text{ bis})$$

$$h'_C = min\{\eta^*, h_C\} \quad (5.33 \text{ bis})$$

Therefore, the solution for the Figure 5-20 resultant force F_{Lat} is given as

h_C = 0.305 m or 1 ft (from Tables B.3-13 and B.2-14)

Location 1: $\eta^* = 0.75 * (1 + \cos(0 \text{ deg})) * 1.211 \text{ m} = 1.817 \text{ m}$ (5.96 ft)

Location 2: $\eta^* = 0.75 * (1 + \cos(0 \text{ deg})) * 1.382 \text{ m} = 2.074 \text{ m}$ (6.80 ft)

since $\eta^* > h_C$, from Equation 5.26,

Location 1: $P_4 = 7272\ N/\text{m}\text{^}2 * \left(1 - \frac{0.305\text{m}}{1.817\text{m}}\right) = 6052\ N/\text{m}^2$ (126.4 lb/ft²)

Location 2: $P_4 = 8354\ N/\text{m}\text{^}2 * \left(1 - \frac{0.305\text{m}}{2.074\text{m}}\right) = 7125\ N/\text{m}^2$ (148.8 lb/ft²)

Location 1: $h_C' = min\{1.817 \text{ m}, 0.305 \text{ m}\} = 0.305 \text{ m}$ (1.0 ft)

Location 2: $h_C' = min\{2.074 \text{ m}, 0.305 \text{ m}\} = 0.305 \text{ m}$ (1.0 ft)

Location 1: $F_{Lat} = 0.5 * \left(7272 \frac{N}{\text{m}^2} + 2432 \frac{N}{\text{m}^2}\right) * 3.353 \text{ m} + 0.5 * \left(7272 \frac{N}{\text{m}^2} + 6052 \frac{N}{\text{m}^2}\right) * 0.305 \text{ m} = 18{,}301 \frac{N}{\text{m}}$ (1254 lb/ft)

Location 2: $F_{Lat} = 0.5 * \left(8354 \frac{N}{\text{m}^2} + 2975 \frac{N}{\text{m}^2}\right) * 3.353 \text{ m} + 0.5 * \left(8354 \frac{N}{\text{m}^2} + 7125 \frac{N}{\text{m}^2}\right) * 0.305 \text{ m} = 21{,}354\ N/\text{m}$ (1463 lb/ft)

The total uplift force per linear width on the T-Wall is calculated as

Location 1: $U_P = 0.5 * P_U * L_B = 0.5 * 2386 \frac{N}{\text{m}^2} * 2.4 \text{ m} = 2863\ N/\text{m}$ (196.1 lb/ft)

Location 2: $U_P = 0.5 * P_U * L_B = 0.5 * 2902 \frac{N}{\text{m}^2} * 2.4 \text{ m} = 3483\ N/\text{m}$ (238.6 lb/ft).

Using the relationships given in Chapter 6 and in Hite et al. for spillway gates, the one-third/one-sixth (1/3:1/6) rule is applied to calculate the elevation of the resultant forces along the vertical face of the T-Wall (Equation 5.341). Based on the parameters listed in Tables B.3-13 and B.3-14 and the wind-speed and wave data in Tables B.3-11 and B.3-12 for the mean value, the pressure and lateral force acting on the floodwall was computed from the Goda (2010) formulations and are shown in Tables B.3-14 and B.3-15, along with h_{Lat} calculations from Equation 5.34.

$$h_{Lat} = \frac{(h_4 - h_1)\left(\frac{P_4}{3} + \frac{P_1}{6}\right)h_4 + (h_4 - h_1)\left(\frac{P_4}{6} + \frac{P_1}{3}\right)h_1 + (h_1 - h_3)\left(\frac{P_1}{3} + \frac{P_3}{6}\right)h_1}{F_{Lat}} \quad \text{(5.34 bis)}$$

Location 1: h_{Lat} = 2.127 m = 6.976 ft

Location 2: h_{Lat} = 2.114 m = 6.935 ft

The definition of Goda's parameters shown in Table B.3-15 and B.3-16 is illustrated in Figure B.3-17.

Table B.3-15. Location 1 – wave force and pressure distribution computations using Goda's (2010) procedure for data in Table B.3-12 for a flood level, SWL, of EL 713.5.

Statistic	Wind Speed (mph)	η^*, m	η^*, ft	P_1, N/m²	P_3, N/m²	P_4, N/m²	P_u, N/m²	F_{lat}, kN/m	h_{lat}, m	h_{lat}, ft	P_1, lb/ft²	P_3, lb/ft²	P_4, lb/ft²	P_u, lb/ft²	F_{lat}, lb/ft
+3σ	41.24	1.94	6.35	7770	2679	6546	2621	19.70	2.12	6.96	162.3	55.95	136.7	54.75	411.5
+2σ	40.16	1.90	6.22	7600	2593	6377	2539	19.22	2.12	6.96	158.7	54.15	133.2	53.03	401.4
+1σ	39.08	1.86	6.09	7441	2514	6220	2464	18.77	2.12	6.97	155.4	52.50	129.9	51.46	392.1
Mean	38.00	1.82	5.96	7272	2432	6052	2386	18.30	2.13	6.98	151.9	50.79	126.4	49.82	382.2
-1σ	36.92	1.78	5.83	7104	2350	5884	2308	17.83	2.13	6.98	148.4	49.09	122.9	48.20	372.4
-2σ	35.84	1.74	5.70	6935	2271	5717	2232	17.36	2.13	6.99	144.8	47.43	119.4	46.61	362.7
-3σ	34.76	1.70	5.58	6768	2193	5550	2156	16.90	2.13	7.00	141.3	45.79	115.9	45.04	353.0

Table B.3-16. Location 2 – wave force and pressure distribution computations using Goda's (2010) procedure for data in Table B.3-13 for a flood level, SWL, of EL 713.5.

Statistic	Wind Speed (mph)	η^*, m	η^*, ft	P_1, N/m^2	P_3, N/m^2	P_4, N/m^2	P_u, N/m^2	F_{lat}, kN/m	h_{lat}, m	h_{lat}, ft	P_1, lb/ft^2	P_3, lb/ft^2	P_4, lb/ft^2	P_u, lb/ft^2	F_{lat}, lb/ft
+3σ	47.98	2.16	7.09	8724	3176	7492	3092	22.42	2.11	6.92	182.2	66.33	156.5	64.57	468.3
+2σ	47.15	2.13	7.00	8607	3104	7377	3024	22.07	2.11	6.93	179.8	64.84	154.1	63.16	461.0
+1σ	46.31	2.10	6.90	8480	3042	7251	2965	21.72	2.11	6.93	177.1	63.53	151.4	61.93	453.6
Mean	45.48	2.07	6.80	8354	2975	7125	2902	21.35	2.11	6.93	174.5	62.14	148.8	60.62	446.0
-1σ	44.65	2.04	6.71	8227	2910	6999	2840	20.99	2.12	6.94	171.8	60.77	146.2	59.32	438.5
-2σ	43.82	2.01	6.61	8101	2844	6874	2778	20.63	2.12	6.94	169.2	59.39	143.6	58.01	430.9
-3σ	42.98	1.99	6.52	7987	2783	6761	2720	20.30	2.12	6.95	166.8	58.12	141.2	56.80	424.0

Appendix C: Using Sparse Data to Determine Geotechnical Soil Property Distributions/Statistics

C.1 Introduction

It is often the case in geotechnical work that a scarcity of material property data makes it difficult to describe the range and statistical distribution of values that characterize the soil material. This appendix discusses one approach used by geotechnical engineers to develop mean and standard deviations values for engineering material parameters describing soils, particularly regarding shear strength parameters. In the absence of enough data to describe a distribution, a bell-shaped distribution (e.g., the Gaussian normal distribution) can be used to estimate the parameter spread of values.

This approach makes use of the range in values for a variable, where range is defined as the difference between the lowest conceivable value (LCV) and the highest conceivable value (HCV) for the data.

$$Range = HCV - LCV \tag{C.1}$$

Because of the sparsity and the magnitude of scatter in geotechnical engineering data, this characterization is found to be especially helpful when assigning a standard deviation value. Baecher and Christian (2003) observe that the dispersion from a small number of tests can be made from the sample range. In statistics, variance (equal to the square of the standard deviation, σ^2) is the measure of dispersion.

C.2 The importance of accurate standard deviation values in a reliability analysis

Sleep and Duncan (2014) make several important observations regarding the application of reliability analysis to geotechnical engineering and the importance of providing accurate mean and standard deviation values. When considering the challenge the engineer faces in developing values of standard deviation for the soil strength variables given sparse data, these points are worth repeating:

- The accuracy of the means and the standard deviations of the variables considered in the Duncan and Sleep (2014) reliability problem model dictate the precision with which P_f can be computed. Considering the interrelationship between P_f and β, this conclusion extends to β as well.
- Considering the often-sparse geotechnical engineering data and challenge in estimating the standard deviations of these data, computed values of P_f cannot be expected to be highly precise.
- Values of standard deviation of geotechnical engineering parameters can be estimated using available data, combined with engineering judgement.
- Application of expertise with informed judgement is an important part of the process used to devise values of standard deviations and mean values for each of the geotechnical engineering, material-characterization variables (e.g., unit weights, shear strength parameters).

Estimating material parameter distributions with the least amount of error directly impacts the accuracy of reliability analyses. The cumulative effect of material properties drawn from distributions affects capacity estimates and limit state(s) calculations, which directly impact P_f, β and LRFD values.

C.3 A quick estimate for the mean value

Baecher and Christian (2003) suggest that a quick and often good estimate of the central tendency is the median value. For data that are symmetrically distributed about its central value and for small numbers of clustered data, the sample median is a good estimate of the mean.[21] Data that are normally distributed is an example of a symmetrical distribution.

A second shortcut suggested by Baecher and Christian (2003) is that in some instances, the mean value μ can be approximated using

$$\mu = \frac{HCV+LCV}{2} \tag{C.2}$$

They caution that this estimate requires expertise to determine the smallest concievable range. It is recognized that experts tend to

[21] The mean is the arithmetic average of a set of numbers, or distribution. The median is described as the numeric value separating the higher half of a sample, a population, or a probability distribution, from the lower half.

underestimate the range, as discussed in subsection C.4.2. Therefore, Equation C.2 should be used with caution. Ellingwood also cites this relationship for a *bell-shaped* PDF (e.g., a normally distributed variable) and when 95% of the values lie between the LCV and HCV values.

If the PDF is skewed in the positive direction, as is natural for geotechnical engineering material parameters that rarely have values that are less than 0.0, Ellingwood suggests a mean estimate can be based on

$$\mu = 0.65 * LCV + 0.35 * HCV \tag{C.3}$$

Graphical N_σ approach: In the graphical approach described in Duncan et al. (2014) and Sleep and Duncan (2014) for interpreting a plot of sparse data (e.g.,consisting of undrained shear strength S_u versus depth [or pressure]), a straight line or a curve is drawn through the data that represent the most likely variation of the S_u with depth (or pressure). In the case of triaxial test results, a straight line is drawn through the data of Mohr-circles at failure for each of the triaxial test data that represent the most likely variation of a Mohr-Coulomb shear strength envelope with pressure for triaxial tests, which are usually run at different confining pressures (Figure C-1).

Figure C-1. Development of average, average plus one standard deviation, and average minus one standard deviation strength envelopes using the 2-σ rule (N_σ= 4).

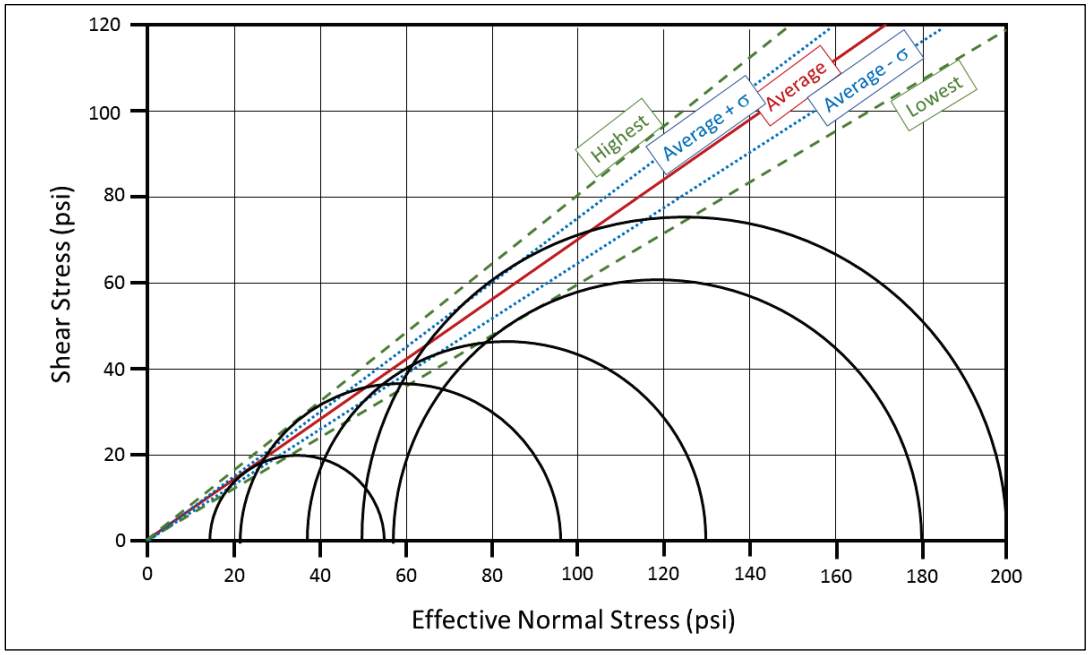

Application of expertise with informed engineering judgement is an important part of the graphical N_σ process. This is because of the influence of sample disturbance, the sensitivity of test data to the quality of the overall execution of the laboratory (or in situ in the field) soil testing process, differences in measured strength results for different types of soil strength tests due to stress anisotropy, etc. Sample disturbance is a *catch-all* term used in geotechnical site characterization to reflect the effect of disturbance on an engineering material characterization parameter (e.g., S_u) that can occur during the drilling and sampling process, during sample extraction from the field and transport to the soil testing laboratory, and during sample storage and handling of the sample in the laboratory.

C.4 A quick estimate for the value of the standard deviation

C.4.1 A statistical procedure using collected data

Because of sparse geotechnical data, one approach cited by Baecher and Christian (2003), Foye et al. (2006), Sleep and Duncan (2014), and Duncan et al. (2014) is what is sometimes referred to as the **N_σ-rule** to estimate the standard deviation σ of geotechnical engineering material parameter (e.g., S_u). Citing the work of Tippett (1925), Foye et al. (2006) state this rule as

$$\sigma = \frac{Range}{N_\sigma} \tag{C.4}$$

for a normally distributed variable. The value for N_σ varies with the number of sample measurements for the parameter (e.g., S_u), from a low of 1.128 for 2 samples to a high approaching 6.5 for 1,000 samples. Table C-1 summarizes N_σ values for different sample sizes according to Tippett (1925) and Burlington and May (1970).

Table C-1. Values of sample range (N_σ) for normally distributed variable with $\sigma = 1$ and n sample measurements (after Tippett [1925] and Burington and May [1970]).

Sample Size, n	N_σ
2	1.128
3	1.693
4	2.059
5	2.326
6	2.534
7	2.704
8	2.847
9	2.970
10	3.078
11	3.173
12	3.258
13	3.336
14	3.407
15	3.472
16	3.532
17	3.588
18	3.640
19	3.689
20	3.735
30	4.09
50	4.5
75	4.81
100	5.02
200	5.49
300	5.756
400	5.936
500	6.073
1,000	6.483

C.4.2. A procedure using expert judgement

It is not uncommon that collected geotechnical data either have too few samples for statistical processing or have values that experienced geotechnical engineers can readily identify as outliers that lie beyond the actual variance of the data trends. Again, the application of expertise with informed engineering judgement is an important part of this process. This is because of the influence of sample disturbance, the sensitivity of test data to the quality of the overall execution of the laboratory (or in situ in the field) soil testing process, differences in measured strength results for different types of soil strength tests due to stress anisotropy, etc. When this occurs, geotechnical expertise is required to specify the actual (e.g., S_u) values for HCV and LCV. The following rules provide a qualified estimate for the probabilities of occurance at the expert-provided HCV and LCV, therefore assigning a standard deviation.

Dai and Wang (1992), Withiam et al. (1997), Foye et al. (2006), and Professor Duncan in his earlier, 2000 publication on the topic of reliabilty analysis in geotechnical engineering all recommended using a value of 6 for N_σ. The basis for the N_σ equal to 6, also called the *three-sigma rule* (Duncan 2000), lies in the fact that for a normally distributed variable, three standard deviations in either direction from the mean of a normal distribution encompases 99.74% of all possible values.

Christian and Baecher (2001) suggested changing the value of N_σ from 6 to 4 after reviewing the Duncan (2000) paper with the following realizations:

- First, if the person making the the estimate for standard deviation uses sparse data with sample sizes of 20 to 30 values, then a better estimate would be made using N_σ equal to 4 rather than 6. This can be seen in the Table C-1 information which interprets the data statistically.
- Second, Duncan and Wright (2005), Duncan, et al. (2014), Sleep and Duncan (2014), and Christian and Baecher (2001) discuss studies that show there is a tendency for people, including statisticians as well as experienced geotechnical engineers, to be overconfident in their ability to estimate the range from LCV to HCV. In other words, their estimated value for the range (Equation C.1) between LCV and HCV is typically too small, resulting in distributions that overestimate values close to the mean.

For geotechnical engineers working with sparse data, it is the opinon of the authors of this ERDC report that the second point is especially relevant to geotechnical material characterization. In summary, these two points encourage using a value of 4 for N_σ when data are scarce for the determination of engineering material parameter distributions for soils that will be used in geotechnical reliability applications.

Duncan and Wright (2005), Sleep and Duncan (2014), Duncan et al. (2014) have since recommended assigning a value of N_σ equal to 4. Professor Duncan refers to this as the "two-sigma rule," which reflects that the range value encompasses 2 times σ above the mean value and 2 times σ less than the mean. Ellingwood also recommends the use of N_σ equal to 4 for a PDF that is bell shaped or is skewed in the positive direction.

Graphical N_σ approach: Duncan and Wright (2005), Duncan et al. (2014), Sleep and Duncan (2014) provide examples of applying the N_σ equal to 4, two-sigma rule graphically to sparse data consisting of undrained shear strength S_u versus depth data or Mohr-circles at failure for triaxial data with different confining pressures that are used to define the angle of internal friction. First, a straight line or a curve is drawn through the data that represent the most likely variation of the parameter with depth (or with pressure). Next, straight lines or curves are drawn through the data that represent the highest conceivable bound and lowest conceivable bounds on the data. These become the two-sigma lines, with N_σ equal to 4. Finally, straight lines or curves that represent the average plus one standard deviation and the average minus one standard deviation are drawn halfway between the average and the lowest and highest concevible lines. Figure 14 in Sleep and Duncan (2014) and Figure 13-1 in Duncan et al. (2014) demonstrate this procedure using undrained shear strength S_u data with depth. This graphical approach is also demonstrated in Figure C-1 for triaxial test data in this appendix.

Appendix D: Values for Coefficient of Variation and Scale of Fluctuation for Soils

D.1 Introduction

Geotechnical site investigations are designed with two objectives in mind: (1) to identify the soil layers contained in the foundation for the project and (2) to characterize the geotechnical engineering soil properties of each of the soil layers. During the site investigation, soil specimens are recovered from each of the foundation soil layers. Some specimens are used to identify the soil type(s) while other specimens are selected for transportation to a laboratory where they are subjected to a variety of geotechnical tests, especially strength data. These soil tests generate geotechnical engineering data that are used to characterize the strength and/or stiffness of the various soil layers from which high quality *undisturbed* samples were recovered. Some of the geotechnical laboratory tests that are conducted include unconfined compression tests, various types of triaxial tests, direct shear tests, direct simple shear tests, ring shear tests, and 1-D consolidation tests. The site investigation may also involve the use of a variety of in situ tests conducted at the project site that result in measurements used to indicate and/or correlate to engineering shear strength and stiffness parameters of the soils within the layers of foundation soils. Examples of these in situ tests include the SPT, various types of CPT, Vane Shear Test (VST), as well as the less frequently used dilatometer tests and pressuremeter tests. The measurements and/or interpreted geotechnical engineering material properties generated for each of the foundation soil layers from the laboratory and/or in situ test results inherently possess *scatter*. Geotechnical engineers have found that reliability-based statistical procedures are one means for quantifying this scatter and formally incorporating it in the engineering analysis. Calculation of an *average trend function* that characterizes the spatial average of the geotechnical engineering data within each of the soil layers, along with the calculation of the data's *statistical* variance about this trend function is an approach to statistically interpret data possessing scatter.

The COV of a geotechnical engineering property for a particular type of soil is an important parameter when formulating a resistance factor in LRFD format, as evidenced by its presence in the LRFD resistance factor,

φ_R, Equation 2.36 (and Equation 2.39). Recall, COV is the standard deviation divided by the mean value for a specified parameter. The COV is frequently used as an index for the variance of an engineering parameter. Recall, variance is the square of the standard deviation, σ^2. This appendix summarizes COV values obtained from geotechnical articles whose COV data were reviewed for pertinence to the geotechnical portion of this USACE LRFD research effort. The focus of this geotechnical parameters COV data collection is on shear strength parameters for different soil categories (e.g., clay, sand). COV data are further grouped according to the type of laboratory or field test used to generate the strength data. Some of the selected geotechnical publications present these data as a range in COV values while others as approximate guidelines for design soil property variability.

D.1.1 Geotechnical data in the vertical and horizontal directions

A geotechnical site investigation consisting of drilled bore holes and in situ tests (e.g., CPT) usually are performed in the vertical direction. The foundation soil types and layering are identified using these data. The in situ measurements and laboratory soil test data are processed and interpreted for each of the soil layers. This data collection and soil type interpretation is conducted in the vertical direction, using the data recovered from different boreholes and/or in situ measurements made across the site. Soil profiles are then constructed across the site. The typical geologic site formation process for soils allows for a site characterization process that is oriented in the vertical and horizontal directions within each of the soil layers.

D.1.2 Sparse data and typical COV values

Phoon and Kulhawy (1999a) and others in the geotechnical community observe that ideally, appropriate resistance factors (in an LRFD-based design procedure) should be based on the variability of the soil data collected at the project site. However, when these data are not yet available or are too limited for meaningful statistical analysis, guidelines on the likely range of soil property COV are useful. The COV data contained in this appendix are intended to bridge this gap in knowledge. These data also serve the purpose of allowing geotechnical engineers to develop an appreciation for the probable range in COV values and to identify unusual values for soil variance, as expressed in a COV value.

D.1.3 Point estimate versus spatial average and variance reduction

Vanmarcke (1977b) points out that probabilistic distributions are primarily needed along a potential failure surface in a clay foundation for each spatially averaged geotechnical engineering soil parameter, like the undrained shear strength S_u. A full description of these parameters is provided by a PDF from which the mean and standard deviation can be calculated. These spatial averages will have narrower PDFs than the corresponding point estimate property of a statistically homogeneous soil because the longer the distance over which this spatial averaging occurs, the uncorrelated fluctuations in S_u tend to cancel during the process of spatial averaging. This tends to cause a reduction in the standard deviation (and variance) in S_u as the size of the averaging length increases. This attribute is referred to as variance reduction within the zone of influence for the structure. Thus, the statistical characterization of the variance in S_u, which can be expressed in terms of its COV value for S_u, needs to account for this variance reduction that occurs when spatial averaging estimates are made for soils properties within a zone of influence (e.g., along a potential slip plane) rather than for a statistical characterization of S_u at discrete points/locations (El-Ramly et al. 2003a,b).

Phoon and Kulhawy (1999a) make an important observation that relates to the fact that there are different methods to quantify COV for geotechnical engineering parameters for soils. Their observation is that soil property statistics reported in several pre-1999 geotechnical publications were determined from total variability analyses that implicitly assume a uniform source of uncertainty, as reflected in their method used to gather and statistically process the geotechnical data. Because of this, they conclude that these earlier results are not suitable for use in a geotechnical reliability analysis. Variance estimates of soil properties based on spatial average are needed. With an intended use in geotechnical reliability analysis, Phoon and Kulhawy take care in their 1999 studies to distinguish a point estimate value of COV in a particular soil layer from the COV value pertaining to spatial average in that layer. The authors of this report recognize the importance of these observations to reliability computations for the USACE hydraulic structures that are in contact with the earth, especially those that retain earth.

Li (1992) provides an explanation supported by informative graphics (Figure D-1(a),(b) to distinguish a point estimate for a geotechnical engineering soil property in what Li refers to as a uniform soil layer from

the spatial average for that soil property in that layer. Li notes that in "early works" on probabilistic analysis, soil properties were commonly modeled using what he referred to as a single-random-variable (SRV) approach in which the random variation of the soil property (x) within the entire soil layer is represented by one single random variable. Figure D-1(a) illustrates that this SRV approach, which implies that all realizations (i.e., simulations) of the soil property (x) are the same at every depth (z) although the exact magnitude of the realization for (x) remains a random variable. A normal distribution is assumed, as shown in this figure at the depth z in which the simulation occurs. Li observes that this approach is inappropriate for geotechnical engineering site characterization because it infers that the actual magnitude of the soil parameter (x) at all depths in the soil layer can be determined with absolute certainty by measuring the value of the soil property using one sample taken anywhere within the soil layer. Modeling the engineering soil property (x) within the soil layer as a random field (Vanmarcke 1977a, 1983) is considered to be more realistic by Li (1992), Phoon and Kulhawy (1999a,b), and others. In this approach, the values of the soil property (x) at different depths z are treated as separate random variables, as depicted in Figure D-1(b). The actual mean value for the soil property of undrained shear strength (S_u) within the soil layer is shown as a constant labeled $\bar{x}$ and designated by a dashed line in these two figures.

Figure D-1. Inherent soil variability of the geotechnical engineering soil property undrained shear strength (S_u) at depth z; (a) point estimate; (b) random field (after Li [1992]).

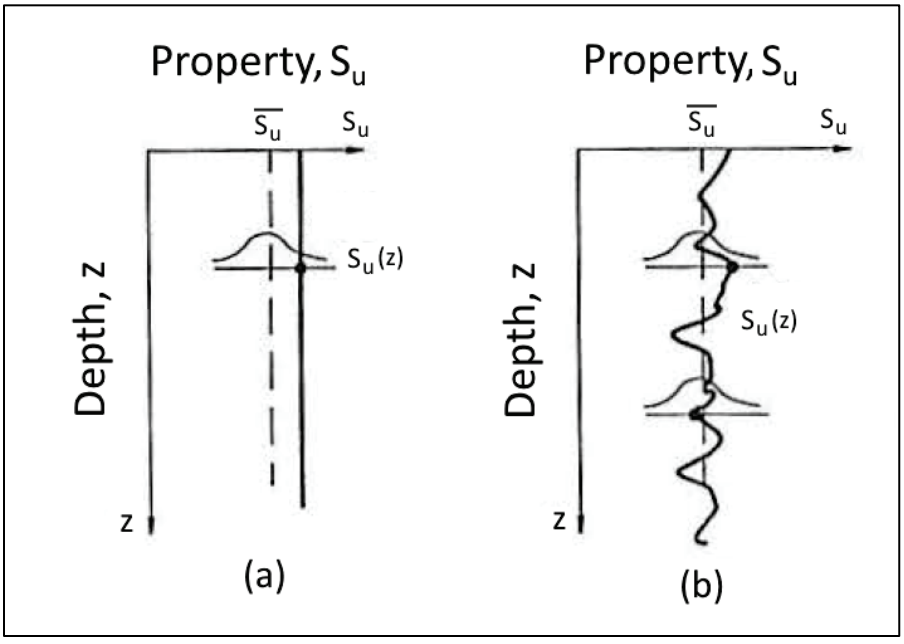

D.1.4 The Phoon and Kulhawy (1999a,b) procedure for computing spatial average for a soil layer

The Phoon and Kulhawy approach for defining variances, standard deviations and COV values based on spatial average is best explained using Figure D-2. This figure displays an engineering soil property they designate as ξ, which varies with depth, z. This Figure D-2 engineering soil property (ξ) is equivalent to Li's engineering soil property (x) shown in Figure D-1. ξ could be the undrained shear strength, S_u, of the soil, for example. In Figure D-2 for soil layer j, ξ is shown to vary with depth z below the ground surface.

Figure D-2. Graphical definition of inherent soil variability (w) with depth, z, within a soil layer (after Phoon and Kulhawy [1999a]).

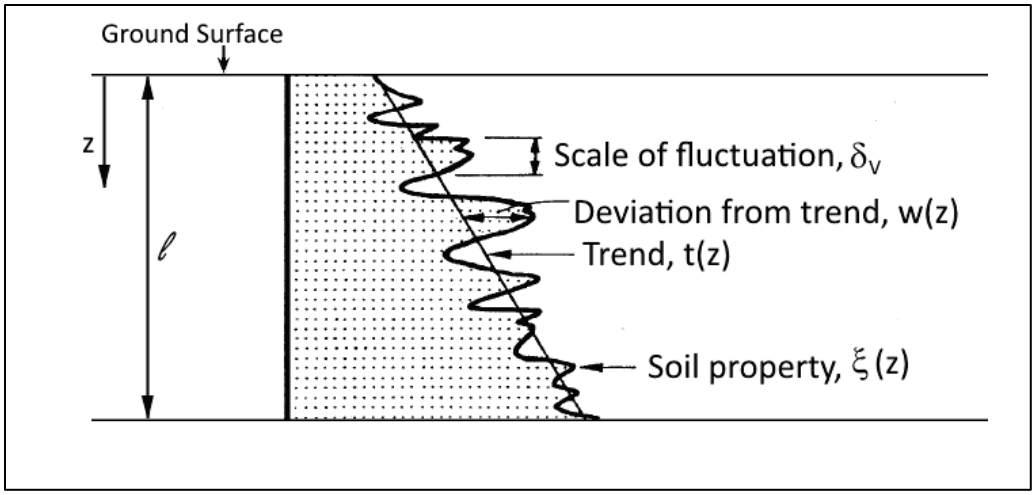

This figure depicts the soil property ξ(z) varying about a trend function t(z), with t(z) assumed to be a linear function with elevation in Figure D-2.[22] This ξ(z) deviation from the trend function t(z) is designated w(z) and is given by the relationship

$$\xi(z) = t(z) + w(z) \tag{D.1}$$

The fluctuating component $w(z)$ represents the inherent soil variability within soil layer j.

[22] Note that the trend function $t(z)$ does not have to be a linear trend function as depicted in Figure D-2. For example, Jaksa et al. (1997) used a quadratic trend function when interpreting CPT tip resistance data. A quadratic trend function was also used by Doherty and Gavin (2010) in their interpretation of CPT data for use in pile design.

Inherent soil variability: Rearranging, Equation D.1, the inherent soil variability $w(z)$ is defined mathematically as the difference between $\xi(z)$ and $t(z)$:

$$w(z) = \xi(z) - t(z) \tag{D.2}$$

It is important to the resulting statistics that the soil property data from different soil layers are not mixed. This requirement is also portrayed in Figure D-2. Additionally, the application of Equation D.2 ensures that deterministic trends in the soil property data are removed by subtracting the trend line function $t(z)$. The inherent soil variability $w(z)$ is modeled as random field (Vanmarcke 1983, 2010) and is considered to statistically homogeneous for a homogeneous soil layer when two statistical criteria are met for the data: Phoon and Kulhawy (1999a) state that these criteria are met if (1) the mean and variance of w does not change with depth and (2) the correlation between the deviations at two different depths is a function only of their separation distance, rather than their absolute positions. The standard deviation of the inherent soil variability $w(z)$ is designated as SD_w and evaluated in the usual manner using

$$SD_w = \sqrt{\frac{1}{n-1} * \sum_{i=1}^{n} |w(z_i)|^2} \tag{D.3}$$

with $w(z_i)$ being the fluctuation at depth z_i about the trend function. The coefficient of variation of inherent soil variability $w(z)$ is

$$COV_w = \frac{SD_w}{t} \tag{D.4}$$

with t being the mean soil property trend for the soil layer in this equation.

D.1.5 Scale of fluctuation; autocorrelation distance; characteristic length

Another statistical parameter used to describe inherent soil variability in a soil layer is the autocorrelation distance, designated r_o by DeGroot and Baecher (1993) and Keaveny et al. (1989). Mollon et al. (2011) observe that an infinite autocorrelation length corresponds to a homogeneous field, while an autocorrelation length equal to zero corresponds to a non-correlated field (i.e., a soil in which the value of the geotechnical engineering soil parameter at each point is totally uncorrelated with the ones of surrounding points). The autocorrelation distance r_o is also

referred to as the characteristic length. For a simple and commonly used exponentially decaying autocorrelation function, ρ,

$$\rho(r) = b * e^{-\left(|r|/r_o\right)} \tag{D.5}$$

the Vanmarcke (1977a) scale of fluctuation, δ, is given by[23]

$$\delta = 2 * r_o \tag{D.6}$$

In equation D.5, r is separation (lag) distance between points, and b is a value between 0 and 1, depending upon measurement noise (Keaveny et al. 1989). The scale of fluctuation, δ, is related to the autocorrelation distance, r_o, but differs in numeric value by a constant associated with the model used (e.g., Equation D.5) to define the autocorrelation function with distance.

The scale of fluctuation represents the length of a range where all values should show correlation whereas the autocorrelation distance is the distance from a certain location until properties are uncorrelated (much like a diameter and radius). Both parameters r_o and δ possess units of length. The value for r_o or δ is a measure of the spatial extent within which a soil property shows a strong correlation. Vanmarcke (1977a) comments that at two points that lie within a distance δ, the corresponding values of the soil parameter are likely to be either both above or both below the soil layers trend function within this region. A large value for r_o (or δ) implies that the soil property is highly correlated over a large spatial extent, resulting in a smooth variation within the soil profile about a mean trend function and a small value of r_o (or δ) implies the fluctuation of the soil property is large, giving rise to a rapid spatial variation of soil property about a mean trend function (Li and Lee 1991; Wickremesinghe and Campanella 1993).

Because of soil anisotropy, a distinction is made between the scale of fluctuation in the vertical and in the horizontal direction. Note that the vertical direction is designated by the subscript v in this appendix and the horizontal direction is designated by the subscript h.

[23] For other mathematical options that may be used to describe the autocorrelation function with distance, refer to Table 1 of Keaveny et al. (1989); Figure 2 of DeGroot and Baecher (1993); Table 2 of Li and Lee (1991); Table 1 of Jaksa et al. (2000); Section 5.1 in Vanmarcke (1983, 2010); or Table 1 of Vanmarcke (1977a).

A simplified approach for assessing the value for δ_v is described in Vanmarcke (1977a) and outlined using Figure D-3. Given sufficient geotechnical material property data ξ with depth z within a soil layer, as depicted in Figure D-3, a simple approximation for the vertical scale of fluctuation δ_v is given by Vanmarcke (1977a) to be

$$\delta_v = 0.8 * \bar{d} \tag{D.7}$$

in which $\bar{d}$ is the average distance between intersections of the fluctuating soil property ξ and its trend function $t(z)$.

Figure D-3. Estimation of vertical scale of fluctuation (after Phoon and Kulhawy [1999a]).

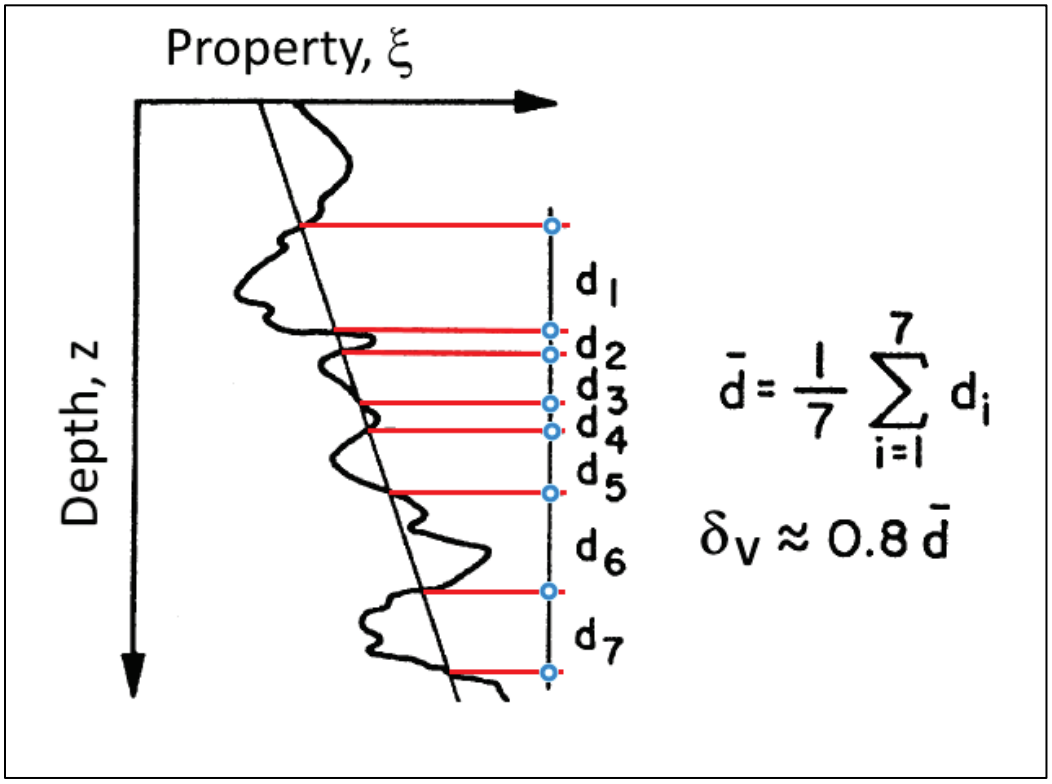

D.1.6 Geology's influence on horizontal and vertical scales of fluctuation

Fenton and Vanmarcke (1991) and others suggest that the scale of fluctuation is largely dependent on the geological process of the soil layer deposition rather than the specific soil property being studied. During a review of the geotechnical literature on autocorrelation distance of in situ soils (versus manmade soil layer(s)), the authors of this report observed that the values for autocorrelation distance (i.e., characteristic length) r_o and for the scale of fluctuation δ differ in the vertical direction from the

value in the horizontal direction, within the same soil layer. This is logical from a geologic point of view when the depositional environment for the soil layer is considered: For example, Baecher and Christian (2006) comment that for fluvial soils, the correlation distance might be small while for lacustrine soil the correlation distance might be large. El-Ramley et al. (2003a) also encourage approaching the assignment of r_o and δ values from a geologic viewpoint. They cite the example of a marine sediment tending to be homogeneous with continuous patterns of variability and large autocorrelation distances whereas tills and residual soils tend to be more erratic with notable variabilities over small distances and with small autocorrelation distances. By the observations cited in this paragraph, the authors of this report recognize the importance of geologic depositional characteristics to r_o and δ values and subsequently, their impact on a reliability computation for the USACE hydraulic structures in contact with earth.

D.1.7 Anisotropy in δ_v and δ_h values: site-specific data

Table D-1 is a collection of values of the vertical and horizontal autocorrelation distances and/or vertical and horizontal scales of fluctuation for different engineering tests made in different soil types. Nearly all the soils cited are naturally formed soils. Two exceptions are the hydraulic fill sand sites that were described in Onisiphorou (2000), as cited in Hicks and Samy (2002) and in Popescu et al. (1997). The soil data reported in this table focus almost entirely on strength tests results. The data in this table support the observation that as a result of the geologic process and within a given layer, soil properties tend to be more variable in the vertical direction than in the horizontal direction, as reflected in smaller r_o (and δ) values in the vertical direction as compared to those for the horizontal direction.

Table D-1. Summary of autocorrelation and scale of fluctuation distances of some geotechnical engineering soil properties charactering the strength of soils.

Test Type	Soil Property	Soil Type	Autocorrelation Distance, r_o (m)		Scale of Fluctuation, δ (m)		Horizontal / Vertical	Reference
			Vert.	Horiz.	Vert.	Horiz.		
Unconfined compressive strength	q_u	Chicago clay	0.4		0.79			Wu (1974)
CPT	q_c	Clay	0.52		1.04			Alonzo and Krizek (1975)
Vane	S_u	New Liskeard Clay			5	46	9.2	Vanmarcke (1977b)
Unconfined Compressive Strength	S_u	Nagoya Port Marine clay, Japan; NC			1.25			Matsuo and Asaoka (1977)
Unconfined Compressive Strength	S_u	Nagoya Port Marine clay, Japan; NC			2.5			Matsuo and Asaoka (1977)
Unconfined Compressive Strength	S_u	Horikawa bridge Marine clay, Japan; NC			1.82			Matsuo and Asaoka (1977)
CPT	q_c	North Sea clay		30				Tang (1979)
Vane	S_u	Organic soft clay, New York City	1.2					Asaoka and A-Grivas (1982)
Vane	S_u	Organic soft clay, New York City	3.1					Asaoka and A-Grivas (1982)
Unconsolidated Undrained	S_u	Offshore soil	3.6		7.1			Keaveny et al. (1989)
Direct Simple Shear	S_u	Offshore soil	1.4		2.8			Keaveny et al. (1989)
CPT	q_c	Offshore soil; CPT at 7m depth		13.9		24.6		Keaveny et al. (1989)
CPT	q_c	Offshore soil; CPT at 9m depth		37.5		66.5		Keaveny et al. (1989)
Vane	S_u	Marine clay Quebec, Canada	3	30			10	Soulie et al. (1990)
Unconfined Compressive Strength	q_u	Soft clay	2	40			20	Honjo and Kuroda (1991)
CPT	q_c	Muddy silty clay; Shanghai, China			0.4 to 0.8			Gao and Li (1993)

Test Type	Soil Property	Soil Type	Autocorrelation Distance, r_o (m)		Scale of Fluctuation, δ (m)		Horizontal / Vertical	Reference
			Vert.	Horiz.	Vert.	Horiz.		
CPT	q_c	Muddy soft clay; Shanghai, China			1.0 to 1.5			Gao and Li (1993)
CPT	q_c	Greyish silty clay; Shanghai, China			0.6 to 1.2			Gao and Li (1993)
CPT	q_c	Dark green clay; Shanghai, China; (OCR>1)			0.5 to 0.8			Gao and Li (1993)
Vane	S_u	Clay		21.4				Christian et al. (1994)
Triaxial and Direct Shear	SHANSEP, S_u	Clay		7				Christian et al. (1994)
Vane	S_u	Very soft Bangkok clay	1.1	22.1			20	Bergado et al. (1994)
Piezocone and Vane	q_c	Sensitive clay, Saint-Hilaire, Canada	2					Chiasson et al. (1995)
CPT	q_c	Silty clay	1					Lacasse and de Lamballerie (1995)
CPT	q_c	Laminated clay		9.6				Lacasse and Nadim (1996)
CPT	q_c	Kelswick Clay; homogeneous; (OCR > 1)	0.88	0.97	-	-	1.1	Jaksa et al. (1997)
CPT	q_c	Kelswick Clay; homogeneous; (OCR > 1)			0.15	0.14 to 2	0.93 to 13.3	Jaksa et al. (2000)
CPT	q_c	Upper (yellow) clay; clayey silt to silty clay; Taranto, Italy; (OCR > 1); five tests			0.33 ave. (0.2 to 0.44)			Cafaro and Cherubini (2002); Cherubini et al. (2006)
		Lower (gray) clay; clayey silt to silty clay; Taranto, Italy; (OCR > 1); five tests			0.4 ave. (0.19 to 0.72)			
CPT	q_{c1N}	Clay			0.32			Uzielli et al. (2005)

Test Type	Soil Property	Soil Type	Autocorrelation Distance, r_o (m)		Scale of Fluctuation, δ (m)		Horizontal / Vertical	Reference
			Vert.	Horiz.	Vert.	Horiz.		
CPT	q_{c1N}	Silty clay and clayey silt; Brindisi, Italy; (OCR > 1)			1.6			Cherubini and Vessia (2006)
CPT	q_c	Clean, uniform sand; Eglin Field, FL	1.1		2.2			Alonzo and Krizek (1975)
CPT	Friction ratio	Clean, uniform sand; Eglin Field, FL	0.625		1.25			Alonzo and Krizek (1975)
CPT	q_c	Clean sand	1.6					Kulatilake and Ghosh (1988)
CPT	q_c	Fine sand; Shanghai, China; Medium density			0.25 to 0.6			Gao and Li (1993)
CPT	q_c	Dense sand		37.5				Lacasse and Nadim (1996)
CPT	q_{c1N}	Sand			0.7			Uzielli et al., (2005)
CPT	q_{c1N}	Silty sand			0.35			Uzielli et al., (2005)
CPT	q_{c1N}	Silt			0.76			Uzielli et al., (2005)
CPT	q_c	Sand; three tests per each of two sites				0.3		Wickremesinghe and Campanella (1993)
		Hydraulic sandfill slope			0.7			Onisiphorou (2000), as cited in Hicks and Samy (2002)
CPT	q_c	North Sea soil		13.9				Keaveny et al. (1989)
CPT	q_c	North Sea soil		37.5				Keaveny et al. (1989)
CPT	q_c	Sand, hydraulic fill artificial island	0.95	12.1	-	-	12.7	Popescu et al. (1997)

Test Type	Soil Property	Soil Type	Autocorrelation Distance, r_o (m)		Scale of Fluctuation, δ (m)		Horizontal / Vertical	Reference
			Vert.	Horiz.	Vert.	Horiz.		
CPT	q_c	Dense Sand, Wicklow, Ireland; four tests	0.25		0.4 to 0.83			Doherty and Gavin (2010)
Wave Velocity Tests; Down-Hole	P-wave	Alluvial Deposit; Fivizzano Village in Tuscany, Italy; two tests			1.8 to 2			Cherubini and Vessia (2006)
	SH-wave				1.4 to 2.6			

Notes

CPT is the cone penetration test, q_c is its tip resistance, and q_{c1N} is a normalized tip resistance.

In clays, silty clays, clayey silts, etc., variability in CPT indices as q_c and q_{c1N} correspond to variability of undrained shear resistance S_u.

OCR is the overconsolidation ratio; OCR > 1 means the soil is overconsolidated. NC means the soil is normally consolidated.

δ may be approximated as 2 times r_o for an exponentially decaying autocorrelation function.

D.1.8 Anisotropy in δ_v and δ_h values – generalizations published in the technical literature

Over the last 20 years, engineers researching the spatial correlation of engineering soil properties have collected and studied the vertical and horizontal scale of fluctuation (or autocorrelation) engineering soil property data and some have made generalized observations. Tables D-2 and D-3 list some of their generalized observations. For example, based on her (limited) study of values cited in the geotechnical literature on vertical and horizontal scale of fluctuation for CPT and undrained shear strength data for natural (versus manmade) soils, Cherubini (2000) concludes that the values of the vertical scale of fluctuation, δ_v , are generally found between 0.5 and 2 m while for the horizontal scale of fluctuation, δ_h , are generally on the order of 12 m. The Phoon and Kulhawy (1999a) data suggest values of r_o and δ in the horizontal direction to be more than one order of magnitude greater than the values in the vertical direction. Babu (2014) citing a Uzielli et al. (2005) vertical random field modeling of soil variability assessment of 40 CPT profiles in mostly sandy soils that were collected at five regional sites, makes this same conclusion.

Differences are to be expected among the (Table D-2) generalizations due to consideration of the amount and type(s) of engineering soil property data available and collected at the time each generalization is made. However, these generalizations appear to be consistent. Among the

researchers, the Phoon and Kulhawy (1999a,b) studies contained the largest soil test results data base(s). The Table D-1 data are for the most part for soil strength tests. These data collected by the authors of this report support these Table D-2 and D-3 generalized observations.

Table D-2. Generalizations on the magnitude of the vertical and horizontal scale of fluctuation distances of select geotechnical engineering soil properties charactering the strength of soils.

Reference	Range in Vertical Scale of Fluctuation, δ_v (m)	Range in Horizontal Scale of Fluctuation, δ_h (m)	Notes
Cherubini (1997)	0.5 to 2 m	10 to 30 m	
Cherubini (2000)	0.5 to 2 m	On the order of 12 m	
Phoon and Kulhawy (1999a)	1 to 2 m	40 to 60 m	Laboratory measurement of undrained shear strength
	<1 m		Cone tip resistance
	<0.5 m		Corrected cone tip resistance
	2 to 6 m		Vane shear and standard penetration tests

Table D-3. Generalizations on the magnitude of the vertical and horizontal autocorrelation distances of select geotechnical engineering soil properties charactering the strength of soils.

Reference	Range in Vertical Autocorrelation Distance, $(r_o)_v$ (m)	Range in Horizontal Autocorrelation Distance, $(r_o)_h$ (m)	Notes
El-Ramly (2001)	1 to 3 m	20 to 40 m	Generalized observations based on data reported in the geotechnical literature.
El-Ramly et al. (2002b, 2003a,b)	1 to 3 m	10 to 40 m	

Note: δ may be approximated as 2 times r_o for an exponentially decaying autocorrelation function.

D.1.9 Is the value of δ (and r_o) a property of the soil mass?

Citing the study of different (engineering) soil properties of the same soil made by Bao et al. (1993), Cherubini (1997) asserts that δ would seem an attribute of a soil mass. During the technical review for this report, the authors noted that Bao et al. (1993) article does not present supporting data but cites a 1992 Bao-authored article (published in Chinese) as the basis for this observation. However, the soil property data obtained from different laboratory engineering strength and in situ vane and CPT tests that were reported in Phoon and Kulhawy (1999a) do appear to support the assertion that δ would seem an attribute of a soil mass.

D.1.10 Value of the anisotropy factor, δ_h/δ_v

Hicks and Samy (2002) conclude that the clay data of Vanmarcke (1977b) supports an anisotropy factor (= δ_h/δ_v) of 9; the Soulie et al. (1990) data support a factor of 10; and the Phoon and Kulhawy (1999a) data support a factor of 13 (using mean VST results). Using CPT profiles taken from a hydraulic sandfill, Popescu et al. (1997) found δ_h to be on average 12 times greater than δ_v. Note that although the hydraulic sandfill structure was manmade, the value for the resulting anisotropy factor is consistent with those from natural geologic depositional environments that were discussed in this paragraph. One exception to these trends is the lower end estimate made by Jaksa et al. (1997) and Jaksa et al. (2000) for a homogeneous, stiff, overconsolidated Kelswick Clay of Adelaide, Australia, that indicates an anisotropy factor between 0.93 and 13.3 (using vertical and horizontal CPT profiles). These limited data on clay suggest that the degree of overconsolidation can influence the magnitude of the anisotropy factor; higher overconsolidation ratios, OCRs, reduce the value for the anisotropy factor.

D.1.11 Impact of directionality of the scale of fluctuation on foundations

Because of the significant difference in δ_h and δ_v values, El-Ramley et al. (2003a) and others point out the importance to identify the direction in which the variability of geotechnical engineering properties has a dominant impact on the stability model used in the analysis. Three examples can be cited:

- The earth pressure on a retaining structure being controlled by the variability of the coefficient of earth pressure with depth.

- The soil-to-pile resistance of vertical or batter pile foundations.

In these first two examples, the spatial variability in the vertical direction is likely to be more important to the reliability analysis.

- The stability of slopes in presheared or jointed formations with shallow dip angles is controlled by the variability of strength parameters along a long, near-horizontal rupture surface. This example comes from a probabilistic stability analysis of a tailings dike on pre-sheared clay shale made by El-Ramly et al. (2003a). Autocorrelation distances in horizontal directions are thus more relevant in this case.

In this third example of a sliding stability analysis, the spatial variability in the horizontal direction may be more important to the reliability analysis of system consisting of driving, structural, and resisting wedges if the structural wedge dominates the stability calculation.

D.1.12 Equivalent scale of fluctuation distance

Within a given layer, as a result of the geologic process, soil properties tend to be anisotropic and specifically, more variable in the vertical direction than in the horizontal direction. This is borne out by the Table D-1 data. Therefore, for sliding stability computations, the challenge is to account for scale of fluctuation anisotropy along the (potential) slip planes of driving and resisting soil wedges when these slip planes are not oriented along a plane that is neither vertical nor horizontal but is inclined (relative to these two orientations). Appendix E discusses four methodologies presented in the engineering literature for dealing with anisotropic scales of fluctuation. Each of these methodologies determine an equivalent scale of fluctuation.

D.1.13 Scale of fluctuation dependent upon the type of engineering soil test and engineering parameter

Although the general trend of the Table D-1 strength data is in support of Cherubini's (1997) assertion that δ would seem an attribute of a soil mass, it was also observed in the published data that the exact values for r_o and δ will differ among the geotechnical engineering soil parameters according to the type of soil test conducted (e.g., strength, stiffness, index properties, water contents).

D.1.14 Sampling interval

Lesser known but also important is the DeGroot and Baecher (1993) and Phoon and Kulhawy (1999a) observation that the r_o and δ values are strongly influenced by the sampling interval. Jaska et al. (1997) and Jaksa et al. (2000) also demonstrated this fact as well as the dependence of r_o on the degree of trend (i.e., order of polynomial) removed from the data using vertical and horizontal CPT data obtained from a relatively homogeneous, overconsolidated clay known as Keswick clay. It possesses properties similar to London clay.

D.2 Variability of design soil properties

To evaluate geotechnical soil property variability on a general basis that facilitates the use of reliability-based geotechnical design procedures, Phoon and Kulhaway (1999b) recognized that it is necessary to describe total soil variability in terms of

- inherent soil variability (w)
- soil test measurement error (e)
- transformation uncertainty (ε).

Each source of variability is assessed separately in the Phoon and Kulhawy procedure of probabilistic analysis. Inherent soil variability, caused primarily by the natural geologic processes that are involved in soil formation, was discussed in the previous section. It is depicted as $w(z)$ in Figure D-2 and labeled "deviation from trend." Soil test measurement error is because the process of measurement introduces variability into the soil data. It arises from equipment, procedural-operator, and random testing effects (Phoon and Kulhawy 1999a). The direct measurement from a geotechnical test typically is not directly applicable to the geotechnical engineering design property. Instead, a transformation model is needed to relate the test measurement to an appropriate design property. One such example is the uncertainty in the correlation (i.e., the transformation model) between the SPT field test measurement and the unconfined compressive soil strength parameter, q_u, (Table 45.2 in Terzaghi and Peck [1967]) for clays. S_u is equal to $q_u/2$. The SPT-N value measured in the field is not a geotechnical engineering soil property, but the unconfined compressive soil strength value is.

D.2.1 Spatial average

Considering pile foundation design, Phoon and Kulhawy (1999b) suggest the use of a spatial average of design geotechnical property ξ_d (e.g., $\xi_d(z) = S_u(z)$) over some (vertical) length l_v rather than the design property at a point. The spatial average of variable ξ_d is defined as

$$\xi_a = \frac{1}{l_v} * \int_{l_v} \xi_d(z)dz \tag{D.8}$$

In the design of a pile embedded in a homogeneous soil (i.e., a single soil layer), l_v would be the pile's embedment depth.

For embankments, slopes, retaining structures, hydraulic structures, etc., founded on a soil stratum consisting of weak horizontal layer(s) where more horizontal-type sliding surfaces are of concern, the length used in Equation D.8 becomes l_h, a near-to-horizontal distance along the potential slip surface within each homogeneous soil layer. Examples of reliability studies of this type are discussed in detail for the proposed Canadian James Bay dike project in Christian et al. (1994) and for a tailings dike founded on a presheared clay-shale in El-Ramly et al. (2003a).

D.2.2 $COV_{\xi a}$ of spatial average

Phoon and Kulhawy (1999b) express the total COV for $COV_{\xi a}$ of the spatial average (ξ_a) of the soil property as

$$COV_{\xi a}^2 = \Gamma^2(l_v) * COV_w^2 + COV_e^2 + COV_\varepsilon^2 \tag{D.9}$$

where the three components of variance are determined based on values of the COV_w of inherent soil variability, COV_e of measurement error and COV_ε of transformation uncertainty. A variance reduction function $\Gamma^2(l_v)$ is also used in this computation. The value of $\Gamma^2(l_v)$ ranges from a low of zero to a high of 1 and depends on the length of the averaging interval, l_v. The approach used to define the variance reduction term applied to the Equation D.9 coefficient of variation term makes use of the following Vanmarcke (1983, 2010) approximations: For the vertical scale of fluctuation δ_v greater than or equal to the vertical averaging length l_v,

$$\Gamma^2(l_v) = 1 \tag{D.10}$$

while

$$\Gamma^2(l_v) = \frac{\delta_v}{l_v} \tag{D.11}$$

with δ_v less than l_v. For a potential foundation sliding limit state in which horizontal layering is of concern, δ_h is substituted for δ_v in the qualifying criteria for Equation D.10 and in Equation D.11, and l_v is measured in the horizontal direction and now designated as l_h. For directions that are neither perfectly vertical nor horizontal, please refer to Appendix E and procedures used to compute an equivalent scale of fluctuation, δ_E. The distance of the slip plane of any orientation is given as L ($L = L_{Active}$ in Figure 5-7). The results from research by the authors of this report into this topic for hydraulic structures is discussed in Chapters 4 and 5.

Observation

For the approach suggested by Phoon and Kulhawy (1999a,b), inherent soil variability is modeled as random field (Vanmarcke 1983), with its COV_w value adjusted by a variance reduction function $\Gamma^2(l_v)$ in Equation D.9. The significance of Equation D.11 is that the COV_ξ of the spatial average is smaller in comparison to the COV_w of inherent soil variability when the averaging length l_v is greater than the (vertical) scale of fluctuation δ_v value.

The scale of fluctuation value δ_v reflects the autocorrelation distance of the design soil property. Consequently, the authors of this report find it useful to recall that the scale of fluctuation is approximately twice the autocorrelation distance (i.e., $\delta = 2\ r_o$) for the exponentially decaying autocorrelation function, whose value of δ reflects the correlation distance of the soil's engineering design property.

Inherent soil variability is caused primarily by the natural geologic processes that are involved in soil formation. Depending on the type of laboratory or field soil test involved, each type of test will have a unique COV due to measurement errors for that testing procedure.

D.2.3 COV values for soil strengths compared to those for steel resistances

As pointed out by Phoon and Kulhawy (1999b) and others, the difference between geotechnical and structural variabilities is significant and is accounted for differently in a reliability analysis. Most structural COV are fairly small compared to geotechnical COV. They point out that, for example, the COV of undrained shear strength (S_u) of clays can vary from 10% to 60%, depending upon its form of measurement (e.g., direct laboratory measurement or correlated with a field measurement). In contrast to geotechnical materials and citing the landmark study made by Ellingwood et al. (1980), they observe that uncertainties in structural resistances typically fall within a range of 10% to 20% for a wide range of materials (e.g., concrete, steel, aluminum) and resistance model (e.g., tension, flexure, shear). Consequently, the differences between geotechnical and structural variability, as reflected in COV values, impact the development of reliability-based design procedures for geotechnical engineering, in contrast to those developed for structural engineering.

D.2.4 Point and spatial average COV values from the Phoon and Kulhawy (1999b) soil strength data assessment

Phoon and Kulhawy (1999b) point out that structural loads and resistances usually can be modeled adequately as lumped parameters in a reliability calibration process. In contrast, they point out that it is no longer realistic to model geotechnical capacities as lumped parameters because of spatial correlation of materials. Therefore, Phoon and Kulhawy (1999a,b) took care to distinguish inherent variability of strength properties for COV point estimates from those pertaining to spatial average COV values[24]. Table D-4 summarizes Phoon and Kulhawy (1999b) approximate guidelines for design soil property variability in terms of the two COV values for different soil types. Note that they used vertical spatial average COV values in contrast to horizontal spatial average values. Additionally, the vertical spatial average was computed over a vertical distance (L) of 5 m.

[24] Chapter 3 in Ebeling and White (2019) addresses variance reduction techniques that are used to quantify vertical and horizontal spatial average COV values. Application of variance reduction techniques of the type suggested by Phoon and Kulhawy (1999a,b) lower the magnitude of COV values for use in geotechnical engineering applications from point estimate COV values by as much as 50%. Vanmarcke expressed this general trend in his 1977a reference on random fields that it is not soil parameter values at a point but the average over a certain size of line, area, or volume (i.e., the local average) that controls geotechnical limit state(s) performances.

Table D-4. A summary of Phoon and Kulhawy (1999b; Table 5) approximate guidelines for design soil property variability.

Design Strength Parameter	Test	Soil Type	Point COV (%)	Vertical Spatial Average COV (%) with L = 5 m
S_u (UC)	Direct (lab)	Clay	20-55	10-40
S_u (UU)	Direct (lab)	Clay	10-35	7-25
S_u (CIUC)	Direct (lab)	Clay	20-45	10-30
S_u (field)	Correlated to a VST (field)	Clay	15-50	15-50
S_u (UU)	Correlated to a cone tip resistance (q_T)	Clay	30-40	30-35
S_u (CIUC)	Correlated to a cone tip resistance (q_T)	Clay	35-50	35-40
S_u (UU)	Correlated to a SPT blow count N value (field)	Clay	40-60	40-55
S_u (field)	Correlated to a dilatometer horizontal stress index K_D value	Clay	30-55	30-55
S_u (field)	Correlated to a PI value (for UU, UC and VST Su values)	Clay	30-55	-
ϕ'	Direct (lab)	Clay, sand	7-20	6-20
ϕ' (TC)	Correlated to a cone tip resistance (q_T)	Sand	10-15	10
ϕ'CV	Correlated to a PI	Clay	15-20	15-20

Note: [a]S_u, undrained shear strength; UC, unconfined compression test; UU, unconsolidated undrained triaxial test; CIUC, consolidated isotopically undrained triaxial test – compression; ϕ', effective angle of internal friction; ϕ'_{CV}, constant-volume effective angle of internal friction.

Appendix E in Ebeling and White (2019) discusses four techniques used to quantify vertical and horizontal spatial average COV values into an equivalent scale of fluctuation. Application of variance reduction techniques of the type suggested by Phoon and Kulhawy (1999a,b) lower the magnitude of COV values for use in geotechnical engineering applications from point estimate COV values by as much as 50%. Vanmarcke expressed this general trend in his 1977a reference on random fields that it is not soil parameter values at a point but the average over a certain size of line, area or volume (i.e., the local average, that controls geotechnical limit state(s) performances).

D.3 The width of 3-D slope failures

A method of probabilistic 3-D limit equilibrium analysis stability of long earth slopes was first discussed in Varmarcke (1977b, 1980). This method accounts for the spatial variability of the shear strength. The spatial variability takes into account the correlation effects of soils near the initial failure cross section, so this model predicts that slope failure events involving very long or very short widths of the failure zone are highly improbable. The contribution of 3-D end resisting moment effects, the value for the horizontal scale of fluctuation, δ_h, and the variance reduction function (into the third dimension) play important roles in 3-D probabilistic slope stability analyses and likely slope failure widths. Vanmarcke (2011) matured this probabilistic engineering methodology vision in his 2011 paper on the risk of limit-equilibrium failure of long earth slopes and how it depends on length. Again, the value of the horizontal scale of fluctuation in the third dimension (of slope width) and the correlation structure of the resisting moment/force as represented by the variance reduction function in the third dimension (i.e., along the slope) plays a dominant role in the dictating the width along the slope axis of the 3-D slope failure in the analysis. A third Vanmarcke paper published in 2013 (Vanmarcke and Otsubo 2013), extended the Vanmarcke 3-D reliability analysis to long multi-segment earth slopes.

Unit Conversion Factors

Multiply	By	To Obtain
atmosphere (standard)	101.325	kilopascals
cubic feet	0.02831685	cubic meters
cubic inches	1.6387064 E-05	cubic meters
cubic yards	0.7645549	cubic meters
degrees (angle)	0.01745329	radians
feet	0.3048	meters
foot-pounds force	1.355818	joules
gallons (US liquid)	3.785412 E-03	cubic meters
inches	0.0254	meters
inch-pounds (force)	0.1129848	newton meters
microinches	0.0254	micrometers
microns	1.0 E-06	meters
miles (nautical)	1,852	meters
miles (US statute)	1,609.347	meters
mils	0.0254	millimeters
pounds (force)	4.448222	newtons
pounds (force) per foot	14.59390	newtons per meter
pounds (force) per inch	175.1268	newtons per meter
pounds (force) per square foot	47.88026	pascals
pounds (force) per square inch	6.894757	kilopascals
pounds (mass)	0.45359237	kilograms
pounds (mass) per cubic foot	16.01846	kilograms per cubic meter
pounds (mass) per cubic inch	2.757990 E+04	kilograms per cubic meter
pounds (mass) per square foot	4.882428	kilograms per square meter
pounds (mass) per square yard	0.542492	kilograms per square meter
slugs	14.59390	kilograms
square feet	0.09290304	square meters
square inches	6.4516 E-04	square meters
square miles	2.589998 E+06	square meters
square yards	0.8361274	square meters
tons (force)	8,896.443	newtons
tons (force) per square foot	95.76052	kilopascals
tons (long) per cubic yard	1,328.939	kilograms per cubic meter
tons (2,000 pounds, mass)	907.1847	kilograms
tons (2,000 pounds, mass) per square foot	9,764.856	kilograms per square meter
yards	0.9144	meters

Abbreviations

1-D	One-dimensional
2-D	Two-dimensional
3-D	Three-dimensional
AASHTO	American Association of State Highway and Transportation Officials
AC	Allowable compression
ACC	Axial compression capacity
ACE	Annual Chance of Exceedance
ACI	American Concrete Institute
AFOSM	Advanced First Order Second Moment
ALF	Axial load factor
ASCE	American Society of Civil Engineers
ASD	Allowable stress design
ASM	Advanced Second Moment
AT	Allowable tension
CBF	Combined Bending Factor
CDF	Cumulative Distribution Function
CE	Chance of Exceedance
CEM	Coastal Engineering Manual
CHBDC	Canadian highway bridge design code
COV	Coefficient of Variation
CPT	Cone Penetration Testing
DL	Dead load
EL	Elevation
ERDC	US Army Engineer Research and Development Center
FoS	Factors of safety
FOSM	First Order Second Moment
GEV	Generalized Extreme Value
GFI	Grand Forks International Airport
GLF	Global Load Factor
HCV	Highest conceivable value
IEM	Iowa Environmental Mesonet
LCV	Lowest conceivable value
LL	Live load

LRFD	Load and Resistance Factor Design
LSF	Load Scale Factor
MML	Marshall/Ryan Airport
MPF12	Minnesota Pile Formula 2012
MSP	Minneapolis-Saint Paul International Airport
MVFOSM	Mean Value First Order Second Moment Method
MVP	USACE St. Paul District
NGVD	National Geodetic Vertical Datum
NOAA	National Oceanic and Atmospheric Administration
OCR	Overconsolidation ratio
OHB	Oxbow-Hickson-Bakke
OSF	Overstress Factor
PAU	Pressure aeration units
PDF	Probability density function
PUP	Probability of Unsatisfactory Performance
R&D	Research and Development
RP	Return period
RSF	Resistance Scale Factor
SCC	St. Charles County Airport
SHANSEP	Stress History and Normalized Soil Engineering Parameters
SLR	St. Louis Regional Airport
SLS	Serviceability Limit State
SPT	Standard Penetration Test
SRV	Single-random-variable
SSI	Soil structure interaction
STP	St. Paul Downtown Airport
SWL	Still water level
ULS	Ultimate Limit States
USACE	US Army Corps of Engineers
VRF	Variance reduction factor
VST	Vane Shear Test
WIWL	Wind-induced wave loading
WSDOT	Washington State Department of Transportation
XS	Cross section

REPORT DOCUMENTATION PAGE

Form Approved
OMB No. 0704-0188

The public reporting burden for this collection of information is estimated to average 1 hour per response, including the time for reviewing instructions, searching existing data sources, gathering and maintaining the data needed, and completing and reviewing the collection of information. Send comments regarding this burden estimate or any other aspect of this collection of information, including suggestions for reducing the burden, to Department of Defense, Washington Headquarters Services, Directorate for Information Operations and Reports (0704-0188), 1215 Jefferson Davis Highway, Suite 1204, Arlington, VA 22202-4302. Respondents should be aware that notwithstanding any other provision of law, no person shall be subject to any penalty for failing to comply with a collection of information if it does not display a currently valid OMB control number.
PLEASE DO NOT RETURN YOUR FORM TO THE ABOVE ADDRESS.

1. REPORT DATE	2. REPORT TYPE	3. DATES COVERED *(From - To)*
June 2023	Final Report	FY19–FY21

4. TITLE AND SUBTITLE

Load and Resistance Factors from Reliability Analysis Probability of Unsatisfactory Performance (PUP) of Flood Mitigation, Batter Pile-Founded T-Walls Given a Target Reliability Index (β)

5a. CONTRACT NUMBER

5b. GRANT NUMBER

5c. PROGRAM ELEMENT NUMBER

6. AUTHOR(S)

Robert M. Ebeling, Barry C. White, John E. Hite, James R. Tallent, Locke M. Williams, Brad C. McCoy, Aaron Hill, Cameron Dell, Jake Bruhl, and Kevin McMullen

5d. PROJECT NUMBER

5e. TASK NUMBER

5f. WORK UNIT NUMBER

7. PERFORMING ORGANIZATION NAME(S) AND ADDRESS(ES)
(see reverse)

8. PERFORMING ORGANIZATION REPORT NUMBER
ERDC TR-23-9

9. SPONSORING/MONITORING AGENCY NAME(S) AND ADDRESS(ES)
Navigation Systems Research Program (NavSys)
Vicksburg, MS 39180-6199

10. SPONSOR/MONITOR'S ACRONYM(S)
NavSys

11. SPONSOR/MONITOR'S REPORT NUMBER(S)

12. DISTRIBUTION/AVAILABILITY STATEMENT
Approved for public release; distribution is unlimited.

13. SUPPLEMENTARY NOTES
Funding Account Code: U4375151; AMSCO Code 031391

14. ABSTRACT

This technical report documents the research and development (R&D) study in support of the development of a combined Load and Resistance Factor Design (LRFD) methodology that accommodates both geotechnical and structural design limit states for design of the US Army Corps of Engineers (USACE) batter pile-founded, reinforced concrete flood walls. Development of the required reliability and corresponding LRFD procedures has been progressing slowly in the geotechnical topic area as compared to those for structural limit state considerations, and therefore this has been the focus of this first-phase R&D effort. This R&D effort extends reliability procedures developed for other non-USACE structural systems, primarily bridges and buildings, for use in the design of batter pile-founded USACE flood walls. Because the foundation system includes batter piles under flood loading, the design procedure involves frame analysis with significant soil structure interaction. Three example batter pile-founded T-Wall flood structures on three different rivers have been examined considering 10 geotechnical and structural limit states. Numerical procedures have been extended to develop precise multiple limit state Reliability calculations and for complete LRFD analysis of the example batter pile-founded, T-Wall reinforced concrete, flood walls.

15. SUBJECT TERMS

Geotechnical engineering, Load factor design, Soil-structure interaction, Structural design, Structural dynamics

16. SECURITY CLASSIFICATION OF:			17. LIMITATION OF ABSTRACT	18. NUMBER OF PAGES	19a. NAME OF RESPONSIBLE PERSON
a. REPORT	b. ABSTRACT	c. THIS PAGE			Barry C. White
Unclassified	Unclassified	Unclassified	SAR	491	19b. TELEPHONE NUMBER *(Include area code)* 601-634-4575

7. PERFORMING ORGANIZATION NAME(S) AND ADDRESS(ES) (continued)

Information Technology Laboratory
US Army Engineer Research and Development Center
3909 Halls Ferry Road
Vicksburg, MS 39180-6199

Coastal and Hydraulics Laboratory
US Army Engineer Research and Development Center
3909 Halls Ferry Road
Vicksburg, MS 39180-6199

United States Military Academy, West Point
606 Thayer Road
West Point, New York 10996